



Sebastian Schmitt  
Molecular Simulation and Entropy Scaling Modeling of Transport Properties  
Scientific Report Series Volume 50  
2024

Scientific Report Series  
Laboratory of Engineering Thermodynamics (LTD)  
RPTU Kaiserslautern  
P.O. Box 3049  
67663 Kaiserslautern  
Germany

ISSN 2195-7606  
ISBN 978-3-944433-49-3

© LTD all rights reserved







# **Molecular Simulation and Entropy Scaling Modeling of Transport Properties**

Vom Fachbereich Maschinenbau und Verfahrenstechnik  
der Rheinland-Pfälzischen Technischen Universität  
Kaiserslautern-Landau  
zur Verleihung des akademischen Grades

**Doktor-Ingenieur (Dr.-Ing.)**

genehmigte

**Dissertation**

von

M.Sc. Sebastian Schmitt  
aus Neunkirchen/Saar

Dekan: Prof. Dr. rer. nat. Roland Ulber  
Berichterstatter: Prof. Dr.-Ing. Hans Hasse  
Jun. Prof. Dr.-Ing. Dr. rer. nat. Simon Stephan  
Prof. Dr.-Ing. Jadran Vrabec

Tag der mündlichen Prüfung: 22. November 2024

D 386



# Danksagung

Die vorliegende Dissertation entstand im Rahmen meiner Tätigkeit als wissenschaftlicher Mitarbeiter am Lehrstuhl für Thermodynamik (LTD) an der RPTU Kaiserslautern-Landau. Ich möchte mich an dieser Stelle herzlich bei den vielen Menschen bedanken, ohne die diese Arbeit so nicht möglich gewesen wäre.

Ich möchte mich bei Prof. Hans Hasse und Jun. Prof. Simon Stephan für die hervorragende Betreuung meiner Arbeit bedanken. Insbesondere möchte ich mich bei dir, Hans, für die wertvollen fachlichen Diskussionen sowie die wissenschaftliche Freiheit bedanken, die du ermöglicht hast. Bei dir, Simon, möchte ich mich für die freundschaftliche Zusammenarbeit bedanken sowie die oft langen Diskussionen, bei denen nicht selten ganz neue Ideen entstanden sind. Ich möchte mich zudem bei Prof. Jadran Vrabec für die Begutachtung meiner Arbeit bedanken sowie bei Prof. Eberhard Kerscher für die Übernahme des Prüfungsvorsitzes.

Ein ganz besonderer Dank gilt dem gesamten Team des LTD. Viele Kolleginnen und Kollegen sind mittlerweile zu guten Freunden geworden. Für diesen Zusammenhalt und die vielen Events, Partys, Urlaube etc., die wir zusammen erleben durften, bin ich sehr dankbar. Darüber hinaus hat auch der fachliche Austausch mit euch einen erheblichen Beitrag zu dieser Arbeit geleistet und mir oftmals neue Blickwinkel eröffnet. Ebenso danke ich dem Sekretariat für die immer herzliche Hilfe bei allen möglichen größeren und kleineren Problemen. Gleiches gilt für das gesamte Laborteam. Ohne eure Unterstützung wäre die Labortätigkeit nicht in dieser Weise möglich gewesen. Zudem möchte ich mich bei den Studierenden bedanken, die ich während meiner Promotion betreuen durfte und die einen erheblichen Beitrag zum Gelingen dieser Arbeit beigetragen haben.

Bei meiner Familie möchte ich mich für die Unterstützung auf all meinen Lebenswegen bedanken. Ihr habt mir die Möglichkeit gegeben, mich frei zu entfalten, und euch war auch kein Weg zu weit, mich bei Auslandsaufenthalten zu besuchen. Für all das bin ich euch sehr dankbar. Zuletzt möchte ich mich bei dir, Babette, für deine Unterstützung in den letzten Jahren bedanken. Du hast die Zeit am LTD noch etwas schöner gemacht und ich freue mich auf viele weitere gemeinsame Momente.

Kaiserslautern, Dezember 2024

Sebastian Schmitt



# Abstract

Knowledge on transport properties of fluids is important for the design of many industrial processes in chemical and mechanical engineering, but experimental data are often scarce. Therefore, reliable models for predicting transport properties are required. In the present thesis, two ways for modeling transport properties were explored, which both stem from the field of molecular thermodynamics: Molecular dynamics (MD) simulations and entropy scaling. In both fields, various open questions were addressed: A comprehensive database on MD simulation data of the viscosity, thermal conductivity, and self-diffusion coefficient of the Lennard-Jones fluid was established. The assessment of the data yields, among others, insights in the reproducibility of the simulation of transport properties. Moreover, the results obtained from different force fields for the transport properties of a set of lubricants at very high pressures were compared, with the aim of identifying force fields that are suitable for modeling lubricants. By extending an online force field database to transferable force fields, their application in molecular simulations was facilitated. Furthermore, detailed studies of the heat transfer across solid-liquid interfaces on the nanoscopic level were carried out by non-equilibrium molecular dynamics (NEMD) simulations. In contrast to MD simulations, entropy scaling provides an analytical theory for modeling transport properties based on equations of state (EOS). The reliability of the underlying EOS model is crucial for the application of entropy scaling. Therefore, new EOS models were parameterized for alcohols and their extrapolation ability was tested. This was done based on high-pressure density data measured in this work. A new entropy scaling framework was developed that covers the entire fluid region. The framework was successfully applied for modeling the viscosity, the thermal conductivity, and the self-diffusion coefficient of different fluids in a wide range of states based on few experimental data. The excellent extrapolation behavior of the method is demonstrated. The approach was also extended to modeling diffusion coefficients in mixtures. This enables, for the first time, the prediction of self-diffusion coefficients and mutual diffusion coefficients in binary mixtures in a consistent way.



# Kurzfassung

Kenntnisse über die Transporteigenschaften von Fluiden sind für die Entwicklung vieler industrieller Prozesse in der chemischen Industrie und im Maschinenbau wichtig. Es liegen allerdings oft nur wenige experimentelle Daten vor. Daher werden zuverlässige Modelle zur Vorhersage von Transporteigenschaften benötigt. In der vorliegenden Arbeit wurden zwei Modellierungsansätze für Transporteigenschaften aus dem Bereich der molekularen Thermodynamik untersucht: Molekulardynamik (MD)-Simulationen und Entropieskalierung. In beiden Bereichen wurden verschiedene offene Fragen behandelt: Es wurde eine umfassende Datenbank mit MD-Simulationsdaten für die Transporteigenschaften des Lennard-Jones-Modellfluids erstellt. Die Auswertung der Daten liefert u.a. Erkenntnisse über die Reproduzierbarkeit der Simulation von Transporteigenschaften. Darüber hinaus wurden die Ergebnisse verschiedener Kraftfelder für die Transporteigenschaften einiger Schmierstoffe bei sehr hohen Drücken verglichen, um geeignete Kraftfelder zur Modellierung von Schmierstoffen zu ermitteln. Durch die Erweiterung einer Online-Kraftfelddatenbank auf übertragbare Kraftfelder wurde deren Anwendung in MD-Simulationen erleichtert. Darüber hinaus wurde mittels Nicht-Gleichgewichts-MD Simulationen der Wärmeübergang an Fest-Flüssig-Grenzflächen auf nanoskopischer Ebene untersucht. Im Gegensatz zu MD-Simulationen bietet die Entropieskalierung eine analytische Methode zur Modellierung von Transporteigenschaften auf der Grundlage von Zustandsgleichungen. Die Zuverlässigkeit der zugrundeliegenden Zustandsgleichung ist für die Anwendung der Entropieskalierung von entscheidender Bedeutung. Daher wurden neue Zustandsgleichungs-Modelle für Alkohole parametrisiert und deren Extrapolationsfähigkeit getestet. Dies erfolgte auf der Grundlage von Hochdruck-Dichtedaten, die im Rahmen dieser Arbeit gemessen wurden. Es wurde ein neues Rahmenwerk zur Anwendung der Entropieskalierung entwickelt, das den gesamten fluiden Zustandsbereich abdeckt. Das Rahmenwerk wurde erfolgreich zur Modellierung der Viskosität, der Wärmeleitfähigkeit und des Selbstdiffusionskoeffizienten verschiedener Fluide in einem breiten Zustandsbereich angewandt. Zudem wurde das gute Extrapolationsverhalten der Methode gezeigt. Der Ansatz wurde auch auf die Modellierung von Diffusionskoeffizienten in Mischungen erweitert. Dies ermöglicht erstmals eine konsistente Vorhersage der Selbst- und Transportdiffusionskoeffizienten in binären Mischungen.





# Contents

<b>1</b>	<b>Introduction</b>	<b>1</b>
<b>2</b>	<b>Database and Data Assessment of Transport Properties of the Lennard-Jones Fluid</b>	<b>5</b>
2.1	Introduction . . . . .	5
2.2	Database of Transport Properties of the Lennard-Jones Fluid . . . . .	9
2.3	Assessment of the Data . . . . .	22
2.3.1	Outlier Detection for Homogeneous States . . . . .	23
2.3.2	Assessment by the Chapman-Enskog Zero-Density Limit . . . . .	25
2.4	Discussion . . . . .	29
2.5	Conclusions . . . . .	30
<b>3</b>	<b>Evaluation of Force Fields for the Simulation of Thermophysical Properties of Long Alkanes</b>	<b>33</b>
3.1	Introduction . . . . .	33
3.2	Methodology . . . . .	36
3.2.1	Simulation Details and Evaluation . . . . .	36
3.2.2	Force Fields . . . . .	40
3.2.3	Data Analysis . . . . .	43
3.3	Results . . . . .	44
3.3.1	Density . . . . .	45
3.3.2	Viscosity . . . . .	46
3.3.3	Self-diffusion Coefficient . . . . .	49
3.3.4	Computational Costs . . . . .	52
3.4	Conclusions . . . . .	53
<b>4</b>	<b>Online Database for Transferable Force Fields</b>	<b>55</b>
4.1	Introduction . . . . .	55
4.2	TUK-FFDat: Data Scheme and Data Format for Transferable Force Fields	60
4.2.1	Classification of Force Fields . . . . .	60
4.2.2	Definition of Data Scheme . . . . .	64
4.2.3	SQL-based Data Format . . . . .	72

4.2.4	Application of Data Format . . . . .	77
4.2.5	Conversion Tools . . . . .	80
4.2.6	Conclusions . . . . .	80
4.3	<i>MolMod</i> Database: Extension to Transferable Force Fields . . . . .	81
4.3.1	MolMod Transferable . . . . .	81
4.3.2	Implemented Transferable Force Fields . . . . .	85
4.3.3	Available Input Formats . . . . .	89
4.3.4	Data Management and Data Integrity . . . . .	90
4.3.5	Exemplary Application . . . . .	92
4.3.6	Conclusions . . . . .	93
<b>5</b>	<b>Non-Equilibrium Molecular Simulations of Interfacial Heat Transfer in a Model System</b>	<b>95</b>
5.1	Introduction . . . . .	95
5.2	Molecular Model . . . . .	97
5.3	Methods . . . . .	98
5.3.1	Simulation Details . . . . .	98
5.3.2	Theoretical Background . . . . .	100
5.4	Influencing Factors and Overview of the Simulations . . . . .	101
5.5	Results and Discussion . . . . .	107
5.5.1	Empirical Correlation for the Kapitza Length $L_K$ . . . . .	107
5.5.2	Influence of Solid-Fluid Interaction Energy . . . . .	109
5.5.3	Influence of Solid-Solid Interaction Energy . . . . .	110
5.5.4	Influence of Mass of Solid Particles . . . . .	111
5.5.5	Influence of Fluid Temperature . . . . .	112
5.5.6	Influence of Fluid Density . . . . .	113
5.5.7	Introducing the Kapitza Interface Number $Ki$ . . . . .	114
5.5.8	Describing Heat Transfer with Convection and Scale-up . . . . .	116
5.6	Conclusions . . . . .	118
<b>6</b>	<b>Measurements and Equation of State Modeling of the Density of 1-Alcohols at High Pressures</b>	<b>121</b>
6.1	Introduction . . . . .	121
6.2	Experimental Methods . . . . .	122
6.2.1	Chemicals and Sample Preparation . . . . .	122
6.2.2	Measurements . . . . .	122
6.3	Computational Methods . . . . .	125
6.3.1	Empirical Correlation $\rho(T, p)$ . . . . .	125
6.3.2	Molecular-based Equation of State Modeling . . . . .	126

---

6.3.3	Evaluation of Models . . . . .	129
6.4	Results and Discussion . . . . .	130
6.4.1	Experimental Results . . . . .	130
6.4.2	EOS Modeling Results . . . . .	140
6.5	Conclusions . . . . .	145
<b>7</b>	<b>Framework for Modeling Transport Properties using Entropy Scaling</b>	<b>147</b>
7.1	Introduction . . . . .	147
7.2	Model . . . . .	150
7.2.1	Molecular-based EOS . . . . .	151
7.2.2	Scaling of the Transport Properties . . . . .	152
7.2.3	Component-Specific Correlation . . . . .	156
7.2.4	Molecular Simulations and Adjustment of the Universal Parameters	156
7.2.5	Extension to Mixtures . . . . .	159
7.2.6	Remarks Regarding the Physical Basis of the Model Framework .	161
7.3	Applications . . . . .	162
7.3.1	Overview . . . . .	162
7.3.2	Pure Components . . . . .	165
7.3.3	Mixtures . . . . .	172
7.4	Conclusions . . . . .	174
<b>8</b>	<b>Entropy Scaling for Modeling Diffusion Coefficients in Mixtures</b>	<b>177</b>
8.1	Introduction . . . . .	177
8.2	Methods . . . . .	180
8.2.1	Entropy Scaling of Infinite Dilution Diffusion Coefficients . . . . .	180
8.2.2	Predicting Diffusion Coefficients in Mixtures . . . . .	181
8.3	Results . . . . .	182
8.3.1	Infinite Dilution Diffusion Coefficients . . . . .	182
8.3.2	Application to Mixtures of OMEs with Alkanes . . . . .	185
8.3.3	Prediction of Diffusion Coefficients in Mixtures by Entropy Scaling	188
8.4	Conclusions . . . . .	194
<b>9</b>	<b>Conclusions</b>	<b>195</b>
	<b>Literature</b>	<b>196</b>
	<b>Appendix</b>	<b>275</b>
<b>A</b>	<b>Supporting Information for Chapter 2</b>	<b>275</b>
A.1	Simulation Details . . . . .	275
A.2	Discussion of Data Sets . . . . .	276

A.3	Overview of Other Properties Reported in the References . . . . .	280
A.4	Heat Maps of the Statistical Uncertainties of the Data . . . . .	281
A.5	Outliers in the Phase Diagram . . . . .	281
A.6	Evaluation of the Critical Region . . . . .	282
A.7	Artifact of Kolafa-Nezbeda EOS at High Temperatures and Densities . .	284
A.8	Deviation Plots of Selected Data Sets . . . . .	285
<b>B</b>	<b>Supporting Information for Chapter 3</b>	<b>287</b>
B.1	Finite Size Analysis . . . . .	287
B.2	Choice of Integrator for All-atom Simulations . . . . .	288
B.3	Long $NpT$ Run . . . . .	289
B.4	Influence of the Cutoff Criterion in the TDM . . . . .	289
B.5	Force Field Parameters . . . . .	290
B.5.1	UA Force Fields . . . . .	291
B.5.2	OPLS . . . . .	293
B.5.3	L-OPLS . . . . .	294
B.5.4	COMPASS . . . . .	295
B.5.5	MARTINI . . . . .	298
B.5.6	Reactive Force Fields . . . . .	300
B.6	Validation . . . . .	300
B.7	Correlations of Experimental Data . . . . .	304
B.8	Correlations of Simulation Data . . . . .	304
B.9	Radius of Gyration . . . . .	306
B.10	OPLS Simulations of $n$ -Icosane and $n$ -Triacontane . . . . .	307
B.11	Relation Between Viscosity and Self-diffusion . . . . .	310
B.12	Results for the MARTINI Force Field with Time Scaling . . . . .	312
B.13	Uncertainties of the Simulations for the Computational Costs . . . . .	313
<b>C</b>	<b>Supporting Information for Chapter 4</b>	<b>315</b>
C.1	Further Details on the Data Scheme and Data Format . . . . .	315
C.1.1	Tags of Interaction Sites Modeling Hydrogen Atoms . . . . .	315
C.1.2	Tags of Interaction Sites Modeling Cyclic Structures . . . . .	316
C.1.3	Non-Transferable Models of Molecules in the Data Scheme . . . .	317
C.1.4	Details on Rigid, Flexible, and Semi-Flexible Force Fields . . . . .	318
C.1.5	Specifications for Special Cis/Trans Torsion Potentials . . . . .	318
C.2	Application to the TraPPE-UA, OPLS-AA, and Potoff Force Fields . . .	318
C.3	Building a TUK-FFDat Force Field File . . . . .	319
C.4	The Handling of the Conversion Tools . . . . .	319
C.5	Comparison with Literature Data . . . . .	320

<b>D</b>	<b>Supporting Information for Chapter 5</b>	<b>323</b>
D.1	Cumulative Kinetic Energy . . . . .	323
D.2	Influence of the Channel Width $H$ and the Wall Temperature $T_w$ . . . . .	323
D.3	Density Profiles Near the Solid Surface . . . . .	325
<b>E</b>	<b>Supporting Information for Chapter 6</b>	<b>327</b>
E.1	Multi-parameter EOS of Calibration Fluids . . . . .	327
E.2	Estimation of the Calibration Uncertainty $u_{\text{cal,r}}(\rho)$ . . . . .	327
E.3	Parameters of Empirical Correlations $\rho_{\text{corr}}(T, p)$ . . . . .	327
E.4	Literature Data . . . . .	329
E.5	Details on the Fitting Procedure . . . . .	331
E.6	Comparison of the Second-Order Derivative Properties to Literature Data	333
E.7	EOS Parameters from the Literature . . . . .	333
E.8	<i>Brown's</i> Characteristic Curves . . . . .	336
<b>F</b>	<b>Supporting Information for Chapter 7</b>	<b>338</b>
F.1	Phase Diagrams of Viscosity, Thermal Conductivity, and Self-Diffusion . . . . .	338
F.2	Scaled Chapman-Enskog Transport Properties $\eta_{\text{CE}}^+$ , $\lambda_{\text{CE}}^+$ , and $D_{\text{CE}}^+$ . . . . .	339
F.3	Isentropes of the LJ fluid . . . . .	340
F.4	EOS Parameters . . . . .	340
F.5	Component-Specific Entropy Scaling Parameters . . . . .	344
F.6	Details on Entropy Scaling Framework . . . . .	346
F.7	Implementation of the Entropy Scaling Framework . . . . .	347
F.8	Comparison of EOS for Modeling the Viscosity of Methane . . . . .	348
F.9	LJTS Mixture . . . . .	349
F.10	Thermal Conductivity of Mixture Benzene + $n$ -Hexane . . . . .	349
<b>G</b>	<b>Supporting Information for Chapter 8</b>	<b>352</b>
G.1	Entropy Scaling of infinite dilution diffusion coefficients . . . . .	352
G.2	Entropy Scaling of Diffusion Coefficients in Mixtures . . . . .	354
G.3	Simulation Details . . . . .	356
G.4	Component-Specific EOS Models . . . . .	358
G.5	Entropy Scaling Models . . . . .	359
G.6	Established Methods for Predicting Infinite Dilution Diffusion Coefficients	361
G.7	Scaling Behavior of Pure Components and at Infinite Dilution . . . . .	361
G.8	Results for the Lennard-Jones Mixtures at Different Pressures . . . . .	363
G.9	Comparison of Entropy Scaling to the Vignes and Darken Models . . . . .	364
G.10	Scaled Diffusion Coefficient of Mixtures . . . . .	365



# List of Symbols

## Latin symbols

$A$	area
$a$	molar Helmholtz energy
$a_Y, b_Y, c_Y$	parameters (specific for transport property $Y$ )
$B$	second virial coefficient
$B_1, \dots, B_9$	bond-dihedral cross parameters
$c_p$	isobaric heat capacity
$c_v$	isochoric heat capacity
$c_0, \dots, c_6$	empirical parameters for density correlation
$c_0, \dots, c_7$	torsion energy parameters
$cpu_h$	CPU hours
$D, D_i$	self-diffusion coefficient (of component $i$ )
$D_{ij}$	Fickian diffusion coefficient
$\mathcal{D}_{ij}$	Maxwell-Stefan diffusion coefficient
$E$	energy
$f_\eta, f_\lambda, f_D$	correction terms for the Chapman-Enskog properties
$f_1, f_2$	empirical functions
$G$	Gibbs energy
$g$	universal parameter
$H$	channel width
$J_p$	stress tensor
$Ka$	Kapitza number
$k_B$	Boltzmann's constant
$Ki$	Kapitza interface number
$k_2, k_3, k_4$	bond parameters
$L$	box length
$L_K$	Kapitza length
$L_1, \dots, L_6$	angle-dihedral cross parameters
$l_2, l_3, l_4$	angle parameters
$M$	particle mass

---

$M_1, \dots, M_3$	angle-angle-dihedral cross parameters
$M_i$	molar mass of component $i$
$m$	attractive Mie exponent
$m$	segment number
$N$	number of particles/molecules
$n$	repulsive Mie exponent
$N_{\text{pub}}$	number of publications
$N_{\text{tot}}$	number of data points
$N_1, N_2$	bond-angle cross parameters
$n_1, \dots, n_4$	torsion parameters
$N_A$	Avogadro's constant
$Nu$	Nusselt number
$p$	pressure
$P$	uncertainty measure
$p^s$	vapor pressure
$p_{\text{cm}}$	pseudo critical pressure
$q_i$	charge of site $i$
$q$	heat flux
$r$	distance
$R$	thermal resistance
$R$	universal gas constant
$R_g$	radius of gyration
$R_h$	hydrodynamic radius
$R_K$	Kapitza resistance
$r_{\text{AB}}$	association radius
$r_c$	cutoff radius
$\mathbf{r}_i$	position vector of site $i$
$r_{\text{min}}$	distance of potential minimum
$r_0$	equilibrium bond distance
$s$	molar entropy
$T$	temperature
$t$	time
$T_{\text{cm}}$	pseudo critical temperature
$u$	internal/potential energy
$u$	standard uncertainty
$U$	expanded uncertainty
$v$	(specific) volume
$V$	volume
$W$	transition function



---

$x$	mole fraction
$x, y, z$	Cartesian coordinates
$Y$	transport property
$Z$	compressibility factor

## Superscripts

$+$	modified Rosenfeld scaling
$\alpha\beta$	non-diagonal tensor entries
$\infty$	long-term limit
$\infty$	infinite dilution
assoc	associating contribution
branching	branching contribution
c	critical property
cal	calibration
CE	Chapman-Enskog property
chain	chain contribution
cold	cold wall
cond	conductive
conf	configurational
conv	convection
corr	correlation value
D	dipolar contribution
disp	dispersive contribution
ES	entropy scaling value
exp	experimental value
f	fluid
ff	fluid-fluid interaction
hot	hot wall
$i$	neighbor index
$i, j$	component/site index
id	ideal contribution
$j$	data point index
lit	literature value
mix	mixture value
mod	model value
Q	quadrupolar contribution
r	relative

---

rep	repulsive contribution
s	solid
sf	solid-fluid interaction
sim	simulation value
src	source
ss	solid-solid interaction
th	this work
total	total value
tr	triple point value
w	wall

## Greek symbols

$\alpha$	thermal expansion coefficient
$\alpha$	energy parameter in CPA EOS
$\alpha, \beta_1, \beta_2$	viscosity fit parameters
$\alpha_{\text{conv}}$	convective heat transfer coefficient
$\beta$	isothermal compressibility
$\Gamma$	thermodynamic factor
$\Delta$	statistical uncertainty, objective function
$\delta$	relative deviation
$\varepsilon$	Lennard-Jones energy parameter
$\varepsilon_{\text{AB}}$	association energy
$\varepsilon_0$	vacuum permittivity
$\eta$	viscosity
$\Theta$	bond angle
$\Theta_0$	equilibrium bond angle
$\kappa_{\text{AB}}$	association volume
$\lambda$	thermal conductivity
$\Lambda$	diffusion coefficient (general)
$\lambda_{\text{a}}$	attractive exponent in SAFT-VR Mie
$\lambda_{\text{r}}$	repulsive exponent in SAFT-VR Mie
$\mu$	chemical potential
$\xi$	binary interaction parameter
$\rho$	density
$\rho_{\text{N}}$	number density
$\sigma$	Lennard-Jones size parameter
$\tau$	time variable

---

$\Phi$	torsion angle
$\Phi_0$	equilibrium torsion angle
$\Phi_1, \dots, \Phi_4$	torsion angle parameters
$\Psi$	out of plan angle
$\Psi_0$	equilibrium out of plane angle
$\Omega^{(1,1)}, \Omega^{(2,2)}$	collision integrals

## Abbreviations

AA	all-atom
AAD	average absolute deviation
ACF	auto correlation function
AIREBO	adaptive intermolecular reactive empirical bond order potential
AMM	acoustic mismatch model
C	critical region
CAS	chemical abstracts service
CE	Chapman-Enskog
CFD	computational fluid dynamics
CG	coarse-grained
CHARMM	chemistry at Harvard macromolecular mechanics
COMPASS	condensed-phase optimized molecular potentials for atomistic simulation studies
CPA	cubic-plus-association
DDB	Dortmund database
DOI	digital object identifier
EMD	equilibrium molecular dynamics
EOS	equation of state
Ex-T	extreme temperature region
FCC	face-centered cubic
FFT	fast Fourier transform
G	gas region
GROMOS	Groningen molecular simulation
HD	high-density
HD-L	high-density liquid region
HD-Su	high-density supercritical region
L	liquid region
LD	low-density
LJ	Lennard-Jones

---

LJTS	Lennard-Jones truncated and shifted
Lo-T	low temperature region
MAD	median absolute deviation
MC	Monte Carlo
MD	molecular dynamics
MoDOD	model distance-based outlier detection
MSD	mean squared displacement
MU	vapor-liquid metastable/unstable region
NEMD	non-equilibrium molecular dynamics
$NpT$	isothermal-isobaric
$NVT$	canonical ensemble
$n$ -C10	$n$ -decane
$n$ -C20	$n$ -icosane
$n$ -C30	$n$ -triacontane
OME	poly(oxymethylene) dimethyl ethers
OPLS	optimized potentials for liquid simulations
PACT	perturbed-anisotropic-chain theory
PAO	poly- $\alpha$ -olefines
PC-SAFT	perturbed-chain SAFT
PES	potential energy surface
PeTS	perturbed truncated and shifted
RESPA	reverse reference system propagator algorithm
SAFT	statistical association fluid theory
SAFT-VR Mie	SAFT variable range Mie EOS
SI	système international d'unités
SLE	solid-liquid equilibrium, solid-metastable region
SQU	squalane
Su	supercritical region
TAMie	transferable anisotropic Mie-potential
TCF	time correlation function
TDM	time decomposition method
TraPPE	transferable potentials for phase equilibria
TRI	1-decene trimer
TUK-FFDat	data scheme and data format for transferable force fields
UA	united-atom
VLE	vapor-liquid equilibrium

# 1 Introduction

Transport phenomena like viscous momentum transport, heat transfer, and mass diffusion occur in most natural and technical processes. They always act in a way, that the system undergoes a transition in which it approaches an equilibrium state by transferring momentum, heat, and mass. In technical applications, transport phenomena are often crucial for the functionality and efficiency of a process [1–4]. For example, the lubricant and its properties determine the friction in a tribological system [5]. In separation processes and reactors, the diffusion is often the limiting factor [1]. In microelectronic devices, the heat transfer is highly important [6]. Reliable modeling of the transport phenomena is therefore crucial in many applications. It enables the development of efficient processes and machines with a lower energy consumption.

Transport phenomena are described mathematically by transport equations, which connect a flux to a corresponding gradient. The proportionality coefficient between the flux and the gradient is called transport property, a substance-specific property, which depends on the thermodynamic state. The viscosity relates the momentum flux with the velocity gradient (*Newton's law of viscosity*), the thermal conductivity relates the heat flux to the temperature gradient (*Fourier's law*), and the diffusion coefficient relates the mass flux to either the gradient of the chemical potential (Maxwell-Stefan equation) or the concentration gradient (*Fick's law*). These transport equations and their corresponding transport coefficients form the basis of many simulation methods used to model and design industrial processes, like computational fluid dynamics (CFD) simulations or rate-based process simulations. For solving the transport equations, information on the transport properties is a prerequisite.

As experimental data of transport properties are often not available for the substance and thermodynamic state of interest, modeling transport properties is an important task [7–11]. For the prediction of transport properties at extreme conditions where experiments cannot be conducted, physical models with a robust extrapolation behavior are required [12]. This includes, for example, the thermophysical properties of lubricants at extremely high pressure ( $p > 1$  GPa), as it occurs in the narrow contact zone of bearings [2]. Also for diffusion coefficients in mixtures, the availability of data is very limited due to large number of systems and the complexity of experiments [13].

Molecular dynamics (MD) simulations and molecular-based equations of state (EOS) in combination with entropy scaling are sound physical routes for predicting transport properties. In MD simulations, many-particle systems are described based on *Newton's* equations of motion and underlying models for the interaction between the particles (i.e. molecules), the so-called force fields [14, 15]. From the numerical solution of the equations, thermodynamic and transport properties can be calculated [16]. Often, transferable force fields are used in MD simulations. They are modular force fields allowing to build up molecules – in contrast to component-specific force fields which are only applicable for a specific substance. Transferable force fields enable the simulation of substances, for which no experimental data are available. Besides substance properties, MD simulations also enable the simulation of nanoscopic processes, which allows investigating transport phenomena on the nanoscale [17–21].

In contrast to the computationally expensive MD simulations, molecular-based EOS provide analytical models which enable the calculation of all (static) thermodynamic properties [22, 23]. In combination with entropy scaling, also transport properties can be modeled [24]. Entropy scaling makes use of the observation that transport properties, when properly scaled, can often be described by a monovariate function of the configurational entropy [25, 26]. The configurational entropy is taken from an EOS in entropy scaling models.

Both concepts – MD simulations and entropy scaling – are used in this work for modeling transport properties and phenomena. The first part (Chapters 2 - 5) focuses on MD simulations and the second part (Chapters 6 - 8) on molecular-based EOS and entropy scaling.

The Lennard-Jones fluid [27] is a simple model fluid often used in molecular thermodynamics for the development of new theories and techniques [28–32]. In Chapter 2, literature data on the shear viscosity, thermal conductivity, and self-diffusion coefficient of the Lennard-Jones fluid sampled by molecular dynamics simulations are reviewed and critically assessed. The transport property literature data were complemented by new simulation data from this work. The accuracy of the data was assessed with two methods: (i) An outlier detection method based on entropy scaling and (ii) an assessment based on the Chapman-Enskog theory for low densities. Among others, the study provides information on the reproducibility of MD simulation results of transport properties.

For real fluids, the quality of predictions by MD simulations primarily depends on the applied force field. In Chapter 3, a systematic comparison of classical transferable force fields for the prediction of the density, the viscosity, and the self-diffusion coefficient is presented. Nine transferable force fields were applied for simulating three linear and two branched alkanes at extreme conditions with pressures up to 400 MPa – as

they are encountered in tribological applications. The force fields were evaluated using experimental data. Besides the accuracy of the force fields, their computational costs were taken into account.

Additionally, an online database for transferable force fields was created, cf. Chapter 4. For this purpose, a generalized data scheme and data format for transferable force fields was developed. The tools supplied with the database also support the building of component-specific force fields which can be readily applied in MD simulations. The online database includes eight different force fields: OPLS-UA [33], OPLS-AA [34], COMPASS [35], CHARMM [36], GROMOS, TraPPE [37], Potoff [38], and TAMie [39]. The download of ready-to-use input files for different simulation engines enables easy workflow integration.

In Chapter 5, results from non-equilibrium molecular dynamics (NEMD) simulations are presented in which the heat transfer across solid-fluid interfaces on the nanoscale was investigated. The studied system consists of a fluid confined between two parallel atomistic walls. Both the fluid and the solid were modeled with the Lennard-Jones truncated and shifted (LJTS) potential. The heat transfer resistance across the solid-liquid interface, also called Kapitza resistance, was quantified by the Kapitza length and different influencing parameters were varied in the simulations. Based on the simulation results, a correlation for the Kapitza length was developed. A dimensionless number is introduced, the Kapitza interface number  $Ki$ , which describes the Kapitza resistance in the stagnant fluid and is zero in the absence of the Kapitza effect. The results from Chapter 5 can be used to describe heat transfer in cases in which the Kapitza resistance plays a role, or simply to assess whether the Kapitza resistance plays a role in a given system.

Molecular-based EOS are the basis for the application of entropy scaling. A reliable prediction of the configurational entropy by the EOS is required, especially at extreme conditions. Therefore, a set of EOS models for long-chain alcohols was developed in Chapter 6. Since data at high pressure is scarce, experiments were carried out with a vibrating-tube densimeter. The density of five 1-alcohols was measured at pressures up to 120 MPa and temperatures between 298.15 K and 423.15 K. The new data were used in combination with vapor-liquid equilibrium (VLE) data to parameterize new EOS models of the studied substances using four molecular-based EOS, namely PC-SAFT [40], SAFT-VR Mie [41], soft SAFT [42], and CPA [43]. The extrapolation behavior of the EOS models was assessed by means of *Brown's* characteristic curves and by considering the model predictions for metastable states.

In Chapter 7, a new entropy scaling framework for modeling transport properties is presented. It can be applied for modeling the viscosity, the thermal conductivity, and the self-diffusion coefficient. The framework was formulated in a general way such that

it can be coupled with any EOS. It is demonstrated that the framework, when coupled to a suitable molecular-based EOS, provides not only good descriptions of existing data but also reasonable predictions in a wide range of states covering the liquid, gaseous, supercritical, and metastable region. The universal parameters of the model were fitted to MD simulation data of the Lennard-Jones fluid. This procedure provides inherently a robust form of the basic scaling function. Thereby, only few data points are required for the determination of the component-specific model parameters. The applicability of the framework is demonstrated for model fluids as well as for a wide variety of real substances including non-polar, polar, and associating pure fluids and mixtures.

In Chapter 8, the entropy scaling approach is extended to diffusion coefficients of mixtures. This is the first time that entropy scaling is applied to these important mixture properties. The new method yields results for the self-diffusion coefficients, Maxwell-Stefan diffusion coefficients, and Fickian diffusion coefficients in binary mixtures. The diffusion coefficients in the mixture are described consistently and in a fully predictive way – also for strongly non-ideal mixtures and for all fluid states. The new methodology is based on the monovariate scaling behavior of infinite dilution diffusion coefficients. It is demonstrated that the approach works reliably both for model fluids as well as for mixtures of real substances.



# 2 Database and Data Assessment of Transport Properties of the Lennard-Jones Fluid

## 2.1 Introduction

The Lennard-Jones (LJ) potential is of central importance in physical chemistry, computational physics, and soft matter physics [28, 29]. It is defined as

$$u_{\text{LJ}} = 4\varepsilon \left[ \left( \frac{\sigma}{r} \right)^{12} - \left( \frac{\sigma}{r} \right)^6 \right] \quad (1)$$

where  $r$  is the distance between two interacting particles and  $u_{\text{LJ}}$  their potential energy [27, 44, 45]. Its parameters  $\sigma$  and  $\varepsilon$  characterize the size of the particles and the magnitude of the dispersive interactions, respectively. The (virtual) substance described by the Lennard-Jones fluid [30], i.e. spherical particles interacting by the Lennard-Jones potential, has an outstanding role. It is important for the development and testing of new molecular simulation methods [17, 31, 32, 46], the development and parametrization of fluid theories and models [47–52], and for studying the fundamentals of the relations between macroscopic properties and the atomistic interactions [53–62]. The LJ substance also provides a realistic representation of simple real fluids like argon and methane [63–65] such that results from simulations and theories can be compared to laboratory measurements [66, 67]. Due to the importance of the simple substance described by the Lennard-Jones potential in physical chemistry, it is often referred to as Lennard-Jonesium and its properties are generally reported in its own unit system [14, 30, 68, 69].

Thermophysical properties of the Lennard-Jonesium have been studied by many authors since the first computer experiments carried out by *Alder and Wainwright* [70], *Rahman* [71] and *Metropolis et al.* [72]. In a recent study [73], time-independent thermodynamic property data of the LJ fluid were reviewed and a critically evaluated database that contains data for homogeneous state points and the vapor-liquid equilibrium was pro-

vided. Transport properties, i.e. time-dependent thermodynamic properties, were not considered therein.

Transport properties, such as the shear viscosity, thermal conductivity, and self-diffusion coefficient are important in many technical applications as well as in natural phenomena [4, 8, 74–76]. Since laboratory experiments for determining transport properties are tedious and costly, molecular simulations have become an attractive alternative to access such data [77–83]. For brevity, the self-diffusion coefficient is also designated as a transport property here, even though it does not directly describe transient processes, as transport properties should, and the shear viscosity and the thermal conductivity do. However, it is a time-dependent property that is closely related to the transport property mutual diffusion coefficient, which is, however, only defined for mixtures, whereas only pure fluid properties are considered in the present chapter.

The first studies for determining transport properties of the Lennard-Jones fluid were already undertaken by *Jones* himself in 1924 [66] and *Rahman* in 1964 [71]. *Jones* used predictions for the shear viscosity from the Chapman-Enskog theory for estimating the potential parameters of argon [66]. *Rahman* determined for the first time a transport coefficient, namely the self-diffusion coefficient, with molecular dynamics simulation [71]. Since then, the transport properties of Lennard-Jonesium have been studied by many authors. However, no consolidated database is available yet and this work closes this gap.

As in laboratory experiments, also in molecular simulation computer experiments, systematic errors can occur that compromise and obscure the results. Determining transport properties of fluids by molecular simulations is a challenging task [84–86], which can be addressed by different techniques [14, 87]. The development and improvement of simulation techniques for determining transport coefficients is still a very active field with open questions [84, 88, 89], which requires reliable benchmark data. The critical assessment of literature data contributes to establishing such benchmark data. Sampling transport properties is in general more complex and computationally expensive than the simulation of time-independent thermodynamic bulk properties, such as the internal energy or pressure at given temperature and density. The applicability of a given simulation technique and adequate simulation settings for a given specific simulation, i.e. determining a given transport property for a given force field, thermodynamic state etc., is generally not a priori known. The corresponding choices that have to be made may have an important influence on the simulation result and are prone to errors [90–92]. Poor choices can lead to systematic errors. Moreover, computational aspects, like code compilation, parallelization, and even hardware, may influence the simulation results. In particular, simulation algorithms like the thermostat and integrator may affect the results [93–96]. Benchmark data for transport properties are scarce. In this

chapter, transport property data for the Lennard-Jones fluid from the literature are reviewed and critically evaluated. In fluid regions where data are scarce, new simulations were carried out.

In principle, transport properties can be determined with two main techniques: Equilibrium molecular dynamics (EMD) and non-equilibrium molecular dynamics (NEMD) simulations [14]. Transport properties cannot be determined with Monte-Carlo (MC) simulations due to the absence of the physical property time. The sampling of transport properties by EMD simulations is either based on the Green-Kubo formalism [97, 98] or the Einstein [14] relations, which are closely linked [16]. The Green-Kubo relations link the microscopic fluctuation of a specific property under equilibrium conditions to a given macroscopic transport property (e.g. the particle velocity fluctuations are linked to the self-diffusion coefficient) [99]. Therein, the linear response of the system to the fluctuation is evaluated by means of the time correlation functions and the macroscopic transport property is calculated by their integration. The Einstein relations can be derived from the respective Green-Kubo relations by integration [14]. The reliable application of these EMD methods requires sufficiently long simulations (such that the time correlation functions can be determined with sufficient statistical weight and to capture the decay to zero) and usually requires more particles than the simulation of static bulk properties [16, 100]. A review of EMD simulation methods for determining transport coefficients is given in Refs. [14, 16].

In contrast to EMD simulations, a gradient is applied in NEMD simulations and the transport coefficients are calculated from the system response [99]. Hence, the transport equations are directly evaluated for determining the corresponding linear transport coefficients. There is a large variety of NEMD simulation methods for determining transport coefficients [31, 87, 101–106]. Yet, this strategy can only be applied for the shear viscosity and the thermal conductivity since the self-diffusion is not related to a transport ansatz. A review of NEMD simulation methods can be found in Ref. 87. EMD as well as NEMD methods differ significantly, but are similar in their complexity and require the specification of simulation meta parameters that influence the quality of the simulation results, e.g. the length of the autocorrelation function [16] or the magnitude of the applied gradient [99]. In this chapter, transport properties of the Lennard-Jones fluid sampled with both EMD and NEMD simulations are considered.

In the literature, also modifications of the Lennard-Jones potential are often considered, e.g. the Lennard-Jones truncated and shifted potential (LJTS)[107, 108] and the splined Lennard-Jones potential (sLJ) [109, 110]. Yet, these potentials do not truly describe the LJ fluid, but only similar fluids with somewhat different properties [111, 112] and are therefore not considered here. Similarly, the transport properties of Lennard-Jonesium are affected by the long-range interactions and the potential cutoff. Their influence is

two-fold: (i) The sampled transport properties themselves depend to some extent on the attractive tail of the potential. An influence of the cutoff radius has been reported mainly for cutoff radii smaller than  $2.5\sigma$  – for larger cutoff radii, the transport properties are reported to be not significantly dependent on the cutoff radius [113–117]. However, some authors also call for a larger cutoff radius, e.g. a cutoff radius of  $4.5\sigma$  was suggested by Refs [118, 119]. (ii) The state point properties specifying the thermodynamic condition depend on the attractive tail of the potential. A given transport property  $Y$  is to be specified as  $Y = Y(a, b)$ , where  $a$  and  $b$  describe at least two out of the three state variables  $p\nu T$ . The pressure strongly depends on the tail correction. As a consequence, also the transport properties, when required at a pair of temperature and pressure, indirectly, but strongly depend on the tail correction [112, 120]. Also, the size of the simulation volume, i.e. the particle number, plays an important role for determining transport properties. Finite-size effects have been reported for all three properties considered here [114, 118, 119, 121, 122]. To eliminate finite-size effects, an extrapolation to the thermodynamic limit ( $N \rightarrow \infty$ ) can be applied which requires multiple simulations for a given state point. For EMD simulations of the shear viscosity and thermal conductivity, these finite size effects are negligible when choosing an appropriate number of particles ( $N > 1000$ ) [119, 122]. For the self-diffusion coefficient, the finite-size effect is more pronounced [118, 122] and analytical correction terms have been proposed [122, 123]. Some NEMD simulation methods can also be subject to finite-size effects [114, 121].

Transport properties of simple fluids at low densities  $\rho \rightarrow 0$  can be described with the Chapman-Enskog theory [75], which is rigorously derived from statistical mechanics and is based on a statistical consideration of particle collisions [124]. For a simple fluid with soft repulsive and dispersive interactions, the so-called collision integrals of the fluid are required for applying Chapman-Enskog theory. This approach is practically exact for very simple fluids, such as the hard sphere fluid [124, 125]. For the LJ fluid, highly accurate collision integrals are available [126] and the Chapman-Enskog theory can be applied for the transport properties at  $\rho \rightarrow 0$  with high accuracy. For dense states, no rigorous analytical model is available today. Yet, different liquid state theories have been developed for modeling transport properties at high density fluid states [7, 25, 26, 127], e.g. friction theory or entropy scaling. The latter must be coupled with a model for the entropy of the fluid, which is usually an equation of state (EOS). [52, 128–134]. Thereby, entropy scaling exploits that the transport properties, when properly scaled, are a largely monovariate function of the configurational entropy. These two theoretical frameworks, i.e. Chapman-Enskog theory and entropy scaling, were used as a tool in this chapter for evaluating the accuracy of transport property data of the Lennard-Jones fluid. For the database on the (time-independent) properties of the Lennard-Jones fluid

[73], different consistency and outlier detection tests were applied. For detecting outliers in homogeneous state regions, the scatter of data points in the neighborhood of a given data point was considered in Ref. 73. The underlying algorithm (MoDOD – model distance-based outlier detection) rests on a model of the considered property as a base line [135]. Yet, this method uses the model only indirectly as a reference such that the outlier detection does not depend on the accuracy of the model itself (details are given below). In this chapter, the MoDOD method was applied for critically evaluating the transport property data of the LJ fluid. As a model, the entropy scaling approach from Ref. 52 in combination with the Kolafa-Nezbeda EOS [136] was used. Moreover, outliers were identified based on the deviations to the Chapman-Enskog theory at low densities.

Only fluid state points, i.e. gaseous, liquid and supercritical, were considered in this chapter. The established database contains 17,286 data points (including outliers) from a total of 102 references. New simulations were carried out in a wide fluid state range to complement the data in regions where information was only sparsely available.

The chapter is organized as follows: The database is presented in the first part including the references and statistics. In the second part, the data quality of the database is assessed. Finally, conclusions are drawn.

## 2.2 Database of Transport Properties of the Lennard-Jones Fluid

Table 1 gives an overview of the LJ fluid database for the shear viscosity, thermal conductivity, and self-diffusion coefficient including the reference, the year of publication, the number of data points, and the temperature range.

**Table 1:** Overview of the database of the shear viscosity, thermal conductivity, and self-diffusion coefficient of the Lennard-Jones fluid. The columns indicate (from left to right): Reference, year of publication, temperature range, and number of data points (with the number of outliers in parenthesis). The entries are sorted chronologically for each transport property.

Authors	Year	$T/\varepsilon k_{\text{B}}^{-1}$	#
Shear viscosity			
<i>Gosling et al.</i> [137]	1973	0.94 - 1.16	3 (0)
<i>Levesque et al.</i> [138]	1973	0.72 - 0.72	1 (1)

*Continued on next page*

Authors	Year	$T/\varepsilon k_B^{-1}$	#
<i>Ashurst and Hoover</i> [139]	1975	0.67 - 29.7	51 (4)
<i>Heyes et al.</i> [140]	1980	0.72 - 0.72	4 (0)
<i>Hoover et al.</i> [141]	1980	0.72 - 0.73	9 (0)
<i>Singer et al.</i> [142]	1980	0.7 - 0.99	12 (0)
<i>Fincham and Heyes</i> [143]	1983	0.71 - 2.7	11 (1)
<i>Heyes</i> [144]	1983	0.68 - 4.58	52 (18)
<i>Michels and Trappeniers</i> [145]	1985	1.3 - 10.0	36 (25)
<i>Schoen and Hoheisel</i> [146]	1985	0.68 - 4.42	14 (0)
<i>Evans and Morriss</i> [147]	1987	0.72 - 0.72	1 (0)
<i>Heyes</i> [148]	1987	1.46 - 1.46	16 (0)
<i>Levesque and Verlet</i> [149]	1987	0.72 - 2.74	3 (0)
<i>Erpenbeck</i> [150, 151]	1988	0.72 - 0.72	1 (0)
<i>Hammonds and Heyes</i> [152]	1988	0.72 - 10.0	51 (1)
<i>Heyes</i> [153]	1988	0.72 - 12.3	210 (5)
<i>Vogelsang et al.</i> [154]	1988	0.74 - 3.56	14 (1)
<i>Evans et al.</i> [155]	1989	0.72 - 0.72	1 (0)
<i>Borgelt et al.</i> [156]	1990	0.66 - 2.71	46 (10)
<i>Heyes and Powles</i> [157]	1990	0.72 - 6.0	26 (3)
<i>Ferrario et al.</i> [158]	1991	0.72 - 0.72	1 (0)
<i>Moon et al.</i> [159]	1991	0.79 - 0.79	2 (0)
<i>Pas and Zwolinski</i> [160]	1991	0.97 - 0.97	2 (0)
<i>Pas and Zwolinski</i> [161]	1991	0.55 - 1.17	16 (1)
<i>Heyes et al.</i> [162]	1993	0.71 - 6.02	4 (0)
<i>Lee and Cummings</i> [163]	1993	0.95 - 1.13	8 (5)
<i>Hoheisel</i> [164]	1994	0.62 - 3.94	9 (2)
<i>Stassen and Steele</i> [165]	1995	1.26 - 1.26	5 (0)
<i>Rowley and Painter</i> [166]	1997	0.8 - 4.0	171 (5)
<i>Canales and Padro</i> [167]	1999	0.53 - 1.89	3 (1)
<i>Ohara and Suzuki</i> [168]	2001	0.84 - 0.84	1 (1)
<i>Lee et al.</i> [169]	2003	0.79 - 0.79	4 (0)

*Continued on next page*

Authors	Year	$T/\varepsilon k_{\text{B}}^{-1}$	#
<i>Meier et al.</i> [119]	2004	0.71 - 0.72	3 (0)
<i>Vasquez et al.</i> [170]	2004	0.7 - 6.0	104 (7)
<i>Galliéro et al.</i> [171]	2005	0.6 - 4.0	80 (0)
<i>Laghaei et al.</i> [57]	2005	0.7 - 1.8	72 (4)
<i>Mountain</i> [172]	2006	0.74 - 3.56	28 (0)
<i>Galliéro et al.</i> [173]	2007	1.0 - 2.5	35 (0)
<i>Lee</i> [174]	2007	0.79 - 0.79	4 (0)
<i>Sun et al.</i> [175]	2007	0.57 - 1.13	4 (3)
<i>Thomas and Rowley</i> [176]	2007	0.8 - 4.0	241 (30)
<i>Viscardy et al.</i> [177]	2007	0.72 - 0.72	1 (0)
<i>Galliéro and Boned</i> [178]	2008	1.0 - 2.5	7 (0)
<i>Lee</i> [179]	2008	0.79 - 0.79	1 (0)
<i>Strak and Krukowski</i> [180, 181]	2008	2.56 - 6.24	23 (0)
<i>Adebayo et al.</i> [182]	2010	0.75 - 0.75	1 (0)
<i>Oderji et al.</i> [183]	2011	0.7 - 30.2	152 (0)
<i>Baidakov et al.</i> [184]	2012	0.4 - 2.0	216 (7)
<i>Lee</i> [185]	2013	1.18 - 28.74	10 (9)
<i>Lee</i> [186]	2014	2.28 - 2.28	3 (3)
<i>Lee</i> [186]	2014	0.79 - 0.79	6 (1)
<i>Delage et al.</i> [187, 188]	2015	0.8 - 6.0	121 (5)
<i>Ohtori and Ishii</i> [189]	2015	0.72 - 1.17	7 (1)
<i>Nichele et al.</i> [190]	2016	1.22 - 2.62	96 (27)
<i>Ghimire and Adhikari</i> [191]	2017	1.68 - 3.02	13 (0)
<i>Ohtori et al.</i> [192]	2017	1.16 - 2.33	77 (1)
<i>Heyes et al.</i> [193]	2019	0.72 - 205.58	7 (0)
<i>Bell et al.</i> [194]	2021	1.35 - 100.0	136 (0)
<i>Heyes et al.</i> [195]	2021	0.72 - 1.0	2 (0)
<i>Rizk et al.</i> [196, 197]	2022	0.57 - 22.5	296 (0)
<i>Viet et al.</i> [133]	2022	0.75 - 3.0	59 (0)
<i>Fertig and Stephan</i> [112]	2023	0.79 - 2.1	26 (1)

*Continued on next page*

Authors	Year	$T/\varepsilon k_B^{-1}$	#
<i>Šlepavičius et al.</i> [198]	2023	1.0 - 1.16	5 (0)
<i>Chaparro and Müller</i> [199]	2024	0.68 - 10.0	506 (23)
<i>Fleckenstein et al.</i> [200]	2024	0.1 - 95.01	2736 (421)
<i>Ramkumar et al.</i> [201]	2024	0.09 - 1.37	15 (15)
<i>Saric et al.</i> [202]	2024	1.06 - 5.29	120 (0)
<i>Schmitt et al.</i> [52]	2024	0.69 - 20.0	173 (12)
this work	2024	0.55 - 100.05	870 (46)
Thermal conductivity			
<i>Levesque et al.</i> [138]	1973	0.72 - 0.72	1 (1)
<i>Ashurst and Hoover</i> [139]	1975	0.67 - 29.7	24 (13)
<i>Heyes</i> [203]	1984	0.71 - 4.58	36 (22)
<i>Paolini et al.</i> [204]	1986	0.72 - 0.72	3 (0)
<i>Levesque and Verlet</i> [149]	1987	0.72 - 2.74	3 (0)
<i>Hammonds and Heyes</i> [152]	1988	0.72 - 10.0	50 (0)
<i>Heyes</i> [153]	1988	0.72 - 12.3	212 (2)
<i>Vogelsang et al.</i> [154]	1988	0.74 - 3.56	14 (0)
<i>Borgelt et al.</i> [156]	1990	0.66 - 2.71	46 (0)
<i>Heyes and Powles</i> [157]	1990	0.72 - 6.0	26 (1)
<i>Moon et al.</i> [159]	1991	0.79 - 0.79	2 (0)
<i>Pas and Zwolinski</i> [160]	1991	0.97 - 0.97	2 (0)
<i>Pas and Zwolinski</i> [161]	1991	0.55 - 1.17	16 (1)
<i>Heyes et al.</i> [162]	1993	0.71 - 6.02	4 (0)
<i>Hoheisel</i> [164]	1994	0.62 - 3.94	9 (0)
<i>Canales and Padro</i> [167]	1999	0.53 - 1.89	3 (0)
<i>Lee et al.</i> [169]	2003	0.79 - 0.79	4 (2)
<i>Andrade and Stassen</i> [205]	2004	0.72 - 0.72	1 (1)
<i>McGaughey and Kaviany</i> [206]	2004	0.67 - 0.83	3 (0)
<i>Hulse et al.</i> [207]	2005	0.74 - 7.39	68 (3)
<i>Mountain</i> [172]	2006	0.74 - 3.56	28 (0)
<i>Nasrabad et al.</i> [208]	2006	0.9 - 2.0	67 (0)

*Continued on next page*



Authors	Year	$T/\varepsilon k_{\text{B}}^{-1}$	#
<i>Lee</i> [174]	2007	0.79 - 0.79	4 (0)
<i>Sarkar and Selvam</i> [209]	2007	0.71 - 0.71	1 (0)
<i>Sun et al.</i> [175]	2007	0.57 - 1.13	4 (2)
<i>Bugel and Galliéro</i> [114]	2008	0.6 - 4.0	103 (0)
<i>Galliéro and Boned</i> [178]	2008	1.0 - 2.5	7 (0)
<i>Lee</i> [179]	2008	0.79 - 0.79	1 (0)
<i>Galliéro and Boned</i> [210]	2009	0.8 - 8.0	36 (0)
<i>Lee</i> [185]	2013	1.18 - 28.74	10 (9)
<i>Baidakov and Protsenko</i> [211]	2014	0.4 - 2.0	235 (0)
<i>Lee</i> [186]	2014	2.28 - 2.28	3 (1)
<i>Lee</i> [186]	2014	0.79 - 0.79	6 (0)
<i>Nichele et al.</i> [190]	2016	1.22 - 2.62	96 (17)
<i>Ghimire and Adhikari</i> [191]	2017	1.68 - 3.02	13 (0)
<i>Heyes et al.</i> [193]	2019	0.72 - 205.58	7 (0)
<i>Fertig and Stephan</i> [112]	2023	0.79 - 2.1	26 (2)
<i>Chaparro and Müller</i> [199]	2024	0.68 - 10.0	461 (9)
<i>Fleckenstein et al.</i> [200]	2024	0.45 - 95.44	1245 (76)
<i>Ramkumar et al.</i> [201]	2024	0.09 - 1.37	15 (15)
<i>Saric et al.</i> [202]	2024	1.06 - 5.29	120 (0)
<i>Schmitt et al.</i> [52]	2024	0.69 - 20.0	173 (10)
this work	2024	0.55 - 100.05	871 (30)
Self-diffusion coefficient			
<i>Rahman</i> [71]	1964	0.79 - 1.08	2 (1)
<i>Levesque and Verlet</i> [212]	1970	0.72 - 5.09	23 (11)
<i>Kushick and Berne</i> [213]	1973	0.74 - 5.13	5 (2)
<i>Schofield</i> [214]	1973	0.73 - 1.1	3 (3)
<i>Michels and Trappeniers</i> [215]	1975	1.5 - 3.0	22 (22)
<i>Chen and Rahman</i> [216]	1977	0.68 - 2.16	7 (4)
<i>Michels and Trappeniers</i> [217]	1978	1.3 - 5.56	43 (43)
<i>Heyes et al.</i> [140]	1980	0.72 - 0.72	4 (2)

*Continued on next page*

Authors	Year	$T/\varepsilon k_B^{-1}$	#
<i>Fincham and Heyes</i> [143]	1983	0.71 - 2.7	22 (3)
<i>Heyes</i> [218]	1983	0.68 - 2.55	32 (14)
<i>Heyes</i> [144]	1983	0.68 - 4.58	54 (17)
<i>Heyes</i> [148]	1987	1.46 - 1.46	16 (9)
<i>Erpenbeck</i> [150]	1988	0.72 - 0.72	1 (0)
<i>Hammonds and Heyes</i> [152]	1988	0.72 - 10.0	51 (14)
<i>Heyes</i> [153]	1988	0.72 - 12.3	212 (73)
<i>Hoheisel and Vogelsang</i> [219]	1988	0.9 - 0.93	4 (0)
<i>Borgelt et al.</i> [156]	1990	0.66 - 2.71	46 (22)
<i>Heyes and Powles</i> [157]	1990	0.72 - 6.0	26 (3)
<i>Moon et al.</i> [159]	1991	0.79 - 0.79	2 (1)
<i>Pas and Zwolinski</i> [160]	1991	0.97 - 0.97	2 (2)
<i>Pas and Zwolinski</i> [161]	1991	0.55 - 1.17	16 (5)
<i>Straub</i> [220]	1992	0.75 - 4.0	35 (10)
<i>Heyes et al.</i> [162]	1993	0.71 - 6.02	4 (0)
<i>Nuevo et al.</i> [221]	1997	0.71 - 4.45	30 (6)
<i>Rowley and Painter</i> [166]	1997	0.8 - 4.0	171 (59)
<i>Canales and Padro</i> [167]	1999	0.53 - 1.89	3 (1)
<i>Coelho et al.</i> [222]	2002	1.5 - 2.0	12 (3)
<i>Lee et al.</i> [169]	2003	0.79 - 0.79	4 (0)
<i>Meier et al.</i> [118]	2004	0.7 - 6.0	368 (6)
<i>Yeh and Hummer</i> [122]	2004	2.75 - 2.75	1 (0)
<i>Marinakis and Samios</i> [223]	2005	0.96 - 1.62	127 (125)
<i>Lee</i> [174]	2007	0.79 - 0.79	2 (0)
<i>Sarkar and Selvam</i> [209]	2007	0.71 - 0.71	1 (1)
<i>Sun et al.</i> [175]	2007	0.57 - 1.13	4 (1)
<i>Galliéro and Boned</i> [178]	2008	1.0 - 2.5	7 (0)
<i>Lee</i> [179]	2008	0.79 - 0.79	1 (0)
<i>Wei-Zhong et al.</i> [224]	2008	0.75 - 1.09	5 (1)
<i>Baidakov et al.</i> [225]	2011	0.35 - 2.0	396 (11)

*Continued on next page*

Authors	Year	$T/\varepsilon k_{\text{B}}^{-1}$	#
<i>Oderji et al.</i> [183]	2011	0.7 - 30.2	152 (14)
<i>Lee</i> [185]	2013	1.18 - 28.74	20 (4)
<i>Lee</i> [186]	2014	2.28 - 2.28	6 (1)
<i>Lee</i> [186]	2014	0.79 - 0.79	12 (0)
<i>Ohtori and Ishii</i> [189]	2015	0.72 - 1.17	7 (2)
<i>Ghimire and Adhikari</i> [191]	2017	1.68 - 3.02	13 (5)
<i>Ohtori et al.</i> [192]	2017	1.16 - 2.33	77 (10)
<i>Heyes et al.</i> [193]	2019	0.72 - 205.58	7 (0)
<i>Lopez Flores et al.</i> [226, 227]	2021	1.0 - 4.5	54 (45)
<i>Toxvaerd</i> [228]	2021	1.25 - 1.25	1 (0)
<i>Ji</i> [229]	2022	1.67 - 1.67	14 (5)
<i>Rizk et al.</i> [196, 197]	2022	0.57 - 22.5	211 (59)
<i>Atamas et al.</i> [230, 231]	2023	0.71 - 0.92	6 (6)
<i>Fertig and Stephan</i> [112]	2023	0.79 - 2.1	26 (0)
<i>Marchioni et al.</i> [232]	2023	4.0 - 4.0	12 (5)
<i>Šlepavičius et al.</i> [198]	2023	0.91 - 1.97	19 (0)
<i>Chaparro and Müller</i> [199]	2024	0.6 - 10.0	607 (5)
<i>Fleckenstein et al.</i> [200]	2024	0.45 - 95.01	1996 (282)
<i>Ramkumar et al.</i> [201]	2024	0.09 - 1.37	15 (15)
<i>Saric et al.</i> [202]	2024	1.06 - 5.29	120 (0)
<i>Schmitt et al.</i> [52]	2024	0.69 - 20.0	173 (2)
this work	2024	0.55 - 100.05	871 (14)

The transport property database is provided as an `.xlsx` spreadsheet in the electronic Supporting Information of Ref. [233]. In that electronic database, there is one tab for each property, listing the actual data points regarding the thermodynamic condition ( $T$ ,  $\rho$  and/or  $p$ ), the transport property value ( $\eta$ ,  $\lambda$ ,  $D$ ), (if provided in the reference) its corresponding statistical uncertainty ( $\Delta\eta$ ,  $\Delta\lambda$ ,  $\Delta D$ , respectively), and the reference. Each data point possesses a digital tag (0 or 1), which indicates whether it was identified to be an outlier or not, according to the assessment described below.

The general behavior of the three transport properties as a function of the pressure

and the temperature is shown in Fig. 1. The purpose of Fig. 1 is to give an overview

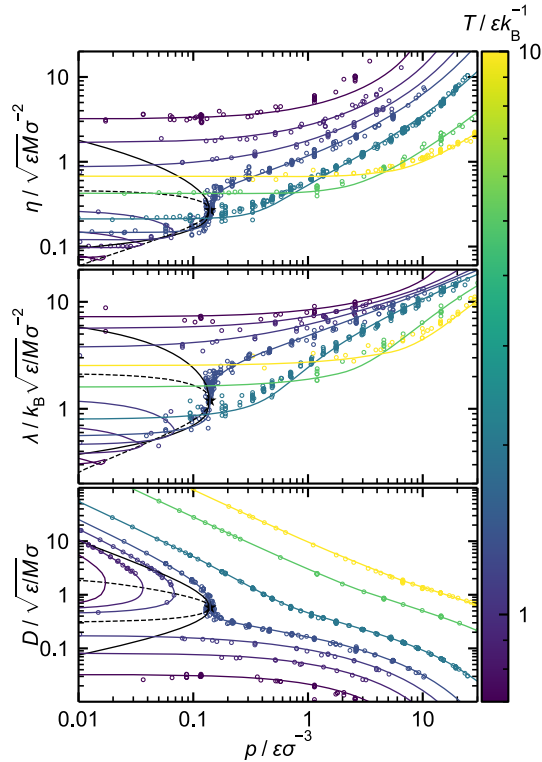


**Figure 1:** Shear viscosity  $\eta$  (top), thermal conductivity  $\lambda$  (middle), and self-diffusion coefficient  $D$  (bottom) as a function of the pressure  $p$  at selected temperatures  $T \in \{0.7, 0.9, 1.1, 1.34, 2, 5, 10\} \varepsilon k_B^{-1}$  (see color scale). Lines: Results from the entropy scaling model. Symbols: Computer experiment data points from the database at the selected temperatures ( $\pm 0.02 \varepsilon k_B^{-1}$ ).

on the range of the transport property values that are relevant for the LJ fluid and for illustrating the topology of the three transport properties. The depicted isotherms were chosen such that all fluid regions (gas, liquid, supercritical, metastable) are covered. Moreover, the transport properties on the vapor-liquid equilibrium binodal and spinodal are depicted. Both, MD data and results from the entropy scaling model adapted from Ref. 52 are shown. The entropy scaling model rests on the Kolafa-Nezbeda EOS, which is known to yield a realistic fluid description in a wide state range [50, 234].

The entropy scaling model represents the computer experiment data of the selected isotherms overall well. The topologies of the shear viscosity and the thermal conductivity are similar (see Fig. 1 top and middle): With rising pressure, both quantities increase for all stable and metastable states. In the unstable region, a *van der Waals* loop-type behavior is observed. In contrast, the temperature dependence varies in different phase regions: In the zero-density limit, shear viscosity and thermal conductivity increase with rising temperature as predicted by Chapman-Enskog theory [75]. This changes at higher density, where both quantities fall with increasing temperature. Thus, different supercritical isotherms may cross each other. The self-diffusion coefficient behaves

differently. It decreases with rising pressure, except for unstable states. The temperature dependence is always the same – the self-diffusion coefficient increases with rising temperature throughout and no crossing of isotherms occurs. At the critical point, the transport properties are estimated to be  $\eta_c = 0.26 \sqrt{\varepsilon M} \sigma^{-2}$ ,  $\lambda_c = 1.24 k_B \sqrt{\varepsilon/M} \sigma^{-2}$ , and  $D_c = 0.59 \sqrt{\varepsilon/M} \sigma$ . The transport properties exhibit a particular behavior near the critical point, the so-called critical enhancement [235–237]. For the Lennard-Jonesium, this is most pronounced for the thermal conductivity and not prominent for the shear viscosity and the self-diffusion coefficient [128]. The critical enhancement is due to large fluctuations that decay very slowly [235].

The LJ transport property database was compiled from data in peer-reviewed publications that were obtained from molecular simulation computer experiments. Data predicted by theories (that are subject to assumptions and simplifications) were not included. Only data for the full LJ potential was included in the database. Data from modified LJ potentials, e.g. the LJs and LJTS potential, were not considered. Simulation data were only included if the cutoff was at least  $2.5\sigma$ . In cases, where the specifications on that were not fully conclusive, data were nevertheless mostly included. In several cases where these specifications were vague, the data turned out to be identified as outliers by the data assessment (see below). The self-diffusion coefficient data included in the database were taken uncorrected. For data of studies that only published the final (corrected) values and that reported the applied correction, the original values were recalculated and the applied procedure was reported in the Appendix A with the conversion. All of the studies where values were uncorrected used the method proposed by *Yeh and Hummer* [122]. Overall, only few studies even report the handling of the long-range corrections (see below).

The total number of data points  $N_{\text{tot}}$  comprised in the transport property LJ database (cf. Table 1) and the number of publications  $N_{\text{pub}}$  from which those data were retrieved is reported in Fig. 2. The number of data points for the thermal conductivity (4059) is significantly lower than that for the shear viscosity (7044) and the self-diffusion coefficient (6183). All three properties are among the most studied properties of the LJ fluid (compare Ref. 73), which underpins their importance.

Fig. 3 shows the state points for which transport property data are available (cf. Table 1), in  $\rho - T$  diagrams. Fig. 4 introduces the symbols distinguished by shape and color used for a given reference throughout this chapter. For all three transport properties, data are available in all fluid state regions. Ten different state regions were distinguished that are depicted in Fig. 5. All data points are assigned to a fluid region according to Fig. 5. In some cases, simulations were also carried out in the metastable/unstable state regions. As expected, for extreme conditions, especially for temperatures  $T > 10 \varepsilon k_B^{-1}$ , the data become sparse. Fig. 3 also contains the data sampled in this work (details on

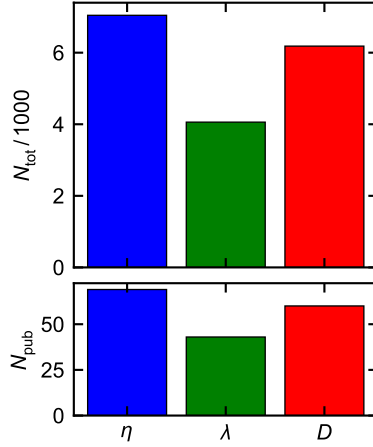


**Figure 2:** Total number of data points  $N_{\text{tot}}$  (top) and number of publications  $N_{\text{pub}}$  (bottom) for the shear viscosity  $\eta$ , thermal conductivity  $\lambda$ , and self-diffusion coefficient  $D$ .

the simulation methodology are given in the Appendix A). They extend the range in which data are available, but also cover regions with more data to allow for comparisons. They were handled as the literature data, in particular, they were subjected to the same tests.

For the vast majority of the transport property data in the database, both  $T$  and  $\rho$  are available specifying the state point. In about 50 % of the cases, also the pressure was reported. Less than 2 % of the data are reported for given  $T$  and  $p$ , i.e. without providing the density. For these state points, the density was calculated with the Kolafa-Nezbeda EOS [136] where required (e.g. for applying the MoDOD test). Moreover, in some cases additional (time-independent) thermodynamic properties were reported, see Appendix A for details. For the three considered transport properties, the availability of data in the different fluid regions is similar. Around 44 % of the transport property data are in the supercritical region (Su), 14 % in the extreme temperature region (Ex-T), 12 % in the liquid region (L), 10 % in the vapor-liquid metastable region (MU), 4 % in the solid-metastable (SLE) region, 4 % in the gas region (G), 3 % in the high-density liquid region (HD-L), 3 % in the critical region (C), 2 % in the high-density supercritical region (HD-Su), and 2 % in at temperatures below the triple point (Lo-T).

The statistical uncertainties of the data points  $\Delta\eta$ ,  $\Delta\lambda$ , and  $\Delta D$  were included in the database – if reported by the authors. Fig. 6 shows histograms of the values of the relative statistical uncertainties. Statistical uncertainties are available for 80 %, 76 %, and 66 % of the data points for the shear viscosity, thermal conductivity, and self-diffusion coefficient, respectively. For the shear viscosity and thermal conductivity, the vast majority of the reported relative statistical uncertainties  $\Delta\eta/\eta$  are below 0.1. For the self-diffusion coefficient, significantly smaller relative statistical uncertainties are reported with  $\Delta D/D < 0.01$  for most of the data. This is due to the fact that the self-

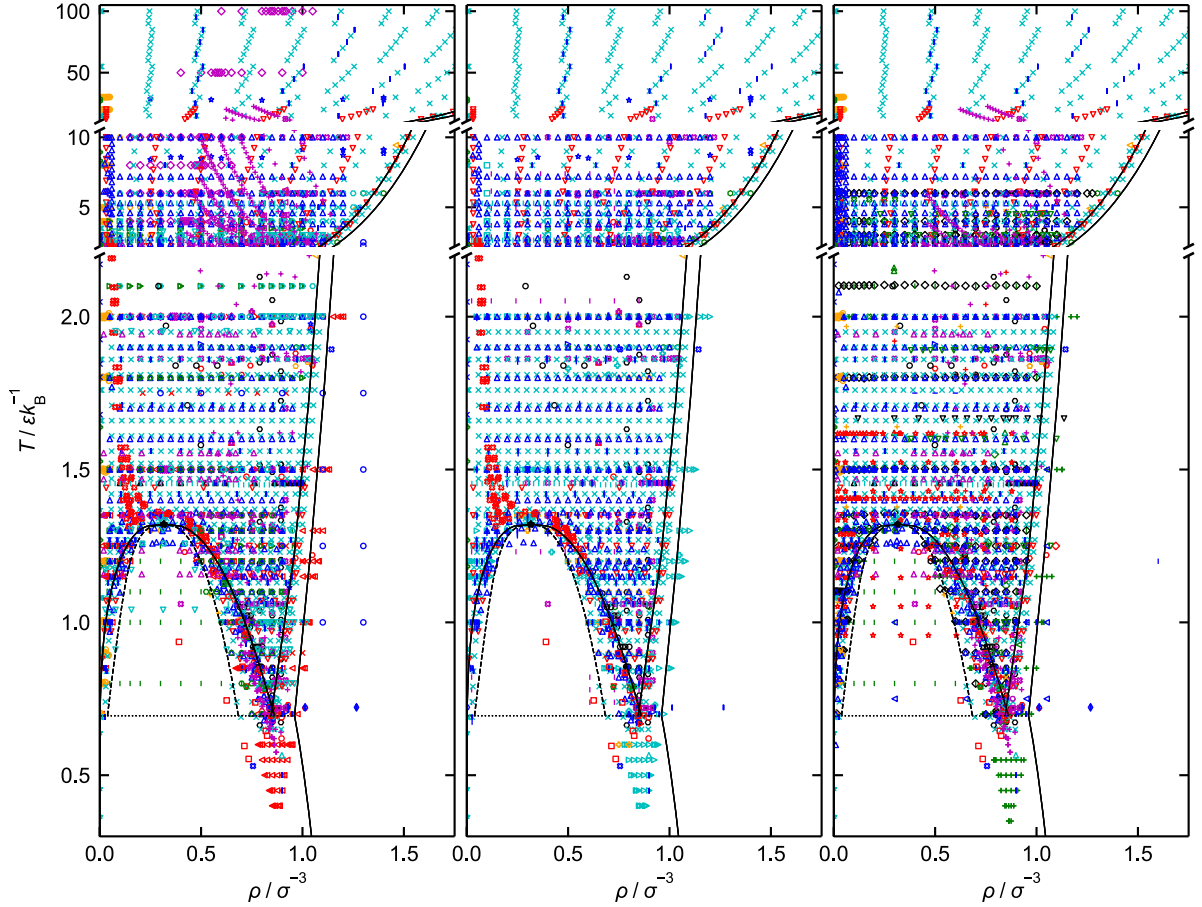


**Figure 3:** Overview of the state points of all available transport property simulation data included in the database for the shear viscosity (left), thermal conductivity (middle), and self-diffusion coefficient (right) in the  $T$ - $\rho$  plane. The symbols are as given in Fig. 4. The binodal, spinodal, critical point, and triple point were taken from Ref. 73, and the freezing and melting lines are from Refs. 238, 239. All data refer to fluid state points, some lie in regions that are not stable.

diffusion coefficient can be sampled for each particle individually. Thus, the self-diffusion coefficient can be obtained as the average of the individual particles, which gives excellent statistics. This is not the case for the shear viscosity or the thermal conductivity, where only one value is computed for the entire simulation volume. Furthermore, the statistical uncertainty depends on the region, where the studied state point lies. This is discussed in the Appendix A using heat maps showing the uncertainty as a function of  $T$  and  $\rho$ .

Simulations for determining transport properties of the LJ fluid that are compiled in the database were carried out with a large number of different simulation codes, hardware, simulation methods, and simulation settings, such as particle number, time steps etc. There is a consensus that publications should report not only the simulation results and their uncertainties, but also meta data on the simulation method – with the main goal to allow for a reproduction of the simulations [90, 240–243]. However, there is no

References (alphabetically)	Viscosity	Thermal conductivity	Self-diffusion coefficient
	<ul style="list-style-type: none"> <li>◇ Adebayo et al. (2010)</li> <li>★ Ashurst and Hoover (1975)</li> <li>◀ Baidakov et al. (2012)</li> <li>◇ Bell et al. (2021)</li> <li>○ Borgelt et al. (1990)</li> <li>■ Canales and Padron (1999)</li> <li>▲ Chaparro and Müller (2024)</li> <li>▽ Delage-Santacreu et al. (2015)</li> <li>- Erpenbeck (1988)</li> <li>◇ Evans and Morriss (1987)</li> <li>◇ Evans et al. (1989)</li> <li>◇ Ferraro et al. (1991)</li> <li>○ Fertig and Stephan (2023)</li> <li>○ Fincham and Heyes (1983)</li> <li>! Fleckenstein et al. (2024)</li> <li>× Galliero et al. (2005)</li> <li>○ Galliéro et al. (2007)</li> <li>▽ Galliéro and Boned (2008)</li> <li>× Ghimire and Adhikari (2017)</li> <li>★ Gosling et al. (1973)</li> <li>★ Hammonds and Heyes (1988)</li> <li>▲ Heyes et al. (2019)</li> <li>▶ Heyes et al. (1993)</li> <li>Heyes (1983)</li> <li>○ Heyes (1983)</li> <li>■ Heyes (1988)</li> <li>▲ Heyes (1987)</li> <li>- Heyes et al. (2021)</li> <li>◇ Heyes et al. (1980)</li> <li>○ Heyes and Powles (1990)</li> <li>○ Hoheisel (1994)</li> <li>○ Hoover et al. (1980)</li> <li>○ Laghaei et al. (2005)</li> <li>◆ Lee (2013)</li> <li>- Lee (2007)</li> <li>◇ Lee et al. (2003)</li> <li>○ Lee (2014)</li> <li>○ Lee (2014)</li> <li>○ Lee (2014)</li> <li>× Lee (2008)</li> <li>■ Lee and Cummings (1993)</li> <li>■ Levesque et al. (1973)</li> <li>★ Levesque and Verlet (1987)</li> <li>▶ Meier et al. (2004)</li> <li>Meier et al. (2004)</li> <li>○ Michels and Trappeniers (1985)</li> <li>◆ Changman Moon et al. (1991)</li> <li>▲ Mountain (2006)</li> <li>■ Nichele et al. (2016)</li> <li>○ Oderji et al. (2011)</li> <li>◇ Ohara and Suzuki (2001)</li> <li>○ Ohtori and Ishii (2015)</li> <li>▲ Ohtori et al. (2017)</li> <li>! Pas and Zwolinski (1991)</li> <li>□ Pas and Zwolinski (1991)</li> <li>★ Ramkumar et al. (2024)</li> <li>★ Rizk et al. (2022)</li> <li>! Rowley and Painter (1997)</li> <li>! Saric et al. (2024)</li> <li>▽ Schmitt et al. (2024)</li> <li>□ Schoen and Hoheisel (1985)</li> <li>★ Singer et al. (1980)</li> <li>★ Slepavicius et al. (2023)</li> <li>■ Stassen and Steele (1995)</li> <li>◀ Strąk and Krukowski (2008)</li> <li>▲ Sun et al. (2007)</li> <li>▶ Thomas and Rowley (2007)</li> <li>○ Vasquez et al. (2004)</li> <li>○ Viet et al. (2022)</li> <li>○ Viscardy et al. (2007)</li> <li>◆ Vogelsang et al. (1988)</li> <li>× this work</li> </ul>	<ul style="list-style-type: none"> <li>○ Andrade and Stassen (2004)</li> <li>★ Ashurst and Hoover (1975)</li> <li>▶ Baidakov and Protsenko (2014)</li> <li>○ Borgelt et al. (1990)</li> <li>◆ Bugel and Galliero (2008)</li> <li>■ Canales and Padron (1999)</li> <li>▲ Chaparro and Müller (2024)</li> <li>○ Fertig and Stephan (2023)</li> <li>! Fleckenstein et al. (2024)</li> <li>□ Galliero and Boned (2009)</li> <li>▽ Galliéro and Boned (2008)</li> <li>× Ghimire and Adhikari (2017)</li> <li>× Hammonds and Heyes (1988)</li> <li>▲ Heyes et al. (2019)</li> <li>▶ Heyes et al. (1993)</li> <li>◆ Heyes (1984)</li> <li>■ Heyes (1988)</li> <li>○ Heyes and Powles (1990)</li> <li>○ Hoheisel (1994)</li> <li>! Hulse et al. (2005)</li> <li>◆ Lee (2013)</li> <li>- Lee (2007)</li> <li>◇ Lee et al. (2003)</li> <li>○ Lee (2014)</li> <li>○ Lee (2014)</li> <li>○ Lee (2014)</li> <li>× Lee (2008)</li> <li>■ Levesque et al. (1973)</li> <li>★ Levesque and Verlet (1987)</li> <li>▶ McGaughy and Kaviany (2004)</li> <li>◆ Changman Moon et al. (1991)</li> <li>▲ Mountain (2006)</li> <li>- Nasrabad et al. (2006)</li> <li>■ Nichele et al. (2016)</li> <li>○ Paolini et al. (1986)</li> <li>! Pas and Zwolinski (1991)</li> <li>□ Pas and Zwolinski (1991)</li> <li>★ Ramkumar et al. (2024)</li> <li>! Saric et al. (2024)</li> <li>★ Sarkar and Selvam (2007)</li> <li>▽ Schmitt et al. (2024)</li> <li>▲ Sun et al. (2007)</li> <li>◆ Vogelsang et al. (1988)</li> <li>× this work</li> </ul>	<ul style="list-style-type: none"> <li>○ Atamas et al. (2023)</li> <li>★ Baidakov et al. (2011)</li> <li>○ Borgelt et al. (1990)</li> <li>■ Canales and Padron (1999)</li> <li>▲ Chaparro and Müller (2024)</li> <li>▲ Chen and Rahman (1977)</li> <li>- Coelho et al. (2002)</li> <li>- Erpenbeck (1988)</li> <li>○ Fertig and Stephan (2023)</li> <li>○ Fincham and Heyes (1983)</li> <li>! Fleckenstein et al. (2024)</li> <li>▽ priv. comm. Lopez Flores et al. (2021)</li> <li>▽ Galliéro and Boned (2008)</li> <li>× Ghimire and Adhikari (2017)</li> <li>★ Hammonds and Heyes (1988)</li> <li>▲ Heyes et al. (2019)</li> <li>▶ Heyes et al. (1993)</li> <li>◆ Heyes (1983)</li> <li>○ Heyes (1983)</li> <li>■ Heyes (1988)</li> <li>▲ Heyes (1987)</li> <li>◇ Heyes et al. (1980)</li> <li>○ Heyes and Powles (1990)</li> <li>◀ Hoheisel and Vogelsang (1988)</li> <li>▽ Ji (2022)</li> <li>× Kushick and Berne (1973)</li> <li>◆ Lee (2013)</li> <li>- Lee (2007)</li> <li>◇ Lee et al. (2003)</li> <li>○ Lee (2014)</li> <li>○ Lee (2014)</li> <li>○ Lee (2014)</li> <li>× Lee (2008)</li> <li>★ Levesque and Verlet (1970)</li> <li>◀ Marchioni et al. (2023)</li> <li>★ Marinakis and Samios (2005)</li> <li>Meier et al. (2004)</li> <li>◇ Meier et al. (2004)</li> <li>◆ Michels and Trappeniers (1975)</li> <li>■ Michels and Trappeniers (1978)</li> <li>◆ Changman Moon et al. (1991)</li> <li>○ Nuevo et al. (1997)</li> <li>○ Oderji et al. (2011)</li> <li>○ Ohtori and Ishii (2015)</li> <li>▲ Ohtori et al. (2017)</li> <li>! Pas and Zwolinski (1991)</li> <li>□ Pas and Zwolinski (1991)</li> <li>★ Rahman et al. (1964)</li> <li>★ Ramkumar et al. (2024)</li> <li>★ Rizk et al. (2022)</li> <li>! Rowley and Painter (1997)</li> <li>! Saric et al. (2024)</li> <li>★ Sarkar and Selvam (2007)</li> <li>▽ Schmitt et al. (2024)</li> <li>◇ Schofield (1973)</li> <li>★ Slepavicius et al. (2023)</li> <li>◀ Straub (1992)</li> <li>▲ Sun et al. (2007)</li> <li>◇ Toxvaerd (2021)</li> <li>■ Wei-Zhong et al. (2008)</li> <li>▲ Yeh and Hummer (2004)</li> <li>× this work</li> </ul>

**Figure 4:** Legend of the symbols used for each source throughout this chapter. Each line in the legend indicates one reference with a unique symbol and color combination.



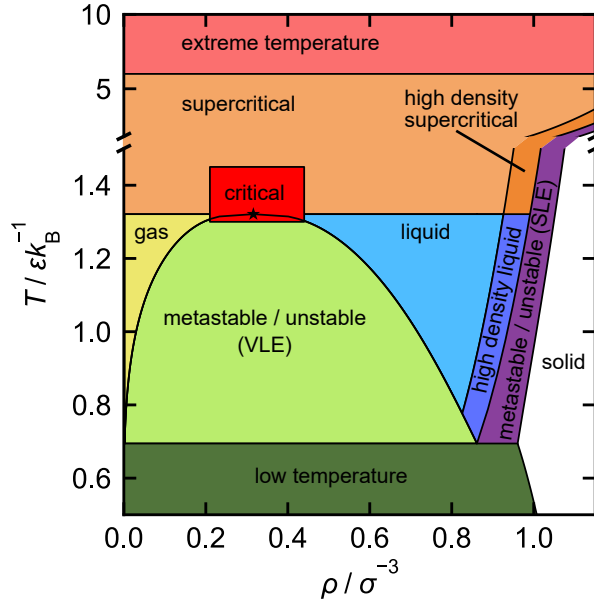


**Figure 5:** Definition of characteristic fluid regions (colored) of the LJ fluid used for the evaluation of the LJ transport property data: Metastable/unstable (MU), gas (G), liquid (L), critical (C), supercritical (Su), high density liquid (HD-L), high density supercritical (HD-Su), extreme temperature (Ex-T), low temperature (Lo-T), and metastable/unstable SLE (SLE). Details on the definitions of the boundaries of the regions are given in Ref. 234.

consensus on the level of detail of these meta data. A full specification seems infeasible – and be it only for practical reasons, given the limitations of a standard publication. In the vast majority of the considered publications, the meta data are far too vague to allow for a serious replication attempt. In the following, a list is presented of what was considered to be a good compromise between disclosing sufficient detail to reproduce essential features of the simulation on the one side and conciseness and feasibility on the other. For molecular simulations of transport data of bulk fluids, it is recommended to include the following meta data: Sampling method, production time, equilibration time, time step, software, ensemble, number of particles, cutoff radius, treatment of the long-range interactions, and handling of finite size effects. Moreover, for EMD simulations with the Green-Kubo method, the time correlation (TCF) length, the number of TCF functions, and the frequency in which the respective quantity is used in the TCF should be specified. In case of the Einstein method, the length of the slope, which was used for calculating the transport property should be stated. For NEMD simulations, details on the imposed gradients and the geometric setup should be provided. Moreover, details on the applied definition and computation of the statistical uncertainty should be provided.

The availability of these meta data was assessed in the publications from the compiled database (cf. Table 1). For this purpose, ten EMD studies and ten NEMD studies were randomly selected and evaluated with respect to the availability of the meta data. More

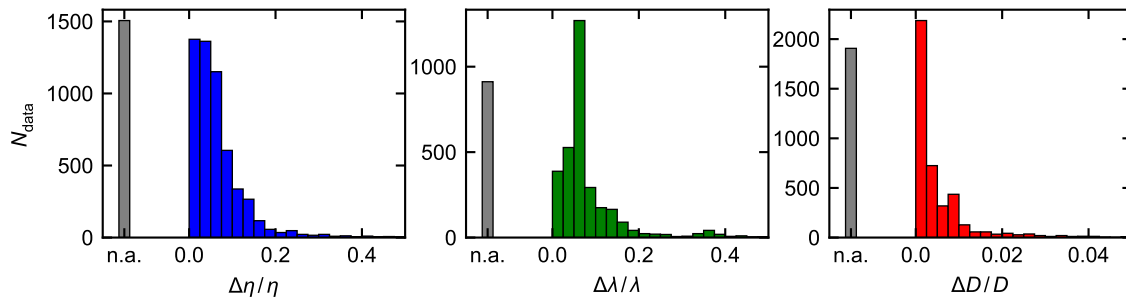


**Figure 6:** Histograms of the relative uncertainty of the data points for the viscosity  $\Delta\eta/\eta$  (left), the thermal conductivity  $\Delta\lambda/\lambda$  (middle), and the self-diffusion coefficient  $\Delta D/D$  (right). The grey bars (n.a.) represent the number of data points published without specifying uncertainty.

than 90 % of these studies (both EMD and NEMD) provided all general parameters, like the production time, time step, and number of particles. The equilibration time is only given in around 30 % of the studies. Around 80 % of the studies report the cutoff radius; but only 20 % specify the treatment of the long-range interactions explicitly. The applied software package is only mentioned by around 20 % of the publications, especially older publications often used unpublished in-house codes. Also, 50 % of the Green-Kubo studies specify the TCF length, the number of TCF, and the sampling frequency of the TCF. For the Einstein method studies, the length of the evaluated slope is only given in around 30 % of the publications. In all inspected NEMD studies, the applied gradient is given explicitly or implicitly by reporting the boundary conditions of the simulations. Unfortunately, several studies do not even report the numerical values of the transport property simulation results [100, 244–249]. In these cases, it was tried to obtain simulation data via private communications for the preparation of this work, but this approach is obviously tedious and limited. The digitization of data from papers from the literature, usually available in pdf file format, is a tedious and error-prone task. After a preliminary application of the outlier detection (see below), data points identified to be gross outliers as well as data sets with particularly high outlier rates were re-checked based on the respective publication. In some cases, copy-paste typos were found and corrected.

## 2.3 Assessment of the Data

The LJ fluid transport property data compiled in this work were assessed using two approaches with the aim of identifying outliers: (1) A model-based procedure was applied to the full data set using an entropy scaling model [52]. (2) The zero-density limit transport properties from Chapman-Enskog theory were used for the assessment of low-density data.

### 2.3.1 Outlier Detection for Homogeneous States

The data points reported in the database were assessed by the model distance-based outlier detection method (MoDOD) adapted from Refs. [73, 135]. The basic principle of the MoDOD test and how it is combined with the entropy scaling model from Ref. 52 is described in the following. The MoDOD test evaluates each data point individually by comparing it with a model value and computer experiment data in its vicinity. It is designed to make a binary decision: Either a data point is an outlier or not. The assessment is based on the relative deviation

$$\delta Y = \frac{Y_{\text{sim}} - Y_{\text{mod}}}{Y_{\text{mod}}} \quad \text{with } Y \in \{\eta, \lambda, D\}, \quad (2)$$

where  $Y_{\text{sim}}$  is the computer experiment value at a given  $T, \rho$  and  $Y_{\text{mod}}$  is the model value determined for the same  $T, \rho$ . In this chapter, the entropy scaling model from Ref. 52 in combination with the Kolafa-Nezbeda EOS [136] was used for obtaining  $Y_{\text{mod}}$  in the MoDOD test. Many EOS models are available for the LJ fluid. The one proposed by *Kolafa and Nezbeda* was found to yield the most accurate and robust description of the LJ fluid in a wide temperature and pressure range for describing both thermal and entropic properties [50, 234] so that it was used in this work. Fig. 1 shows that the entropy scaling model from Ref. 52 combined with the Kolafa-Nezbeda EOS [136] yields a good description of the transport properties of the LJ fluid. Especially for the self-diffusion coefficient, it yields a high accuracy in a large state range. Nonetheless, it should be pointed out that the global accuracy of the model is no prerequisite for its application in the MoDOD test.

To assess a given state point  $j$ , state points from its neighborhood were determined by means of the a weighted euclidean distance in the  $T - \rho$  plane (see Ref. 135 for details). The neighbors  $i = 1 \dots M_j$  were used for the assessment of the data point  $j$ , where the number of neighbors  $M_j$  is up to 20 (depending on the availability of data). The idea of the test is to compare the mean deviation of the  $M_j$  data points in the vicinity of the assessed data point  $j$  from the model and to identify  $j$  as an outlier if its deviation from the model is very different from the deviations of its neighbors. The measure  $P_j$  used to detect outliers by the MoDOD test is

$$P_j = \frac{\left| \delta Y_j - \text{median}_{i=1}^{M_j} (\delta Y_i) \right|}{\text{MAD}_j}, \quad (3)$$

where  $\text{MAD}_j$  is the mean absolute deviation defined as

$$\text{MAD}_j = k \cdot \text{median}_{i=1}^{M_j} \left( \left| \delta Y_i - \text{median}_{i=1}^{M_j} (\delta Y_i) \right| \right), \quad (4)$$

with  $k = 1.4826$  [73].  $MAD_j$  was used here as a measure for the average local deviation of the data points from the reference model. If  $P_j \geq P_{\max} = 4$ , data point  $j$  is identified as an outlier. Otherwise, the data point  $j$  is considered as 'confirmed' by the MoDOD method. The choice  $P_{\max} = 4$  is conservative, i.e. false outlier identifications are unlikely, but not excluded [135].

Fig. 7 shows the results of the MoDOD outlier assessment for each of the three transport properties. In total, for all considered transport property data, about 10 % were

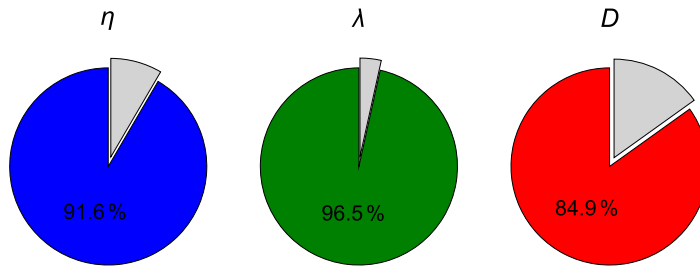


**Figure 7:** Pie charts of the share of confirmed data points of the total number of data points (colored areas) for shear viscosity  $\eta$  (left), thermal conductivity  $\lambda$  (middle), and self-diffusion coefficient  $D$  (right). The grey area represents the share of outlier data.

identified as outliers. Most outliers were identified for the self-diffusion coefficient, which is due to the fact that the literature data have relatively small statistical uncertainties and scatter little, so that the  $MAD_j$  is usually small and comparatively small deviations of data point  $j$  lead to its classification as an outlier. Also the handling of the finite-size correction is not consistent throughout the data due to a lack of reporting which can lead to systematic deviations. The fraction of data points that were identified as outliers does not vary strongly for the different regions in the phase diagram. Details are given in the Appendix A.

Fig. 8 shows some examples for the results for the MoDOD test for the three transport properties. The data for selected isotherms in the homogeneous region are shown and all data points identified as outliers are marked. For the three properties, the MoDOD test works well and is able to identify gross outliers. Despite the fact that the model exhibits some systematic deviations, e.g. for the shear viscosity and thermal conductivity at low pressure and high temperatures, the MoDOD test reliably and autonomously detects outlier data points. For the thermal conductivity, the simulation data exhibit more significant scatter compared to the self-diffusion coefficient. Therefore, the MoDOD test is only able to detect very gross outliers among the thermal conductivity data, whereas, for the self-diffusion coefficient, the MoDOD test acts more rigorously and detects dubious data even in cases where they deviate only slightly from the data in

their neighborhood.

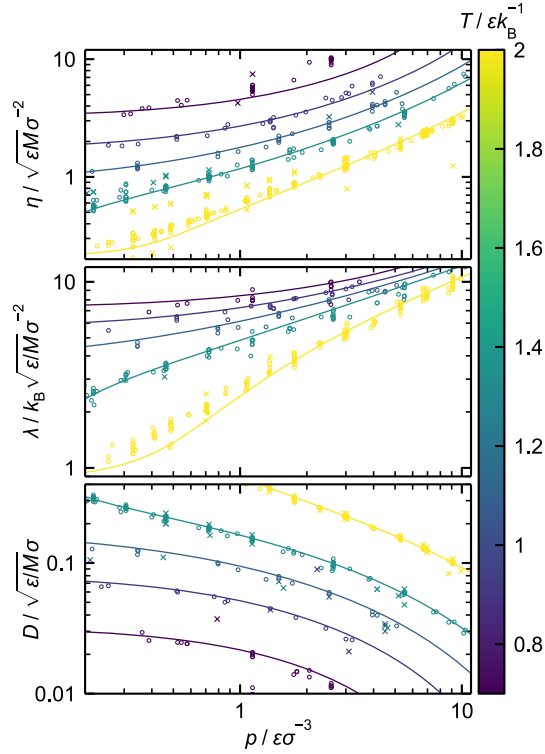


**Figure 8:** Examples for results of the outlier detection with the MoDOD test. Confirmed data points are solid circles, outliers are crosses. Data for the shear viscosity  $\eta$  (top), thermal conductivity  $\lambda$  (middle), and self-diffusion coefficient  $D$  (bottom) as a function of the pressure  $p$  for selected temperatures  $T \in \{0.7, 0.9, 1.1, 1.34, 2\} \varepsilon k_B^{-1}$  in a double-logarithmic plot. The temperature is color coded. Lines: Entropy scaling model. Symbols: Data that are at temperatures within  $\Delta T = \pm 0.02 \varepsilon k_B^{-1}$  of the isotherms.

### 2.3.2 Assessment by the Chapman-Enskog Zero-Density Limit

In the second assessment approach, the low density data were compared to the zero-density limit of the transport properties  $\eta$ ,  $\lambda$ , and  $D$  calculated analytically with the Chapman-Enskog theory, addressed as 'CE test' in the following. The zero-density limit of the Lennard-Jones fluid can be calculated with high accuracy from the Chapman-Enskog equations that originate from kinetic gas theory [124]. Based on Chapman-

Enskog theory, the transport properties in the zero-density limit are given by

$$\eta_{\text{CE}} = \frac{5}{16} \sqrt{\frac{M k_{\text{B}} T}{\pi}} \frac{1}{\sigma^2 \Omega^{(2,2)}} f_{\eta}^{(3)}, \quad (5)$$

$$\lambda_{\text{CE}} = \frac{75}{64} k_{\text{B}} \sqrt{\frac{k_{\text{B}} T}{M \pi}} \frac{1}{\sigma^2 \Omega^{(2,2)}} f_{\lambda}^{(3)}, \quad (6)$$

$$D_{\text{CE}} \rho = \frac{3}{8} \sqrt{\frac{k_{\text{B}} T}{\pi M}} \frac{1}{\sigma^2 \Omega^{(1,1)}} f_D^{(2)}, \quad (7)$$

where  $M$  is the particle mass and  $\Omega^{(1,1)}$  or  $\Omega^{(2,2)}$  are the collision integrals, which are a function of the temperature, i.e.  $\Omega^{(1,1)} = \Omega^{(1,1)}(T/\varepsilon k_{\text{B}}^{-1})$  and  $\Omega^{(2,2)} = \Omega^{(2,2)}(T/\varepsilon k_{\text{B}}^{-1})$ . The collision integrals were computed from an accurate empirical correlation that was developed by *Kim et al.* [126]. Therein, the uncertainty of the collision integral models was specified as  $\Delta\Omega = 0.007\%$  up to  $T = 400 \varepsilon k_{\text{B}}^{-1}$  [126]. The terms  $f_{\eta}^{(3)}$ ,  $f_{\lambda}^{(3)}$ , and  $f_D^{(2)}$  in Eqs. (5) - (7) are 3<sup>rd</sup> order (for shear viscosity and thermal conductivity) and 2<sup>nd</sup> order (for self-diffusion coefficient) correction terms. With these correction terms, the uncertainty of Eqs. (5) - (7) was reported to be below 0.01% [250, 251], which is significantly better than the simulation uncertainties (cf. Fig. 6).

For the CE test of a given data point  $Y_{\text{sim}}(T, \rho)$ , its relative deviation  $\delta_{\text{CE}}Y$  from the corresponding Chapman-Enskog value  $Y_{\text{CE}}(T)$  was computed:

$$\delta_{\text{CE}}Y = (Y_{\text{sim}} - Y_{\text{CE}})/Y_{\text{CE}} \quad \text{with} \quad Y \in \{\eta, \lambda, D\}, \quad (8)$$

where  $Y_{\text{CE}}$  was determined with Eqs. (5) - (7). The CE test was only applied to simulation data at densities  $\rho < 0.2 \sigma^{-3}$ . Starting at  $\rho \rightarrow 0$ , the Chapman-Enskog theory values  $Y_{\text{CE}}$  are expected to deviate from the simulation data with rising density. The magnitude of this deviation is not a priori known. For the assessment of the simulation data within the CE test, the deviations  $\delta_{\text{CE}}Y$  were initially described by the simple empirical function

$$\delta_{\text{CE}}Y^{(\text{expected})}(\rho) = a_Y (\rho/\sigma^3)^{b_Y}, \quad (9)$$

where  $a_Y$  and  $b_Y$  are adjustable parameters that were fitted for a given transport property  $Y \in \{\eta, \lambda, D\}$  to all simulation data with  $\rho < 0.2 \sigma^{-3}$  because no significant temperature dependence of the deviations from the CE values was observed. Outliers detected by the MoDOD test were not considered in this fit. The obtained parameters  $a_y$  and  $b_y$  are reported in the Appendix A. To detect outliers, two additional, empirical functions were defined as

$$f_1(\rho) = 3 \cdot a_Y (\rho/\sigma^3)^{b_Y} + c_Y, \quad (10)$$

$$f_2(\rho) = -c_Y, \quad (11)$$

providing an upper and lower threshold. Data points outside of this range were identified as outliers by the CE test. In Eqs. (10) - (11),  $c_Y$  is an empirical offset chosen as  $c_\eta = c_\lambda = 0.1$  for the shear viscosity and the thermal conductivity and  $c_D = -0.01$  for the self-diffusion coefficient, which reflects the statistical uncertainty and the scatter of the simulation data.

Fig. 9 shows the results of the CE test by plotting  $\delta_{\text{CE}}Y$  as a function of the density for all data points with  $\rho < 0.2 \varepsilon k_B^{-1}$ . It also depicts the curves describing the expected

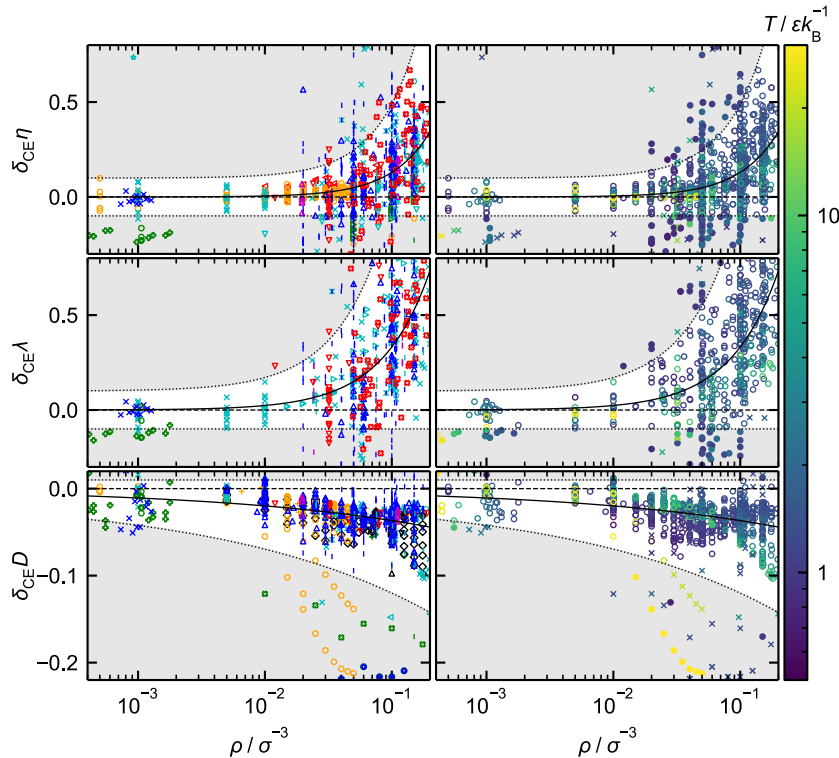


**Figure 9:** Results from the CE test. Relative deviations of the simulation data from Chapman-Enskog theory (cf. Eq. (9)) for the shear viscosity  $\delta_{\text{CE}}\eta$  (top), thermal conductivity  $\delta_{\text{CE}}\lambda$  (middle), and self-diffusion coefficient  $\delta_{\text{CE}}D$  (bottom) as a function of the density  $\rho$  (logarithmic scale) for  $\rho < 0.2 \sigma^{-3}$ . The solid line is the result of the empirical fit, cf. Eq. (9). The dotted lines indicate the upper and lower thresholds defined by Eqs. (10) - (11), containing the confirmed data points (white area). Data outside of this band (grey area), are outliers. Left column: Symbols as introduced in Fig. 4. Right column: Open circles are data points confirmed by both the CE test and the MoDOD test; solid circles are outliers identified only by the CE test and crosses in the white area are outliers identified only by the MoDOD test; crosses located in the grey area were identified as outliers by both methods. Color indicates the temperature.

deviations as well as the thresholds. For all three properties, the deviation to the zero-density limit  $\delta_{\text{CE}}Y$  decreases for  $\rho \rightarrow 0$ , as expected. The deviations  $\delta_{\text{CE}}Y$  are significantly smaller for the self-diffusion than for the other two properties. The vast

majority of the simulation data lies in the threshold band defined by Eqs. (10) - (11). Data points outside of this band were identified as outliers by the CE test. For the shear viscosity, the number of outliers above and below the band is roughly the same. For the thermal conductivity and the self-diffusion coefficient, the number of outliers below the band is significantly larger than that above the band.

With the CE test, 271, 99, and 159 outliers were detected among the shear viscosity, thermal conductivity, and self-diffusion coefficient data, respectively. Fig. 10 shows the share of the confirmed data points and outliers identified by the CE method and the MoDOD test for all three transport properties. The results from the MoDOD outlier

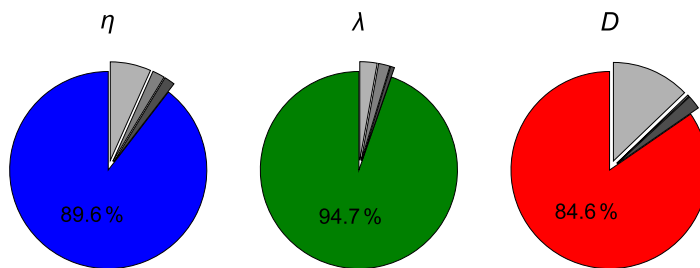


**Figure 10:** Pie charts of the share of confirmed data points (colored areas) and outliers identified by the MoDOD test alone (light grey), the CE test alone (grey), and by both tests (dark grey) for the shear viscosity  $\eta$  (left), thermal conductivity  $\lambda$  (middle), and self-diffusion coefficient  $D$  (right).

detection agree overall well with the results from the CE test. For the shear viscosity and the thermal conductivity, the CE test identified a significant amount of data points as outliers that were not identified by the MoDOD test. For the self-diffusion coefficient, few outliers were identified only by the CE test, cf. Fig. 10. This is due to the small statistical uncertainties of the self-diffusion data, which allow for a more rigorous outlier detection with the MoDOD test. For the shear viscosity and the thermal conductivity, the CE test identified several data points as outliers that were not identified as such by the MoDOD test. Due to the use of the known behavior of the transport properties in the zero-density limit  $\rho \rightarrow 0$ , the CE test can be used in an overall more rigorous way than the rather conservative MoDOD test. Thus, using the zero-density limit allows for an additional designation of gross outliers based on physical knowledge that reasonably complements and confirms the MoDOD test. For the final data evaluation, data points were identified as outliers if at least one of the two tests identified it as such. In the following, 'outliers' refer solely to that aggregated evaluation.



## 2.4 Discussion

Fig. 11 shows the relative deviations  $\delta Y$  (cf. Eq. (2)) of the entropy scaling model and the simulation data for the shear viscosity, thermal conductivity, and self-diffusion coefficient, respectively. Only the confirmed simulation data is depicted in Fig. 11.

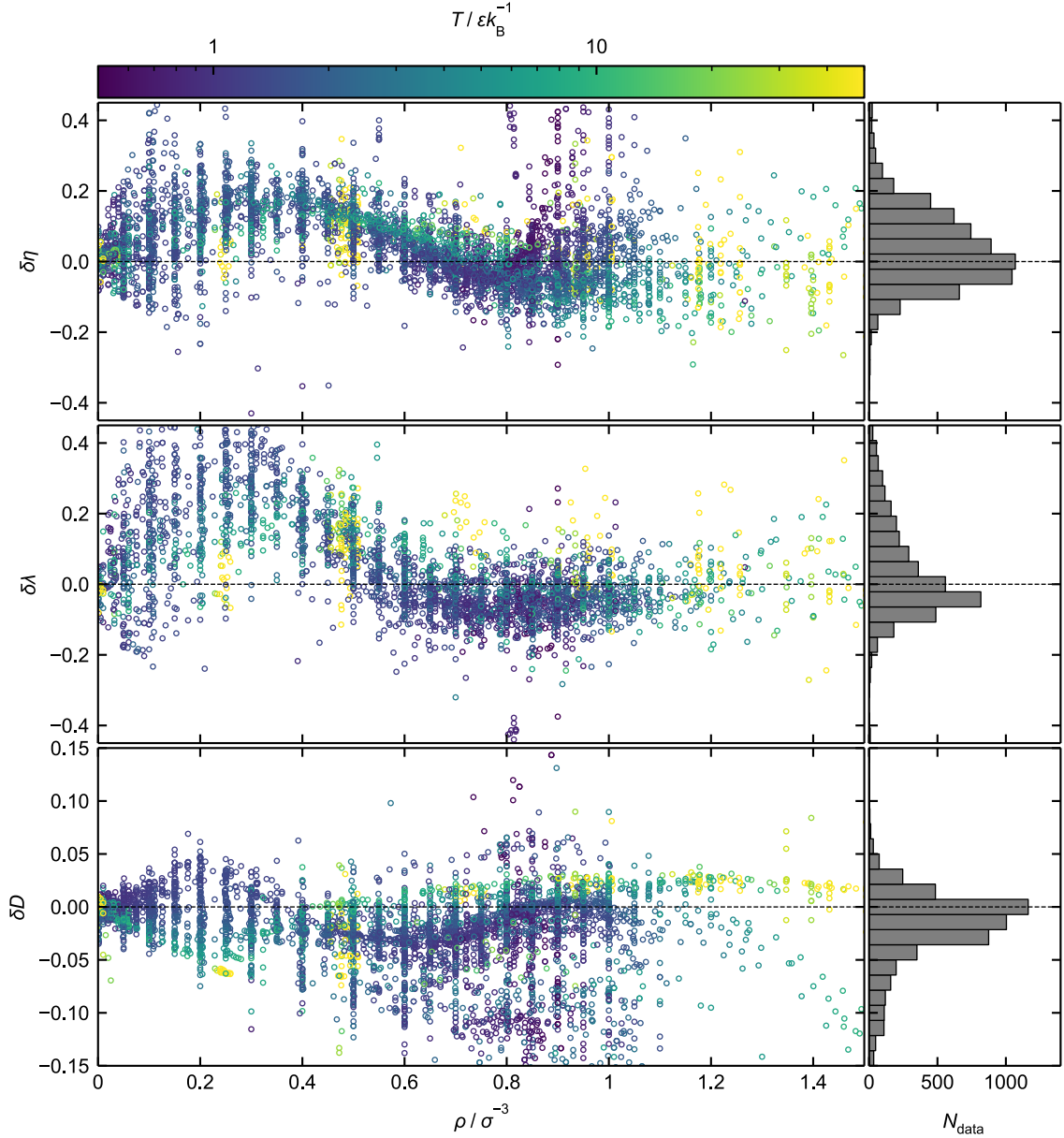


**Figure 11:** Relative deviation of the simulation data from the entropy scaling model for the shear viscosity  $\delta\eta$  (top), thermal conductivity  $\delta\lambda$  (middle), and self-diffusion coefficient  $\delta D$  (cf. Eq. (2)) as a function of the density (left) and corresponding histograms of the relative deviations (right). Only confirmed data are shown. The dashed line represents the entropy scaling model. Error bars are omitted to avoid visual clutter. The color indicates the temperature.

These deviation plots can be used to assess the availability and quality of the simulation

data. They also confirm that the entropy scaling model describes the simulation data robustly in the entire, very wide range of states for which data are available. A discussion of details of the performance of the entropy scaling model is not entered here, the focus lies solely on the simulation data here. The intention of Fig. 11 is to visualize the data such that dubious data points become visible and give an impression of their scatter. A similar representation of the relative deviations  $\delta Y$  with an encoding of the publication including the outliers is discussed in the appendix (Figs. A.1 - A.3).

For the shear viscosity and the thermal conductivity (cf. Fig. 11 top and middle), most of the data points scatter within  $\pm 20\%$  from the entropy scaling model. For the self-diffusion coefficient (Fig. 11 bottom), the deviations are significantly smaller, mostly within  $\pm 5\%$ . This corresponds to the magnitude of the given uncertainties for the three transport properties which behave similarly (cf. Fig. 6). The deviations are independent of temperature for all three properties. Some data sets can be highlighted that contain many data points with a small number of outliers for the shear viscosity [171, 183, 194, 196, 197, 199, 202], thermal conductivity [114, 153, 199, 202, 211], and self-diffusion coefficient [52, 118, 183, 199]. These collections of data sets cover a wide range of state points and provide good accuracy. In the Appendix A, they are plotted analogously to Fig. 11.

## 2.5 Conclusions

In this chapter, molecular simulation data for the Lennard-Jones fluid, i.e. shear viscosity, thermal conductivity, and self-diffusion coefficient, were collected, reviewed, and assessed. The transport property data (around 17,000 data points) were digitized, evaluated, and provided as a consistent database to complement the Lennard-Jones database on (time-independent) thermodynamic properties [73]. This database contains data in all fluid regions, including gaseous, liquid, and supercritical states as well as the vapor-liquid and the solid-liquid metastable regions. Approximately 11 %, 5 %, and 16 % of the shear viscosity, thermal conductivity, and self-diffusion data points, respectively, were identified as outliers by the applied tests. For the assessment of the data quality, two tests were applied, namely the MoDOD test [135] that was coupled with an entropy scaling model and a test procedure based on the Chapman-Enskog zero-density limit of the transport properties. The detected outliers are homogeneously and randomly distributed across the different fluid regions. The relatively large ratio of outliers identified among the self-diffusion coefficient data can be attributed to the fact that the outlier detection can be applied in a more rigorous way due to the high overall accuracy of the self-diffusion coefficient data. This is expressed by the relatively small statistical uncertainty as well as by small deviations to the model (which are connected).

---

The transport properties of the Lennard-Jones fluid are of high interest since its potential model was originally proposed [66, 71]. Consequently, many studies have examined the transport properties of the Lennard-Jones fluid. The present chapter summarizes knowledge on the transport properties of Lennard-Jonesium and provides high quality benchmark data. It thereby also contributes to determining the reproducibility of transport properties by molecular simulation. Systematic uncertainties between the results from different studies, i.e. based on different sampling methods, simulations codes, hardware, etc. were identified. Since the Lennard-Jones fluid can be considered as one of the simplest molecular models, these systematic uncertainties can be considered as a lower limit to what has to be expected for more complex real substance molecular models.



# 3 Evaluation of Force Fields for the Simulation of Thermophysical Properties of Long Alkanes

## 3.1 Introduction

Thermophysical properties of lubricants at extreme pressures are highly important for the design of processes in mechanical engineering [12]. Especially the density and the transport properties determine the performance of the lubricant in the lubrication gap. The pressure in tribological systems with small contact areas are often higher than 1,000 MPa [2]. For such conditions, experimental data are rare due to high costs and complexity of the measurements [252]. Hence, reliable predictive models are needed. Molecular simulation is an attractive method for this.

Molecular dynamics (MD) simulations have been used often for the prediction of thermophysical bulk properties of lubricants [19, 253–259], wetting, and interfacial properties on solid walls [59, 260–262], as well as for the simulation of tribological contact processes [263–270]. Simulations of lubricants usually aim at predicting transport properties, in particular the viscosity, using either equilibrium molecular dynamics (EMD) [62, 112, 271–273] or non-equilibrium molecular dynamics (NEMD) simulations [255, 274–277]. Both methods are challenging: EMD simulations require a large computational effort to compute the viscosity, especially for higher viscosities due to the slow convergence of the auto correlation function (ACF) [84]. In NEMD simulations, the shear rate has to be small enough to reach the Newtonian regime which can require very long simulation times due to the bad signal-to-noise ratio at small shear rates [87]. As the viscosity becomes very large at high pressures [278], the prediction of transport properties at high pressures is a challenging task with high computational costs. Special methods have been applied for tackling this task, such as the time decomposition method [84].

MD simulations of lubricants require force fields that model the inter- and intramolecular interactions. Especially for the quantitative prediction of bulk properties, the choice of

an adequate force field is crucial. There is a large number of different force fields that can be used for modeling lubricants [63, 279, 280]. The choice of the force field is not trivial as different force fields have different strengths and weaknesses, and comparisons on equal terms are usually difficult from the information that is available in the literature alone. The most important attribute of the force field is its the ability to predict the target properties with the desired accuracy. Another attribute is the type of the force field, i.e. the approach that is taken to model the atomistic architectures and their interactions. This is decisive for the computational cost but also relevant for the choice of the simulation tool, as not all programs can handle all types of force fields. Three different basic modeling levels are distinguished in the present chapter (cf. Fig. 12): all-atom (AA), united-atom (UA), and coarse-grained (CG) force fields.

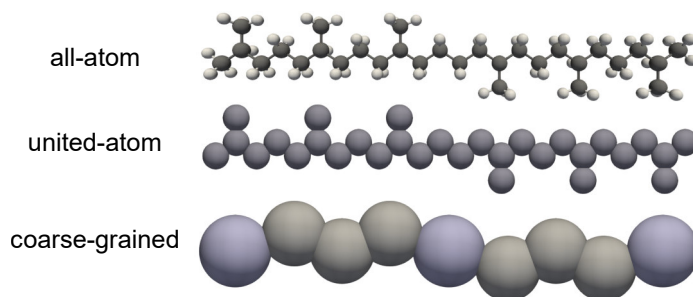


**Figure 12:** Sketch of a squalane molecule modeled by the different types of force fields.

In AA force fields, every atom is assigned to an individual interaction site. They are also often called 'explicit hydrogen' models. In contrast, UA force fields assign multiple atoms to a single interaction site. Usually, methylene and methyl groups are modeled by a single interaction site. The modeling by CG force field goes a step further and chain segments of multiple heavy atoms are combined to a single interaction site. For AA force fields, two subtypes can be further distinguished: (i) reactive AA force fields, which explicitly model chemical bonds (that can form and break during the simulation), and (ii) classical AA force fields, which are built using intramolecular potentials that do not break, e.g. a harmonic potential.

Nine force fields were applied in the present chapter for the modeling of five linear and branched alkanes, which are typical components of poly- $\alpha$ -olefines (PAO) or used as simple model lubricants. PAOs are an important group of lubricants [281]. The substances include the three linear alkanes *n*-decane ( $C_{10}H_{22}$ ), *n*-icosane ( $C_{20}H_{42}$ ), and *n*-triacontane ( $C_{30}H_{62}$ ) as well as two isomers of *n*-triacontane: 1-decene trimer and squalane (both  $C_{30}H_{62}$ ). The chemical structures of the five substances investigated in this chapter are depicted in Fig. 13. In the following, the substances are abbreviated as *n*-C10, *n*-C20, *n*-C30, TRI, and SQU (cf. Fig. 13). Hence, the study comprises alkanes with different chain lengths as well as different structure for a given molecular

Name	Structural formula	Chemical formula
<i>n</i> -decane ( <i>n</i> -C10)		C <sub>10</sub> H <sub>22</sub>
<i>n</i> -icosane ( <i>n</i> -C20)		C <sub>20</sub> H <sub>42</sub>
<i>n</i> -triacontane ( <i>n</i> -C30)		C <sub>30</sub> H <sub>62</sub>
1-decene trimer (TRI)		
squalane (SQU)		

**Figure 13:** Overview of substances included in this chapter.

formula. The molecule 1-decene trimer is the simplest (long branched) representative of poly-(1-decene) and it is an important component of PAO base oils [281]. Squalane (SQU) is frequently used as a model lubricant in experiments [274, 282] and also an important substance in cosmetics [283]. The predictions for the density, the viscosity, and the self-diffusion coefficient of these substances were systematically compared to experimental data. Moreover, the computational costs of the different force fields were assessed. The study covers pressures up to 400 MPa, the temperature is always 373.15 K. The properties of lubricants at high pressure are of particular interest due to the high pressure conditions occurring in tribological applications [2]. Furthermore, the linear alkanes are common components of diesel fuels, whose properties at high pressure are also of high practical interest [284].

Comparisons of different force fields have been published for a wide variety of substances. They address the prediction of phase equilibria [285, 286] as well as bulk properties like the density [272, 273, 280, 287–290], isothermal compressibility [280, 286], and the speed of sound [287]. In some of the works, the ability of the force fields to predict thermophysical properties at elevated temperatures and pressures was explicitly addressed [64, 289, 291]. Studies explicitly addressing the properties of lubricants are sparse. *Lin et al.* calculated the density and viscosity of a polyol ester (POE) lubricant at ambient pressure with three different force fields and compared them to experimental data [290]. *Ewen et al.* compared ten UA and AA force fields in their ability to predict the density and the viscosity of *n*-hexadecane up to 200 MPa [273]. The viscosity and the self-diffusion coefficient of branched alkanes as model lubricants have been studied by *Kondratyuk et al.* [272]. A broad systematic comparison of force fields of different types regarding their ability to predict properties that are important for lubrication, i.e. density and viscosity, up to high pressures was, however, not available up to now. This gap is closed by this work.

The different force fields lead to different computational costs of the molecular simulations. For example, the number of interaction sites per molecule varies for different

force fields and has a strong influence. The computational costs normally scale linearly with the number of interaction sites for systems without electrostatic interactions [292]. With AA force fields, the number of interaction sites is approximately three times higher compared to UA force fields for alkanes. As CG force fields combine multiple UA sites to one site, the computational are further reduced. Another advantage of coarser modeling of the molecular structure consists of preventing high frequency oscillations (e.g. CH stretching bonds), which enables a larger time step. Furthermore, the type of interaction potentials to be evaluated strongly influences the computational costs, for example multibody or electrostatic interactions increase the computational time considerably [293, 294]. Overall, multiple factors influence the computational cost of a simulation with a given force field and the costs can not be predicted a priori. Presently, no systematic comparison of the computational costs of different transferable force field types is available.

The following text is organized as follows: first, the methodology of the study is described which includes details of the conducted simulations, the sampling of the observables, information on the applied force fields, and the methods applied for the evaluation of the results. Then, the results for the three examined properties, the density, the viscosity, and the self-diffusion coefficient, for all studied substances are presented and discussed. Thereafter, the computational costs of simulations with different force fields are compared. Finally, conclusions are drawn.

## 3.2 Methodology

### 3.2.1 Simulation Details and Evaluation

Equilibrium molecular dynamics simulations were carried out to calculate the density, the viscosity, and the self-diffusion coefficient of the studied pure substances. A cubic simulation box with periodic boundary conditions was used. The number of particles was chosen such that there were at least 200 molecules or 4000 interaction sites. The finite size dependency of the simulations was assessed by simulations with different numbers of molecules and extrapolating to the thermodynamic limit ( $N \rightarrow \infty$ ). Details are given in the Appendix B. The results show that no significant finite size dependency applies to the results. The time step and integrator were chosen depending on the force fields and are summarized in Table 2. For the AA force field (excluding the reactive force fields), the RESPA multiple timestep method was used to reduce the computational costs. Thereby, the simulation time was reduced by a factor of at least 8 compared to the classical Velocity Verlet integrator with a time step of 0.25 fs. Details are given in



**Table 2:** Time step and integrator used in the simulations.

Force field type	Time step / fs	Integrator
AA	0.25 (bonds, angles), 0.5 (dihedrals), 1 (nonbonded)	RESPA [295]
AA (reactive)	0.25	
UA	0.5	Velocity-Verlet [14]
CG	10	

the Appendix B. The cutoff radius was set to 14 Å throughout. An analytical long-range correction for the pressure was applied for the dispersive interactions [14]. Rigid bonds were realized using the SHAKE algorithm [296]. The electrostatic interactions were calculated by the particle-particle particle-mesh algorithm [297]. All simulations were carried out with the LAMMPS package (Version 3 March 2020) [298]. The initial configuration was built up by randomly inserting molecules into the box. For the reactive force fields, the molecules were inserted on a lattice to eliminate overlapping, which could lead to false molecule geometries as the geometry of the molecule is only given by the initial position. This insertion was done at a low density to avoid unphysical overlapping. Subsequently, the energy of the system was minimized by moving the particles to avoid large forces at the start of the MD simulations. After the energy minimization, the box volume was reduced to the target density within a short MD run of 100 ps. After this initialization phase, the actual simulations started.

For each substance and force field, five state points were studied. The pressures were  $p \in \{0.1, 10, 100, 200, 400\}$  MPa and the temperature was  $T = 373.15$  K in all cases. The density was determined by  $NpT$  simulations. The Nosé-Hoover thermostat and barostat [299–301] were used to control the temperature and the pressure in the simulations. The damping times comprised 100 timesteps for the thermostat and 1000 timesteps for the barostat, as recommended in the LAMMPS documentation [298]. Each  $NpT$  simulation had an equilibration time of 1 ns and a production time of 2 ns. To ensure that the simulation is sufficiently long enough, longer simulations have been run. More details are given in the Appendix B. To reduce the statistical uncertainty, each  $NpT$  simulation was replicated five times and the density of each state point was calculated as the average of these five replica simulations. This density was then taken as input for  $NVT$  simulations to determine the viscosity and the self-diffusion coefficient. To calculate the transport properties, 20 independent  $NVT$  simulations were carried out for each state point. The equilibration time was 1 ns. The production time varied from 2 to 10 ns and was determined individually for each state point and substance, and was chosen to obtain convergence of the correlation functions. Details are summarized in Table 3.

**Table 3:** Simulation times in ns for the different substances and state points.

$p/\text{MPa}$	Substance		
	$n\text{-C10}$	$n\text{-C20}$	$n\text{-C30, TRI, SQU}$
0.1	2	3	4
10	2	3	4
100	2	4	6
200	2	6	8
400	4	6	10

The viscosity was calculated using the Green-Kubo relations [97, 98] given by

$$\eta(\tau) = \frac{1}{Vk_{\text{B}}T} \int_0^{\tau \rightarrow \infty} \langle J_{\text{p}}^{\alpha\beta}(t + \tilde{\tau}) \cdot J_{\text{p}}^{\alpha\beta}(t) \rangle d\tilde{\tau}, \quad (12)$$

where  $V$  is the box volume,  $k_{\text{B}}$  the Boltzmann constant,  $T$  the temperature,  $t$  the reference time,  $\tau$  the time variable, and  $J_{\text{p}}^{\alpha\beta}$  the non-diagonal entries of the stress tensor [14]. The pressure tensor was sampled every 4 fs during the  $NVT$  simulations. Each of the sampled time steps was taken as reference time  $t$  to achieve best possible statistics. The time decomposition method (TDM) [84] was applied in this work, which enables the reliable calculation of high viscosities by EMD simulations. Therefore, the viscosity time evolution  $\eta(\tau)$  was calculated for all 20  $NVT$  simulations during the production run. For the calculation of the ACF, a fast Fourier transform (FFT) technique was used [302]. Contributions from all six independent entries of the pressure tensor  $p_{\alpha\beta}$  were averaged to calculate the viscosity as proposed by Ref. [303]. The cutoff time  $\tau_{\text{cut}}$  for the ACFs (to circumvent the ACF long-term noise) were determined from the standard deviations  $\sigma_{\eta}(\tau)$  as  $\frac{\sigma_{\eta}(\tau_{\text{cut}})}{\eta(\tau_{\text{cut}})} = 0.4$  as recommended in Ref. [84]. Different numbers  $\frac{\sigma_{\eta}(\tau_{\text{cut}})}{\eta(\tau_{\text{cut}})}$  for the cutoff time have been compared in the Appendix B. The bootstrapping method [84] with 200 iterations was used to calculate the final value and its uncertainty for the viscosity. Therefore, 200 combinations of the 20 simulations were created randomly whereas multiple appearances of individual simulations were allowed. For each combination, an average viscosity  $\bar{\eta}(\tau)$  was calculated and the function given in Eq. (13) was fitted to  $\bar{\eta}(\tau)$  where  $\eta_{\infty}$  is the long term limit.

$$\eta(\tau) = \eta_{\infty} \frac{\alpha\beta_1 \left(1 - e^{-\frac{\tau}{\beta_1}}\right) + (1 - \alpha)\beta_2 \left(1 - e^{-\frac{\tau}{\beta_2}}\right)}{\alpha\beta_1 + (1 - \alpha)\beta_2} \quad (13)$$

Fig. 14 illustrates the TDM method for two state points showing the viscosity sampled during the production phase  $\eta(\tau)$ . The results for all 20 simulation replica are shown. The two simulations have different cutoff times  $\tau_{\text{cut}}$ , which compensates differences of long-term noise behavior. On the right-hand side of Fig. 14, also the final values and

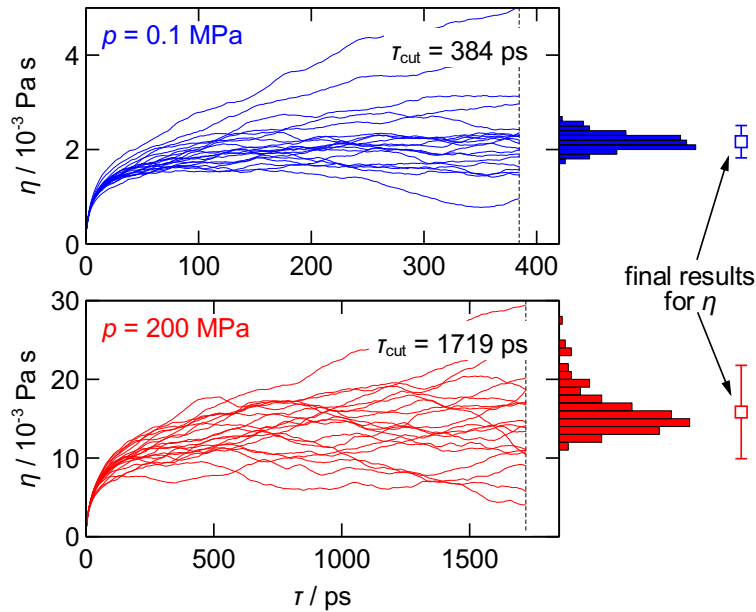


**Figure 14:** Illustration of the TDM method. Results for the sampled viscosity from 20 independent runs  $\eta(\tau)$  over time  $\tau$  of TRI at  $p = 0.1$  MPa (top) and  $p = 200$  MPa (bottom) ( $T = 373.15$  K for both). Histograms of the corresponding bootstrapping results and the final result of the bootstrapping method.

the histograms consisting of 200  $\eta_\infty$  values as obtained from the bootstrapping method are shown. The statistical uncertainties were computed from the histogram as the 95 % confidence interval. The individual results for  $\eta(\tau)$  show in parts a wide scattering that increases with time, which is a well-known phenomenon [304]. The time required to reach a stable plateau of the viscosity differs strongly which can also be seen by the different cutoff times. Overall, the TDM method provides relatively low statistical uncertainties and enables a reliable calculation of the viscosity.

The self-diffusion coefficient  $D$  was calculated by the Einstein relation [14]

$$D = \lim_{\tau \rightarrow \infty} \frac{d}{d\tau} \frac{1}{6} \left\langle \frac{1}{N} \sum_{i=1}^N |\mathbf{r}_i(t + \tau) - \mathbf{r}_i(t)|^2 \right\rangle, \quad (14)$$

where  $N$  is the number of particles in the box and  $\mathbf{r}_i$  is the position vector of center of mass of the molecule or particle  $i$ . A calculation of the self-diffusion coefficient by the Green-Kubo relation and the TDM method was not feasible as it would require to write out the velocity vector of all atoms with a high frequency. The Einstein relation requires the positional data of all atoms less frequently. The positional data were written out every 10 ps. The term  $|\mathbf{r}_i(t + \tau) - \mathbf{r}_i(t)|^2$  is the mean squared displacement (MSD). It is possible to calculate the MSD either from the atomic or the molecular center of mass [305]. In this chapter, the molecular center of mass was used. The MSD was calculated by making use of the FFT method [302]. The self-diffusion coefficient  $D$  was calculated

individually for each  $NVT$  simulation using Eq. (14). By averaging the results of the 20 independent simulations, a single value for  $D$  was obtained for every state point. The statistical uncertainty of  $D$  was calculated as the standard error as

$$\Delta D = \sqrt{\frac{1}{N_{\text{rep}}} \sum_{i=1}^{N_{\text{rep}}} (D_i - D)^2}, \quad (15)$$

with  $N_{\text{rep}} = 20$ . The self-diffusion is subject to finite size effects that are not negligible [306]. There are two methods to obtain the self-diffusion coefficient in the thermodynamic limit (i.e. infinite box size). The classical brute force approach is conducting multiple simulations with different box sizes and extrapolating to the thermodynamic limit. This is not feasible in this chapter since a large number of state points and force fields are studied. Instead, the analytical correction term proposed by *Yeh and Hummer* [122] was applied as

$$D_{L \rightarrow \infty} = D(L) + \frac{k_{\text{B}} T \xi}{6\pi\eta L}, \quad (16)$$

where  $L$  is the box length of the simulation,  $\eta$  the viscosity, and  $\xi = 2.837297$  is a dimensionless constant (adopted from Ref. [122]).

### 3.2.2 Force Fields

Table 4 gives an overview of the force fields studied in this chapter and their assignment to force field classes. All force field parameters used in this chapter and validations of the implementations are given in the Appendix B.

**Table 4:** Overview of all force fields used in this chapter.

Name	Type	Refs.	Published
OPLS	AA	[34]	1996
COMPASS	AA	[35]	1998
L-OPLS	AA	[307]	2012
ReaxFF	AA (reactive)	[308]	2001
AIREBO-M	AA (reactive)	[309]	2015
TraPPE	UA	[37, 310]	1998
Potoff	UA	[38, 311]	2009
TAMie	UA	[39, 312]	2015
MARTINI	CG	[313]	2007

### All-atom Force Fields (AA)

In this chapter, the AA force fields COMPASS [35], OPLS [34], L-OPLS [307], ReaxFF [314], and AIREBO-M [309, 315] were used. The latter two force fields are so-called reactive all-atom force fields that allow bond breaking. However, no bond breaking was observed in the simulations carried out in this chapter, hence, no special distinctions from the other all-atom force fields are necessary here. All AA force fields except AIREBO-M include Coulomb interactions. The COMPASS force field models the dispersive interactions by a 9-6 Mie potential. The intramolecular interactions include bonds, angles, dihedrals, impropers as well as cross terms, which include mixed bond, angle, and dihedral contributions. The parameters of the COMPASS force field were determined from a fit to quantum-mechanical (QM) data (charges and intramolecular potentials) and to liquid state properties (dispersive potential) [35]. In the OPLS force field, the classical Lennard-Jones (LJ) 12-6 potential is used for modeling the dispersive interactions. The bond and angle parameters of the OPLS force field were adopted from the CHARMM/22 force field [34, 36]. The torsional and the dispersive parameters were fitted to QM data and different thermodynamic and structural properties, respectively. The L-OPLS force field adopts the majority of the OPLS parameters but dihedral and dispersive parameters as well as the charges were refined to improve the modeling of longer hydrocarbons [307]. Additionally, the bonds between carbon and hydrogen were constrained to a constant distance in the L-OPLS force field. It is known that the L-OPLS provides better predictions for bulk properties compared to the OPLS force field [273]. As the OPLS force field is still widely used in its original version, it was also included in this chapter.

The ReaxFF [314] and AIREBO-M [309, 315] force fields include explicit calculations of the bond order, which enables them to model chemical reactions [293]. The *CHON-2017\_weak* version of the ReaxFF force field [308] was implemented in this chapter. It includes parameter adjustments that aim at improving the density prediction of the condensed phase [308]. The AIREBO-M force field [309] was derived from the AIREBO force field [315] by replacing the LJ potential interactions by a Morse potential. Its parameters were adjusted to layer spacing of graphite up to pressures of 14 GPa and to QM data of small alkanes. Both reactive force fields were only applied to *n*-decane (*n*-C10) in the present chapter due to their extremely high computational costs.

### United-atom Force Fields (UA)

The TraPPE [37], Potoff [38], and TAMie [39] UA force fields were used in this chapter. The TraPPE force field uses the classical 12-6 LJ potential. These LJ parameters were fitted to critical temperatures and saturated liquid densities. The Potoff and the TAMie

force fields use  $n$ -6 Mie potentials for the non-bonded interactions. In both force fields, the repulsive parameter  $n$  of the Mie potential was additionally adjusted in the fitting procedure. For the TAMie and the Potoff force fields, the non-bonded parameters were fitted to saturated liquid densities and vapor pressures. The cutoff distance of the Potoff force field was set to 10 Å as recommended [38]. In contrast to the AA force fields, there are no Coulomb interactions for UA models of hydrocarbons as all interaction sites are electrostatically neutral. In this chapter, flexible bonds between the interaction sites were applied. Therefore, a harmonic potential was used with the given bond length as equilibrium bond length. The energy parameter of the bond potential was taken from the OPLS force field. Despite the fact that the TraPPE, Potoff, and TAMie force fields were originally developed using rigid bond lengths, it is common practice to adapt them with flexible bonds [316–318]. Moreover, it was shown that the flexible bonds do not influence the results if the bond force constant is well chosen [94, 291]. The angle and dihedral potentials are the same for all three UA force fields as they were mainly adopted from the OPLS-UA [33] and OPLS-AA [34] force fields.

### Coarse Grained Force Field (CG)

In this chapter, the MARTINI CG force field was used. There are two approaches to parameterize CG force fields: bottom-up by derivation from a finer resolved force field (e.g. AA) and top-down by fitting parameters directly to experimental data [319]. The MARTINI force field [313] is based on the top-down approach. It was parameterized to the free energy of hydration and vaporization as well as the partitioning free energies between water and multiple organic substances [313]. A four-to-one mapping is applied by the MARTINI force field in general, which means four heavy atoms (all atoms except hydrogen atoms) are fused to a single interaction site. The force field consists of the LJ potential for non-bonded parameters and harmonic potentials for the angle and bond interactions. There are no dihedral potentials. The mapping of molecules to CG beads is not strictly defined. There are several methods to create CG models from a given molecular topology [320–322]. In this chapter, the automatic mapping algorithm from *Potter et al.* [322] was applied. As the mapping may in general have an influence on the force field predictions, the MARTINI results should be considered as results obtained from "MARTINI + Potter mapping". For brevity, only "MARTINI" is used in the following. The bond lengths of the created models were adjusted as suggested in Ref. [322] for the prediction of thermodynamic bulk properties. The MARTINI 2 [313] version was used in this work instead of the recently published MARTINI 3 force field [323] as the MARTINI 2 version has been widely applied in recent years – and as different auxiliary tools are available for MARTINI 2.

### 3.2.3 Data Analysis

The simulation results for the density, the viscosity, and the self-diffusion coefficient were analyzed in a consistent way as described in the following. As a basis, correlations to all available experimental literature data were developed. An overview of the available data for the five considered substances and the three considered thermophysical properties is given in Table 5. The functions, parameters, and accuracy of the corre-

**Table 5:** Overview of available experimental literature data (references given) and the corresponding maximum pressures for the different substances and properties examined in the current study. "n.a." indicates that no literature data were found.

	$\rho$		$\eta$		$D$	
	Ref.	$p/\text{MPa}$	Ref.	$p/\text{MPa}$	Ref.	$p/\text{MPa}$
<i>n</i> -C10	[324–327]	279	[325, 328]	300	[329]	200
<i>n</i> -C20	[330, 331]	500	[332]	243	n.a.	
<i>n</i> -C30	[330]	500	n.a.		[333]	600
TRI	n.a.		[278]	1298	n.a.	
SQU	[282, 334–337]	243	[278, 338]	1298	n.a.	

lations are reported in the Appendix B. They represent the experimental data within relative deviations of up to 0.3 % ( $\rho$ ), 5.2 % ( $\eta$ ), and 2.6 % ( $D$ ). Furthermore, also correlations for the properties where no experimental data was available are provided in the Appendix B. These correlations were created on the basis of the simulation data of the Potoff force field (which turns out to be clearly the most accurate force field among those studied here). Their parameters are also reported in the Appendix B. For the assessment of the force fields with respect to the experimental data, the deviations of the simulation results to the correlations of the experimental data were calculated from

$$\delta Y_{\text{exp}} = \frac{Y_{\text{sim}} - Y_{\text{corr}}}{Y_{\text{corr}}} \quad \text{for } Y \in \{\rho, \eta, D\}. \quad (17)$$

The total average deviation  $\overline{\delta Y}$  of a force field was calculated as the mean value of  $|\delta Y_{\text{exp}}|$  ( $Y \in \{\rho, \eta, D\}$ ) averaged over all state points and substances for which experimental data were available (cf. Table 5).

### 3.3 Results

In the following, the simulation results for the density  $\rho$ , the viscosity  $\eta$ , and the self-diffusion coefficient  $D$  are presented and discussed. Where available, also the experimental data is included in the discussion. Furthermore, correlations of the experimental data (cf. Section 3.2.3) are shown and used as a reference for the deviation plots. Where no experimental data were available, a correlation of the simulation data of the Potoff force field were used as a reference. Fig. 15 shows three snapshots of different  $n$ -decane ( $n$ -C10) simulations, one for each force field type. It illustrates the different abstraction

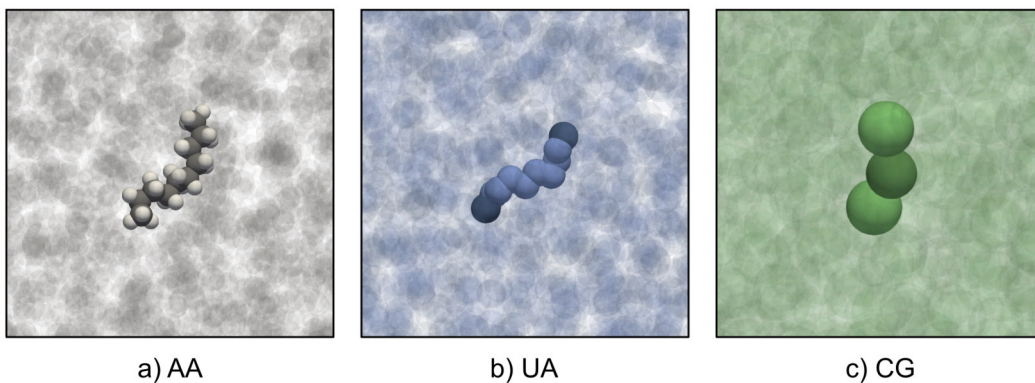


**Figure 15:** Snapshots of three  $n$ -decane simulations ( $p = 0.1$  MPa). The force fields are: (a) L-OPLS (AA), (b) TraPPE (UA), and (c) MARTINI (CG). The length scale is the same for all snapshots. One molecule is highlighted in each snapshot. The single sites are colored as follows: light green - end site of the CG model, dark green - central site of the CG model, light blue -  $\text{CH}_2$ , dark blue -  $\text{CH}_3$ , gray - carbon, white - hydrogen.

levels at which the molecules were modeled by the different force field types. The structure of the molecules was evaluated by the radius of gyration. Details are given in the Appendix B.

Fig. 16 gives an overview of the total average deviations  $\overline{\delta Y}$  of all force fields for the three studied properties, the density, the viscosity, and the self-diffusion coefficient ( $Y \in \{\rho, \eta, D\}$ ). The total deviations are lowest for the density with up to  $\overline{\delta \rho} = 6.4$  %. The deviations for the viscosity and the self-diffusion are substantially larger (up to  $\overline{\delta \eta} = 210.1$  % and  $\overline{\delta D} = 70$  %). For a given force field, the deviations of the viscosity and self-diffusion predictions are very similar for most force fields. As can be seen from Fig. 16, there is no direct indication that the deviation depends on the force field type as the deviations scatter also within the different force field types (AA, UA, and CG). This indicates that the individual parametrization of a force field (cf. Section 3.2.2) is more important for the deviations produced by the force field. The total average deviations of the single force fields are discussed in detail in the following sections.



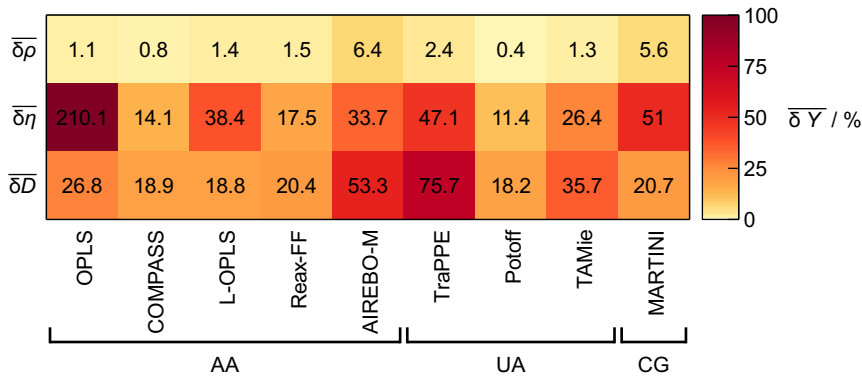


**Figure 16:** Total average deviations of the simulation results to the correlations of experimental data (values given in %) for the density  $\overline{\delta\rho}$ , the viscosity  $\overline{\delta\eta}$ , and the self-diffusion coefficient  $\overline{\delta D}$ .

### 3.3.1 Density

The simulation results for the density are shown in Fig. 17 in comparison to experimental data (where available). The corresponding deviation plots are shown in Fig. 18. The Potoff UA force field gives excellent predictions of the density, the average deviation from the experimental data  $\overline{\delta\rho}$  is only 0.4 %. The predictions obtained with the TAMie UA force field are also good ( $\overline{\delta\rho} = 1.3$  %). The third studied UA force field, TraPPE, yields poorer results ( $\overline{\delta\rho} = 2.4$  %). The TraPPE force field tends to overestimate the density, especially for the linear alkanes.

Despite their higher complexity, the AA force fields OPLS, L-OPLS, and COMPASS generally do not yield better results than the UA force fields. Among the AA force fields, COMPASS ( $\overline{\delta\rho} = 0.8$  %) is slightly better than the two others (OPLS:  $\overline{\delta\rho} = 1.1$  %, L-OPLS:  $\overline{\delta\rho} = 1.4$  %). In assessing the results from the OPLS force field, it has to be considered that it predicts *n*-C20 and *n*-C30 to be solid for the conditions studied here. This is in line with findings from the literature [339], which report that the OPLS force field predicts the liquid-solid phase transition for long alkanes at temperatures that are much higher than the experimental melting temperature [307]. More details on this are given in the Appendix B. The OPLS data for *n*-C20 and *n*-C30 are excluded for the present discussion.

The reactive AA force fields ReaxFF and AIREBO-M were only applied to *n*-C10. ReaxFF ( $\overline{\delta\rho} = 1.5$  %) overestimates the density, AIREBO-M ( $\overline{\delta\rho} = 6.4$  %) strongly underestimates it, cf. Fig. 18. The latter yields the poorest prediction of the density. The CG force field MARTINI ( $\overline{\delta\rho} = 5.9$  %) also shows high deviations.

The pressure dependency of the density  $(d\rho/dp)_T$  is predicted generally quite well by most of the models (cf. Fig. 17). Among the UA force fields, the TraPPE force field

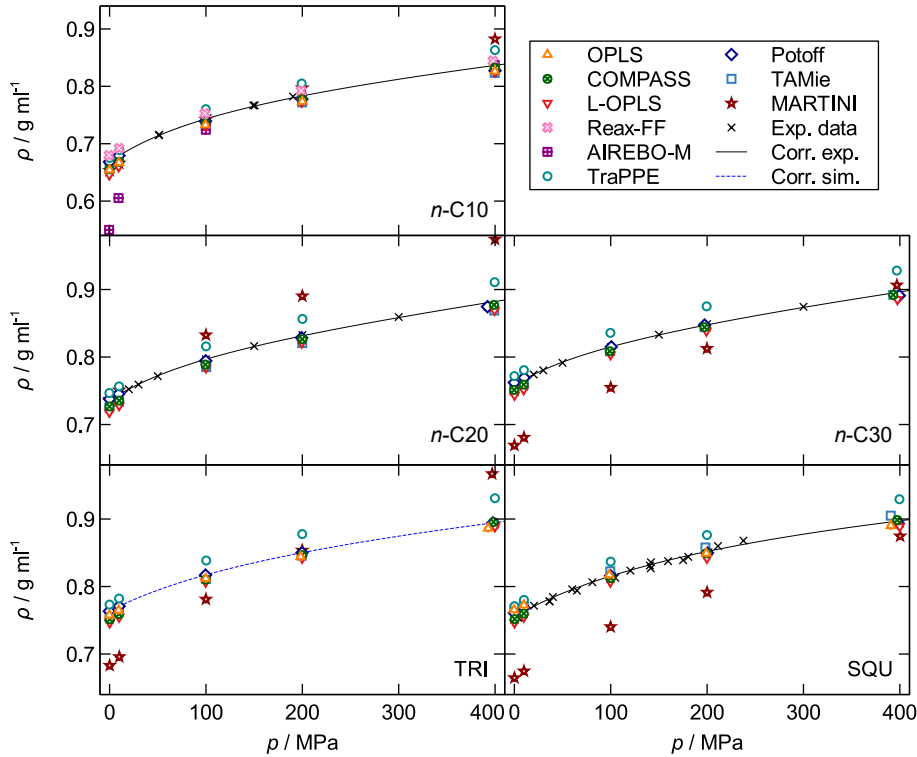


**Figure 17:** Density  $\rho$  of  $n$ -C10,  $n$ -C20,  $n$ -C30, TRI, and SQU at  $T = 373.15$  K as a function of the pressure  $p$ . Colored symbols indicate the simulation results for the different force fields and the black crosses are experimental data points (cf. Table 5). Black solid lines are correlations of the experimental data, blue broken lines are correlations of the simulation data with the Potoff force field.

yields the poorest prediction of the pressure dependency of the density as it overestimates  $(d\rho/dp)_T$ . While the Potoff force field slightly underestimates  $(d\rho/dp)_T$ , the results obtained from the TAMie force field do not show this tendency. This difference originates from the different repulsive Mie coefficients  $n$  of the TraPPE ( $n = 12$ ), the TAMie ( $n = 14$ ), and the Potoff ( $n = 16$ ) force fields. The higher the repulsive coefficient, the lower is  $(d\rho/dp)_T$ . This also holds for the three classical AA force fields, which also utilize a Mie potential (OPLS:  $n = 12$ , COMPASS:  $n = 9$ , L-OPLS:  $n = 12$ ) and overestimate  $(d\rho/dp)_T$ . Besides the potential, also the choice of the state points used for parametrization influences the results. This can especially be seen for the AIREBO-M force field, which was fitted including state points at high pressure. Its predictions of the density are best for the highest investigated pressure (400 MPa).

### 3.3.2 Viscosity

The results for the viscosity are shown in Fig. 19 using a logarithmic scale as a function of pressure. The corresponding deviation plots are shown in Fig. 20. Again, the results

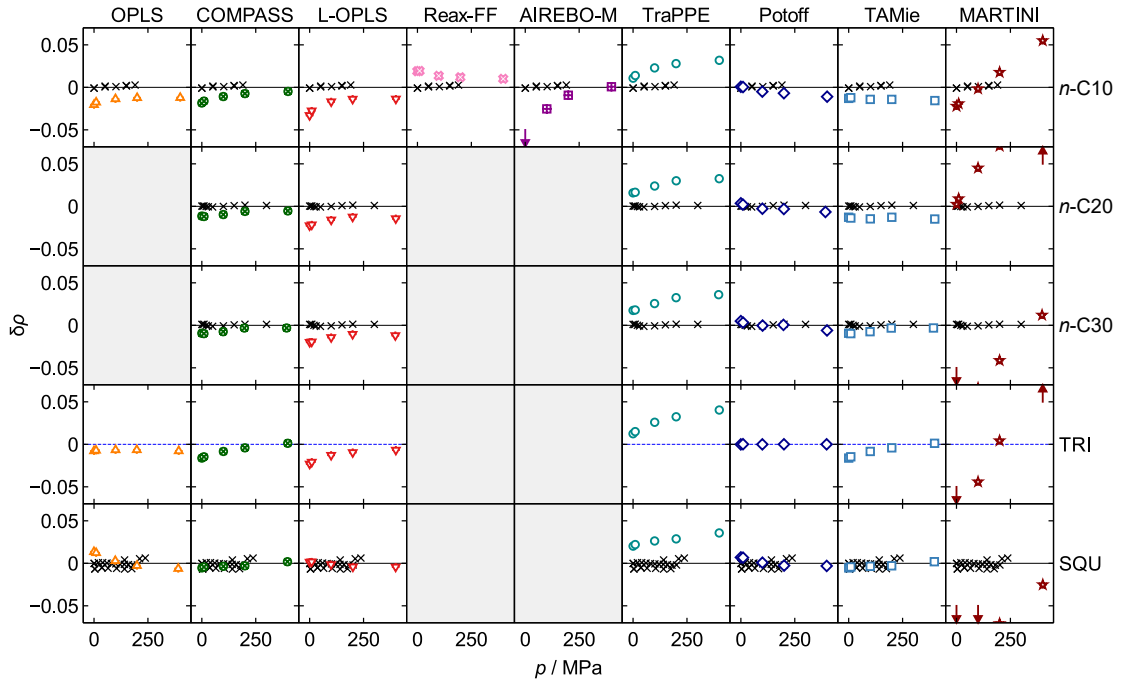


**Figure 18:** Relative deviation of the density  $\delta\rho$  (cf. Eq. (17)) at  $T = 373.15$  K as a function of the pressure  $p$  for all studied force fields and substances. The relative deviation (cf. Eq. (17)) refers to the correlation, which was obtained from either experimental data (black crosses, cf. Table 5) or the simulation data with the Potoff force field (dark blue diamonds).

for  $n$ -C20 and  $n$ -C30 obtained with OPLS are discarded from the discussion as they refer to solids (cf. Appendix B). As expected, the viscosity of all substances increases approximately exponentially with increasing pressure. Moreover, the viscosity of the linear alkanes ( $n$ -C10 to  $n$ -C30) increases with increasing chain length. This behavior is described well by all studied force fields. In contrast to the predictions of the density, the scattering of the results is larger and the predictions from the different force fields deviate in a range of an order of magnitude. This scattering is larger for the two branched alkanes (TRI, SQU) compared to the linear alkanes ( $n$ -C10 to  $n$ -C30).

As already seen for the density results, the Potoff UA force field gives the best predictions for the viscosity with  $\overline{\delta\eta} = 11.4$  %. The deviations obtained with the TAMie UA force field are doubled ( $\overline{\delta\eta} = 26.4$  %) compared to the Potoff UA force field and show an underestimation of the viscosity, especially for high pressures. *Messerly et al.* [291] found similar deviations for the Potoff and TAMie force fields for the viscosity of shorter alkanes. The TraPPE UA force field strongly underestimates the viscosity and yields the largest deviations from the experimental data among the UA force fields ( $\overline{\delta\eta} = 47.1$  %). The underestimation of the viscosity by the TraPPE force field was already stated in literature [287, 291, 340]. The only CG force field, MARTINI, has similar deviations from the experimental correlations with  $\overline{\delta\eta} = 51$  %, which is in accordance with results

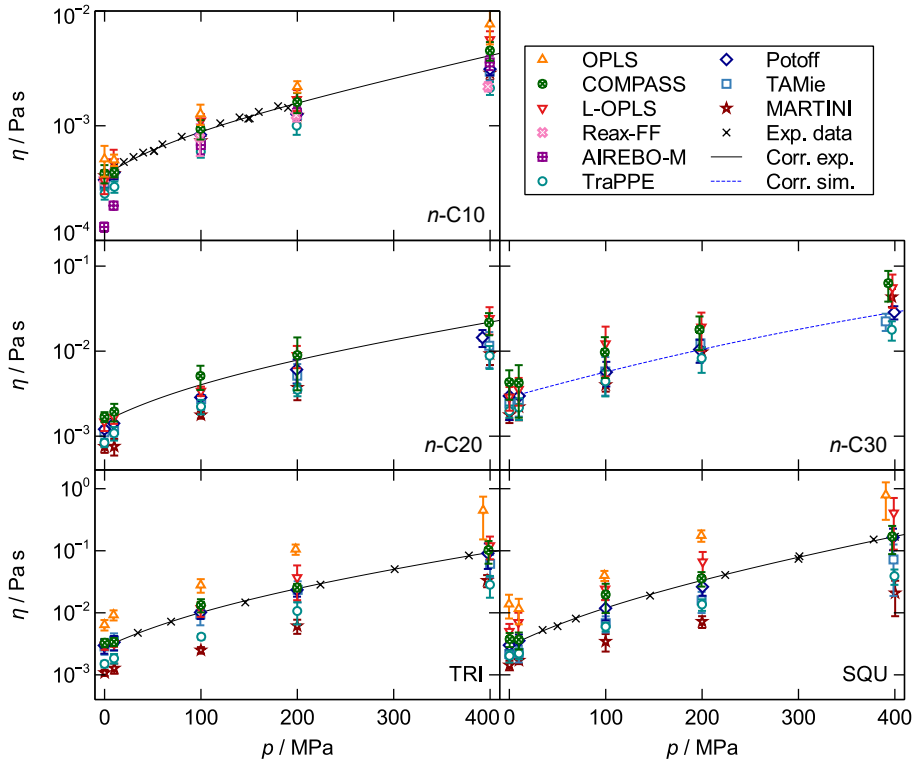


**Figure 19:** Viscosity  $\eta$  of  $n$ -C10,  $n$ -C20,  $n$ -C30, TRI, and SQU at  $T = 373.15$  K as a function of the pressure  $p$ . Colored symbols indicate the simulation results for the different force fields and the black crosses are experimental data points (cf. Table 5). Black solid lines are correlations of the experimental data, blue broken lines are correlations of the simulation data with the Potoff force field.

reported in literature [289]. The time scale, which is crucial for the calculation of the viscosity (cf. Section 3.2.1), is often scaled in CG simulations as CG models usually exhibit faster dynamics compared to higher resolution atomistic models. Therefore, a time scaling factor of 4 is often applied [313]. In the Appendix B, results for the viscosity calculated by the MARTINI force field are given with a time scaling factor of 4. For the three linear alkanes, the results do not improve compared to the results without conversion factor. The scaled results overestimate the experimental values. For the two branched alkanes, the scaling improves the results and decreases the deviations to the experimental data. More details are given in the Appendix B. Yet, in the main part of this chapter, results without a scaling factor are presented.

The AA force fields show very different behaviors. The COMPASS ( $\overline{\delta\eta} = 14.1\%$ ) and the ReaxFF ( $\overline{\delta\eta} = 17.5\%$ ) force fields yield good predictions for the viscosity. The latter predicts the viscosity accurately up to a pressure of around 100 MPa which is in accordance with findings reported by *Morrow and Harrison* [280] for alkanes and other thermophysical properties. For higher pressure, the viscosity is underestimated by the ReaxFF force field. For the COMPASS force field, there is a tendency for overestimation

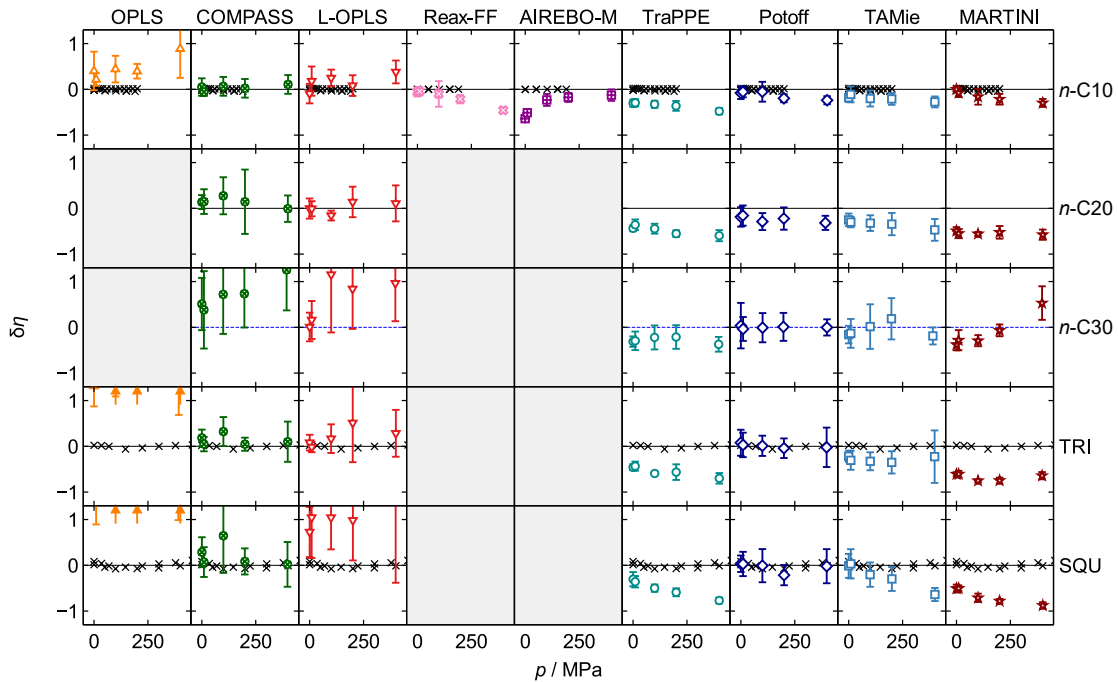


**Figure 20:** Relative deviation of the viscosity  $\delta\eta$  (cf. Eq. (17)) at  $T = 373.15$  K as a function of the pressure  $p$  for all studied force fields and substances. The relative deviation (cf. Eq. (17)) refers to the correlation, which was obtained from either experimental data (black crosses, cf. Table 5) or the simulation data with the Potoff force field (dark blue diamonds).

of the viscosity predicted (which has also been reported by Refs. [256, 272]). The AIREBO-M force field predicts the viscosity with  $\overline{\delta\eta} = 33.7$  %. Its deviations decrease with increasing pressure. The L-OPLS force field deviates with  $\overline{\delta\eta} = 38.4$  % from the experimental data on average. Thus, it shows a good improvement to the closely related OPLS force field [273, 341], which yields by far the worst predictions for the viscosity ( $\overline{\delta\eta} = 210.1$  %). The poor prediction ability of the viscosity by the OPLS force field was already reported for shorter alkanes [272, 340, 341]. In general, the AA force fields have larger error bars compared to the UA and CG force fields, especially for the large molecules  $n$ -C30, TRI, and SQU.

### 3.3.3 Self-diffusion Coefficient

The results for the self-diffusion coefficient using a logarithmic scale as function of pressure and the corresponding deviation plot are shown in Fig. 21 and 22, respectively.

Here, also the results of the OPLS force field for  $n$ -C20 and  $n$ -C30 are discarded and can be found in the Appendix B. The self-diffusion coefficient decreases with increasing pressure for all substances and force fields – as expected. The close relation of the self-diffusion coefficient and the viscosity [342] can be observed in the MD simulation results:

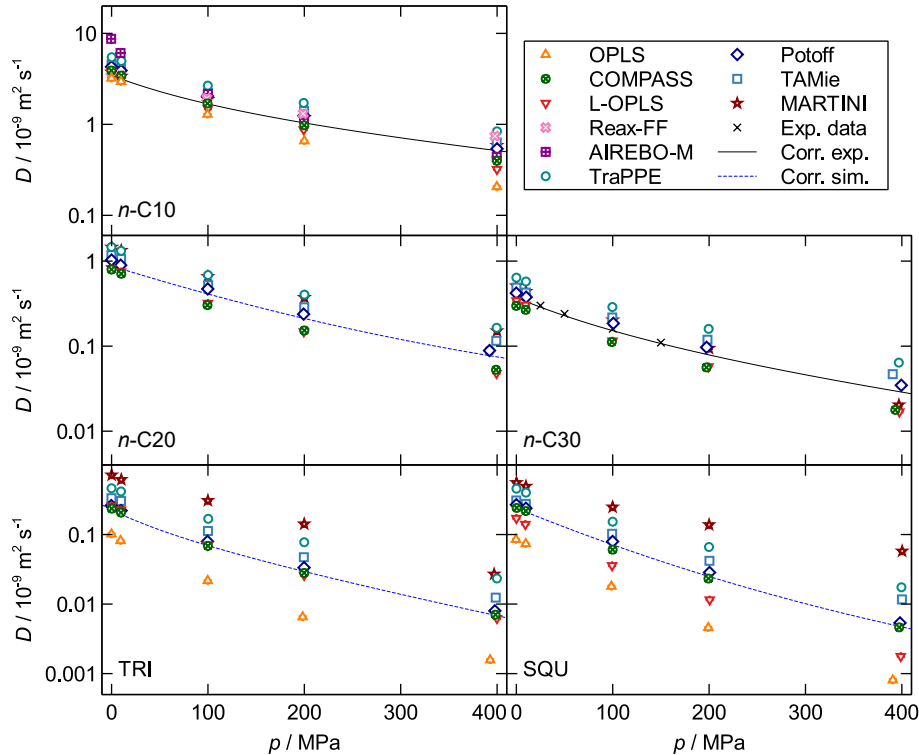


**Figure 21:** Self-diffusion coefficient  $D$  of  $n$ -C10,  $n$ -C20,  $n$ -C30, TRI, and SQU at  $T = 373.15$  K as a function of the pressure  $p$ . Colored symbols indicate the simulation results for the different force fields and the black crosses are experimental data points (cf. Table 5). Black solid lines are correlations of the experimental data, blue broken lines are correlations of the simulation data with the Potoff force field.

high values for the viscosity go along with low values for the self-diffusion and vice versa. Therefore, the self-diffusion coefficient shows opposite characteristics compared to the viscosity (cf. Section 3.3.2) regarding the deviations of the single force fields. In the Appendix B, figures of the viscosity plotted as a function of the self-diffusion coefficient are shown to underline their close relation.

The predictions for the self-diffusion coefficient with the Potoff force field are again the best and show the lowest deviations from the experimental data with  $\overline{\delta D} = 18.2\%$ . This is in line with the results for the density and the viscosity. The TAMie force field overestimates the self-diffusion for all substances with a total deviations of  $\overline{\delta D} = 35.7\%$ . The TraPPE force field also predicts too high values for the self-diffusion coefficient but with a much higher total deviation ( $\overline{\delta D} = 75.7\%$ ). For both the TAMie and the TraPPE force fields, the deviations increase with increasing pressure. The MARTINI CG force field predicts the self-diffusion coefficient surprisingly well with a total deviation of  $\overline{\delta D} = 20.7\%$ . Like the viscosity, the self-diffusion coefficient is a time-dependent property and thus, it is also influenced by time scaling, as often applied in CG simulations. As for the viscosity, results with time scaling are given for the self-diffusion coefficient

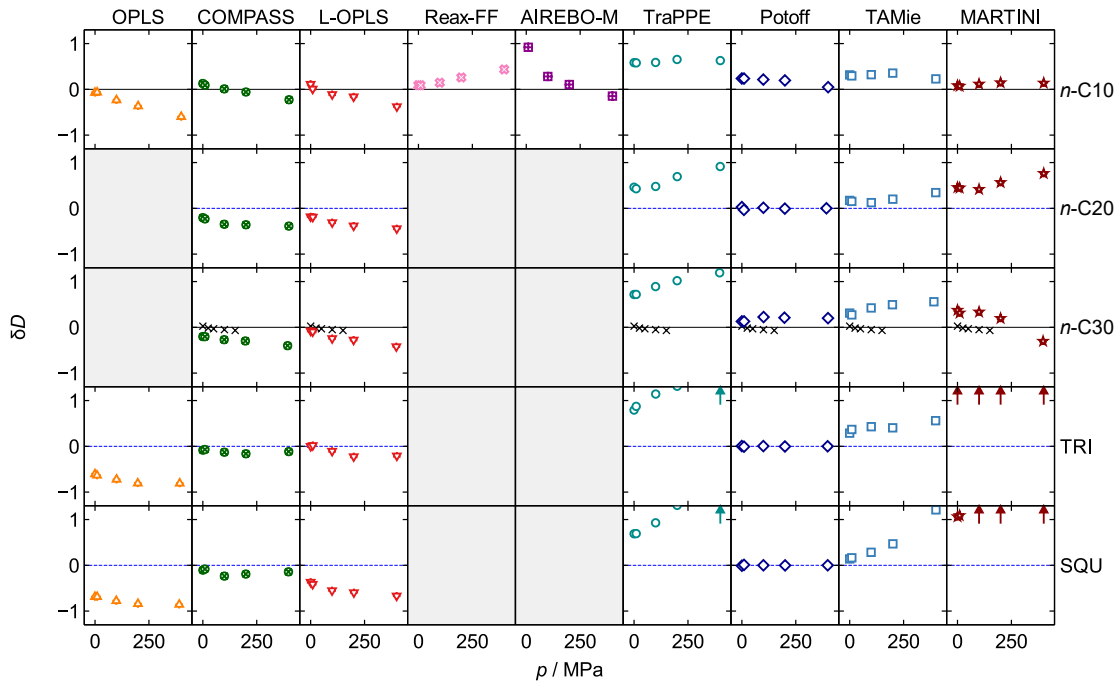


**Figure 22:** Relative deviation of the self-diffusion coefficient  $\delta D$  (cf. Eq. (17)) at  $T = 373.15$  K as a function of the pressure  $p$  for all studied force fields and substances. The relative deviation (cf. Eq. (17)) refers to the correlation, which was obtained from either experimental data (black crosses, cf. Table 5) or the simulation data with the Potoff force field (dark blue diamonds).

in the Appendix B. The results are similar to those for the viscosity: For the linear alkanes, results worsen compared to experimental values and the self-diffusion coefficient is underestimated. For the two branched alkanes, the predictions improve compared to the experimental data. More details are given in the Appendix B. In the main part of this chapter, results without a scaling factor are presented.

The COMPASS ( $\overline{\delta D} = 18.9\%$ ) and the L-OPLS ( $\overline{\delta D} = 18.8\%$ ) force fields exhibit nearly the same total deviations. Their predictions are very good and similar to those of the Potoff force field. With  $\overline{\delta D} = 20.4\%$ , also the ReaxFF force field shows good predictions for the self-diffusion coefficient. They both slightly overestimate the self-diffusion coefficient. The OPLS force field also overestimates the self-diffusion coefficient with a total deviation of  $\overline{\delta D} = 26.8\%$ . This was already reported in literature for simulations of  $n$ -hexane with the OPLS force field [343]. The deviations of the OPLS force field are much lower for the self-diffusion compared to the viscosity as only  $n$ -C10 is included in the calculation of the total deviation. The AIREBO-M force field shows the second largest total deviations ( $\overline{\delta D} = 53.3\%$ ) for the self-diffusion coefficient.

### 3.3.4 Computational Costs

The computational costs of the different force fields were evaluated by additional simulations for *n*-C10 at one state point ( $T = 373.15$  K and  $\rho = 0.67982$  g/ml). 20 replica simulations were conducted for each force field and the viscosity and the self-diffusion coefficient were calculated as described in Section 3.2.3. As the density strongly influences the computational costs, the same density was prescribed to the simulations for all force fields. All simulations for the determination of the computational costs were executed on the same machine with *Intel XEON SP 6126* processors and with the same simulation parameters (200 molecules, 1 ns equilibration, 2 ns production run, cutoff radius of 14 Å). Different number of cores have been used for the different simulations (AA: 24 cores, UA: 8 cores, CG: 1 core) to ensure perfect parallel efficiency. The computational costs were measured using the CPU hours (*cpuh*), i.e.  $cpuh = \text{number of processors} \times \text{simulation time}$  required for a given simulation. The results for the computational costs are shown in Fig. 23. The computational costs are normalized with respect to the OPLS force field computational costs. The statistical

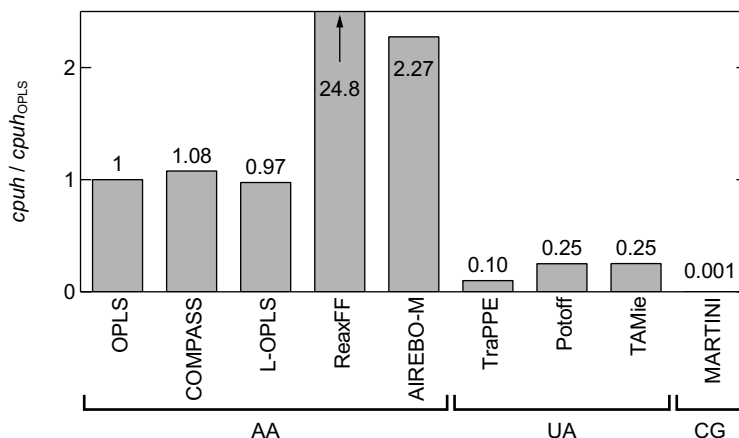


**Figure 23:** Computational costs *cpuh* of all force fields normalized with respect to the computational costs of the OPLS force field  $cpuh_{OPLS}$  for 20 replica simulations with  $T = 373.15$  K and  $\rho = 0.67982$  g/ml.

uncertainties obtained from these simulations are reported in the Appendix B.

The three classical AA force fields, OPLS, COMPASS, and L-OPLS, require similar computational costs, as expected. The slightly increased computational costs of the COMPASS force field compared to the OPLS and the L-OPLS force field are due to the use of more complex functions for computing the interactions in the COMPASS force field (including cross terms, e.g. bond-angle interactions). The two reactive AA force fields, ReaxFF and AIREBO-M, require substantially higher computational costs. The ReaxFF force field requires by far the highest costs with approximately 25 times the costs of the classical AA force fields.



The three UA force fields require lower computational costs than the AA force fields with 10 % - 25 % of the costs of the AA force fields. For studying the computational costs, the cutoff radius of the Potoff force field was set to 14 Å (equal to the other force fields). The higher computational costs of the Potoff and the TAMie force fields compared to the TraPPE force field are due to the use of the Mie potential instead of the 12-6 LJ potential. The latter is computationally more efficient as the repulsive part (exponent  $n = 12$ ) and the attractive part (exponent  $m = 6$ ) can be evaluated simultaneously benefiting from  $r^{12} = (r^6)^2$ . Furthermore, the calculation of the mixed exponent for Mie parameters produces an additional computational overhead. The low computational costs of the MARTINI CG force field are due to the small number of interaction sites and the larger time step used in the MARTINI simulations.

The uncertainties of the simulations are given in the Appendix B. The statistical uncertainties for the viscosity are about an order of magnitude larger compared to the self-diffusion coefficient results. For a given property, the different force fields yield similar statistical uncertainties.

## 3.4 Conclusions

The ability of different force fields to predict the density, the viscosity, and the self-diffusion coefficient of model lubricants was investigated. Pure linear ( $n$ -decane,  $n$ -icosane,  $n$ -triacontane) and branched alkanes (1-decene trimer, squalane) up to C30 were studied. The results were compared to experimental data where such data were available. The force fields consisted of five AA force fields (OPLS, L-OPLS, COMPASS, AIREBO-M, ReaxFF), three UA force fields (TraPPE, Potoff, TAMie), and one CG force field (MARTINI). The Potoff UA force field yields the best results for all three properties and is at the same time still computationally relatively cheap. The COMPASS and the ReaxFF AA force fields provide a good accuracy predicting the density, the viscosity, and the self-diffusion coefficient. For all force fields (except AIREBO-M), the deviations from experimental data increase with increasing pressure. The reason that AIREBO-M AA force field performs relatively well at extreme pressure is probably due to the applied parametrization which included data at high pressure [309]. The CG force field MARTINI simplifies the molecular architecture most. It yields large deviations from experimental data. The unphysical prediction of a solid-like phase by the OPLS force field for long linear alkanes [307] was confirmed by the conducted simulations. The optimized version for long linear alkanes of the OPLS force field, the L-OPLS force field [307], shows significantly better results. If no experimental data are available, the predictions by the force fields can provide good estimates to fill this gap. The Potoff force field is recommended for this purpose. The accuracy of predictions of experimental

data for the studied substances with this model was found to be about 0.5 % for the density, 10 % for the viscosity, and 18 % for the self-diffusion coefficient. As a convenient tool, also the empirical correlations developed in the present chapter based on the Potoff predictions can be used. The results from this chapter can be taken as a benchmark for testing the performance of new force fields under extreme conditions.

# 4 Online Database for Transferable Force Fields

## 4.1 Introduction

Molecular simulation is a powerful tool for predicting macroscopic thermophysical properties [58, 273, 344–351] as well as for the modeling of nanoscopic processes [19, 20, 59, 60, 352–355]. Molecular simulation, namely molecular dynamics (MD) and Monte Carlo (MC) simulation, have become an indispensable tool in many scientific disciplines such as computational physics [19, 20, 354, 356], physical chemistry [346, 357–359], molecular biology [360–364], and engineering [347, 365–367]. In MD and MC simulations, matter is modeled on the atomistic level based on molecular interactions, which are described by so-called force fields. A force field is the mathematical description of the molecular interactions. The quality of molecular simulation results primarily depends on the quality of the employed force field [77, 273, 286, 368–371]. Hence, an important focus has been in the past decades on the force field development and, accordingly, a large number of force fields is available today [14]. Also, the development of new force fields is still a very active field. Yet, the electronic availability, transparency, and usability of molecular force fields remains unsatisfactory [372]. Despite their importance, data science aspects (databases, data formats, interoperability, ontologies, FAIR principles [373] etc.) of force fields are still in their infancy.

While molecular interactions can be modeled today using first principle quantum mechanics, such simulation methods are computationally too expensive for the simulation of many particle systems as required for example in molecular biology. Therefore, molecular simulations based on Newton's mechanics and classical force fields are widely used today. In classical force fields, the molecular interactions are modeled by interaction potentials describing the potential energy as a function of the distance and orientation  $U(\mathbf{r})$ . These interaction potentials provide a relatively simple approximation of the 'true' molecular interactions. Yet, these force fields have proven very powerful and are successfully used across many scientific fields today.

A force field is a collection of parametric equations and corresponding parameter values

describing the interaction potentials between interaction sites representing atoms or groups of atoms. Force fields are used in molecular dynamics simulations to calculate forces between interaction sites. Based on these forces, the trajectories of the interaction sites are computed. Alternatively, the potential energy is directly used in Monte Carlo simulations for evaluating the probability that a given randomly generated atomistic configuration exists.

Transferable force fields for molecular substances are a particularly powerful tool as they can be used for modeling a large number of substances. A transferable force field is a generalized chemical construction plan for substance classes, e.g. characterizing the interaction between two chlorine atoms or the angle potential in an aromatic ring. Therefore, a transferable force field itself cannot be directly used for carrying out molecular simulations. However, based on a transferable force field, component-specific force fields can be uniquely derived by a user and then employed in a simulation. Hence, the strength of transferable force fields lies in their generalized description of molecular interactions, which comes at the cost of a high abstraction level and challenges in the usability.

A large number of transferable force fields, i.e. construction plans, is available today, for example DREIDING [374], UFF [375], AMBER [376], PCFF8 [377], TraPPE-UA [37, 310, 378–387], OPLS-AA [34, 376, 388–390], Potoff [38, 311, 391, 392], and CVFF [393]. They are mostly used for modeling fluid states. The coverage of the transferable force fields for modeling different types of substances strongly varies, i.e. the variety of chemical groups and interactions captured in the construction plan. For example, some force fields are restricted to hydro- or halocarbons [38] and others cover a large range of the periodic system [34]. Hence, transferable force fields can consist of hundreds of parameters. Moreover, this parameter data is heterogeneous as the potentials of a transferable force field describe different types of interactions, e.g. intermolecular and intramolecular. Usually, the parametrization of the building block parameters is carried out with a limited number of components and the obtained force field parameters are then transferred to other substances containing the same building blocks. Therefore, the development of transferable force fields is a demanding and tedious task.

Among transferable force fields, there are different approaches to model the atomistic architecture. Three types of force fields are often distinguished: all-atom (AA), united-atom (UA), and coarse-grained (CG) force fields [14]. In AA force fields, all atoms are represented by individual interaction sites. In contrast, UA force fields combine multiple atoms to one interaction site. Mostly,  $\text{CH}_x$  groups are modeled as one interaction site in which the H atoms are only implicitly modeled. In CG force fields, larger molecule segments (or multiple molecules) are merged into a single interaction site.

Different data aspects of molecular simulations have been addressed in recent years for

increasing the transparency, reproducibility [90, 372, 394, 395], and interoperability of molecular simulations [241, 396–403]. Yet, these attempts mostly focus on the simulation scenario setup and the simulation results. Thereby, multiple data formats for atomistic configurations, i.e. snapshots of simulations, have been well established, e.g. the *.xyz* file format or the *.pdb* file format for proteins [404]. Also, data formats for specific individual molecules are available which includes data formats for (small) molecules such as CML [405] format, SYBYL Line Notation [406], SMIRNOFF format [407], MCDL [408], and SMILES [409] as well as for macromolecules such as proteins, peptides, and polymers such as HELM [410] and SPICES [411]. Moreover, some transferable force fields are electronically accessible for users, e.g. the CHARMM force field in Ref. [412], the Amber force field in Ref. [413], the AMOEBA force field in Ref. [413], the TraPPE force field in Refs. [414, 415], the Merck force field in Ref. [416], and the OPLS force field in Refs. [415, 417]. Yet, most of these use individual data formats designed for the respective force field or computational framework. Also, most of these tools provide component-specific force field files (built from an implemented transferable force field), i.e. they are atom typing tools for generating force fields for a given individual molecule. The OpenKIM [418], the OpenMM [413, 419], and the MoSDeF [397, 415, 420] platform provide a digital infrastructure for atom typing and storing force field parameters, which can also be used for different molecular modeling and simulations tasks, e.g. setting up simulation scenarios and coupling with simulation engines.

For building a component-specific force field from a transferable force field construction plan, multiple challenges arise. Publications on transferable force fields use many different notations, units systems, mathematical forms of interaction potentials etc., which makes it difficult to use different force fields in one workflow. Also, the atomistic coordinates of the interaction sites in a molecule are only implicitly described by transferable force fields by the global minimum of the intramolecular interaction potentials. Moreover, different atomistic configurations, i.e. conformations, of a given molecule are often feasible and the equilibrium conformation (or distribution of conformations) is usually not a priori known. Furthermore, several force field features are treated and implemented differently in different simulation engines, e.g. electrostatic multipoles, long-range forces, and rigidity constraints, which can cause deviations in the results [90]. Moreover, important differences are present in the design concepts of different transferable force fields, which makes switching from one to another transferable force field in a workflow tedious and error-prone. No broad database for transferable force fields of fluids has been established yet. Some force field databases are available [63, 414, 417, 421, 422], but they mostly cover just one specific transferable force field (usually developed by the creators of the respective database) or potential models for solid states [423].

In this work, a generalized data scheme for transferable force fields is proposed, which formalizes the underlying general chemical construction plan and is applicable for a large variety of transferable force fields. Based on the developed data scheme, a concrete SQL-based data format is proposed. The data scheme developed in chapter is based on identifiers that are both human-readable as well as machine-readable. The latter in particular enables the integration in automated workflows. Also, the syntax is chemically consistent such that for example bond order rules are correctly captured. The data scheme is moreover designed to be simple, flexible, and extendable. The applicability of the data scheme and data format is demonstrated for different types of transferable force fields. The data scheme and data format proposed in this chapter (termed TUK-FFDat) enables an interoperable data exchange between publications of new transferable force fields, users of different molecular simulation engines, and force field databases (cf. Fig. 24).

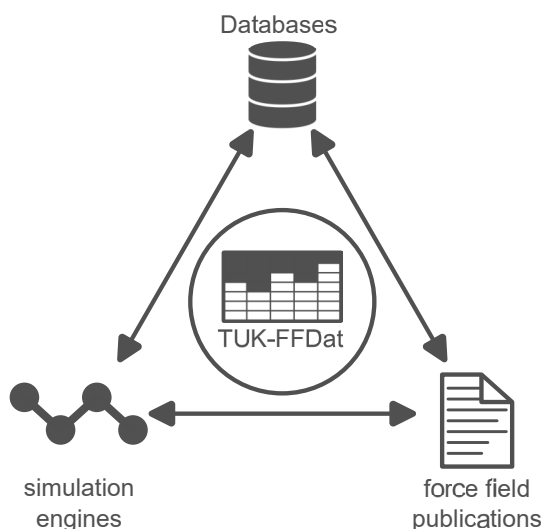


**Figure 24:** Applicability of the TUK-FFDat data scheme and data format for establishing a link between databases, simulation engines, and force field publications.

Additionally, as described in the second part of this chapter, a broad database for transferable force fields was developed and implemented in the existing *MolMod* database [63], which so far only considered component-specific force fields. Fig. 25 gives an overview of the structure of the *MolMod* Database including the 'component-specific' part as well as the 'transferable' part presented in this chapter. The two parts share the same front end, but have individual back end kernels and data structures.

The *MolMod Transferable* database is able to handle both AA and UA force fields. Table 21 gives an overview of the transferable force fields that are presently implemented in the *MolMod* database. Presently, *MolMod Transferable* contains eight transferable force fields, namely: TraPPE [37], TAMie [39], Potoff [38], COMPASS [35], CHARMM

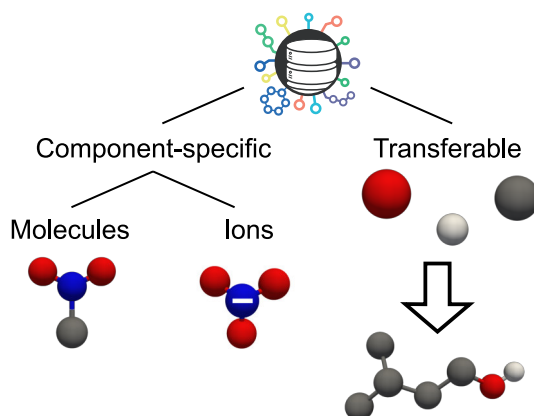


**Figure 25:** *MolMod* database consisting of the 'component-specific' part (left) and the new 'transferable' part.

[36], GROMOS [424], OPLS-AA [34], and OPLS-UA [33]. These force fields were taken from the literature and cover in general different chemical substance classes (details are given below). The data infrastructure of *MolMod Transferable* uses the force field data ontology and data format proposed in Refs. [399, 400, 425]. Based on these interoperable data standards, further transferable force fields can readily be integrated into the *MolMod* database. A graphical user interface is provided on the website that can be used for defining a molecular structure. The website directly displays the transferable force field parameters for that given molecule based on a chosen transferable force field. Moreover, *MolMod Transferable* provides input files for different simulation engines that can be downloaded in different formats.

This chapter consists of two parts: (1) The description of the TUK-FFDat data scheme and data format; (2) the extension of the *molMod* database to transferable force fields. The first part is organized as follows: First, different classification approaches and features of transferable force fields are introduced. Based on this ontology, the novel data scheme is built. Then, the implementation of the data scheme in an SQL-based data format is presented followed by an exemplary application of the presented data format to three transferable force fields. Conversion tools that translate the data scheme information from a user-friendly .xls spreadsheet format to the SQL database format is described in the Method section. The second part describing the extension of the *MolMod* database is organized as follows: first, the operating principles of *MolMod Transferable* are explained. Then, the implementation of the force fields and the available input formats are described. Afterwards, comments on the data infrastructure, data management, and data integrity are given. Finally, the work is summarized and an outlook to future work is presented.

## 4.2 TUK-FFDat: Data Scheme and Data Format for Transferable Force Fields

### 4.2.1 Classification of Force Fields

Force fields can be classified using different attributes. Fig. 26 shows a systematic classification of force fields regarding the modeling approach, the model detail level, the interaction potential types, and the parametrization approach. Blue highlights in the

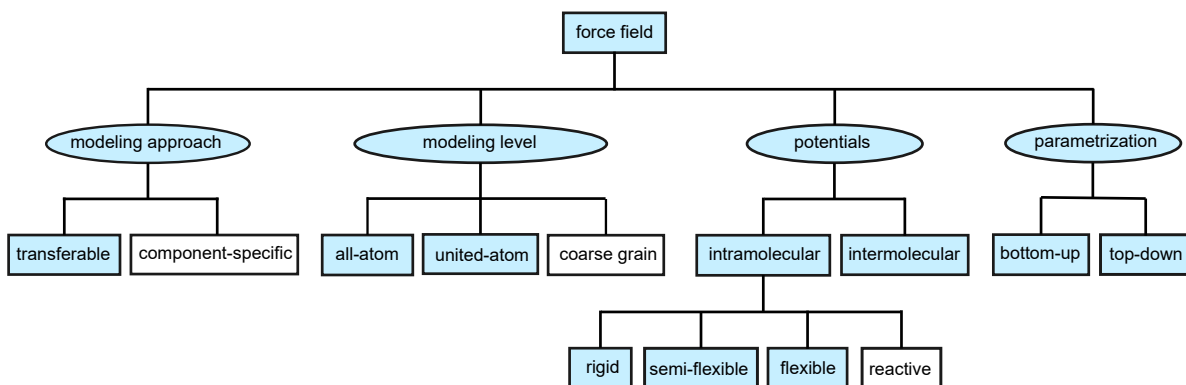


**Figure 26:** Force field ontology and classification used in this work. Blue indicates attributes covered by the TUK-FFDat data scheme and data format.

ontology (Fig. 26) indicate the coverage of the data scheme developed in this work.

There are two main modeling approaches for molecular force fields: (i) component-specific, where the layout of the interaction sites, the choices for the parameter functions as well as the parametrization procedure is carried out for a specific substance, e.g. ethanol. This usually results in a relatively accurate model since the focus was on that substance alone. The downside of that approach is that the developed model is only valid for that substance and no parts of the model can in general be transferred and re-used for modeling other substances. In the transferable force field approach (ii), molecular features and interactions are modeled in a generalized way based on building blocks, e.g. single atoms or groups of atoms. These force fields will usually (but not necessarily) be less accurate than component-specific force fields for a given substance since the objective during the development was broader. Yet, transferable force fields can be applied in a wider sense since the molecular features are captured in building blocks.

Different modeling levels can be used for developing force fields, namely (i) all-atom; (ii) united-atom; and (iii) coarse grain. Fig. 27 shows these different approaches – using *n*-butane as an example. Going from (i) to (iii), the degree of abstraction of the molecular model increases, which also increases the computational efficiency as less details are



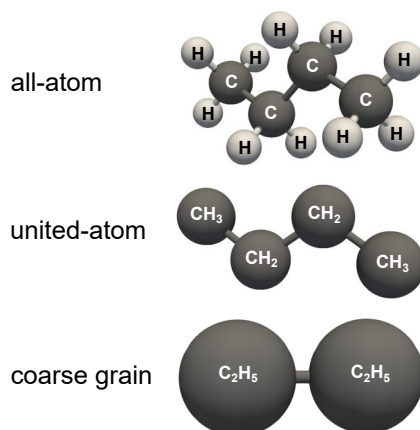


**Figure 27:** Classification of force fields according to the modeling level used to model molecules based on interaction sites (spheres).

included. However, the accuracy for predicting macroscopic thermophysical properties does not necessarily depend on the degree of abstraction [77, 288]. Usually, the ability to extrapolate to state regions that were not considered in the fit usually decreases with increasing the degree of abstraction. In all-atom force fields, each atom in a molecule is explicitly modeled by an interaction site, including small hydrogen atoms. In united-atom force fields, small groups of atoms are modeled as an interaction site. In this approach, usually, chemical groups, e.g. methyl or methylene groups, are fused to a single interaction site, cf. Fig. 27. In united-atom force fields, especially hydrogen atoms are often substituted within the nearest larger neighbor atom. In coarse grain force fields, larger sections of molecules (or even multiple molecules) are modeled as an interaction site, cf. Fig. 27. For each modeling level, an interaction site is represented by a geometrical point. However, in visualizations, interaction sites are usually represented by spheres, cf. Fig. 27, representing the extend of the repulsive interactions of the respective potential (in a simplified way).

The mathematical form of the interaction potentials is an important force field attribute (cf. Fig. 26). Interaction potentials are parametric functions that describe the potential energy between the interaction sites. Both intramolecular interaction potentials (between sites of the same molecule) and intermolecular interaction potentials (between sites of different molecules) exist, cf. Fig. 26. The intramolecular interaction potentials establish the molecule flexibility and allow molecular vibrations. Different types of intramolecular interactions can be applied for a force field: A molecule can be fully *flexible*, meaning that all interaction sites have three independent translational degrees of freedom. Force fields that have intramolecular potentials, but have certain fixed bond lengths, fixed bond angles, or fixed torsion angles are called *semi-flexible*. Thereby, stretching between direct neighbor interaction sites is often constraint to be rigid (this

allows the use of a larger time step and faster exploration of the phase space [14]). In the limiting case where all intramolecular interactions are constraint, the force field is *rigid* and no intramolecular degrees of freedom, i.e. no change in the molecular geometry and vibrations, occur. This is usually only meaningful for relatively small molecules. *Reactive* force fields are a special type of flexible force fields. In reactive force fields [314], bonds are modeled by bond order potentials, which describe the state of a bond between two interaction sites. This enables a dynamic mapping of interaction sites during a simulation and thereby chemical reactions. Most available transferable force fields are of the flexible or semi-flexible type.

Force fields consist of different types of intramolecular and intermolecular interaction potentials, Fig. 28. For fully flexible force fields, different types of intramolecular potentials

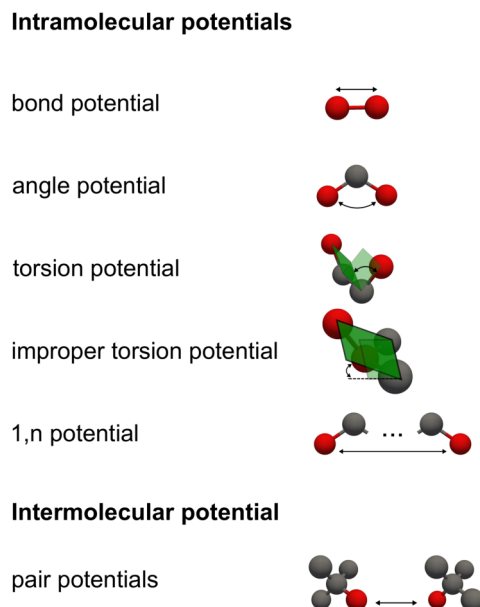


**Figure 28:** Classification of force fields based on the potential types.

can occur: Interaction potentials describing the potential energy between two bonded interaction sites are called *bond potentials* – modeling a strongly localized chemical bond [426]. Bond potentials are parametric functions that usually depend on the bond length of the bond between the interaction sites under consideration. Intramolecular potentials describing the potential energy between three directly neighbored interaction sites are called *angle potentials*. The angle potentials are a function of the angle between three sites. Intramolecular potentials describing the potential energy between four directly neighbored interaction sites (for example the four carbon atoms in *n*-butane, cf. Fig. 27) are called *torsion potentials*. Dihedral potentials have an important impact on the molecular configurations and the macroscopic thermophysical properties. In force fields describing branched molecules, so-called *improper torsion potentials* are used at times. These potentials describe the potential energy between four directly neighbored

interaction sites, whereby three interaction sites are bonded to a fourth central interaction site. Improper torsion or dihedral potentials are usually formulated as a function of the 'out of plane' angle, cf. Fig. 28. Intramolecular potentials describing the potential energy between two interaction sites that belong to the same molecule and have a distance of  $n - 1$  bonds, are called  $1, n$  interaction potentials (where  $n > 1$ ). The  $1, n$  potentials model dispersive and repulsive interactions between interaction sites in a molecule that are not close neighbors. This is particularly relevant for large curled molecules. Usually, the  $1, n$  interactions are described by scaled intermolecular potentials (see below). The van der Waals and the electrostatic interactions are usually scaled individually.

There are (in practically all cases) two types of intermolecular interactions: Electrostatic interactions, dispersive (attractive) interactions, and repulsive interactions. The latter two model attractive forces at moderate distances (a.k.a. van der Waals forces) and repulsive forces at short distances (mimicking the overlap of electron orbitals) [14, 426]. In most cases, effective pair potentials are used for describing intermolecular interactions. For these interactions, mostly the Lennard-Jones [66, 73, 427] potential or the Mie [428] potential is used. The electrostatic interactions are mostly modeled by simple point charges, but also higher multipole interaction sites are used in force fields at times. These relatively simple electrostatic interactions model the molecular orbital charge distribution (that is in reality much more complex), e.g. the charge distribution in alcohol groups and  $\pi$ -orbitals in aromatic components. To describe the potential energy between different types of interaction sites (kinds of atoms or groups of atoms), in practically all cases, the same mathematical functions are used within a given transferable force field and the cross-interaction parameters are determined using combination rules.

Both the intermolecular and the intramolecular potential functions have parameters that – together – describe the chemical and physical nature of the interactions. For the development of force fields, different strategies for determining the parameter values have been applied in the literature (cf. Fig. 26). Two main routes are established today: (i) a bottom-up approach and (ii) a top-down approach.

In the bottom-up approach, the 'true' molecular interactions are determined using quantum mechanical simulations [429–432]. Based on the results, both the intermolecular and the intramolecular interactions in force fields can in general be determined. The parameter values of the intramolecular potentials are often fitted to first principle quantum chemical simulation results for the potential energy surface (PES). Yet, using quantum mechanical simulations for fitting the intermolecular potential parameters is conceptually and computationally challenging, e.g. since multi-body interactions are mapped to pair interactions.

In the top-down approach, the parameter values of the potential functions are deter-

mined using macroscopic thermophysical property data. The parameters are tuned such that the force field describes a given set of macroscopic properties well. For force fields for fluids, mostly vapor–liquid equilibrium properties and self-diffusion data is used for the parametrization. In many cases, the top-down approach and the bottom-up approach are combined such that intramolecular interactions are determined from quantum chemical simulation results and intermolecular interactions using macroscopic thermophysical property data.

Furthermore, force fields can be sub-classified based on the mathematical functions employed in a force field. Also, machine learning force fields have been developed in recent years as a novel class [433]. In machine learning force fields, the potential functions and their parameters are determined using machine learning (mostly using large PES data sets). Machine learning force fields can be considered a sub-type of the bottom-up parametrization strategy.

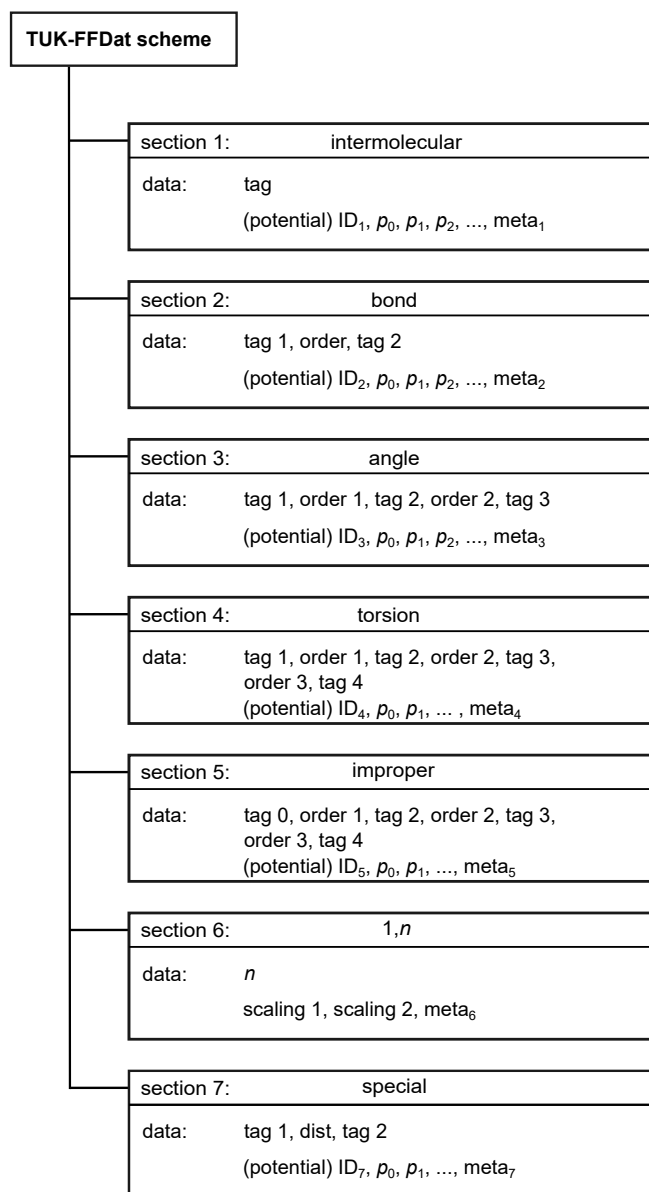
The generalized data scheme proposed in this chapter captures a large variety of transferable force field types (blue highlighting in Fig. 26). Based on the ontology and terminology introduced in Fig. 26, the new data scheme is presented in the following.

## 4.2.2 Definition of Data Scheme

The data scheme proposed in this chapter consists of seven sections that formalize the definition of a transferable force field construction plan. Fig. 29 gives an overview of the data scheme. In the  $i = 1..7$  sections, the interaction potentials constituting a transferable force field are stored as follows: (1) intermolecular interactions; (2) bond intramolecular interactions; (3) angle intramolecular interactions; (4) torsion intramolecular interactions; (5) improper intramolecular interactions; (6)  $1, n$  interactions; and (7) special case interactions.

A 'tag' notation is introduced defining the interaction site type, i.e. atom or group of atoms (in the case of a united-atom force field). Tag tuples are used in the different sections to indicate the combination of interaction site types defining a specific interaction, e.g. a bond between a hydrogen atom and a carbon atom. Using the tag notation and the bond order between the interaction sites, the interaction potentials acting between a given set of sites is defined in a generalized way.

A tag consists of four parts that are separated by a hyphen '-'. The first two parts are strings and the third and fourth part are integer values. Details are given in Table 6. Fig. 30 shows a united-atom 3-methyl-1-butene ( $C_5H_{10}$ ) molecule model illustrating the definition of the tag. The first part of the tag is an abbreviation representing the functional group to which the interaction site is assigned. Table 7 gives a list of

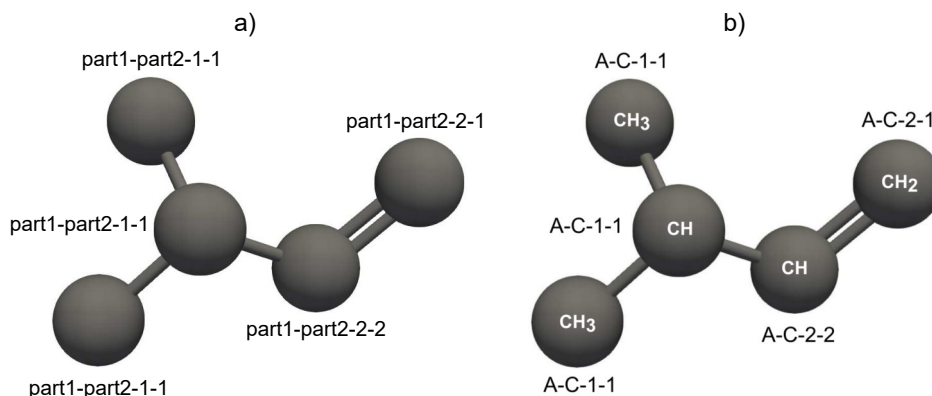


**Figure 29:** Schematic overview of TUK-FFDat data scheme for transferable force fields.

chemical groups and their abbreviations used in the data scheme. The second part of the tag indicates the type of atom or group of atoms modeled by the interaction site under consideration. For atoms, the classical periodic table notation is used [434]. For sites modeling a group of atoms (in an united-atom force field), fused hydrogen and carbon atoms are indicated by a 'C'. Hence, in this part of the tag hydrogen atoms are neglected in united-atom models unless a site explicitly models a single hydrogen atom. The third part of the tag is the number of bonds the interaction site forms with other (non-hydrogen) interaction sites. The fourth part of the tag indicates the highest bond order the interaction site under consideration enters into. The tag 'A-C-2-1', cf. Fig. 30, for example indicates a carbon atom C (fused with the substituted hydrogen atoms) in an alkane group A forming one '1' bond with (non-hydrogen) interaction

**Table 6:** Definition of tag notation `part1-part2-part3-part4` characterizing a given interaction site and data type of the individual tag entries.

Part	Value	Description
<code>part1</code>	string	functional group of which interaction site is part of (cf. Table 7)
<code>part2</code>	string	atom or group of atoms modeled by interaction site
<code>part3</code>	integer	number of bonds of interaction site (with non-hydrogen atoms)
<code>part4</code>	integer	highest bond order of interaction site

**Figure 30:** Exemplaric definition of tag identifier notation (cf. Table 6) for interaction sites (atoms or groups of atoms) using 3-methyl-1-butene: a) last two parts of the tag specifying bond structure in a molecule (details given in the text); b) first two parts of the tag specifying the atom type and site structure of the model.

sites, which has a bond order of '2', i.e. a double bond. The tag notation also enables a direct distinction of a particular atom type that is modeled differently, i.e. different parameters, in different chemical environments. Details on the tag notation are given in Appendix C.

In the seven sections of the data scheme (cf. Fig. 29), chemical sub-structures (i.e. formations of two sites (bonds), three sites (angles) etc.) are characterized using tuples of tags indicating the participating interaction sites. This constitutes the chemical construction plan. Each of the seven sections of the data scheme has a list of entries defining the interaction potentials and their parameters assigned to a given chemical structure, i.e. combination of types of interaction sites. The interaction potentials are represented by parametric functions with the parameters  $p_0, p_1, \dots, p_n$  (cf. Fig. 29). The mathematical functions used for describing a given interaction are represented by the 'ID<sub>*i*</sub>' with  $i = 1 \dots 7$ . Each section has its own ID and interaction potential list. For example, for the bond potential  $i = 2$ , the classical harmonic function has the  $ID_2 = 1$ . Moreover, meta data indicating the origin of the data (in most cases the parameter values) is appended for each structural information. For this purpose, the DOI numbers are used as references, which provide a unique link to the respective references [435].

**Table 7:** Functional groups included in the data scheme (first part of the tag, cf. Table 6).

Abbreviation	Type	Functional group
A*	$\text{CH}_x\text{-CH}_x^a$ , $\text{CH}_x=\text{CH}_x^b$ , $\text{CH}_x\equiv\text{CH}_x^c$	alkane
Ac	$\text{CH}_x\text{-O-C(=O)-CH=CH}_2^a$	acrylate
Ace	$\text{CH}_x\text{-O-C(-X)}_2\text{-O-CH}_x^{a,d}$	acetal
Ad	$\text{CH}_x\text{-C(=O)-N-X}_2^{a,d}$	amide
Ak	$\text{CH}_x\text{-O-H}^a$	alcohol
Al	$\text{X-C(-H)=O}^{a,d}$	aldehyde
Am	$\text{CH}_x\text{-N-X}_2^{a,d}$	amine
B**	CH-CH (arom.)	benzene
CA**	$\text{CH}_2\text{-CH}_2$ (cyc.)	cycloalkane with $6 < (\text{ring size}) < 18$
CA5**	$\text{CH}_2\text{-CH}_2$ (cyc.)	cycloalkane with ring size 5
CA6**	$\text{CH}_2\text{-CH}_2$ (cyc.)	cycloalkane with ring size 6
Cac	$\text{CH}_x\text{-C(=O)-O-H}^a$	carboxylic acid
DS	$\text{CH}_x\text{-S-S-CH}_x^a$	disulfide
E	$\text{CH}_x\text{-O-CH}_x^a$	ether
Es	$\text{CH}_x\text{-C(=O)-O-CH}_x^a$	ester
K	$\text{CH}_x\text{-C(=O)-CH}_x^a$	ketone
mAc	$\text{CH}_x\text{-O-C(=O)-C(-CH}_3\text{)=CH}_2^a$	methacrylate
Nl	$\text{CH}_x\text{-C}\equiv\text{N}^a$	nitrile
No	$\text{CH}_x\text{-N-O}_2^a$	nitro
Sd	$\text{CH}_x\text{-S-CH}_x^a$	sulfide
Tl	$\text{CH}_x\text{-S-H}^a$	thiol

<sup>a</sup>  $x \in [0, 1, 2, 3]$ , <sup>b</sup>  $x \in [0, 1, 2]$ , <sup>c</sup>  $x \in [0, 1]$ , <sup>d</sup>  $X \in [\text{H}, \text{CH}_x]$ .

\* Both, alkenes ( $\text{sp}^2$ ) and alkynes ( $\text{sp}^1$ ) are abbreviated 'A' in the first part of the tag.

\*\* Functional groups inside cycloalkanes or aromatic benzene rings are also abbreviated 'CA' and 'B', respectively, in the first part of the tag.

In the following, the structure and syntax of each of the seven sections is introduced in detail. It should be noted that the equilibrium structure (bonds, bond angles, ...) of a given molecule is implicitly given by a global minimum of its total potential energy, which is therefore not explicitly described by the data scheme.

The first section of the data scheme is termed *intermolecular* and contains the information on the intermolecular interaction potentials between interaction sites. The assignment of the individual intermolecular potential functions by the corresponding IDs is given in Table 8. The *intermolecular* section explicitly lists potential functions

**Table 8:** Intermolecular potential functions and their parameters (first section of data scheme, cf. Fig. 29), where  $r_{ij}$  indicates the distance between the considered interaction sites  $i$  and  $j$ ,  $\varepsilon_0$  the vacuum permittivity,  $k_B$  the Boltzmann constant,  $q$  the charge,  $\varepsilon$  the dispersion energy,  $\sigma$  the size parameter, and  $n$  the potential exponent.

ID <sub>1</sub>	Function	P1	P2	P3	P4
1	$4\varepsilon_{ij} \left[ \left( \frac{\sigma_{ij}}{r_{ij}} \right)^{12} - \left( \frac{\sigma_{ij}}{r_{ij}} \right)^6 \right] + \frac{1}{4\varepsilon_0\pi} \frac{q_{ij}}{r_{ij}}$ with: $q_{ij} = q_{ii}q_{jj}, \varepsilon_{ij} = \sqrt{\varepsilon_{ii}\varepsilon_{jj}}, \sigma_{ij} = \frac{\sigma_{ii} + \sigma_{jj}}{2}$	$q_{ii}$	$\varepsilon_{ii}$	$\sigma_{ii}$	-
2	$C_n \varepsilon_{ij} \left[ \left( \frac{\sigma_{ij}}{r_{ij}} \right)^{n_{ij}} - \left( \frac{\sigma_{ij}}{r_{ij}} \right)^6 \right] + \frac{1}{4\varepsilon_0\pi} \frac{q_{ij}}{r_{ij}}$ with: $n_{ij} = \frac{n_{ii} + n_{jj}}{2}, C_n = \left( \frac{n_{ij}}{n_{ij}-6} \right) \left( \frac{n_{ij}}{6} \right)^{\frac{6}{n_{ij}-6}}, q_{ij} = q_{ii}q_{jj},$ $\varepsilon_{ij} = \sqrt{\varepsilon_{ii}\varepsilon_{jj}}, \sigma_{ij} = \frac{\sigma_{ii} + \sigma_{jj}}{2}$	$q_{ii}$	$\varepsilon_{ii}$	$\sigma_{ii}$	$n_{ii}$
3	$4\varepsilon_{ij} \left[ \left( \frac{\sigma_{ij}}{r_{ij}} \right)^{12} - \left( \frac{\sigma_{ij}}{r_{ij}} \right)^6 \right] + e^2 \frac{q_{ij}}{r_{ij}}$ with: $q_{ij} = q_{ii}q_{jj}, \varepsilon_{ij} = \sqrt{\varepsilon_{ii}\varepsilon_{jj}}, \sigma_{ij} = \frac{\sigma_{ii} + \sigma_{jj}}{2}$	$q_{ii}$	$\varepsilon_{ii}$	$\sigma_{ii}$	-
4	$\varepsilon_{ij} \left[ \left( \frac{r_{\min, ij}}{r_{ij}} \right)^{12} - \left( \frac{r_{\min, ij}}{r_{ij}} \right)^6 \right] + \frac{1}{\varepsilon_l} \frac{q_{ij}}{r_{ij}}$ with: $q_{ij} = q_{ii}q_{jj}, \varepsilon_{ij} = \sqrt{\varepsilon_{ii}\varepsilon_{jj}}, r_{\min, ij} = \frac{r_{\min, ii} + r_{\min, jj}}{2}$	$q_{ii}$	$\varepsilon_{ii}$	$r_{\min, ii}$	-

with its corresponding parameters and a combination rule. The interaction sites in the first section of the data scheme are defined by a single corresponding tag. The potential functions used for modeling the interactions between given site types are encoded in the ID<sub>1</sub> (cf. Table 8). Also the combination rule type describing the interaction potential between unlike interaction sites is comprised in the ID<sub>1</sub>. For a given transferable force field, the ID<sub>1</sub> is constant. In the list of intermolecular interaction potential functions (cf. Table 8), also the meaning of the parameter values is specified.

The second section of the data scheme is termed *bond* and contains the specifications for the bond potentials for different combinations of two directly neighbored interaction sites. Hence, all information on intramolecular bond potentials within the given transferable force field are stored in the second data scheme section. A bond interaction is specified by the tags of the two involved interaction sites 'tag 1' and 'tag 2' as well as the bond 'order' between the considered interaction sites (cf. Fig. 29). The bond potential specification for two interaction sites consists of a bond potential function and its parameters – analogously to the intermolecular potential section. The bond potential



function is encoded by the ID<sub>2</sub>. Details on the potential functions are given in Table 9.

**Table 9:** Bond potential functions and their parameters (second section of data scheme, cf. Fig. 29), where  $r_{ij}$  is the distance between the considered interaction sites  $i$  and  $j$ , and  $k$  parameters of the potentials.

ID <sub>2</sub>	Function	p <sub>1</sub>	p <sub>2</sub>	p <sub>3</sub>	p <sub>4</sub>
1	$\frac{k_2}{2} (r_{ij} - r_0)^2$	$k_2$	$r_0$	-	-
2	$k_2 (r_{ij} - r_0)^2 + k_3 (r_{ij} - r_0)^3 + k_4 (r_{ij} - r_0)^4$	$k_2$	$k_3$	$k_4$	$r_0$
3	$\frac{k_4}{4} (r_{ij}^2 - r_0^2)^2$	$k_4$	$r_0$	-	-

The third section of the data scheme is termed *angle*. It contains the specifications for the angle potentials for different combinations of three directly neighbored interaction sites. An angle interaction potential is specified by the tags of the three involved types of interaction sites 'tag 1', 'tag 2', and 'tag 3' and the two bond orders 'order 1' and 'order 2'. The 'order 1' indicates the bond order between the central interaction site indicated by 'tag 2' and the first interaction site 'tag 1'. The 'order 2' indicates the bond order between the 'tag 2' and 'tag 3' interaction sites. The interaction potential functions are encoded by the ID<sub>3</sub>. The list of mathematical functions and the corresponding parameters is given in Table 10.

**Table 10:** Angle potential functions and their parameters (third section of data scheme, cf. Fig. 29), where  $i$  and  $k$  are the interaction sites that are bond to the interaction site  $j$ , such that  $i$ ,  $j$  and  $k$  form the bond angle  $\Theta$ ,  $r_{ij}$  is the distance between the interaction sites  $i$  and  $j$ ,  $r_{jk}$  is the distance between the interaction sites  $j$  and  $k$ .

ID <sub>3</sub>	Function	p <sub>1</sub>	p <sub>2</sub>	p <sub>3</sub>	p <sub>4</sub>	p <sub>5</sub>	p <sub>6</sub>	p <sub>7</sub>	p <sub>8</sub>	p <sub>9</sub>
1	$\frac{l_2}{2} (\Theta - \Theta_0)^2$	$l_2$	$\Theta_0$	-	-	-	-	-	-	-
2	$l_2 (\Theta - \Theta_0)^2 + l_3 (\Theta - \Theta_0)^3 + l_4 (\Theta - \Theta_0)^4 + k_2 (r_{ij} - r_1) (r_{jk} - r_2) + N_1 (r_{ij} - r_1) (\Theta - \Theta_0) + N_2 (r_{jk} - r_2) (\Theta - \Theta_0)$	$l_2$	$l_3$	$l_4$	$\Theta_0$	$k_2$	$r_1$	$r_2$	$N_1$	$N_2$
3	$c \frac{(\cos \Theta - \cos \Theta_0)^2}{2}$	$\Theta_0$	$c$	-	-	-	-	-	-	-

The fourth section of the data scheme is termed *torsion* and contains the specifications for the torsion potentials for different combinations of four directly neighbored in-line (no branching) interactions sites. This type of interaction is also often named dihedral. A torsion potential is specified by the tags of the four involved types of interaction

sites 'tag 1', 'tag 2', 'tag 3', and 'tag 4' and the three bond orders 'order 1', 'order 2', and 'order 3'. The interaction sites indicated by 'tag 1' and 'tag 4' are the tail interaction sites of a torsion structure; the interaction sites indicated by 'tag 2' and 'tag 3' are the central interaction sites. Accordingly, the 'order 1' and 'order 3' specify the bond order of the tail bonds of a torsion structure; the 'order 2' specifies the bond order of the central bond. The potential function types are encoded by the ID<sub>4</sub>. The list of mathematical functions and the corresponding parameters is given in Table 11. Details on the specifications of special cis/trans isomerism-dependent torsion potentials are given in Appendix C.

**Table 11:** Torsion potential functions and their parameters (fourth section of data scheme, cf. Fig. 29), where  $\Phi$  is the torsion angle formed by the interaction sites under consideration and  $c$  and  $n$  are potential parameters.

ID <sub>4</sub>	Function	P <sub>1</sub>	P <sub>2</sub>	P <sub>3</sub>	P <sub>4</sub>	P <sub>5</sub>	P <sub>6</sub>	P <sub>7</sub>	P <sub>8</sub>	P <sub>9</sub>	P <sub>10</sub>	P <sub>11</sub>	P <sub>12</sub>
1	$c_0 + c_1 (1 + \cos \Phi) + c_2 (1 - \cos 2\Phi) + c_3 (1 + \cos 3\Phi)$	$c_0$	$c_1$	$c_2$	$c_3$	-	-	-	-	-	-	-	-
2	$c \frac{(\Phi - \Phi_0)^2}{2}$	$c$	$\Phi_0$	-	-	-	-	-	-	-	-	-	-
3	$\sum_{i=0}^6 c_i \cos i\Phi$	$c_0$	$c_1$	$c_2$	$c_3$	$c_4$	$c_5$	$c_6$	-	-	-	-	-
4	$c_0 [1 - \cos (2\Phi + \Phi_0)]$	$c_0$	$\Phi_0$	-	-	-	-	-	-	-	-	-	-
5	$\sum_{i=0}^7 c_i \cos^i \Phi$	$c_0$	$c_1$	$c_2$	$c_3$	$c_4$	$c_5$	$c_6$	$c_7$	-	-	-	-
6	$\sum_{i=1}^4 c_i [1 + \cos (n_i \Phi - \Phi_i)]$	$c_1$	$n_1$	$\Phi_1$	$c_2$	$n_2$	$\Phi_2$	$c_3$	$n_3$	$\Phi_3$	$c_4$	$n_4$	$\Phi_4$

The fifth section of the data scheme is termed *improper*. It contains the specifications for improper torsion potentials of a branching intersection of four directly neighbored interaction sites. Hence, the improper torsion potential is specified by the four involved types of interaction sites 'tag 0', 'tag 1', 'tag 2', and 'tag 3' and the three bond orders 'order 1', 'order 2', and 'order 3' – as for the in-line torsion potential (see above). In a branched structure modeled by an improper torsion, one interaction site is the central one – indicated by the 'tag 0' in the data scheme. The three remaining interaction sites 'tag 1', 'tag 2', and 'tag 3' have a direct bond to the central one. Accordingly, 'order 1', 'order 2', and 'order 3' specify the bond order from the central interaction site to the respective neighboring interaction site. The three interaction sites indicated by 'tag 0', 'tag 1', and 'tag 2' span a specific plane (which is relevant for some improper torsion potential functions). The potential functions used for modeling the improper torsion differs in most cases from those used for modeling the in-line torsion. The improper

torsion potential function types are encoded by the ID<sub>5</sub>. The list of mathematical functions and the corresponding parameters is given in Table 12.

**Table 12:** Improper torsion potential functions and their parameters (fifth section of data scheme, cf. Fig. 29), where  $\Psi$  is the out of the plane angle formed by the interaction sites under consideration and  $l$  are potential parameters.

ID <sub>5</sub>	Function	p <sub>1</sub>	p <sub>2</sub>
1	$l_2 \frac{(\Psi - \Psi_0)^2}{2}$	$l_2$	$\Psi$

The sixth section of the data scheme is termed  $1,n$ . It contains the information on the  $1,n$  intramolecular interaction potentials, i.e. the potential acting between an interaction site and its  $n$ th neighbor. For modeling these intramolecular interactions, scaled intermolecular potentials are used. The individual parts modeling the van der Waals interactions and the electrostatic interaction of the intermolecular potential are scaled individually. Hence, the mathematical functions are adopted from the first section, but scaled by a factor. The  $1,n$  section of the data scheme contains two values, i.e.  $n$  indicating the distance of two sites in a molecule and two corresponding 'scaling' values. The 'scaling 1' contains the information on the scaling for the van der Waals interactions and 'scaling 2' the information on the scaling for the electrostatic interactions. If not specified otherwise, the scaling factor is taken to be 0 for  $n \leq 4$  and 1 for  $n > 4$  for both the van der Waals and the electrostatic potentials within the data scheme.

The seventh section of the data scheme is termed *special* and contains special interaction potential cases that may occur in specific transferable force fields that are not covered within the sections one to six. The syntax used for the special potential cases is similar to the  $1,n$  interactions introduced above. Hence, special interaction potentials are specified between two interaction sites. Special potentials model the potential energy between specific interaction sites, which have a certain distance with respect to direct bonding neighbors. The information structure in the *special* potential section is similar to the *bond* section. A *special* interaction is specified by the tags of the two involved types of interaction sites 'tag 1', 'tag 2', and 'dist' (cf. Fig. 29). The latter specifies distance of the involved sites by counting the number of direct bonds between the sites 'tag 1' and 'tag 2'. The potential functions and the corresponding parameters are encoded by the ID<sub>7</sub>. The list of mathematical functions and the corresponding parameters is given in Table 13. The dimensions of the parameters used in Tables 8 - 13 are given in Table 14.

The seven data scheme sections generalize and formalize a transferable force field construction plan. Therein, for a given transferable force field, the ID-vector  $\mathbf{ID} = \{\text{ID}_1,$

**Table 13:** Special potential functions and their parameters (seventh section of data scheme, cf. Fig. 29), where  $r_{ij}$  indicates the distance between the considered interaction sites  $i$  and  $j$ , and  $k$  parameters of the potentials.

ID <sub>7</sub>	Function	p <sub>1</sub>
1	$k_{12}/r_{ij}^{12}$	$k_{12}$

**Table 14:** Force field parameters (cf. Tables 8 – 12) and their physical dimensions as well as their units used in the TUK-FFDat data format.

Parameter	Dimension	Unit
$\varepsilon_{ii}, c$	energy	eV
$\sigma, r$	length	Å
$n$	n	1
$q$	charge	e
$k_i$	energy/length <sup><math>i</math></sup>	eV/Å <sup><math>i</math></sup>
$l_i$	energy/angle <sup><math>i</math></sup>	eV/deg <sup><math>i</math></sup>
$\Theta, \Phi, \Psi$	angle	deg
$N$	energy/(angle length)	eV/(Å deg)

ID<sub>2</sub> ... ID<sub>7</sub>} specifies the mathematical structure of the model. The outlined data scheme can be applied to all-atom and united-atom force fields. Also, force fields parameterized by the bottom-up and top-down approach can be described using the data scheme. Regarding the molecular architecture and potentials, rigid, flexible, and semi-flexible force fields can be described by the data scheme. For semi-flexible force fields it is possible that individual bond lengths, bond angles or torsion angles are constrained. Details are given in Appendix C.

The tag notation in combination with the bond order and the systematization of the potential types provides a formalization for transferable force field construction plans. The proposed data scheme can be used for electronically documenting and defining a large variety of transferable force fields, cf. Fig. 26. Therefore, the data scheme is implemented in an SQL-based data format.

### 4.2.3 SQL-based Data Format

The data scheme introduced above is implemented as an SQL-based data format to make it interoperable and directly usable in automated workflows, e.g. in simulation engines, databases, and for publishing new transferable force fields.

The information contained in each of the seven sections of the data scheme is translated into an SQL table structure in the data format. The data comprised in each of the sections of the data scheme (cf. Fig. 29) are translated to the columns of the tables. The tag notation (cf. Table 6) introduced above is used for specifying interaction sites within the tables.

The data format syntax and data type used in the seven tables is specified in Table 15. For each table, the name of each column and the data type (string, real number, integer, etc.) stored in the column is specified in Table 15. To avoid redundant or duplicate entries within a section and to keep the tables compact, a short-hand notation is introduced. Thereby, an 'X' indicates either a part of a tag or a bond order. The 'X' syntax serves as a placeholder for an arbitrary entry. For example, the bond identifier (tag 1, order, tag 2) = (A-C-X-X, 1, A-C-X-X) specifies all types of bonds in alkanes. Hence, they would all be modeled by the same mathematical function and parameters.

**Table 15:** Data structure of TUK-FFDat data format.

Column	Value	Description
First table: intermolecular		
tag	tag	tag of atom or group of atoms of interaction site (cf. Table 6)
ID1	integer	identifier for potential function for intermolecular interactions and combining rule encoded in ID <sub>1</sub> (cf. Table 8)
p1	real number	parameter of intermolecular potential function
p2	real number	parameter of intermolecular potential function
...	...	...
ref	string	DOI of the reference in which the potential parameters were published
Second table: bond		
tag1	tag	tag of interaction site (cf. Table 6) involved in the considered bond
order	integer	bond order of considered bond
tag2	tag	tag of interaction site (cf. Table 6) involved in the considered bond

*Continued on next page*

---

Column	Value	Description
ID2	integer or "none"	identifier for bond potential function encoded in ID <sub>2</sub> , cf. Table 9 ("none" indicating a fixed bond length)
p1	real number	if ID2 == 'none': bond length, else: parameter of bond potential function
p2	real number	parameter of bond potential function
...	...	...
ref	string	DOI of the reference in which the potential parameters were published

---

Third table: angle

tag1	tag	tag of central interaction site (cf. Table 6) involved in the considered angle
order1	integer	bond order of the bond between the sites represented by tag1 and tag2
tag2	tag	tag of interaction site (cf. Table 6) involved in the considered angle
order2	integer	bond order of the bond between the sites represented by tag2 and tag3
tag3	tag	tag of the interaction site (cf. Table 6) involved in the considered angle
ID3	integer or "none"	identifier for angle potential function encoded in ID <sub>3</sub> , cf. Table 10 ("none" indicating a fixed bond angle)
p1	real number	if ID3 == 'none': bond angle, else: parameter of angle potential function
p2	real number	parameter of angle potential function
...	...	...
ref	string	DOI of the reference in which the potential parameters were published

---

Fourth table: torsion

tag1	tag	tag of interaction site (cf. Table 6) involved in the considered torsion angle
------	-----	--

---

*Continued on next page*

---

Column	Value	Description
order1	integer	bond order of the bond between the sites represented by tag1 and tag2
tag2	tag	tag of interaction site (cf. Table 6) involved in the considered torsion angle
order2	integer	bond order of the bond between the sites represented by tag2 and tag3
tag3	tag	tag of interaction site (cf. Table 6) involved in the considered torsion angle
order3	integer	bond order of the bond between the sites represented by tag3 and tag4
tag4	tag	tag of interaction site (cf. Table 6) involved in the considered torsion angle
ID4	integer or "none"	identifier for torsion angle potential function encoded in ID <sub>4</sub> , cf. Table 11 ("none" indicating a fixed torsion angle)
p1	real number	if ID4 == 'none': torsion angle, else: parameter of torsion potential function
p2	real number	parameter of torsion potential function
...	...	...
ref	string	DOI of the reference in which the potential parameters were published

---

Fifth table: improper

tag0	tag	tag of central interaction site (cf. Table 6) involved in the considered improper torsion angle
order1	integer	bond order of the bond between the sites represented by tag0 and tag1
tag1	tag	tag of interaction site (cf. Table 6) involved in the considered improper torsion angle
order2	integer	bond order of the bond between the sites represented by tag0 and tag2
tag2	tag	tag of interaction site (cf. Table 6) involved in the considered improper torsion angle

---

*Continued on next page*

---

Column	Value	Description
order3	integer	bond order of the bond between the sites represented by tag0 and tag3
tag3	tag	tag of interaction site (cf. Table 6) involved in the considered improper torsion angle
ID5	integer or "none"	identifier for improper torsion angle potential function encoded in ID <sub>5</sub> , cf. Table 12 ("none" indicating a fixed improper torsion angle)
p1	real number	if ID5 == 'none': improper torsion angle, or: parameter of improper torsion potential function
p2	real number	parameter of improper torsion potential function
...	...	...
ref	string	DOI of the reference in which the potential parameters were published

---

Sixth table: 1n\_potential

n	integer	distance between the two sites involved in the 1, <i>n</i> potential given in number of bonds between them
scaling1	real number	scaling factor applied to the potential modeling van der Waals interactions
scaling2	real number	scaling factor applied to the potential modeling electrostatic interactions
ref	string	DOI of the reference in which the potential parameters were published

---

Seventh table: special

tag1	tag	tag of interaction site (cf. Table 6)
dist	integer	distance between the two sites involved in the special potential given in number of bonds between them
tag2	tag	tag of second interaction site (cf. Table 6)
ID7	integer or "none"	potential function for special potentials encoded in ID <sub>7</sub>
p1	real number	parameter of the special potential function
p2	real number	parameter of the special potential function

---

*Continued on next page*



---

Column	Value	Description
...	...	...
ref	string	DOI of the reference in which the potential parameters were published

---

---

#### 4.2.4 Application of Data Format

The TUK-FFDat format proposed in this chapter is applied to three transferable force fields of different type. The three transferable force fields are:

- the TraPPE-UA force field [37, 310, 378–387] (semi-flexible, united-atom),
- the OPLS-AA force field [34, 376, 388–390] (flexible, all-atom), and
- the Potoff force field [38, 311, 391, 392] (semi-flexible, united-atom).

The TraPPE-UA and the Potoff transferable force field have been developed within the chemical engineering community. They are widely used for predicting thermodynamic properties – in particular of hydrocarbons [37, 38, 310, 311]. The OPLS-AA transferable force field has been developed within the molecular biology community and is accordingly mostly used for modeling bio systems, e.g. predicting structural protein properties [364].

The TUK-FFDat implementations of all three transferable force fields (TraPPE-UA, OPLS-AA, and Potoff) are available on Zenodo [436]. In this work, a representative part of the TraPPE-UA transferable force field is depicted and discussed as examples (cf. Tables 16 - 20). This selection represents the alkane and alcohol part of the TraPPE-UA transferable force field. In the main body of the manuscript (Tables 16 - 20), the manuscript references are used instead of the DOIs (see online repository [436]).

**Table 16:** First table (intermolecular) of the data format, cf. Table 15, for the TraPPE-UA force field for alkanes and alcohols.

tag	ID1	p1	p2	p3	ref
A-C-0-0	1	0	148	3.73	[37]
A-C-1-1	1	0	98	3.75	[37]
A-C-2-1	1	0	46	3.95	[37]
A-C-3-1	1	0	10	4.68	[310]
A-C-4-1	1	0	0.5	6.4	[310]
Ak-O-2-1	1	-0.7	93	3.02	[379]
Ak-H-1-1	1	0.435	0	0	[379]
Ak-C-1-1	1	0.265	98	3.75	[379]
Ak-C-2-1	1	0.265	46	3.95	[379]
Ak-C-3-1	1	0.265	10	4.33	[379]
Ak-C-4-1	1	0.265	0.5	5.8	[379]

**Table 17:** Second table (bonds) of the data format, cf. Table 15, for the TraPPE-UA force field for alkanes and alcohols.

tag1	order	tag2	ID2	p1	ref
X-C-X-1	1	X-C-X-1	none	1.54	[37]
Ak-C-X-X	1	Ak-O-2-1	none	1.43	[379]
Ak-H-1-1	1	Ak-O-2-1	none	0.945	[379]

**Table 18:** Third table (angles) of the data format, cf. Table 15, for the TraPPE-UA force field for alkanes and alcohols.

tag1	order1	tag2	order2	tag3	ID3	p1	p2	ref
X-C-X-X	1	X-C-2-1	1	X-C-X-X	1	62500	114	[37]
X-C-X-X	1	X-C-3-1	1	X-C-X-X	1	62500	112	[310]
X-C-X-X	1	X-C-4-1	1	X-C-X-X	1	62500	109.47	[310]
X-C-X-X	1	Ak-C-X-1	1	Ak-O-2-1	1	50400	109.47	[379]
Ak-C-X-1	1	Ak-O-2-1	1	Ak-H-1-1	1	55400	108.5	[379]

**Table 19:** Fourth table (torsion) of the data format, cf. Table 15, for the TraPPE-UA force field for alkanes and alcohols

tag1	order1	tag2	order2	tag3	order3	tag4	ID4	p1	p2	p3	p4	ref
X-C-X-X	1	X-C-2-1	1	X-C-2-1	1	X-C-X-X	1	0	355.03	-68.19	791.32	[37]
X-C-X-X	1	X-C-2-1	1	X-C-3-1	1	X-C-X-X	1	-251.06	428.73	-111.85	441.27	[310]
X-C-X-X	1	X-C-2-1	1	X-C-4-1	1	X-C-X-X	1	0	0	0	461.29	[310]
X-C-X-X	1	X-C-3-1	1	X-C-3-1	1	X-C-X-X	1	-251.06	428.73	-111.85	441.27	[310]
X-C-X-X	1	X-C-2-1	1	X-C-3-2	1	X-C-X-X	1	0	0	0	461.29	[310]
X-C-X-X	1	Ak-C-2-1	1	Ak-O-2-1	1	Ak-H-1-1	1	0	209.82	-29.17	187.93	[379]
X-C-X-X	1	Ak-C-3-1	1	Ak-O-2-1	1	Ak-H-1-1	1	215.96	197.33	31.46	-173.92	[379]
X-C-X-X	1	Ak-C-4-1	1	Ak-O-2-1	1	Ak-H-1-1	1	0	0	0	163.56	[379]
X-C-X-X	1	X-C-2-X	1	X-C-2-1	1	X-O-2-1	1	0	176.62	-53.34	769.93	[379]
X-C-X-X	1	X-C-X-1	1	X-O-2-1	1	X-C-X-1	1	0	725.35	-163.75	558.2	[380]
X-O-2-1	1	X-C-2-1	1	X-C-2-1	1	X-O-2-1	1	503.24	0	-251.62	1006.47	[380]

**Table 20:** Seventh table (special) of the data format, cf. Table 15, for the TraPPE-UA force field for alkanes and alcohols.

tag1	dist	tag2	ID7	p1	ref
Ak-O-X-X	4	X-H-1-1	1	75000000	[380]
Ak-O-X-X	5	X-H-1-1	1	75000000	[380]

The TraPPE-UA transferable force field is a semi-flexible united-atom force field. In the TraPPE-UA force field, all bonds between interaction sites are constrained to be rigid. This translates in the data format as `none` entries in the second data format table, cf. Table 17. The TraPPE-UA transferable force field does not contain improper torsion potentials. Accordingly, the fifth table of the data format remains empty (not shown). Despite the fact that the TraPPE-UA is a united-atom force field, hydrogen atoms are explicitly modeled in some chemical structures, e.g. specific polar functional groups. Details are given in Appendix C.

#### 4.2.5 Conversion Tools

The SQL-based data format presented here can be favorably used for process automation. For human interaction and creating the tables, the classical `.xls` spreadsheet format can, however, be more convenient. An auxiliary tool is provided in the online repository [436] for converting the data scheme from the `.xls` format to the SQL-based format and vice versa. Therefore, two Python scripts are provided in the online repository [436]. For testing, example `.xls` and SQL transferable force field files are also provided. The script named `xlsx2SQL.py` reads an `.xls` spreadsheet file in which a transferable force field is defined and creates an SQL database containing the corresponding transferable force field. The second script reads a transferable force field from an SQL database and creates the corresponding `.xls` spreadsheet files. The handling of these scripts is described in detail in Appendix C. The `.xls` spread files are intended for constructing the actual SQL-based data format files of a given transferable force field.

#### 4.2.6 Conclusions

A generalized data scheme for transferable force fields was presented that can be applied to various types of force fields such as rigid and flexible as well as all-atom and united-atom force fields. The data scheme is implemented into an SQL-based file format. Thereby, the data scheme is fully machine readable and provides uniquely defined

data structures. It is called TUK-FFDat. The TUK-FFDat data scheme and data format is specifically designed for transferable force fields (opposite to component-specific force fields), i.e. it provides data structures for generalized chemical construction plans that define model building blocks for substance classes. Three applications of the data scheme and data format are given (the TraPPE-UA, OPLS-AA, and Potoff transferable force fields). These three examples show important differences, which demonstrates the general applicability of the data scheme. The data scheme and data format proposed in this chapter can be favorably used for increasing the force field interoperability in the molecular simulations community. The data scheme and data format can be used for sharing transferable force field data between different actors, e.g. database developers, force field developers, and simulators.

The data scheme and data format presented here can readily be extended in different directions. New interaction potentials can easily be added in the corresponding potential lists (cf. Tables 8 - 12) by adding a new  $ID_i$ -value. Also, new chemical groups can be added in the corresponding functional group list, cf. Table 7. Also, in the case that the topology of the transferable force field is to be extended, new sections can be added to the data scheme. Also, the ongoing development of a given transferable force field can favorably be carried out based on the data scheme by adding entries in the different section tables. If new interaction site types are added to a transferable force field, the new entries specifying the different potential interactions can be readily appended in the lists of the seven sections. For future work, the data scheme proposed in this chapter can be extended to coarse grain, reactive, and machine learned force fields.

## 4.3 *MolMod* Database: Extension to Transferable Force Fields

### 4.3.1 *MolMod* Transferable

The *MolMod Transferable* database can be accessed at [molmod.boltzmann-zuse.de/](http://molmod.boltzmann-zuse.de/). The purpose of *MolMod Transferable* is to provide findable, accessible, and interoperable access to force field models for molecules based on transferable force fields. The main task of *MolMod Transferable* is to build a component-specific force field for a given molecule based on a given transferable force field and to provide simulation engine input files. The workflow of *MolMod Transferable* is depicted in Fig. 31. The *user input* (left side of Fig. 31) consists of the specification of the molecule and the transferable force field to be used. The molecule specification is to be provided by specifying the molecule structure. The geometry of the molecule can be specified by a drawing of the

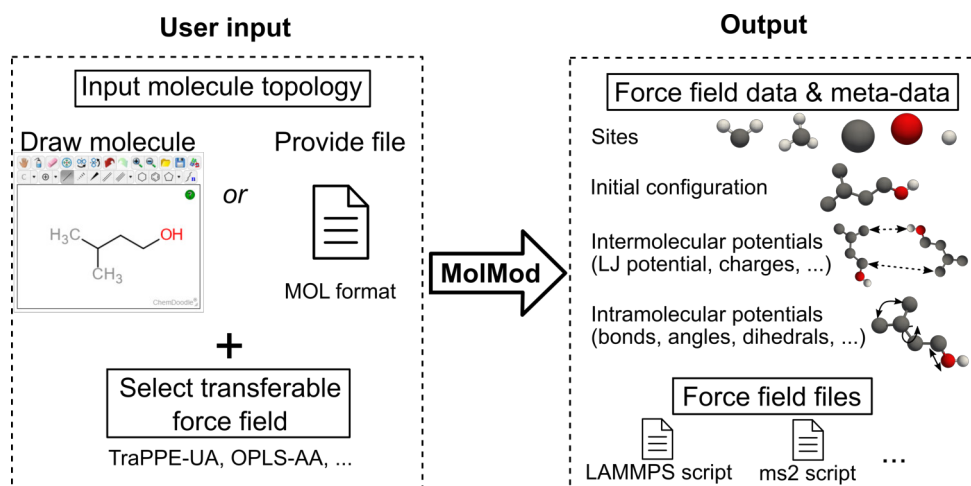


**Figure 31:** Workflow for users of *MolMod Transferable*.

structural formula or by providing a MOL file [437]. The drawing can be done by the *ChemDoodle* sketcher [438], which is integrated into the *MolMod* website. Additionally, the user has to select a transferable force field among those currently available in the *MolMod* database.

*MolMod* displays the component-specific force field model for the considered molecule on-the-fly on the front end of the website. For identifying the functional groups of a given molecule, an algorithm based on the method proposed by *Ertl* [439] was implemented in *MolMod Transferable*. The kernel of *MolMod Transferable* builds a component-specific force field model by assigning the model parameters from the generalized transferable construction plans to a concrete molecular structure. Presently, *MolMod Transferable* covers only molecules that can be represented by the scheme of *Kanagalingam et al.* [425], which comprises a large number of organic substances (see below for details). If this is the case, the component-specific force field can be built; otherwise the user is informed by the website that the transferable force field cannot be used in the present case. Changes of the molecular structure via the structure drawing tool or changing the transferable force field are quasi-instantaneously depicted on the website. Both, the data of the force field and the meta-data are displayed on the website. The actual force field data consists of the force field parameters, i.e., variables and their numeric values and units that define the interaction sites, the initial configuration, and the intermolecular as well as the intramolecular potentials acting between the interaction sites. The meta-data of a user-built component-specific force field comprises the information on the references that published the transferable force field parameters in use for the given model. For some molecules, this might be multiple publications, e.g., for an alcohol where the methyl and methylene group parameters were published separately from the hydroxyl group parameters. Moreover, input files for MD or MC simulation engines of the component-specific force field model built by the user are directly provided by the

*MolMod* database.

Besides being a tool for simulators, the *MolMod Transferable* database is also a useful tool for force field developers to distribute newly developed force fields. The force field parameters in the *MolMod Transferable* database are stored in the generalized data format proposed in Ref. [425]. The format is both human-readable and interoperable with *MolMod Transferable*. Thus, it is straightforward to integrate new transferable force fields into the *MolMod Transferable* database. Details on the implementation of force fields and the general workflow to upload new force fields are given below.

Fig. 32 shows a screenshot of the user interface of the *MolMod Transferable* front end. The *MolMod Transferable* front end consists of five sections (top to bottom). In the user input section (highlighted in red in Fig. 32), which is entitled *Builder*, the user specifies the structure of the molecule by drawing the structure formula or providing a MOL file and specifies the transferable force field via a drop-down menu.

The section *Overview* (highlighted in green in Fig. 32) contains meta-data information on the component-specific force field, including the molecular formula, identifiers for the references used for building the model, the number of interaction sites in the force field, and the name of the underlying transferable force field.

The *Force Field* section (highlighted in blue in Fig. 32) contains the full specification of the actual component-specific force field by providing its parameters in separate tables. The first subsection contains the specification of the sites and the equilibrium configuration, the second and third subsections contain the specifications of the inter- and intramolecular interactions.

In the first subsection, the first table *Sites* provides a list of the interaction sites, their names, their functional groups as well as their molar masses. In the second table, the *Initial Configuration* is given (xyz coordinates of each interaction site in an equilibrium configuration). Details on the calculation of the initial configuration are given below. The *Intermolecular Potential Parameters* subsection provides the parameters for the intermolecular interactions. Depending on the types of interactions used in a given component-specific force field, the corresponding tables are depicted, i.e., a table for the dispersive-repulsive interactions (e.g. Lennard-Jones or Mie potential parameters) and a table for charges and multipoles (no charges are applicable in the ethane model exemplarily shown in Fig. 32). Also, a link to the nomenclature section of the *MolMod* database is given that provides details on the underlying mathematical equations used for the modeling of the interactions. The *Intramolecular Potential Parameters* subsection provides the parameters for the intramolecular interactions as well as the specifications of intramolecular constraints. In this section, tables for the specification of the bond, angle, dihedral, and improper interactions are displayed (latter three are not

**Builder** (User input section)

ChemDoodle<sup>®</sup>

Select the Force Field: TraPPE

**Overview** (General information and meta-data on molecule and force field)

Molecular Formula: C<sub>2</sub>H<sub>6</sub>  
 References: [Martin, 1998]  
 Number of Sites: 2  
 Force Field: TraPPE

**Force Field** (Force field parameters for the chosen molecule)

**Sites**

Site-ID	Site-name	Funktional Group	Group-ID	M / g mol <sup>-1</sup>
1	CH <sub>3</sub>	-	-	15.03452
2	CH <sub>3</sub>	-	-	15.03452

**Initial Configuration**

Site-ID	Site-name	x-Position / Å	y-Position / Å	z-Position / Å
1	CH <sub>3</sub>	-0.77	0	0
2	CH <sub>3</sub>	0.77	0	0

**Intermolecular Potential Parameters**

Lennard-Jones 12-6

Site-ID	Site-name	ε/k <sub>B</sub> / K	σ / Å	Ref.
1	CH <sub>3</sub>	98	3.75	[Martin, 1998]
2	CH <sub>3</sub>	98	3.75	[Martin, 1998]

**Intramolecular Potential Parameters**

**Bond**

Bond-ID	Site-IDs	Site-names	Bond-length / Å	Potential	p0 / K	p1 / K	p2 / K	p3 / K	Type	Ref.
1	1-2	CH <sub>3</sub> -CH <sub>3</sub>	1.54	-	-	-	-	-	rigid	[Martin, 1998]

**Downloads** (Input files download section)

**Further Specification of the Model**

Input Files Format

LAMMPS  
 ms2  
 Gromacs

Download

**References** (Citations used for molecule)

[Martin, 1998] M. G. Martin and J. I. Siepmann: Transferable Potentials for Phase Equilibria. 1. United-Atom Description of n-Alkanes, Journal of Physical Chemistry B 102, 14, 2569-2577 (1998), 10.1021/jp972543+.

**Figure 32:** Screenshot of the user interface of the *MolMod Transferable* front end. As an example, the modeling of ethane C<sub>2</sub>H<sub>6</sub> with the TraPPE-UA transferable force field is considered.

applicable in the example shown in Fig. 32).

The individual tables contain all information needed to identify the interaction potential (an ID for each interaction type, the IDs and names of the sites that are part of the interaction, the potential ID, the actual potential parameters, the type of interaction



(rigid or flexible), and the reference to the publication in which the parameters were first published).

In the *Downloads* section (highlighted in yellow in Fig. 32), *MolMod Transferable* provides files for download that contain the data and meta-data of the considered component-specific force field. Different file formats are available that correspond to input file formats of popular simulation engines. More details on the input files are given below in 'Data Management and Data Integrity'.

The last section *References* (highlighted in light blue in Fig. 32) provides the details on the literature sources that were used to construct the component-specific model. In some cases, it might contain only a single reference, but multiple references will be listed when the information was spread in several papers or if erratums were considered. The references are specified using the full author list, title, journal title, volume, page number, year, and the DOI number including a web-link.

### 4.3.2 Implemented Transferable Force Fields

*MolMod Transferable* covers both UA and AA transferable force fields. Table 21 gives an overview of the force fields presently implemented in *MolMod Transferable*. These

**Table 21:** Overview of transferable force fields presently implemented in the *MolMod* database. Both united-atom (UA) and all-atom (AA) force fields are available. Sorted chronologically. The number of citations was taken from the *Web of Science* (<https://www.webofscience.com>) as of June 26<sup>th</sup>, 2023. The number of citations is the sum of citations of the references given in the third column.

Name	Type	References	First publication	Citations
OPLS-UA	UA	[33, 440–451]	1984	6433
OPLS-AA	AA	[34, 389, 390]	1996	11429
TraPPE-UA	UA	[37, 310, 378–387]	1998	5181
COMPASS	AA	[35]	1998	4406
CHARMM	AA	[36]	1998	11617
GROMOS	UA	[424]	2001	753
Potoff	UA	[38, 311, 391, 392]	2009	150
TAMie	UA	[39, 312, 452–455]	2015	105

transferable force fields differ significantly in the chemical groups for which parameters are available, cf. Table 22. Furthermore, the force fields were developed at different times, e.g., the OPLS-UA force field was in most parts developed in the 1980ies, whereas

**Table 22:** Substance classes and functional groups implemented in the *MolMod* database (1<sup>st</sup> and 2<sup>nd</sup> column). The 3<sup>rd</sup> column lists the transferable force fields that comprise a given functional group.

Substance class	Functional group	Force fields
alkanes	$\text{CH}_x\text{-CH}_x^a$	OPLS-UA, OPLS-AA, TraPPE-UA, COMPASS, CHARMM, GROMOS, Potoff, TAMie
alkenes	$\text{CH}_x\text{=CH}_x^b$	OPLS-UA, TraPPE-UA, Potoff, TAMie
alkynes	$\text{CH}_x\equiv\text{CH}_x^c$	Potoff
(meth)acrylates	$\text{CH}_x\text{-O-C(=O)-CX=CH}_2^{a,d}$	TraPPE-UA
alcohols	$\text{CH}_x\text{-O-H}^a$	OPLS-UA, OPLS-AA, TraPPE-UA, TAMie
aldehydes	$\text{X-C(-H)=O}^{a,d}$	TraPPE-UA, TAMie
aromatic rings	$\text{CH-CH (arom.)}$	OPLS-AA, TraPPE-UA, CHARMM
cycloalkanes	$\text{CH}_2\text{-CH}_2$ (cyc.)	TraPPE-UA, GROMOS, TAMie
disulfides	$\text{CH}_x\text{-S-S-CH}_x^a$	OPLS-UA, OPLS-AA, TraPPE-UA
ethers	$\text{CH}_x\text{-O-CH}_x^a$	OPLS-UA, OPLS-AA, TraPPE-UA, TAMie
ketones	$\text{CH}_x\text{-C(=O)-CH}_x^a$	OPLS-AA, TraPPE-UA, TAMie
nitriles	$\text{CH}_x\text{-C}\equiv\text{N}^a$	OPLS-UA, TraPPE-UA
sulfides	$\text{CH}_x\text{-S-CH}_x^a$	OPLS-UA, OPLS-AA, TraPPE-UA
thiols	$\text{CH}_x\text{-S-H}^a$	OPLS-UA, OPLS-AA, TraPPE-UA

<sup>a</sup>  $x \in [0, 1, 2, 3]$ , <sup>b</sup>  $x \in [0, 1, 2]$ , <sup>c</sup>  $x \in [0, 1]$ , <sup>d</sup>  $X \in [\text{H}, \text{CH}_x]$ .

the Potoff and TAMie force field were developed in the past two decades. Transferable force fields presently implemented in the *MolMod* database use the Lennard-Jones potential or the generalized Mie potential for modeling the dispersive-repulsive interactions and point charges for modeling the polarities for describing intermolecular interactions. For the intramolecular interactions, different approaches are used, i.e., some transferable force fields use constraint stretching and bending bonds (i.e. rigid), whereas other transferable force fields use harmonic springs for modeling the stretching and bending. Most force fields use a torsion potential for modeling the intramolecular rotations. Yet, different force fields mostly use different torsional potential functions.

The force fields are stored in the *MolMod* database using the data format proposed in the previous section. This data format is based on tags that are attributed to every site and that contain information on the functional groups, the modeled atoms or group of atoms, the neighboring interaction sites, the number of bonds, and the highest bond

order of the site. In particular, the data format provides a high interoperability and is well-defined [425], which enables an easy integration of new force fields in the database. Presently, eight transferable force fields are integrated in *MolMod Transferable*. In the following a brief overview of these transferable force fields (cf. Table 21 and Table 22) is given. For some transferable force fields, multiple versions are available in the literature, i.e., multiple parameter sets for a given functional group have been proposed. In the *MolMod* database, only a single version for each transferable force field is implemented – as indicated by the references in Table 21.

The united-atom OPLS-UA transferable force field (Optimized Potentials for Liquid Simulations) [33] was developed by *Jorgensen* and co-workers. The basis of the OPLS-UA force field was published in 1984 and has been extended in the following years. Today, it can be applied to a wide range of structural groups (cf. Table 21). The intermolecular interactions are represented by charges and Lennard-Jones interaction sites. The bond lengths and bond angles are fixed in OPLS-UA. The bond length and bond bending angle values were determined using spectroscopic data. The intramolecular torsion is considered by explicit potentials and the potential parameters were obtained using quantum chemical data. Parameters for the charges and the non-bonded dispersive-repulsive interactions were optimized with respect to macroscopic thermodynamic data and structural data.

Also the all-atom OPLS-AA transferable force field [34] is implemented in the *MolMod* database. It was also developed by *Jorgensen* and co-workers and is today widely used, e.g., in computational biology. For the OPLS-AA force field [34], the bond and bending angle parameters were adopted from the AMBER [376] and the CHARMM force field [456]. The torsional potential parameters were fitted to QM data. The non-bonded dispersive-repulsive interaction parameters (modeled by the Lennard-Jones potential) and charges were fitted to thermodynamic and structural property data (in parts adopted from the OPLS-UA [33]).

The TraPPE-UA transferable force field (Transferable Potentials for Phase Equilibria) comprises a large number of functional group building blocks, cf. Table 21. It was developed by *Siepmann* and co-workers [414]. In the *MolMod* database, presently the UA force field (TraPPE-UA) is implemented, which has to be distinguished from the AA force field TraPPE-AA [457–459]. The TraPPE-UA force field is today one of the most widely used transferable force fields, cf. Table 21. The basis of the TraPPE-UA force field was published in 1998 and has been substantially extended since. The nonbonded dispersive-repulsive interactions are represented by the classical Lennard-Jones potential. The Lennard-Jones interaction parameters were fitted to experimental data for the vapor-liquid equilibrium of selected components. The parameters for the charges and the intramolecular interactions were either taken from the literature or

fitted to quantum-mechanical (QM) calculation results. In most cases, the bending parameters were adopted from AMBER [376]; the dihedral parameters as well as charge parameters were adopted from OPLS-UA [33, 446].

The AA COMPASS (Condensed-phase Optimized Molecular Potentials for Atomistic Simulation Studies) transferable force field is an all-atom force field that was first published in 1998 [35]. The force field was developed to describe simultaneously thermodynamic condensed phase properties and vibrational molecular properties. Hence, an important focus was also on the intramolecular interaction parameters [14]. Therefore, besides the bond, bending, dihedral, and improper interactions, also cross terms are included in the transferable force field. These cross terms model the coupling between the different intramolecular interactions, e.g., the bond-bond, bond-angle, angle-angle, bond-torsion, and angle-torsion couplings. The bond and angle potentials are described by functions with quartic terms. The dispersive-repulsive interactions are modeled by a 9-6 Mie potential. The parameters of the COMPASS force field were determined from a fit to QM data (charges and intramolecular potentials) and to thermodynamic liquid state properties (dispersive-repulsive potential).

The AA CHARMM (Chemistry at HARvard Macromolecular Mechanics) transferable force field version C22/CMAP [36] is implemented in the *MolMod* database. The CHARMM force field was originally developed for modeling bio-molecules such as lipids and proteins, but is today also used for other applications. The CHARMM force field is one of the most popular force fields, cf. Table 21. As for most force fields, the intramolecular parameters were fitted to structural data. Therefore, data from different spectroscopic methods were used in addition to ab initio QM data. The charges were fitted to QM data. The dispersive-repulsive interaction parameters were fitted to experimental solvation data for model compounds in water. As a water model, TIP3P [460] was used in the optimization process.

The UA GROMOS transferable force field (Groningen Molecular Simulation) was developed by *Van Gunsteren* and *Berendsen* and co-workers and was primarily designed for describing aqueous bio-molecular systems. In the *MolMod* database, the GROMOS version 45A3[461] is implemented. The intermolecular parameters of the 45A3 GROMOS version were fitted to experimental data for the bulk liquid density, the enthalpy of vaporization, and the free energy of hydration. The simple point charge (SPC) [462] water model was used in the optimization process. The intramolecular parameters of the 45A3 GROMOS version were adopted from earlier versions, where they were in most parts fitted to quantum chemical data and in parts fine-tuned to macroscopic liquid phase properties [461].

The UA Potoff transferable force field [38], named here after the principal developer, *J. Potoff*, was first published in 2009. Compared to other transferable force fields, the

Potoff force field presently comprises only a small number of functional group building blocks, such that alkanes, alkenes, and alkynes as well as perfluoralkanes, perfluoroalkenes, and perfluoroalkynes can be modeled. The Potoff force field uses the Mie potential for modeling the dispersive-repulsive interactions. The Mie parameters were fitted to experimental vapor-liquid equilibrium data. The intramolecular potential parameters were adopted from the TraPPE force field. The Potoff force field has recently been found to be remarkably accurate for predicting properties and state regions that were not considered in the model parametrization [77].

The UA TAMie (Transferable Anisotropic Mie) transferable force field [39] was developed by *Gross* and co-workers and uses the Mie potential for modeling the dispersive-repulsive interactions. For the TAMie force field, the intramolecular potential parameters were adopted from the TraPPE force field. In contrast to the TraPPE force field, the TAMie force field framework uses an anisotropic approach regarding the bond length between terminal methyl groups and neighboring interaction sites to better account for the hydrogen atoms. In its fitting procedure, parameters for the dispersive-repulsive interactions, partial charges, and the repulsive exponent of the Mie potential were simultaneously fitted to experimental vapor-liquid equilibrium data. The dispersive exponent was set to 6 in all cases.

### 4.3.3 Available Input Formats

The component-specific force fields built by *MolMod Transferable* can be directly downloaded by the user as input files for different common simulation engines. These input files contain the actual force field data written in the corresponding simulation engine syntax as well as the force field meta-data to make the input files transparently reusable.

Presently, *MolMod Transferable* provides download input files for three simulation engines, namely for LAMMPS [298], *ms2* [463, 464], and Gromacs [465]. The files contain the calculated initial configuration of all sites as well as the force field parameters in the respective formats for the molecule of interest.

The LAMMPS input files provided by the *MolMod* database consists of two files: the `.int` file contains the force field parameters for all types of interactions applicable to the model. It is written as a LAMMPS script file and, thus, can be readily integrated into any LAMMPS simulation script. The second file (`.molecule`) contains the geometry of the molecule (bond topology as well as the initial coordinates). For *ms2*, a `.pm` file is provided containing the geometry as well as the potential parameters. The Gromacs input files provided by *MolMod Transferable* consist of four `.itp` files containing the force field parameters, which are split into a main file, a file defining general force field

properties, and two files for defining bonded and non-bonded interactions. Additionally, the initial coordinates are stored in a `.pdb` file.

#### 4.3.4 Data Management and Data Integrity

In the following, the operating principle of the *MolMod* database for using transferable force fields and the corresponding data management system is presented. Fig. 33 schematically shows the interplay between the different database parts, users, and developers. The *MolMod* database is designed such that users can easily find and access force

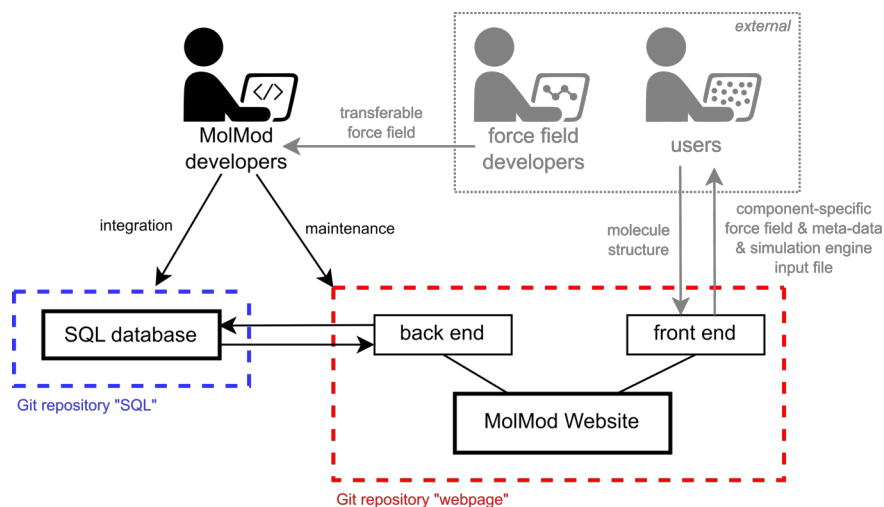


**Figure 33:** Operating principle of the *MolMod Transferable* database and the interaction of the *MolMod* developers, the user, and force field developers with the *MolMod Transferable* database.

field data. For adding new force field models to the *MolMod* database, force field developers are invited to submit their force fields along with the corresponding meta-data to the *MolMod* developers ([info.molmod@boltzmann-zuse.de](mailto:info.molmod@boltzmann-zuse.de)). The data is then checked for consistency and integrated into the database. For submitting new force fields, the data format specified in Ref. [425] should be used, which is directly compatible with the *MolMod* database.

The *MolMod* database is hosted at the RPTU computer center. The *MolMod* database consists of two parts: the *MolMod* database website (highlighted in red in Fig. 33) and the actual database comprising the data and meta-data of the force fields (highlighted in blue in Fig. 33). The latter is stored in an SQL database. Both parts are stored in an individual Git repository, which provides a basic and robust data integrity level. The SQL database is setup within a Git repository that is updated once a day. Hence, a backup is written every 24 h and changes, that eventually crash the website or alter force field data, can be traced back. Also the code for the actual *MolMod* website is

developed within a (separate) Git repository. Thereby, the integrated database system (cf. Fig. 33) is well maintainable, and the data quality traceable. Moreover, the system is designed in a modular way such that it can be well extended, e.g., new transferable force fields can be easily integrated using the SQL data format defined in Ref. [425] and new user features implemented in the back end or front end of the website, e.g., new interaction potential functions.

The *MolMod* website itself consists of a back end and a front end (cf. Fig. 34). The

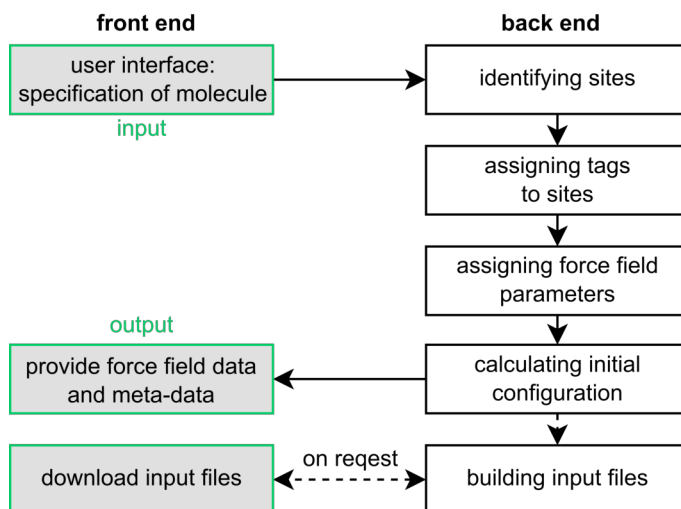


**Figure 34:** Operating principle of *MolMod Transferable* for a user request for building a component-specific force field for a given component based on a given transferable force field and providing an input file for a certain simulation engine.

back end contains the routines for building a component-specific force field based on the molecule structure specifications of the user and a transferable force field. Therefore, the back end retrieves the required force field parameters from the SQL database. Then, the back end builds the component-specific force field as well as determines an equilibrium configuration based on a heuristic approach that determines a (local) minimum of the total intramolecular potential energy [466]. Also, the back end constructs the simulation engine input files and carries out conversions, e.g., between xyz and internal coordinates and different multipole representations [467]. The results are then returned and depicted for the user on the front end.

Both the force field data and meta-data of *MolMod Transferable* are stored in an SQL database. The SQL database (here the version *MySQL 8.0.32* was used) contains the force field parameters within multiple tables (cf. Ref. [425] for details of the data architecture) for the sites, masses, bonds, angles, dihedrals, and special interactions, which also include references to the original publications using DOI identifiers. The data format [425] used in the SQL database generalizes the transferable force field construction

plans such that different transferable force fields can be stored in a homogenized and well-defined machine readable way.

An overview of the internal operating principle for a user request for building a component-specific model for a given molecule structure is depicted in Fig. 34. Accordingly, the front end and the back end interact upon a user request. The molecule structure is in an intermediate step stored in an internal format that includes the information of the chemical groups and the molecule bonding structure. The molecular structure is converted into a collection of sites specifying chemical groups and their bonding structure. Based on this basic layout, the applicable types of intermolecular interactions and intramolecular interactions are identified. Then, a tag ID (following the data scheme embedded in the data format [425]) is assigned to each site according to the atom or group of atoms they represent, which also includes the information on the functional group they are part of. The details of this step evidently differ for UA and AA force fields. Based on the tags, the force field parameters for the intramolecular as well as intermolecular interactions are requested from the SQL database. That request is carried out for all implemented transferable force fields returning the information on which transferable force field actually contains parameters for all functional groups present in the molecule specified by the user. The information, which transferable force field is applicable for the considered component is then provided to the user via the force field drop down menu, cf. Fig. 32 – red-colored section. Thereby, users can quickly screen the availability of force field models for a given substance.

Finally, the initial configuration of the considered molecule is computed based on the intramolecular force field potentials. Due to the increasing computational effort with increasing number of sites, the use of the *MolMod* database is only recommended for molecules up to 100 sites. Moreover, users have a limited open-access budget. Once all relevant parameters and the corresponding meta-data for a given component-specific force field are assigned and compiled, the data is sent to the front end and provided to the user. Moreover, the user can optionally request input files for different software packages. Such files are created upon explicit user request to save computer time when input files are not required.

### 4.3.5 Exemplary Application

The application of the *MolMod Transferable* website is demonstrated in the following. Therefore, molecular dynamics simulations of *n*-decane ( $C_{10}H_{22}$ ) at a temperature of  $T = 373.15$  K and three pressures  $p \in \{20, 90, 160\}$  MPa were conducted for each of the eight force fields. The force fields were used as implemented in the *MolMod Transferable*



database. For the TraPPE-UA, COMPASS, Potoff, and TAMie force field, simulations were carried out using LAMMPS. For the OPLS-UA, OPLS-AA, CHARMM, and GROMOS force field, simulations were carried out with Gromacs. All simulations were conducted in the  $NpT$  ensemble with 500 molecules. The time step was  $\Delta\tau = 0.1$  fs. The simulations were equilibrated for  $10^5$  time steps. The production ran for  $10^6$  time steps. In the simulation with LAMMPS, the Nosé-Hoover thermostat and barostat [299–301] were applied. In the Gromacs simulations, the Nosé-Hoover thermostat [299, 300] and the Parinello-Rahman barostat [468] were used.

Fig. 35 shows the results for the sampled density as function of the pressure in comparison with experimental data (experimental data points and correlation of experimental data). All considered force fields yield reasonable results for the density. It is out of

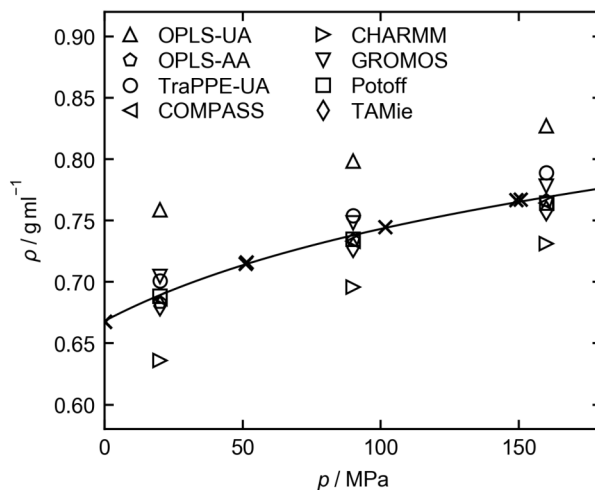


**Figure 35:** Density of *n*-decane as function of the pressure at  $T = 373$  K. Open symbols: simulation results from eight different force fields; line: correlation to experimental data [77]; crosses: experimental values from Ref. [325].

the scope of this chapter to compare the performance of different force fields. Such comparisons have been carried out in the literature, e.g., Refs. [77, 273].

### 4.3.6 Conclusions

In this work, the *MolMod* database was extended to transferable force fields. Therefore, a new workflow was developed and implemented that establishes a link between a user request for a component-specific force field for a given molecule and a transferable force field. The user specifies a molecule structure and a transferable force field; based on that, the database constructs the corresponding component-specific force field and provides both a comprehensive description as well as input files for popular molecular simulation engines. Various transferable force fields were included in *MolMod Transferable*, namely

OPLS-UA, OPLS-AA, COMPASS, CHARMM, GROMOS, TraPPE, Potoff, and TAMie. The data architecture used to obtain a unified description of these models is based on a force field data standard developed in Section 4.2. Thereby, new transferable force fields can readily be integrated into the *MolMod* database. Force field developers are invited to submit their transferable force fields to the *MolMod* developers for integration in the database. *MolMod Transferable* provides ready-to-use input files for different popular molecular dynamics and Monte Carlo simulation engines. *MolMod Transferable* is open-access for the scientific community. Presently, *MolMod Transferable* comprises UA and AA force field frameworks. It would be interesting to extend this to CG force fields in the future.

The development and maintenance of molecular simulation infrastructure such as the *MolMod* database is a highly interdisciplinary task. Experience in multiple programming languages, interfaces, data science aspects, chemistry, and computational physics are closely interconnected. *MolMod Transferable* provides a new level of accessibility and interoperability of transferable force fields, and, by reducing the risk of input errors, also to the reliability of molecular simulations based on transferable force fields.

# 5 Non-Equilibrium Molecular Simulations of Interfacial Heat Transfer in a Model System

## 5.1 Introduction

The heat transfer across solid-fluid interfaces plays an important role in many technical and natural processes. For describing macroscopic heat transfer, it is generally sufficient to assume that thermal equilibrium is established at the interface. As dimensions get smaller, surface phenomena become increasingly important and interfacial effects begin to play a significant role. This chapter deals with the interfacial effects associated with heat transfer that were systematically studied first by *Pyotr Leonidovich Kapitza* [469].

The heat transfer between a solid and a fluid phase requires energy transfer between the particles in the solid and those in the fluid. There is a heat transfer resistance associated with this, which is known as Kapitza resistance  $R_K$  [470] and often expressed in terms of the Kapitza length  $L_K$  [471]. In heat transfer theory, the Kapitza length  $L_K$  plays a similar role as the slip length  $L_S$  in fluid dynamics, which replaces on the microscale the assumption of zero slip used for describing macroscopic flow processes. In macroscopic heat transfer theory, the Kapitza resistance is usually neglected and replaced by the assumption of thermal equilibrium between both phases at the interface.

The Kapitza resistance is difficult to study experimentally. Therefore, molecular dynamics (MD) simulations have been frequently used in the literature to study its influence on heat transfer [471–479]. The available results show that the Kapitza resistance plays an important role in heat transfer on the nanoscale. Notably, there is a temperature jump at the interface, which has to be accounted for and which is directly related to the Kapitza length  $L_K$ . The Kapitza resistance at solid-fluid interfaces of many material pairings has been studied by NEMD simulations [480–483], often with water as fluid component [6, 484, 485]. Besides the variation of the material pairings, the influence of single simulation parameters like the channel width [486, 487], the surface

geometry [481, 488], the temperature or the thermostating [484, 489–491], the fluid density [492, 493], and the solid-fluid [472, 477, 478, 485, 494–496] as well as the solid-solid interaction [471, 474, 497, 498] were determined by MD simulations.

While numbers for  $L_K$  have been determined for various situations, no relations have been established yet that allow an estimation of  $L_K$  for a wide range of conditions. We have therefore carried out a comprehensive MD study of the Kapitza resistance for a model system for which different influencing parameters were varied systematically and used the results for establishing an empirical correlation.

The simulation scenario used in this work consists of a fluid confined between two parallel fixed plane walls: a hot and a cold one. There is no convection. Both the fluid and the walls were modeled with the Lennard-Jones potential truncated and shifted at the cutoff radius  $r_c = 2.5 \sigma$  (LJTS). This potential is well studied regarding both bulk [108, 113, 499] and interfacial properties [60, 63, 260, 264, 500–502] and is often used to study processes on the nanoscale [103, 263, 352, 503, 504]. Moreover, the LJTS potential provides a simple yet realistic model for simple spherical substances [63]. The effects of different influencing factors (solid-fluid interaction, solid-solid interaction, mass of the solid particles, temperature difference between fluid and solid, fluid temperature, fluid density, and channel width) on the heat transfer between the walls and the stagnant fluid were thereby studied systematically. Based on these results, an empirical correlation was developed in this work that describes the heat transfer resistance at the interface as a function of those influencing factors. Furthermore, a dimensionless number is introduced, which is called Kapitza interface number  $Ki$ , to distinguish it from the well-known Kapitza number  $Ka$  [505]. The latter describes the flow of a fluid down an inclined surface, another phenomenon that has been studied by *Pyotr Leonidovich Kapitza*. The Kapitza interface number  $Ki$  relates the Kapitza length  $L_K$  to a characteristic macroscopic length of the heat transfer problem, called  $H$  here, i.e.  $Ki = L_K/H$ . It is straightforward to show that  $Ki$  can be interpreted as the ratio of the Kapitza resistance  $R_K$  and the heat transfer resistance due to heat conduction in the fluid  $R_{\text{cond}}$ , i.e.  $Ki = R_K/R_{\text{cond}}$ . If the characteristic macroscopic length  $H$  is large,  $Ki$  goes to zero and the Kapitza resistance becomes much smaller compared to the conductive resistance.

Surprisingly, there are only few studies available in which the interfacial heat transfer on the microscale was related to that on the macroscale [506, 507]. In the presence of convection, the macroscopic heat transfer is usually described by the Nusselt number  $Nu$ . Formally, the Nusselt number can also be applied when there is no convection. This results in  $Nu = 1$  [508], if the usual definition is applied. The interfacial heat transfer resistance reduces that number [506, 507], but as dimensions increase, the limit of  $Nu = 1$  is finally attained, as long as there is no convection. It has been shown that the interfacial heat transfer resistance is hardly influenced by convection, even for large

streaming velocities [506], such that results obtained for stagnant conditions, as those reported in this work, can also be used for estimating the heat transfer conditions if convection is present.

This chapter is organized as follows: first, details on the molecular model are given. Then, the MD simulation setup and sampling procedure for the observables are presented. Furthermore, the dimensionless quantities used are introduced and an overview of the set of simulations that were carried out is presented. In the subsequent section, the results are reported including a discussion of the effect on the molecular level. Then, the correlation describing the heat transfer based on the simulation data is presented and it is shown how that can be applied in also more complex heat transfer problems. Finally, conclusions are drawn.

## 5.2 Molecular Model

All molecular interactions were modeled using the LJTS potential, which is based on the Lennard-Jones (LJ) potential:

$$u^{\text{LJTS}}(r_{ij}) = \begin{cases} u^{\text{LJ}}(r_{ij}) - u^{\text{LJ}}(r_c) & r_{ij} < r_c \\ 0 & r_{ij} \geq r_c \end{cases} \quad (18a)$$

$$u^{\text{LJ}}(r_{ij}) = 4\varepsilon \left[ \left( \frac{\sigma}{r_{ij}} \right)^{12} - \left( \frac{\sigma}{r_{ij}} \right)^6 \right], \quad (18b)$$

where  $r_{ij}$  is the intermolecular distance between two particles  $i$  and  $j$ ,  $\sigma$  is the size parameter, and  $\varepsilon$  is the energy parameter. The truncation radius is  $r_c = 2.5\sigma$  for all molecular interactions and in all simulations of this work.

All size parameters are the same:  $\sigma_{\text{ff}} = \sigma_{\text{ss}} = \sigma_{\text{sf}}$ , where “ff” stands for interactions in the fluid f, “ss” stands for interactions in the solid s, and “sf” stands for solid-fluid interactions. The influence of the attractive solid-solid and solid-fluid interactions as well as the mass of the solid particles on the interfacial heat transfer resistance was studied systematically by varying the corresponding parameters  $\varepsilon_{\text{ss}}$ ,  $\varepsilon_{\text{sf}}$ , and  $M_s$ , respectively.

All physical quantities are reported using classical reduced Lennard-Jones units, i.e. all quantities are reported with respect to the parameters of the LJTS potential of the fluid: the energy parameter  $\varepsilon_{\text{ff}}$ , the size parameter  $\sigma_{\text{ff}}$ , and the mass  $M_f$ . The reduced units system obtained in this way should be distinguished from dimensionless quantities introduced to lower the number of independent parameters for describing a physical

problem, such as the Nusselt number  $Nu$  or the Kapitza interface number  $Ki$ . The latter can be formulated either directly with physical SI unit quantities or, equivalently, with the corresponding reduced Lennard-Jones unit quantities.

## 5.3 Methods

### 5.3.1 Simulation Details

The simulation setup consists of a hot and a cold wall, which confine a stagnant fluid. A snapshot of the simulation setup is depicted in Fig. 36.

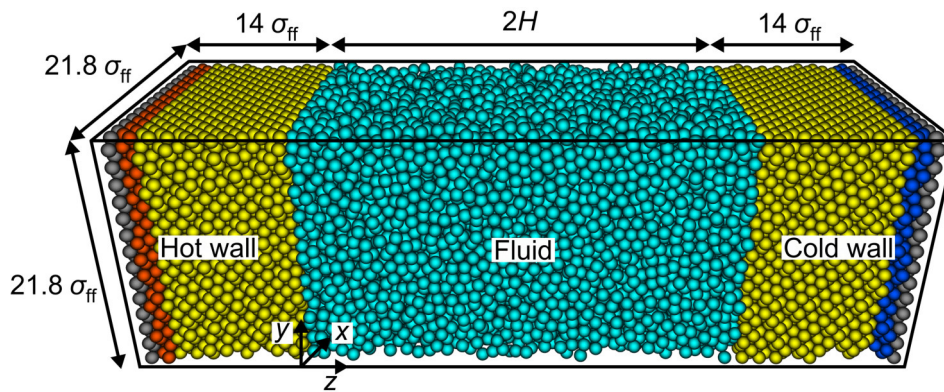


**Figure 36:** Snapshot of the simulation setup. The cyan particles represent the fluid. The remaining particles (gray, red, blue, and yellow) belong to the solid walls, including two fixed layers at the boundaries in  $z$ -direction (gray particles) and two thermostatted regions next to those with  $T_{\text{hot}}$  (red particles) and  $T_{\text{cold}}$  (blue particles). The thermostats induce a temperature gradient in the channel. The yellow particles of the walls are unconstrained. The box boundaries are depicted as black lines. The dimensions of the simulation box are given. The length  $H$  is half the channel width and was systematically varied in this work.

The solid walls had an FCC crystal structure and the (001) surface at the solid-fluid interface. The coordinate system used is depicted in Fig. 36:  $z = 0$  indicates the initial position of the first solid layer of the hot wall that is in direct contact with the fluid. The dimensions of the box in the  $x$ - and  $y$ -direction were  $\Delta x = \Delta y = 21.8 \sigma_{\text{ff}}$ . The thickness of each solid wall in the  $z$ -direction was  $14 \sigma_{\text{ff}}$ . The fluid channel width was  $2H$ , where  $H$  is the distance from  $z = 0$  to the center of the channel. The wall position  $z = 0$  was defined as the average  $z$ -position of all particles of the first layer (directly in contact with the fluid particles) of the left wall (cf. Fig. 36). The channel width was systematically varied in this work.

Periodic boundary conditions were applied in the  $x$ - and  $y$ -directions. The two layers of the hot and the cold walls next to the fixed layers were thermostatted (red and blue

particles in Fig. 36). The temperature was high in one wall ( $T_{\text{hot}}$ ) and low in the other ( $T_{\text{cold}}$ ). Thus, a heat flux in positive  $z$ -direction was induced and measured as described below. Due to the geometry of the setup, the temperature of the fluid in the center of the channel is approximately  $T_f = (T_{\text{hot}} + T_{\text{cold}})/2$ .

All simulations were carried out using the LAMMPS package [509]. The simulation time step was  $0.002 \sigma_{\text{ff}}(M_f/\varepsilon_{\text{ff}})^{1/2}$ . Each simulation run started by 1 million time steps of equilibration in the  $NVT$  ensemble. During that equilibration, a Nosé-Hoover thermostat was applied to the entire system for thermostatization to the temperature  $T_f$ . Subsequently, non-equilibrium conditions were prescribed for 4 million time steps, in which a Langevin thermostat was used to control the temperature in the thermostatted zones of the hot wall and the cold wall. The temperature of the walls were  $T_{\text{hot}} = T_f + \Delta T_w$  and  $T_{\text{cold}} = T_f - \Delta T_w$ , where  $\Delta T_w$  is a system parameter that was systematically varied in the study. Within that non-equilibrium simulation phase, a steady state with a stationary temperature profile was built up during the first 1 million time steps. The following 3 million time steps were used for the sampling of the results. No drift of the total energy appeared in the sampling phase of the simulations.

The simulation volume was uniformly discretized in  $z$ -direction for the sampling of local properties. The local density and temperature were determined in bins of the thickness  $\Delta z_\rho = 0.1 \sigma_{\text{ff}}$  and  $\Delta z_T = 0.5 \sigma_{\text{ff}}$ , respectively. An exemplaric temperature profile and a fluid density profile obtained from the simulations from the hot wall to the middle of the channel is shown in Fig. 37. There, the layering of the fluid at the wall, i.e. the adsorption layer, can be seen. The adsorption in solid-fluid dispersive systems has been extensively studied in the literature [261, 501, 502, 510–514]. At the depicted state point (cf. Fig. 37), multiple layers of particles are observed in the adsorption film, which reaches approximately  $z = 8 \sigma_{\text{ff}}$ . Fluid particles at larger distances from the wall, i.e.  $z > 8 \sigma_{\text{ff}}$  are considered as ‘bulk fluid’ in the following. Therefore, the smallest considered channel width in this chapter was chosen as  $H = 10 \sigma_{\text{ff}}$  such that there was a small bulk region present in all cases. The uncertainty of the sampled Kapitza length  $L_K$  was calculated by block averaging. For this purpose, the sampling part of the non-equilibrium simulation phase was divided into ten blocks, each of a length of 300,000 time steps and the Kapitza length was calculated for each block. The given uncertainties are the standard deviation of the ten values. The results reported for  $L_K$  are the mean values of the ten block results.

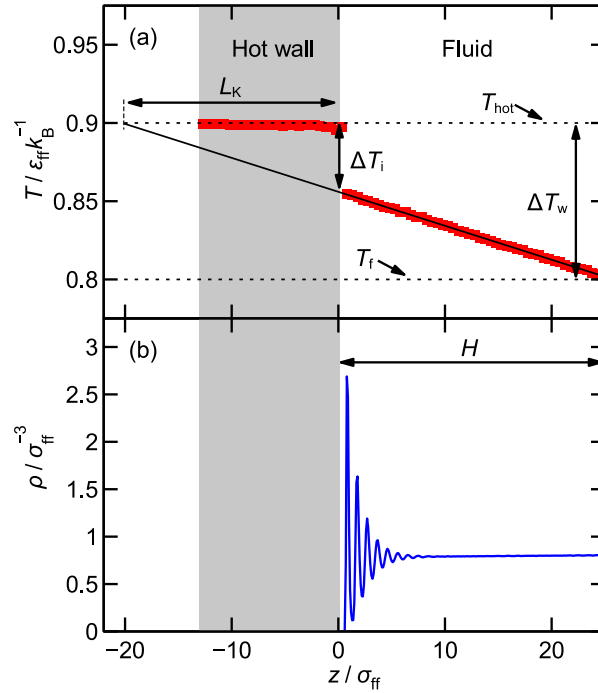


**Figure 37:** Exemplaric simulation result for (a) a temperature profile in the simulation box and (b) a density profile of the fluid for the hot side of the simulation box. The wall is indicated by the gray shaded area. The black solid line in (a) is a linear fit of the fluid temperature profile. The horizontal dashed lines in (a) indicate both the temperature of the hot wall  $T_{\text{hot}}$  and the fluid temperature  $T_f$  (i.e. the temperature in the middle of the channel). The temperature difference at the interface  $\Delta T_i$  and the temperature difference between the hot wall and the fluid in the middle of the channel  $\Delta T_w$  are also depicted.

### 5.3.2 Theoretical Background

From the temperature profiles sampled during the simulations, the temperature jump at the interface  $\Delta T_i$  and the Kapitza length  $L_K$  were determined as indicated in Fig. 37 at both the hot and the cold side. Furthermore, the heat flux  $q$  was determined from

$$q = \frac{1}{A_s} \frac{dE}{dt}, \quad (19)$$

where  $dE/dt$  is the slope of the cumulative kinetic energy added to the hot wall and removed from the cold wall with respect to the time (see Appendix D for details) determined by linear regression and  $A_s$  is the cross-sectional area of the solid-fluid interface, which was computed as the cross-section of the simulation box  $A_s = \Delta x \Delta y$ .

Applying *Fourier's* law of heat conduction to the bulk fluid region, here to the hot side of the simulation box (cf. Fig. 37, analogously applicable to the cold side of the simulation box), yields



$$\frac{q}{\lambda} = -\frac{dT}{dz} = \frac{\Delta T_i}{L_K} = \frac{T_{\text{hot}} - T_f}{H + L_K}, \quad (20)$$

where  $dT/dz$  indicates the slope of the temperature profile determined from a linear fit to the sampled simulation results in the bulk fluid region (cf. Fig. 37). In Eq. (20),  $\lambda$  is the thermal conductivity of the bulk fluid, which is assumed to be constant in the channel. The numbers for  $\lambda$  were determined by the slope of the temperature of the fluid in the channel in the stationary phase and the heat transferred from the hot to the cold wall (cf. Eq. (20)). The values obtained were compared to an empirical correlation from Ref. [113]. Good agreement (AAD of 2.9%) of the simulated values and the empirical correlation from *Lautenschlaeger and Hasse* [113] in the range of validity of the correlation ( $\rho_f > 0.2 \sigma_{\text{ff}}^{-3}$ ) was found. The uncertainty of the empirical correlation was estimated to be 2.4% [113]. The temperature jump at the interface is indicated as  $\Delta T_i$ . The Kapitza length  $L_K$  can be determined either from Eq. (21a) or from Eq. (21b):

$$L_K = \frac{\lambda}{q} \Delta T_i, \quad (21a)$$

$$L_K = \frac{\lambda}{q} (T_{\text{hot}} - T_f) - H, \quad (21b)$$

which are equivalent as long as the temperature profile in the fluid is linear, which was well satisfied by all simulation results from this work. As the statistical uncertainties were found to be smaller when  $L_K$  was determined using Eq. (21b), this route was applied in the present work.

## 5.4 Influencing Factors and Overview of the Simulations

The following influencing factors on the heat transfer at the microscale were considered in this work:

- the dispersion energy  $\varepsilon_{sf}$  describing the solid-fluid interactions,
- the dispersion energy  $\varepsilon_{ss}$  describing the solid-solid interactions,
- the mass of the solid particles  $M_s$ ,
- the temperature difference between the mean fluid temperature and the walls  $\Delta T_w$ ,
- the mean fluid temperature  $T_f$ ,

- the fluid density  $\rho_f$ , and
- the channel width  $H$ .

The interaction parameters  $\varepsilon_{sf}$ ,  $\varepsilon_{ff}$ , and  $\varepsilon_{ss}$  are not independent due to the reduced units system, which is why  $\varepsilon_{ff}$  was not varied here.

**Table 23:** Overview of the simulations of this work and results obtained for the heat flux  $q$  and the Kapitza length  $L_K$ . The variables of the settings are described in the text. Simulation 1 is the *default simulation*. Plain entries of settings have the same value as the default simulation.

Sim.	Setting							Results	
	$\frac{T_f}{\varepsilon_{ff} k_B^{-1}}$	$\frac{\Delta T_w}{\varepsilon_{ff} k_B^{-1}}$	$\frac{\rho_f}{\sigma_{ff}^{-3}}$	$\frac{\varepsilon_{sf}}{\varepsilon_{ff}}$	$\frac{\varepsilon_{ss}}{\varepsilon_{ff}}$	$\frac{M_s}{M_f}$	$\frac{H}{\sigma_{ff}}$	$\frac{q}{\varepsilon_{ff} \sigma_{ff}^{-3} (M_f / \varepsilon_{ff})^{-1/2}}$	$\frac{L_K}{\sigma_{ff}}$
1	0.80	0.10	0.80	1.00	30	2.0	10	0.01934	21.665
2	0.85		0.80					0.02011	19.638
3	0.90		0.81					0.02118	20.075
4	0.95		0.80					0.02202	17.965
5	1.00		0.80					0.02278	17.856
6	1.05		0.81					0.02436	15.850
7	1.10		0.81					0.02512	15.216
8	1.20		0.81					0.02613	13.798
9	1.30		0.80					0.02792	13.032
10			0.81	0.25				0.00554	105.270
11			0.81	0.50				0.01000	51.330
12			0.80	0.75				0.01441	31.112
13			0.81	1.25				0.02299	16.434
14			0.80	1.50				0.02554	12.891
15			0.80	1.75				0.02773	11.358
16			0.80	2.00				0.03005	9.425
17			0.80	2.25				0.03111	8.169
18			0.80	2.50				0.03307	7.184
19			0.81		10			0.03831	5.259
20			0.80		20			0.02645	12.392
21			0.80		40			0.01401	32.836

*Continued on next page*

Sim.	$\frac{T_f}{\varepsilon_{ff} k_B^{-1}}$	$\frac{\Delta T_w}{\varepsilon_{ff} k_B^{-1}}$	$\frac{\rho_f}{\sigma_{ff}^{-3}}$	$\frac{\varepsilon_{sf}}{\varepsilon_{ff}}$	$\frac{\varepsilon_{ss}}{\varepsilon_{ff}}$	$\frac{M_s}{M_f}$	$\frac{H}{\sigma_{ff}}$	$\frac{q}{\varepsilon_{ff} \sigma_{ff}^{-3} (M_f / \varepsilon_{ff})^{-1/2}}$	$\frac{L_K}{\sigma_{ff}}$
22			0.81					0.01052	50.686
23			0.81					0.00833	61.388
24			0.80					0.00644	84.316
25			0.80					0.00521	88.298
26			0.80					0.00394	134.559
27			0.80					0.00359	174.420
28			0.81				15	0.01636	22.441
29			0.80				20	0.01476	22.373
30			0.80				25	0.01279	21.725
31			0.80				50	0.00853	21.691
32			0.80				75	0.00642	21.944
33	1.00		0.80				15	0.01984	18.844
34	1.00		0.80				20	0.01713	17.402
35	1.00		0.80				25	0.01489	17.186
36	1.00		0.80				50	0.00967	17.944
37	1.00		0.80				75	0.00674	19.239
38	1.30		0.80				15	0.02401	13.340
39	1.30		0.80				20	0.01985	13.244
40	1.30		0.80				25	0.01786	13.424
41	1.30		0.80				50	0.01049	14.644
42	1.30		0.80				75	0.00773	13.765
43			0.81	0.25			15	0.00526	107.881
44			0.81	0.25			20	0.00514	107.452
45			0.81	0.25			25	0.00476	110.885
46			0.80	0.25			50	0.00403	101.094
47			0.80	0.25			75	0.00338	107.178
48			0.80	2.50			15	0.02609	7.318
49			0.80	2.50			20	0.02134	7.695
50			0.80	2.50			25	0.01843	7.620

*Continued on next page*

Sim.	$\frac{T_f}{\varepsilon_{\text{ff}} k_{\text{B}}^{-1}}$	$\frac{\Delta T_{\text{w}}}{\varepsilon_{\text{ff}} k_{\text{B}}^{-1}}$	$\frac{\rho_f}{\sigma_{\text{ff}}^{-3}}$	$\frac{\varepsilon_{\text{sf}}}{\varepsilon_{\text{ff}}}$	$\frac{\varepsilon_{\text{ss}}}{\varepsilon_{\text{ff}}}$	$\frac{M_s}{M_f}$	$\frac{H}{\sigma_{\text{ff}}}$	$\frac{q}{\varepsilon_{\text{ff}} \sigma_{\text{ff}}^{-3} (M_f / \varepsilon_{\text{ff}})^{-1/2}}$	$\frac{L_{\text{K}}}{\sigma_{\text{ff}}}$
51			0.80	2.50			50	0.01062	8.450
52	0.79		0.80	2.50			75	0.00722	7.892
53	0.79		0.80		10		15	0.02922	5.388
54	0.79		0.80		10		20	0.02328	5.268
55	0.79		0.80		10		25	0.01965	5.433
56	0.79		0.80		10		50	0.01094	6.130
57	0.79		0.80		10		75	0.00748	5.520
58			0.80		100		15	0.00343	173.528
59			0.80		100		20	0.00321	158.409
60			0.80		100		25	0.00325	152.951
61			0.80		100		50	0.00300	163.039
62			0.80		100		75	0.00256	174.058
63	0.85	0.04	0.80					0.00836	20.803
64	0.85	0.06	0.80					0.01204	20.403
65	0.85	0.08	0.80					0.01628	20.458
66	0.85	0.12	0.80					0.02360	20.548
67	0.85	0.14	0.80					0.02841	20.323
68	0.85	0.16	0.80					0.03162	20.795
69	1.20	0.04	0.80					0.01053	15.354
70	1.20	0.06	0.81					0.01598	13.550
71	1.20	0.08	0.81					0.02077	15.157
72	1.20	0.12	0.81					0.03153	14.754
73	1.20	0.14	0.81					0.03685	13.855
74	1.20	0.16	0.81					0.04235	14.683
75			0.81			0.5		0.00683	77.124
76			0.81			1.0		0.01264	37.883
77			0.81			1.5		0.01677	28.314
78			0.80			2.5		0.02073	18.497
79			0.81			5.0		0.02346	15.482

*Continued on next page*

Sim.	$\frac{T_f}{\varepsilon_{ff} k_B^{-1}}$	$\frac{\Delta T_w}{\varepsilon_{ff} k_B^{-1}}$	$\frac{\rho_f}{\sigma_{ff}^{-3}}$	$\frac{\varepsilon_{sf}}{\varepsilon_{ff}}$	$\frac{\varepsilon_{ss}}{\varepsilon_{ff}}$	$\frac{M_s}{M_f}$	$\frac{H}{\sigma_{ff}}$	$\frac{q}{\varepsilon_{ff} \sigma_{ff}^{-3} (M_f / \varepsilon_{ff})^{-1/2}}$	$\frac{L_K}{\sigma_{ff}}$
80			0.80			7.5		0.02364	14.437
81			0.80			10		0.02274	15.447
82			0.80			15		0.02153	17.841
83			0.81			25		0.01828	22.723
84			0.81			50		0.01157	42.811
85			0.80			75		0.00819	62.876
86			0.81			100		0.00643	87.765
87			0.69					0.01468	16.606
88			0.71					0.01525	18.085
89			0.73					0.01596	18.743
90			0.75					0.01680	18.747
91			0.77					0.01705	20.989
92			0.79					0.01835	19.936
93			0.82					0.02011	21.181
94			0.85					0.02109	22.837
95			0.86					0.02166	21.789
96			0.88					0.02288	23.678
97	1.30		0.08					0.00345	3.855
98	1.30		0.12					0.00505	3.531
99	1.30		0.16					0.00656	4.276
100	1.30		0.21					0.00761	4.401
101	1.30		0.27					0.00893	4.450
102	1.30		0.33					0.00939	5.690
103	1.30		0.39					0.01089	6.625
104	1.30		0.45					0.01193	7.746
105	1.30		0.51					0.01329	8.573
106	1.30		0.56					0.01473	9.514
107	1.30		0.61					0.01647	10.392
108	1.30		0.65					0.01899	11.872

*Continued on next page*

Sim.	$\frac{T_f}{\varepsilon_{\text{ff}} k_{\text{B}}^{-1}}$	$\frac{\Delta T_{\text{w}}}{\varepsilon_{\text{ff}} k_{\text{B}}^{-1}}$	$\frac{\rho_f}{\sigma_{\text{ff}}^{-3}}$	$\frac{\varepsilon_{\text{sf}}}{\varepsilon_{\text{ff}}}$	$\frac{\varepsilon_{\text{ss}}}{\varepsilon_{\text{ff}}}$	$\frac{M_s}{M_f}$	$\frac{H}{\sigma_{\text{ff}}}$	$\frac{q}{\varepsilon_{\text{ff}} \sigma_{\text{ff}}^{-3} (M_f / \varepsilon_{\text{ff}})^{-1/2}}$	$\frac{L_{\text{K}}}{\sigma_{\text{ff}}}$
109	1.30		0.71					0.02114	12.961
110	1.30		0.76					0.02387	13.124
111	1.30		0.85					0.03274	14.000
112	1.30		0.90					0.03632	14.709
113	1.30		0.95					0.04062	13.998

Table 23 gives an overview of the simulations carried out in this chapter and also reports the simulation results for the sampled heat flux  $q$  and the Kapitza length  $L_{\text{K}}$ . In total, 113 simulations were carried out. Simulation 1 (see first column in Table 23) is defined as the *default simulation*. The parameters of the default simulation were chosen such that they are in the middle of the studied parametric ranges and similar to cases that were studied in the literature [113, 471, 473, 477–479, 502, 503, 507, 510, 515]. The temperature of the fluid  $T_f$ , the solid-fluid interaction energy  $\varepsilon_{\text{sf}}$ , and the solid-solid interaction energy  $\varepsilon_{\text{ss}}$  were varied separately in the ranges  $0.8 \leq T_f / \varepsilon_{\text{ff}} k_{\text{B}}^{-1} \leq 1.3$ ,  $0.25 \leq \varepsilon_{\text{sf}} / \varepsilon_{\text{ff}} \leq 2.5$ , and  $10 \leq \varepsilon_{\text{ss}} / \varepsilon_{\text{ff}} \leq 100$ , while the other parameters were kept constant, i.e. their values are identical to those from the default simulation. Such single parametric variations were carried out in simulations 2 – 27. In simulations 28 – 62, the effect of the channel width  $H$  was studied with either the maximum or the minimum value of each of the three influencing factors  $\varepsilon_{\text{sf}}$ ,  $\varepsilon_{\text{ss}}$ , and  $T_f$ . The channel width  $H$  was varied between 10 and 75. In simulations 1 – 62, the temperature difference between the walls and the fluid temperature in the middle of the channel was always  $\Delta T_{\text{w}} = 0.1 \varepsilon_{\text{ff}} k_{\text{B}}^{-1}$ . In order to study the influence of the temperature difference  $\Delta T_{\text{w}}$ , simulations with different wall temperatures were carried out for the two fluid temperatures  $0.85 \varepsilon_{\text{ff}} k_{\text{B}}^{-1}$  and  $1.20 \varepsilon_{\text{ff}} k_{\text{B}}^{-1}$  (cf. Table 23, simulations 63 – 74) to generate  $\Delta T_{\text{w}}$  in the range of  $0.04 \varepsilon_{\text{ff}}$  and  $0.16 \varepsilon_{\text{ff}}$ . The mass of the solid particles  $M_s$  was varied in simulations 75 – 86 in the range  $0.5 \leq M_s / M_f \leq 100$ , while the other simulation parameters were set to the default values of simulation 1. In the remaining simulations 87 – 113, the fluid density was varied along the two isotherms  $T_f = 0.8 \varepsilon_{\text{ff}} k_{\text{B}}^{-1}$  and  $1.3 \varepsilon_{\text{ff}} k_{\text{B}}^{-1}$ . The critical temperature of the LJTS fluid is at approximately  $T_c = 1.1 \varepsilon_{\text{ff}} k_{\text{B}}^{-1}$  [63]. Hence, the isotherm  $T_f = 0.8 \varepsilon_{\text{ff}} k_{\text{B}}^{-1}$  is in the subcritical liquid region, whereas the isotherm  $T_f = 1.3 \varepsilon_{\text{ff}} k_{\text{B}}^{-1}$  is in the supercritical region. For the supercritical isotherm ( $T_f = 1.3 \varepsilon_{\text{ff}} k_{\text{B}}^{-1}$ ), simulations with fluid bulk densities in the range  $\rho_f = 0.08 \sigma_{\text{ff}}^{-3}$  and  $0.96 \sigma_{\text{ff}}^{-3}$  were carried out. For the subcritical isotherm ( $T_f = 0.8 \varepsilon_{\text{ff}} k_{\text{B}}^{-1}$ ), the density was varied in the liquid state region ( $0.69 \leq \rho_f / \sigma_{\text{ff}}^{-3} \leq 0.89$ ). Simulations with lower density have also been carried out in preliminary tests, but showed a phase separation, i.e. vapor bubbles in the metastable vapor-liquid region.

The resulting state points sampled are shown in Fig. 38. Only simulation results with a homogeneous fluid bulk phase are reported here.

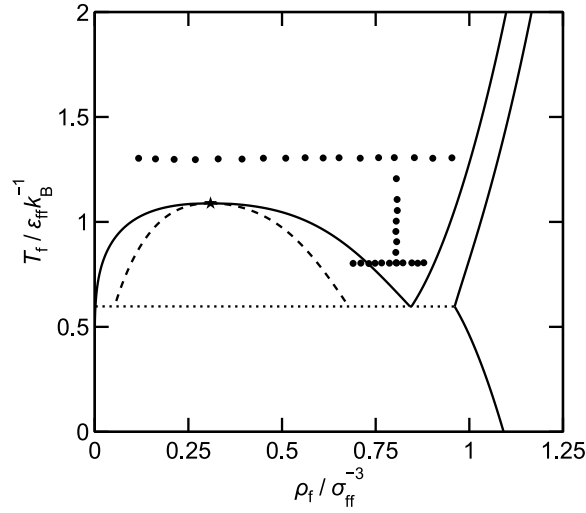


**Figure 38:** Representation of the studied state points of the fluid. The filled black circles represent the simulated state points ( $\bullet$ ). The binodal and the spinodal for the vapor-liquid equilibrium of the LJTS fluid were computed from an equation of state [501]. The other phase boundaries (the sublimation, melting, and freezing line) were adopted from LJ potential data [238]. The critical point is marked by a star ( $\star$ ). The dotted line indicates the triple point temperature [63].

## 5.5 Results and Discussion

### 5.5.1 Empirical Correlation for the Kapitza Length $L_K$

The results obtained from varying  $\Delta T_w$  and  $H$  show that these two simulation parameters have no significant influence on the Kapitza length  $L_K$ . More information is given in Appendix D. Hence, the Kapitza length  $L_K$  is discussed in the following as a function of five variables  $L_K = L_K(\epsilon_{sf}, \epsilon_{ss}, M_s, T_f, \rho_f)$ . The results presented in Table 23 were used to develop a simple empirical correlation, which describes the Kapitza length  $L_K$  as function of the solid-fluid interaction energy  $\epsilon_{sf}$ , the solid-solid interaction energy  $\epsilon_{ss}$ , the mass of the solid particles  $M_s$ , the fluid temperature  $T_f$ , and the fluid density  $\rho_f$ . The mathematical form of the empirical correlation is

$$\frac{L_K}{\sigma_{ff}} = \alpha + \beta \left( \frac{T_f}{\epsilon_{ff} k_B^{-1}} \frac{\epsilon_{sf}}{\epsilon_{ff}} \right)^\gamma \left( \frac{\epsilon_{ss}}{\epsilon_{ff}} \right)^\delta \left( \frac{\epsilon \left( \frac{M_s}{M_f} \right)^2 + \zeta}{\frac{M_s}{M_f}} \right) \left( \frac{\rho_f}{\sigma_{ff}^{-3}} \right)^{\eta \frac{T_f}{\epsilon_{ff} k_B^{-1}} + \theta}. \quad (22)$$

The numeric values of the parameters  $\alpha$ ,  $\beta$ ,  $\gamma$ ,  $\delta$ ,  $\epsilon$ ,  $\zeta$ ,  $\eta$ , and  $\theta$  are given in Table 24. The correlation yields an absolute average deviation (AAD) of 5.1% to the data used

for the fit.

Eq. (22) in connection with Table 24 reveals that the Kapitza length  $L_K$  increases with decreasing fluid temperature  $T_f$  and decreasing solid-fluid interaction  $\varepsilon_{sf}$ . In contrast, increasing the solid-solid interaction energy  $\varepsilon_{ss}$  and increasing the density of the fluid  $\rho_f$  results in an increase of the Kapitza length  $L_K$ . A more complex behaviour is found for the dependency on  $M_s$ : The Kapitza length passes through a minimum in the studied range  $M_s$ . In the following sections, the individual influencing factors are discussed in detail.

**Table 24:** Numeric values of the empirical correlation model for the Kapitza length (cf. Eq. (22)).

Parameter	Value
$\alpha$	2.447
$\beta$	0.324
$\gamma$	-1.238
$\delta$	1.781
$\epsilon$	0.00635
$\zeta$	0.267
$\eta$	-0.621
$\theta$	2.057

Fig. 39 shows the performance of the empirical model (cf. Eq. (22)) in a parity plot in comparison to the simulation results. For most data points, the model describes the simulation results with a relative deviation of 10% or less. Especially for moderate to high values of the Kapitza length ( $10 < L_{K,\text{sim}} / \sigma_{\text{ff}} < 100$ ) where many data points are available, the correlation provides a good fit to the simulation results. For smaller values of the Kapitza length, there are more outliers. Nevertheless, most data points in this region have a relative deviation smaller than 10%.



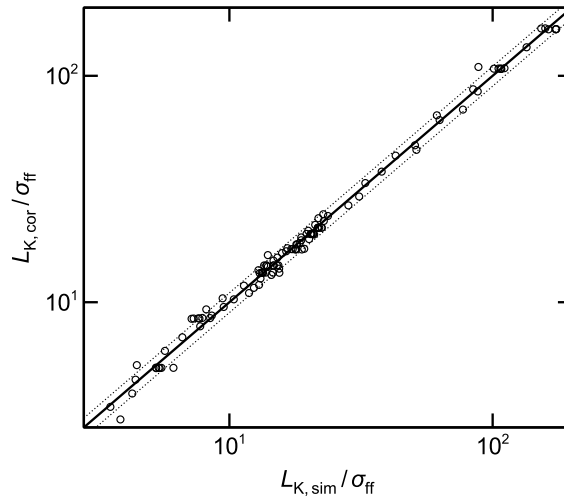


**Figure 39:** Parity plot of the Kapitza length calculated from the empirical correlation (cf. Eq. (22))  $L_{K,cor}$  plotted over the simulation results  $L_{K,sim}$ . Both axes have a log scale. Symbols indicate the simulation results. The black solid line represents the case  $L_{K,cor} = L_{K,sim}$ . The dotted lines represent deviations  $\pm 10\%$ .

### 5.5.2 Influence of Solid-Fluid Interaction Energy

The solid-fluid interaction energy is known to have a strong influence on the microscopic heat transfer at solid-fluid interfaces [264, 493, 496, 502]. Fig. 40 shows the results obtained in present chapter for the Kapitza length as a function of the solid-fluid interaction energy  $\varepsilon_{sf}$  in the simulations 1 and 10 – 18 (cf. Table 23). As the solid-fluid interaction energy  $\varepsilon_{sf}$  increases, the Kapitza length  $L_K$  decreases, i.e. the transport resistance at the interface decreases. Hence, a strong solid-fluid interaction and thereby a strong coupling enables a high heat transfer across the solid-fluid interface, as expected. This is due to a stronger attractive coupling of the solid and fluid particles at the interface, which enables a better transfer of kinetic energy across the interface. For small values of the solid-fluid interaction energy, the Kapitza length exhibits large values, which is due to the repulsive interactions dominating the interactions at the interface, which acts as a hindrance for heat transfer. As the attractive interactions at the interface become important (with increasing  $\varepsilon_{sf}$ ), the dependence of the Kapitza length on  $\varepsilon_{sf}$  becomes weaker and the curve flattens (cf. Fig. 40). Similar observations for the dependency on the solid-fluid interaction energy were also observed for tribological properties of the same LJTS model system studied in scratching simulations [264], i.e. a strong influence of the solid-fluid interaction energy for  $\varepsilon_{sf}/\varepsilon_{ff} < 1$  and only a moderate influence for  $\varepsilon_{sf}/\varepsilon_{ff} > 1$ .

Furthermore, the influence of  $\varepsilon_{sf}$  on the adsorption layer, which describes the layering structure at the interface, was investigated. As shown in Ref. [502], the adsorption layer

may have an important influence on interfacial processes. The results for the adsorption layer are presented and discussed in Appendix D.

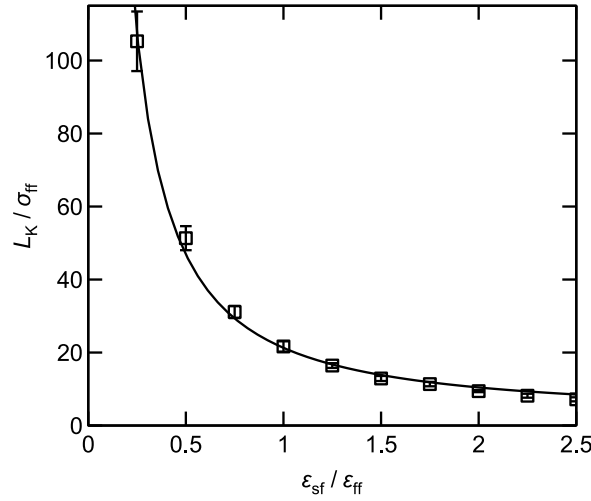


**Figure 40:** Kapitza length  $L_K$  as a function of solid-fluid interaction energy  $\epsilon_{sf}$ . Results from simulations 1 and 10 – 18 (symbols) (cf. Table 23). The solid line indicates the empirical correlation (cf. Eq. (22)). For all shown data points, the simulation parameters  $\epsilon_{ss}$ ,  $M_s$ ,  $T_f$ ,  $\Delta T_w$ ,  $\rho_f$ , and  $H$  were constant (cf. Table 23).

### 5.5.3 Influence of Solid-Solid Interaction Energy

Fig. 41 shows the Kapitza length  $L_K$  as a function of the solid-solid interaction energy  $\epsilon_{ss}$  as obtained from simulations 1 and 19 – 27 (cf. Table 23). Within the studied range, the Kapitza length  $L_K$  increases with increasing  $\epsilon_{ss}$ . This is in accordance with the acoustic mismatch model (AMM), which predicts a deterioration of the energy transport between a solid and a fluid phase as a result of a mismatch between the solid and fluid interaction energies [470, 516]. Moreover, according to the AMM, a linear relation between the misfit and the heat transfer resistance is expected. In contrast, the simulation results depicted in Fig. 41 show a non-linear relation – especially for small  $\epsilon_{ss}$  values. This behaviour is in line with findings from studies, which showed partial failure of AMM for predicting the interfacial thermal resistance [473, 477].

For large values of  $\epsilon_{ss}$ , the heat transfer between the solid and the fluid basically breaks down; the AMM predicts:  $L_K \rightarrow \infty$  for  $\epsilon_{ss} \rightarrow \infty$  [470, 517]. In principle, one could expect that for  $\epsilon_{ss}/\epsilon_{ff} \rightarrow 1$  the Kapitza length  $L_K \rightarrow 0$ . However, this would require that also all other differences between the solid and the liquid vanish, which is not the case in the present study as the mass of the solid particles was  $M_s/M_f = 2$  in simulations 19 – 27. The influence of  $M_s$  on the results is the subject of the next section.

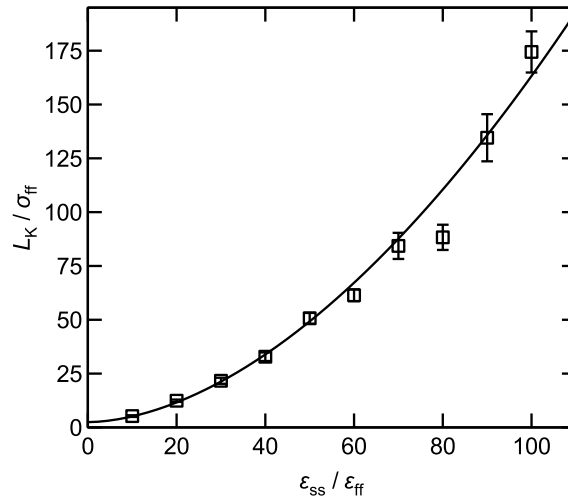


**Figure 41:** Kapitza length  $L_K$  as a function of the solid-solid interaction energy  $\varepsilon_{ss}$ . Results from simulations 1 and 19 – 27 (symbols) (cf. Table 23). The solid line indicates the empirical correlation (cf. Eq. (22)). For all shown data points, the simulation parameters  $\varepsilon_{sf}$ ,  $M_s$ ,  $T_f$ ,  $\Delta T_w$ ,  $\rho_f$ , and  $H$  were constant (cf. Table 23).

#### 5.5.4 Influence of Mass of Solid Particles

The influence of the mass of the solid particles  $M_s$  was studied by simulations 75 – 86. The range  $0.5 \leq M_s/M_f \leq 100$  covers also extreme mass ratios to investigate the limits of the Kapitza length. For  $M_s/M_f < 0.5$  and  $M_s/M_f > 100$ , the heat flux is close to zero, which leads to large statistical uncertainties for the sampled Kapitza length. Therefore, only simulations in the range  $0.5 \leq M_s/M_f \leq 100$  were included in the study. In Fig. 42, the results for the variation of  $M_s$  are shown.

The Kapitza length  $L_K$  exhibits a minimum at approximately  $M_s/M_f = 7.5$ . For larger masses of the solid particles, the Kapitza length increases, which is covered well by the correlation (cf. Eq. (22)). According to AMM, a linear dependency of  $L_K$  on the elastic properties of the solid [470], i.e.  $M_s$ , is expected, which is confirmed by the simulations from this work only for  $M_s/M_f > 15$ . At about  $M_s/M_f = 7$ , the Kapitza length has a minimum of about  $L_K = 13 \sigma_{ff}$ . For smaller values, the Kapitza length  $L_K$  increases with decreasing mass of the solid particles. This behaviour is a result of the decreasing momentum of the solid particles and, therefore, the decreasing energy being transferred between solid and fluid particles when they collide. The correlation (cf. Eq. (22)) describes the complex dependence of the Kapitza length on the mass of the solid particles overall well.

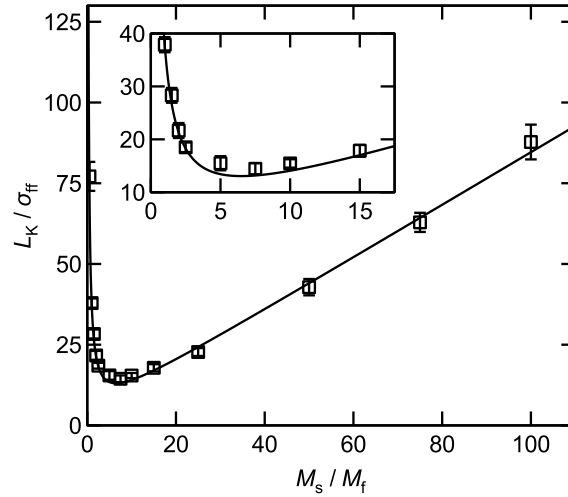


**Figure 42:** Kapitza length  $L_K$  as a function of the mass of the fluid particles  $M_s$ . Results from simulations 1 and 75 – 86 (symbols) (cf. Table 23). The solid line indicates the empirical correlation (cf. Eq. (22)). For all shown data points, the simulation parameters  $\varepsilon_{sf}$ ,  $\varepsilon_{ss}$ ,  $T_f$ ,  $\Delta T_w$ ,  $\rho_f$ , and  $H$  were constant (cf. Table 23).

### 5.5.5 Influence of Fluid Temperature

Fig. 43 shows the results for the Kapitza length  $L_K$  as a function of the mean fluid temperature  $T_f$  as obtained from simulations 1 – 9. In the studied temperature range,  $L_K$  decreases with increasing  $T_f$ . This qualitative behaviour of the Kapitza resistance was also reported by previous studies [478, 482, 493, 497]. A higher mean fluid temperature  $T_f$  leads to a higher temperature of both the fluid and the solid particles in the vicinity of the interface. The effect of the fluid temperature on the structuring of the adsorption layer is shown and discussed in detail in Appendix D. In general, the structuring of the adsorption layer can have an influence on the local transport properties of fluids [518, 519]. However, it was found that the effective transport properties averaged across the entire adsorption layer exhibit only minor deviations from the corresponding bulk phase values [502] for systems as the ones studied here.

With increasing temperature, the mean undirected kinetic energy of the particles and thus their mobility increases, which yields higher collision rates in both, bulk phases and at the interface, which decreases interfacial heat transfer resistance and thereby the Kapitza length. The Fluid structure at the interface (see Appendix D) becomes less prominent with increasing temperature, which counteracts the aforementioned effect. As the interfacial structuring of the fluid decreases with increasing temperature, both phases become more unlike and fewer fluid particles are permanently coupled to solid-phase particles at the interface. This hinders the heat transfer through the interface and is also in accordance with AMM [470]. In the simulation results from this work, the

temperature effect on the overall particle mobility dominates the adverse effect from the adsorption structure. Yet, even for the highest temperature (which is slightly above the critical point of the LJTS fluid [500]) studied here, the Kapitza length  $L_K$  remains fairly high.

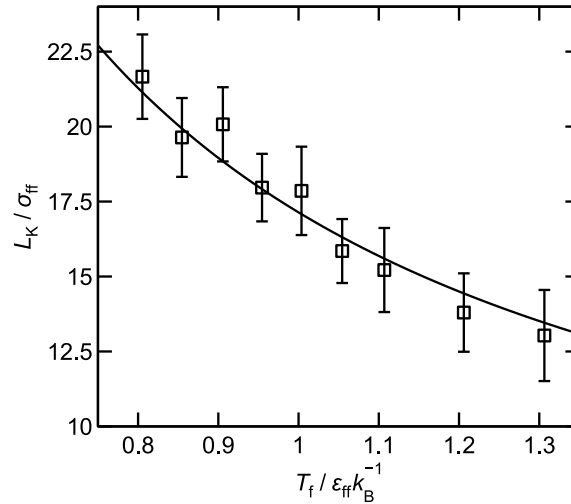


**Figure 43:** Kapitza length  $L_K$  as a function of the fluid temperature  $T_f$ . Results from simulations 1 – 9 (symbols) (cf. Table 23). The solid line indicates the empirical correlation (cf. Eq. (22)). For all shown data points, the simulation parameters  $\varepsilon_{sf}$ ,  $\varepsilon_{ss}$ ,  $M_s$ ,  $\Delta T_w$ ,  $\rho_f$ , and  $H$  were constant (cf. Table 23).

### 5.5.6 Influence of Fluid Density

The influence of the fluid density  $\rho_f$  was studied in the liquid phase region ( $T_f = 0.8 \varepsilon_{ff} k_B^{-1}$ ) and at supercritical conditions ( $T_f = 1.3 \varepsilon_{ff} k_B^{-1}$ , cf. Fig. 38). The corresponding simulation results are shown in Fig. 44. For both isotherms, the Kapitza length  $L_K$  increases monotonically with increasing fluid density. Such behavior was already reported by *Amani et al.* [493] for liquid phase state points. The results for  $T_f = 1.3 \varepsilon_{ff} k_B^{-1}$  show that this also holds at supercritical conditions and for low densities of the fluid. Yet, the density dependence is found to be more prominent at low temperatures, i.e. the slope of  $L_K(\rho_f)$  is larger at low temperatures. Moreover, it can be seen that the influence of temperature and density on  $L_K$  plays an important role. The developed empirical correlation describes the behavior well for both, the sub- and the supercritical temperature.

An increasing Kapitza length with increasing fluid density may be considered counter-intuitive: one might expect an improvement of the heat transfer as the particles bump into each other more often at higher densities. This would lead to larger transfer of momentum between the solid and the fluid particles and, therefore, decrease the interfacial heat resistance. However, this mechanism is counteracted by an increasing structuring in adsorption layers with increasing density and an increasing dominance of repulsive

interactions. The adsorption layers are shown in Appendix D for ten state points with  $0.08 \leq \rho_f / \sigma_{\text{ff}}^{-3} \leq 0.96$  and  $T_f = 1.3 \varepsilon_{\text{ff}} k_{\text{B}}^{-1}$ . With increasing density, the number of adsorption layers increases, while the individual layers become thinner at the same time. This leads to a decrease of the mobility of the particles in the vicinity of the interface, especially perpendicular to the surface, and thereby also to an increase of the interfacial heat resistance.

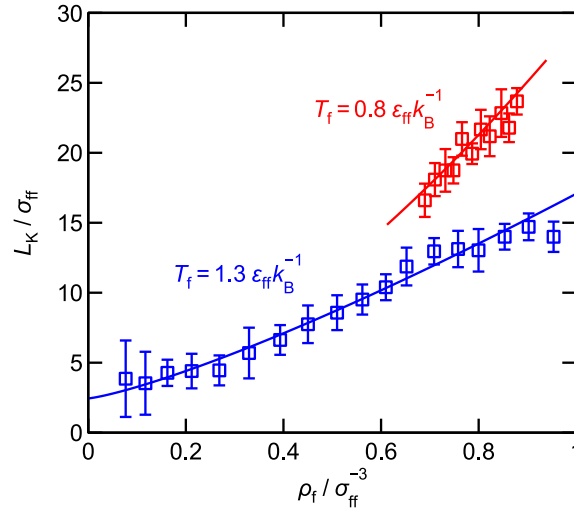


**Figure 44:** Kapitza length  $L_K$  as a function of the fluid density  $\rho_f$  for the temperatures  $T_f = 0.8 \varepsilon_{\text{ff}} k_{\text{B}}^{-1}$  (red) and  $T_f = 1.3 \varepsilon_{\text{ff}} k_{\text{B}}^{-1}$  (blue). Results from simulations 1 and 87 – 113 (symbols), (cf. Table 23). The solid lines indicate the empirical correlation (cf. Eq. (22)). For all shown data points, the simulation parameters  $\varepsilon_{\text{sf}}$ ,  $\varepsilon_{\text{ss}}$ ,  $M_s$ ,  $\Delta T_w$  and  $H$  were constant (cf. Table 23).

### 5.5.7 Introducing the Kapitza Interface Number $Ki$

In the heat transfer simulation scenario studied here (cf. Fig. 36), heat conduction in the fluid plays an important role. Even in the case of total absence of the Kapitza effect (i.e. for  $L_K = 0$ ), there is the heat transfer resistance due to the heat conduction in the fluid between the two planar walls, which is simply

$$R_{\text{cond}} = \frac{H}{\lambda}, \quad (23)$$

where  $H$  is the channel width and  $\lambda$  is the thermal conductivity of the fluid. Here, we assume that the mean thermal conductivity in the adsorption layer is the same as in the bulk fluid, which is a reasonable approximation, as the temperature profiles that were observed in the liquid were basically linear in all cases studied in the present work. For a systematic investigation of the thermal conductivity of the LJTS fluid near walls, see Ref. [502].

It is, therefore, interesting to relate the Kapitza heat transfer resistance  $R_K$ , which is simply

$$R_K = \frac{L_K}{\lambda} \quad (24)$$

to  $R_{\text{cond}}$ . The quotient  $R_K/R_{\text{cond}}$  is a dimensionless number, which is called Kapitza interface number  $Ki$ . It follows from Eq. (23) and (24) that

$$Ki = \frac{R_K}{R_{\text{cond}}} = \frac{L_K}{H}, \quad (25)$$

which gives a descriptive geometric interpretation of  $Ki$  as the ratio of the Kapitza length  $L_K$  and the characteristic macroscopic length of the problem, which is  $H$  here.

The total thermal resistance  $R_{\text{total}}$  in a system without convection, as it was considered in this work, is defined as the sum of the conductive thermal resistance  $R_{\text{cond}}$  and the Kapitza resistance  $R_K$

$$R_{\text{total}} = R_K + R_{\text{cond}} = \frac{H}{\lambda} (Ki + 1). \quad (26)$$

Here, the conductive thermal resistance of the walls is neglected and a constant wall temperature is assumed (cf. Fig. 37). For the LJTS system studied here, this is an excellent assumption due to the much higher thermal conductivity in the solid compared to the fluid [113, 520].

The dimensionless number  $Ki$  characterizes the influence of the Kapitza interface resistance on the total thermal resistance. Due to its definition (see Eq. (25)),  $Ki$  goes to zero for large channel widths  $H$ , and the influence of the Kapitza resistance on the total heat transfer resistance  $R_{\text{tot}}$  vanishes, see Eq. (26). Fig. 45 shows the dependency of the results for the  $Ki$  number obtained from the simulations of the present work on the channel width  $H$ . As expected,  $Ki$  decreases inversely proportional to  $H$ , which indicates that the numbers for  $L_K$  are independent of the channel width  $H$ , which is also shown in Appendix D and is in line with findings from the literature [486, 487]. As can be seen in Fig. 45, the empirical correlation developed in this chapter agrees well with the simulation results. Only for simulations 19 and 53 – 57 ( $\triangleleft$ ) with weak solid-solid interaction energies and, therefore, small values for the Kapitza length  $L_K$  (cf. section 5.5.3), the correlation shows some deviations from the simulation results as already discussed in section 5.5.1. Fig. 45 illustrates that the dimensionless number  $Ki$  is particularly high for weak solid-fluid interaction energies  $\varepsilon_{\text{sf}}$  ( $\triangle$ ) and large solid-solid interaction energies  $\varepsilon_{\text{ss}}$  ( $\triangleright$ ). For both simulation series ( $\triangle$  and  $\triangleright$ ),  $Ki > 1$  holds for all conducted simulations. In Fig. 45, the results from the correlation are deliberately shown for a very large range of  $H$  covering values up to 1000, which is much higher than

the maximum channel width studied here, which was about  $H_{\max} = 75 \sigma_{\text{ff}}$ . Values of  $Ki > 1$  indicate that the Kapitza resistance  $R_K$  is larger than the resistance due to heat conductivity  $R_{\text{cond}}$ , but even for  $Ki = 0.1$  the Kapitza resistance  $R_K$  is 10% of  $R_{\text{cond}}$ , and hence, not negligible. Fig. 45 illustrates that this is true in many cases even for channel widths as large as 2000 molecular diameters ( $H = 1000 \sigma_{\text{ff}}$ ).

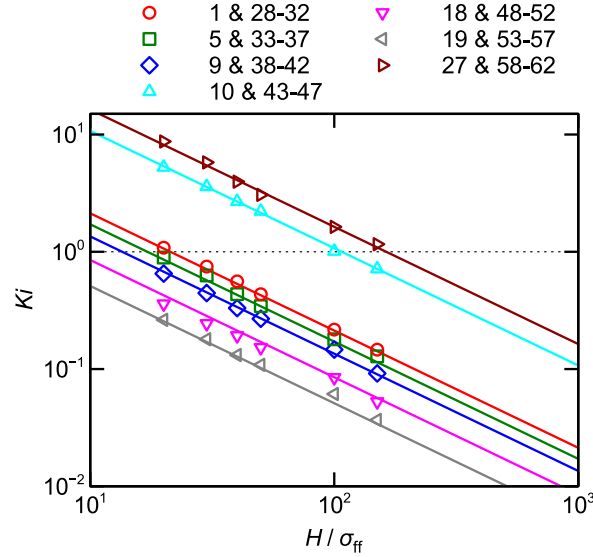


**Figure 45:** Kapitza interface number  $Ki$  as function of the channel width  $H$  as log-log plot. Symbols indicate simulation results; the numbers given in the legend correspond to the simulation numbers given in Table 23. The solid lines represent the values for  $Ki$  obtained from the empirical correlation for  $L_K$  (Eq. (22) and Eq. (25)).

### 5.5.8 Describing Heat Transfer with Convection and Scale-up

In general, the application of the correlation given in Eq. (22) on real substance systems requires the estimation of the parameters, which describe the molecular interactions and the size of the molecules, namely  $\varepsilon_{\text{ff}}$ ,  $\varepsilon_{\text{sf}}$ ,  $\varepsilon_{\text{ss}}$ , and  $\sigma_{\text{ff}}$ . These parameters can be estimated by different methods. For the parameters of the fluid  $\varepsilon_{\text{ff}}$  and  $\sigma_{\text{ff}}$ , there are many parameter sets given in the literature, mainly for small, spherical molecules [63, 107]. Estimations for the solid-solid interaction energy  $\varepsilon_{\text{ss}}$  are also available for different materials, e.g. for some metals [521]. The solid-fluid interaction energy  $\varepsilon_{\text{sf}}$  can be derived from the wetting behavior of the material pairing [260]. With these four parameters given, all quantities involved in a given problem (e.g.  $T$  or  $H$ ) can be reduced and the correlation in conjunction with Eq. (25) can be used to estimate  $Ki$ . *Merabia et al.* [522] showed that such a mapping of results from a Lennard-Jones model system to real systems of nanoparticles based on a corresponding states principle yields good results.



In the following, it is briefly discussed, how the results for  $Ki$  that were obtained in this work can be applied for describing heat transfer with convection. Also the scale-up from nanoscale channels to macroscale channels is discussed. As an example, the following situation is considered: a fluid flows between two parallel planar walls of the temperature  $T_w$ , which differs from the fluid temperature  $T_f$ , which is defined here as the temperature of the fluid in the middle of the channel for the sake of simplicity. The characteristic length  $L$  of such a scenario is usually defined in terms of the channel width, i.e.  $L = 2H$  [523, 524]. The Kapitza interface number  $Ki$  (cf. Eq. (25)) accounts for the Kapitza resistance in the absence of convection.

The heat transfer from a solid surface with the temperature  $T_w$  to a bulk fluid with the temperature  $T_f$  is described by

$$q = \frac{T_w - T_f}{R_{\text{total}}} , \quad (27)$$

where  $R_{\text{total}}$  is the total thermal resistance, which can be written as

$$R_{\text{total}} = R_K + R_{\text{conv}} . \quad (28)$$

The term  $R_{\text{conv}}$  includes the convective and the conductive contribution to the thermal resistance such that Eq. (26) is extended to systems with convection. The summation of the resistances in Eq. (28) is adapted from Refs. [525–527]. Usually, the transport resistance  $R_{\text{conv}}$  is calculated in engineering from the Nusselt number  $Nu$ :

$$R_{\text{conv}} = \frac{1}{\alpha_{\text{conv}}} = \frac{L}{Nu \lambda} = \frac{2 H}{Nu \lambda} , \quad (29)$$

where  $\alpha_{\text{conv}}$  is the convective heat transfer coefficient. From Eqs. (25), (28), and (29), it follows that

$$R_{\text{total}} = \frac{H}{\lambda} \left( Ki + \frac{2}{Nu} \right) . \quad (30)$$

Eq. (30) accounts for the interfacial resistance, the conductive, and convective heat transfer effects. Heat conduction in the flowing bulk fluid is incorporated in the Nusselt number  $Nu$ . Different Nusselt number correlations have been proposed in the literature [528], which may yield different limits for zero flow velocity. In many cases, the limit is zero, i.e. heat conduction is neglected. To be consistent with the discussion above, the limit of the Nusselt number for zero flow velocity should be  $Nu = 2$  (cf. Eq. (26) and 30).

Eq. (30) also enables discussing the influence of the scale of the problem on the heat transfer. The scale is determined by the geometric parameter  $H$ . As  $H$  increases,  $Ki$  approaches 0 and the right side of Eq. (30) is dominated by  $Nu$ . On the other side, for small  $H$ ,  $Ki \gg 1$  and there is a significant contribution of the term  $Ki$  to the total heat transfer resistance. Fig. 45 shows that, even for a simple fluid as studied in this work, the contribution from  $Ki$  may play a role up to  $H = 1000 \sigma_{ff}$ . For a fairly small organic molecule with  $\sigma_{ff} = 0.5$  nm this corresponds to  $H = 0.5$   $\mu\text{m}$ . This is only a ballpark estimate. The correlation presented in Eq. (22) enables more accurate considerations for specific situations.

## 5.6 Conclusions

In this chapter, the heat transfer across a solid-fluid interface was studied in a model system using molecular dynamics simulations. In the simulation scenario, a stagnant fluid was confined between two planar fixed walls with different temperatures. The heat transfer resistance between the two thermostatted walls can be split up in a formal way into two contributions: firstly, a resistance that would be present if the entire channel was filled with the stagnant bulk fluid, and secondly, a contribution that accounts for the heat transfer resistance at the interfaces, which is known as the Kapitza resistance and usually characterized by the Kapitza length.

A model system is studied, where both the fluid and the wall particles were described with the Lennard-Jones truncated and shifted potential. The influence of different parameters on the heat transfer was studied systematically: the strength of the solid-fluid interaction, the strength of the solid-solid interaction, the mass of the solid particles, the fluid density, the fluid temperature, the temperature difference between solid and fluid as well as the channel width. The obtained results for the dependencies of the Kapitza length  $L_K$  on these parameters were correlated by a simple analytical function. The temperature of the wall and the channel width were found to have no significant influence on the interfacial heat transfer resistance. For the fluid temperature  $T_f$ , an increasing  $T_f$  yields a decreasing interfacial heat transfer resistance. Furthermore, a strong mismatch between the solid-solid interaction and the fluid-fluid interaction energies leads to a high heat transfer resistance at the interface, while a strong solid-fluid interaction decreases that resistance. These findings are in line with results reported in the literature [472, 477, 478, 493, 498]. An increase of the fluid density leads to an increase of the Kapitza length for both studied temperatures, the subcritical and the supercritical isotherms. For liquid states, this behavior was also reported by *Amani et al.* [493]. The mass of the solid particles has a more complex influence on the interfacial heat transfer resistance: the Kapitza length exhibits a minimum as a function of the

mass of the solid particles. The Kapitza length is found to be minimal for a reduced mass of the solid particles of about  $M_s/M_f \approx 7.5$ . For future work, it would be interesting to analyze the different contributions to the heat flux, i.e. the kinetic and the configurational contributions [210, 529], in the adsorption layer to elucidate different mechanisms in detail.

Furthermore, the study yields information on the scale of the problem. The influence of the interfacial thermal resistance and the bulk fluid thermal resistance of the heat transfer can readily be estimated using the dimensionless number proposed in this chapter. For large scales, the heat transfer is dominated by heat conduction and the Kapitza resistance is negligible. But as the scale becomes smaller, the influence of the Kapitza resistance increases. It can play a role in channels with widths corresponding to several hundred diameters of the fluid molecules. The results of this work provide a simple yet effective tool to estimate the relevance of the interfacial heat transfer resistance in a given heat transfer problem.



# 6 Measurements and Equation of State Modeling of the Density of 1-Alcohols at High Pressures

## 6.1 Introduction

Linear primary alcohols with carbon backbone lengths between 6 and 10 are important chemicals. For instance, they are utilized as alternative biofuels [530–535]. They exhibit good combustion characteristics [530] and can be used as additives in biodiesel [535, 536]. This is of particular interest as long alcohols can be produced from biomass [531, 532]. Long chain 1-alcohols are also used as lubricant additives, e.g. in manufacturing processes [537–539]. Furthermore, they are important chemical intermediates and frequently used as solvents (e.g. for extraction processes) in chemical industry [540–543].

The density (at given temperature and pressure) is a basic thermodynamic property and data on the density and derived properties, such as the compressibility and the thermal expansion coefficient, are needed in many engineering tasks [8, 544]. The accurate description of the density is also an important requirement in the development of equations of state (EOS)[545]. In many applications, also information on the density at extreme conditions is needed. E.g., pressures up to 250 MPa are reached in injection systems of combustion engines and pressures in lubricated contacts may exceed 1,000 MPa [2, 74, 353, 537, 546]. To be able to model such processes accurately, knowledge on the density at such high pressures, where experiments are difficult, is required. As experimental data of the density is often unavailable, especially at extreme conditions, EOS are needed that enable robust predictions.

There are different methods to measure the density at elevated pressure [547–549]. Vibrating-tube densimeters are well-established for such measurements as they yield precise results in a wide temperature and pressure range [549–551]. The density in those devices is calculated from the period of the tube vibrations, which is the primarily measured quantity. This requires, however, a suitable calibration with calibration fluids of known density [552].

For predictive modeling of thermodynamic properties, molecular-based EOS are an attractive choice [22, 23, 108, 234]. Molecular-based EOS are usually formulated as fundamental equations describing the Helmholtz energy of the studied substance and explicitly account for different types of molecular interactions and molecular architecture. Due to their physical basis, they often yield reliable predictions for properties at conditions that were not considered in the training of the model [324, 331, 336, 553, 554]. For the modeling of substances with hydrogen bonding, molecular-based EOS using the statistical association fluid theory (SAFT) [555, 556] are the state of the art. Several molecular-based EOS models comprising SAFT have been proposed in the literature [41–43, 557].

In this chapter, the density of 1-hexanol, 1-heptanol, 1-octanol, 1-nonanol, and 1-decanol was measured at temperatures between 298.15 K and 423.15 K and pressures up to 120 MPa with a vibrating-tube densimeter. The experimental results complement and extend the range of existing literature data. Literature data were used to validate the measurement results. The measurements were then used to model the density, the thermal expansion coefficient, and the isothermal compressibility using four molecular-based EOS, namely the PC-SAFT [40], the SAFT-VR Mie [41], the soft SAFT [558], and the CPA EOS [43]. Therefore, new component-specific models were fitted to experimental data (both from this work and from the literature), which enables a fair comparison.

## 6.2 Experimental Methods

### 6.2.1 Chemicals and Sample Preparation

The CAS registry numbers, suppliers, and purities of the chemicals used for sample preparation are given in Table 25. All chemicals were used without further purification. Toluene and ethanol were used as calibration fluids for the calibration.

### 6.2.2 Measurements

The measurements were conducted with a density-measuring cell (DMA HPM, Anton Paar) in combination with an evaluation unit (mPDS 5, Anton Paar) for digital data processing. A scheme of the experimental setup is shown in Fig. 46. The setup has two parts: A hydraulic and a sample part, which are separated by a separator piston. The pressure is induced by a hand spindle pump. The pressure in the sample part is measured by a digital pressure transducer from WIKA (S-20) with a standard uncertainty of  $u(p) = 0.05$  MPa (specified by the manufacturer). The pressure in the hydraulic part

**Table 25:** Chemical specifications.

Substance	CAS reg. no.	Supplier	Mole fraction purity <sup>a</sup>	Lot number
toluene	108-88-3	Sigma-Aldrich	99.98 %	MKCF6188
ethanol	64-17-5	Merck Supelco	≥ 99.9 %	K52680280
1-hexanol	111-27-3	ThermoScientific	99.3 %	10238077
1-heptanol	111-70-6	ThermoScientific	99.8 %	10237915
1-octanol	111-87-5	Merck Supelco	99.5 %	K54568191
1-nonanol	143-08-8	TCI	99.7 %	AD6TI
1-decanol	112-30-1	Merck	99.8 %	S7025863

<sup>a</sup> As specified by the supplier.

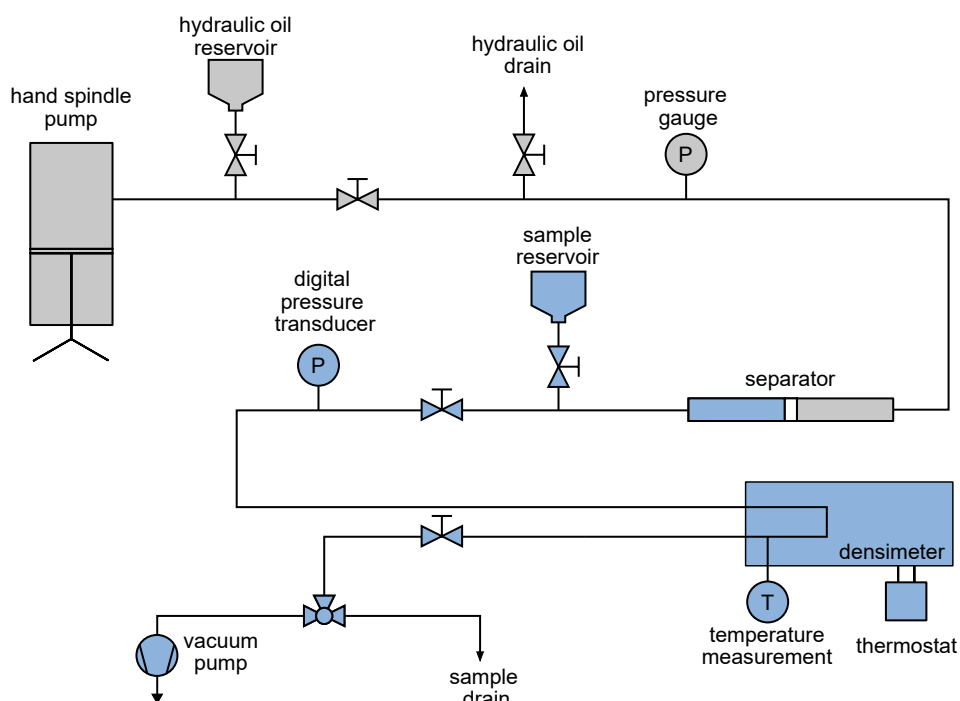


**Figure 46:** Scheme of the experimental setup (grey: Hydraulic part, blue: Sample part).

is monitored by an analog pressure gauge. The temperature is measured by a built-in temperature sensor (Pt1000 resistance thermometer from ABB AG) in the measuring cell with a standard uncertainty of  $u(T) = 0.1$  K (specified by the manufacturer). All components were chosen to withstand a pressure of at least 140 MPa. To avoid the accidental buildup of higher pressure, safety valves were installed in both the hydraulic and the sample parts (not shown in Fig. 46). For each substance (see Table 25), six isotherms were studied  $T/\text{K} \in \{298.15, 323.15, 348.15, 373.15, 398.15, 423.15\}$  at 13 pressures  $p/\text{MPa} \in \{0.1, 10, 20, 30, 40, 50, 60, 70, 80, 90, 100, 110, 120\}$ . Only liquid states were studied. Hence, combinations that led to solid or gas states were excluded. All samples were degassed by a vacuum pump before loading the system. The evacuation of the sample was conducted in the sample reservoir. The temperature  $T$ , the pressure  $p$ , and the period  $\tau$  of the vibrating tube were recorded digitally for two minutes at each state point using this setup. The valve between the densimeter and the sample reservoir was closed during the measurements to reduce external influences, which slightly increased the pressure. Therefore, the target pressure given above was not always met exactly.

To calculate densities from the measured periods, the density-measuring cell was calibrated by calibration fluids with known density. Several empirical models for correlating the density have been proposed in the literature [559–561]. A model proposed by Anton Paar was used, which describes the relation between the density  $\rho$  and the measured period  $\tau$ , temperature  $T$ , and pressure  $p$  as

$$\begin{aligned} \rho/\text{kg m}^{-3} = & a_1 + a_2(T/\text{K}) + a_3(p/\text{MPa}) + a_4(T/\text{K})^2 + a_5(p/\text{MPa})^2 \\ & + (a_6 + a_7(T/\text{K}) + a_8(p/\text{MPa}) + a_9(T/\text{K})^2 + a_{10}(p/\text{MPa})^2) (\tau/\text{s})^2 \\ & + a_{11}(\tau/\text{s})^4, \end{aligned} \quad (31)$$

where  $a_1 \dots a_{11}$  are eleven device constants, which were determined by a fit to the measurements of the calibration fluids (which provides  $\rho, \tau, T, p$  data sets). Ethanol and toluene were used as calibration fluids. The calibration fluids were selected such that their densities cover the complete expected density range of the samples, i.e. one calibration fluid (ethanol) has a lower density and one calibration fluid (toluene) a higher density than the target substances. The density for the calibration fluids was taken from the multi-parameter EOS from Ref. 562 for ethanol and from Ref. 563 for toluene. They are both valid in the entire considered range of conditions. The uncertainties for the density are specified by the developers of the EOS as  $u_r(\rho) = 0.002$  for ethanol [562] and  $u_r(\rho) = 0.002$  for  $p \leq 300$  MPa or  $u_r(\rho) = 0.005$  else for toluene [563]. For the conditions considered here, the uncertainties of both EOS are significantly smaller, as shown in Appendix E. For both calibration fluids, the density was measured at the state points stated above, excluding state points above the boiling temperature at the corresponding pressure ( $T \geq 373.15$  K at  $p = 0.1$  MPa for ethanol and  $T \geq 398.15$  K at  $p = 0.1$  MPa for



toluene). The parameters of the calibration function  $a_1 \dots a_{11}$  were determined from a least-squares fit. The relative standard uncertainty of the calibration is estimated to be  $u_{\text{cal,r}}(\rho) = 0.0005$ .

The overall expanded uncertainty of the density  $U_r(\rho)$  with  $k = 2$  was calculated from the individual uncertainties [564] as

$$U(\rho) = k \sqrt{\left(\left(\frac{\partial \rho}{\partial T}\right)_{p,\tau} u(T)\right)^2 + \left(\left(\frac{\partial \rho}{\partial p}\right)_{T,\tau} u(p)\right)^2 + \left(\left(\frac{\partial \rho}{\partial \tau}\right)_{T,p} u(\tau)\right)^2 + (u_{\text{cal,r}}\rho)^2}, \quad (32)$$

where the coverage factor  $k$  was chosen to be 2 throughout this chapter and  $u(\tau)$  is the standard uncertainty of the primary data of the measured period  $\tau$ . The partial derivatives of the density with respect to temperature, pressure, and period were calculated from Eq. (31). The resulting relative expanded uncertainty is approximately  $U_r(\rho) = 0.0016$  in the entire temperature and pressure range.

## 6.3 Computational Methods

### 6.3.1 Empirical Correlation $\rho(T, p)$

For each studied substance, an empirical correlation of the density data  $\rho(T, p)$  was established to evaluate the results and compare them to literature data. Therefore, the polynomial function  $\rho(T, p)$  given in Eq. (33) was chosen based on preliminary tests.

$$\begin{aligned} \rho_{\text{corr}} / \text{kg m}^{-3} = & c_0 + c_1(T/\text{K}) + c_2(T/\text{K})^2 + c_3(p/\text{MPa}) + \\ & c_4(T/\text{K})^3(p/\text{MPa}) + c_5(T/\text{K})(p/\text{MPa})^3 + c_6(T/\text{K})^2(p/\text{MPa})^2 \end{aligned} \quad (33)$$

The seven adjustable parameters of Eq. (33) were fitted to the experimental results for each substance individually. Due to their empirical nature, the resulting correlations are not suited for extrapolation beyond the temperature and pressure range of the data to which it was fitted. The parameters are given in the Appendix E.

The thermal expansion coefficient  $\alpha$  and the isothermal compressibility  $\beta$  were computed as

$$\alpha = -\frac{1}{\rho} \left( \frac{\partial \rho}{\partial T} \right)_p \quad \text{and} \quad (34)$$

$$\beta = \frac{1}{\rho} \left( \frac{\partial \rho}{\partial p} \right)_T. \quad (35)$$

The thermal expansion coefficient  $\alpha$  and the isothermal compressibility  $\beta$  were computed directly from the empirical density model  $\rho_{\text{corr}} = \rho_{\text{corr}}(T, p)$ , cf. Eq. (33). Both

properties were computed for the state points studied experimentally (see above). Additionally, the data are compared to literature data in Appendix E. The obtained  $\alpha$  and  $\beta$  data are referred to as 'pseudo experimental' data in the following. The expanded uncertainty of the derived quantities  $U(\alpha)$  and  $U(\beta)$  are estimated by error propagation as

$$U(\alpha) = k \sqrt{\left(\frac{\partial \alpha}{\partial \rho}\right) \rho + \sum_{i=0}^6 \left(\frac{\partial \alpha}{\partial c_i}\right) u(c_i)} \quad \text{and} \quad (36)$$

$$U(\beta) = k \sqrt{\left(\frac{\partial \beta}{\partial \rho}\right) \rho + \sum_{i=0}^6 \left(\frac{\partial \beta}{\partial c_i}\right) u(c_i)}, \quad (37)$$

where  $u(c_i)$  are the standard errors of the parameter  $c_i$  calculated from the results of the linear regression in Eq. (33) [565]. For 1-hexanol, 1-heptanol, 1-octanol, and 1-nonanol, the average uncertainties were calculated to be  $U_r(\alpha) = U_r(\beta) = 0.08$ . For 1-decanol, the uncertainties are slightly larger with  $U_r(\alpha) = 0.12$  and  $U_r(\beta) = 0.14$ .

### 6.3.2 Molecular-based Equation of State Modeling

The density, the thermal expansion coefficient, and the isothermal compressibility of the 1-alcohols were modeled using four molecular-based EOS: PC-SAFT [40, 557], SAFT-VR Mie [41], soft SAFT [558], and CPA [43]. The applied EOS are formulated in the molar Helmholtz energy  $a$  as function of the temperature and the density, i.e.  $a = a(T, \rho)$ . The considered molecular-based EOS models are composed of different contributions to the Helmholtz energy as

$$a = a_{\text{id}} + a_{\text{rep}} + a_{\text{disp}} + a_{\text{chain}} + a_{\text{assoc}}, \quad (38)$$

where  $a_{\text{id}}$  is the ideal gas contribution,  $a_{\text{rep}}$  and  $a_{\text{disp}}$  are the contributions due to repulsive and dispersive interactions, respectively,  $a_{\text{chain}}$  is the contribution due to chain formation, and  $a_{\text{assoc}}$  represents the associating (H-bonding) interaction. The PC-SAFT EOS and the SAFT-VR Mie employ the hard sphere model from *Boublik and Mansoori* [566, 567]. Both EOS use a monomer dispersion term specifically designed for the EOS, cf. Refs. [40] and [41], respectively. The soft SAFT EOS uses the Lennard-Jones EOS from *Johnson et al.* as monomer term for modeling the repulsive and dispersive interactions [568]. The CPA EOS uses the Soave-Redlich-Kwong EOS as monomer term. All four considered EOS frameworks use versions of the SAFT model proposed by *Chapman* [555] for describing the association. For the chain contribution, the PC-SAFT EOS uses a hard chain reference fluid model from *Boublik and Mansori* [566, 567]. The soft SAFT EOS is based on the chain model (describing Lennard-Jones chains) proposed by *Johnson et al.* [569]. The SAFT-VR Mie EOS chain term is formulated as a model for tangential bonded Mie segment chains [41]. No explicit chain contribution is used in

**Table 26:** PC-SAFT component-specific models developed in in this work: The column indicate the segment number  $m$ , segment diameter  $\sigma$ , segment dispersion energy  $\varepsilon$ , association volume  $\kappa_{AB}$ , and association energy  $\varepsilon_{AB}$ .

Substance	$m$	$\sigma / \text{\AA}$	$\varepsilon / k_{\text{B}}\text{K}$	$\kappa_{AB} / 10^{-3}$	$\varepsilon_{AB} / k_{\text{B}}\text{K}$
1-hexanol	2.6387	4.0904	296.28	2.2982	2985.1
1-heptanol	3.1386	4.0206	287.29	2.5257	2943.2
1-octanol	3.5238	4.0157	285.27	2.3575	2944.9
1-nonanol	3.9179	4.0033	280.35	2.3733	3010.5
1-decanol	4.3381	3.9888	278.38	2.0959	3018.7

**Table 27:** SAFT-VR Mie component-specific models developed in in this work: The column indicate the segment number  $m$ , segment diameter  $\sigma$ , segment dispersion energy  $\varepsilon$ , repulsive exponent  $\lambda_{\text{r}}$ , association radius  $r_{AB}$ , and association energy  $\varepsilon_{AB}$ . The attractive exponent was  $\lambda_{\text{a}} = 6$  in all cases.

Substance	$m$	$\sigma / \text{\AA}$	$\varepsilon / k_{\text{B}}\text{K}$	$\lambda_{\text{r}}$	$r_{AB} / \sigma$	$\varepsilon_{AB} / k_{\text{B}}\text{K}$
1-hexanol	2.0411	4.5361	370.31	13.532	0.27932	3192.6
1-heptanol	2.2228	4.6161	406.97	15.566	0.2834	3108.3
1-octanol	2.3588	4.7289	456.3	18.936	0.29574	2912.8
1-nonanol	2.6733	4.66	419.34	16.579	0.28245	3182.2
1-decanol	3.0053	4.6078	407.63	15.97	0.27674	3224.8

the CPA EOS. For most of the studied alcohols, component-specific models for the four EOS frameworks are available in the literature [570–574]. The results using models from the literature are shown and compared in Appendix E. Yet, those were parameterized using different reference data sets and fitting methods. To enable a fair comparison of the performance of the EOS frameworks, component-specific models for the five alcohols was developed in this work using the same reference data sets and fitting routines for all EOS frameworks. All models include association by the SAFT term [555], but no polar contributions. The 2B association scheme was applied. The component-specific model parameters were fitted in this work for all five substances using the density results from this work in combination with experimental data from the literature [570, 575–588] for the vapor pressure  $p^{\text{s}}$  and the saturated liquid density  $\rho^{\text{s}}$ . Only vapor pressure and saturated liquid density data with  $T < 0.9T_{\text{c}}$  were used as the critical point is not well described by molecular-based EOS [589]. The squared relative error was used for the fitting. Details are given in Appendix E. For the SAFT-VR Mie, six parameters were used in the models in contrast to only five parameters used for the other three EOS frameworks. The resulting parameters are given in Tables 26 - 29.

**Table 28:** Soft SAFT component-specific models developed in in this work: The column indicate the segment number  $m$ , segment diameter  $\sigma$ , segment dispersion energy  $\varepsilon$ , association volume  $\kappa_{AB}$ , and association energy  $\varepsilon_{AB}$ .

Substance	$m$	$\sigma / \text{\AA}$	$\varepsilon / k_B\text{K}$	$\kappa_{AB}$	$\varepsilon_{AB} / k_B\text{K}$
1-hexanol	3.176	3.8521	276.96	35.46	3279.5
1-heptanol	3.5617	3.8604	280.8	31.755	3254.7
1-octanol	3.8077	3.9316	288.16	21.411	3332.8
1-nonanol	3.8409	4.0513	296.6	14.501	3584.1
1-decanol	4.0642	4.1128	301.34	11.182	3672.3

**Table 29:** CPA component-specific models developed in in this work: The column indicate the energy parameter  $\alpha$ , pseudo critical temperature  $T_{cm}$ , pseudo critical pressure  $p_{cm}$ , association volume  $\kappa_{AB}$ , and association energy  $\varepsilon_{AB}$ .

Substance	$\alpha$	$T_{cm} / \text{K}$	$p_{cm} / \text{bar}$	$\kappa_{AB} / 10^{-3}$	$\varepsilon_{AB} / k_B\text{K}$
1-hexanol	0.94524	596.9	38.149	2.0513	2837.7
1-heptanol	0.95308	636.87	35.364	0.92934	3025.8
1-octanol	0.95976	668.74	33.052	0.52529	3217.9
1-nonanol	1.1088	682.79	30.174	0.51068	3093.2
1-decanol	1.1686	706.71	28.578	0.31068	3171

**Table 30:** Overview of *Brown's* characteristic curves including the name, the abbreviation, and the definition.

Name	Abbreviation	Definition
Zeno curve	Z	$Z = \frac{vp}{RT} = 1$
Amagat curve	A	$\left(\frac{\partial Z}{\partial T}\right)_\rho = 0$
Boyle curve	B	$\left(\frac{\partial Z}{\partial 1/\rho}\right)_T = 0$
Charles curve	C	$\left(\frac{\partial Z}{\partial 1/\rho}\right)_p = 0$

*Brown's* characteristic curves [590] were used to assess the extrapolation behavior of the EOS models. The characteristic curves define lines on the thermodynamic  $p\rho T$  surface, along which the compressibility factor  $Z$  or its derivatives are identical to the corresponding ideal gas values. Details are given in Refs. 348, 590, 591. The thermodynamic definitions of the four curves are given in Table 30. Based on these characteristics, the consistency of EOS can be tested [592, 593]. *Brown* postulated several criteria for the characteristic curves to be thermodynamically consistent [348, 590, 591, 594, 595]. These criteria were originally derived for simple fluids, i.e. spherical particles with repulsive and dispersive interactions. Yet, it has been shown based on first principle molecular simulation data [348] that the criteria are applicable to associating, elongated, and polar fluids [348, 594, 595]. Therefore, *Brown's* tests were applied to the 1-alcohol EOS models developed in this chapter. Yet, successfully passing this test is only a necessary, but not sufficient condition for the models to be thermodynamically consistent.

### 6.3.3 Evaluation of Models

To quantify the deviations from a given model (empirical correlation or EOS) and experimental data, two deviation measures are used in this chapter: The average absolute deviation (AAD) and the median absolute deviation (MAD) given as

$$\text{AAD}_{Y,\text{mod}}^{\text{src}} = \frac{1}{N_{\text{exp}}} \sum_i^{N_{\text{exp}}} \left| \frac{Y_{\text{mod},i} - Y_{\text{exp},i}^{\text{src}}}{Y_{\text{exp},i}^{\text{src}}} \right| \quad \text{and} \quad (39)$$

$$\text{MAD}_{Y,\text{mod}}^{\text{src}} = \text{Median} \left\{ \left| \frac{Y_{\text{mod},i} - Y_{\text{exp},i}^{\text{src}}}{Y_{\text{exp},i}^{\text{src}}} \right| \right\}, \quad (40)$$

where  $Y_{\text{exp},i}^{\text{src}}$  are the experimental data (source (src) is either this work (th) or literature (lit)) and  $Y_{\text{mod},i}$  the corresponding value calculated either from an empirical correlation model (corr), cf. Eq. (33), or an EOS model.

## 6.4 Results and Discussion

### 6.4.1 Experimental Results

The experimental results for the density of the studied 1-alcohols are given in Table 31.

**Table 31:** Results for the density measurements for 1-hexanol, 1-heptanol, 1-octanol, 1-nonanol, and 1-decanol. The standard uncertainties of the temperature  $T$  and pressure  $p$  are  $u(T) = 0.1$  K and  $u(p) = 0.05$  MPa. The combined expanded uncertainties for the density is  $U(\rho) = 1.3$  kg m<sup>-3</sup> ( $k = 2$ ).

$p$ /MPa	$\rho$ /kg m <sup>-3</sup>	$p$ /MPa	$\rho$ /kg m <sup>-3</sup>	$p$ /MPa	$\rho$ /kg m <sup>-3</sup>
1-hexanol					
$T = 298.15$ K		$T = 323.15$ K		$T = 348.15$ K	
0.2	815.1	0.14	796.6	0.12	777.4
10.2	821.6	10.19	804.1	10.32	786.1
20.14	827.6	20.21	810.8	20.15	793.5
30.16	833.3	30.31	817.1	30.2	800.5
40.13	838.5	40.24	822.9	40.14	806.9
50.3	843.6	50.29	828.4	50.21	813.0
60.29	848.4	60.26	833.5	60.05	818.5
70.24	852.9	70.25	838.4	70.22	823.9
80.22	857.2	80.28	843.0	80.06	828.9
89.97	861.2	90.12	847.4	90.26	833.8
100.04	865.3	100.17	851.7	100.13	838.3
110.18	869.2	110.1	855.8	110.03	842.7
120.04	872.8	120.07	859.7	120.18	846.9
$T = 373.15$ K		$T = 398.15$ K		$T = 423.15$ K	
0.2	757.3	0.12	734.7	0.3	710.5
10.22	767.1	10.36	746.3	10.32	724.2
20.07	775.7	20.2	756.2	20.3	735.8
30.33	783.7	30.27	765.0	30.33	745.8
40.3	790.7	40.12	772.9	40.11	754.7
50.34	797.4	50.14	780.2	50.25	762.9
60.25	803.0	60.18	787.0	60.25	770.6

*Continued on next page*

$p/\text{MPa}$	$\rho/\text{kg m}^{-3}$	$p/\text{MPa}$	$\rho/\text{kg m}^{-3}$	$p/\text{MPa}$	$\rho/\text{kg m}^{-3}$
70.2	808.7	70.17	793.3	70.21	777.5
80.23	814.2	80.16	799.2	80.04	783.8
90.1	819.3	90.12	804.8	90.05	789.9
100.24	824.3	100.32	810.2	100.13	795.6
110.01	828.9	110.09	815.2	110.18	801.2
120.08	833.6	120.18	820.1	120.24	806.3
1-heptanol					
$T = 298.15\text{ K}$		$T = 323.15\text{ K}$		$T = 348.15\text{ K}$	
0.39	819.1	0.32	800.9	0.22	782.1
10.24	825.3	10.44	808.1	10.29	790.3
20.38	831.3	20.25	814.5	20.18	797.5
30.51	836.8	30.24	820.5	30.28	804.3
40.2	841.8	40.28	826.2	40.22	810.5
50.39	846.8	50.29	831.5	50.3	816.4
60.42	851.4	60.4	836.6	60.24	821.8
70.34	855.8	70.47	841.3	70.2	827.0
80.47	860.0	80.3	845.8	80.27	832.0
90.38	864.1	90.24	850.1	90.23	836.6
100.39	868.0	100.27	854.4	100.19	841.1
110.33	871.7	110.37	858.4	110.11	845.3
120.17	875.3	120.07	862.2	120.26	849.5
$T = 373.15\text{ K}$		$T = 398.15\text{ K}$		$T = 423.15\text{ K}$	
0.18	762.3	0.35	740.6	0.26	717.9
10.18	771.6	10.32	751.3	10.3	730.8
20.3	780.0	20.34	760.9	20.16	741.6
30.33	787.6	30.33	769.4	30.14	751.2
40.18	794.3	40.25	777.1	40.34	760.0
50.2	800.8	50.13	784.1	50.3	767.8
60.17	806.7	60.3	790.7	60.27	774.8
70.33	812.6	70.1	796.7	70.39	781.9

*Continued on next page*

$p/\text{MPa}$	$\rho/\text{kg m}^{-3}$	$p/\text{MPa}$	$\rho/\text{kg m}^{-3}$	$p/\text{MPa}$	$\rho/\text{kg m}^{-3}$
80.28	817.8	80.33	802.7	80.37	788.1
90.2	822.8	90.14	808.1	90.23	793.8
100.42	827.7	100.23	813.2	100.19	799.4
110.3	832.2	110.43	818.2	110.22	804.7
120.3	836.6	120.24	822.8	120.23	809.7
1-octanol					
$T = 298.15 \text{ K}$		$T = 323.15 \text{ K}$		$T = 348.15 \text{ K}$	
0.15	822.0	0.21	803.8	0.12	785.4
10.14	828.2	10.14	810.7	10.11	793.2
20.14	833.8	20.17	817.0	20.14	800.4
30.24	839.2	30.4	823.0	30.22	807.0
40.38	844.3	40.33	828.5	40.28	813.1
50.26	849.0	50.24	833.6	50.25	818.7
60.31	853.5	60.12	838.4	60.24	824.1
70.32	857.9	70.29	843.2	70.14	829.1
80.3	862.0	80.3	847.7	80.32	834.0
90.25	865.9	90.21	851.9	90.12	838.5
100.26	869.7	100.11	856.0	100.17	842.9
110.19	873.4	110.13	859.9	110.08	847.1
120.1	877.0	120.16	863.7	120.25	851.2
$T = 373.15 \text{ K}$		$T = 398.15 \text{ K}$		$T = 423.15 \text{ K}$	
0.29	765.9	0.25	745.3	0.17	723.2
10.26	775.2	10.21	755.7	10.17	735.5
20.18	783.1	20.28	764.9	20.11	746.0
30.14	790.4	30.2	772.9	30.24	755.4
40.3	797.3	40.14	780.4	40.37	763.8
50.11	803.3	50.26	787.4	50.11	771.2
60.38	809.4	60.12	793.6	60.05	778.2
70.24	814.7	70.26	799.7	70.48	785.0
80.31	820.0	80.29	805.3	80.32	791.1

*Continued on next page*



$p/\text{MPa}$	$\rho/\text{kg m}^{-3}$	$p/\text{MPa}$	$\rho/\text{kg m}^{-3}$	$p/\text{MPa}$	$\rho/\text{kg m}^{-3}$
90.19	824.9	90.11	810.5	90.16	796.7
100.16	829.6	100.25	815.7	100.22	802.3
110.35	834.2	110.33	820.6	110.33	807.5
120.26	838.4	120.17	825.2	120.29	812.4
1-nonanol					
$T = 298.15\text{ K}$		$T = 323.15\text{ K}$		$T = 348.15\text{ K}$	
0.17	825.2	0.27	807.6	0.14	789.1
10.14	831.0	10.21	814.3	10.15	796.8
20.1	836.6	20.21	820.5	20.12	803.7
30.29	841.8	30.24	826.2	30.25	810.2
40.16	846.7	40.35	831.6	40.21	816.1
50.24	851.4	50.16	836.6	50.29	821.7
60.22	855.8	60.21	841.4	60.1	826.8
70.35	860.0	70.19	845.9	70.22	831.8
80.24	864.1	80.38	850.4	80.31	836.6
90.17	867.9	90.3	854.6	90.26	841.1
100.22	871.7	100.25	858.6	100.2	845.3
110.27	875.3	110.36	862.4	110.2	849.5
120.0	878.7	120.22	866.1	120.39	853.5
$T = 373.15\text{ K}$		$T = 398.15\text{ K}$		$T = 423.15\text{ K}$	
0.16	770.3	0.3	750.1	0.17	728.5
10.21	779.0	10.15	760.0	10.28	740.3
20.14	786.8	20.1	768.7	20.37	750.5
30.22	794.0	30.29	776.9	30.22	759.3
40.19	800.6	40.25	784.1	40.18	767.5
50.18	806.7	50.18	790.8	50.28	774.9
60.14	812.4	60.17	797.0	60.2	781.6
70.21	817.8	70.32	802.8	70.13	788.0
80.24	822.8	80.21	808.3	80.31	794.0
90.17	827.7	90.36	813.5	90.22	799.6

*Continued on next page*

$p/\text{MPa}$	$\rho/\text{kg m}^{-3}$	$p/\text{MPa}$	$\rho/\text{kg m}^{-3}$	$p/\text{MPa}$	$\rho/\text{kg m}^{-3}$
100.2	832.3	100.3	818.6	100.12	804.9
110.24	836.7	110.26	823.3	110.38	810.2
120.14	840.8	119.9	827.6	119.96	814.7
1-decanol					
$T = 298.15 \text{ K}$		$T = 323.15 \text{ K}$		$T = 348.15 \text{ K}$	
0.22	827.2	0.29	810.1	0.16	791.9
10.22	833.0	10.22	816.6	10.17	799.4
20.33	838.5	20.29	822.6	20.11	806.2
30.23	843.6	30.21	828.2	30.26	812.5
40.3	848.4	40.17	833.5	40.19	818.4
50.2	853.0	50.32	838.6	50.17	823.8
60.17	857.4	60.35	843.3	60.2	829.0
70.17	861.7	70.19	847.8	70.18	833.8
80.34	865.9	80.24	852.1	80.31	838.5
90.25	869.6	90.2	856.2	89.99	842.8
100.44	873.5	100.27	860.2	100.26	847.2
		110.38	864.0	110.14	851.3
		120.2	867.7	120.22	855.2
$T = 373.15 \text{ K}$		$T = 398.15 \text{ K}$		$T = 423.15 \text{ K}$	
0.2	773.6	0.31	752.4	0.22	729.5
10.18	782.1	10.38	762.6	10.13	740.5
20.23	789.7	20.23	770.7	20.31	750.5
30.28	796.6	30.2	778.3	30.1	759.2
40.29	803.2	40.3	785.8	40.3	767.0
50.37	809.2	50.29	792.3	50.27	774.4
60.29	814.8	60.36	798.4	60.28	781.2
70.3	820.1	70.25	804.1	70.22	787.6
80.28	825.0	80.27	809.6	80.23	793.3
90.15	829.6	90.0	814.7	90.16	798.8
100.21	834.2	100.36	819.6	100.43	804.2

*Continued on next page*

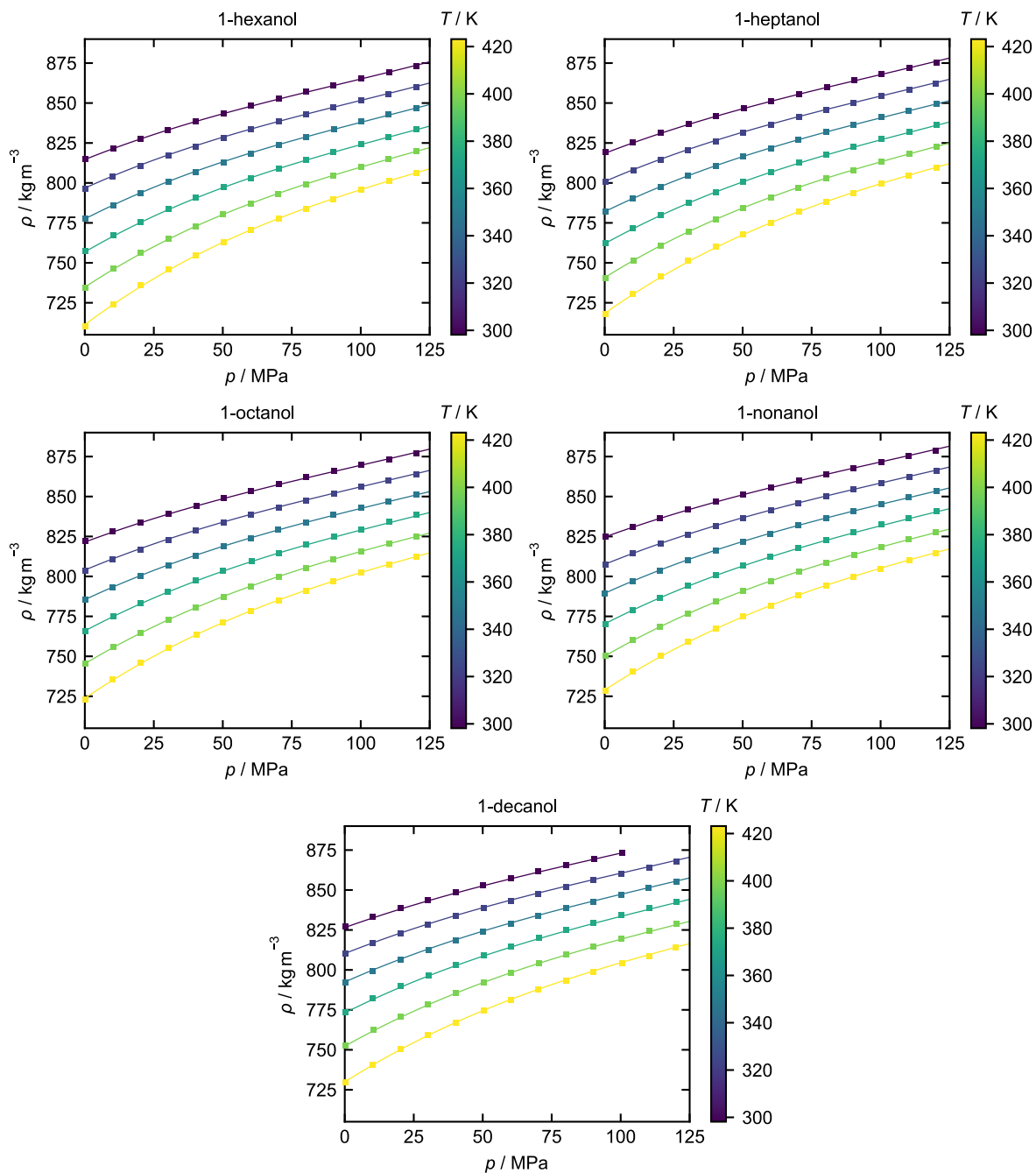
$p/\text{MPa}$	$\rho/\text{kg m}^{-3}$	$p/\text{MPa}$	$\rho/\text{kg m}^{-3}$	$p/\text{MPa}$	$\rho/\text{kg m}^{-3}$
110.39	838.6	110.33	824.4	110.27	808.8
120.1	842.8	120.31	829.0	120.05	814.1

Fig. 47 shows the measured densities of the five 1-alcohols as a function of the pressure. Also the results from the empirical correlations of the data, cf. Eq. (33), are shown. The density of the 1-alcohols increases with increasing chain length. Only liquid state points were studied, i.e. state points where the sample was (partially) solidified were discarded. This was evidenced by an increased density at these points and an abrupt pressure drop during compression, indicating a phase transition. A solidification was observed only for 1-decanol at  $T = 298.15\text{ K}$  and  $p \geq 110\text{ MPa}$ . Both state points are above the measured solidification pressure at this temperature [596] (see also Appendix E).

The results from this work were compared to literature data. Refs. 550, 577, 586, 597–647 report data on the studied 1-alcohols. An overview of the available literature data for each of the five substances is given in the Appendix E. For 1-hexanol, data are available in the entire range of conditions that were studied in this work. For the longer 1-alcohols (1-heptanol to 1-decanol), data are sparse. The experimental data from this work significantly extend and complement the available data for these substances.

For comparing the different data sets, the relative deviation between the data and the empirical correlations is used here. The relative deviations of all studied 1-alcohols at ambient pressure are shown in Fig. 48 as a function of the temperature. Overall, the experimental data from this work agree well with the literature data. Most of the literature data deviate not more than  $\pm 0.2\%$  from the empirical correlations over the entire temperature range. The experimental data from this work are generally well within the scattering of the literature data from the different groups, especially for lower temperatures, where more experimental data are available.

Fig. 49 shows the relative deviations of the experimental data and the empirical correlations for 1-hexanol, 1-heptanol, and 1-octanol as a function of the pressure for the different studied temperatures. Fig. 50 shows the corresponding results for 1-nonanol and 1-decanol. The literature data at elevated pressure scatter more than those at ambient pressure. At temperatures above  $348\text{ K}$ , literature data are scarce, especially at high pressures. For 1-nonanol and 1-decanol, in general, few data are available in literature. The experimental results from this work are in very good agreement with the literature data, especially for 1-hexanol and 1-heptanol. For 1-octanol, the results from this work lie slightly below the majority of the literature data for  $T \leq 348.15\text{ K}$ . However, the



**Figure 47:** Density  $\rho$  of the studied 1-alcohols as a function of pressure  $p$ . Symbols: Experimental results from this work; lines: Empirical correlation based on Eq. (33).

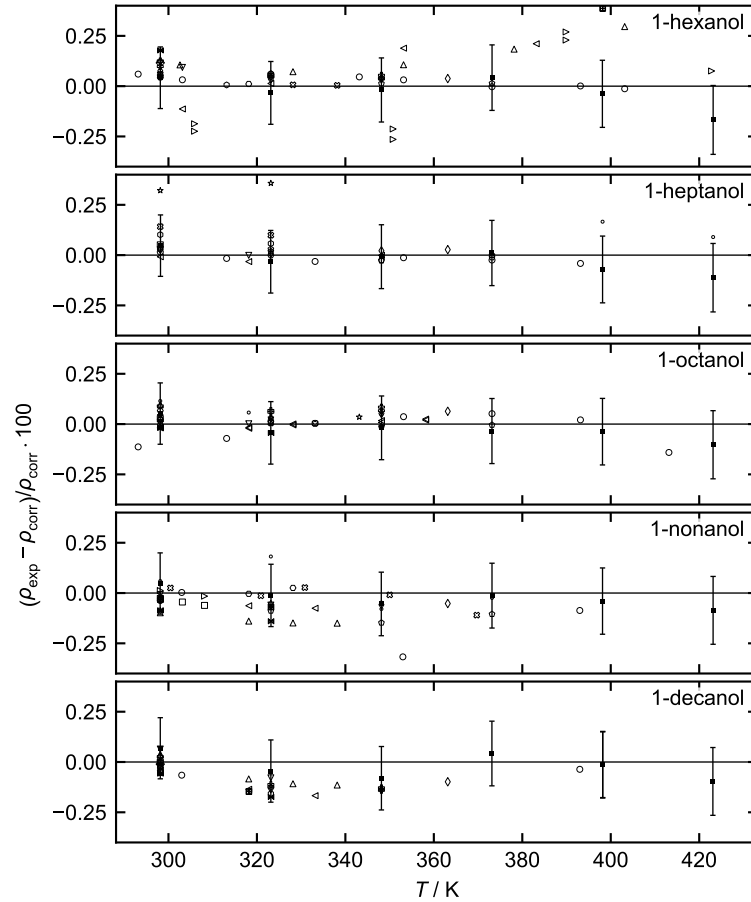


**Figure 48:** Relative deviation between experimental density data at ambient pressure (symbols) and the empirical correlations of the data from this work, cf. Eq. (33), (baseline) as a function of the temperature  $T$ . Solid squares indicate results from this work (with error bars  $U(\rho)$  ( $k = 2$ )) and open symbols indicate data from the literature [550, 577, 586, 597–647] (symbols are defined according to the legends in Figs. 49 and 50).

deviations are still within the given expanded combined uncertainty ( $k = 2$ ). Also, at  $T > 373.15$  K, the data from this work agrees well with most of the literature data.

Overall, the experimental data from the literature confirm the experimental results of this work. This is also shown by the  $AAD_{\rho, \text{corr}}$  and  $MAD_{\rho, \text{corr}}$  (cf. Eqs. (39) and (40)) between the empirical correlations and the experimental data. The two deviation measures were computed for the two experimental data sets, i.e. the literature data  $AAD_{\rho, \text{corr}}^{\text{lit}}$  and the data from this work  $AAD_{\rho, \text{corr}}^{\text{th}}$ . The results for the AAD and the MAD of the five substances are given in Table 32. The empirical correlations describe the experimental results with relative mean absolute deviation of less than 0.05%, which is significantly below the expanded uncertainty specified above. The small deviations between the experimental data from this work and the empirical correlations are measures for the accuracy of the empirical correlations, which were fitted to the experimental data from this work alone. With one exception, also both  $AAD_{\rho, \text{corr}}^{\text{lit}}$  and  $MAD_{\rho, \text{corr}}^{\text{lit}}$ , which quantify

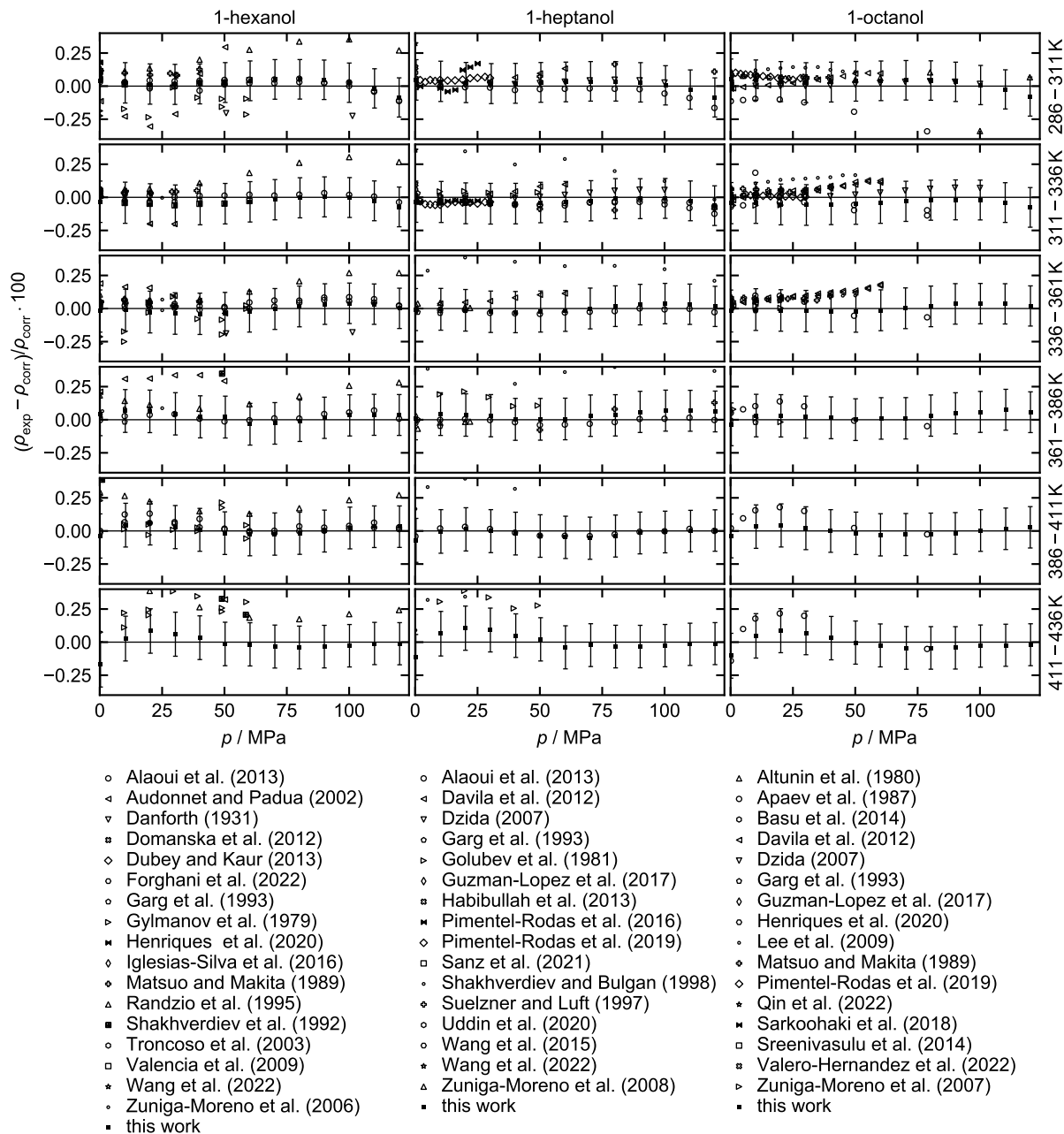


**Figure 49:** Relative deviation between experimental density data (symbols) and the empirical correlations, cf. Eq. (33), (baseline) for 1-hexanol, 1-heptanol, and 1-octanol as a function of the pressure  $p$ . Solid squares indicate results from this work (with error bars  $U(\rho)$  ( $k = 2$ )) and open symbols indicate data from the literature [550, 577, 586, 597–647].

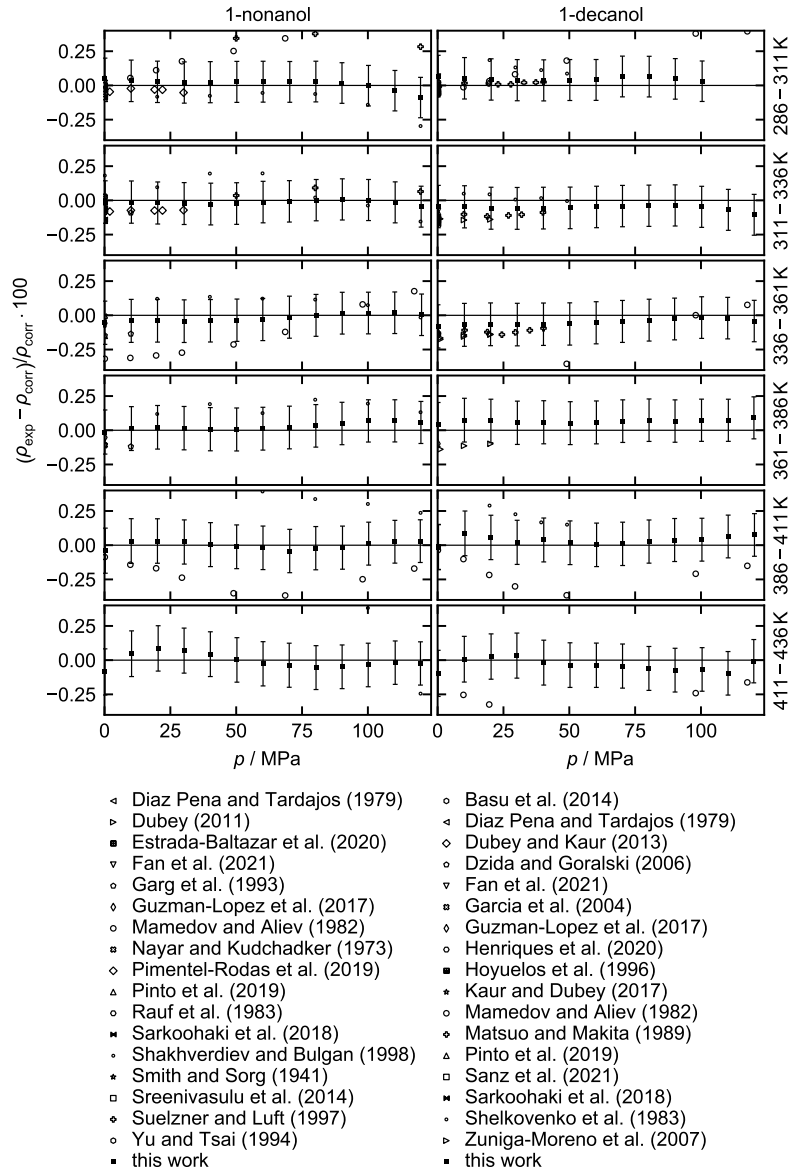


**Figure 50:** Relative deviations between experimental density data (symbols) and the empirical correlations, cf. Eq. (33), (baseline) for 1-nonanol and 1-decanol as a function of the pressure  $p$ . Solid squares indicate results from this work (with error bars  $U(\rho)$  ( $k = 2$ )) and open symbols indicate data from the literature [550, 577, 586, 597–647].

**Table 32:** Deviations of the literature data and the measurement data from this work to the empirical correlations (cf. Eq. (33)). The columns indicate (left to right) the substance name, the average deviations  $\text{AAD}_{\rho,\text{corr}}^{\text{lit}}$  as well as the median deviations  $\text{MAD}_{\rho,\text{corr}}^{\text{lit}}$  of the literature data, and the average deviations  $\text{AAD}_{\rho,\text{corr}}^{\text{th}}$  as well as the median deviations  $\text{MAD}_{\rho,\text{corr}}^{\text{th}}$  of the measurement data from this work (cf. Eqs. (39) and (40)).

Substance	$\text{AAD}_{\rho,\text{corr}}^{\text{lit}} / \%$	$\text{MAD}_{\rho,\text{corr}}^{\text{lit}} / \%$	$\text{AAD}_{\rho,\text{corr}}^{\text{th}} / \%$	$\text{MAD}_{\rho,\text{corr}}^{\text{th}} / \%$
1-hexanol	0.16	0.07	0.03	0.03
1-heptanol	0.10	0.04	0.03	0.03
1-octanol	0.07	0.06	0.03	0.03
1-nonanol	0.23	0.13	0.03	0.03
1-decanol	0.14	0.11	0.05	0.05

the deviations of the literature data from the empirical correlations of the present data, are within the expanded uncertainty  $U(\rho)$  ( $k = 2$ ) of the present data of 0.16 %. The only exception is the  $\text{AAD}_{\rho,\text{corr}}^{\text{lit}} = 0.23 \%$  obtained for 1-nonanol, which can be attributed to some large outliers in the literature data (see Appendix E for a discussion). Overall, the values shown in Table 32 confirm the good agreement of the results from this work with the literature data, as already demonstrated in Figs. 48 - 50.

### 6.4.2 EOS Modeling Results

By using the same fitting procedure and reference data for the different EOS models, a fair comparison of the different EOS frameworks (PC-SAFT, SAFT-VR Mie, soft SAFT, and CPA) is possible. An additional evaluation of component-specific models from the literature for the considered EOS frameworks is given in the Appendix E. The results of the fit from this work, i.e. the AADs obtained for the vapor pressure, saturated liquid density, and homogeneous state density are reported in Table E.2 in the Appendix. The description of VLE properties, i.e. the vapor pressure and the saturated liquid density, is similar for all EOS frameworks. The vapor pressure data are overall described with  $\text{AAD}_{p^s,\text{EOS}}^{\text{lit}}$  values of up to around 1 %. The corresponding values for the saturated liquid density are slightly smaller for the PC-SAFT and the SAFT-VR Mie than for the other two EOS. For the soft SAFT and the CPA EOS, the  $\text{AAD}_{\rho^s,\text{EOS}}^{\text{lit}}$  is significantly larger with values between 1 % and 2 %. The performance of the EOS models with respect to the density and its derived properties is discussed in detail in the following.

Fig. 51 shows the deviations of the EOS model results from the empirical correlations (cf. Eq. (33)) as a function of the pressure for 1-hexanol, 1-octanol, and 1-nonanol. Fig. 52 shows the corresponding results for 1-nonanol and 1-decanol. Additionally,



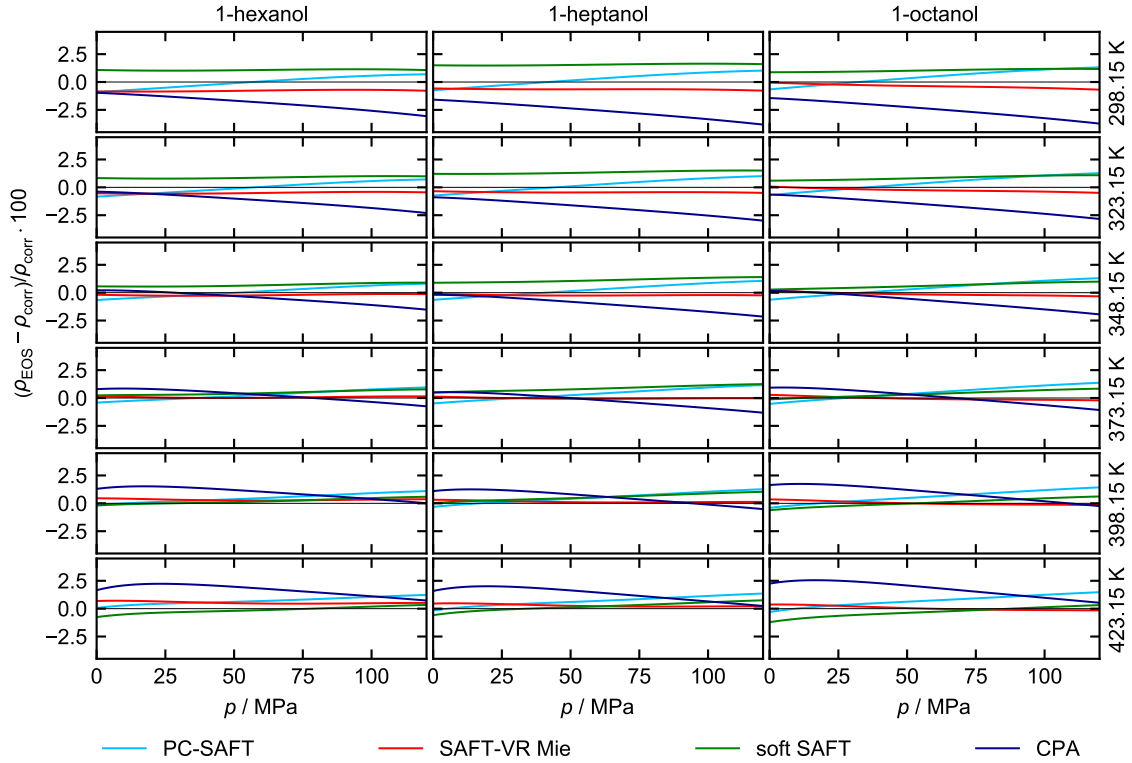


**Figure 51:** Relative deviation between the results for the density from the four EOS frameworks and the empirical correlations from this chapter (cf. Eq. (33)) for 1-hexanol, 1-heptanol, and 1-octanol as a function of the pressure  $p$ . Each rows shows results for a constant temperature.

the AADs for the density  $\rho$ , the thermal expansion coefficient  $\alpha$ , and the isothermal compressibility  $\beta$ , i.e.  $\text{AAD}_{Y,\text{EOS}}^{\text{th}}$ , were calculated for the four EOS and five substances. For the density  $\rho$ , the experimental data from this work were used. For the thermal expansion coefficient  $\alpha$  and the isothermal compressibility  $\beta$ , the pseudo-experimental data from this work were used (see above). Fig. 53 shows the AADs for  $\rho$ ,  $\alpha$ , and  $\beta$  for all substances and EOS.

The findings for all five alcohols are similar. First of all, the deviations for the EOS are overall about an order of magnitude larger than the deviations for the empirical correlations for describing the experimental data, cf. Figs. 49 and 50. In the entire considered temperature and pressure range, the deviations for the density are in the range  $\pm 3\%$  for all EOS and substances. Also, the EOS-deviations of the second-order derivative properties  $\alpha$  and  $\beta$  are about one order of magnitude larger than the deviations obtained for the density, which is, among other reasons, due to larger uncertainties of the pseudo-experimental data of  $\alpha$  and  $\beta$  (up to 14 %, see above). For both second-order derivative properties, the deviations reach values up to 50 % across all studied EOS frameworks – yet with significant differences between the individual EOS frameworks.

The PC-SAFT results overestimate the density for most substances and states, cf.

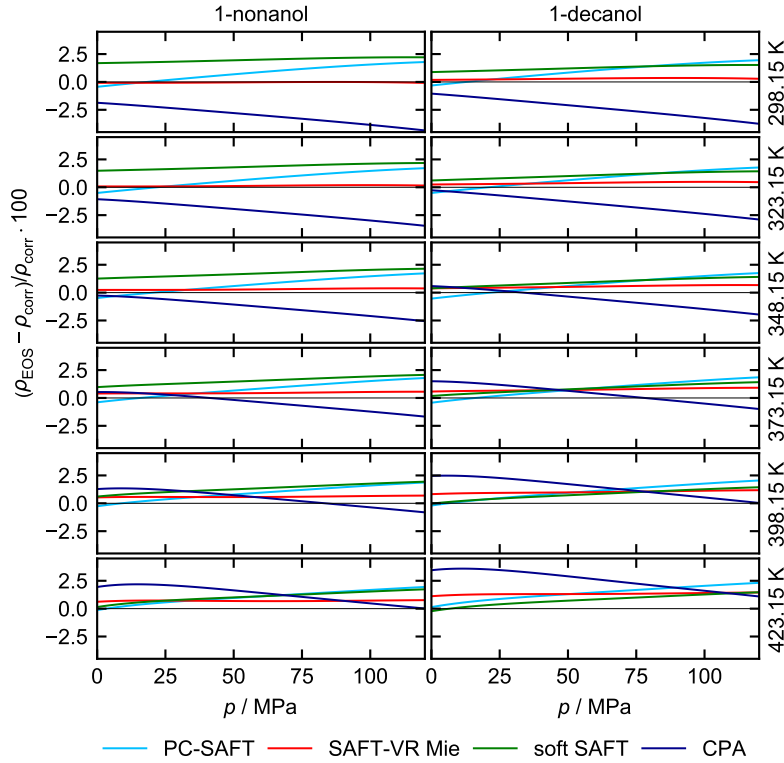


**Figure 52:** Relative deviation between the results for the density from the four EOS frameworks and the empirical correlations from this chapter (cf. Eq. (33)) for 1-nonanol and 1-decanol as a function of the pressure  $p$ . Each rows shows results for a constant temperature.

Figs. 51 and 52. While the density results of the PC-SAFT EOS often agree well with the experimental data at ambient pressure, the density is overestimated at elevated pressure. The thermal expansion coefficient, a measure for the temperature dependence of the density, is well described by the PC-SAFT EOS with  $AAD_{\alpha, \text{EOS}}^{\text{th}}$  values between 4% and 10% (cf. Fig. 53 middle). The pressure dependence of the density, i.e. the isothermal compressibility  $\beta$ , is less accurately described by the PC-SAFT EOS (cf. Fig. 53 bottom). The  $AAD_{\beta, \text{EOS}}^{\text{th}}$  for the PC-SAFT EOS is the second largest of the different EOS and increases with increasing chain length with values from 18% (1-hexanol) up to 36% (1-decanol).

The SAFT-VR Mie EOS yields the lowest deviations among the studied EOS for the density for all studied substances with a lowest  $AAD_{\rho, \text{EOS}}^{\text{th}}$  of  $<0.2\%$  and a maximum  $AAD_{\rho, \text{EOS}}^{\text{th}}$  of around 0.7% (cf. Fig. 53 top). This is also reflected in the deviations for  $\alpha$  and  $\beta$ . Similar to the PC-SAFT EOS, the SAFT-VR Mie EOS provides a good description of the thermal expansion coefficient  $\alpha$ , which is line with findings from previous studies [648, 649]. Only for 1-hexanol and 1-heptanol, the  $AAD_{\alpha, \text{EOS}}^{\text{th}}$  obtained from the SAFT-VR Mie EOS is relatively large with values up to 14% (for 1-hexanol). The pressure dependence of the density, i.e. the isothermal compressibility, of the alcohols is described remarkably well by the SAFT-VR Mie EOS (cf. Fig. 53 bottom). The values

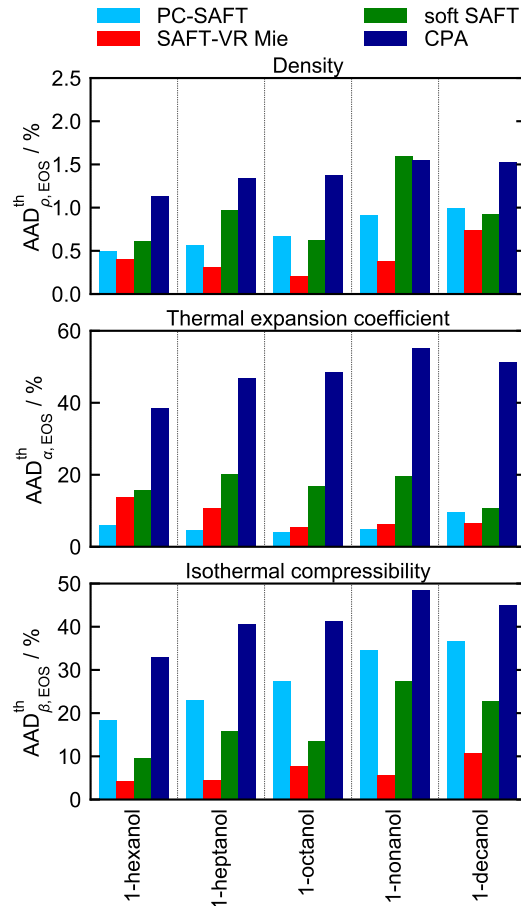


**Figure 53:** Average absolute deviation of the EOS results  $\text{AAD}_{Y,\text{EOS}}^{\text{th}}$  (cf. Eq. (39)) for the density  $\rho$ , the thermal expansion coefficient  $\alpha$ , and the isothermal compressibility  $\beta$  for the five 1-alcohols. The AADs were computed with respect to the reference data from this work 'th'.

for the  $\text{AAD}_{\beta,\text{EOS}}^{\text{th}}$  are the smallest for all substances with a maximum of 10%. The good performance of the SAFT-VR Mie EOS is probably to some extent due to the fact that a higher degree of freedom was used in the fitting procedure since the additional parameter  $\lambda_r$  is used in the models. However, increasing the repulsive exponent  $\lambda_r$  in force fields for molecular simulations yields similar improvements for the description of the density and the pressure dependence of the density [77, 291].

The performance of the soft SAFT EOS for describing the density is similar to the performance of PC-SAFT. Only for the density of 1-heptanol and 1-nonanol, the deviations obtained for the soft SAFT EOS are significantly larger than those of the PC-SAFT, cf. Fig. 53 top. The density is overestimated by the soft SAFT EOS for most of the substances and conditions, especially for the lower temperatures (cf. Figs. 51 and 52). This is also reflected in the deviations obtained by soft SAFT for the thermal expansion coefficient  $\alpha$ , which are slightly larger than those obtained from the PC-SAFT and SAFT-VR Mie EOS. The pressure dependence of the density is slightly overestimated by the soft SAFT EOS (similar to the PC-SAFT) yielding  $\text{AAD}_{\beta,\text{EOS}}^{\text{th}}$  between 9% and

28 %.

The results from the CPA EOS show the largest deviations for all three properties (cf. Fig. 53): The CPA EOS yields the largest deviations for the density with values  $\text{AAD}_{\rho,\text{EOS}}^{\text{th}} > 1\%$  for all substances (see Fig. 53 top). At ambient conditions ( $T = 298.15\text{ K}$  and  $p = 0.1\text{ MPa}$ ), the deviations for the density are relatively small (see Figs. 51 and 52). At high temperatures, the density at ambient pressure is overestimated with deviations of more than 2% by the CPA EOS. The AAD for describing the thermal expansion coefficient by the CPA EOS, i.e.  $\text{AAD}_{\alpha,\text{EOS}}^{\text{th}}$ , is the largest among the studied EOS with values between 35% and more than 50% (cf. Fig. 53 middle). Also, the pressure dependency of the density (cf. Fig. 53 bottom) is not well reproduced by the CPA EOS: The slope  $\partial\rho/\partial p$  is too small (cf. Figs. 51 and 52), i.e. the CPA EOS underestimates the isothermal compressibility  $\beta$ . This results in large  $\text{AAD}_{\beta,\text{EOS}}^{\text{th}}$  values of up to 35%. The overall relatively high deviations obtained for the CPA EOS are possibly due to the fact that the molecule elongation is not explicitly represented in the CPA EOS.

Overall, there is a tendency for the deviations to increase with increasing chain length of the 1-alcohols, i.e. the smallest deviations are observed for 1-hexanol and the largest deviations are observed for 1-decanol. This is the case for the CPA EOS for all three studied properties ( $\rho$ ,  $\alpha$ ,  $\beta$ ) and the case for PC-SAFT and soft SAFT for one or two properties. This indicates that the chain contribution (which is coupled with the monomer contribution [40–42]) causes systematic deviations and that the molecular structure is not ideally described by it. Only for the SAFT-VR Mie EOS, no systematic deviations are obtained for the molecule size dependency. This is in line with the fact that the lowest overall deviations were obtained for the SAFT-VR Mie EOS.

The extrapolation behavior of the EOS models was also evaluated by studying the characteristic curves and assessing the behavior in the vapor-liquid two-phase region. Fig. 54 shows the characteristic curve results for 1-octanol for the PC-SAFT, SAFT-VR Mie, soft SAFT, and CPA EOS. 1-Octanol was chosen as an example here; the results for the other studied 1-alcohols are qualitatively the same (see Appendix E). The SAFT-VR Mie EOS yields realistic predictions of all four characteristic curves. The other three EOS frameworks yield realistic Zeno, Charles, and Boyle curves, but a distorted Amagat curve. These findings are in line with the performance of the four EOS frameworks reported for other substances [50, 650, 651]. For the PC-SAFT EOS, the distorted Amagat curve has been attributed to the employed soft repulsion in the monomer term [651]. For the soft SAFT, a distorted Amagat curve has also been attributed to the underlying monomer term [50], i.e. the Johnson Lennard-Jones EOS [568]. Hence, for both PC-SAFT and soft SAFT, the defects in the Amagat curve are a result of the monomer term. Since all four EOS frameworks applied in this chapter use the SAFT term for describing the H-bonding association and a thermodynamically

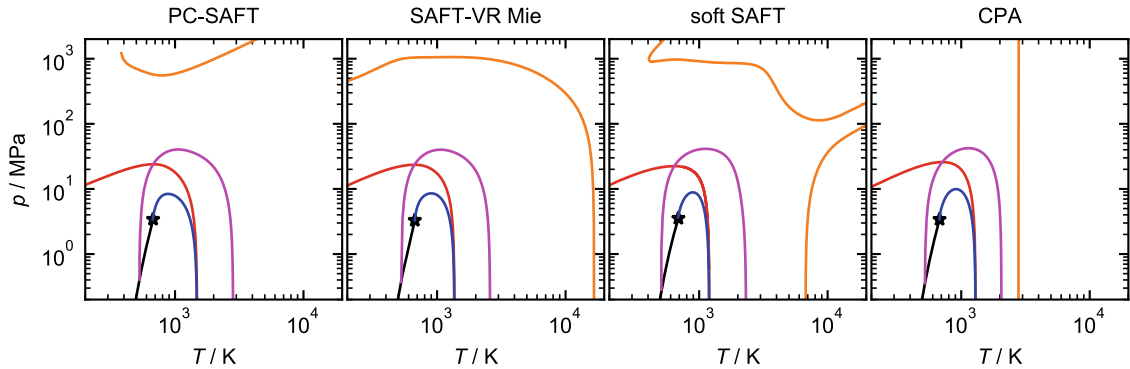


**Figure 54:** Characteristic curves of 1-octanol obtained from the PC-SAFT EOS, SAFT-VR Mie EOS, soft SAFT EOS, and CPA EOS (left to right) including the Zeno curve (red), Amagat curve (orange), Boyle curve (blue), and Charles curve (purple). Black solid line and star represents the vapor pressure curve and the critical point, respectively, as calculated by the corresponding EOS.

consistent Amagat curve is obtained for the SAFT-VR Mie EOS, the SAFT term does most likely not contribute to the defects in the depicted case. Since the CPA EOS comprises only the SAFT term and the Soave-Redlich-Kwong term, the latter probably causes the defects in the Amagat curve. Hence, among the studied models, only the SAFT-VR Mie EOS should be used for extrapolation to extreme states.

The extrapolation behavior in the vapor-liquid metastable and unstable region was also tested. A physically reasonable behavior, i.e. a single spinodal and no undulations of isotherms and a smooth *van der Waals* loop, is for example critical for the application of an EOS model within density gradient theory for describing interfacial properties [500, 652, 653]. The results for 1-octanol from the SAFT-VR Mie EOS are depicted in Fig. 55. Additionally, isotherms are depicted, where density data were determined in this work. The SAFT-VR Mie EOS yields single smooth van der Waals loops in a wide temperature range for 1-octanol. This is in line with results reported in Ref. [234] for the underlying monomer.

## 6.5 Conclusions

In this chapter, the density of the 1-alcohols 1-hexanol, 1-heptanol, 1-octanol, 1-nonanol, and 1-decanol was measured at pressures up to 120 MPa with a high pressure vibrating-tube densimeter. The available density data for the five 1-alcohols was significantly extended and supplemented by this work – especially at elevated temperatures and pressures. Based on that experimental data, an empirical correlations was developed that describes the data with an accuracy of 0.05%. This was used to determine pseudo-

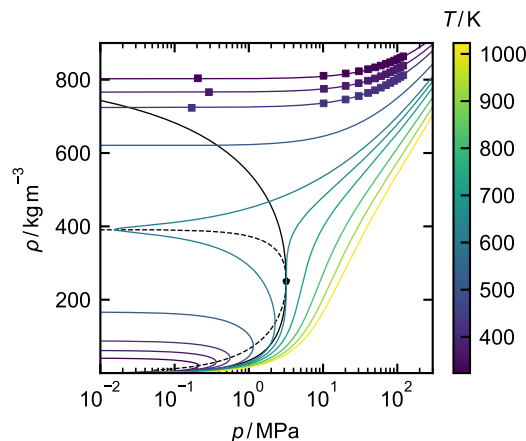


**Figure 55:** Density of 1-octanol as function of the pressure for ten isotherms between 323.15 K and 1023.15 K. Lines are results from the SAFT-VR Mie EOS: Black solid line, black dashed line, and star represents the vapor-liquid equilibrium curve, the spinodal curve, and the critical point, respectively; colored lines are isotherms with the color coded according to the color scale. The squares are the experimental results from this work.

experimental data for the thermal expansion coefficient and the isothermal compressibility.

The density, the thermal expansion coefficient, and the isothermal compressibility were modeled using molecular-based EOS, namely the PC-SAFT, SAFT-VR Mie, soft SAFT, and CPA. Therefore, new parameter sets were fitted using the new experimental data from this work in combination with vapor-liquid equilibrium data from the literature. Overall, the SAFT-VR Mie EOS yields the best results: i) It is the most accurate model for describing the density, the thermal expansion coefficient, and the isothermal compressibility and at the same time describes the vapor-liquid equilibrium data very well; ii) it yields a thermodynamically consistent extrapolation behavior regarding *Brown's* curves as well as into the vapor-liquid two-phase region. Yet, the deviations are about an order of magnitude larger compared to the uncertainty of the experimental data.

# 7 Framework for Modeling Transport Properties using Entropy Scaling

## 7.1 Introduction

Transport properties of pure fluids and fluid mixtures are important in many disciplines of science and engineering [4, 8]. In many cases, also transport properties at conditions, that are far away from the region in which data are available, have to be known. For example, in tribological applications [353, 654], information on the viscosity at pressures above 1 GPa is required [12]. Other examples stem from carbon capture and storage [655], petroleum industry [7, 656], power engineering [10, 76], process engineering [8, 17, 60, 657], and combustion processes [658]. Experimental transport property data are often only available for moderate conditions and for pure fluids; transport property data for extreme conditions and mixtures are scarce. Moreover, for a large number of relevant substances, even at moderate conditions, only little or no data are available. For modeling dynamic processes at interfaces [17, 59, 659], information on transport properties is also required in the metastable and unstable region [60, 352, 502], where practically no experimental data are available. Hence, reliable and predictive models for transport properties are required – which is challenging as transport properties vary strongly depending on the chosen conditions. Fig. 56 illustrates the viscosity, the thermal conductivity, and the self-diffusion coefficient for a molecular fluid in a phase diagram [660]; a detailed discussion of these topologies is given in Appendix F.

Entropy scaling is an interesting method for the modeling of the viscosity, thermal conductivity, and self-diffusion coefficient. It is based on the discovery that the three properties are (within certain limits) monovariate functions of the configurational entropy – when properly scaled by the density and the temperature. The entropy scaling approach was originally proposed by *Rosenfeld* in 1977 [25] and 1999 [26]. Entropy scaling can be favorably coupled with equations of state (EOS)[24] that are used for modeling the configurational entropy as a function of, for example, temperature

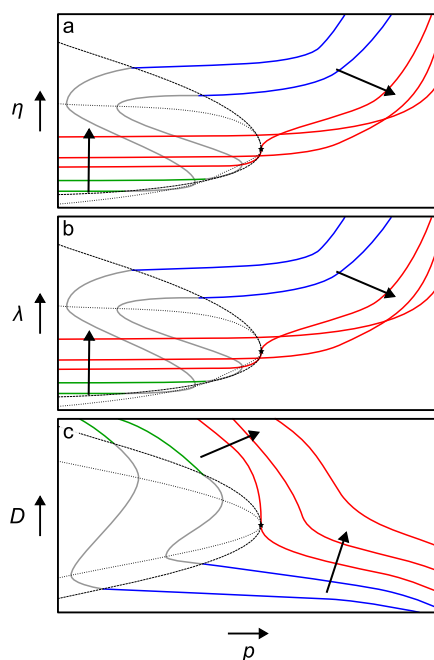


**Figure 56:** Schematic diagrams with subcritical and supercritical isotherms for the viscosity (a), thermal conductivity (b), and self-diffusion coefficient (c) as a function of the pressure  $p$ . The isotherms are: two subcritical isotherms in the homogeneous liquid phase region (blue), in the homogeneous gas phase region (green), the metastable and the unstable region (grey), and the critical and supercritical (red) region. The binodal is indicated as solid line, the spinodal as dotted line, and the critical point by a star. The arrows indicate increasing temperature of the isotherms. The diagrams were drawn based on the entropy scaling models of a simple fluid.

and pressure  $s_{\text{conf}} = s_{\text{conf}}(T, p)$ . Therefore, an accurate description of the configurational entropy is crucial for entropy scaling. For predicting the transport properties in state regions where no experimental data are available, a reliable extrapolation behavior of the entropy scaling model itself is required as well as reliable predictions for the configurational entropy  $s_{\text{conf}} = s_{\text{conf}}(T, p)$  in that region. Several entropy scaling approaches have been proposed in recent years using empirical multi-parameter EOS models [128, 661–666]. Empirical EOS, however, often lack of a robust extrapolation behavior. Molecular-based EOS, on the other hand, enable reliable extrapolations including mixtures [22, 23, 58, 83, 112, 667, 668]. Some entropy scaling models that use molecular-based EOS have been proposed in the past: *Gross* and co-workers have developed entropy scaling models specifically for PC-SAFT [669–675]. The PC-SAFT EOS was also used by other authors to create entropy scaling models for the viscosity, the thermal conductivity, and the self-diffusion coefficient [676–682]. Yet, the PC-SAFT EOS has a physically unrealistic behavior at extreme conditions [50, 651, 683, 684]. Also cubic EOS were used in entropy scaling models [130, 679–681, 685]. Entropy scaling was also applied to the transport properties of model fluids like the Lennard-Jones (LJ) fluid



using specific LJ EOS [128, 132, 686, 687]. As these models were specifically developed for a given EOS, they cannot be straightforwardly transferred to other EOS (that might provide a better description of the thermodynamic properties of the fluid). Hence, no generalized entropy scaling model has been developed yet that can be straightforwardly coupled with different molecular-based EOS.

The core of the entropy scaling approach is the conversion of the transport properties to the so-called 'macroscopically scaled' quantities. *Rosenfeld* [25, 26] found a monovariate relation of a macroscopically scaled transport property as a function of the configurational entropy  $s_{\text{conf}}$ . These findings were later elaborated in the isomorph theory [688, 689]. The macroscopic *Rosenfeld* [25, 26] scaling is only exact for some simple model potentials, e.g. for the inverse power-law potential [24]. For more complex model potentials (even the LJ potential) and real substances, there are deviations from this monovariate behavior [690] and the relation between the configurational entropy and the transport properties cannot be predicted a priori from the theory. Therefore, (component-specific) adjustable parameters are introduced for these substances.

In this work, a generalized framework for the application of entropy scaling in conjunction with molecular-based EOS is proposed, which can be used for modeling transport properties of model fluids as well as real substances. The framework is designed such that the viscosity, the thermal conductivity, and the self-diffusion coefficient can be described. The new framework is based on a scaling of the three properties, that combines the *Rosenfeld* scaling with a scaling for the zero-density limit. The transition between the two approaches is achieved in a convenient, yet not physically rigorously deducible way. The universal parameters of the entropy scaling framework were fitted to computer experiment data for transport properties and the entropy of the LJ fluid, so that they do not depend on the chosen EOS. Therefore, simulations of the LJ fluid were conducted in which the transport properties and the entropy were sampled simultaneously. This makes the model on one hand robust and on the other hand flexible as it can be straightforwardly coupled with basically any EOS. For modeling a specific real substance, the entropy scaling model requires component-specific parameters, which have to be adjusted to experimental data of transport properties. The number of component-specific parameters of the model is 2-5 and can be chosen depending on the amount and quality of transport data that are available for the training. Hence, the model can also be applied in a meaningful way if only very few data are available. Based on the component-specific parameters for the pure substances, the framework can be applied to predict the viscosity and the thermal conductivity of mixtures without any additional information.

The flexibility of the entropy scaling framework was demonstrated by applying it to nine different molecular-based EOS. Also, the robust extrapolation behavior of the framework

to high pressures, metastable and unstable states, as well as mixtures is demonstrated. For mixtures, it is shown that transport properties can be predicted by the framework without the adjustment of additional parameters – even for highly non-ideal mixtures.

The chapter is organized as follows: First, the entropy scaling framework is described, including the scaling procedure, the treatment of the zero-density limit, and the determination of the universal parameters. Then, the applicability of the framework is demonstrated for different pure substances and mixtures. Finally, conclusions are drawn.

## 7.2 Model

The principles of the entropy scaling framework developed in this chapter are depicted in Fig. 57. It can be applied for modeling the viscosity, the thermal conductivity, and

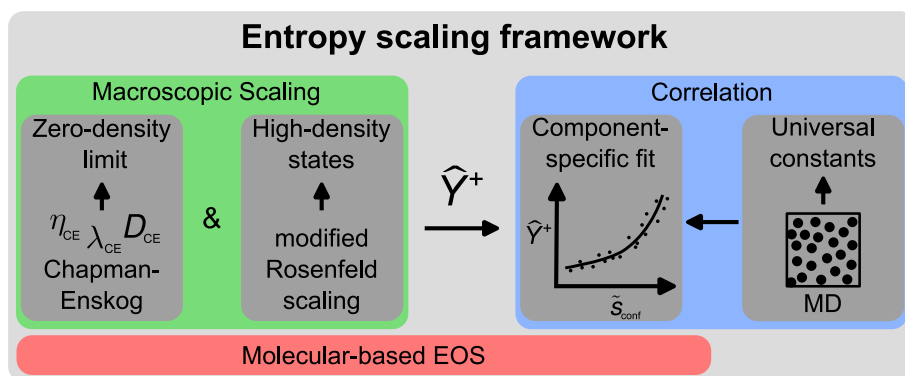


**Figure 57:** Scheme of the entropy scaling framework proposed in this chapter.

the self-diffusion coefficient of pure component fluids; and for modeling the viscosity and the thermal conductivity of fluid mixtures. The entropy scaling framework consists of two parts: a suitable macroscopic scaling of the transport properties (green part in Fig. 57) and correlations that describe the scaled data (blue part in Fig. 57). The scaling part comprises two different methods, one for the low-density region and one for the high-density region. The scaling is carried out so that the scaled properties from both regions fall onto a single continuous smooth curve describing the dependency of the scaled property on the configurational entropy. The mathematical function that is used here for describing this relation has both universal parameters that determine basic features of the function and component-specific parameters that have to be fitted to experimental data. The universal parameters were fitted to molecular dynamics (MD) simulation results of the transport properties and the entropy of the LJ fluid determined in this chapter, i.e. without using an EOS. For applying the entropy scaling framework, it is coupled with a molecular-based EOS that yields the configurational entropy for the

state point of interest, i.e.  $s_{\text{conf}}(T, \rho, \underline{x})$ , where  $\underline{x}$  indicates the composition vector of a mixture.

### 7.2.1 Molecular-based EOS

Molecular-based EOS are algebraic models for describing thermodynamic properties of fluids and fluid mixtures [22, 23]. They are usually formulated in the Helmholtz energy per particle  $a = A/N$  as a function of the temperature, density, and composition, i.e.  $a = a(T, \rho, \underline{x})$ , since this is a thermodynamic fundamental expression. All other thermodynamic properties can be derived from it [545]. In molecular-based EOS, the formulation of the Helmholtz energy is physically motivated and can be divided into an ideal gas and a configurational (or residual) contribution. The configurational contribution is usually constructed as a sum of terms in molecular-based EOS, each modeling the effect of a given molecular interaction or molecular architecture feature on the Helmholtz energy, for example, repulsion, attraction, association [555], electrostatic interactions [22], the chain formation [40] and branching in the molecular structure [691]. Hence, the configurational Helmholtz energy  $a_{\text{conf}}$  can be written as

$$a_{\text{conf}} = a_{\text{rep}} + a_{\text{disp}} + a_{\text{chain}} + a_{\text{branching}} + a_{\text{assoc}} + a_{\text{D}} + a_{\text{Q}}, \quad (41)$$

where  $a_{\text{rep}}$ ,  $a_{\text{disp}}$ ,  $a_{\text{chain}}$ ,  $a_{\text{branching}}$ ,  $a_{\text{assoc}}$ ,  $a_{\text{D}}$ , and  $a_{\text{Q}}$  indicate the contributions due to repulsive and dispersive interactions of monomers, the chain formation of multiple monomers, branching, associating (H-bonding) interactions, dipole interactions, and quadrupole interactions, respectively [692]. The terms contain different component-specific parameters, which can be physically interpreted. In different molecular-based EOS, different terms are combined to constitute the EOS. Component-specific parameters are for example the segment diameter  $\sigma$ , the segment dispersion energy  $\varepsilon$ , and the chain length, i.e. segment number or elongation parameter  $m$ . These component-specific parameters are usually fitted to experimental data – in particular to vapor-liquid equilibrium (VLE) properties and liquid phase densities.

Many different molecular-based EOS have been described in the literature [22], e.g. the BACKONE EOS family of *Fischer* and co-workers [693, 694], the PACT EOS family of *Prausnitz* and co-workers [695, 696], the EOS family that uses the statistical association fluid theory (SAFT) of *Chapman, Jackson, and Gubbins* [555, 556], and the CPA EOS family of *Kontogeorgis* and co-workers [43, 697]. Since different molecular-based EOS are based on different modeling approaches and approximations, they differ in parts significantly in their mathematical formulation. Accordingly, for a given component, the component-specific parameters are not transferable among different molecular-based EOS.

Due to their sound physical basis, molecular-based EOS often enable reliable predictions for states and properties that were not considered in the training [22, 23, 348, 651, 692, 698], i.e. many of them can be reliably applied not only for describing stable gas, liquid, and supercritical states, but also metastable and to some extent unstable states (which is for example relevant for interfaces). Yet, without further modifications [589], the critical point is not well described by most EOS. They overestimate the critical temperature and pressure (due to the underlying critical scaling behavior). For modeling mixtures with molecular-based EOS, mixing and combination rules are applied [22, 47, 58, 667, 699]. Thereby, it is usually sufficient to use a single state independent parameter  $\xi_{ij}$ , which is generally introduced in the Berthelot term, with which the binary dispersive cross-interactions  $\varepsilon_{ij}$  are described [700]

$$\varepsilon_{ij} = \xi_{ij} \sqrt{\varepsilon_i \varepsilon_j}, \quad (42)$$

where  $\varepsilon_i$  and  $\varepsilon_j$  are the dispersive interaction parameters of the pure components.

For entropy scaling, the calculation of the molar configurational entropy  $s_{\text{conf}}$  at a given state point  $(T, \rho, \underline{x})$  is required. It can be calculated from the configurational Helmholtz energy  $a_{\text{conf}}$  as the derivative with respect to temperature  $T$  at constant volume  $v$  and composition  $\underline{x}$

$$s_{\text{conf}} = - \left( \frac{\partial a_{\text{conf}}}{\partial T} \right)_{v, \underline{x}}. \quad (43)$$

In this chapter, nine molecular-based EOS were used: three LJ EOS (Kolafa-Nezbeda [136], PeTS [108], *Stephan et al.* [234]), three from the SAFT EOS family (PC-SAFT [40], SAFT-VR Mie [41], soft SAFT [558]), one from the PACT EOS family (PACT+B [695]), one from the BACKONE family [694], and one from the cubic EOS family (sCPA [43, 701]). The pure component model parameters were taken from the literature [40, 41, 62, 63, 558, 694, 695, 697, 702–704]. Details are given in Appendix F.

## 7.2.2 Scaling of the Transport Properties

The scaling of the viscosity  $\eta$ , the thermal conductivity  $\lambda$ , and the self-diffusion coefficient  $D$  with respect to temperature and density is the core of entropy scaling [25, 26].

Here, a modified *Rosenfeld* scaling from *Bell* [128, 690] (indicated by  $^+$ ) is adopted:

$$\eta^+ = \eta \frac{\rho_N^{-2/3}}{\sqrt{MTk_B/N_A}} \left( \frac{-s_{\text{conf}}}{R} \right)^{2/3}, \quad (44)$$

$$\lambda^+ = \lambda \frac{\rho_N^{-2/3}}{k_B \sqrt{RT/M}} \left( \frac{-s_{\text{conf}}}{R} \right)^{2/3}, \quad (45)$$

$$D^+ = D \frac{\rho_N^{1/3}}{\sqrt{RT/M}} \left( \frac{-s_{\text{conf}}}{R} \right)^{2/3}, \quad (46)$$

where  $\rho_N$  is the number density in  $1/\text{m}^3$ ,  $M$  the molar mass in  $\text{kg}/\text{mol}$ ,  $R = k_B N_A$  the universal gas constant,  $k_B$  the *Boltzmann* constant, and  $N_A$  the *Avogadro* number. The scaled transport properties  $Y^+$  with  $Y \in \{\eta, \lambda, D\}$  obtained from Eqs. (44) - (46) are dimensionless. This scaling approach yields an approximately monovariate dependency of  $Y^+$  on the configurational entropy for dense states. However, this does not hold for low density states [26, 705]. To overcome this drawback, a reduction using the Chapman-Enskog (CE) transport properties is applied here for low-densities as explained in more detail below.

Fig. 58 schematically shows the scaling procedure introduced in this chapter starting from  $Y^+$  (green, cf. Eqs. (44) - (46)). In the framework, the reduced configurational

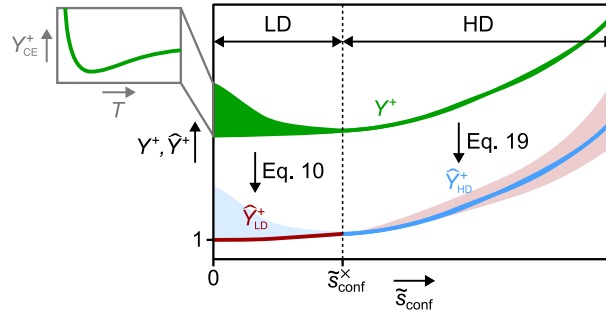


**Figure 58:** Scheme illustrating the modeling principle of the entropy scaling framework. LD and HD indicate the low-density and the high-density region, respectively. Green indicates the scaled transport property  $Y^+$  for a given substance with  $Y \in \{\eta, \lambda, D\}$ .  $Y_{\text{CE}}^+$  (left inset) indicates the zero-density limit transport property ( $\rho \rightarrow 0$ ,  $\tilde{s}_{\text{conf}} \rightarrow 0$ ) obtained from Chapman-Enskog theory as function of the temperature  $T$ .  $\hat{Y}_{\text{LD}}^+$  indicates the CE-scaled transport property in the LD region (cf. Eq. (54)) and  $\hat{Y}_{\text{HD}}^+$  the CE-scaled transport property in the HD region (cf. Eq. (55)). The light red and light blue areas are not used.

entropy  $\tilde{s}_{\text{conf}}$  is defined as

$$\tilde{s}_{\text{conf}} = \frac{-s_{\text{conf}}}{mR}. \quad (47)$$

Therein, the segment number  $m$  describes the elongation of a molecule in a given molecular-based EOS and is used to scale  $s_{\text{conf}}$  such that the values of  $\tilde{s}_{\text{conf}}$  are within a

similar range for molecules of different sizes [669]. Moreover,  $\tilde{s}_{\text{conf}}$  is also a dimensionless property. The limit  $\tilde{s}_{\text{conf}} \rightarrow 0$  corresponds to the limit  $\rho \rightarrow 0$ . Based on  $\tilde{s}_{\text{conf}}$ , a split for individually describing the low-density (LD) and high-density (HD) region is applied. The LD region covers all states  $\tilde{s}_{\text{conf}} < \tilde{s}_{\text{conf}}^*$  and the HD region all states  $\tilde{s}_{\text{conf}} \geq \tilde{s}_{\text{conf}}^*$ . Here, a value of  $\tilde{s}_{\text{conf}}^* = 0.5$  was chosen based on preliminary studies.

The scaling with Eqs. (44) - (46) usually yields very good results for the HD region, but scattering results for the LD region (cf. Fig. 58, green part in the LD region). This scattering can be understood as a consequence of the known temperature-dependence of the results for  $\rho \rightarrow 0$ , as described by the Chapman-Enskog theory, cf. insert in Fig. 58. Applying Eqs. (44) - (46) to the results from the Chapman-Enskog theory yields:

$$\eta_{\text{CE}}^+ = \frac{5}{16\sqrt{\pi}} \frac{1}{\sigma_{\text{CE}}^2 \Omega^{(2,2)}} \left( T \left( \frac{dB}{dT} \right) + B \right)^{2/3}, \quad (48)$$

$$\lambda_{\text{CE}}^+ = \frac{75}{64\sqrt{\pi}} \frac{1}{\sigma_{\text{CE}}^2 \Omega^{(2,2)}} \left( T \left( \frac{dB}{dT} \right) + B \right)^{2/3}, \quad (49)$$

$$D_{\text{CE}}^+ = \frac{3}{8\sqrt{\pi}} \frac{1}{\sigma_{\text{CE}}^2 \Omega^{(1,1)}} \left( T \left( \frac{dB}{dT} \right) + B \right)^{2/3}, \quad (50)$$

where the relation

$$\lim_{\rho_{\text{N}} \rightarrow 0} \left( \frac{\partial(-s_{\text{conf}}/R)}{\partial \rho_{\text{N}}} \right)_T = T \frac{dB}{dT} + B \quad (51)$$

is exploited with  $B$  being the second virial coefficient (computed from the EOS) and  $\Omega^{(1,1)}$  and  $\Omega^{(2,2)}$  are the reduced collision integrals [75], which are functions of the reduced temperature  $Tk_{\text{B}}/\varepsilon_{\text{CE}}$ , i.e.  $\Omega^{(1,1)} = \Omega^{(1,1)}(Tk_{\text{B}}/\varepsilon_{\text{CE}})$  and  $\Omega^{(2,2)} = \Omega^{(2,2)}(Tk_{\text{B}}/\varepsilon_{\text{CE}})$ . The two parameters  $\sigma_{\text{CE}}$  and  $\varepsilon_{\text{CE}}$  characterize the molecular size and dispersion energy, respectively. The scaled Chapman-Enskog transport properties  $\eta_{\text{CE}}^+$ ,  $\lambda_{\text{CE}}^+$ , and  $D_{\text{CE}}^+$  are solely functions of the temperature. In Appendix F, the Eqs. (48) - (50) are derived from the Chapman-Enskog equations. The LJ fluid is taken as a reference fluid for calculating the zero-density limit transport properties; the empirical correlations for the collision integrals for the LJ fluid from *Kim* and *Monroe* were used [126]. To determine the parameters  $\sigma_{\text{CE}}$  and  $\varepsilon_{\text{CE}}$ , the LJ model is mapped to a given real substance by applying the corresponding states principle. Hence,  $\sigma_{\text{CE}}$  and  $\varepsilon_{\text{CE}}$  are determined from the critical temperature  $T_{\text{c}}$  and pressure  $p_{\text{c}}$  of the considered substance and the critical temperature and pressure of the LJ fluid as

$$\varepsilon_{\text{CE}} = \frac{T_{\text{c}}}{T_{\text{c,LJ}}/\varepsilon_{\text{LJ}}}, \quad (52)$$

$$\sigma_{\text{CE}} = \left( \frac{(p_{\text{c,LJ}} \sigma_{\text{LJ}}^3 / \varepsilon_{\text{LJ}}) \varepsilon_{\text{CE}}}{p_{\text{c}}} \right)^{1/3}, \quad (53)$$

where  $\varepsilon_{\text{LJ}}$  and  $\sigma_{\text{LJ}}$  indicate the size and energy parameter of the LJ potential, respec-

tively. The reduced critical temperature and pressure of the LJ fluid were taken from the literature:  $T_{c,LJ} = 1.321 \varepsilon_{LJ}/k_B$  and  $p_{c,LJ} = 0.316 \varepsilon_{LJ}/\sigma_{LJ}^3$  [73]. Thus, Eqs. (52) - (53) establish a link between the real substance model described by the molecular-based EOS and the LJ model in the zero-density limit. The critical parameters  $T_c$  and  $p_c$  for a given substance are taken from the EOS.

The CE-scaled transport property for the LD region  $\widehat{Y}_{LD}^+$  (with  $Y \in \{\eta, \lambda, D\}$ ) is calculated from  $Y_{LD}^+$  as

$$\widehat{Y}_{LD}^+ = \frac{Y_{LD}^+}{Y_{CE}^+}. \quad (54)$$

As illustrated in Fig. 58,  $\widehat{Y}_{LD}^+$  provides a monovariate function with respect to the reduced configurational entropy  $\tilde{s}_{conf}$ . In the case of exact representation of the zero-density limit of the transport properties by the Chapman-Enskog theory, Eq. (54) yields unity ( $\widehat{Y}^+ = 1$ ) for  $\tilde{s}_{conf} \rightarrow 0$ . Applying Eq. (54) to all states including the HD region would, however, yield a distinctly poorer scaling than in the LD region, as illustrated in Fig. 58. As the modified *Rosenfeld* scaling already yields a decent behavior in the HD region, the scaled transport property for the HD region  $Y_{HD}^+$  only has to be shifted in a suitable way to obtain a smooth transition in  $\widehat{Y}^+$  from the LD to the HD region at  $\tilde{s}_{conf}^*$ . Preliminary studies showed that this can be achieved by simply dividing  $Y^+$  by a constant factor for which the minimum of the scaled Chapman-Enskog transport property  $\min(Y_{CE}^+(T))$  was chosen, i.e.

$$\widehat{Y}_{HD}^+ = \frac{Y_{HD}^+}{\min(Y_{CE}^+(T))}. \quad (55)$$

The rationale behind this choice is that the scattering of  $Y^+$  can be understood as positive deviations from a master curve that extends the results from the HD region (cf. green part in Fig. 58). By dividing the results from the HD region by the minimum value from the Chapman-Enskog theory, it can be expected to recover this curve, albeit in a version that is shifted.

To avoid having to work with a distinction of cases (LD vs. HD), a continuous function  $\widehat{Y}^+$  is introduced:

$$\widehat{Y}^+ = \widehat{Y}_{LD}^+ W + \widehat{Y}_{HD}^+ (1 - W), \quad (56)$$

with

$$W = \frac{1}{1 + \exp(20(\tilde{s}_{conf} - \tilde{s}_{conf}^*))}, \quad (57)$$

where  $W = 1$  for  $\tilde{s}_{conf} \ll \tilde{s}_{conf}^*$  and  $W = 0$  for  $\tilde{s}_{conf} \gg \tilde{s}_{conf}^*$ . The CE-scaled transport property  $\widehat{Y}^+$  is a monovariate function of the reduced configurational entropy  $\tilde{s}_{conf}$  (cf. Fig. 58) in all state regions as shown below. Details of the framework are given in Appendix F and an implementation is available on GitHub.

### 7.2.3 Component-Specific Correlation

CE-scaled transport properties are approximate monovariate functions of the configurational entropy  $\tilde{s}_{\text{conf}}$ . Yet, the shape of this monovariate function is different for the three transport properties and for different components. The relation  $\widehat{Y}^+(\tilde{s}_{\text{conf}})$  is described here by an empirical, rational function

$$\left. \begin{array}{l} \ln(\widehat{\eta}_i^+(\tilde{s}_{\text{conf}})) \\ \widehat{\lambda}_i^+(\tilde{s}_{\text{conf}}) \\ \ln(\widehat{D}_i^+(\tilde{s}_{\text{conf}})) \end{array} \right\} = \frac{\alpha_{0,i}^{(Y)} + \alpha_{\ln,i}^{(Y)} \ln(\tilde{s}_{\text{conf}} + 1) + \alpha_{1,i}^{(Y)} \tilde{s}_{\text{conf}} + \alpha_{2,i}^{(Y)} (\tilde{s}_{\text{conf}})^2 + \alpha_{3,i}^{(Y)} (\tilde{s}_{\text{conf}})^3}{1 + g_1^{(Y)} \ln(\tilde{s}_{\text{conf}} + 1) + g_2^{(Y)} \tilde{s}_{\text{conf}}}. \quad (58)$$

The parameters  $\alpha_{0,i}^{(Y)}$ ,  $\alpha_{\ln,i}^{(Y)}$ ,  $\alpha_{1,i}^{(Y)}$ ,  $\alpha_{2,i}^{(Y)}$ , and  $\alpha_{3,i}^{(Y)}$  are specific for the studied component  $i$  as well as for the transport property  $Y$ . They are fitted for each substance to reference data. The number of parameters, i.e. terms, used in the nominator of Eq. (58) can be conveniently chosen for a given problem. The parameters  $g_1^{(Y)}$  and  $g_2^{(Y)}$  in the denominator are universal parameters for the transport property  $Y$ . All parameters of Eq. (58), i.e.  $\alpha_{0,i}^{(Y)}$ ,  $\alpha_{\ln,i}^{(Y)}$ ,  $\alpha_{1,i}^{(Y)}$ ,  $\alpha_{2,i}^{(Y)}$ ,  $\alpha_{3,i}^{(Y)}$ ,  $g_1^{(Y)}$ , and  $g_2^{(Y)}$ , are dimensionless. The mathematical form (cf. Eq. (58)) and choice for the universal parameters (see below) provides well behaving functions for the resulting model, i.e. no pole for  $\tilde{s}_{\text{conf}} > 0$ , and a defined limit for  $\tilde{s}_{\text{conf}} \rightarrow 0$ , i.e.  $\alpha_{0,i}^{(Y)}$ .

### 7.2.4 Molecular Simulations and Adjustment of the Universal Parameters

The universal parameters, i.e.  $g_1^{(Y)}$  and  $g_2^{(Y)}$  (cf. Eq. (58)), were fitted to LJ simulation data. As suitable data were not available in the literature, homogeneous bulk phase MD simulations were carried out in this work with the software *ms2*[463, 464]. The simulations were carried out for liquid, vapor, supercritical, metastable VLE and metastable solid-liquid equilibrium (SLE) regions as well as on the VLE binodal and the freezing line. In total, 173 state points were studied. The studied state points are depicted in Fig. 59.

Each simulation consisted of 5000 particles. The gear predictor-corrector integrator was used with a time step of  $\Delta t = 0.001 ((\sigma^2 M / N_A) / \varepsilon)^{1/2}$ . The simulations were conducted in the  $NVT$  ensemble with  $1 \times 10^5$  equilibration time steps and  $5 \times 10^6$  production time steps. Periodic boundary conditions were applied in all directions. The viscosity, the thermal conductivity, and the self-diffusion coefficient were sampled using the Green-Kubo [97, 98] formalism with a correlation length of  $10^4$  time steps for  $\rho \geq 0.1\sigma^{-3}$  and  $10^5$  time steps for  $\rho < 0.1\sigma^{-3}$ . Details on the computational procedure of the Green-



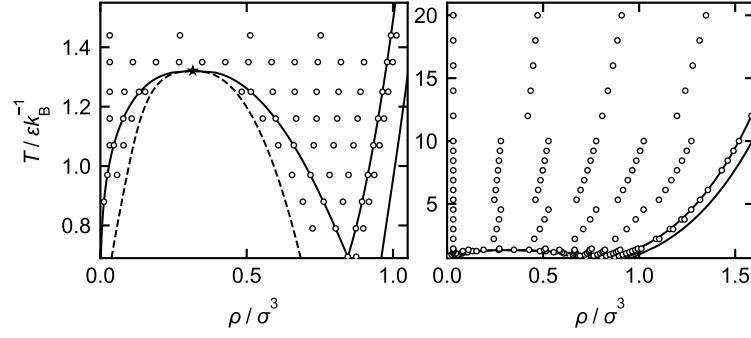


**Figure 59:** Overview of the 173 state points (circles) of the LJ fluid that were studied in this chapter. The binodal and the critical point (star) were taken from Ref. [73], the spinodal from Ref. [706], and the freezing and melting lines from Ref. [238].

Kubo implementation in *ms2* are given in Refs. [707, 708]. The viscosity, the thermal conductivity, and the self-diffusion coefficient data obtained from the simulations were CE-scaled according to Eqs. (44) - (56). The second virial coefficient  $B$  of the LJ fluid and its derivative with respect to  $T$  used in Eqs. (48) - (50) were calculated analytically from the interaction potential [709]. Moreover, the configurational entropy was determined from the simulations. Therefore, the chemical potential  $\mu_{\text{conf}}$  was sampled using *Widom's* test particle method [710]. From that, the configurational Helmholtz energy  $a_{\text{conf}}$  was calculated as [464]

$$a_{\text{conf}} = -\frac{\partial a_{\text{conf}}}{\partial \rho} \rho + \mu_{\text{conf}} = \frac{p}{\rho} + \mu_{\text{conf}}. \quad (59)$$

The configurational entropy  $s_{\text{conf}}$  was then calculated as

$$s_{\text{conf}} = \frac{u_{\text{conf}}}{T} - \frac{a_{\text{conf}}}{T}, \quad (60)$$

with  $u_{\text{conf}}$  being the configurational internal energy. Thereby, data for  $s_{\text{conf}}$ ,  $\widehat{\eta}^+$ ,  $\widehat{\lambda}^+$ , and  $\widehat{D}^+$  of the LJ fluid were obtained in a wide state range. Details are discussed in Appendix F. Moreover, the numeric data of the MD simulation results are provided in Ref. 52.

The sampled entropy data were converted to the reduced configurational entropy  $\tilde{s}_{\text{conf}}$  using Eq. (47) and  $m = 1$ . The universal parameters  $g_1^{(Y)}$  and  $g_2^{(Y)}$  for the correlations for  $Y \in \{\eta, \lambda, D\}$  (cf. Eq. (58)) were obtained from a fit to the computer experiment data  $\widehat{\eta}^+(\tilde{s}_{\text{conf}})$ ,  $\widehat{\lambda}^+(\tilde{s}_{\text{conf}})$ , and  $\widehat{D}^+(\tilde{s}_{\text{conf}})$ . The results are given in Table 33.

**Table 33:** Universal parameters of the entropy scaling framework, i.e. Eq. (58), as well as the component-specific parameters used for the fits of the universal parameters for the viscosity, the thermal conductivity, and the self-diffusion coefficient.

Property	$f(\tilde{s}_{\text{conf}})$	$g_1^{(Y)}$	$g_2^{(Y)}$	$\alpha_{0,\text{LJ}}^{(Y)}$	$\alpha_{\text{ln,LJ}}^{(Y)}$	$\alpha_{1,\text{LJ}}^{(Y)}$	$\alpha_{2,\text{LJ}}^{(Y)}$	$\alpha_{3,\text{LJ}}^{(Y)}$
viscosity	$\ln(\widehat{\eta}^+(\tilde{s}_{\text{conf}}))$	-1.6386	1.3923	0	0	0	1	0
thermal conductivity	$\widehat{\lambda}^+(\tilde{s}_{\text{conf}})$	-1.9107	1.0725	1	0	0	0	1
self-diffusion	$\ln(\widehat{D}^+(\tilde{s}_{\text{conf}}))$	0.6632	9.4714	0	0	0	0	-1

The component-specific parameters  $\alpha_{0,\text{LJ}}^{(Y)}$ ,  $\alpha_{\text{ln,LJ}}^{(Y)}$ ,  $\alpha_{1,\text{LJ}}^{(Y)}$ ,  $\alpha_{2,\text{LJ}}^{(Y)}$ , and  $\alpha_{3,\text{LJ}}^{(Y)}$  were a priori fixed to constant values for the fit (see Table 33). The value of  $\alpha_{0,\text{LJ}}^{(Y)}$  determines the low-density limit of the studied property, which is zero for  $\ln(\widehat{\eta}^+)$  and  $\ln(\widehat{D}^+)$  and 1 for  $\widehat{\lambda}^+$ . The logarithmic term and the linear term in the denominator of Eq. (58) were not used, i.e.  $\alpha_{\text{ln,LJ}}^{(Y)} = \alpha_{1,\text{LJ}}^{(Y)} = 0$ . The numbers for  $\alpha_{2,\text{LJ}}^{(Y)}$  and  $\alpha_{3,\text{LJ}}^{(Y)}$  were, depending on the property, set either to 0 or 1, so that the numerator of Eq. (58) is either a quadratic (viscosity) or a cubic function (thermal conductivity and self-diffusion coefficient) of the reduced configurational entropy  $\tilde{s}_{\text{conf}}$ . As the denominator of Eq. (58) is linear, this results in a linear asymptote for  $\tilde{s}_{\text{conf}} \rightarrow \infty$  for the viscosity, which accounts for the approximately linear behavior of the CE-scaled viscosity as function of the configurational entropy [128]. For the thermal conductivity and the self-diffusion coefficient, the CE-scaled transport properties can be described more accurately by a quadratic asymptote. The values for the parameters given in Table 33 are valid for the LJ fluid, but they can also be used as default and starting values for individual fits to data for other fluids. Fig. 60 shows the result of the fit for the CE-scaled properties as function of the reduced configurational entropy for the LJ fluid. The data are well represented by the fit. The mean relative deviations of the fits are  $\overline{\delta\widehat{\eta}^+} = 9.12\%$ ,  $\overline{\delta\widehat{\lambda}^+} = 11.49\%$ , and  $\overline{\delta\widehat{D}^+} = 2.01\%$  and were calculated as

$$\overline{\delta Y} = \frac{1}{N_{\text{exp}}} \sum_j^{N_{\text{exp}}} |\delta Y_j| \quad (61)$$

$$\text{with } \delta Y_j = \frac{Y_{\text{exp},j} - Y_{\text{ES},j}}{Y_{\text{exp},j}}, \quad (62)$$

with  $N_{\text{exp}}$  being the number of data points,  $Y_{\text{exp}}$  the (computer) experiment value, and  $Y_{\text{ES}}$  the values obtained from the entropy scaling model. Since the studied state points cover a large range of states with respect to temperature and density (cf. Fig. 59), also a large range of states with respect to the configurational entropy is covered (see Appendix

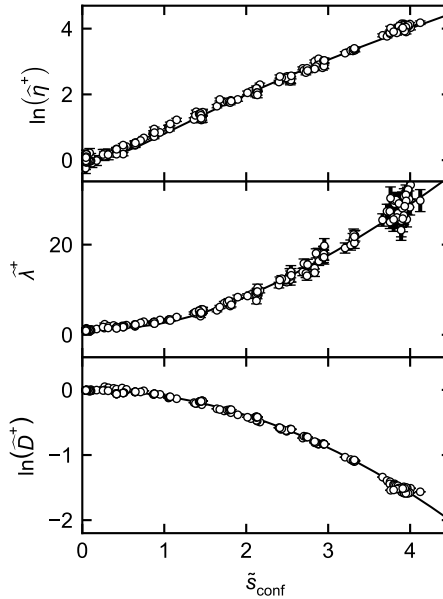


**Figure 60:** CE-scaled viscosity  $\hat{\eta}^+$ , thermal conductivity  $\hat{\lambda}^+$ , and self-diffusion coefficient  $\hat{D}^+$  of the LJ fluid as function of the reduced configurational entropy  $\tilde{s}_{\text{conf}}$ . Symbols represent MD simulation results (state points as shown in Fig. 59) and the solid line is the global fit to these results (cf. Eq. (58) and Table 33). All shown properties are dimensionless.

F). For the viscosity and the thermal conductivity, the vast majority of the data points is described by the entropy scaling model with a deviation below 5 %; that number is 2 % for the self-diffusion coefficient. The deviations are larger for the data points at the largest configurational entropies which corresponds to very high densities, where the sampling of both the entropy and the transport properties is challenging. These deviations are of the same order as the relative statistical uncertainties of the simulation data for the viscosity and the thermal conductivity, which are on average 7.4 % and 8.5 %, respectively. For the self-diffusion coefficient, the corresponding uncertainty for the simulation data is 0.15 %.

Fig. 60 also indicates that the strategy proposed in this work, that is based on different procedures for the LD region and the HD region, works well. The curves are smooth, also in the vicinity of the threshold at  $\tilde{s}_{\text{conf}} = 0.5$ .

### 7.2.5 Extension to Mixtures

Also for mixtures, an approximately monovariate relation between the transport properties and the configurational entropy has been observed [62, 672]. Therefore, the entropy scaling model for the viscosity and the thermal conductivity of pure components described above was extended to modeling mixture properties. The extension to self-diffusion coefficients is less straightforward, as there is one self-diffusion coefficient for

each component, so this issue is not discussed here and left open for future work. In the approach, the mixture is treated as a pure pseudo-component following the one-fluid theory mixing rule concept [28, 711].

Transport properties of mixtures are represented here as a function of the temperature, density, and composition  $\underline{x}$ , i.e.  $Y_{\text{mix}}(T, \rho, \underline{x})$ , and described by the entropy scaling model as  $\widehat{Y}_{\text{mix}}^+(\tilde{s}_{\text{conf}}(T, \rho, \underline{x}))$ . In Eqs. (44) - (46),  $M$  is now the mean molar mass of the mixture

$$M = \sum_i^N x_i M_i, \quad (63)$$

where  $N$  is the number of components and  $x_i$  and  $M_i$  are the mole fraction and the molar mass of component  $i$ . The reduced configurational entropy of the mixture  $\tilde{s}_{\text{conf}}(T, \rho, \underline{x})$  is calculated from the molecular-based EOS using Eq. (47), where the segment number  $m$  of the pseudo-component representing the mixture is calculated from

$$m = \sum_i^N x_i m_i, \quad (64)$$

where  $m_i$  is the segment number of the component  $i$ . The zero-density transport properties of the mixture were calculated as follows: the viscosity of the mixture in the zero-density limit  $\eta_{\text{CE,mix}}^+$  was calculated according to *Wilke* [712]

$$\eta_{\text{CE,mix}}^+ = \sum_i^N \frac{x_i \eta_{\text{CE},i}^+}{\sum_{j=1}^N x_j \phi_{ij}}, \quad (65)$$

with  $\phi_{ij} = \frac{(1 + (\eta_{\text{CE},i}^+ / \eta_{\text{CE},j}^+)^{1/2} (M_i / M_j)^{1/4})^2}{(8(1 + M_i / M_j))^{1/2}},$

where  $\eta_{\text{CE},i}^+$  and  $\eta_{\text{CE},j}^+$  are the pure component Chapman-Enskog values for the viscosity (cf. Eq. (48)). The thermal conductivity of the mixture in the zero-density limit  $\lambda_{\text{CE,mix}}^+$  was calculated according to *Wassiljewa* [713] and *Mason and Saxena* [714] from

$$\lambda_{\text{CE,mix}}^+ = \sum_i^N \frac{x_i \lambda_{\text{CE},i}^+}{\sum_{j=1}^N x_j \phi_{ij}}, \quad (66)$$

with  $\phi_{ij} = \frac{(1 + (\lambda_{\text{CE},i}^+ / \lambda_{\text{CE},j}^+)^{1/2} (M_i / M_j)^{1/4})^2}{(8(1 + M_i / M_j))^{1/2}},$

where  $\lambda_{\text{CE},i}^+$  and  $\lambda_{\text{CE},j}^+$  are the pure component Chapman-Enskog values for the thermal conductivity (cf. Eq. (49)). In Eq. (58), which describes the mathematical form of the

generalized function  $\widehat{Y}_{\text{conf}}^+(\tilde{s}_{\text{conf}})$ , linear mixing rules are applied for the parameters, i.e.

$$\beta_{\text{mix}} = \sum_i^N x_i \beta_i \quad \text{with} \quad \beta_i \in \{\alpha_{0,i}^{(Y)}, \alpha_{\text{ln},i}^{(Y)}, \alpha_{1,i}^{(Y)}, \alpha_{2,i}^{(Y)}, \alpha_{3,i}^{(Y)}\} \quad (67)$$

$$\text{and} \quad \beta_{\text{mix}} \in \{\alpha_{0,\text{mix}}^{(Y)}, \alpha_{\text{ln},\text{mix}}^{(Y)}, \alpha_{1,\text{mix}}^{(Y)}, \alpha_{2,\text{mix}}^{(Y)}, \alpha_{3,\text{mix}}^{(Y)}\}.$$

Here,  $\beta_{\text{mix}}$  is the resulting parameter for the mixture,  $N$  is the number of components,  $x_i$  is the mole fraction of component  $i$ , and  $\beta_i$  indicates the component-specific parameters. The values for the universal parameters  $g_1^{(Y)}$  and  $g_2^{(Y)}$  (cf. Table 33) are the same for pure components and mixtures. Additional information on the entropy scaling framework for mixtures is given in Appendix F.

### 7.2.6 Remarks Regarding the Physical Basis of the Model Framework

The outlined entropy scaling framework is a physically-motivated model designed to be coupled with molecular-based EOS. The framework provides a basis for the modeling and prediction of transport properties in a wide range of thermodynamic states, different substance classes, and different EOS models (see applications below). Yet, the physical aspects of the entropy scaling model also comprise several assumptions and simplifications that influence the performance and are briefly critically summarized here. Moreover, while the entropy scaling framework is designed to be coupled with molecular-based EOS, it can in general be also used with empirical EOS. Yet, this route is not further exploited here.

In the zero-density limit, the Chapman-Enskog theory, which assumes spherical particles, is applied in the proposed model. By applying the model, it is assumed that the Chapman-Enskog theory, coupled with the corresponding states principle, also works for more complex molecules. This is a relatively crude assumption for highly non-ideal fluids, e.g. H-bonding fluids. Furthermore, the thermal conductivity of gases depends on internal degrees of freedom, which are not considered in the Chapman-Enskog theory [75]. Hence, also the model developed in this chapter does not consider the influence of the internal degrees of freedom on the thermal conductivity [75], which can cause problems with predictions for fluids at low densities. However, fitting the parameter  $\alpha_{0,i}^{(Y)}$  and not using the default value of 0 or 1 offers a pragmatic work-around that can alleviate some of these problems. More details are given in the applications section below and in Appendix F. In principle, the framework proposed in this chapter could be extended by adding a model for the intramolecular degrees of freedom.

Furthermore, the smoothness of the transition between the LD and the HD region

depends on the (presence of the) minimum of the function  $Y_{\text{CE}}^+(T)$ , which depends on the description of the second virial coefficient by the employed EOS. In cases where the second virial coefficient is not described well by a given EOS, a work-around can be used – see Appendix F.

Moreover, in this chapter, molecular-based EOS with a classical scaling behavior were used such that systematic errors in the critical region have to be expected (overestimation of the critical temperature). The latter could be overcome by using more sophisticated EOS models, e.g. based on renormalization group theory [589], which were, however, not applied in this work.

Furthermore, the entropy scaling model itself does not account for near-critical effects, i.e. the critical enhancement [235]. In principle, additional contributions in the entropy scaling approach could be used to account for this, but this was not considered here, so that the model should not be used without modifications in the near-critical region.

## 7.3 Applications

### 7.3.1 Overview

The new entropy scaling framework was applied in this chapter to pure substances and binary mixtures. To demonstrate the flexibility, different molecular-based EOS were used for the modeling. In total, 15 pure components, four binary mixtures, and a quaternary mixture were studied. Table 34 gives an overview of the studied pure components.

**Table 34:** Overview of the studied pure components: the columns indicate (from left to right) the substance name, the EOS used for the modeling, the references for the pure component model.  $N_{\text{exp}}$  is the number of experimental data points used for the parameter adjustment and model evaluation,  $N_{\text{par}}$  the number of entropy scaling parameters used.  $\overline{\delta Y}$  indicates the mean relative deviation (cf. Eq. (61)) for the viscosity  $\eta$ , the thermal conductivity  $\lambda$ , and the self-diffusion coefficient  $D$ .

Substance	EOS	Ref.	Viscosity			Thermal conductivity			Self-diffusion		
			$N_{\text{exp}}$	$N_{\text{par}}$	$\overline{\delta\eta}/\%$	$N_{\text{exp}}$	$N_{\text{par}}$	$\overline{\delta\lambda}/\%$	$N_{\text{exp}}$	$N_{\text{par}}$	$\overline{\delta D}/\%$
LJ	Kolafa-Nezbeda [136]	-	654	4	5.57	529	4	4.66	947	4	3.69
LJTS	PeTS [108]	-	348	4	4.54	348	4	3.91	348	2	5.22
methane	<i>Stephan et al.</i> [234]	[715]	2588	4	2.99	3082	5	5.84	318	4	5.53
<i>n</i> -butane	PC-SAFT [40]	[40]	973	4	4.36	2859	5	4.68	42	2	7.71
<i>n</i> -hexane	SAFT-VR Mie [41]	[41]	1487	4	3.36	1845	5	3.01	12	2	1.31
<i>n</i> -hexane <sup>a</sup>	SAFT-VR Mie [41]	[41]	867	4	3.18	-	-	-	-	-	-
<i>n</i> -hexadecane	PC-SAFT [40]	[40]	592	4	5.7	431	3	1.81	109	2	8.63
propene	soft SAFT [558]	[558]	244	4	5.61	172	5	12.59	-	-	-
cyclohexane	PACT+B [695]	[695]	895	4	4.59	294	3	2.37	15	2	3
benzene	SAFT-VR Mie [41]	[41]	1379	4	3.63	803	5	2.93	426	2	4.02
nitrogen	SAFT-VR Mie [41]	[702]	2826	5	1.49	2223	5	2.86	-	-	-
carbon dioxide	PC-SAFT [40, 703]	[703]	2911	4	2.82	1968	5	8.49	324	1	14.72
methanol	sCPA [43, 701]	[697]	1233	5	3.84	609	5	4.81	103	3	4.78
1-propanol	SAFT-VR Mie [41]	[41]	896	2	5.44	273	5	4.82	-	-	-
1-octanol	PC-SAFT [40, 557, 716]	[704]	341	4	3.59	197	5	3.8	19	2	19.95
R134a	BACKONE [694]	[694]	742	4	3.71	6478	5	5.79	-	-	-

<sup>a</sup>extrapolation study (details below)

Table 35 gives an overview of the studied mixtures. The results for the mixtures are

**Table 35:** Overview of the studied mixtures: the columns indicate (from left to right) the components, the EOS used for modeling, the Berthelot combination rule parameter  $\xi_{ij}$ ,  $N_{\text{exp}}$  is the number of experimental data points used for the evaluation,  $\overline{\delta Y}$  indicates the mean relative deviation (computed from Eq. (61)) for the viscosity  $\eta$  and the thermal conductivity  $\lambda$ . The size parameter  $\sigma$  was the same for both LJTS components, the pure component models for the other four (real) components were the same as in Table 34. No parameters were adjusted to the mixture data.

Components	EOS	$\xi_{ij}$	Viscosity		Thermal conductivity	
			$N_{\text{exp}}$	$\overline{\delta\eta}/\%$	$N_{\text{exp}}$	$\overline{\delta\lambda}/\%$
LJTS ( $\varepsilon_1$ ) + LJTS ( $\varepsilon_2 = 0.9 \varepsilon_1$ )	PeTS	1.2	55	4.71	55	5.42
LJTS ( $\varepsilon_1$ ) + LJTS ( $\varepsilon_2 = 0.9 \varepsilon_1$ )	PeTS	0.85	51	4.85	51	4.55
1-octanol + <i>n</i> -hexadecane	PC-SAFT	1	42	2.39	-	-
benzene + <i>n</i> -hexane	SAFT-VR Mie	1	-	-	19	3.47
<i>n</i> -decane + <i>n</i> -dodecane + <i>n</i> -tetradecane + <i>n</i> -hexadecane	PC-SAFT	1	18	1.97	-	-

predictions based on the pure component models (cf. Table 34) and the mixing rules (cf. Eqs. (63) - (67)), i.e. they were obtained without any adjustment to experimental mixture data of transport properties. Also for the EOS mixture models, fully predictive mixing and combination rules were used.

Nine different molecular-based EOS were used to model the different substances (cf. Tables 34 and 35). The choice of the EOS models was not optimized to create entropy scaling models with low deviations, but to show the general applicability and robustness of the framework. The individual choices were made so as to obtain examples that reflect realistic applications, e.g. the BACKONE EOS is often used for modeling refrigerants in the literature [717, 718]. It was out of the scope of this chapter to compare the performance of different EOS. The EOS pure component parameters were adopted from the literature (see Appendix F for details). The entropy scaling parameters (cf. Eq. (58)) were fitted to transport property data taken from the literature. The number of parameters for each model (cf. Table 34) was chosen so that no overfitting occurred for the function  $\widehat{Y}^+(\tilde{s}_{\text{conf}})$ . For the viscosity, four parameters were used in most cases. For the thermal conductivity, five parameters were used since also the value  $\alpha_{0,i}^{(\lambda)}$  had to be adjusted to get a good representation of the zero-density limit, for the reasons discussed in Section 7.2.6. Only for the spherical model fluids (LJ and LJTS), the parameter  $\alpha_{0,i}^{(\lambda)}$  was not fitted for the thermal conductivity due to the absence of internal degrees of freedom in this radial-symmetric model. For the self-diffusion coefficient, the data basis



is smaller for all substances. Except for the LJ fluid and methane, only one to three parameters were used in the entropy scaling model. All experimental data were used for adjusting the entropy scaling parameters, except in the case of *n*-hexane modeled by the SAFT-VR Mie EOS (cf. Table 34). To test the extrapolation capability of the model to states that were not considered in the fit, the model parameters for *n*-hexane were adjusted using state points  $p \leq 10$  MPa alone. The model performance was then evaluated using data at  $p > 10$  MPa, which includes state points up to  $p = 1000$  MPa. Both the pure component EOS parameters and the entropy scaling parameters used in this chapter are reported in Appendix F.

The experimental data for the real substances were taken from the Dortmund Database (DDB) [719] and from the database from *Suárez-Iglesias et al.* [329]. For the model fluids, i.e. the LJ and the Lennard-Jones truncated and shifted (LJTS) fluid, data were taken from Refs. [62, 114, 118, 153, 176, 184, 211, 225]. Data from different fluid regions were considered for the entropy scaling modeling, i.e. gaseous, liquid, and supercritical (and in some cases also metastable) states in a large temperature and pressure range. In total, 43,750 data points were considered for the 15 pure components and 291 data points for the five mixtures. Overall, the availability of data on the transport properties of mixtures is significantly lower than that for the pure components. In all cases, the data compiled from the literature was screened for gross outliers which were removed for the fit and model evaluation. Also, data in the direct vicinity of the critical point were omitted.

### 7.3.2 Pure Components

The mean relative deviation results for the pure components are given in Table 34. They are in a range from 1.49% to 19.95%. For the vast majority of the studied pure components, a mean relative deviation below 6% is obtained. This is impressive considering the fact that not more than five parameters were used for the fit that describes large data sets covering a wide range of conditions. Four typical examples are presented and discussed in detail in the main body of this paper, namely the viscosity of *n*-butane and *n*-hexane, the thermal conductivity of nitrogen, and the self-diffusion coefficient of benzene (cf. Table 34).

Fig. 61 shows the entropy scaling plot  $\widehat{Y}^+ = \widehat{Y}^+(\tilde{s}_{\text{conf}})$  for the viscosity of *n*-butane, the thermal conductivity of nitrogen, and the self-diffusion coefficient of benzene (the corresponding plot for the viscosity of *n*-hexane is shown at the end of this chapter). In all three plots, the CE-scaled transport properties are distinct monovariate functions of the reduced configurational entropy in the entire range of  $\tilde{s}_{\text{conf}}$ . The scattering of

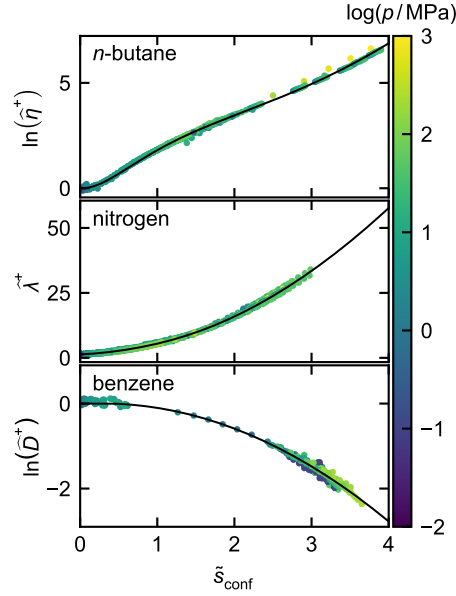


**Figure 61:** CE-scaled viscosity  $\widehat{\eta}^+$  of *n*-butane (top), CE-scaled thermal conductivity of nitrogen  $\widehat{\lambda}^+$  (middle), and CE-scaled self-diffusion coefficient  $\widehat{D}^+$  as function of the reduced configurational entropy  $\widehat{s}_{\text{conf}}$ . Symbols are the data points derived from experimental data ( $\eta$ ,  $\lambda$ , and  $D$  from experimental data and  $\widehat{s}_{\text{conf}}$  from the EOS). The EOS applied for the three substances are given in Table 34. The color indicates the pressure. The black line is the entropy scaling model.

the data points is very small for all properties and substances. In all cases, a smooth transition between the LD and the HD region is observed.

In the following, the results for the four selected systems are discussed in detail by means of Figs. 62 - 65. For each example, the results from the entropy scaling model are compared to the reference data for selected isotherms (plot a in Figs. 62 - 65). Additionally, a deviation plot is shown (plot b in Figs. 62 - 65), which comprises all considered experimental data. Furthermore, a parity plot (plot e in Figs. 62 - 65) is given together with histograms of the temperature and pressure distributions of the considered state points (plots c and d in Figs. 62 - 65).

Fig. 62 shows the results for the viscosity of *n*-butane. Four parameters (cf. Eq. (58)) were adjusted to 973 experimental data points. The experimental data were in the range  $0.0267 \text{ MPa} < p < 1000 \text{ MPa}$  and  $140 \text{ K} < T < 511 \text{ K}$ , which includes gaseous, liquid, as well as supercritical states. Most state points are in the temperature range from 300 to 500 K and pressure of 0.1 MPa to 100 MPa (cf. Fig. 62 c & d). The EOS was PC-SAFT. The viscosity of *n*-butane is described well by the model with a mean relative deviation of  $\overline{\delta\eta} = 4.36\%$ .

The supercritical isotherms cross each other in the vicinity of the critical point, which reflects the change of the temperature dependency. At low pressure, the viscosity in-

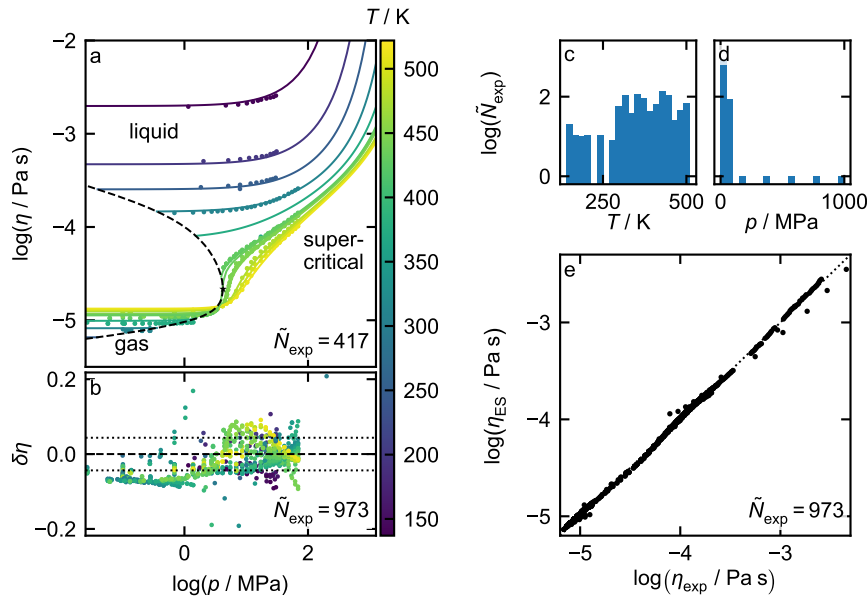


**Figure 62:** Results for the viscosity  $\eta$  of *n*-butane. a: Viscosity  $\eta$  as function of the pressure  $p$  for 12 isotherms obtained from the entropy scaling model (lines) and experimental data (colored symbols). The viscosity computed from entropy scaling for the saturated liquid and saturated vapor (dashed line), and the critical point (star) are also given. b: Relative deviation between entropy scaling results and experimental data  $\delta\eta$  (cf. Eq. (62)) as function of the pressure  $p$  (all considered data). The black dotted line indicates the mean average deviation  $\overline{\delta\eta} = \pm 4.36\%$ . a and b: The color indicates the temperature. c and d: Histograms of the number of experimental data points  $N_{\text{exp}}$  regarding their temperature (plot c) and pressure (plot d). e: Parity plot for the viscosity computed from the entropy scaling model  $\eta_{\text{ES}}$  vs. experimental data  $\eta_{\text{exp}}$  (all considered data). The entropy scaling results were obtained with the PC-SAFT EOS.  $\tilde{N}_{\text{exp}}$  indicates the number of data points depicted in a given plot.

creases with increasing temperature as predicted by the Chapman-Enskog theory; at high pressure at liquid-like states, the viscosity decreases with increasing temperature, which is as expected [75, 660].

Overall, the entropy scaling model yields an excellent description of the viscosity over the whole temperature and pressure range. Only for pressures  $p < 1$  MPa, the experimental values are slightly systematically overestimated by the entropy scaling model (cf. Fig. 62 b). This is due to an overestimation of the zero-density limit by the Chapman-Enskog theory in combination with the corresponding states principle.

Fig. 63 shows the results for the thermal conductivity of nitrogen modeled by the entropy scaling model in conjunction with the SAFT-VR Mie EOS. The 2223 state points comprise temperatures in the range  $77\text{K} < T < 2473\text{K}$  and pressures in the range  $0.009\text{MPa} < p < 1000\text{MPa}$  (cf. Fig. 63 c & d), which includes a large amount of su-

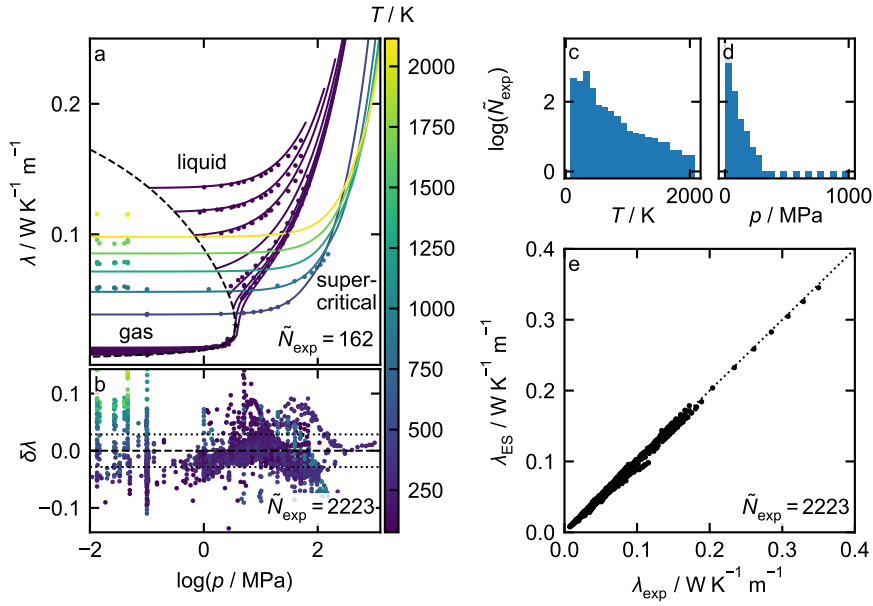


**Figure 63:** Results for the thermal conductivity  $\lambda$  of nitrogen. a: Thermal conductivity  $\lambda$  as function of the pressure  $p$  for 13 isotherms obtained from the entropy scaling model (lines) and experimental data (colored symbols). The thermal conductivity computed from entropy scaling for the saturated liquid and saturated vapor (dashed line), and the critical point (star) are also given. b: Relative deviation between entropy scaling results and experimental data  $\delta\lambda$  (cf. Eq. (62)) as function of the pressure  $p$  (all considered data). The black dotted line indicates the mean average deviation  $\overline{\delta\lambda} = \pm 2.86\%$ . a and b: The color indicates the temperature. c and d: Histograms of the number of experimental data points  $N_{\text{exp}}$  regarding their temperature (plot c) and pressure (plot d). e: Parity plot for the thermal conductivity computed from the entropy scaling model  $\lambda_{\text{ES}}$  vs. experimental data  $\lambda_{\text{exp}}$  (all considered data). The entropy scaling results were obtained with the SAFT-VR Mie EOS.  $\tilde{N}_{\text{exp}}$  indicates the number of data points depicted in a given plot.

percritical state points as well as some gas and few liquid state points. The structure of the  $\lambda - \log(p)$  diagram regarding the different state regions (cf. Fig. 63 a) is similar to that for the viscosity. The isotherms with low temperatures are shown up to the solidification pressure (data taken from *Grace et al.* [720]).

The mean relative deviation is  $\overline{\delta\lambda} = 2.86\%$ , which is impressive considering that only five parameters were fitted to a very large and diverse data set. Some larger deviations (up to  $\delta\lambda = 15\%$ ) are observed in the gas region at low pressure ( $\log(p/\text{MPa}) \leq -1$ ). These deviations slightly increase with increasing temperature. This is likely due to the fact that the Chapman-Enskog model does not consider internal degrees of freedom. On the other hand, state points at large pressures up to 1000 MPa and moderate temperatures are described very well (cf. Fig. 63 b), i.e. with  $\delta\lambda < 1.5\%$ . These state points can also be identified in the parity plot (cf. Fig. 63 e) as the ones with  $\lambda > 0.2 \text{ W K}^{-1} \text{ m}^{-1}$ , which

indicates the robustness of the macroscopic scaling used for dense states (cf. Eq. (56)).

Fig. 64 shows the results for the self-diffusion coefficient of benzene. Only two component-

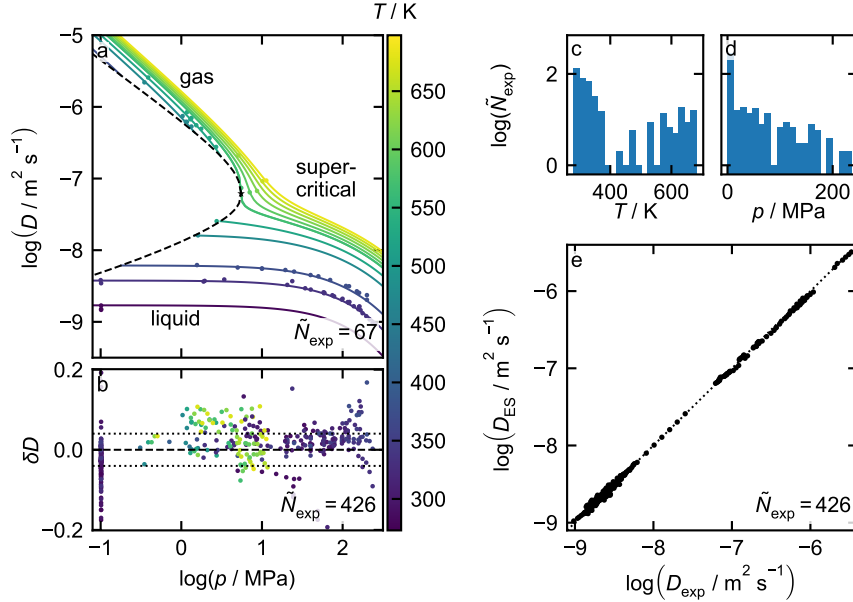


**Figure 64:** Results for the self-diffusion coefficient  $D$  of benzene. a: Self-diffusion coefficient  $D$  as function of the pressure  $p$  for 12 isotherms obtained from the entropy scaling model (lines) and experimental data (colored symbols). The self-diffusion coefficient computed from entropy scaling for the saturated liquid and saturated vapor (dashed line), and the critical point (star) are also given. b: Relative deviation between entropy scaling results and experimental data  $\delta D$  (cf. Eq. (62)) as function of the pressure  $p$  (all considered data). The black dotted line indicates the mean average deviation  $\overline{\delta D} = \pm 4.02\%$ . a and b: The color indicates the temperature. c and d: Histograms of the number of experimental data points  $N_{\text{exp}}$  regarding their temperature (plot c) and pressure (plot d). e: Parity plot for the self-diffusion coefficient computed from the entropy scaling model  $D_{\text{ES}}$  vs. experimental data  $D_{\text{exp}}$  (all considered data). The entropy scaling results were obtained with the SAFT-VR Mie EOS.  $\tilde{N}_{\text{exp}}$  indicates the number of data points depicted in a given plot.

specific parameters were used. The experimental data of the self-diffusion coefficient for benzene ( $N_{\text{exp}} = 426$ ) cover temperatures in the range  $279 \text{ K} < T < 684 \text{ K}$  and pressures in the range  $0.1 \text{ MPa} \leq p < 236 \text{ MPa}$ , which corresponds to liquid, gaseous, and super-critical states. The majority of the data points is at temperatures below  $373.15 \text{ K}$  and ambient pressure, i.e. liquid states. The parity plot (cf. Fig. 64 e) reveals two groups of points, for liquid-like states ( $D < 10^{-8} \text{ m}^2\text{s}^{-1}$ ) and for gas-like states ( $D \geq 10^{-7} \text{ m}^2\text{s}^{-1}$ ). This distribution of the state points makes benzene an interesting candidate for testing the entropy scaling framework. The self-diffusion coefficient exhibits a qualitatively different behavior  $D = D(p, T)$  compared to the viscosity and thermal conductivity. For

all fluid states,  $D$  increases with increasing temperature and decreases with increasing pressure.

The self-diffusion coefficient of benzene is described with a mean average deviation of  $\overline{\delta D} = 4.02\%$ . This is impressive considering the fact that only two adjustable parameters were used. The description of the different state regions is overall similar. Hence, no region shows particularly high deviations, which indicates that the splitting approach between the low-density and high-density states in the entropy scaling framework works well. This is supported by the fact that also the gaseous state points at high temperatures  $T > 550$  K are well described by the model.

Fig. 65 shows the results for the viscosity of  $n$ -hexane. Here, a different fitting strategy

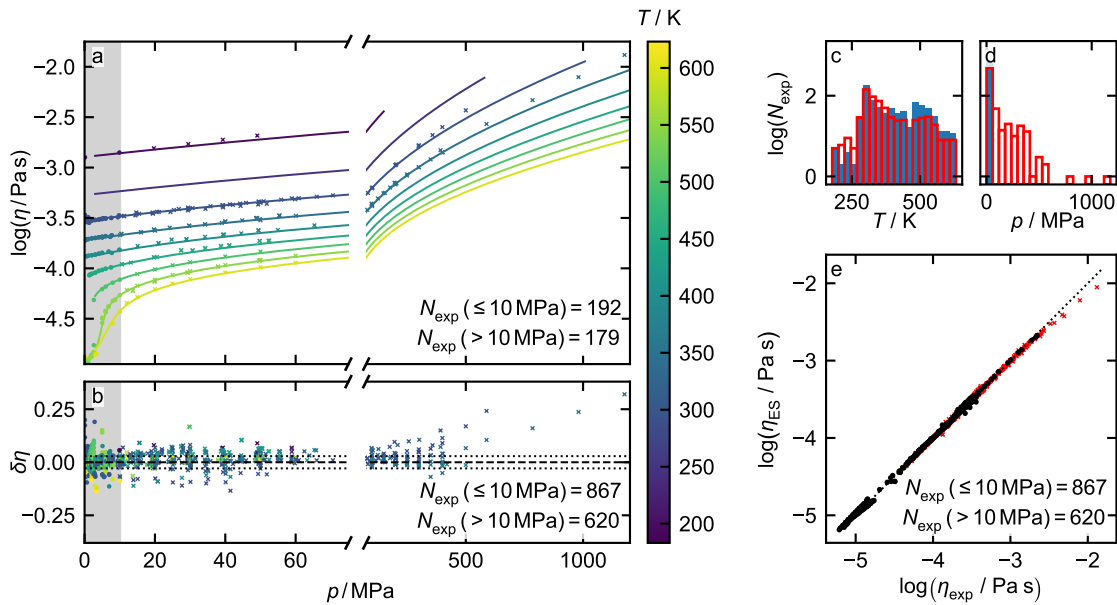


**Figure 65:** Results for the viscosity  $\eta$  of  $n$ -hexane. a: Viscosity  $\eta$  as function of the pressure  $p$  for 9 isotherms computed from the entropy scaling model (lines) and experimental data (symbols). b: Relative deviation between entropy scaling model and experimental data  $\delta\eta$  as function of the pressure  $p$  (all available experimental data). The black dotted line indicates the mean average deviation  $\overline{\delta\eta} = \pm 3.18\%$ . a and b: The circles denote the data points at  $p \leq 10$  MPa (grey area, used for fitting) and the crosses the data points at  $p > 10$  MPa. The color indicates the temperature. c and d: Histograms of the number of experimental data points  $N_{\text{exp}}$  (blue: used for fit ( $p \leq 10$  MPa), red: data points at  $p > 10$  MPa) regarding their temperature (plot c) and pressure (plot d). e: Parity plot for the viscosity computed by the entropy scaling model  $\eta_{\text{ES}}$  vs. experimental data  $\eta_{\text{exp}}$  (black circles: state points used for fit ( $p \leq 10$  MPa), red crosses: data points at  $p > 10$  MPa). The entropy scaling results were obtained with the SAFT-VR Mie EOS.  $\tilde{N}_{\text{exp}}$  indicates the number of data points depicted in a given plot.

was used in order to test the extrapolation behavior of the entropy scaling framework:

the experimental data were divided into two sets based on the pressure, state points at  $p \leq 10$  MPa were used for fitting the component-specific parameters of the entropy scaling model; state points at  $p > 10$  MPa were used for the assessment of the predictions of the entropy scaling model. Accordingly, 867 experimental state points were used for the parametrization and 620 state points were used for the evaluation of the predictions (cf. Table 34). For *n*-hexane, all considered experimental data points for the assessment of the entropy scaling model are at supercritical pressure (up to 1000 MPa), but sub- and supercritical isotherms are shown, cf. Fig. 65 (the critical temperature and pressure are  $T_c = 507.6$  K and  $p_c = 3.02$  MPa [721], respectively). Four component-specific parameters were used in the fit. The entropy scaling model describes the data used for the fit ( $p < 10$  MPa) very well with a mean relative deviation of  $\overline{\delta\eta} = 3.18\%$ . Upon using the entropy scaling model for extrapolation ( $p > 10$  MPa), a mean relative deviation of  $\overline{\delta\eta} = 2.88\%$  is obtained. The vast majority of predicted data points yields a deviation well below 10 %. For the data points at  $p > 500$  MPa (where also experiments are challenging to carry out), a larger deviation up to 38 % is obtained. Yet, the trends are qualitatively captured well at these extreme pressures. Hence, the entropy scaling model is capable of making reliable predictions for the viscosity across two orders of magnitude in the pressure. Also the temperature dependency is very well described by the model.

The main reasons for the robust extrapolation behavior of the framework lie in the robust extrapolation behavior of the molecular-based EOS and the basic principle of the entropy scaling concept – correlating transport coefficients that are in general a function of two state variables, e.g.  $T$  and  $p$ , by only the configurational entropy  $s_{\text{conf}}$  (which is a function of  $T$  and  $p$  in the example). This leads to situations, where an extrapolation in the  $T, p$  space is an interpolation in the  $\tilde{s}_{\text{conf}}$  space. This is illustrated in Fig. 66 for the *n*-hexane case discussed above. It shows the CE-scaled viscosity  $\widehat{\eta}^+$  as function of the reduced configurational entropy  $\tilde{s}_{\text{conf}}$ . For all considered experimental data points, the configurational entropy was computed (cf. Eq. (43)) from the EOS. The data points considered for the entropy scaling model fit ( $p < 10$  MPa) lie in the range  $0 < \tilde{s}_{\text{conf}} < 5$  (cf. Fig. 66 a). For the vast majority of the data points at  $p > 10$  MPa, the reduced configurational entropy  $\tilde{s}_{\text{conf}}$  is also in the range  $0 < \tilde{s}_{\text{conf}} < 5$  (cf. Fig. 66 b). Hence, the vast majority of data points predicted by the model at high pressure  $p > 10$  MPa are actually interpolated by the kernel of the model, i.e. in the entropy space. Only few state points are in fact extrapolations in the  $\tilde{s}_{\text{conf}}$  space, which are the state points with large viscosities at extremely high pressure (cf. Fig. 65). This principle could be favorably used in the design of experiment for determining most useful data for the parametrization of entropy scaling models.

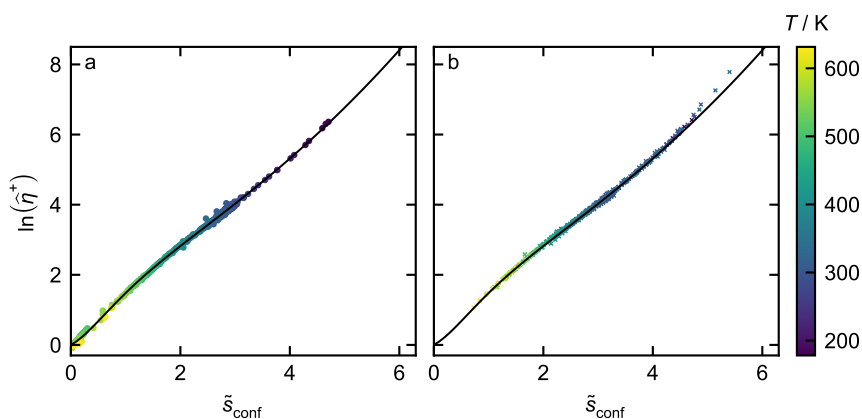


**Figure 66:** CE-scaled viscosity  $\hat{\eta}^+$  as function of the reduced configurational entropy  $\tilde{s}_{\text{conf}}$  for *n*-hexane. Symbols are data points derived from experimental data ( $\eta$  from experimental data and  $\tilde{s}_{\text{conf}}$  from the SAFT-VR Mie EOS). The color indicates the temperature. The black line is the entropy scaling model. a: Data points at  $p \leq 10$  MPa (used for fit). b: Data points at  $p > 10$  MPa (testing extrapolation behavior). Both  $\hat{\eta}^+$  and  $\tilde{s}_{\text{conf}}$  are dimensionless properties.

### 7.3.3 Mixtures

The entropy scaling framework was also used for predicting transport properties of mixtures based on the pure component models discussed above. Five mixtures were studied (cf. Table 35). The results for three mixtures are presented and discussed in the main part of this work; the results for the other two mixtures are presented in Appendix F. For all studied mixtures, no parameters were fitted to the experimental data of the mixtures, i.e. the mixture results are pure predictions.

Fig. 67 shows the results for the viscosity and the thermal conductivity of an LJTS model mixture with  $\sigma_2 = \sigma_1$ ,  $M_1 = M_2$ ,  $\varepsilon_2 = 0.9\varepsilon_1$ , and  $\xi = 1.2$  [62]. The PeTS EOS [108] was used for modeling the LJTS mixtures. Results are shown for a wide temperature range and the entire composition range. The mixture exhibits a high-boiling azeotropic phase behavior for all studied temperatures [62]. All studied data points for the LJTS mixture are liquid phase state points. The predictions from the entropy scaling model are in excellent agreement with the reference data, which is astonishing considering the fact that the mixture is highly non-ideal. For all studied temperatures, both the viscosity and the thermal conductivity exhibit a maximum at  $x_2 \approx 0.4 \text{ mol mol}^{-1}$ , which corresponds approximately to the azeotropic composition [62]. For the vast majority of data points, the entropy scaling predictions agree with the computer experiment results within their uncertainties. The mean relative deviations of the entropy scaling model are  $\overline{\delta\eta} = 4.71\%$  and  $\overline{\delta\lambda} = 5.42\%$ . These deviations are even slightly below the mean relative deviations obtained for the pure LJTS component (cf. Table 34) which



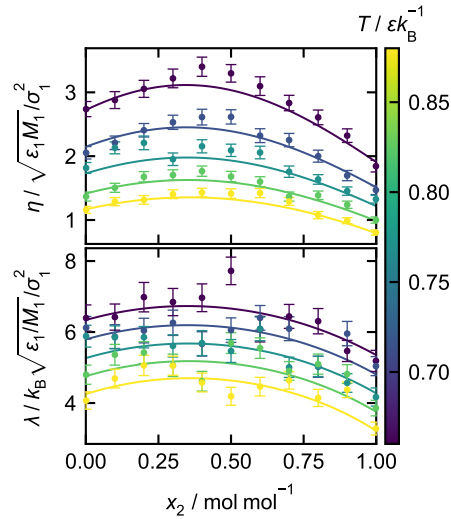


**Figure 67:** Viscosity  $\eta$  (top) and thermal conductivity  $\lambda$  (bottom) of the LJTS mixture with  $\sigma_2 = \sigma_1$ ,  $\varepsilon_2 = 0.9\varepsilon_1$ , and  $\xi = 1.2$  [62] as function of the mole fraction  $x_2$ . Molecular simulation data (symbols) from Ref. [62] and predictions with entropy scaling (lines). The color indicates the temperature. The pressure is  $p = 0.1 \varepsilon/\sigma^3$ . The entropy scaling results were obtained with the PeTS EOS.

emphasizes the predictive capabilities of the entropy scaling framework for modeling mixtures. The success of the predictions justifies the use of the simple linear mixing rules for the component-parameters of the fit function (cf. Eq. (58)) and emphasizes that the deviations from ideality are a result of the modeling of the entropy of the mixture by the EOS. The results for another LJTS mixture with same  $\sigma$  and  $\varepsilon$  values, but a mixing parameter  $\xi = 0.85$  (cf. Table 35), a mixture with a low-boiling azeotrope, are reported in Appendix F. Also for this LJTS mixture, the performance of the entropy scaling framework is excellent.

Fig. 68 shows the results for the viscosity of the mixture 1-octanol + *n*-hexadecane. Predictions from the entropy scaling model are compared with experimental data for three different temperatures from 298.15 K to 308.15 K at ambient pressure in the entire composition range. All considered state points are liquid. The predictions of the entropy scaling model are in excellent agreement with the experimental data. For mole fractions  $x_{C_{16}H_{32}} \gtrsim 0.8 \text{ mol mol}^{-1}$ , the experimental viscosity data exhibit a plateau for all temperatures. The entropy scaling model predicts a faint minimum in that region. It is astonishing that such details of the behavior are predicted by a model that was not trained to mixture data. Both the temperature and composition dependency of the viscosity are predicted well by the entropy scaling model. This is also reflected by the mean relative deviation of  $\overline{\delta\eta} = 2.39\%$ .

Fig. 69 shows the results for the quaternary mixture *n*-decane + *n*-dodecane + *n*-tetradecane + *n*-hexadecane. The predictions from entropy scaling are compared with

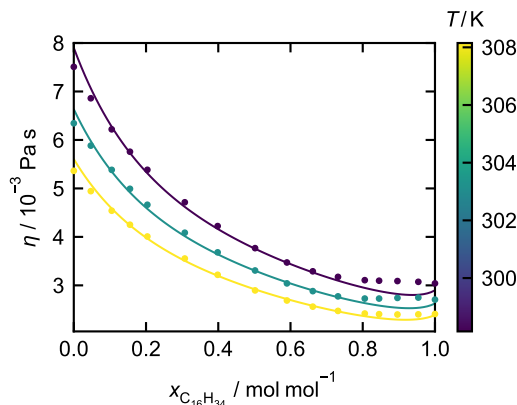


**Figure 68:** Viscosity  $\eta$  of the mixture 1-octanol +  $n$ -hexadecane as function of the mole fraction of  $n$ -hexadecane  $x_{C_{16}H_{34}}$  at ambient pressure  $p = 0.1$  MPa. Experimental data [722] (symbols) and entropy scaling (lines). The color indicates the temperature. The entropy scaling results were obtained with the PC-SAFT EOS.

experimental data for three different temperatures (313.15 K, 333.15 K, and 353.15 K) as a function of the pressure. All considered state points are liquid. The entropy scaling model provides a very good description of the experimental data over the whole temperature and pressure range. Thus, the mean relative deviation is  $\overline{\delta\eta} = 1.97\%$ .

## 7.4 Conclusions

An entropy scaling framework was developed for modeling transport properties of pure fluids and mixtures. The entropy scaling framework proposed in this chapter combines multiple physical theories and concepts such as the Chapman-Enskog theory, the *Rosenfeld* scaling theory, a LJ model at the kernel, the corresponding states principle, and molecular-based EOS. The aim of entropy scaling is to obtain a master curve that relates a suitably scaled transport property to the configurational entropy of the studied fluid. In the entropy scaling framework proposed in this chapter, the *Rosenfeld* scaling is used for describing high-density states and the Chapman-Enskog theory for low-density states. The two approaches are connected in a convenient way using the lowest number obtained for the scaled zero-density limit from the Chapman-Enskog theory. This leads to a smooth transition between the scaled Chapman-Enskog data at low densities and the *Rosenfeld*-scaled data at high densities, which can be described easily as a function of the configurational entropy. The kernel of the entropy scaling framework comprises a LJ model such that the LJ critical parameters and the LJ collision integrals were adapted. A generalized mathematical form for this master curve was proposed that contains both component-specific parameters as well as universal parameters. The latter were fitted in this work to transport data for the LJ fluid. The number of component-specific pa-

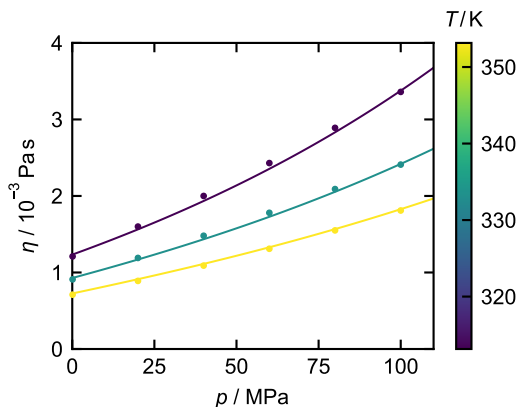


**Figure 69:** Viscosity  $\eta$  of the mixture *n*-decane + *n*-dodecane + *n*-tetradecane + *n*-hexadecane as function of the pressure  $p$  with constant mole fractions  $x_{\text{C}_{10}\text{H}_{22}} = 0.31 \text{ mol mol}^{-1}$ ,  $x_{\text{C}_{12}\text{H}_{26}} = 0.26 \text{ mol mol}^{-1}$ ,  $x_{\text{C}_{14}\text{H}_{30}} = 0.23 \text{ mol mol}^{-1}$  and  $x_{\text{C}_{16}\text{H}_{34}} = 0.20 \text{ mol mol}^{-1}$ . Experimental data [723] (symbols) and entropy scaling (lines). The color indicates the temperature. The entropy scaling results were obtained with the PC-SAFT EOS.

rameters can be varied, depending on the amount of available data. The mathematical form contains five component-specific parameters, but usually only some of these have to be adjusted to obtain good correlations of the available transport data of a given fluid. By applying simple mixing rules to these parameters, also transport properties of mixtures can be predicted from the pure component models. The applicability and good performance of this framework has been demonstrated in this chapter for several pure fluids and also for some mixtures.

Entropy scaling requires a suitable model for calculating the entropy, which is usually accomplished by an EOS. The entropy scaling framework proposed in this chapter is designed to be coupled with molecular-based EOS, which provide in many cases robust extrapolation capabilities to conditions not used in the model development. The EOS are integrated in the entropy scaling framework model in a consistent way by adapting the second virial coefficients, the critical point parameters, molecular property parameters, and the configurational entropy from the EOS. Based on that coupling, the entropy scaling framework can be flexibly used in conjunction with practically any molecular-based EOS (and in general also with empirical EOS). This was demonstrated by applying several molecular-based EOS, without, however, aiming at a systematic comparison of their performance.

The big advantage of combining entropy scaling with molecular-based EOS is that, based only on a few data points, transport properties can be predicted for a wide range of states. What may be a bold extrapolation in terms of the transport data in variables of temperature and pressure may turn out to be a simple interpolation in the scaled transport data as a function of the configurational entropy.

Due to the strong physical basis of the framework, transport properties can be described in a large range of states with very few adjustable parameters. Even two parameters can provide a good description of transport property data in a wide state range. The entropy scaling framework was shown to yield excellent predictions also for states that were not considered for the parametrization, i.e. for metastable states, extreme pressure and temperature as well as for mixtures.

# 8 Entropy Scaling for Modeling Diffusion Coefficients in Mixtures

## 8.1 Introduction

Diffusion in mixtures is important in many natural and technical processes. And, numbers for diffusion coefficients are needed in many applications, e.g. for the design of fluid separation processes and reactors or for modeling combustion processes. However, experimental data on diffusion coefficients are notoriously scarce, so that reliable models for their prediction are needed. A new model type is introduced that is based on entropy scaling and enables predictions that were previously infeasible.

In diffusion, two phenomena are distinguished: Self-diffusion (a.k.a. tracer diffusion) and mutual (transport) diffusion. Self-diffusion and the corresponding self-diffusion coefficient  $D_i$  of a component  $i$  describes the Brownian movement of individual particles and is defined for pure components and mixtures. In contrast, mutual diffusion is only defined in mixtures and describes the motion of particle collectives of the different components that results in macroscopic mass transfer. Obviously, self-diffusion and mutual diffusion are closely related, but there exist no generally applicable equations that relate self-diffusion coefficients and mutual diffusion coefficients. The different diffusion coefficients are schematically depicted in Fig. 70 for a binary mixture.

For describing mutual diffusion [724], there are two common frameworks: Those of *Fick* and Maxwell-Stefan. The corresponding diffusion coefficients are the Fickian diffusion coefficients  $D_{ij}$  (related to the concentration gradient as driving force) and the Maxwell-Stefan diffusion coefficients  $\mathcal{D}_{ij}$  (related to the chemical potential gradient as driving force). The two frameworks are thermodynamically consistent representations and can be transformed into each other. For a binary mixture, these diffusion coefficients are related by

$$D_{ij} = \mathcal{D}_{ij}\Gamma_{ij}, \quad (68)$$

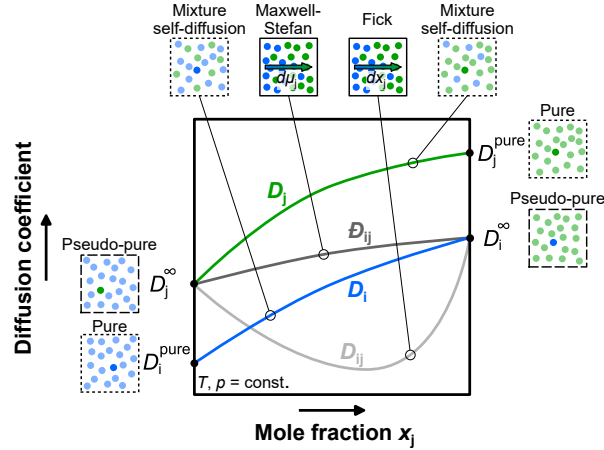


**Figure 70:** Schematic representation of the diffusion coefficients in a binary mixture as a function of the mole fraction. Lines indicate the self-diffusion coefficient of component  $i$   $D_i$  (blue) and component  $j$   $D_j$  (green), the Maxwell-Stefan diffusion coefficient  $\mathcal{D}_{ij}$  (dark grey), and the Fickian diffusion coefficient  $D_{ij}$  (light grey). The limiting cases  $D_i^{\text{pure}}$ ,  $D_j^{\text{pure}}$  (both pure cases) and  $D_i^{\infty}$ ,  $D_j^{\infty}$  (both pseudo-pure cases) are also depicted.

where  $\Gamma_{ij}$  is the thermodynamic factor, which is defined by

$$\Gamma_{ij} = \frac{x_i x_j}{RT} \frac{\partial^2 G}{\partial x_i^2}, \quad (69)$$

where  $x_i$  and  $x_j$  are the mole fractions of components  $i$  and  $j$ , respectively,  $R$  is the universal gas constant, and  $G$  is the Gibbs energy of the mixture.

Evidently, the two coefficients  $D_{ij}$  and  $\mathcal{D}_{ij}$  become equal if the thermodynamic factor is unity, which is the case in the infinite dilution limit (and for ideal mixtures). Furthermore, self-diffusion coefficient and the mutual diffusion coefficients are related in the infinite dilution limit (cf. Fig. 70). Thus, the following relations apply for the infinite dilution limit:

$$x_i \rightarrow 0: \quad \mathcal{D}_{ij} = D_{ij} = D_i = D_i^{\infty} \quad (70)$$

$$x_j \rightarrow 0: \quad \mathcal{D}_{ij} = D_{ij} = D_j = D_j^{\infty} \quad (71)$$

where  $D_i^{\infty}$  is the diffusion coefficient of component  $i$  infinitely diluted in component  $j$ ,  $D_j^{\infty}$  the diffusion coefficient of component  $j$  infinitely diluted in component  $i$ . Modeling the different diffusion coefficients in a mixture in a consistent way is a challenging task. In this work, a new methodology that provides such a framework is proposed.

Physical models for predicting mixture diffusion coefficients at gaseous states are known and established for a long time within kinetic gas theory [9] - see Appendix G for details. The prediction of mixture diffusion coefficients at states where significant intermolecular

interactions prevail, on the other hand, is still an unresolved problem. Einstein has proposed a method for estimating infinite dilution diffusion coefficients in liquids [342], for which several modifications exist today [9, 675, 725]. For estimating the concentration dependence of mutual diffusion coefficients in mixtures, several empirical models have been proposed, e.g. the Vignes model and the generalized Darken model [13, 726, 727]. However, these models often fail for strongly non-ideal mixtures (see Appendix G).

In recent years, entropy scaling has received significant attention for modeling transport properties [24, 669, 728]. It is based on the discovery of Rosenfeld [25, 26], that dynamic properties (i.e. viscosity, thermal conductivity, and self-diffusion coefficient) of pure components, when properly scaled by the density and temperature, are a monovariate function of the configurational entropy  $s_{\text{conf}}$ . This scaling behavior is physically based and related to isomorph theory [24, 688] (however, it is not yet fully understood). For describing the entropy with respect to the desired state point (e.g. given by  $T, p$ ), usually an equation of state (EOS) is used. Entropy scaling can be favorably combined with molecular-based EOS [22], which enables predictions beyond the available data [52, 74]. Entropy scaling is well established for predicting the viscosity and thermal conductivity of mixtures [664, 672]. The corresponding models are based on combination and mixing rules and often enable a reliable prediction of mixture viscosities and thermal conductivities. However, entropy scaling for mixture diffusion coefficients – as depicted in Fig. 70 – has not yet been developed. So far, only the pure component limiting cases for the self-diffusion coefficients  $D_1^{\text{pure}}$  and  $D_2^{\text{pure}}$  (cf. Fig. 70) can be described by entropy scaling models from the literature [52, 128, 130, 671, 679]. Molecular dynamics simulation results indicate that also mixture diffusion coefficients might be subject to a scaling with respect to the entropy [62, 686, 728]. However, no modeling framework for describing mixture diffusion coefficients has been developed yet.

In this work, an entropy scaling model for predicting mixture diffusion coefficients, namely the self-diffusion coefficients as well as the (Fickian and MS) mutual diffusion coefficients, without any adjustable mixture parameters is proposed. The physical framework developed here for predicting diffusion coefficients in mixtures is unique and can be characterized as follows: (1) It can be applied in the entire fluid region, i.e. it covers gases, liquids, and supercritical fluids, phase equilibria, and even metastable states. (2) It describes both self-diffusion and mutual diffusion in a consistent way. (3) It comprises the dependence of the diffusion coefficients on temperature, pressure and composition in the entire fluid region. The applicability of the model is demonstrated for binary mixtures in this work.

The approach developed in this work is based on three central ideas and concepts: (1) Infinite dilution diffusion coefficients are treated as pseudo-pure components that exhibit a monovariate scaling behavior, which can be treated by classical entropy scaling [52]. (2)

Therefore, the mixture diffusion coefficient limiting cases, i.e. the pure component and pseudo-pure component self-diffusion coefficients (cf. Fig. 70), are modeled as functions of the entropy. This requires at least one reference data point for each limiting case. (3) Based on the information of the limiting cases, the concentration dependence of the diffusion coefficients  $D_i$ ,  $D_j$ ,  $D_{ij}$ , and  $D_{ij}$  are predicted using combination and mixing rules. It is demonstrated that these predictions can succeed without any adjustable mixture parameter. The performance of the new approach is demonstrated using model fluids as well as real substance systems. In this work, molecular-based EOS models are used. Yet, also other EOS types such as multiparameter [545] or cubic EOS [43] could be used.

## 8.2 Methods

The framework proposed in this work consists of two new elements: (1) Treating the infinite dilution self-diffusion coefficient as a pseudo pure component to obtain a monovariate scaling; (2) The application of mixing and combination rules for predicting the different diffusion coefficients in a mixture.

### 8.2.1 Entropy Scaling of Infinite Dilution Diffusion Coefficients

The infinite dilution diffusion coefficient  $D_i^\infty(T, p)$  is treated as a pseudo-pure component property such that the corresponding scaled property  $\widehat{D}_i^{\infty, \circ}(s_{\text{conf}})$  exhibits a monovariate function with respect to the configurational entropy  $s_{\text{conf}}$ . For testing this postulate, the ES model for pure component diffusion coefficients from Ref. 52 is adopted here. Thereby, the infinite dilution self-diffusion coefficient is transformed using a modified Rosenfeld scaling (marked by  $\circ$ ) as

$$D_i^{\infty, \circ} = D_i^\infty \frac{\rho_{\text{N}}^{1/3}}{\sqrt{RT/M_{\text{CE}}}} \left( \frac{-s_{\text{conf}}}{R} \right)^{2/3}, \quad (72)$$

where  $\rho_{\text{N}}$  is the number density of the solvent at given  $T$  and  $p$ . The reference mass  $M_{\text{CE}}$  is adopted from the Chapman-Enskog (CE) theory as

$$M_{\text{CE}} = \frac{2}{1/M_i + 1/M_j}, \quad (73)$$

where  $M_i$  and  $M_j$  are the molar masses of the pure components. For the zero-density limit, the scaled Chapman-Enskog infinite dilution diffusion coefficient  $D_{\text{CE}, i}^{\infty, \circ}$  is computed using a Lennard-Jones kernel (see Appendix G for details). Therefore, the



Lennard-Jones cross-interaction size and energy parameters  $\sigma_{ij}$  and  $\varepsilon_{ij}$  are calculated by the Lorentz-Berthelot combining rules here [700, 729]. Finally, the CE-scaled infinite dilution diffusion coefficient  $\widehat{D}_i^{\infty,\circ}$  is described by a split between the low-density (LD) and the high-density (HD) region as

$$\widehat{D}_i^{\infty,\circ} = \underbrace{\frac{D_i^{\infty,\circ}}{D_{\text{CE},i}^{\infty,\circ}}}_{\text{LD}} W(\tilde{s}_{\text{conf}}) + \underbrace{\frac{D_i^{\infty,\circ}}{\min(D_{\text{CE},i}^{\infty,\circ})}}_{\text{HD}} (1 - W(\tilde{s}_{\text{conf}})), \quad (74)$$

where  $\tilde{s}_{\text{conf}} = -s_{\text{conf}}/(Rm)$  is the reduced configurational entropy using the segment parameter  $m$  of molecular-based EOS and  $W$  is a smoothed step function. The CE-scaled infinite dilution diffusion coefficient  $\widehat{D}_i^{\infty,\circ}(\tilde{s}_{\text{conf}})$  is then described by a function with up to five adjustable parameters  $\alpha_k$  (see Appendix G). In this work, one or two system-dependent parameters were used for the real substance systems. A detailed description of the entropy scaling framework for infinite dilution diffusion coefficients is given in Appendix G. To test and validate this new scaling approach for infinite dilution diffusion coefficients, two model systems and a real substance system (all strongly non-ideal systems) were studied in this work using molecular dynamics simulations using the molecular simulation engine ms2 [464]. Simulations were conducted in all fluid regions, i.e. liquid, gaseous, supercritical, and metastable states (details are given in Appendix G).

### 8.2.2 Predicting Diffusion Coefficients in Mixtures

For predicting the diffusion coefficients  $D_i(x_j)$ ,  $D_j(x_j)$ ,  $\mathcal{D}_{ij}(x_j)$ , and  $D_{ij}(x_j)$  in a mixture, the entropy scaling framework is extended using combining and mixing rules. It is briefly outlined how this is done here; details are given in Appendix G. Diffusion coefficients in mixtures are predicted based on the limiting case models for the self-diffusion coefficient of pure components and the (infinite dilution) pseudo-pure component. The scaled diffusion coefficient  $\widehat{\Lambda}^\circ \in \{\widehat{D}_i^\circ, \widehat{D}_j^\circ, \widehat{\mathcal{D}}_{ij}^\circ\}$  is computed using the configurational entropy of the mixture  $s_{\text{conf}}^{\text{mix}} = s_{\text{conf}}^{\text{mix}}(T, \rho, \underline{x})$  and a mixture model for the scaled function  $\widehat{\Lambda}^\circ = \widehat{\Lambda}^\circ(s_{\text{conf}}^{\text{mix}}, \alpha_{k,\text{mix}})$ , which is computed from the limiting case scaling functions. The final (unscaled) diffusion coefficient  $\Lambda \in \{D_i, D_j, \mathcal{D}_{ij}\}$  is calculated as

$$\Lambda = \frac{\widehat{\Lambda}^\circ}{\frac{W(\tilde{s}_{\text{conf}}^{\text{mix}})}{\Lambda_{\text{CE}}^\circ} + \frac{1-W(\tilde{s}_{\text{conf}}^{\text{mix}})}{\min(\Lambda_{\text{CE}}^\circ)}} \cdot \frac{\sqrt{RT/M_{\text{ref}}}}{\rho_{\text{N}}^{1/3}} \left( \frac{-s_{\text{conf}}^{\text{mix}}}{R} \right)^{-2/3}, \quad (75)$$

where  $\Lambda_{\text{CE}}^\circ$  is the Chapman-Enskog property of the mixture,  $\rho_{\text{N}}$  is the number density of the mixture, and  $M_{\text{ref}}$  is the reference mass of the mixture. The Fickian diffusion coefficient is obtained from the Maxwell-Stefan diffusion coefficient by the ther-

modynamic factor as predicted by the EOS (see Eq. (68)). Details on the calculation of the Chapman-Enskog property of the mixture  $\Lambda_{\text{CE}}^\circ$ , the reference mass  $M_{\text{ref}}$ , and  $\widehat{\Lambda}^\circ = \widehat{\Lambda}^\circ(s_{\text{conf}}^{\text{mix}}, \alpha_{k,\text{mix}})$  are given in Appendix G. All required quantities are obtained using predictive combination rules and mixing rules and the EOS mixture model. No adjustable mixture parameters are introduced. The non-ideality of the mixture is primarily taken into account by the underlying EOS via the predicted mixture entropy. The combination of the EOS and entropy scaling enables the consistent calculation of the diffusion coefficients ( $D_i$ ,  $D_j$ ,  $D_{ij}$ ,  $D_{ij}$ ), homogeneous bulk properties ( $pvT$ ,  $s_{\text{conf}}$ ,  $\Gamma_{ij}$ , etc.), and phase equilibria (e.g. vapor-liquid and liquid-liquid equilibria).

## 8.3 Results

First, the applicability of a monovariate scaling to the infinite dilution self-diffusion coefficients by treating  $D_i^\infty$  as a pseudo-pure component is demonstrated. This enables the prediction of  $D_i^\infty$  to practically all fluid states based on very little data. Then, results for the prediction of the different mixture diffusion coefficients for selected examples are presented.

### 8.3.1 Infinite Dilution Diffusion Coefficients

Fig. 71a demonstrates the monovariate scaling behavior (cf. Eqs. (72) - (74)) for infinite dilution diffusion coefficients  $\widehat{D}_2^{\infty,\circ}$  for a binary Lennard-Jones mixture. This is impressive considering the fact that a large range of states was studied, cf. Fig. 71a-inset. The quality of the scaling of  $\widehat{D}_2^{\infty,\circ}$  (i.e. how well the data can be described by a monovariate function) is essentially the same as that found for the pure component diffusion coefficient  $D_2$ . This supports the picture introduced in this work that  $D_2^\infty$  can be considered as a pseudo-pure component property. This picture is physically meaningful considering the fact that in both cases, the mobility of a single particle in a homogeneous environment is described. The Chapman-Enskog diffusion coefficient agrees well with the low-density simulation results – as indicated by the convergence of  $\widehat{D}_2^{\infty,\circ} \rightarrow 1$  for  $s_{\text{conf}}/R \rightarrow 0$ . In Appendix G, the results for a second binary Lennard-Jones system that support the findings discussed here. For the two Lennard-Jones model systems, the "global" parameters from Ref. 52 were sufficient for describing  $\widehat{D}_2^{\infty,\circ}$ . This finding was not expected and demonstrates the broad applicability of the universal parameters  $g_1$  and  $g_2$  in the correlation, that were determined in Ref. 52.

From the models for the pure component self-diffusion coefficient  $\widehat{D}_2^{\text{pure}}(\tilde{s}_{\text{conf}})$  [52] and the infinite dilution diffusion coefficient  $\widehat{D}_2^\infty(\tilde{s}_{\text{conf}})$ , both  $D_2^{\text{pure}}$  and  $D_2^\infty$  can be predicted

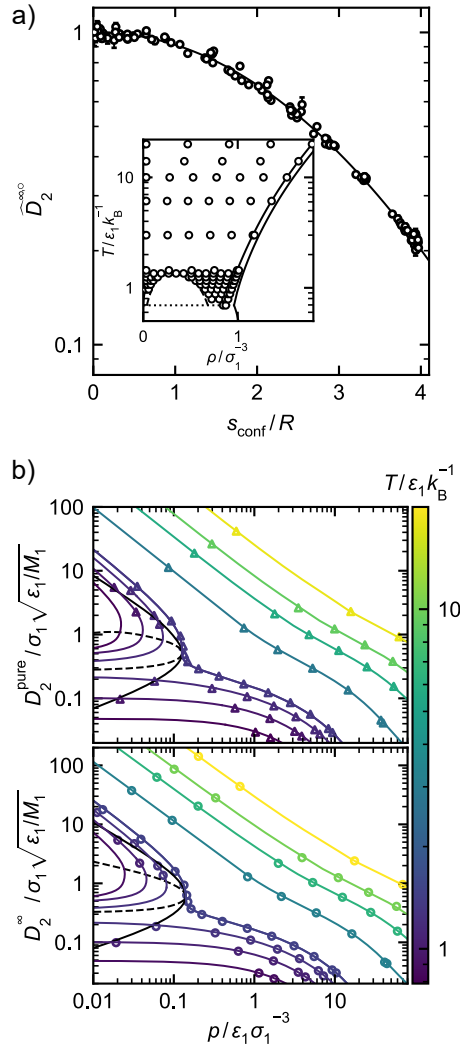


**Figure 71:** Entropy scaling of diffusion coefficients in a Lennard-Jones mixture with  $\sigma_2 = \sigma_1$ ,  $\varepsilon_2 = 0.9\varepsilon_1$ , and  $\varepsilon_{12} = 1.2\sqrt{\varepsilon_1\varepsilon_2}$ . a) Scaled infinite dilution diffusion coefficient of component 2  $\widehat{D}_2^{\infty,0}$  as a function the reduced configurational entropy  $s_{\text{conf}}/R$ . The line indicates the entropy scaling model. Symbols are MD simulation data from this work. The inset shows the simulation state points in the temperature-density phase diagram of component 1. Therein, solid lines indicate the phase envelopes from Refs. 73, 238. b) Self-diffusion coefficient of component 2  $D_2$  (top) and infinite dilution diffusion coefficient of component 2  $D_2^{\infty}$  (bottom) as function of the pressure. Lines are the entropy scaling model and symbols are simulation results from Ref. 52 ( $D_2^{\text{pure}}$ ) and from this work ( $D_2^{\infty}$ ). The black solid lines indicates the vapor-liquid equilibrium and the black dashed line the corresponding spinodal. Colors indicate the temperature.

in a wide range of states. For the Lennard-Jones mixture, the configurational entropy was taken from the Kolafa-Nezbeda EOS [136]. Fig. 71b shows the results of the entropy scaling models for  $D_2$  and  $D_2^{\infty}$  in comparison to the MD results. The agreement between both methods is excellent, which is a result of the good performance of the EOS as well

as of the fact that both properties show a monovariate relation with respect to the entropy.

Besides the Lennard-Jones models systems, also the scaling behavior of two real substance mixtures was investigated based on simulation data and experimental data. Fig. 72 shows the simulation results for the real substance system benzene + isobutane. The simulation state points cover the gas, liquid, and the supercritical region. The scaled infinite dilution diffusion coefficient of benzene  $\widehat{D}_1^{\infty, \circ}$  shows a monovariate

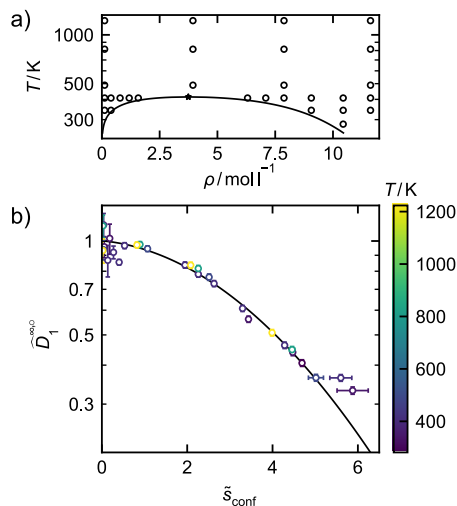


**Figure 72:** Scaling behavior of the infinite dilution diffusion coefficient of benzene in the system benzene (1) + isobutane (2). a) Simulation state points (symbols) in the temperature-density phase diagram of the solvent isobutane. The line indicates the vapor-liquid equilibrium and the star the critical point as calculated from the PC-SAFT EOS [40]. b) Scaled diffusion coefficient of benzene infinitely diluted in isobutane  $\widehat{D}_1^{\infty, \circ}$  as a function of the configurational entropy  $\tilde{s}_{\text{conf}}$ . The symbols are the simulation results (color indicates the temperature) and the line the entropy scaling model (fitted to the simulation results).

behavior with respect to the reduced configurational entropy  $\tilde{s}_{\text{conf}}$  – similar to the results for the Lennard-Jones systems (see Fig. 77).

Experimental infinite dilution self-diffusion coefficient data in a large range of states (as considered for the model systems) are unfortunately not available. For the system toluene + *n*-hexane, experimental data of infinite dilution diffusion coefficients at different pressures and temperatures are available, but only for the liquid phase. Fig. 73 shows the scaled infinite dilution diffusion coefficients of the system toluene (1) + *n*-hexane (2) as function of the reduced configurational entropy, i.e.  $\widehat{D}_1^{\infty, \circ}(\tilde{s}_{\text{conf}})$  and  $\widehat{D}_2^{\infty, \circ}(\tilde{s}_{\text{conf}})$ . Additionally, the system-specific entropy scaling models are shown for both cases. For each case, two system-specific parameters were adjusted (see Tab. G.2 in Appendix G). The scaled experimental data lie on a single curve, i.e. show a monovariate behavior

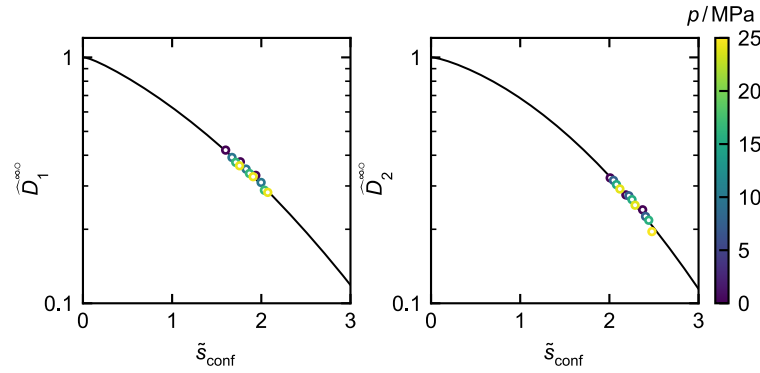


**Figure 73:** Scaling behavior of the infinite dilution diffusion coefficients in the system toluene (1) + *n*-hexane (2) as function of the reduced configurational entropy  $\tilde{s}_{\text{conf}}$ . Left: Scaled diffusion coefficient of toluene infinitely diluted in *n*-hexane  $\widehat{D}_1^{\infty}$ . Right: Scaled diffusion coefficient of *n*-hexane infinitely diluted in toluene  $\widehat{D}_2^{\infty}$ . The line indicates the system-specific entropy scaling model (parameters given in Tab. G.2). The color indicates the pressure.

with respect to  $\tilde{s}_{\text{conf}}$ . The results for both real systems based on simulation data and experimental data confirm the validity of the entropy scaling methodology introduced in this work for real substance systems.

Hence, reliable analytical models for the limiting cases  $D_1$ ,  $D_2$ ,  $D_1^{\infty}$ , and  $D_2^{\infty}$  (cf. Fig. 70) are now available that can be applied in all fluid regions. They are the basis for the next step, the prediction of  $D_1$ ,  $D_2$ ,  $D_{12}$ , and  $D_{12}$  at arbitrary compositions in the mixture.

### 8.3.2 Application to Mixtures of OMEs with Alkanes

Blends of poly(oxyethylene) dimethyl ethers (OME) and hydrogenated vegetable oils (HVO) are interesting new synthetic fuels that can be produced from renewable resources [730–733]. OME are oligomers with the chemical structure  $\text{CH}_3\text{O}(\text{CH}_2\text{O})_n\text{CH}_3$  with  $n \geq 2$ . For synthetic fuels, OME with chain lengths  $n = 3 - 5$  are often used [734]. These oligomers have suitable physical properties to replace fossil diesel, but produce much less soot upon combustion because they contain oxygen in their backbone [735–737]. HVO consist predominantly of *n*-alkanes, with C-numbers between 15 and 20 [737]. For the modeling of production processes and combustion applications, information and models for the transport properties of OME and HVO and their mixtures are required. They are needed, e.g., for calculating the Lewis number  $Le$ , which is the ratio of the heat conductivity and the diffusion coefficient, which must be known to decide whether explosions of droplets in fuel sprays may occur [657, 738].

In this section, the entropy scaling method for modeling infinite dilution diffusion coefficients was applied to the self-diffusion data in binary mixtures of  $\text{OME}_n$  and alkanes,

which were determined from data obtained by PFG-NMR spectroscopy at temperatures between 298.15 and 353.15 K at ambient pressure [134]. The entropy scaling model as well as the experimental results were compared to the models of *Evans et al.* [725] (SEGWE) and *Wilke and Chang* [739] (WC). Details on the SEGWE and WC models are given in Appendix G. The extrapolations over a wide range of conditions enabled by the entropy scaling model is demonstrated.

The entropy scaling model was combined with the PC-SAFT [40] equation of state (EOS). The EOS parameters to model all pure components were taken from the literature, for the alkanes from *Gross and Sadowski* [40] and for the OME<sub>*n*</sub> from *Schappals et al.* [740]. The self-diffusion coefficients of the pure components were scaled as described above. The global and component-specific parameters are given in Appendix G.

Fig. 74 shows the entropy scaling results in comparison with the experimental data. Good agreement is observed. This is not astonishing as two parameters were fitted

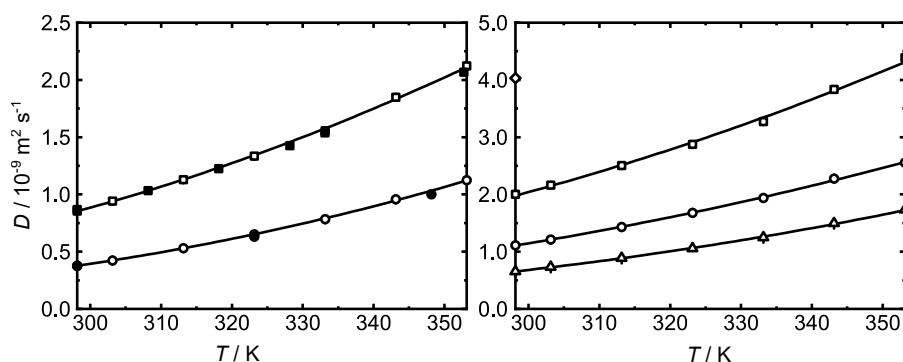


**Figure 74:** Pure component self-diffusion coefficients as a function of temperature. Left: *n*-dodecane (squares) and *n*-hexadecane (C16) (circles). Right: OME<sub>1</sub> (diamond), OME<sub>2</sub> (squares), OME<sub>3</sub> (circle), and OME<sub>4</sub> (triangle). Open symbols are experimental results from Ref. [134] obtained with PFG-NMR spectroscopy and filled symbols are literature data [741–743]. Solid lines are results from entropy scaling. Error bars are within symbol size.

to the data for each studied component, and the data were measured only in a quite narrow temperature range at ambient pressure. Furthermore, as only the temperature was varied, the entropy scaling brings no immediate advantages for correlating the data set. The advantage of entropy scaling is that, based on the limited amount of data that is provided here, self-diffusion coefficients can be predicted for a much wider range of conditions (temperatures and pressures) for all studied components. Such extrapolation yield good results, as has been demonstrated in extensive studies with model fluids [62].

Fig. 75 shows the results for the infinite dilution diffusion coefficients in binary mixtures of OME<sub>*n*</sub> + *n*-dodecane (C12) and OME<sub>*n*</sub> + *n*-hexadecane (C16) at different temperatures. As expected, the diffusion coefficients of OME<sub>*n*</sub> in *n*-dodecane are higher than in *n*-hexadecane, and the diffusion coefficients of *n*-dodecane in a given OME<sub>*n*</sub> are higher

than those of  $n$ -hexadecane in the same  $\text{OME}_n$ , and the diffusion coefficients increase with increasing temperature. The correlation of the data for the infinite dilution diffusion coefficients with entropy scaling was successful for all studied systems. For each pair solute + solvent, two parameters were fitted to the data so that the success of the correlation is not astonishing, but it should be kept in mind that the method enables extrapolations beyond the range that was studied here. The predictions with the SEGWE and the WC model yield only poor results. No clear ranking of the models is possible; sometimes SEGWE is better and sometimes WC.

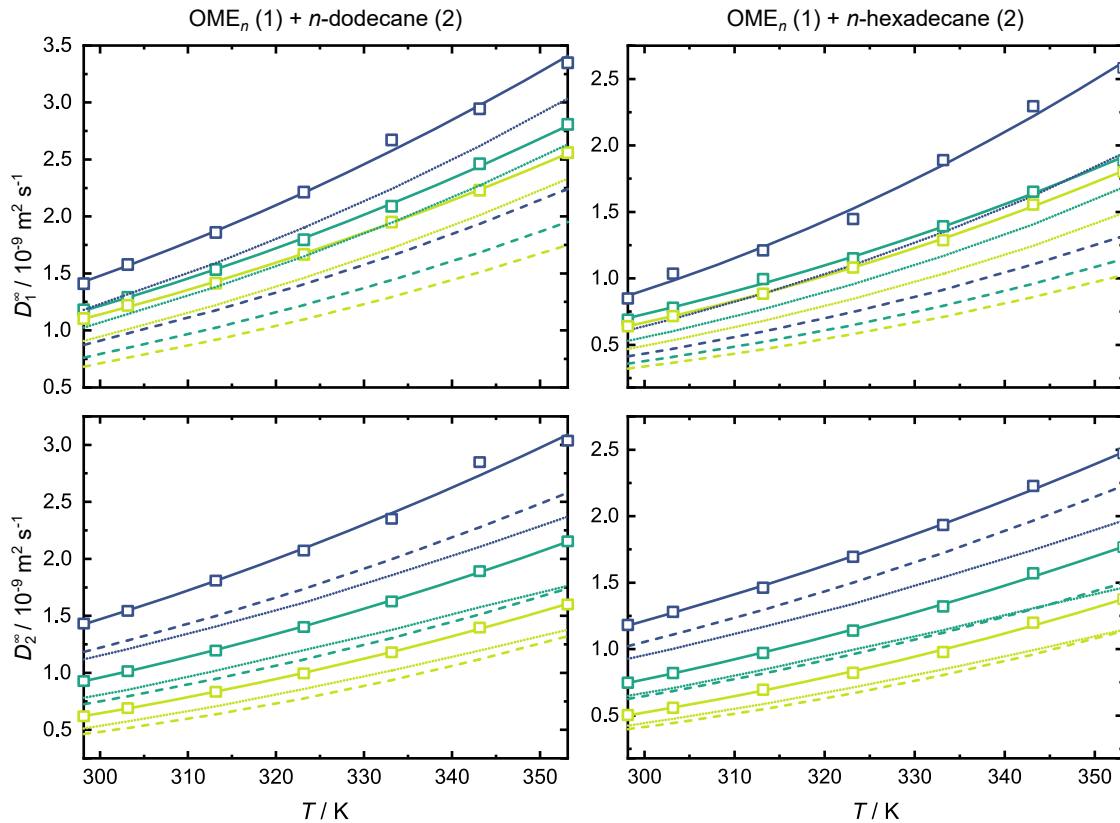


**Figure 75:** Infinite dilution diffusion coefficients in binary mixtures of  $\text{OME}_n$  (1) +  $n$ -dodecane (2) (left) and  $\text{OME}_n(1)$  +  $n$ -hexadecane (2) (right) as a function of temperature. Symbols: Experimental results from Ref. [134] obtained with PFG-NMR spectroscopy. Lines: Entropy scaling model (solid) and predictions with SEGWE (dashed) and WC (dotted). The colors indicate the  $\text{OME}_n$  ( $\text{OME}_2$ : dark blue,  $\text{OME}_3$ : green,  $\text{OME}_4$ : yellow).

An example for the application of the entropy scaling model based on the new data on infinite dilution diffusion coefficients from Ref. [134] is presented in Fig. 76, where the mutual diffusion coefficients in the system  $\text{OME}_2$  +  $n$ -dodecane (C12) are shown for a wide range of temperatures using the Vignes equation. Therein, the numbers of the infinite dilution diffusion coefficients outside the temperature range that was studied by experiments here were obtained from the entropy scaling model. The interpolation by

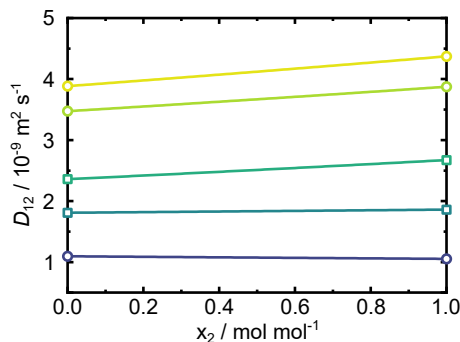


**Figure 76:** Diffusion coefficients of OME<sub>2</sub> + *n*-dodecane (C12) as a function of composition and temperature from NMR data, entropy scaling, and Vignes. Symbols: NMR data from Ref. [134] (squares) and entropy scaling data (circles). Solid lines: Vignes correlation.

the Vignes equation is almost linear in all cases. The results should be interpreted as predictions of the binary Maxwell-Stefan diffusion coefficient. For calculating Fickian diffusion coefficients, the thermodynamic factor should be considered.

### 8.3.3 Prediction of Diffusion Coefficients in Mixtures by Entropy Scaling

The model proposed in this work (see Section 8.2.2) is able to predict all diffusion coefficients in a mixture, which is demonstrated here for binary systems. Fig. 77 shows the model predictions for all four diffusion coefficients ( $D_1$ ,  $D_2$ ,  $D_{12}$ ,  $D_{12}$ ) of two Lennard-Jones mixture for the entire composition range and different temperatures. For comparison, simulation data from Ref. [112] are used. The predictions from the entropy scaling framework and the computer experiment results agree well for all four diffusion coefficients and both studied mixtures (see Fig. 77).

For the first Lennard-Jones mixture with strong cross interactions (cf. Fig. 77 left), the self-diffusion coefficient simulation data, for which the statistical uncertainty is smaller than for the mutual diffusion coefficients, are described mostly within their uncertainty, despite the strong non-ideality that leads to extrema at about  $x_2 \approx 0.4 \text{ mol mol}^{-1}$ . The simulation data for  $D_{12}$  scatter more and have larger error bars than those for  $D_1$  and  $D_2$ . The entropy scaling framework predicts the  $D_{12}$  simulation data very well in the entire composition range. In particular, the strongly non-ideal behavior is captured accurately by the entropy scaling framework in contrast to established empirical models such as the Vignes or Darken model that fail here (see Appendix G). Also the temperature and pressure dependency of the diffusion coefficients are very well described by the model (cf. Fig. 77 and Appendix G, respectively). For the predictions of the Fickian diffusion coefficient, the trends are correctly predicted by the entropy scaling predictions, but



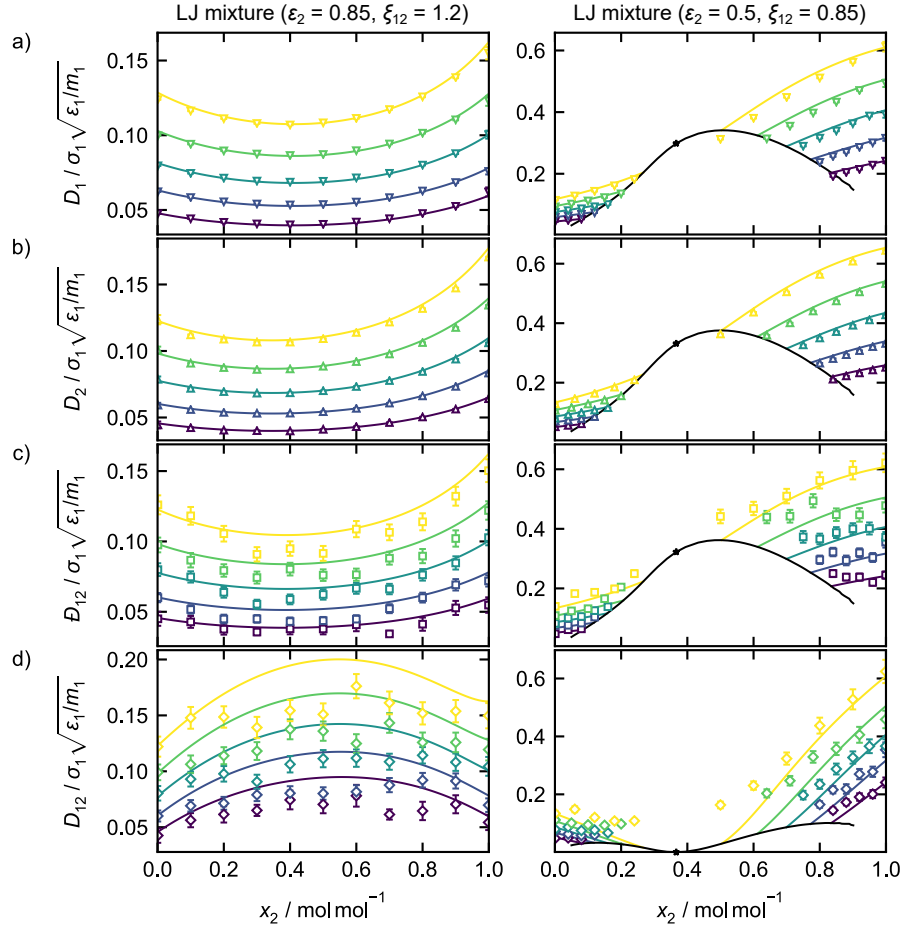


**Figure 77:** Diffusion coefficients in two binary Lennard-Jones mixture with  $\sigma_2 = \sigma_1$ ,  $\varepsilon_2 = 0.9\varepsilon_1$ , and  $\xi_{12} = 1.2$  (left) and  $\sigma_2 = \sigma_1$ ,  $\varepsilon_2 = 0.5\varepsilon_1$ , and  $\xi_{12} = 0.85$  (right) as a function of the mole fraction  $x_2$  at  $p = 0.13\sigma_1^3\varepsilon_1^{-1}$  (left) and  $p = 0.26\sigma_1^3\varepsilon_1^{-1}$  (left). a) Self-diffusion coefficient of component 1  $D_1$ ; b) Self-diffusion coefficient of component 2  $D_2$ ; c) Maxwell-Stefan diffusion coefficient  $D_{12}$ ; d) Fickian diffusion coefficient  $D_{12}$ . Lines are predictions from the entropy scaling framework. Symbols are simulation results from Ref. 112. The entropy scaling framework was used in combination with the Kolafa-Nezbeda EOS [136]. The colors indicate the temperature  $T \in \{0.79, 0.855, 0.92, 0.985, 1.05\} k_B\varepsilon_1^{-1}$  (from blue to yellow). The black lines indicate the vapor-liquid equilibrium and the star the critical point.

deviations are observed, cf. Fig. 77d. The deviations between simulation results and entropy scaling are larger for the Fickian diffusion coefficient, which can be attributed to the inclusion of the thermodynamic factor adding additional complexity to the model predictions (and the MD sampling [62]). In contrast to the other three diffusion coefficients ( $D_1$ ,  $D_2$ ,  $D_{12}$ ), the Fickian diffusion coefficient  $D_{12}$  exhibits a maximum at about  $x_2 \approx 0.55 \text{ mol mol}^{-1}$ , which is in line with values of  $\Gamma_{12} \gg 1$  obtained in this system. Due to the coupling of entropy scaling and EOS, the model is inherently consistent and can be applied over a wide range of states.

The right part of Fig. 77 shows the results from the entropy scaling diffusion coefficient model for the second Lennard-Jones mixture with weak cross interaction, i.e.  $\xi_{12} = 0.85$ , resulting in a liquid-liquid miscibility gap at the considered conditions. The entropy scaling model proposed in this work is able to predict not only the different diffusion coefficients in the bulk phases, but also describes the diffusion coefficients of the coexisting phases of the liquid-liquid equilibrium. The results from entropy scaling are again compared to simulation results from Ref. 112 (cf. Fig. 77 left). For the two self-diffusion coefficients  $D_1$  and  $D_2$ , the agreement between entropy scaling predictions and the simulation data is excellent. The self-diffusion coefficients increase with increasing mole fraction  $x_2$  in both liquid phases. The Maxwell-Stefan diffusion coefficient shows a similar characteristic and is reasonably well described by the entropy scaling model. The Fickian diffusion coefficient has a different qualitative behavior compared to the Maxwell-Stefan diffusion coefficient – due to the non-ideality of the system comprised in the thermodynamic factor. Also the Fickian diffusion coefficient of the liquid-liquid phase equilibrium envelope shows a qualitatively different course compared to the corresponding Maxwell-Stefan coefficient. At the upper critical solution point, the thermodynamic factor becomes zero and so does the Fickian diffusion coefficient ( $x_2 \approx 0.38 \text{ mol mol}^{-1}$ ). This is as expected for the Fickian diffusion coefficient at a critical point [83]. For both mutual diffusion coefficients, the agreement of the entropy scaling model with the simulation data is reasonable considering the fact that the model is fully predictive and the fact that the system is strongly non-ideal. In Ref. 83, it was shown that the Kolafa-Nezbeda EOS exhibits some deviations already for phase equilibria predictions in such strongly non-ideal mixtures.

Fig. 78 shows the results for the diffusion coefficients in two real substance systems: A mixture of alkanes, *n*-hexane ( $\text{C}_6\text{H}_{14}$ ) + *n*-dodecane ( $\text{C}_{12}\text{H}_{26}$ ), and the mixture toluene ( $\text{C}_7\text{H}_8$ ) + *n*-hexane ( $\text{C}_6\text{H}_{14}$ ). For both systems, only little experimental data are available (which is common for practically all real mixtures), which is used for the validation of the predictions. The thermodynamic properties of the systems were modeled by the PC-SAFT EOS [40] and the component-specific models for the pure substances were taken from the literature (see Appendix G for details).

Fig. 78a shows the entropy scaling predictions in comparison to the experimental reference data for both self-diffusion coefficients of the system *n*-hexane + *n*-dodecane at two temperatures. Both components strongly differ in their molar mass. Both self-diffusion coefficients decrease with increasing mole fraction  $x_2$  in a non-linear way, which is predicted well by the framework. The entropy scaling predictions of both self-diffusion coefficients and the experimental data are in excellent agreement.

Fig. 78b shows the results for the Fickian diffusion coefficient in the system toluene + *n*-hexane  $D_{12}$  at four temperatures from 293.15 K to 308.15 K as a function of the mole

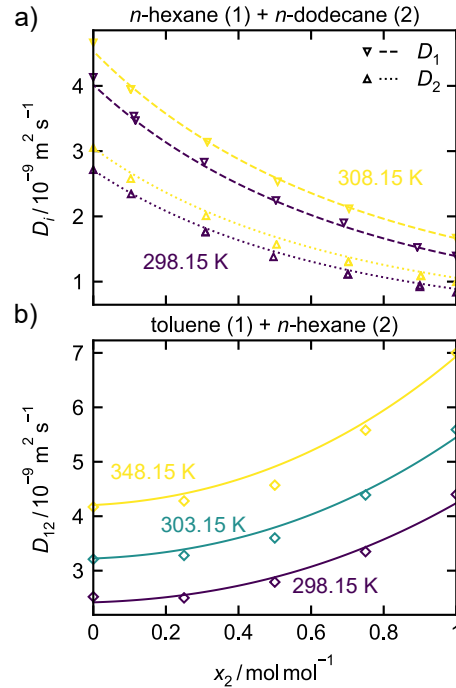


**Figure 78:** Diffusion coefficients of real substance mixtures predicted by entropy scaling. Symbols are experimental data and lines are predictions from the entropy scaling framework. a) Self-diffusion coefficients  $D_1$  in the mixture *n*-hexane (1) + *n*-dodecane (2) as a function of the mole fraction of *n*-dodecane  $x_2$  at  $p = 0.1$  MPa. Experimental data are from Ref. 744. b) Fickian diffusion coefficient  $D_{12}$  in the mixture toluene (1) + *n*-hexane (2) as a function of the mole fraction of *n*-hexane  $x_2$  at  $p = 0.1$  MPa. Experimental data are from Ref. 745.

fraction at ambient pressure. The Fickian diffusion coefficient increases with increasing temperature. Again, the entropy scaling predictions are in excellent agreement with the experimental data.

Fig. 79 shows the predictions for the Maxwell-Stefan diffusion coefficient phase diagrams of the system toluene + *n*-hexane at two pressures:  $p = 0.1$  MPa (top) and  $p = 4$  MPa (bottom). The diffusion coefficients of the coexisting phases can be obtained in a straightforward manner by the framework. At  $p = 0.1$  MPa, both components are subcritical (see inset in Fig. 79 top). The Maxwell-Stefan diffusion coefficient is shown for three isotherms (340 K, 360 K, 385 K). As shown in the inset (see Fig. 79 top), one isotherm is entirely in the liquid phase (340 K), one isotherm passes through the vapor-liquid equilibrium (360 K), and one isotherm is entirely in the gas phase (385 K). The Maxwell-Stefan diffusion coefficient in the gas phase is significantly larger than that in the liquid phase. In the liquid phase, the diffusion coefficient strongly depends on the composition. In the gas phase, the Maxwell-Stefan diffusion coefficient exhibits only a minor dependency on the composition. This is in line with the Chapman-Enskog theory [9] – which is inherently incorporated in the framework. At  $p = 4$  MPa (cf. Fig.

79 bottom), *n*-hexane is supercritical and a critical point exists at about  $T = 547.18\text{ K}$  (see inset). Four isotherms are plotted: One subcritical isotherm ( $T = 540\text{ K}$ ), the critical isotherm ( $T = 547.18\text{ K}$ ), one isotherm passing through the vapor-liquid equilibrium ( $T = 570\text{ K}$ ), and one isotherm entirely in the gas/supercritical phase ( $T = 590\text{ K}$ ). The isotherm at  $T = 540\text{ K}$  exhibits a transition between the two pseudo-pure component limiting cases – from a liquid state at  $x_2 = 0$  to a supercritical state at  $x_2 = 1\text{ mol mol}^{-1}$ . At the critical point, the diffusion coefficient exhibits a large gradient with respect to the composition. Due to the thermodynamic consistency established by the EOS, the framework correctly predicts the Fickian diffusion coefficient to be zero at critical points (see Fig. 77).

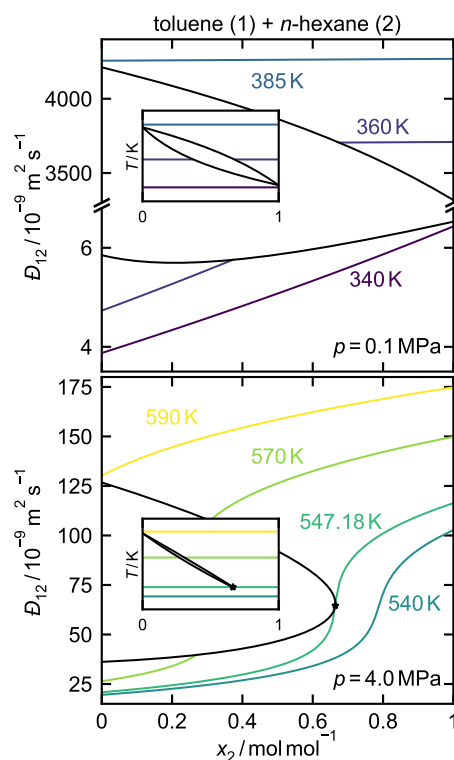


**Figure 79:** Maxwell-Stefan diffusion coefficient  $D_{12}$  in the mixture toluene (1) + *n*-hexane (2) as a function of the mole fraction of *n*-hexane  $x_2$  at  $p = 0.1\text{ MPa}$  (top) and  $p = 4\text{ MPa}$  (bottom). Black lines: Vapor-liquid equilibrium; colored lines: Isotherms. Insets show the  $T-x$  vapor liquid-equilibrium phase diagram at the respective pressure.

Also diffusion coefficients of metastable and unstable states as well as at spinodal states can be described by the framework (which is for example relevant for nucleation). Fig. 80 demonstrates the application of the entropy scaling model to Maxwell-Stefan diffusion coefficients at metastable and unstable states in the mixture toluene (1) + *n*-hexane (2). Therefore, three lines with constant partial densities of *n*-hexane  $\rho_2 = 0.25, 0.75, \text{ or } 1.25\text{ mol l}^{-1}$  were calculated by varying the partial density of toluene in the range  $0\text{ mol l}^{-1} \leq \rho_1 \leq 5.6\text{ mol l}^{-1}$  at a temperature  $T = 560\text{ K}$ , where *n*-hexane is

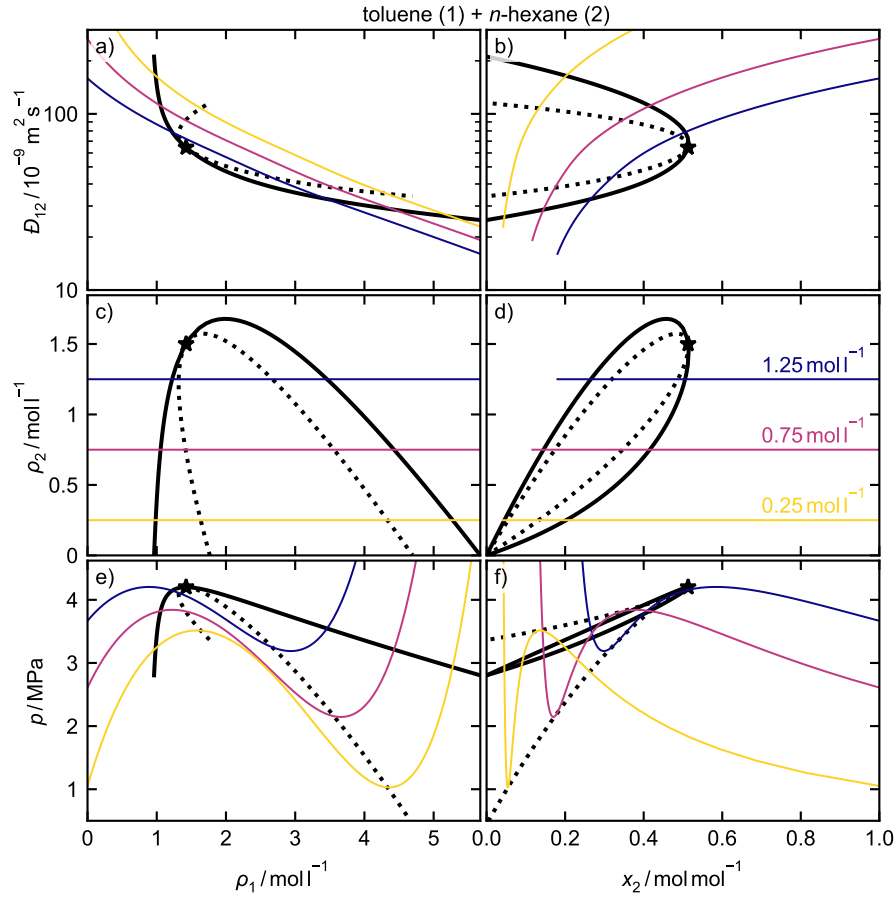


**Figure 80:** Predictions of the VLE properties and the Maxwell-Stefan diffusion coefficient from the entropy scaling + EOS model in the two-phase vapor-liquid equilibrium region of the binary mixture toluene (1) + *n*-hexane (2). Maxwell-Stefan diffusion coefficient  $\bar{D}_{12}$  (top), partial density of *n*-hexane  $\rho_2$  (middle), and pressure  $p$  (bottom) as a function of the partial density of toluene  $\rho_1$  (a, c, and e) and of the mole fraction  $x_2$  (b, d, and f) at  $T = 560$  K. The black solid lines correspond to the vapor-liquid binodal, the dotted line to the vapor-liquid spinodal, and the black star indicates the critical point. The three colored lines are lines with constant partial density of *n*-hexane  $\rho_2$ .

supercritical. This procedure is computationally convenient for calculating metastable and unstable states as the applied PC-SAFT EOS is formulated in the Helmholtz energy  $a$  with its fundamental variables  $T$ ,  $\rho$ , and  $x$ . All three partial isochores cross the vapor-liquid equilibrium. The corresponding pressures undergo a van-der-Waals-like loop with minima and maxima at the spinodals (see Fig. 80). Evidently, the application of the entropy scaling model in metastable states requires an EOS model that shows a physically reasonable behavior in that region, i.e. a single van der Waals loop, which is the case here. Here, only predictions of the Maxwell-Stefan diffusion coefficient are shown. The Maxwell-Stefan diffusion coefficient smoothly transitions from the liquid phase to the gas phase through the vapor-liquid equilibrium including the metastable and unstable

regions. While there is no diffusion coefficient reference data available for validation, these predictions seem physically reasonable. This significantly exceeds the capabilities of all presently available diffusion coefficient models.

## 8.4 Conclusions

In this work, a new methodology for predicting diffusion coefficients in mixtures in a consistent manner for all fluid states is proposed. This includes self-diffusion and mutual diffusion coefficients. The new approach combines several physical concepts, including the Rosenfeld scaling, the Chapman-Enskog theory, and a molecular-based EOS. The framework enables predictions for the mixture diffusion coefficients without any adjustable parameters based on the limiting cases of the pure components and pseudo-pure components (i.e. infinite dilution). Due to the coupling of entropy scaling and EOS, the framework can consistently describe diffusion coefficients in mixtures in different phases (gas, liquid, supercritical, metastable) – including coexisting phases such as vapor-liquid and liquid-liquid equilibria. Also predictions to regions in which no data are available are possible. The strong predictive capabilities are a result of the physical backbone of the framework. The fact that infinite dilution diffusion coefficients exhibit a monovariate scaling behavior was discovered here for the first time. It enables an efficient entropy scaling modeling of the limiting mixture diffusion coefficient cases based on very few data. Since the limiting case diffusion coefficients are monovariate functions with respect to the entropy, extrapolations beyond the temperature and pressure range where data are available are feasible. In the mixture, no general monovariate behavior retains. Nevertheless, the mixture entropy in combination with mixing and combination rules enables predictions of mixture diffusion coefficients, which was demonstrated here for model mixtures as well as real substance systems.

The new entropy scaling framework requires an accurate and robust EOS model that describes mixture thermodynamic properties reliably, i.e. the phase equilibria, the entropy, the thermodynamic factor, and the second virial coefficient. If such a model is available, the entropy scaling framework proposed in this work is a powerful tool. For future work, the extension to multi-component systems would be interesting.

## 9 Conclusions

Information on transport properties is important for the development of industrial processes, e.g. for designing tribological systems and separation processes. In many cases, experimental data are scarce – or not available at all. Therefore, physical models with reliable extrapolation behavior are needed which only require a small set of experimental data as input. In this work, transport properties of pure fluids and fluid mixtures were studied using methods from molecular thermodynamics, namely molecular dynamics (MD) simulation and entropy scaling. Additionally, experiments were carried out for determining reference data. The focus of this work was on the viscosity, thermal conductivity, and diffusion coefficients.

MD simulations were applied for predicting transport properties using different transferable force fields. The investigated state points included high pressure states which are experimentally hardly accessible. In MD simulations, the accuracy of the results strongly depends on the employed force field. Particularly suited force field for the prediction of transport properties were identified in a comprehensive evaluation of force fields. Additionally, a literature review on transport properties of the Lennard-Jones fluid provided insights into general aspects of MD simulation modeling of transport properties, e.g. the accuracy presently achieved by MD simulations for a simple model fluid. Due to the strong predictive capabilities of MD simulations in combination with transferable force fields, even transport properties of substances for which no experimental data are available can be determined, which was demonstrated for several substances. However, conducting MD simulations, especially at extreme conditions, is computationally expensive and requires a high-performance computing infrastructure. Hence, analytical models for describing transport properties are required that provide a robust physical extrapolation behavior.

Therefore, a new modeling framework based on entropy scaling was developed. Entropy scaling makes use of the discovery that properly scaled transport properties of a given substance can usually be represented as a monovariate function of the configurational entropy, which is the basis for the prediction of transport properties for a wide range of fluid states. The new framework enables the consistent modeling of the viscosity, the thermal conductivity, and the self-diffusion coefficients of pure components in the

entire fluid region, including liquid, gaseous, supercritical, and metastable states. By integrating first-principle MD simulation data of the Lennard-Jones fluid, only a small set of experimental data are required for the model parametrization. Although the framework can be coupled with any EOS, it is designed to be used in combination with molecular-based EOS. As shown in this work, excellent extrapolation behavior is obtained in such cases. However, a prerequisite for the reliable extrapolation of the developed transport property modeling framework is the accurate extrapolation behavior of the underlying EOS model. Therefore, new component-specific EOS models for alcohols were developed and their extrapolation behavior was critically assessed. For this purpose, the density of five primary alcohols was measured up to very high pressures. The new data were employed in the parametrization of the component-specific EOS models.

The entropy scaling framework developed in this work was designed such that predictions for mixture transport properties are possible based on the pure component models alone. The viscosity and thermal conductivity of mixtures can reliably be predicted by the framework which is demonstrated for several examples including multicomponent mixtures. While entropy scaling predictions for the viscosity and thermal conductivity of mixtures have been available in the literature before, no entropy scaling model was so far available for predicting mixture diffusion coefficients. Therefore, the framework was extended to enable, for the first time, the modeling of diffusion coefficients in mixtures based on entropy scaling. The framework is able to predict the self-diffusion coefficients and the mutual diffusion coefficients in mixtures consistently and for all fluid states. The entropy scaling framework was successfully applied for predicting transport properties of several model and real substance systems. The new model shows excellent predictive capabilities – considering the fact that no parametrization to mixture data was applied. The predictions of the transport properties by the new framework can be applied in various cases, for example for studying transport phenomena at interfaces or as input for dynamic fluid simulations.



# Literature

- [1] R. Taylor, R. Krishna: Multicomponent mass transfer, Wiley, New York, 1993.
- [2] G. W. Stachowiak: How tribology has been helping us to advance and to survive, *Friction* 5 (2017) 233–247. DOI: 10.1007/s40544-017-0173-7.
- [3] J. H. Lienhard: A heat transfer textbook, 3rd ed., Phlogiston Press, Cambridge, Mass, 2001.
- [4] G. W. Stachowiak, A. W. Batchelor: Engineering tribology, 4th ed., Elsevier/Butterworth-Heinemann, Oxford, 2014.
- [5] S. Bair, C. McCabe: High-pressure rheology for quantitative elastohydrodynamics, number 54 in Tribology and interface engineering series, 1st ed., Elsevier, Amsterdam, Boston, 2007.
- [6] A. Sarode, Z. Ahmed, P. Basarkar, A. Bhargav, D. Banerjee: Role of carbon nanotube on the interfacial thermal resistance: A molecular dynamics approach, in: 2017 16th IEEE Intersociety Conference on Thermal and Thermomechanical Phenomena in Electronic Systems (ITherm), IEEE, Orlando, 2017, pp. 352–356. DOI: 10.1109/ITHERM.2017.7992493.
- [7] H. O. Baled, I. K. Gamwo, R. M. Enick, M. A. McHugh: Viscosity models for pure hydrocarbons at extreme conditions: A review and comparative study, *Fuel* 218 (2018) 89–111. DOI: 10.1016/j.fuel.2018.01.002.
- [8] G. M. Kontogeorgis, R. Dohrn, I. G. Economou, J.-C. de Hemptinne, A. ten Kate, S. Kuitunen, M. Mooijer, L. F. Zilnik, V. Vesovic: Industrial requirements for thermodynamic and transport properties: 2020, *Industrial & Engineering Chemistry Research* 60 (2021) 4987–5013. DOI: 10.1021/acs.iecr.0c05356.
- [9] J. R. Elliott, V. Diky, T. A. Knotts, W. V. Wilding: The properties of gases and liquids, 6th ed., McGraw Hill, New York, Chicago, San Francisco, 2023.
- [10] B. L. Neindre, Y. Garrabos: Transport properties of refrigerants, *The Review of High Pressure Science and Technology* 7 (1998) 1183–1188. DOI: 10.4131/jshpreview.7.1183.

- [11] Advances in Transport Properties of Fluids, in: M. J. Assael, A. R. H. Goodwin, V. Vesovic, W. A. Wakeham (Eds.), *Experimental Thermodynamics Volume IX*, volume 9, Royal Society of Chemistry, Cambridge, 2014. DOI: 10.1039/9781782625254-FP001.
- [12] S. Bair: A traction (friction) curve is not a flow curve, *Lubricants* 10 (2022) 221. DOI: 10.3390/lubricants10090221.
- [13] X. Liu, T. J. Vlugt, A. Bardow: Predictive Darken equation for Maxwell-Stefan diffusivities in multicomponent mixtures, *Industrial & Engineering Chemistry Research* 50 (2011) 10350–10358. DOI: 10.1021/ie201008a.
- [14] M. P. Allen, D. J. Tildesley: *Computer simulation of liquids*, 2nd ed., Oxford University Press, Oxford, 2017.
- [15] B. D. Todd, P. J. Daivis: *Nonequilibrium molecular dynamics: Theory, algorithms and applications*, Cambridge University Press, Cambridge, 2017. DOI: 10.1017/9781139017848.
- [16] E. J. Maginn, R. A. Messerly, D. J. Carlson, D. R. Roe, J. R. Elliott: Best practices for computing transport properties 1. Self-diffusivity and viscosity from equilibrium molecular dynamics [article v1.0], *Living Journal of Computational Molecular Science* 1 (2019). DOI: 10.33011/livecoms.1.1.6324.
- [17] D. Schaefer, S. Stephan, K. Langenbach, M. T. Horsch, H. Hasse: Mass transfer through vapor-liquid interfaces studied by non-stationary molecular dynamics simulations, *The Journal of Physical Chemistry B* 127 (2023) 2521–2533. DOI: 10.1021/acs.jpcc.2c08752.
- [18] D. Schaefer, B. Kunstmann, S. Schmitt, H. Hasse, M. Kohns: Explosions of nanodroplets studied with molecular dynamics simulations, *Physics of Fluids* 36 (2024) 037129. DOI: 10.1063/5.0190455.
- [19] J. P. Ewen, H. A. Spikes, D. Dini: Contributions of molecular dynamics simulations to elastohydrodynamic lubrication, *Tribology Letters* 69 (2021) 24. DOI: 10.1007/s11249-021-01399-w.
- [20] I. Szlufarska, M. Chandross, R. W. Carpick: Recent advances in single-asperity nanotribology, *Journal of Physics D: Applied Physics* 41 (2008) 123001. DOI: 10.1088/0022-3727/41/12/123001.
- [21] S. Schmitt, S. Stephan, B. Kirsch, J. C. Aurich, H. M. Urbassek, H. Hasse: *Molecular Dynamics Simulation of Cutting Processes: The Influence of Cutting Fluids*

- at the Atomistic Scale, in: J. C. Aurich, C. Garth, B. S. Linke (Eds.), *Proceedings of the 3rd Conference on Physical Modeling for Virtual Manufacturing Systems and Processes*, Springer International Publishing, Cham, 2023, pp. 260–280. DOI: 10.1007/978-3-031-35779-4\_14.
- [22] I. Nezbeda: On molecular-based equations of state: Perturbation theories, simple models, and SAFT modeling, *Frontiers in Physics* 8 (2020) 1–17. DOI: 10.3389/fphy.2020.00287.
- [23] E. A. Müller, K. E. Gubbins: Molecular-based equations of state for associating fluids: A review of SAFT and related approaches, *Industrial & Engineering Chemistry Research* 40 (2001) 2193–2211. DOI: 10.1021/ie000773w.
- [24] J. C. Dyre: Perspective: Excess-entropy scaling, *The Journal of Chemical Physics* 149 (2018) 210901. DOI: 10.1063/1.5055064.
- [25] Y. Rosenfeld: Relation between the transport coefficients and the internal entropy of simple systems, *Physical Review A* 15 (1977) 2545–2549. DOI: 10.1103/PhysRevA.15.2545.
- [26] Y. Rosenfeld: A quasi-universal scaling law for atomic transport in simple fluids, *Journal of Physics: Condensed Matter* 11 (1999) 5415–5427. DOI: 10.1088/0953-8984/11/28/303.
- [27] J. E. Lennard-Jones: Cohesion, *Proceedings of the Physical Society* 43 (1931) 461–482. DOI: 10.1088/0959-5309/43/5/301.
- [28] J.-P. Hansen, I. R. McDonald: *Theory of simple liquids: With applications of soft matter*, 4th ed., Elsevier, Amstersdam, 2013.
- [29] J. Fischer, M. Wendland: On the history of key empirical intermolecular potentials, *Fluid Phase Equilibria* 573 (2023) 113876. DOI: 10.1016/j.fluid.2023.113876.
- [30] J. Lenhard, S. Stephan, H. Hasse: A child of prediction. On the history, ontology, and computation of the Lennard-Jonesium, *Studies in History and Philosophy of Science* 103 (2024) 105–113. DOI: 10.1016/j.shpsa.2023.11.007.
- [31] D. J. Evans, G. P. Morriss: Transient-time-correlation functions and the rheology of fluids, *Physical Review A* 38 (1988) 4142–4148. DOI: 10.1103/PhysRevA.38.4142.
- [32] L. Verlet: Computer "experiments" on classical fluids. I. Thermodynamical properties of Lennard-Jones molecules, *Physical Review* 159 (1967) 98–103. DOI: 10.1103/PhysRev.159.98.

- [33] W. L. Jorgensen, J. D. Madura, C. J. Swenson: Optimized intermolecular potential functions for liquid hydrocarbons, *Journal of the American Chemical Society* 106 (1984) 6638–6646. DOI: 10.1021/ja00334a030.
- [34] W. L. Jorgensen, D. S. Maxwell, J. Tirado-Rives: Development and testing of the OPLS all-atom force field on conformational energetics and properties of organic liquids, *Journal of the American Chemical Society* 118 (1996) 11225–11236. DOI: 10.1021/ja9621760.
- [35] H. Sun: COMPASS: An ab initio force-field optimized for condensed-phase applications – Overview with details on alkane and benzene compounds, *The Journal of Physical Chemistry B* 102 (1998) 7338–7364. DOI: 10.1021/jp980939v.
- [36] A. D. MacKerell, D. Bashford, M. Bellott, R. L. Dunbrack, J. D. Evanseck, M. J. Field, S. Fischer, J. Gao, H. Guo, S. Ha, D. Joseph-McCarthy, L. Kuchnir, K. Kuczera, F. T. K. Lau, C. Mattos, S. Michnick, T. Ngo, D. T. Nguyen, B. Prodhom, W. E. Reiher, B. Roux, M. Schlenkrich, J. C. Smith, R. Stote, J. Straub, M. Watanabe, J. Wiórkiewicz-Kuczera, D. Yin, M. Karplus: All-atom empirical potential for molecular modeling and dynamics studies of proteins, *The Journal of Physical Chemistry B* 102 (1998) 3586–3616. DOI: 10.1021/jp973084f.
- [37] M. G. Martin, J. I. Siepmann: Transferable potentials for phase equilibria. 1. United-atom description of n-alkanes, *The Journal of Physical Chemistry B* 102 (1998) 2569–2577. DOI: 10.1021/jp972543+.
- [38] J. J. Potoff, D. A. Bernard-Brunel: Mie potentials for phase equilibria calculations: Application to alkanes and perfluoroalkanes, *The Journal of Physical Chemistry B* 113 (2009) 14725–14731. DOI: 10.1021/jp9072137.
- [39] A. Hemmen, J. Gross: Transferable anisotropic united-atom force field based on the Mie potential for phase equilibrium calculations: n-Alkanes and n-olefins, *The Journal of Physical Chemistry B* 119 (2015) 11695–11707. DOI: 10.1021/acs.jpccb.5b01354.
- [40] J. Gross, G. Sadowski: Perturbed-chain SAFT: An equation of state based on a perturbation theory for chain molecules, *Industrial & Engineering Chemistry Research* 40 (2001) 1244–1260. DOI: 10.1021/ie0003887.
- [41] T. Lafitte, A. Apostolakou, C. Avendaño, A. Galindo, C. S. Adjiman, E. A. Müller, G. Jackson: Accurate statistical associating fluid theory for chain molecules formed from Mie segments, *The Journal of Chemical Physics* 139 (2013) 154504. DOI: 10.1063/1.4819786.

- [42] F. J. Blas, L. F. Vega: Thermodynamic behaviour of homonuclear and heteronuclear Lennard-Jones chains with association sites from simulation and theory, *Molecular Physics* 92 (1997) 135–150. DOI: 10.1080/002689797170707.
- [43] G. M. Kontogeorgis, E. C. Voutsas, I. V. Yakoumis, D. P. Tassios: An equation of state for associating fluids, *Industrial & Engineering Chemistry Research* 35 (1996) 4310–4318. DOI: 10.1021/ie9600203.
- [44] E. Grüneisen: Das Verhältnis der thermischen Ausdehnung zur spezifischen Wärme fester Elemente, *Zeitschrift für Elektrochemie und angewandte physikalische Chemie* 17 (1911) 737–739. DOI: 10.1002/bbpc.191100004.
- [45] E. Grüneisen: Theorie des festen Zustandes einatomiger Elemente, *Annalen der Physik* 344 (1912) 257–306. DOI: 10.1002/andp.19123441202.
- [46] A. Z. Panagiotopoulos: Direct determination of phase coexistence properties of fluids by Monte Carlo simulation in a new ensemble, *Molecular Physics* 61 (1987) 813–826. DOI: 10.1080/00268978700101491.
- [47] S. Stephan, H. Hasse: Molecular interactions at vapor-liquid interfaces: Binary mixtures of simple fluids, *Physical Review E* 101 (2020) 012802. DOI: 10.1103/PhysRevE.101.012802.
- [48] J. Nicolas, K. Gubbins, W. Streett, D. Tildesley: Equation of state for the Lennard-Jones fluid, *Molecular Physics* 37 (1979) 1429–1454. DOI: 10.1080/00268977900101051.
- [49] T. van Westen, J. Gross: A critical evaluation of perturbation theories by Monte Carlo simulation of the first four perturbation terms in a Helmholtz energy expansion for the Lennard-Jones fluid, *The Journal of Chemical Physics* 147 (2017) 014503. DOI: 10.1063/1.4991008.
- [50] S. Stephan, U. K. Deiters: Characteristic curves of the Lennard-Jones fluid, *International Journal of Thermophysics* 41 (2020) 147. DOI: 10.1007/s10765-020-02721-9.
- [51] M. Horsch, J. Vrabec, H. Hasse: Modification of the classical nucleation theory based on molecular simulation data for surface tension, critical nucleus size, and nucleation rate, *Physical Review E* 78 (2008) 011603. DOI: 10.1103/PhysRevE.78.011603.
- [52] S. Schmitt, H. Hasse, S. Stephan: Entropy scaling framework for transport properties using molecular-based equations of state, *Journal of Molecular Liquids* 395 (2024) 123811. DOI: 10.1016/j.molliq.2023.123811.

- [53] P. Rosales-Pelaez, I. Sanchez-Burgos, C. Valeriani, C. Vega, E. Sanz: Seeding approach to nucleation in the NVT ensemble: The case of bubble cavitation in overstretched Lennard Jones fluids, *Physical Review E* 101 (2020) 022611. DOI: 10.1103/PhysRevE.101.022611.
- [54] P. R. ten Wolde, D. Frenkel: Computer simulation study of gas-liquid nucleation in a Lennard-Jones system, *The Journal of Chemical Physics* 109 (1998) 9901–9918. DOI: 10.1063/1.477658.
- [55] S. E. Quiñones-Cisneros, U. K. Deiters, R. E. Rozas, T. Kraska: New model for the correlation of the surface tension based on friction theory, *The Journal of Physical Chemistry B* 113 (2009) 3504–3511. DOI: 10.1021/jp8073255.
- [56] G. A. Mansoori, T. W. Leland: Statistical thermodynamics of mixtures. A new version for the theory of conformal solution, *Journal of the Chemical Society, Faraday Transactions 2: Molecular and Chemical Physics* 68 (1972) 320–344. DOI: 10.1039/F29726800320.
- [57] R. Laghaei, A. Eskandari Nasrabad, B. C. Eu: Statistical-mechanical theory of rheology: Lennard-Jones fluids, *The Journal of Chemical Physics* 123 (2005) 234507. DOI: 10.1063/1.2138700.
- [58] S. Stephan, K. Langenbach, H. Hasse: Interfacial properties of binary Lennard-Jones mixtures by molecular simulation and density gradient theory, *The Journal of Chemical Physics* 150 (2019) 174704. DOI: 10.1063/1.5093603.
- [59] S. Schmitt, T. Vo, M. P. Lautenschlaeger, S. Stephan, H. Hasse: Molecular dynamics simulation study of heat transfer across solid-fluid interfaces in a simple model system, *Molecular Physics* 120 (2022) e2057364. DOI: 10.1080/00268976.2022.2057364.
- [60] F. Diewald, M. P. Lautenschlaeger, S. Stephan, K. Langenbach, C. Kuhn, S. Seckler, H.-J. Bungartz, H. Hasse, R. Müller: Molecular dynamics and phase field simulations of droplets on surfaces with wettability gradient, *Computer Methods in Applied Mechanics and Engineering* 361 (2020) 112773. DOI: 10.1016/j.cma.2019.112773.
- [61] A. Köster, P. Mausbach, J. Vrabec: Premelting, solid-fluid equilibria, and thermodynamic properties in the high density region based on the Lennard-Jones potential, *The Journal of Chemical Physics* 147 (2017) 144502. DOI: 10.1063/1.4990667.

- [62] D. Fertig, H. Hasse, S. Stephan: Transport properties of binary Lennard-Jones mixtures: Insights from entropy scaling and conformal solution theory, *Journal of Molecular Liquids* 367 (2022) 120401. DOI: 10.1016/j.molliq.2022.120401.
- [63] S. Stephan, M. T. Horsch, J. Vrabec, H. Hasse: MolMod - an open access database of force fields for molecular simulations of fluids, *Molecular Simulation* 45 (2019) 806–814. DOI: 10.1080/08927022.2019.1601191.
- [64] B. Saager, J. Fischer: Predictive power of effective intermolecular pair potentials: MD simulation results for methane up to 1000 MPa, *Fluid Phase Equilibria* 57 (1990) 35–46. DOI: 10.1016/0378-3812(90)80011-Y.
- [65] G. Rutkai, M. Thol, R. Span, J. Vrabec: How well does the Lennard-Jones potential represent the thermodynamic properties of noble gases?, *Molecular Physics* 115 (2017) 1104–1121. DOI: 10.1080/00268976.2016.1246760.
- [66] J. E. Jones: On the determination of molecular fields.I. From the variation of the viscosity of a gas with temperature, *Proceedings of the Royal Society of London. Series A, Containing Papers of a Mathematical and Physical Character* 106 (1924) 441–462. DOI: 10.1098/rspa.1924.0081.
- [67] W. W. Wood, F. R. Parker: Monte carlo equation of state of molecules interacting with the Lennard-Jones potential. I. A supercritical isotherm at about twice the critical temperature, *The Journal of Chemical Physics* 27 (1957) 720–733. DOI: 10.1063/1.1743822.
- [68] J. Mick, E. Hailat, V. Russo, K. Rushaidat, L. Schwiebert, J. Potoff: GPU-accelerated Gibbs ensemble Monte Carlo simulations of Lennard-Jonesium, *Computer Physics Communications* 184 (2013) 2662–2669. DOI: 10.1016/j.cpc.2013.06.020.
- [69] B. Chen, J. I. Siepmann, M. L. Klein: Direct Gibbs ensemble Monte Carlo simulations for solidvapor phase equilibria: Applications to Lennard-Jonesium and carbon dioxide, *The Journal of Physical Chemistry B* 105 (2001) 9840–9848. DOI: 10.1021/jp011950p.
- [70] B. J. Alder, T. E. Wainwright: Studies in molecular dynamics. I. General method, *The Journal of Chemical Physics* 31 (1959) 459–466. DOI: 10.1063/1.1730376.
- [71] A. Rahman: Correlations in the motion of atoms in liquid argon, *Physical Review* 136 (1964) A405–A411. DOI: 10.1103/PhysRev.136.A405.

- [72] N. Metropolis, A. W. Rosenbluth, M. N. Rosenbluth, A. H. Teller, E. Teller: Equation of state calculations by fast computing machines, *The Journal of Chemical Physics* 21 (1953) 1087–1092. DOI: 10.1063/1.1699114.
- [73] S. Stephan, M. Thol, J. Vrabec, H. Hasse: Thermophysical properties of the Lennard-Jones fluid: Database and data assessment, *Journal of Chemical Information and Modeling* 59 (2019) 4248–4265. DOI: 10.1021/acs.jcim.9b00620.
- [74] P. Wingertszahn, S. Schmitt, S. Thielen, M. Oehler, B. Magyar, O. Koch, H. Hasse, S. Stephan: Measurement, modelling, and application of lubricant properties at extreme pressures, *Tribologie und Schmierungstechnik* 70 (2023) 5–12. DOI: 10.24053/TuS-2023-0017.
- [75] B. E. Poling, J. M. Prausnitz, J. P. O’Connell: *The properties of gases and liquids*, 5th ed., McGraw-Hill, New York, 2001.
- [76] R. Krauss, K. Stephan: Thermal conductivity of refrigerants in a wide range of temperature and pressure, *Journal of Physical and Chemical Reference Data* 18 (1989) 43–76. DOI: 10.1063/1.555842.
- [77] S. Schmitt, F. Fleckenstein, H. Hasse, S. Stephan: Comparison of force fields for the prediction of thermophysical properties of long linear and branched alkanes, *The Journal of Physical Chemistry B* 127 (2023) 1789–1802. DOI: 10.1021/acs.jpcc.2c07997.
- [78] M. Fischer, G. Bauer, J. Gross: Transferable anisotropic united-atom Mie (TAMie) force field: Transport properties from equilibrium molecular dynamic simulations, *Industrial & Engineering Chemistry Research* 59 (2020) 8855–8869. DOI: 10.1021/acs.iecr.0c00848.
- [79] R. M. de Souza, L. J. A. de Siqueira, M. Karttunen, L. G. Dias: Molecular dynamics simulations of polymer-ionic liquid (1-ethyl-3-methylimidazolium tetracyanoborate) ternary electrolyte for sodium and potassium ion batteries, *Journal of Chemical Information and Modeling* 60 (2020) 485–499. DOI: 10.1021/acs.jcim.9b00750.
- [80] I. Valencia-Jaime, C. Desgranges, J. Delhommelle: Viscosity of a highly compressed methylated alkane via equilibrium and nonequilibrium molecular dynamics simulations, *Chemical Physics Letters* 719 (2019) 103–109. DOI: 10.1016/j.cplett.2019.01.041.
- [81] G. Guevara-Carrion, J. Vrabec, H. Hasse: On the prediction of transport properties of monomethylamine, dimethylamine, dimethylether and hydrogen chlo-



- ride by molecular simulation, *Fluid Phase Equilibria* 316 (2012) 46–54. DOI: 10.1016/j.fluid.2011.12.009.
- [82] X. Nie, Z. Du, L. Zhao, S. Deng, Y. Zhang: Molecular dynamics study on transport properties of supercritical working fluids: Literature review and case study, *Applied Energy* 250 (2019) 63–80. DOI: 10.1016/j.apenergy.2019.04.156.
- [83] I. Antolovi, J. Staubach, S. Stephan, J. Vrabec: Phase equilibria of symmetric Lennard-Jones mixtures and a look at the transport properties near the upper critical solution temperature, *Physical Chemistry Chemical Physics* 25 (2023) 17627–17638. DOI: 10.1039/D3CP01434G.
- [84] Y. Zhang, A. Otani, E. J. Maginn: Reliable viscosity calculation from equilibrium molecular dynamics simulations: A time decomposition method, *Journal of Chemical Theory and Computation* 11 (2015) 3537–3546. DOI: 10.1021/acs.jctc.5b00351.
- [85] C. M. Tenney, E. J. Maginn: Limitations and recommendations for the calculation of shear viscosity using reverse nonequilibrium molecular dynamics, *The Journal of Chemical Physics* 132 (2010) 014103. DOI: 10.1063/1.3276454.
- [86] R. Hafner, G. Guevara-Carrion, J. Vrabec, P. Klein: Sampling the bulk viscosity of water with molecular dynamics simulation in the canonical ensemble, *The Journal of Physical Chemistry. B* 126 (2022) 10172. DOI: 10.1021/acs.jpcc.2c06035.
- [87] J. P. Ewen, D. M. Heyes, D. Dini: Advances in nonequilibrium molecular dynamics simulations of lubricants and additives, *Friction* 6 (2018) 349–386. DOI: 10.1007/s40544-018-0207-9.
- [88] G. Toraman, T. Verstraelen, D. Fauconnier: Impact of ad hoc post-processing parameters on the lubricant viscosity calculated with equilibrium molecular dynamics simulations, *Lubricants* 11 (2023). DOI: 10.3390/lubricants11040183.
- [89] L. F. Mercier Franco, A. Firoozabadi: Computation of shear viscosity by a consistent method in equilibrium molecular dynamics simulations: Applications to 1-decene oligomers, *The Journal of Physical Chemistry B* 127 (2023) 10043–10051. DOI: 10.1021/acs.jpcc.3c04994.
- [90] M. Schappals, A. Mecklenfeld, L. Kröger, V. Botan, A. Köster, S. Stephan, E. J. García, G. Rutkai, G. Raabe, P. Klein, K. Leonhard, C. W. Glass, J. Lenhard,

- J. Vrabec, H. Hasse: Round Robin study: Molecular simulation of thermodynamic properties from models with internal degrees of freedom, *Journal of Chemical Theory and Computation* 13 (2017) 4270–4280. DOI: 10.1021/acs.jctc.7b00489.
- [91] D. A. Kofke, P. T. Cummings: Quantitative comparison and optimization of methods for evaluating the chemical potential by molecular simulation, *Molecular Physics* 92 (1997) 973–996. DOI: 10.1080/002689797169600.
- [92] S. Stephan, M. Dyga, I. Alabd Alhafez, J. Lenhard, H. M. Urbassek, H. Hasse: Reproducibility of atomistic friction computer experiments: A molecular dynamics simulation study, *Molecular Simulation* 47 (2021) 1509–1521. DOI: 10.1080/08927022.2021.1987430.
- [93] X. Yong, L. T. Zhang: Thermostats and thermostat strategies for molecular dynamics simulations of nanofluidics, *The Journal of Chemical Physics* 138 (2013) 084503. DOI: 10.1063/1.4792202.
- [94] M. Fischer, G. Bauer, J. Gross: Force fields with fixed bond lengths and with flexible bond lengths: Comparing static and dynamic fluid properties, *Journal of Chemical & Engineering Data* 65 (2020) 1583 – 1593. DOI: 10.1021/acs.jced.9b01031.
- [95] J. E. Basconi, M. R. Shirts: Effects of temperature control algorithms on transport properties and kinetics in molecular dynamics simulations, *Journal of Chemical Theory and Computation* 9 (2013) 2887–2899. DOI: 10.1021/ct400109a.
- [96] S. C. Harvey, R. K.-Z. Tan, T. E. Cheatham III: The flying ice cube: Velocity rescaling in molecular dynamics leads to violation of energy equipartition, *Journal of Computational Chemistry* 19 (1998) 726–740. DOI: 10.1002/(SICI)1096-987X(199805)19:7<726::AID-JCC4>3.0.CO;2-S.
- [97] M. S. Green: Markoff random processes and the statistical mechanics of time-dependent phenomena. II. Irreversible processes in fluids, *The Journal of Chemical Physics* 22 (1954) 398–413. DOI: 10.1063/1.1740082.
- [98] R. Kubo: Statistical-mechanical theory of irreversible processes. I. General theory and simple applications to magnetic and conduction problems, *Journal of the Physical Society of Japan* 12 (1957) 570–586. DOI: 10.1143/JPSJ.12.570.
- [99] D. J. Evans, G. Morriss: *Statistical mechanics of nonequilibrium liquids*, 2nd ed., Cambridge University Press, Cambridge, 2008.

- [100] T. Chen, B. Smit, A. T. Bell: Are pressure fluctuation-based equilibrium methods really worse than nonequilibrium methods for calculating viscosities?, *The Journal of Chemical Physics* 131 (2009) 246101. DOI: 10.1063/1.3274802.
- [101] D. J. Evans, G. P. Morriss: Nonlinear-response theory for steady planar Couette flow, *Physical Review A* 30 (1984) 1528–1530. DOI: 10.1103/PhysRevA.30.1528.
- [102] F. Müller-Plathe: Reversing the perturbation in nonequilibrium molecular dynamics: An easy way to calculate the shear viscosity of fluids, *Physical Review E* 59 (1999) 4894–4898. DOI: 10.1103/PhysRevE.59.4894.
- [103] M. P. Lautenschlaeger, M. Horsch, H. Hasse: Simultaneous determination of thermal conductivity and shear viscosity using two-gradient non-equilibrium molecular dynamics simulations, *Molecular Physics* 117 (2019) 189–199. DOI: 10.1080/00268976.2018.1504134.
- [104] B. Todd, P. Daivis: Nonequilibrium molecular dynamics simulations of planar elongational flow with spatially and temporally periodic boundary conditions, *Physical Review Letters* 81 (1998) 1118–1121. DOI: 10.1103/PhysRevLett.81.1118.
- [105] P. A. Thompson, M. O. Robbins: Origin of stick-slip motion in boundary lubrication, *Science* 250 (1990) 792–794. DOI: 10.1126/science.250.4982.792.
- [106] J. J. Erpenbeck: Comparison of Green-Kubo and nonequilibrium calculations of the self-diffusion constant of a Lennard-Jones fluid, *Physical Review A* 35 (1987) 218–232. DOI: 10.1103/PhysRevA.35.218.
- [107] J. Vrabec, G. K. Kedia, G. Fuchs, H. Hasse: Comprehensive study of the vapour-liquid coexistence of the truncated and shifted Lennard-Jones fluid including planar and spherical interface properties, *Molecular Physics* 104 (2006) 1509–1527. DOI: 10.1080/00268970600556774.
- [108] M. Heier, S. Stephan, J. Liu, W. G. Chapman, H. Hasse, K. Langenbach: Equation of state for the Lennard-Jones truncated and shifted fluid with a cut-off radius of  $2.5 \sigma$  based on perturbation theory and its applications to interfacial thermodynamics, *Molecular Physics* 116 (2018) 2083–2094. DOI: 10.1080/00268976.2018.1447153.
- [109] B. Hafskjold, K. P. Travis, A. B. Hass, M. Hammer, A. Aasen, O. Wilhelmsen: Thermodynamic properties of the 3D Lennard-Jones/spline model, *Molecular Physics* 117 (2019) 3754–3769. DOI: 10.1080/00268976.2019.1664780.

- [110] K. R. Kristiansen: Transport properties of the simple Lennard-Jones/Spline fluid I: Binary scattering and high-accuracy low-density transport coefficients, *Frontiers in Physics* 8 (2020) 271.
- [111] S. Stephan, H. Hasse: Influence of dispersive long-range interactions on properties of vapour-liquid equilibria and interfaces of binary Lennard-Jones mixtures, *Molecular Physics* 118 (2020) e1699185. DOI: 10.1080/00268976.2019.1699185.
- [112] D. Fertig, S. Stephan: Influence of dispersive long-range interactions on transport and excess properties of simple mixtures, *Molecular Physics* 121 (2023) e2162993. DOI: 10.1080/00268976.2022.2162993.
- [113] M. P. Lautenschlaeger, H. Hasse: Transport properties of the Lennard-Jones truncated and shifted fluid from non-equilibrium molecular dynamics simulations, *Fluid Phase Equilibria* 482 (2019) 38–47. DOI: 10.1016/j.fluid.2018.10.019.
- [114] M. Bugel, G. Galliero: Thermal conductivity of the Lennard-Jones fluid: An empirical correlation, *Chemical Physics* 352 (2008) 249–257. DOI: 10.1016/j.chemphys.2008.06.013.
- [115] O. C. Nwobi, L. N. Long, M. M. Micci: Molecular dynamics studies of properties of supercritical fluids, *Journal of Thermophysics and Heat Transfer* 12 (1998) 322–327. DOI: 10.2514/2.6364.
- [116] Y.-L. Huang, T. Merker, M. Heilig, H. Hasse, J. Vrabec: Molecular modeling and simulation of vapor-liquid equilibria of ethylene oxide, ethylene glycol, and water as well as their binary mixtures, *Industrial & Engineering Chemistry Research* 51 (2012) 7428–7440. DOI: 10.1021/ie300248z.
- [117] C. Hoheisel: Bulk viscosity of model fluids. A comparison of equilibrium and nonequilibrium molecular dynamics results, *The Journal of Chemical Physics* 86 (1987) 2328–2333. DOI: 10.1063/1.452131.
- [118] K. Meier, A. Laesecke, S. Kabelac: Transport coefficients of the Lennard-Jones model fluid. II Self-diffusion, *The Journal of Chemical Physics* 121 (2004) 9526–9535. DOI: 10.1063/1.1786579.
- [119] K. Meier, A. Laesecke, S. Kabelac: Transport coefficients of the Lennard-Jones model fluid. I. Viscosity, *The Journal of Chemical Physics* 121 (2004) 3671–3687. DOI: 10.1063/1.1770695.

- [120] C. Huang, C. Li, P. Y. Choi, K. Nandakumar, L. W. Kostiuk: Effect of cut-off distance used in molecular dynamics simulations on fluid properties, *Molecular Simulation* 36 (2010) 856–864. DOI: 10.1080/08927022.2010.489556.
- [121] G. Galliéro, B. Duguay, J.-P. Caltagirone, F. Montel: Thermal diffusion sensitivity to the molecular parameters of a binary equimolar mixture, a non-equilibrium molecular dynamics approach, *Fluid Phase Equilibria* 208 (2003) 171–188. DOI: 10.1016/S0378-3812(03)00030-X.
- [122] I.-C. Yeh, G. Hummer: System-size dependence of diffusion coefficients and viscosities from molecular dynamics simulations with periodic boundary conditions, *The Journal of Physical Chemistry B* 108 (2004) 15873–15879. DOI: 10.1021/jp0477147.
- [123] B. Dünweg, K. Kremer: Molecular dynamics simulation of a polymer chain in solution, *The Journal of Chemical Physics* 99 (1993) 6983–6997. DOI: 10.1063/1.465445.
- [124] J. O. Hirschfelder, C. F. Curtiss, R. B. Bird: *Molecular theory of gases and liquids*, J. Wiley & Sons, New York, 1963.
- [125] H. C. Longuet-Higgins, J. A. Pople: Transport properties of a dense fluid of hard spheres, *The Journal of Chemical Physics* 25 (1956) 884–889. DOI: 10.1063/1.1743136.
- [126] S. U. Kim, C. W. Monroe: High-accuracy calculations of sixteen collision integrals for Lennard-Jones (12-6) gases and their interpolation to parameterize neon, argon, and krypton, *Journal of Computational Physics* 273 (2014) 358–373. DOI: 10.1016/j.jcp.2014.05.018.
- [127] S. E. Quiñones-Cisneros, C. K. Zéberg-Mikkelsen, E. H. Stenby: The friction theory (f-theory) for viscosity modeling, *Fluid Phase Equilibria* 169 (2000) 249–276. DOI: 10.1016/S0378-3812(00)00310-1.
- [128] I. H. Bell, R. Messerly, M. Thol, L. Costigliola, J. C. Dyre: Modified entropy scaling of the transport properties of the Lennard-Jones fluid, *The Journal of Physical Chemistry B* 123 (2019) 6345–6363. DOI: 10.1021/acs.jpccb.9b05808.
- [129] G. Galliero, C. Boned, J. Fernández: Scaling of the viscosity of the Lennard-Jones chain fluid model, argon, and some normal alkanes, *The Journal of Chemical Physics* 134 (2011) 064505. DOI: 10.1063/1.3553262.
- [130] R. V. Vaz, A. L. Magalhães, D. L. A. Fernandes, C. M. Silva: Universal correlation of self-diffusion coefficients of model and real fluids based on residual entropy

- scaling law, *Chemical Engineering Science* 79 (2012) 153–162. DOI: 10.1016/j.ces.2012.05.006.
- [131] T. Goel, C. N. Patra, T. Mukherjee, C. Chakravarty: Excess entropy scaling of transport properties of Lennard-Jones chains, *The Journal of Chemical Physics* 129 (2008) 164904. DOI: 10.1063/1.2995990.
- [132] T. Nguyen, S. Khennache, G. Galliero, T. Tran, L. Tuong, P. Nguyen, H. Hoang, H. K. Ho: Entropy scaling for viscosity of pure Lennard-Jones fluids and their binary mixtures, *Communications in Physics* 32 (2022) 187–200. DOI: 10.15625/0868-3166/16345.
- [133] T. Q. Q. Viet, S. Khennache, G. Galliero, S. Alapati, P. T. Nguyen, H. Hoang: Mass effect on viscosity of mixtures in entropy scaling framework: Application to Lennard-Jones mixtures, *Fluid Phase Equilibria* 558 (2022) 113459. DOI: 10.1016/j.fluid.2022.113459.
- [134] S. Mross, S. Schmitt, S. Stephan, K. Münnemann, H. Hasse: Diffusion coefficients in mixtures of poly(oxymethylene) dimethyl ethers with alkanes, *Industrial & Engineering Chemistry Research* 63 (2024) 1662–1669. DOI: 10.1021/acs.iecr.3c03839.
- [135] A. Schnorr, D. J. Kaldi, J. Staubach, C. Garth, S. Stephan: Using autonomous outlier detection methods for thermophysical property data, *Journal of Chemical & Engineering Data* 69 (2024) 864–880. DOI: 10.1021/acs.jced.3c00588.
- [136] J. Kolafa, I. Nezbeda: The Lennard-Jones fluid: An accurate analytic and theoretically-based equation of state, *Fluid Phase Equilibria* 100 (1994) 1–34. DOI: 10.1016/0378-3812(94)80001-4.
- [137] E. M. Gosling, I. R. McDonald, K. Singer: On the calculation by molecular dynamics of the shear viscosity of a simple fluid, *Molecular Physics* 26 (1973) 1475–1484. DOI: 10.1080/00268977300102631.
- [138] D. Levesque, L. Verlet, J. Kürkijarvi: Computer "experiments" on classical fluids. IV. Transport properties and time-correlation functions of the Lennard-Jones liquid near its triple point, *Physical Review A* 7 (1973) 1690–1700. DOI: 10.1103/physreva.7.1690.
- [139] W. T. Ashurst, W. G. Hoover: Dense-fluid shear viscosity via nonequilibrium molecular dynamics, *Physical Review A* 11 (1975) 658–678. DOI: 10.1103/physreva.11.658.

- [140] D. M. Heyes, J. J. Kim, C. J. Montrose, T. A. Litovitz: Time dependent nonlinear shear stress effects in simple liquids: A molecular dynamics study, *The Journal of Chemical Physics* 73 (1980) 3987–3996. DOI: 10.1063/1.440624.
- [141] W. G. Hoover, D. J. Evans, R. B. Hickman, A. J. C. Ladd, W. T. Ashurst, B. Moran: Lennard-Jones triple-point bulk and shear viscosities. Green-Kubo theory, Hamiltonian mechanics, and nonequilibrium molecular dynamics, *Physical Review A* 22 (1980) 1690–1697. DOI: 10.1103/physreva.22.1690.
- [142] K. Singer, J. V. L. Singer, D. Fincham: Determination of the shear viscosity of atomic liquids by non-equilibrium molecular dynamics, *Molecular Physics* 40 (1980) 515–519. DOI: 10.1080/00268978000101661.
- [143] D. Fincham, D. M. Heyes: Comparisons between experimental argon and Lennard-Jones 12:6 shear viscosities, *Chemical Physics* 78 (1983) 425–441. DOI: 10.1016/0301-0104(83)85128-3.
- [144] D. M. Heyes: Self-diffusion and shear viscosity of simple fluids. A molecular-dynamics study, *Journal of the Chemical Society (Faraday Transactions 2)* 79 (1983) 1741. DOI: 10.1039/f29837901741.
- [145] J. P. J. Michels, N. J. Trappeniers: Molecular dynamical calculations of the viscosity of Lennard-Jones systems, *Physica A: Statistical Mechanics and its Applications* 133 (1985) 281–290. DOI: 10.1016/0378-4371(85)90067-6.
- [146] M. Schoen, C. Hoheisel: The shear viscosity of a Lennard-Jones fluid calculated by equilibrium molecular dynamics, *Molecular Physics* 56 (1985) 653–672. DOI: 10.1080/00268978500102591.
- [147] D. J. Evans, G. P. Morriss: Asymptotic nonlinear stress tensor in small periodic systems undergoing Couette flow, *Physical Review A* 36 (1987) 4119–4122. DOI: 10.1103/PhysRevA.36.4119.
- [148] D. M. Heyes: Viscosity and self-diffusion of simple liquids. Hard-sphere treatment of molecular dynamics data, *Journal of the Chemical Society, Faraday Transactions 2* 83 (1987) 1985. DOI: 10.1039/f29878301985.
- [149] D. Levesque, L. Verlet: Molecular dynamics calculations of transport coefficients, *Molecular Physics* 61 (1987) 143–159. DOI: 10.1080/00268978700101041.
- [150] J. J. Erpenbeck: Shear viscosity of the Lennard-Jones fluid near the triple point: Green-Kubo results, *Physical Review A* 38 (1988) 6255–6266. DOI: 10.1103/physreva.38.6255.

- [151] J. J. Erpenbeck: Erratum: Shear viscosity of the Lennard-Jones fluid near the triple point: Green-Kubo results, *Physical Review A* 39 (1989) 4893–4893. DOI: 10.1103/physreva.39.4893.
- [152] K. D. Hammonds, D. M. Heyes: Transport coefficients of model simple liquids. A molecular-dynamics study and effective hard-sphere analysis, *Journal of the Chemical Society, Faraday Transactions 2: Molecular and Chemical Physics* 84 (1988) 705–725. DOI: 10.1039/F29888400705.
- [153] D. M. Heyes: Transport coefficients of Lennard-Jones fluids: A molecular-dynamics and effective-hard-sphere treatment, *Physical Review B* 37 (1988) 5677–5696. DOI: 10.1103/PhysRevB.37.5677.
- [154] R. Vogelsang, G. Hoheisel, M. Lucas: Shear viscosity and thermal conductivity of the Lennard-Jones liquid computed using molecular dynamics and predicted by a memory function model for a large number of states, *Molecular Physics* 64 (1988) 1203–1213. DOI: 10.1080/00268978800100813.
- [155] D. J. Evans, G. P. Morriss, L. M. Hood: On the number dependence of viscosity in three dimensional fluids, *Molecular Physics* 68 (1989) 637–646. DOI: 10.1080/00268978900102421.
- [156] P. Borgelt, C. Hoheisel, G. Stell: Exact molecular dynamics and kinetic theory results for thermal transport coefficients of the Lennard-Jones argon fluid in a wide region of states, *Physical Review A* 42 (1990) 789–794. DOI: 10.1103/physreva.42.789.
- [157] D. M. Heyes, J. G. Powles: Information theory applied to the transport coefficients of Lennard-Jones fluids, *Molecular Physics* 71 (1990) 781–800. DOI: 10.1080/00268979000102111.
- [158] M. Ferrario, G. Ciccotti, B. L. Holian, J. P. Ryckaert: Shear-rate dependence of the viscosity of the Lennard-Jones liquid at the triple point, *Physical Review A* 44 (1991) 6936–6939. DOI: 10.1103/physreva.44.6936.
- [159] C. Moon, K. M. Moon, S. H. Lee: Equilibrium and non-equilibrium molecular dynamics simulations of thermal transport coefficients of liquid argon, *Bulletin of The Korean Chemical Society* 12 (1991) 309–315.
- [160] M. F. Pas, B. J. Zwolinski: Computation of the transport coefficients of binary mixtures of argon-krypton, krypton-xenon, and argon-xenon by molecular dynamics, *Molecular Physics* 73 (1991) 483–494. DOI: 10.1080/00268979100101331.



- [161] M. F. Pas, B. J. Zwolinski: Computation of the transport coefficients of dense fluid neon, argon, krypton and xenon by molecular dynamics, *Molecular Physics* 73 (1991) 471–481. DOI: 10.1080/00268979100101321.
- [162] D. M. Heyes, J. G. Powles, J. C. G. Montero: Information theory applied to the transport coefficients of Lennard-Jones fluids II, *Molecular Physics* 78 (1993) 229–234. DOI: 10.1080/00268979300100191.
- [163] S. H. Lee, P. T. Cummings: Shear viscosity of model mixtures by nonequilibrium molecular dynamics. I. Argon-krypton mixtures, *The Journal of Chemical Physics* 99 (1993) 3919–3925. DOI: 10.1063/1.466137.
- [164] C. Hoheisel: Transport properties of molecular liquids, *Physics Reports* 245 (1994) 111–157. DOI: 10.1016/0370-1573(94)90075-2.
- [165] H. Stassen, W. A. Steele: Simulation studies of shear viscosity time-correlation-functions, *The Journal of Chemical Physics* 102 (1995) 932–938. DOI: 10.1063/1.469160.
- [166] R. L. Rowley, M. M. Painter: Diffusion and viscosity equations of state for a Lennard-Jones fluid obtained from molecular dynamics simulations, *International Journal of Thermophysics* 18 (1997) 1109–1121. DOI: 10.1007/bf02575252.
- [167] M. Canales, J. A. Padró: Dynamic properties of Lennard-Jones fluids and liquid metals, *Physical Review E* 60 (1999) 551–558. DOI: 10.1103/physreve.60.551.
- [168] T. Ohara, D. Suzuki: Intermolecular momentum transfer in a simple liquid and its contribution to shear viscosity, *Microscale Thermophysical Engineering* 5 (2001) 117–130. DOI: 10.1080/108939501750397463.
- [169] S. H. Lee, D. K. Park, D. B. Kang: Molecular dynamics simulations for transport coefficients of liquid argon: New approaches, *Bulletin of The Korean Chemical Society* 24 (2003) 178–182. DOI: 10.5012/bkcs.2003.24.2.178.
- [170] V. R. Vasquez, E. A. Macedo, M. S. Zabaloy: Lennard-Jones viscosities in wide ranges of temperature and density: Fast calculations using a steady-state periodic perturbation method, *International Journal of Thermophysics* 25 (2004) 1799–1818. DOI: 10.1007/s10765-004-7736-3.
- [171] G. Galliéro, C. Boned, A. Baylaucq: Molecular dynamics study of the Lennard-Jones fluid viscosity: Application to real fluids, *Industrial & Engineering Chemistry Research* 44 (2005) 6963–6972. DOI: 10.1021/ie050154t.

- [172] R. D. Mountain: System size and control parameter effects in reverse perturbation nonequilibrium molecular dynamics, *The Journal of Chemical Physics* 124 (2006) 104109. DOI: 10.1063/1.2178340.
- [173] G. Galliéro, C. Boned, A. Baylaucq, F. Montel: Influence of the repulsive coefficient  $\alpha$  and approximate corresponding states in Mie  $\alpha$ -6 and exponential  $\alpha$ -6 fluids, *Chemical Physics* 333 (2007) 219–228. DOI: 10.1016/j.chemphys.2007.02.002.
- [174] S. H. Lee: Molecular dynamics simulation study of the transport properties of liquid argon: The Green-Kubo formula revisited, *Bulletin of The Korean Chemical Society* 28 (2007) 1371–1374. DOI: 10.5012/bkcs.2007.28.8.1371.
- [175] H. M. Sun, M. S. Chang, H. L. Song: Transport properties of Ar-Kr mixtures: A molecular dynamics simulation study, *Bulletin of The Korean Chemical Society* 28 (2007) 1689–1696. DOI: 10.5012/bkcs.2007.28.10.1689.
- [176] J. C. Thomas, R. L. Rowley: Transient molecular dynamics simulations of viscosity for simple fluids, *The Journal of Chemical Physics* 127 (2007) 174510. DOI: 10.1063/1.2784117.
- [177] S. Viscardy, J. Servantie, P. Gaspard: Transport and Helfand moments in the Lennard-Jones fluid. I. Shear viscosity, *The Journal of Chemical Physics* 126 (2007) 184512. DOI: 10.1063/1.2724820.
- [178] G. Galliero, C. Boned: Molecular dynamics study of the repulsive form influence of the interaction potential on structural, thermodynamic, interfacial, and transport properties, *The Journal of Chemical Physics* 129 (2008) 074506. DOI: 10.1063/1.2969766.
- [179] S.-H. Lee: Transport properties of Lennard-Jones mixtures: A molecular dynamics simulation study, *Bulletin of the Korean Chemical Society* 29 (2008) 641–646. DOI: 10.5012/bkcs.2008.29.3.641.
- [180] P. Strąk, S. Krukowski: Molecular dynamic simulations of viscosity of argon at high pressures, *High Pressure Research* 28 (2008) 469–476. DOI: 10.1080/08957950802510109.
- [181] P. Strąk: Private communication, data from Ref. 180 (2024).
- [182] G. A. Adebayo, B. C. Anusionwu, A. N. Njah, O. J. Adeniran, B. Mathew, R. S. Sunmonu: Collision frequency of Lennard-Jones fluids at high densities by equilibrium molecular dynamics simulation, *Pramana* 75 (2010) 523–536. DOI: 10.1007/s12043-010-0136-2.

- [183] H. Y. Oderji, H. Ding, H. Behnejad: Calculation of the second self-diffusion and viscosity virial coefficients of Lennard-Jones fluid by equilibrium molecular dynamics simulations, *Physical Review E* 83 (2011) 061202. DOI: 10.1103/physreve.83.061202.
- [184] V. G. Baidakov, S. P. Protsenko, Z. R. Kozlova: Metastable Lennard-Jones fluids. I. Shear viscosity, *The Journal of Chemical Physics* 137 (2012) 164507. DOI: 10.1063/1.4758806.
- [185] S. H. Lee: Equilibrium molecular dynamics simulation study for transport properties of noble gases: The Green-Kubo formula, *Bulletin of The Korean Chemical Society* 34 (2013) 2931–2936. DOI: 10.5012/BKCS.2013.34.10.2931.
- [186] S. H. Lee: Size effect on transport properties of gaseous argon: A molecular dynamics simulation study, *Bulletin of The Korean Chemical Society* 35 (2014) 1559–1561. DOI: 10.5012/BKCS.2014.35.5.1559.
- [187] S. Delage-Santacreu, G. Galliero, H. Hoang, J.-P. Bazile, C. Boned, J. Fernandez: Thermodynamic scaling of the shear viscosity of Mie  $n$ -6 fluids and their binary mixtures, *The Journal of Chemical Physics* 142 (2015) 174501. DOI: 10.1063/1.4919296.
- [188] G. Galliero: Private communication, data from Ref. 187 (2024).
- [189] N. Ohtori, Y. Ishii: Explicit expressions of self-diffusion coefficient, shear viscosity, and the Stokes-Einstein relation for binary mixtures of Lennard-Jones liquids, *The Journal of Chemical Physics* 143 (2015) 164514. DOI: 10.1063/1.4934627.
- [190] J. Nichele, I. Borges, A. B. Oliveira, L. S. Alves: Molecular dynamics simulations of momentum and thermal diffusion properties of near-critical argon along isobars, *The Journal of Supercritical Fluids* 114 (2016) 46–54. DOI: 10.1016/j.supflu.2016.04.004.
- [191] S. Ghimire, N. P. Adhikari: Study of structural and transport properties of argon, krypton, and their binary mixtures at different temperatures, *Journal of Molecular Modeling* 23 (2017) 94. DOI: 10.1007/s00894-017-3261-8.
- [192] N. Ohtori, S. Miyamoto, Y. Ishii: Breakdown of the Stokes-Einstein relation in pure Lennard-Jones fluids: From gas to liquid via supercritical states, *Physical Review E* 95 (2017) 052122. DOI: 10.1103/PhysRevE.95.052122.
- [193] D. M. Heyes, D. Dini, L. Costigliola, J. C. Dyre: Transport coefficients of the Lennard-Jones fluid close to the freezing line, *The Journal of Chemical Physics* 151 (2019) 204502. DOI: 10.1063/1.5128707.

- [194] I. H. Bell, S. Delage-Santacreu, H. Hoang, G. Galliero: Dynamic crossover in fluids: From hard spheres to molecules, *The Journal of Physical Chemistry Letters* 12 (2021) 6411–6417. DOI: 10.1021/acs.jpcllett.1c01594.
- [195] D. M. Heyes, D. Dini, E. R. Smith: Viscuit and the fluctuation theorem investigation of shear viscosity by molecular dynamics simulations: The information and the noise, *The Journal of Chemical Physics* 154 (2021) 074503. DOI: 10.1063/5.0040106.
- [196] F. Rizk, S. Gelin, A.-L. Biance, L. Joly: Microscopic origins of the viscosity of a Lennard-Jones liquid, *Physical Review Letters* 129 (2022) 074503. DOI: 10.1103/physrevlett.129.074503.
- [197] L. Joly: Private communication, data from Ref. 196 (2024).
- [198] J. Šlepavičius, A. Patti, J. L. McDonagh, C. Avendaño: Application of machine-learning algorithms to predict the transport properties of Mie fluids, *The Journal of Chemical Physics* 159 (2023) 024127. DOI: 10.1063/5.0151123.
- [199] G. Chaparro, E. A. Müller: Simulation and data-driven modeling of the transport properties of the Mie fluid, *The Journal of Physical Chemistry B* 128 (2024) 551–566. DOI: 10.1021/acs.jpccb.3c06813.
- [200] F. Fleckenstein, S. Schmitt, D. Fertig, D. Schäfer, J. Lenhard, H. Hasse, S. Stephan: Reproducibility of computer experiments for the prediction of thermophysical properties of the Lennard-Jones fluid, in preparation (2024).
- [201] K. Ramkumar, S. S. Mishra, S. Bhattacharjee: Uncertainties in the transport properties of helium gas at cryogenic temperatures determined using molecular dynamics simulation, *Fluid Phase Equilibria* 577 (2024) 113979. DOI: 10.1016/j.fluid.2023.113979.
- [202] D. Saric, I. H. Bell, G. Guevara-Carrion, J. Vrabec: Influence of repulsion on entropy scaling and density scaling of monatomic fluids, *The Journal of Chemical Physics* 160 (2024) 104503. DOI: 10.1063/5.0196592.
- [203] D. M. Heyes: Thermal conductivity and bulk viscosity of simple fluids. A molecular-dynamics study, *Journal of the Chemical Society, Faraday Transactions 2* 80 (1984) 1363–1394. DOI: 10.1039/f29848001363.
- [204] G. V. Paolini, G. Ciccotti, C. Massobrio: Nonlinear thermal response of a Lennard-Jones fluid near the triple point, *Physical Review A* 34 (1986) 1355–1362. DOI: 10.1103/physreva.34.1355.

- 
- [205] J. de Andrade, H. Stassen: Molecular dynamics studies of thermal conductivity time correlation functions, *Journal of Molecular Liquids* 110 (2004) 169–176. DOI: 10.1016/j.molliq.2003.09.012.
- [206] A. J. H. McGaughey, M. Kaviany: Thermal conductivity decomposition and analysis using molecular dynamics simulations. Part I. Lennard-Jones argon, *International Journal of Heat and Mass Transfer* 47 (2004) 1783–1798. DOI: 10.1016/j.ijheatmasstransfer.2003.11.002.
- [207] R. J. Hulse, R. L. Rowley, W. V. Wilding: Transient nonequilibrium molecular dynamic simulations of thermal conductivity: 1. Simple fluids, *International Journal of Thermophysics* 26 (2005) 1–12. DOI: 10.1007/s10765-005-2349-z.
- [208] A. E. Nasrabad, R. Laghaei, B. C. Eu: Molecular theory of thermal conductivity of the Lennard-Jones fluid, *The Journal of Chemical Physics* 124 (2006) 084506. DOI: 10.1063/1.2166394.
- [209] S. Sarkar, R. P. Selvam: Molecular dynamics simulation of effective thermal conductivity and study of enhanced thermal transport mechanism in nanofluids, *Journal of Applied Physics* 102 (2007) 074302. DOI: 10.1063/1.2785009.
- [210] G. Galliero, C. Boned: Thermal conductivity of the Lennard-Jones chain fluid model, *Physical Review E* 80 (2009) 061202. DOI: 10.1103/PhysRevE.80.061202.
- [211] V. G. Baidakov, S. P. Protsenko: Metastable Lennard-Jones fluids. II. Thermal conductivity, *The Journal of Chemical Physics* 140 (2014) 214506. DOI: 10.1063/1.4880958.
- [212] D. Levesque, L. Verlet: Computer "experiments" on classical fluids. III. Time-dependent self-correlation functions, *Physical Review A* 2 (1970) 2514–2528. DOI: 10.1103/PhysRevA.2.2514.
- [213] J. Kushick, B. J. Berne: Role of attractive forces in self-diffusion in dense Lennard-Jones fluids, *The Journal of Chemical Physics* 59 (1973) 3732–3736. DOI: 10.1063/1.1680543.
- [214] P. Schofield: Computer simulation studies of the liquid state, *Computer Physics Communications* 5 (1973) 17–23. DOI: 10.1016/0010-4655(73)90004-0.
- [215] J. P. J. Michels, N. J. Trappeniers: Molecular-dynamical calculations of the self-diffusion coefficient below the critical density, *Chemical Physics Letters* 33 (1975) 195–200. DOI: 10.1016/0009-2614(75)80136-9.

- [216] S.-H. Chen, A. Rahman: Molecular dynamics simulation of dense gases, *Molecular Physics* 34 (1977) 1247–1262. DOI: 10.1080/00268977700102521.
- [217] J. P. J. Michels, N. J. Trappeniers: The self-diffusion coefficient in the gas phase at moderate densities, obtained by computer simulations, *Physica A: Statistical Mechanics and its Applications* 90 (1978) 179–195. DOI: 10.1016/0378-4371(78)90108-5.
- [218] D. M. Heyes: Molecular dynamics at constant pressure and temperature, *Chemical Physics* 82 (1983) 285–301. DOI: 10.1016/0301-0104(83)85235-5.
- [219] C. Hoheisel, R. Vogelsang: Thermal transport coefficients for one-and two-component liquids from time correlation functions computed by molecular dynamics, *Computer Physics Reports* 8 (1988) 1–69. DOI: 10.1016/0167-7977(88)90007-X.
- [220] J. E. Straub: Analysis of the role of attractive forces in self-diffusion of a simple fluid, *Molecular Physics* 76 (1992) 373–385. DOI: 10.1080/00268979200101391.
- [221] M. J. Nuevo, J. J. Morales, D. M. Heyes: Temperature and density dependence of the self-diffusion coefficient and Mori coefficients of Lennard-Jones fluids by molecular dynamics simulation, *Physical Review E* 55 (1997) 4217–4224. DOI: 10.1103/physreve.55.4217.
- [222] L. Coelho, J. V. de Oliveira, F. W. Tavares, M. A. Matthews: Role of attractive forces in self-diffusion and mutual diffusion in dense simple fluids and real substances, *Fluid Phase Equilibria* 194-197 (2002) 1131–1140. DOI: 10.1016/S0378-3812(01)00662-8.
- [223] S. Marinakis, J. Samios: The temperature and density dependence of fluid xenon self-diffusion coefficients: a comparison between experimental, theoretical and molecular dynamics results, *The Journal of Supercritical Fluids* 34 (2005) 81–89. DOI: 10.1016/j.supflu.2004.10.002.
- [224] L. Wei-Zhong, C. Cong, Y. Jian: Molecular dynamics simulation of self-diffusion coefficient and its relation with temperature using simple Lennard-Jones potential, *Heat Transfer - Asian Research* 37 (2008) 86–93. DOI: 10.1002/htj.20191.
- [225] V. G. Baidakov, S. P. Protsenko, Z. R. Kozlova: The self-diffusion coefficient in stable and metastable states of the Lennard-Jones fluid, *Fluid Phase Equilibria* 305 (2011) 106–113. DOI: 10.1016/j.fluid.2011.03.002.

- [226] L. López Flores, J. M. Olais-Govea, M. Chávez-Páez, M. Medina-Noyola: Effect of attractions on the hard-sphere dynamic universality class, *Physical Review E* 103 (2021) 050602. DOI: 10.1103/PhysRevE.103.L050602.
- [227] L. López Flores: Private communication, data from Ref. 226 (2024).
- [228] S. Toxvaerd: Role of the attractive forces in a supercooled liquid, *Physical Review E* 103 (2021) 022611. DOI: 10.1103/PhysRevE.103.022611.
- [229] X. Ji: Diffusion model of Lennard-Jones fluids based on the radial distribution function, *The Journal of Physical Chemistry B* 126 (2022) 9008–9015. DOI: 10.1021/acs.jpcc.2c04019.
- [230] N. O. Atamas, K. S. Yablochkova, D. A. Gavryushenko, M. M. Lazarenko: Structure and dynamic inhomogeneity of liquids on the liquid-gas coexistence curve near the triple point, *Journal of Phase Equilibria and Diffusion* 44 (2023) 704–713. DOI: 10.1007/s11669-023-01070-y.
- [231] N. O. Atamas: Private communication, data from Ref. 230 (2024).
- [232] L. Marchioni, M. A. Di Muro, M. Hoyuelos: Dependence on the thermodynamic state of self-diffusion of pseudo-hard-sphere and Lennard-Jones potentials, *Physical Review E* 107 (2023) 014134. DOI: 10.1103/PhysRevE.107.014134.
- [233] S. Schmitt, J. Vrabc, H. Hasse, S. Stephan: Transport Properties of the Lennard-Jones Fluid: Database and Data Assessment, in preparation (2024).
- [234] S. Stephan, J. Staubach, H. Hasse: Review and comparison of equations of state for the Lennard-Jones fluid, *Fluid Phase Equilibria* 523 (2020) 112772. DOI: 10.1016/j.fluid.2020.112772.
- [235] J. V. Sengers: Transport properties of fluids near critical points, *International Journal of Thermophysics* 6 (1985) 203–232. DOI: 10.1007/BF00522145.
- [236] R. A. Perkins, J. V. Sengers: A note on the critical enhancement of transport properties and correlation length of fluids, *International Journal of Thermophysics* 34 (2013) 2046–2052. DOI: 10.1007/s10765-013-1519-7.
- [237] I. Bodnár, J. K. G. Dhont: Strong critical enhancement of the shear viscosity of colloidal systems, *Physical Review Letters* 77 (1996) 5304–5307. DOI: 10.1103/PhysRevLett.77.5304.

- [238] A. J. Schultz, D. A. Kofke: Comprehensive high-precision high-accuracy equation of state and coexistence properties for classical Lennard-Jones crystals and low-temperature fluid phases, *The Journal of Chemical Physics* 149 (2018) 204508. DOI: 10.1063/1.5053714.
- [239] A. J. Schultz, D. A. Kofke: Erratum: Comprehensive high-precision high-accuracy equation of state and coexistence properties for classical Lennard-Jones crystals and low-temperature fluid phases [J. Chem. Phys. 149, 204508 (2018)], *The Journal of Chemical Physics* 153 (2020) 059901. DOI: 10.1063/5.0021283.
- [240] E. Braun, J. Gilmer, H. B. Mayes, D. L. Mobley, J. I. Monroe, S. Prasad, D. M. Zuckerman: Best practices for foundations in molecular simulations [article v1.0], *Living Journal of Computational Molecular Science* 1 (2019). DOI: 10.33011/livecoms.1.1.5957.
- [241] M. Abraham, R. Apostolov, J. Barnoud, P. Bauer, C. Blau, A. M. Bonvin, M. Chavent, J. Chodera, K. ondi Jurki, L. Delemotte, H. Grubmüller, R. J. Howard, E. J. Jordan, E. Lindahl, O. H. S. Ollila, J. Selent, D. G. A. Smith, P. J. Stansfeld, J. K. Tiemann, M. Trellet, C. Woods, A. Zhmurov: Sharing data from molecular simulations, *Journal of Chemical Information and Modeling* 59 (2019) 4093–4099. DOI: 10.1021/acs.jcim.9b00665.
- [242] T. A. Soares, Z. Cournia, K. Naidoo, R. Amaro, H. Wahab, K. M. J. Merz: Guidelines for reporting molecular dynamics simulations in JCIM publications, *Journal of Chemical Information and Modeling* 63 (2023) 3227–3229. DOI: 10.1021/acs.jcim.3c00599.
- [243] Reliability and reproducibility checklist for molecular dynamics simulations, *Communications Biology* 6 (2023) 1–2. DOI: 10.1038/s42003-023-04653-0.
- [244] N. Jackson, J. M. Rubi, F. Bresme: Non-equilibrium molecular dynamics simulations of the thermal transport properties of Lennard-Jones fluids using configurational temperatures, *Molecular Simulation* 42 (2016) 1214–1222. DOI: 10.1080/08927022.2016.1168926.
- [245] S. A. Khrapak, A. G. Khrapak: Freezing temperature and density scaling of transport coefficients, *The Journal of Physical Chemistry Letters* 13 (2022) 2674–2678. DOI: 10.1021/acs.jpcllett.2c00408.
- [246] O. O. Odeyemi: Structure and transport coefficients of liquid Argon and neon using molecular dynamics simulation, *IOSR Journal of Applied Physics* 5 (2014) 52–59. DOI: 10.9790/4861-0555259.



- [247] N. Ohtori, Y. Ishii, Y. Togawa, T. Oono, K. Takase: Thermal conductivity of simple liquids: temperature and packing-fraction dependence, *Physical Review. E* 89 (2014) 022129. DOI: 10.1103/PhysRevE.89.022129.
- [248] N. Ohtori, Y. Ishii: Explicit expression for the Stokes-Einstein relation for pure Lennard-Jones liquids, *Physical Review. E* 91 (2015) 012111. DOI: 10.1103/PhysRevE.91.012111.
- [249] N. Tchouar, F. Ould-Kaddour, D. Levesque: Computation of the properties of liquid neon, methane, and gas helium at low temperature by the Feynman-Hibbs approach, *The Journal of Chemical Physics* 121 (2004) 7326–7331. DOI: 10.1063/1.1794651.
- [250] J. Hurly, M. Moldover: Ab initio values of the thermophysical properties of helium as standards, *Journal of Research of the National Institute of Standards and Technology* 105 (2000) 667–688. DOI: 10.6028/jres.105.054.
- [251] L. A. Viehland, A. R. Janzen, R. A. Aziz: High approximations to the transport properties of pure atomic gases, *The Journal of Chemical Physics* 102 (1995) 5444–5450. DOI: 10.1063/1.469272.
- [252] A. Ahuja, R. Lee, Y. M. Joshi: Advances and challenges in the high-pressure rheology of complex fluids, *Advances in Colloid and Interface Science* 294 (2021) 102472. DOI: 10.1016/j.cis.2021.102472.
- [253] V. Jadhao, M. O. Robbins: Probing large viscosities in glass-formers with nonequilibrium simulations, *Proceedings of the National Academy of Sciences* 114 (2017) 7952–7957. DOI: 10.1073/pnas.1705978114.
- [254] C. McCabe, S. Cui, P. T. Cummings: Characterizing the viscosity-temperature dependence of lubricants by molecular simulation, *Fluid Phase Equilibria* 183-184 (2001) 363–370. DOI: 10.1016/S0378-3812(01)00448-4.
- [255] P. Liu, H. Yu, N. Ren, F. E. Lockwood, Q. J. Wang: Pressure-viscosity coefficient of hydrocarbon base oil through molecular dynamics simulations, *Tribology Letters* 60 (2015) 34. DOI: 10.1007/s11249-015-0610-6.
- [256] N. D. Kondratyuk, V. V. Pisarev: Calculation of viscosities of branched alkanes from 0.1 to 1000 MPa by molecular dynamics methods using COMPASS force field, *Fluid Phase Equilibria* 498 (2019) 151–159. DOI: 10.1016/j.fluid.2019.06.023.
- [257] D. Mathas, W. Holweger, M. Wolf, C. Bohnert, V. Bakolas, J. Procelewska, L. Wang, S. Bair, C.-K. Skylaris: Evaluation of methods for viscosity simulations

- of lubricants at different temperatures and pressures: A case study on PAO-2, *Tribology Transactions* 64 (2021) 1138–1148. DOI: 10.1080/10402004.2021.1922790.
- [258] N. D. Kondratyuk, V. V. Pisarev, J. P. Ewen: Probing the high-pressure viscosity of hydrocarbon mixtures using molecular dynamics simulations, *The Journal of Chemical Physics* 153 (2020) 154502. DOI: 10.1063/5.0028393.
- [259] N. D. Kondratyuk, V. V. Pisarev: Predicting shear viscosity of 1,1-diphenylethane at high pressures by molecular dynamics methods, *Fluid Phase Equilibria* 544–545 (2021) 113100. DOI: 10.1016/j.fluid.2021.113100.
- [260] S. Becker, H. M. Urbassek, M. Horsch, H. Hasse: Contact angle of sessile drops in Lennard-Jones systems, *Langmuir* 30 (2014) 13606–13614. DOI: 10.1021/la503974z.
- [261] M. Heier, S. Stephan, F. Diewald, R. Müller, K. Langenbach, H. Hasse: Molecular dynamics study of wetting and adsorption of binary mixtures of the Lennard-Jones truncated and shifted fluid on a planar wall, *Langmuir* 37 (2021) 7405–7419. DOI: 10.1021/acs.langmuir.1c00780.
- [262] T. Q. Vo, B. Park, C. Park, B. Kim: Nano-scale liquid film sheared between strong wetting surfaces: Effects of interface region on the flow, *Journal of Mechanical Science and Technology* 29 (2015) 1681–1688. DOI: 10.1007/s12206-015-0340-6.
- [263] S. Schmitt, S. Stephan, B. Kirsch, J. C. Aurich, E. Kerscher, H. M. Urbassek, H. Hasse: Molecular simulation study on the influence of the scratching velocity on nanoscopic contact processes, 2nd International Conference of the DFG International Research Training Group 2057 - Physical Modeling for Virtual Manufacturing (iPMVM 2020) 89 (2021) 17:1–17:16. DOI: 10.4230/OASIScs.iPMVM.2020.17.
- [264] S. Stephan, M. Dyga, H. M. Urbassek, H. Hasse: The influence of lubrication and the solid-fluid interaction on thermodynamic properties in a nanoscopic scratching process, *Langmuir* 35 (2019) 16948–16960. DOI: 10.1021/acs.langmuir.9b01033.
- [265] S. Stephan, M. P. Lautenschlaeger, I. A. Alhafez, M. T. Horsch, H. M. Urbassek, H. Hasse: Molecular dynamics simulation study of mechanical effects of lubrication on a nanoscale contact process, *Tribology Letters* 66 (2018) 126. DOI: 10.1007/s11249-018-1076-0.

- [266] T. D. Ta, A. K. Tieu, H. Zhu, B. Kosasih, Q. Zhu, H. T. Phan: The structural, tribological, and rheological dependency of thin hexadecane film confined between iron and iron oxide surfaces under sliding conditions, *Tribology International* 113 (2017) 26–35. DOI: 10.1016/j.triboint.2016.12.001.
- [267] Y. Gao, A. Brodyanski, M. Kopnarski, H. M. Urbassek: Nanoscratching of iron: A molecular dynamics study of the influence of surface orientation and scratching direction, *Computational Materials Science* 103 (2015) 77–89. DOI: 10.1016/j.commatsci.2015.03.011.
- [268] I. A. Alhafez, C. J. Ruestes, Y. Gao, H. M. Urbassek: Nanoindentation of hcp metals: A comparative simulation study of the evolution of dislocation networks, *Nanotechnology* 27 (2016) 045706. DOI: 10.1088/0957-4484/27/4/045706.
- [269] H. Washizu, T. Ohmori, A. Suzuki: Molecular origin of limiting shear stress of elastohydrodynamic lubrication oil film studied by molecular dynamics, *Chemical Physics Letters* 678 (2017) 1–4. DOI: 10.1016/j.cplett.2017.04.020.
- [270] S. Tromp, L. Joly, M. Cobian, N. Fillot: Tribological performance of the R1233zd refrigerant in extreme confinement at the nanoasperity level: A molecular dynamics study using an ab initio-based force field, *Tribology Letters* 67 (2019) 67. DOI: 10.1007/s11249-019-1180-9.
- [271] L. I. Kioupis, E. J. Maginn: Molecular simulation of poly- $\alpha$ -olefin synthetic lubricants: Impact of molecular architecture on performance properties, *The Journal of Physical Chemistry B* 103 (1999) 10781–10790. DOI: 10.1021/jp992399n.
- [272] N. Kondratyuk, D. Lenev, V. Pisarev: Transport coefficients of model lubricants up to 400 MPa from molecular dynamics, *The Journal of Chemical Physics* 152 (2020) 191104. DOI: 10.1063/5.0008907.
- [273] J. Ewen, C. Gattinoni, F. Thakkar, N. Morgan, H. Spikes, D. Dini: A comparison of classical force-fields for molecular dynamics simulations of lubricants, *Materials* 9 (2016) 651. DOI: 10.3390/ma9080651.
- [274] P. Liu, J. Lu, H. Yu, N. Ren, F. E. Lockwood, Q. J. Wang: Lubricant shear thinning behavior correlated with variation of radius of gyration via molecular dynamics simulations, *The Journal of Chemical Physics* 147 (2017) 084904. DOI: 10.1063/1.4986552.
- [275] V. Jadhao, M. O. Robbins: Rheological properties of liquids under conditions of elastohydrodynamic lubrication, *Tribology Letters* 67 (2019) 66. DOI: 10.1007/s11249-019-1178-3.

- [276] V. Pisarev, N. Kondratyuk: Prediction of viscosity-density dependence of liquid methane+*n*-butane+*n*-pentane mixtures using the molecular dynamics method and empirical correlations, *Fluid Phase Equilibria* 501 (2019) 112273. DOI: 10.1016/j.fluid.2019.112273.
- [277] M. A. Galvani Cunha, M. O. Robbins: Determination of pressure-viscosity relation of 2,2,4-trimethylhexane by all-atom molecular dynamics simulations, *Fluid Phase Equilibria* 495 (2019) 28–32. DOI: 10.1016/j.fluid.2019.05.008.
- [278] S. Bair: The high pressure rheology of some simple model hydrocarbons, *Proceedings of the Institution of Mechanical Engineers, Part J: Journal of Engineering Tribology* 216 (2002) 139–149. DOI: 10.1243/1350650021543960.
- [279] J. A. Harrison, J. D. Schall, S. Maskey, P. T. Mikulski, M. T. Knippenberg, B. H. Morrow: Review of force fields and intermolecular potentials used in atomistic computational materials research, *Applied Physics Reviews* 5 (2018) 031104. DOI: 10.1063/1.5020808.
- [280] B. H. Morrow, J. A. Harrison: Evaluating the ability of selected force fields to simulate hydrocarbons as a function of temperature and pressure using molecular dynamics, *Energy & Fuels* 35 (2021) 3742 – 3752. DOI: 10.1021/acs.energyfuels.0c03363.
- [281] R. Benda, J. Bullen, A. Plomer: Synthetics basics: Polyalphaolefins – base fluids for high-performance lubricants, *Journal of Synthetic Lubrication* 13 (1996) 41–57. DOI: 10.1002/jsl.3000130105.
- [282] V. Bürk, S. Pollak, S. E. Quiñones-Cisneros, K. A. G. Schmidt: Complementary experimental data and extended density and viscosity reference models for squalane, *Journal of Chemical & Engineering Data* 66 (2021) 1992 – 2005. DOI: 10.1021/acs.jced.0c01058.
- [283] R. Ciriminna, V. Pandarus, F. Béland, M. Pagliaro: Catalytic hydrogenation of squalene to squalane, *Organic Process Research & Development* 18 (2014) 1110–1115. DOI: 10.1021/op5002337.
- [284] A. Verma, R. Cracknell, D. Doyle, I. Rudra: Determination of diesel physical properties at injection pressures and temperatures via all-atom molecular simulations, *SAE International Journal of Fuels and Lubricants* 9 (2016) 567–574. DOI: 10.4271/2016-01-2253.
- [285] S. A. Burrows, I. Korotkin, S. K. Smoukov, E. Boek, S. Karabasov: Benchmarking of molecular dynamics force fields for solid-liquid and solid-solid phase transitions

- in alkanes, *The Journal of Physical Chemistry B* 125 (2021) 5145 – 5159. DOI: 10.1021/acs.jpccb.0c07587.
- [286] M. P. Oliveira, Y. M. H. Gonçalves, S. K. Ol Gheta, S. R. Rieder, B. A. C. Horta, P. H. Hünenberger: Comparison of the united- and all-atom representations of (halo)alkanes based on two condensed-phase force fields optimized against the same experimental data set, *Journal of Chemical Theory and Computation* 18 (2022) 6757–6778. DOI: 10.1021/acs.jctc.2c00524.
- [287] A. W. S. Hamani, J.-P. Bazile, H. Hoang, H. T. Luc, J.-L. Daridon, G. Galliero: Thermophysical properties of simple molecular liquid mixtures: On the limitations of some force fields, *Journal of Molecular Liquids* 303 (2020) 112663. DOI: 10.1016/j.molliq.2020.112663.
- [288] G. C. Q. da Silva, G. M. Silva, F. W. Tavares, F. P. Fleming, B. A. C. Horta: Are all-atom any better than united-atom force fields for the description of liquid properties of alkanes?, *Journal of Molecular Modeling* 26 (2020) 296. DOI: 10.1007/s00894-020-04548-5.
- [289] K. D. Papavasileiou, L. D. Peristeras, A. Bick, I. G. Economou: Molecular dynamics simulation of pure *n*-alkanes and their mixtures at elevated temperatures using atomistic and coarse-grained force fields, *The Journal of Physical Chemistry B* 123 (2019) 6229–6243. DOI: 10.1021/acs.jpccb.9b02840.
- [290] L. Lin, M. A. Kedzierski: Density and viscosity of a polyol ester lubricant: Measurement and molecular dynamics simulation, *International Journal of Refrigeration* 118 (2020) 188–201. DOI: 10.1016/j.ijrefrig.2020.07.004.
- [291] R. A. Messerly, M. C. Anderson, S. M. Razavi, J. R. Elliott: Improvements and limitations of Mie  $\lambda$ -6 potential for prediction of saturated and compressed liquid viscosity, *Fluid Phase Equilibria* 483 (2019) 101–115. DOI: 10.1016/j.fluid.2018.11.002.
- [292] U. Welling, G. Germano: Efficiency of linked cell algorithms, *Computer Physics Communications* 182 (2011) 611–615. DOI: 10.1016/j.cpc.2010.11.002.
- [293] S. J. Plimpton, A. P. Thompson: Computational aspects of many-body potentials, *MRS Bulletin* 37 (2012) 513–521. DOI: 10.1557/mrs.2012.96.
- [294] A. Y. Toukmaji, J. A. Board: Ewald summation techniques in perspective: A survey, *Computer Physics Communications* 95 (1996) 73–92. DOI: 10.1016/0010-4655(96)00016-1.

- [295] M. Tuckerman, B. J. Berne, G. J. Martyna: Reversible multiple time scale molecular dynamics, *The Journal of Chemical Physics* 97 (1992) 1990–2001. DOI: 10.1063/1.463137.
- [296] J.-P. Ryckaert, G. Ciccotti, H. J. Berendsen: Numerical integration of the cartesian equations of motion of a system with constraints: Molecular dynamics of n-alkanes, *Journal of Computational Physics* 23 (1977) 327–341. DOI: 10.1016/0021-9991(77)90098-5.
- [297] E. Pollock, J. Glosli: Comments on P3M, FMM, and the Ewald method for large periodic Coulombic systems, *Computer Physics Communications* 95 (1996) 93–110. DOI: 10.1016/0010-4655(96)00043-4.
- [298] A. P. Thompson, H. M. Aktulga, R. Berger, D. S. Bolintineanu, W. M. Brown, P. S. Crozier, P. J. in 't Veld, A. Kohlmeyer, S. G. Moore, T. D. Nguyen, R. Shan, M. J. Stevens, J. Tranchida, C. Trott, S. J. Plimpton: LAMMPS - a flexible simulation tool for particle-based materials modeling at the atomic, meso, and continuum scales, *Computer Physics Communications* 271 (2022) 108171. DOI: 10.1016/j.cpc.2021.108171.
- [299] S. Nosé: A molecular dynamics method for simulations in the canonical ensemble, *Molecular Physics* 52 (1984) 255–268. DOI: 10.1080/00268978400101201.
- [300] W. G. Hoover: Canonical dynamics: Equilibrium phase-space distributions, *Physical Review A* 31 (1985) 1695–1697. DOI: 10.1103/PhysRevA.31.1695.
- [301] W. Shinoda, M. Shiga, M. Mikami: Rapid estimation of elastic constants by molecular dynamics simulation under constant stress, *Physical Review B* 69 (2004) 134103. DOI: 10.1103/PhysRevB.69.134103.
- [302] V. Calandrini, E. Pellegrini, P. Calligari, K. Hinsén, G. R. Kneller: nMoldyn - Interfacing spectroscopic experiments, molecular dynamics simulations and models for time correlation functions, *École thématique de la Société Française de la Neutronique* 12 (2011) 201–232. DOI: 10.1051/sfn/201112010.
- [303] H. Liu, E. Maginn, A. E. Visser, N. J. Bridges, E. B. Fox: Thermal and transport properties of six ionic liquids: An experimental and molecular dynamics study, *Industrial & Engineering Chemistry Research* 51 (2012) 7242–7254. DOI: 10.1021/ie300222a.
- [304] B. Hess: Determining the shear viscosity of model liquids from molecular dynamics simulations, *The Journal of Chemical Physics* 116 (2002) 209. DOI: 10.1063/1.1421362.

- [305] M. Mondello, G. S. Grest: Viscosity calculations of *n*-alkanes by equilibrium molecular dynamics, *The Journal of Chemical Physics* 106 (1997) 9327–9336. DOI: 10.1063/1.474002.
- [306] O. A. Moulton, Y. Zhang, I. N. Tsimpanogiannis, I. G. Economou, E. J. Maginn: System-size corrections for self-diffusion coefficients calculated from molecular dynamics simulations: The case of CO<sub>2</sub>, *n*-alkanes, and poly(ethylene glycol) dimethyl ethers, *The Journal of Chemical Physics* 145 (2016) 074109. DOI: 10.1063/1.4960776.
- [307] S. W. I. Siu, K. Pluhackova, R. A. Böckmann: Optimization of the OPLS-AA force field for long hydrocarbons, *Journal of Chemical Theory and Computation* 8 (2012) 1459–1470. DOI: 10.1021/ct200908r.
- [308] W. Zhang, A. C. T. van Duin: Improvement of the ReaxFF description for functionalized hydrocarbon/water weak interactions in the condensed phase, *The Journal of Physical Chemistry B* 122 (2018) 4083–4092. DOI: 10.1021/acs.jpcc.8b01127.
- [309] T. C. O'Connor, J. Andzelm, M. O. Robbins: AIREBO-M: A reactive model for hydrocarbons at extreme pressures, *The Journal of Chemical Physics* 142 (2015) 024903. DOI: 10.1063/1.4905549.
- [310] M. G. Martin, J. I. Siepmann: Novel configurational-bias Monte Carlo method for branched molecules. Transferable potentials for phase equilibria. 2. United-atom description of branched alkanes, *The Journal of Physical Chemistry B* 103 (1999) 4508–4517. DOI: 10.1021/jp984742e.
- [311] J. R. Mick, M. Soroush Barhaghi, B. Jackman, L. Schwiebert, J. J. Potoff: Optimized Mie potentials for phase equilibria: Application to branched alkanes, *Journal of Chemical & Engineering Data* 62 (2017) 1806–1818. DOI: 10.1021/acs.jced.6b01036.
- [312] D. Weidler, J. Gross: Individualized force fields for alkanes, olefins, ethers and ketones based on the transferable anisotropic Mie potential, *Fluid Phase Equilibria* 470 (2018) 101–108. DOI: 10.1016/j.fluid.2018.02.012.
- [313] S. J. Marrink, H. J. Risselada, S. Yefimov, D. P. Tieleman, A. H. de Vries: The MARTINI force field: Coarse grained model for biomolecular simulations, *The Journal of Physical Chemistry B* 111 (2007) 7812–7824. DOI: 10.1021/jp071097f.

- [314] A. C. T. van Duin, S. Dasgupta, F. Lorant, W. A. Goddard: ReaxFF: A reactive force field for hydrocarbons, *The Journal of Physical Chemistry A* 105 (2001) 9396–9409. DOI: 10.1021/jp004368u.
- [315] S. J. Stuart, A. B. Tutein, J. A. Harrison: A reactive potential for hydrocarbons with intermolecular interactions, *The Journal of Chemical Physics* 112 (2000) 6472–6486. DOI: 10.1063/1.481208.
- [316] K. S. Rane, S. Murali, J. R. Errington: Monte Carlo simulation methods for computing liquid-vapor saturation properties of model systems, *Journal of Chemical Theory and Computation* 9 (2013) 2552–2566. DOI: 10.1021/ct400074p.
- [317] S. Patel, W. V. Wilding, R. L. Rowley: The use of two-phase molecular dynamics simulations to determine the phase behavior and critical point of propane molecular models, *The Journal of Chemical Physics* 134 (2011) 024101. DOI: 10.1063/1.3528117.
- [318] P. A. Gordon: Development of intermolecular potentials for predicting transport properties of hydrocarbons, *The Journal of Chemical Physics* 125 (2006) 014504. DOI: 10.1063/1.2208359.
- [319] Z. Jarin, J. Newhouse, G. A. Voth: Coarse-grained force fields from the perspective of statistical mechanics: Better understanding of the origins of a MARTINI hangover, *Journal of Chemical Theory and Computation* 17 (2021) 1170–1180. DOI: 10.1021/acs.jctc.0c00638.
- [320] T. Bereau, K. Kremer: Automated parametrization of the coarse-grained Martini force field for small organic molecules, *Journal of Chemical Theory and Computation* 11 (2015) 2783–2791. DOI: 10.1021/acs.jctc.5b00056.
- [321] J. A. Graham, J. W. Essex, S. Khalid: PyCGTOOL: Automated generation of coarse-grained molecular dynamics models from atomistic trajectories, *Journal of Chemical Information and Modeling* 57 (2017) 650–656. DOI: 10.1021/acs.jcim.7b00096.
- [322] T. D. Potter, E. L. Barrett, M. A. Miller: Automated coarse-grained mapping algorithm for the MARTINI force field and benchmarks for membrane-water partitioning, *Journal of Chemical Theory and Computation* 17 (2021) 5777–5791. DOI: 10.1021/acs.jctc.1c00322.
- [323] P. C. T. Souza, R. Alessandri, J. Barnoud, S. Thallmair, I. Faustino, F. Grünewald, I. Patmanidis, H. Abdizadeh, B. M. H. Bruininks, T. A. Wassenaar, P. C. Kroon, J. Melcr, V. Nieto, V. Corradi, H. M. Khan, J. Domaski, M. Javanainen,



- H. Martinez-Seara, N. Reuter, R. B. Best, I. Vattulainen, L. Monticelli, X. Periole, D. P. Tieleman, A. H. de Vries, S. J. Marrink: Martini 3: A general purpose force field for coarse-grained molecular dynamics, *Nature Methods* 18 (2021) 382–388. DOI: 10.1038/s41592-021-01098-3.
- [324] K. Liu, Y. Wu, M. A. McHugh, H. Baled, R. M. Enick, B. D. Morreale: Equation of state modeling of high-pressure, high-temperature hydrocarbon density data, *The Journal of Supercritical Fluids* 55 (2010) 701–711. DOI: 10.1016/j.supflu.2010.10.004.
- [325] D. R. Caudwell, J. P. M. Trusler, V. Vesovic, W. A. Wakeham: Viscosity and density of five hydrocarbon liquids at pressures up to 200 MPa and temperatures up to 473 K, *Journal of Chemical & Engineering Data* 54 (2009) 359–366. DOI: 10.1021/je800417q.
- [326] F. Audonnet, A. A. H. Pádua: Viscosity and density of mixtures of methane and n-decane from 298 to 393 K and up to 75 MPa, *Fluid Phase Equilibria* 216 (2004) 235–244. DOI: 10.1016/j.fluid.2003.10.017.
- [327] C. M. B. P. Oliveira, W. A. Wakeham: The viscosity of five liquid hydrocarbons at pressures up to 250 MPa, *International Journal of Thermophysics* 13 (1992) 773–790. DOI: 10.1007/BF00503906.
- [328] L.-D. Naake, G. Wiegand, E. U. Franck: The viscosity of n-decane to high temperatures of 573 K and high pressures of 300 MPa, *Zeitschrift für Physikalische Chemie* 216 (2002) 1295 – 1310. DOI: 10.1524/zpch.2002.216.11.1295.
- [329] O. Suárez-Iglesias, I. Medina, M. Sanz, C. Pizarro, J. L. Bueno: Self-diffusion in molecular fluids and noble gases: Available data, *Journal of Chemical & Engineering Data* 60 (2015) 2757–2817. DOI: 10.1021/acs.jced.5b00323.
- [330] A. K. Doolittle: Specific volumes of *n*-alkanes, *Journal of Chemical & Engineering Data* 9 (1964) 275–279. DOI: 10.1021/je60021a048.
- [331] Y. Wu, B. Bamgbade, K. Liu, M. A. McHugh, H. Baled, R. M. Enick, W. A. Burgess, D. Tapriyal, B. D. Morreale: Experimental measurements and equation of state modeling of liquid densities for long-chain *n*-alkanes at pressures to 265 MPa and temperatures to 523 K, *Fluid Phase Equilibria* 311 (2011) 17–24. DOI: 10.1016/j.fluid.2011.08.020.
- [332] H. O. Baled, D. Xing, H. Katz, D. Tapriyal, I. K. Gamwo, Y. Soong, B. A. Bamgbade, Y. Wu, K. Liu, M. A. McHugh, R. M. Enick: Viscosity of *n*-hexadecane, *n*-octadecane and *n*-eicosane at pressures up to 243MPa and temperatures up

- to 534K, *The Journal of Chemical Thermodynamics* 72 (2014) 108–116. DOI: 10.1016/j.jct.2014.01.008.
- [333] T. Vardag, N. Karger, H.-D. Lüdemann: Temperature and pressure dependence of self diffusion in long liquid *n*-alkanes, *Berichte der Bunsengesellschaft für physikalische Chemie* 95 (1991) 859–865. DOI: 10.1002/bbpc.19910950803.
- [334] F. Ciotta, G. Maitland, M. Smietana, J. P. M. Trusler, V. Vesovic: Viscosity and density of carbon dioxide + 2,6,10,15,19,23-hexamethyltetracosane (squalane), *Journal of Chemical & Engineering Data* 55 (2010) 4126–4126. DOI: 10.1021/je1008153.
- [335] A. J. Rowane, R. R. Mallepally, A. Gupta, M. Gavaises, M. A. McHugh: High-temperature, high-pressure viscosities and densities of *n*-hexadecane, 2,2,4,4,6,8,8-heptamethylnonane, and squalane measured using a universal calibration for a rolling-ball viscometer/densimeter, *Industrial & Engineering Chemistry Research* 58 (2019) 4303–4316. DOI: 10.1021/acs.iecr.8b05952.
- [336] B. A. Bamgbade, Y. Wu, W. A. Burgess, D. Tapriyal, I. K. Gamwo, H. O. Baled, R. M. Enick, M. A. McHugh: High-temperature, high-pressure volumetric properties of propane, squalane, and their mixtures: Measurement and PC-SAFT modeling, *Industrial & Engineering Chemistry Research* 54 (2015) 6804–6811. DOI: 10.1021/acs.iecr.5b01173.
- [337] K. A. G. Schmidt, D. Pagnutti, M. D. Curran, A. Singh, J. P. M. Trusler, G. C. Maitland, M. McBride-Wright: New experimental data and reference models for the viscosity and density of squalane, *Journal of Chemical & Engineering Data* 60 (2015) 137–150. DOI: 10.1021/je5008789.
- [338] S. Bair: Reference liquids for quantitative elasto-hydrodynamics: Selection and rheological characterization, *Tribology Letters* 22 (2006) 197–206. DOI: 10.1007/s11249-006-9083-y.
- [339] L. L. Thomas, T. J. Christakis, W. L. Jorgensen: Conformation of alkanes in the gas phase and pure liquids, *The Journal of Physical Chemistry B* 110 (2006) 21198–21204. DOI: 10.1021/jp064811m.
- [340] O. A. Moulton, I. N. Tsimpanogiannis, A. Z. Panagiotopoulos, J. P. M. Trusler, I. G. Economou: Atomistic molecular dynamics simulations of carbon dioxide diffusivity in *n*-hexane, *n*-decane, *n*-hexadecane, cyclohexane, and squalane, *The Journal of Physical Chemistry B* 120 (2016) 12890–12900. DOI: 10.1021/acs.jpcc.6b04651.

- [341] N. D. Kondratyuk: Comparing different force fields by viscosity prediction for branched alkane at 0.1 and 400 MPa, *Journal of Physics: Conference Series* 1385 (2019) 012048. DOI: 10.1088/1742-6596/1385/1/012048.
- [342] A. Einstein: Über die von der molekularkinetischen Theorie der Wärme geforderte Bewegung von in ruhenden Flüssigkeiten suspendierten Teilchen, *Annalen der Physik* 322 (1905) 549–560. DOI: 10.1002/andp.19053220806.
- [343] T. J. dos Santos, C. R. Abreu, B. A. Horta, F. W. Tavares: Self-diffusion coefficients of methane/*n*-hexane mixtures at high pressures: An evaluation of the finite-size effect and a comparison of force fields, *The Journal of Supercritical Fluids* 155 (2020) 104639. DOI: 10.1016/j.supflu.2019.104639.
- [344] B. Eckl, J. Vrabec, H. Hasse: On the application of force fields for predicting a wide variety of properties: Ethylene oxide as an example, *Fluid Phase Equilibria* 274 (2008) 16–26. DOI: 10.1016/j.fluid.2008.02.002.
- [345] C. G. Aimoli, E. J. Maginn, C. R. A. Abreu: Thermodynamic properties of supercritical mixtures of carbon dioxide and methane: A molecular simulation study, *Journal of Chemical & Engineering Data* 59 (2014) 3041–3054. DOI: 10.1021/je500120v.
- [346] R. B. Getman, Y.-S. Bae, C. E. Wilmer, R. Q. Snurr: Review and analysis of molecular simulations of methane, hydrogen, and acetylene storage in metal-organic frameworks, *Chemical Reviews* 112 (2012) 703–723. DOI: 10.1021/cr200217c.
- [347] D. Bedrov, J.-P. Piquemal, O. Borodin, A. D. J. MacKerell, B. Roux, C. Schröder: Molecular dynamics simulations of ionic liquids and electrolytes using polarizable force fields, *Chemical Reviews* 119 (2019) 7940–7995. DOI: 10.1021/acs.chemrev.8b00763.
- [348] M. Urschel, S. Stephan: Determining Browns characteristic curves using molecular simulation, *Journal of Chemical Theory and Computation* 19 (2023) 1537–1552. DOI: 10.1021/acs.jctc.2c01102.
- [349] G. Guevara-Carrion, T. Janzen, Y. M. Muñoz-Muñoz, J. Vrabec: Mutual diffusion of binary liquid mixtures containing methanol, ethanol, acetone, benzene, cyclohexane, toluene, and carbon tetrachloride, *The Journal of Chemical Physics* 144 (2016) 124501. DOI: 10.1063/1.4943395.
- [350] I. Nitzke, J. Vrabec: Numerical discrimination of thermodynamic Monte Carlo simulations in all eight statistical ensembles, *Journal of Chemical Theory and Computation* 19 (2023) 3460–3468. DOI: 10.1021/acs.jctc.3c00252.

- [351] I. Nitzke, R. Stierle, S. Stephan, M. Pfitzner, J. Gross, J. Vrabec: Phase equilibria and interface properties of hydrocarbon propellant-oxygen mixtures in the trans-critical regime, *Physics of Fluids* 35 (2023) 032117. DOI: 10.1063/5.0138973.
- [352] S. Stephan, D. Schaefer, K. Langenbach, H. Hasse: Mass transfer through vapour-liquid interfaces: A molecular dynamics simulation study, *Molecular Physics* 119 (2020) e1810798. DOI: 10.1080/00268976.2020.1810798.
- [353] S. Stephan, S. Schmitt, H. Hasse, H. M. Urbassek: Molecular dynamics simulation of the Stribeck curve: Boundary lubrication, mixed lubrication, and hydrodynamic lubrication on the atomistic level, *Friction* 11 (2023) 2342–2366. DOI: 10.1007/s40544-023-0745-y.
- [354] E. Bitzek, J. R. Kermode, P. Gumbsch: Atomistic aspects of fracture, *International Journal of Fracture* 191 (2015) 13–30. DOI: 10.1007/s10704-015-9988-2.
- [355] S. Homes, M. Heinen, J. Vrabec, J. Fischer: Evaporation driven by conductive heat transport, *Molecular Physics* 119 (2021) e1836410. DOI: 10.1080/00268976.2020.1836410.
- [356] C. J. Ruestes, I. A. Alhafez, H. M. Urbassek: Atomistic studies of nanoindentation – A review of recent advances, *Crystals* 7 (2017). DOI: 10.3390/cryst7100293.
- [357] S. Stephan, H. Hasse: Enrichment at vapour-liquid interfaces of mixtures: Establishing a link between nanoscopic and macroscopic properties, *International Reviews in Physical Chemistry* 39 (2020) 319–349. DOI: 10.1080/0144235X.2020.1777705.
- [358] W. F. van Gunsteren, H. J. C. Berendsen: Computer simulation of molecular dynamics: Methodology, applications, and perspectives in chemistry, *Angewandte Chemie International Edition in English* 29 (1990) 992–1023. DOI: 10.1002/anie.199009921.
- [359] M. E. Tuckerman, G. J. Martyna: Understanding modern molecular dynamics: Techniques and applications, *The Journal of Physical Chemistry B* 104 (2000) 159–178. DOI: 10.1021/jp992433y.
- [360] J. Spöner, G. Bussi, M. Krepl, P. Baná, S. Bottaro, R. A. Cunha, A. Gil-Ley, G. Pinamonti, S. Poblete, P. Jureka: RNA structural dynamics as captured by molecular simulations: A comprehensive overview, *Chemical Reviews* 118 (2018) 4177–4338. DOI: 10.1021/acs.chemrev.7b00427.

- [361] O. M. H. Salo-Ahen, I. Alanko, R. Bhadane, A. M. J. J. Bonvin, R. V. Honorato, S. Hossain, A. H. Juffer, A. Kabedev, M. Lahtela-Kakkonen, A. S. Larsen, E. Lescrier, P. Marimuthu, M. U. Mirza, G. Mustafa, A. Nunes-Alves, T. Pantsar, A. Saadabadi, K. Singaravelu, M. Vanmeert: Molecular dynamics simulations in drug discovery and pharmaceutical development, *Processes* 9 (2021). DOI: 10.3390/pr9010071.
- [362] M. Levitt: The birth of computational structural biology, *Nature Structural Biology* 8 (2001) 392–393. DOI: 10.1038/87545.
- [363] S. A. Hollingsworth, R. O. Dror: Molecular dynamics simulation for all, *Neuron* 99 (2018) 1129–1143. DOI: 10.1016/j.neuron.2018.08.011.
- [364] A. D. Mackerell: Empirical force fields for biological macromolecules: Overview and issues, *Journal of Computational Chemistry* 25 (2004) 1584–1604. DOI: 10.1002/jcc.20082.
- [365] J. M. Prausnitz, F. W. Tavares: Thermodynamics of fluid-phase equilibria for standard chemical engineering operations, *AIChE Journal* 50 (2004) 739–761. DOI: 10.1002/aic.10069.
- [366] J. Vrabec, M. Bernreuther, H.-J. Bungartz, W.-L. Chen, W. Cordes, R. Fingerhut, C. W. Glass, J. Gmehling, R. Hamburger, M. Heilig, M. Heinen, M. T. Horsch, C.-M. Hsieh, M. Hülsmann, P. Jäger, P. Klein, S. Knauer, T. Köddermann, A. Köster, K. Langenbach, S.-T. Lin, P. Neumann, J. Rarey, D. Reith, G. Rutkai, M. Schappals, M. Schenk, A. Schedemann, M. Schönherr, S. Seckler, S. Stephan, K. Stöbener, N. Tchipev, A. Wafai, S. Werth, H. Hasse: SkaSim – Scalable HPC software for molecular simulation in the chemical industry, *Chemie Ingenieur Technik* 90 (2018) 295–306. DOI: 10.1002/cite.201700113.
- [367] E. J. Maginn, J. R. Elliott: Historical perspective and current outlook for molecular dynamics as a chemical engineering tool, *Industrial & Engineering Chemistry Research* 49 (2010) 3059–3078. DOI: 10.1021/ie901898k.
- [368] C. Vega, J. L. F. Abascal: Simulating water with rigid non-polarizable models: A general perspective, *Physical Chemistry Chemical Physics* 13 (2011) 19663–19688. DOI: 10.1039/C1CP22168J.
- [369] O. Guvench, A. D. MacKerell: Comparison of Protein Force Fields for Molecular Dynamics Simulations, in: A. Kukol (Ed.), *Molecular Modeling of Proteins*, Springer-Humana Press, Totowa, 2008, pp. 63–88.

- [370] M. Levitt, M. Hirshberg, R. Sharon, V. Daggett: Potential energy function and parameters for simulations of the molecular dynamics of proteins and nucleic acids in solution, *Computer Physics Communications* 91 (1995) 215–231. DOI: 10.1016/0010-4655(95)00049-L.
- [371] A. Albaugh, H. A. Boateng, R. T. Bradshaw, O. N. Demerdash, J. Dziejic, Y. Mao, D. T. Margul, J. Swails, Q. Zeng, D. A. Case, P. Eastman, L.-P. Wang, J. W. Essex, M. Head-Gordon, V. S. Pande, J. W. Ponder, Y. Shao, C.-K. Skylaris, I. T. Todorov, M. E. Tuckerman, T. Head-Gordon: Advanced potential energy surfaces for molecular simulation, *The Journal of Physical Chemistry B* 120 (2016) 9811–9832. DOI: 10.1021/acs.jpcc.6b06414.
- [372] E. J. Maginn: From discovery to data: What must happen for molecular simulation to become a mainstream chemical engineering tool, *AIChE Journal* 55 (2009) 1304–1310. DOI: 10.1002/aic.11932.
- [373] M. D. Wilkinson, M. Dumontier, I. J. Aalbersberg, G. Appleton, M. Axton, A. Baak, N. Blomberg, J.-W. Boiten, L. B. da Silva Santos, P. E. Bourne: The FAIR Guiding Principles for scientific data management and stewardship, *Scientific data* 3 (2016) 1–9. DOI: 10.1038/sdata.2016.18.
- [374] S. L. Mayo, B. D. Olafson, W. A. Goddard: DREIDING: A generic force field for molecular simulations, *The Journal of Physical Chemistry* 94 (1990) 8897–8909. DOI: 10.1021/j100389a010.
- [375] A. K. Rappé, C. J. Casewit, K. Colwell, W. A. Goddard III, W. M. Skiff: UFF, a full periodic table force field for molecular mechanics and molecular dynamics simulations, *Journal of the American Chemical Society* 114 (1992) 10024–10035. DOI: 10.1021/ja00051a040.
- [376] W. D. Cornell, P. Cieplak, C. I. Bayly, I. R. Gould, K. M. Merz, D. M. Ferguson, D. C. Spellmeyer, T. Fox, J. W. Caldwell, P. A. Kollman: A second generation force field for the simulation of proteins, nucleic acids, and organic molecules, *Journal of the American Chemical Society* 117 (1995) 5179–5197. DOI: 10.1021/ja00124a002.
- [377] H. Sun, S. J. Mumby, J. R. Maple, A. T. Hagler: An ab initio CFF93 all-atom force field for polycarbonates, *Journal of the American Chemical Society* 116 (1994) 2978–2987. DOI: 10.1021/ja00086a030.
- [378] C. D. Wick, M. G. Martin, J. I. Siepmann: Transferable potentials for phase equilibria. 4. United-atom description of linear and branched alkenes and alkyl-

- benzenes, *The Journal of Physical Chemistry B* 104 (2000) 8008–8016. DOI: 10.1021/jp001044x.
- [379] B. Chen, J. J. Potoff, J. I. Siepmann: Monte carlo calculations for alcohols and their mixtures with alkanes. Transferable potentials for phase equilibria. 5. United-atom description of primary, secondary, and tertiary alcohols, *The Journal of Physical Chemistry B* 105 (2001) 3093–3104. DOI: 10.1021/jp003882x.
- [380] J. M. Stubbs, J. J. Potoff, J. I. Siepmann: Transferable potentials for phase equilibria. 6. United-atom description for ethers, glycols, ketones, and aldehydes, *The Journal of Physical Chemistry B* 108 (2004) 17596–17605. DOI: 10.1021/jp049459w.
- [381] C. D. Wick, J. M. Stubbs, N. Rai, J. I. Siepmann: Transferable potentials for phase equilibria. 7. Primary, secondary, and tertiary amines, nitroalkanes and nitrobenzene, nitriles, amides, pyridine, and pyrimidine, *The Journal of Physical Chemistry B* 109 (2005) 18974–18982. DOI: 10.1021/jp0504827.
- [382] N. Lubna, G. Kamath, J. J. Potoff, N. Rai, J. I. Siepmann: Transferable potentials for phase equilibria. 8. United-atom description for thiols, sulfides, disulfides, and thiophene, *The Journal of Physical Chemistry B* 109 (2005) 24100–24107. DOI: 10.1021/jp0549125.
- [383] K. A. Maerzke, N. E. Schultz, R. B. Ross, J. I. Siepmann: TraPPE-UA force field for acrylates and Monte Carlo simulations for their mixtures with alkanes and alcohols, *Journal of Physical Chemistry B* 113 (2009) 6415–6425. DOI: 10.1021/jp810558v.
- [384] L. Zhang, J. I. Siepmann: Pressure dependence of the vapor-liquid-liquid phase behavior in ternary mixtures consisting of *n*-alkanes, *n*-perfluoroalkanes, and carbon dioxide, *The Journal of Physical Chemistry B* 109 (2004) 2911–2919. DOI: 10.1021/jp0482114.
- [385] J.-S. Lee, C. D. Wick, J. M. Stubbs, J. I. Siepmann: Simulating the vapour-liquid equilibria of large cyclic alkanes, *Molecular Physics* 103 (2005) 99–104. DOI: 10.1080/00268970412331303341.
- [386] S. J. Keasler, S. M. Charan, C. D. Wick, I. G. Economou, J. I. Siepmann: Transferable potentials for phase equilibria – United atom description of five- and six-membered cyclic alkanes and ethers, *The Journal of Physical Chemistry B* 116 (2012) 11234–11246. DOI: 10.1021/jp302975c.

- [387] C. D. Wick, J. I. Siepmann, W. L. Klotz, M. R. Schure: Temperature effects on the retention of n-alkanes and arenes in helium-squalane gas-liquid chromatography, *Journal of Chromatography A* 954 (2002) 181–190. DOI: 10.1016/S0021-9673(02)00171-1.
- [388] S. J. Weiner, P. A. Kollman, D. T. Nguyen, D. A. Case: An all atom force field for simulations of proteins and nucleic acids, *Journal of Computational Chemistry* 7 (1986) 230–252. DOI: <https://doi.org/10.1002/jcc.540070216>.
- [389] W. Damm, A. Frontera, J. Tirado-Rives, W. L. Jorgensen: OPLS all-atom force field for carbohydrates, *Journal of Computational Chemistry* 18 (1997) 1955–1970. DOI: 10.1002/(SICI)1096-987X(199712)18:16<1955::AID-JCC1>3.0.CO;2-L.
- [390] W. L. Jorgensen, N. A. McDonald: Development of an all-atom force field for heterocycles. Properties of liquid pyridine and diazenes, *Journal of Molecular Structure: THEOCHEM* 424 (1998) 145–155. DOI: [https://doi.org/10.1016/S0166-1280\(97\)00237-6](https://doi.org/10.1016/S0166-1280(97)00237-6).
- [391] J. J. Potoff, G. Kamath: Mie potentials for phase equilibria: Application to alkenes, *Journal of Chemical & Engineering Data* 59 (2014) 3144–3150. DOI: 10.1021/je500202q.
- [392] M. S. Barhaghi, J. R. Mick, J. J. Potoff: Optimised Mie potentials for phase equilibria: Application to alkynes, *Molecular Physics* 115 (2017) 1378–1388. DOI: 10.1080/00268976.2017.1297862.
- [393] P. Dauber-Osguthorpe, V. A. Roberts, D. J. Osguthorpe, J. Wolff, M. Genest, A. T. Hagler: Structure and energetics of ligand binding to proteins: Escherichia coli dihydrofolate reductase-trimethoprim, a drug-receptor system, *Proteins: Structure, Function, and Bioinformatics* 4 (1988) 31–47. DOI: 10.1002/prot.340040106.
- [394] A. Hocquet, F. Wieber: Epistemic issues in computational reproducibility: Software as the elephant in the room, *European Journal for Philosophy of Science* 11 (2021) 38. DOI: 10.1007/s13194-021-00362-9.
- [395] H. H. Loeffler, S. Bosisio, G. Duarte Ramos Matos, D. Suh, B. Roux, D. L. Mobley, J. Michel: Reproducibility of free energy calculations across different molecular simulation software packages, *Journal of Chemical Theory and Computation* 14 (2018) 5567–5582. DOI: 10.1021/acs.jctc.8b00544.



- [396] C. W. Yong: Descriptions and implementations of DL\_f notation: A natural chemical expression system of atom types for molecular simulations, *Journal of Chemical Information and Modeling* 56 (2016) 1405–1409. DOI: 10.1021/acs.jcim.6b00323.
- [397] M. W. Thompson, J. B. Gilmer, R. A. Matsumoto, C. D. Quach, P. Shamaprasad, A. H. Yang, C. R. Iacovella, C. McCabe, P. T. Cummings: Towards molecular simulations that are transparent, reproducible, usable by others, and extensible (TRUE), *Molecular Physics* 118 (2020) e1742938. DOI: 10.1080/00268976.2020.1742938.
- [398] G. Gygli, J. Pleiss: Simulation Foundry: Automated and F.A.I.R. molecular modeling, *Journal of Chemical Information and Modeling* 60 (2020) 1922–1927. DOI: 10.1021/acs.jcim.0c00018.
- [399] M. T. Horsch, S. Chiacchiera, W. L. Cavalcanti, B. Schembera: Data technology in materials modelling, *SpringerBriefs in Applied Sciences and Technology*, Springer International Publishing, Cham, 2021.
- [400] M. T. Horsch, C. Niethammer, G. Boccardo, P. Carbone, S. Chiacchiera, M. Chiricotto, J. D. Elliott, V. Lobaskin, P. Neumann, P. Schiffels, M. A. Seaton, I. T. Todorov, J. Vrabc, W. L. Cavalcanti: Semantic interoperability and characterization of data provenance in computational molecular engineering, *Journal of Chemical & Engineering Data* 65 (2020) 1313–1329. DOI: 10.1021/acs.jced.9b00739.
- [401] S. Kanza, C. Willoughby, C. L. Bird, J. G. Frey: eScience Infrastructures in Physical Chemistry, *Annual Review of Physical Chemistry* 73 (2022) 97–116. DOI: 10.1146/annurev-physchem-082120-041521.
- [402] P. W. Hildebrand, A. S. Rose, J. K. S. Tiemann: Bringing Molecular Dynamics Simulation Data into View, *Trends in Biochemical Sciences* 44 (2019) 902–913. DOI: 10.1016/j.tibs.2019.06.004.
- [403] R. Grunzke, S. Breuers, S. Gesing, S. Herres-Pawlis, M. Kruse, D. Blunk, L. de la Garza, L. Packschies, P. Schäfer, C. Schärfe, T. Schlemmer, T. Steinke, B. Schuller, R. Müller-Pfefferkorn, R. Jäkel, W. E. Nagel, M. Atkinson, J. Krüger: Standards-based metadata management for molecular simulations, *Concurrency and Computation: Practice and Experience* 26 (2014) 1744–1759. DOI: 10.1002/cpe.3116.

- [404] H. M. Berman, J. Westbrook, Z. Feng, G. Gilliland, T. N. Bhat, H. Weissig, I. N. Shindyalov, P. E. Bourne: The protein data bank, *Nucleic Acids Research* 28 (2000) 235–242. DOI: 10.1093/nar/28.1.235.
- [405] P. Murray-Rust, H. S. Rzepa, M. Wright: Development of chemical markup language (CML) as a system for handling complex chemical content, *New Journal of Chemistry* 25 (2001) 618–634. DOI: 10.1039/B008780G.
- [406] S. Ash, M. A. Cline, R. W. Homer, T. Hurst, G. B. Smith: SYBYL line notation (SLN): A versatile language for chemical structure representation, *Journal of Chemical Information and Computer Sciences* 37 (1997) 71–79. DOI: 10.1021/ci960109j.
- [407] D. L. Mobley, C. C. Bannan, A. Rizzi, C. I. Bayly, J. D. Chodera, V. T. Lim, N. M. Lim, K. A. Beauchamp, D. R. Slochower, M. R. Shirts, M. K. Gilson, P. K. Eastman: Escaping atom types in force fields using direct chemical perception, *Journal of Chemical Theory and Computation* 14 (2018) 6076–6092. DOI: 10.1021/acs.jctc.8b00640.
- [408] A. A. Gakh, M. N. Burnett: Modular chemical descriptor language (MCDL): Composition, connectivity, and supplementary modules, *Journal of Chemical Information and Computer Sciences* 41 (2001) 1494–1499. DOI: 10.1021/ci000108y.
- [409] D. Weininger: SMILES, a chemical language and information system. 1. Introduction to methodology and encoding rules, *Journal of Chemical Information and Computer Sciences* 28 (1988) 31–36. DOI: 10.1021/ci00057a005.
- [410] T. Zhang, H. Li, H. Xi, R. V. Stanton, S. H. Rotstein: HELM: A hierarchical notation language for complex biomolecule structure representation, *Journal of Chemical Information and Modeling* 52 (2012) 2796–2806. DOI: 10.1021/ci3001925.
- [411] K. van den Broek, M. Daniel, M. Epple, H. Kuhn, J. Schaub, A. Zielesny: SPICES: A particle-based molecular structure line notation and support library for mesoscopic simulation, *Journal of Cheminformatics* 10 (2018) 1–10. DOI: 10.1186/s13321-018-0294-7.
- [412] J. D. Yesselman, D. J. Price, J. L. Knight, C. L. Brooks III: MATCH: An atom-typing toolset for molecular mechanics force fields, *Journal of Computational Chemistry* 33 (2012) 189–202. DOI: 10.1002/jcc.21963.
- [413] P. Eastman, J. Swails, J. D. Chodera, R. T. McGibbon, Y. Zhao, K. A. Beauchamp, L.-P. Wang, A. C. Simmonett, M. P. Harrigan, C. D. Stern, R. P. Wiewiora, B. R. Brooks, V. S. Pande: OpenMM 7: Rapid development of high

- performance algorithms for molecular dynamics, *PLOS Computational Biology* 13 (2017) 1–17. DOI: 10.1371/journal.pcbi.1005659.
- [414] B. L. Eggimann, A. J. Sunnarborg, H. D. Stern, A. P. Bliss, J. I. Siepmann: An online parameter and property database for the TraPPE force field, *Molecular Simulation* 40 (2014) 101–105. DOI: 10.1080/08927022.2013.842994.
- [415] C. Klein, A. Z. Summers, M. W. Thompson, J. B. Gilmer, C. McCabe, P. T. Cummings, J. Sallai, C. R. Iacovella: Formalizing atom-typing and the dissemination of force fields with foyer, *Computational Materials Science* 167 (2019) 215–227. DOI: 10.1016/j.commatsci.2019.05.026.
- [416] V. Zoete, M. A. Cuendet, A. Grosdidier, O. Michielin: SwissParam: A fast force field generation tool for small organic molecules, *Journal of Computational Chemistry* 32 (2011) 2359–2368. DOI: 10.1002/jcc.21816.
- [417] L. S. Dodda, I. CabezaãdeãVaca, J. Tirado-Rives, W. L. Jorgensen: LigParGen web server: An automatic OPLS-AA parameter generator for organic ligands, *Nucleic Acids Research* 45 (2017) W331–W336. DOI: 10.1093/nar/gkx312.
- [418] E. B. Tadmor, R. S. Elliott, J. P. Sethna, R. E. Miller, C. A. Becker: The potential of atomistic simulations and the knowledgebase of interatomic models, *JOM* 63 (2011) 17–17. DOI: 10.1007/s11837-011-0102-6.
- [419] P. Eastman, M. S. Friedrichs, J. D. Chodera, R. J. Radmer, C. M. Bruns, J. P. Ku, K. A. Beauchamp, T. J. Lane, L.-P. Wang, D. Shukla, T. Tye, M. Houston, T. Stich, C. Klein, M. R. Shirts, V. S. Pande: OpenMM 4: A reusable, extensible, hardware independent library for high performance molecular simulation, *Journal of Chemical Theory and Computation* 9 (2013) 461–469. DOI: 10.1021/ct300857j.
- [420] P. T. Cummings, C. McCabe, C. R. Iacovella, A. Ledeczi, E. Jankowski, A. Jayaraman, J. C. Palmer, E. J. Maginn, S. C. Glotzer, J. A. Anderson, J. Ilja Siepmann, J. Potoff, R. A. Matsumoto, J. B. Gilmer, R. S. DeFever, R. Singh, B. Crawford: Open-source molecular modeling software in chemical engineering focusing on the Molecular Simulation Design Framework, *AIChE Journal* 67 (2021) e17206. DOI: 10.1002/aic.17206.
- [421] M. Yabe, K. Mori, K. Ueda, M. Takeda: Development of PolyParGen software to facilitate the determination of molecular dynamics simulation parameters for polymers, *Journal of Computer Chemistry, Japan -International Edition* 5 (2019) 2018–0034. DOI: 10.2477/jccjie.2018-0034.

- [422] C. Hilpert, L. Beranger, P. C. T. Souza, P. A. Vainikka, V. Nieto, S. J. Marrink, L. Monticelli, G. Launay: Facilitating CG simulations with MAD: The MARTINI database server, *Journal of Chemical Information and Modeling* (2023). DOI: 10.1021/acs.jcim.2c01375.
- [423] C. Becker, Z. Trautt, L. Hale: NIST interatomic potentials repository, 2010. DOI: 10.18434/m37.
- [424] L. D. Schuler, X. Daura, W. F. v. Gunsteren: An improved GROMOS96 force field for aliphatic hydrocarbons in the condensed phase, *Journal of Computational Chemistry* 22 (2001) 1205–1218. DOI: 10.1002/jcc.1078.
- [425] G. Kanagalingam, S. Schmitt, F. Fleckenstein, S. Stephan: Data scheme and data format for transferable force fields for molecular simulation, *Scientific Data* 10 (2023). DOI: 10.1038/s41597-023-02369-8.
- [426] P. Atkins, J. de Paula: *Physical chemistry*, 9th ed., W. H. Freeman and Company, New York, 2010.
- [427] J. E. Jones: On the determination of molecular fields. II. From the equation of state of a gas, *Proceedings of the Royal Society of London. Series A, Containing Papers of a Mathematical and Physical Character* 106 (1924) 463–477. DOI: 10.1098/rspa.1924.0082.
- [428] G. Mie: Zur kinetischen Theorie der einatomigen Körper, *Annalen der Physik* 316 (1903) 657–697. DOI: 10.1002/andp.19033160802.
- [429] A. R. Leach: *Molecular modelling - Principles and applications*, 2nd ed., Pearson Education Limited, Harlow, 2001.
- [430] J. R. Maple, U. Dinur, A. T. Hagler: Derivation of force fields for molecular mechanics and dynamics from *ab initio* energy surfaces, *Proceedings of the National Academy of Sciences* 85 (1988) 5350–5354. DOI: 10.1073/pnas.85.15.5350.
- [431] U. K. Deiters, R. J. Sadus: Fully a priori prediction of the vapor-liquid equilibria of Ar, Kr, and Xe from *ab initio* two-body plus three-body interatomic potentials, *The Journal of Chemical Physics* 151 (2019) 034509. DOI: 10.1063/1.5109052.
- [432] P. Ströker, R. Hellmann, K. Meier: Thermodynamic properties of argon from Monte Carlo simulations using *ab initio* potentials, *Physical Review E* 105 (2022) 064129. DOI: 10.1103/PhysRevE.105.064129.

- [433] O. T. Unke, S. Chmiela, H. E. Sauceda, M. Gastegger, I. Poltavsky, K. T. Schuett, A. Tkatchenko, K. Mueller: Machine learning force fields, *Chemical Reviews* 121 (2021) 10142–10186. DOI: 10.1021/acs.chemrev.0c01111.
- [434] T. L. Brown, H. E. LeMay, B. E. Bursten, C. J. Murphy, P. M. Woodward, M. W. Stoltzfus: *Chemistry: The central science*, 15th ed., Pearson, Harlow, 2022.
- [435] N. Paskin: Toward unique identifiers, *Proceedings of the IEEE* 87 (1999) 1208–1227. DOI: 10.1109/5.771073.
- [436] G. Kanagalingam, S. Schmitt, F. Fleckenstein, S. Stephan: TUK-FFDat - Data scheme and data format for transferable force fields for molecular simulation (1.0.0) [Data set], 2023. DOI: 10.5281/zenodo.8116422.
- [437] A. Dalby, J. G. Nourse, W. D. Hounshell, A. K. I. Gushurst, D. L. Grier, B. A. Leland, J. Laufer: Description of several chemical structure file formats used by computer programs developed at Molecular Design Limited, *Journal of Chemical Information and Computer Sciences* 32 (1992) 244–255. DOI: 10.1021/ci00007a012.
- [438] M. C. Burger: ChemDoodle web components: HTML5 toolkit for chemical graphics, interfaces, and informatics, *Journal of Cheminformatics* 7 (2015) 35. DOI: 10.1186/s13321-015-0085-3.
- [439] P. Ertl: An algorithm to identify functional groups in organic molecules, *Journal of Cheminformatics* 9 (2017) 36. DOI: 10.1186/s13321-017-0225-z.
- [440] W. L. Jorgensen, C. J. Swenson: Optimized intermolecular potential functions for amides and peptides. Structure and properties of liquid amides, *Journal of the American Chemical Society* 107 (1985) 569–578. DOI: 10.1021/ja00289a008.
- [441] W. L. Jorgensen: Optimized intermolecular potential functions for liquid alcohols, *The Journal of Physical Chemistry* 90 (1986) 1276–1284. DOI: 10.1021/j100398a015.
- [442] W. L. Jorgensen: Intermolecular potential functions and Monte Carlo simulations for liquid sulfur compounds, *The Journal of Physical Chemistry* 90 (1986) 6379–6388. DOI: 10.1021/j100281a063.
- [443] W. L. Jorgensen, J. M. Briggs, M. L. Contreras: Relative partition coefficients for organic solutes from fluid simulations, *The Journal of Physical Chemistry* 94 (1990) 1683–1686. DOI: 10.1021/j100367a084.

- [444] W. L. Jorgensen, J. M. Briggs: A priori pKa calculations and the hydration of organic anions, *Journal of the American Chemical Society* 111 (1989) 4190–4197. DOI: 10.1021/ja00194a007.
- [445] W. L. Jorgensen, J. M. Briggs: Monte Carlo simulations of liquid acetonitrile with a three-site model, *Molecular Physics* 63 (1988) 547–558. DOI: 10.1080/00268978800100371.
- [446] J. M. Briggs, T. Matsui, W. L. Jorgensen: Monte Carlo simulations of liquid alkyl ethers with the OPLS potential functions, *Journal of Computational Chemistry* 11 (1990) 958–971. DOI: 10.1002/jcc.540110808.
- [447] W. L. Jorgensen, E. R. Laird, T. B. Nguyen, J. Tirado-Rives: Monte Carlo simulations of pure liquid substituted benzenes with OPLS potential functions, *Journal of Computational Chemistry* 14 (1993) 206–215. DOI: 10.1002/jcc.540140208.
- [448] W. L. Jorgensen, T. B. Nguyen: Monte Carlo simulations of the hydration of substituted benzenes with OPLS potential functions, *Journal of Computational Chemistry* 14 (1993) 195–205. DOI: 10.1002/jcc.540140207.
- [449] J. M. Briggs, T. B. Nguyen, W. L. Jorgensen: Monte Carlo simulations of liquid acetic acid and methyl acetate with the OPLS potential functions, *The Journal of Physical Chemistry* 95 (1991) 3315–3322. DOI: 10.1021/j100161a065.
- [450] M. D. Harmony, V. W. Laurie, R. L. Kuczkowski, R. H. Schwendeman, D. A. Ramsay, F. J. Lovas, W. J. Lafferty, A. G. Maki: Molecular structures of gasphase polyatomic molecules determined by spectroscopic methods, *Journal of Physical and Chemical Reference Data* 8 (1979) 619–722. DOI: 10.1063/1.555605.
- [451] S. Cradock, P. B. Liescheski, D. W. H. Rankin, H. E. Robertson: The r.alpha. structures of pyrazine and pyrimidine by the combined analysis of electron diffraction, liquid-crystal NMR, and rotational data, *Journal of the American Chemical Society* 110 (1988) 2758–2763. DOI: 10.1021/ja00217a011.
- [452] A. Hemmen, A. Z. Panagiotopoulos, J. Gross: Grand canonical Monte Carlo simulations guided by an analytic equation of state – Transferable anisotropic Mie potentials for ethers, *The Journal of Physical Chemistry B* 119 (2015) 7087–7099. DOI: 10.1021/acs.jpcc.5b01806.
- [453] D. Weidler, J. Gross: Transferable anisotropic united-atom force field based on the Mie potential for phase equilibria: aldehydes, ketones, and small cyclic alkanes, *Industrial & Engineering Chemistry Research* 55 (2016) 12123–12132. DOI: 10.1021/acs.iecr.6b02182.

- [454] A. Hemmen: Entwicklung eines übertragbaren Kraftfeldes (TAMie) für Phasengleichgewichte mit Monte Carlo Simulationen im groSSkanonischen Ensemble, Dissertation, Universität Stuttgart, Stuttgart, 2019.
- [455] J. Baz, N. Hansen, J. Gross: Transferable anisotropic Mie-potential force field for n-alcohols: Static and dynamic fluid properties of pure substances and binary mixtures, *Industrial & Engineering Chemistry Research* 59 (2020) 919–929. DOI: 10.1021/acs.iecr.9b05323.
- [456] B. R. Brooks, R. E. Bruccoleri, B. D. Olafson, D. J. States, S. Swaminathan, M. Karplus: CHARMM: A program for macromolecular energy, minimization, and dynamics calculations, *Journal of Computational Chemistry* 4 (1983) 187–217. DOI: 10.1002/jcc.540040211.
- [457] B. Chen, J. I. Siepmann: Transferable potentials for phase equilibria. 3. Explicit-hydrogen description of normal alkanes, *The Journal of Physical Chemistry B* 103 (1999) 5370–5379. DOI: 10.1021/jp990822m.
- [458] N. Rai, J. I. Siepmann: Transferable potentials for phase equilibria. 9. Explicit hydrogen description of benzene and five-membered and six-membered heterocyclic aromatic compounds, *The Journal of Physical Chemistry B* 111 (2007) 10790–10799. DOI: 10.1021/jp0735861.
- [459] N. Rai, J. I. Siepmann: Transferable potentials for phase equilibria. 10. Explicit-hydrogen description of substituted benzenes and polycyclic aromatic compounds, *The Journal of Physical Chemistry B* 117 (2013) 273–288. DOI: 10.1021/jp307328x.
- [460] W. L. Jorgensen, J. Chandrasekhar, J. D. Madura, R. W. Impey, M. L. Klein: Comparison of simple potential functions for simulating liquid water, *The Journal of Chemical Physics* 79 (1983) 926–935. DOI: 10.1063/1.445869.
- [461] L. D. Schuler, W. F. Van Gunsteren: On the choice of dihedral angle potential energy functions for n-alkanes, *Molecular Simulation* 25 (2000) 301–319. DOI: 10.1080/08927020008024504.
- [462] H. J. C. Berendsen, J. P. M. Postma, W. F. van Gunsteren, J. Hermans: Interaction models for water in relation to protein hydration, in: B. Pullman (Ed.), *Intermolecular Forces: Proceedings of the Fourteenth Jerusalem Symposium on Quantum Chemistry and Biochemistry Held in Jerusalem, Israel, April 13-16, 1981*, Springer Netherlands, Dordrecht, 1981, pp. 331–342.

- [463] G. Rutkai, A. Köster, G. Guevara-Carrion, T. Janzen, M. Schappals, C. W. Glass, M. Bernreuther, A. Wafai, S. Stephan, M. Kohns, S. Reiser, S. Deublein, M. Horsch, H. Hasse, J. Vrabec: ms2: A molecular simulation tool for thermodynamic properties, release 3.0, *Computer Physics Communications* 221 (2017) 343–351. DOI: 10.1016/j.cpc.2017.07.025.
- [464] R. Fingerhut, G. Guevara-Carrion, I. Nitzke, D. Saric, J. Marx, K. Langenbach, S. Prokopev, D. Celný, M. Bernreuther, S. Stephan, M. Kohns, H. Hasse, J. Vrabec: ms2: A molecular simulation tool for thermodynamic properties, release 4.0, *Computer Physics Communications* 262 (2021) 107860. DOI: 10.1016/j.cpc.2021.107860.
- [465] M. J. Abraham, T. Murtola, R. Schulz, S. Páll, J. C. Smith, B. Hess, E. Lindahl: GROMACS: High performance molecular simulations through multi-level parallelism from laptops to supercomputers, *SoftwareX* 1-2 (2015) 19–25. DOI: 10.1016/j.softx.2015.06.001.
- [466] J. Parsons, J. B. Holmes, J. M. Rojas, J. Tsai, C. E. M. Strauss: Practical conversion from torsion space to Cartesian space for in silico protein synthesis, *Journal of Computational Chemistry* 26 (2005) 1063–1068. DOI: 10.1002/jcc.20237.
- [467] C. Engin, J. Vrabec, H. Hasse: On the difference between a point multipole and an equivalent linear arrangement of point charges in force field models for vapour-liquid equilibria; partial charge based models for 59 real fluids, *Molecular Physics* 109 (2011) 1975–1982. DOI: 10.1080/00268976.2011.601604.
- [468] M. Parrinello, A. Rahman: Crystal structure and pair potentials: A molecular-dynamics study, *Physical Review Letters* 45 (1980) 1196–1199. DOI: 10.1103/PhysRevLett.45.1196.
- [469] P. L. Kapitza: The study of heat transfer in helium II, *Journal of Physics (USSR)* 4 (1941) 181.
- [470] G. L. Pollack: Kapitza resistance, *Reviews of Modern Physics* 41 (1969) 48–81. DOI: 10.1103/RevModPhys.41.48.
- [471] M. R. Hasan, T. Q. Vo, B. Kim: Manipulating thermal resistance at the solid-fluid interface through monolayer deposition, *RSC Advances* 9 (2019) 4948–4956. DOI: 10.1039/C8RA08390H.
- [472] M. Barisik, A. Beskok: Temperature dependence of thermal resistance at the water/silicon interface, *International Journal of Thermal Sciences* 77 (2014) 47–54. DOI: 10.1016/j.ijthermalsci.2013.10.012.



- [473] B. H. Kim, A. Beskok, T. Cagin: Molecular dynamics simulations of thermal resistance at the liquid-solid interface, *The Journal of Chemical Physics* 129 (2008) 174701. DOI: 10.1063/1.3001926.
- [474] T. Q. Vo, B. Kim: Interface thermal resistance between liquid water and various metallic surfaces, *International Journal of Precision Engineering and Manufacturing* 16 (2015) 1341–1346. DOI: 10.1007/s12541-015-0176-0.
- [475] T. Q. Vo, B. Kim: Transport phenomena of water in molecular fluidic channels, *Scientific Reports* 6 (2016) 33881. DOI: 10.1038/srep33881.
- [476] T. Q. Vo, B. Kim: Physical origins of temperature continuity at an interface between a crystal and its melt, *The Journal of Chemical Physics* 148 (2018) 034703. DOI: 10.1063/1.5004545.
- [477] L. Xue, P. Keblinski, S. R. Phillpot, S. U.-S. Choi, J. A. Eastman: Two regimes of thermal resistance at a liquid-solid interface, *The Journal of Chemical Physics* 118 (2003) 337–339. DOI: 10.1063/1.1525806.
- [478] G. Song, C. Min: Temperature dependence of thermal resistance at a solid/liquid interface, *Molecular Physics* 111 (2013) 903–908. DOI: 10.1080/00268976.2012.756990.
- [479] R. Khare, P. Keblinski, A. Yethiraj: Molecular dynamics simulations of heat and momentum transfer at a solid-fluid interface: Relationship between thermal and velocity slip, *International Journal of Heat and Mass Transfer* 49 (2006) 3401–3407. DOI: 10.1016/j.ijheatmasstransfer.2006.03.005.
- [480] S. Alosious, S. K. Kannam, S. P. Sathian, B. D. Todd: Nanoconfinement effects on the Kapitza resistance at water-CNT interfaces, *Langmuir* 37 (2021) 2355–2361. DOI: 10.1021/acs.langmuir.0c03298.
- [481] Z. Liang, K. Sasikumar, P. Keblinski: Thermal transport across a substrate – Thin-film interface: Effects of film thickness and surface roughness, *Physical Review Letters* 113 (2014) 065901. DOI: 10.1103/PhysRevLett.113.065901.
- [482] H.-C. Dan, Z.-M. Zou, Z. Zhang, J.-W. Tan: Effects of aggregate type and SBS copolymer on the interfacial heat transport ability of asphalt mixture using molecular dynamics simulation, *Construction and Building Materials* 250 (2020) 118922. DOI: 10.1016/j.conbuildmat.2020.118922.
- [483] H. Han, C. Schlawitschek, N. Katyal, P. Stephan, T. Gambaryan-Roisman, F. Leroy, F. Müller-Plathe: Solid-liquid interface thermal resistance affects the

- evaporation rate of droplets from a surface: A study of perfluorohexane on chromium using molecular dynamics and continuum theory, *Langmuir* 33 (2017) 5336–5343. DOI: 10.1021/acs.langmuir.7b01410.
- [484] J. Vera, Y. Bayazitoglu: Temperature and heat flux dependence of thermal resistance of water/metal nanoparticle interfaces at sub-boiling temperatures, *International Journal of Heat and Mass Transfer* 86 (2015) 433–442. DOI: 10.1016/j.ijheatmasstransfer.2015.02.033.
- [485] A. T. Pham, M. Barisik, B. Kim: Interfacial thermal resistance between the graphene-coated copper and liquid water, *International Journal of Heat and Mass Transfer* 97 (2016) 422–431. DOI: 10.1016/j.ijheatmasstransfer.2016.02.040.
- [486] S. Alosious, S. K. Kannam, S. P. Sathian, B. D. Todd: Kapitza resistance at water-graphene interfaces, *The Journal of Chemical Physics* 152 (2020) 224703. DOI: 10.1063/5.0009001.
- [487] D. Alexeev, J. Chen, J. H. Walther, K. P. Giapis, P. Angelikopoulos, P. Koumoutsakos: Kapitza resistance between few-layer graphene and water: Liquid layering effects, *Nano Letters* 15 (2015) 5744–5749. DOI: 10.1021/acs.nanolett.5b03024.
- [488] H. Hu, Y. Sun: Effect of nanopatterns on Kapitza resistance at a water-gold interface during boiling: A molecular dynamics study, *Journal of Applied Physics* 112 (2012) 053508. DOI: 10.1063/1.4749393.
- [489] A. T. Pham, M. Barisik, B. Kim: Molecular dynamics simulations of Kapitza length for argon-silicon and water-silicon interfaces, *International Journal of Precision Engineering and Manufacturing* 15 (2014) 323–329. DOI: 10.1007/s12541-014-0341-x.
- [490] Z.-Y. Ong: Thickness-dependent Kapitza resistance in multilayered graphene and other two-dimensional crystals, *Physical Review B* 95 (2017) 155309. DOI: 10.1103/PhysRevB.95.155309.
- [491] D. Ghatage, G. Tomar, R. K. Shukla: Thermostat-induced spurious interfacial resistance in non-equilibrium molecular dynamics simulations of solid-liquid and solid-solid systems, *The Journal of Chemical Physics* 153 (2020) 164110. DOI: 10.1063/5.0019665.
- [492] A. Pham, M. Barisik, B. Kim: Pressure dependence of Kapitza resistance at gold/water and silicon/water interfaces, *The Journal of Chemical Physics* 139 (2013) 244702. DOI: 10.1063/1.4851395.

- [493] A. Amani, S. M. H. Karimian, M. Seyednia: A molecular dynamics simulation on the effect of different parameters on thermal resistance of graphene-argon interface, *Molecular Simulation* 43 (2016) 276–283. DOI: 10.1080/08927022.2016.1265959.
- [494] Z. H. Kou, M. L. Bai, G. C. Zhao: Molecular dynamics simulations of thermal transport at the nanoscale solid-liquid interface, *Applied Mechanics and Materials* 291-294 (2013) 1999–2003. DOI: 10.4028/www.scientific.net/AMM.291-294.1999.
- [495] S. Murad, I. K. Puri: Molecular simulation of thermal transport across hydrophilic interfaces, *Chemical Physics Letters* 467 (2008) 110–113. DOI: 10.1016/j.cplett.2008.10.068.
- [496] F. Jabbari, A. Rajabpour, S. Saedodin, S. Wongwises: Effect of water/carbon interaction strength on interfacial thermal resistance and the surrounding molecular nanolayer of CNT and graphene flake, *Journal of Molecular Liquids* 282 (2019) 197–204. DOI: 10.1016/j.molliq.2019.03.003.
- [497] A. France-Lanord, P. Soukiassian, C. Glattli, E. Wimmer: Ab initio parameterization of a charge optimized many-body forcefield for Si-SiO<sub>2</sub>: Validation and thermal transport in nanostructures, *The Journal of Chemical Physics* 144 (2016) 104705. DOI: 10.1063/1.4943396.
- [498] S. Ge, M. Chen: Vibrational coupling and Kapitza resistance at a solid-liquid interface, *International Journal of Thermophysics* 34 (2013) 64–77. DOI: 10.1007/s10765-012-1362-2.
- [499] K. R. S. Shaul, A. J. Schultz, D. A. Kofke: The effect of truncation and shift on virial coefficients of Lennard-Jones potentials, *Collection of Czechoslovak Chemical Communications* 75 (2010) 447–462. DOI: 10.1135/cccc2009113.
- [500] S. Stephan, J. Liu, K. Langenbach, W. G. Chapman, H. Hasse: Vapor-liquid interface of the Lennard-Jones truncated and shifted fluid: Comparison of molecular simulation, density gradient theory, and density functional theory, *The Journal of Physical Chemistry C* 122 (2018) 24705–24715. DOI: 10.1021/acs.jpcc.8b06332.
- [501] M. Heier, F. Diewald, M. T. Horsch, K. Langenbach, R. Müller, H. Hasse: Molecular dynamics study of adsorption of the Lennard-Jones truncated and shifted fluid on planar walls, *Journal of Chemical & Engineering Data* 64 (2019) 386–394. DOI: 10.1021/acs.jced.8b00927.

- [502] M. P. Lautenschlaeger, H. Hasse: Thermal, caloric and transport properties of the Lennard-Jones truncated and shifted fluid in the adsorbed layers at dispersive solid walls, *Molecular Physics* 118 (2019) 1–10. DOI: 10.1080/00268976.2019.1669838.
- [503] M. P. Lautenschlaeger, S. Stephan, M. T. Horsch, B. Kirsch, J. C. Aurich, H. Hasse: Effects of lubrication on friction and heat transfer in machining processes on the nanoscale: A molecular dynamics approach, *Procedia CIRP* 67 (2018) 296–301. DOI: 10.1016/j.procir.2017.12.216.
- [504] J. Liu, M. Heier, W. G. Chapman, K. Langenbach: Adsorption in purely dispersive systems from molecular simulation, density gradient theory, and density functional theory, *Journal of Chemical & Engineering Data* 65 (2020) 1222–1233. DOI: 10.1021/acs.jced.9b00585.
- [505] I. Mudawwar, M. El-Masri: Momentum and heat transfer across freely-falling turbulent liquid films, *International Journal of Multiphase Flow* 12 (1986) 771–790. DOI: 10.1016/0301-9322(86)90051-0.
- [506] D. C. Marable, S. Shin, A. Yousefzadi Nobakht: Investigation into the microscopic mechanisms influencing convective heat transfer of water flow in graphene nanochannels, *International Journal of Heat and Mass Transfer* 109 (2017) 28–39. DOI: 10.1016/j.ijheatmasstransfer.2017.01.100.
- [507] S. Ge, Y. Gu, M. Chen: A molecular dynamics simulation on the convective heat transfer in nanochannels, *Molecular Physics* 113 (2015) 703–710. DOI: 10.1080/00268976.2014.970593.
- [508] A. Pellew, R. V. Southwell: On maintained convective motion in a fluid heated from below, *Proceedings of the Royal Society of London. Series A. Mathematical and Physical Sciences* 176 (1940) 312–343. DOI: 10.1098/rspa.1940.0092.
- [509] S. Plimpton: Fast parallel algorithms for short-range molecular dynamics, *Journal of Computational Physics* 117 (1995) 1–19. DOI: 10.1006/jcph.1995.1039.
- [510] Y. Akkus, C. T. Nguyen, A. T. Celebi, A. Beskok: A first look at the performance of nano-grooved heat pipes, *International Journal of Heat and Mass Transfer* 132 (2019) 280–287. DOI: 10.1016/j.ijheatmasstransfer.2018.12.022.
- [511] Q. V. Dinh, T. Q. Vo, B. Kim: Viscous heating and temperature profiles of liquid water flows in copper nanochannel, *Journal of Mechanical Science and Technology* 33 (2019) 3257–3263. DOI: 10.1007/s12206-019-0621-6.

- [512] C. T. Nguyen, M. Barisik, B. Kim: Wetting of chemically heterogeneous striped surfaces: Molecular dynamics simulations, *AIP Advances* 8 (2018) 065003. DOI: 10.1063/1.5031133.
- [513] J. Ghorbanian, A. Beskok: Scale effects in nano-channel liquid flows, *Microfluidics and Nanofluidics* 20 (2016) 121. DOI: 10.1007/s10404-016-1790-6.
- [514] Y. Noh, T. Vo, B. Kim: Subatomic-level solid/fluid boundary of Lennard-Jones atoms: A molecular dynamics study of metal-inert fluid interface, *Applied Sciences* 9 (2019). DOI: 10.3390/app9122439.
- [515] M. P. Lautenschlaeger, H. Hasse: Thermal and caloric properties of fluids from non-equilibrium molecular dynamics simulations using the two-gradient method, *The Journal of Chemical Physics* 149 (2018) 244106. DOI: 10.1063/1.5063985.
- [516] D. G. Cahill, W. K. Ford, K. E. Goodson, G. D. Mahan, A. Majumdar, H. J. Maris, R. Merlin, S. R. Phillpot: Nanoscale thermal transport, *Journal of Applied Physics* 93 (2003) 793–818. DOI: 10.1063/1.1524305.
- [517] S. A. Khrapak: Sound velocities of Lennard-Jones systems near the liquid-solid phase transition, *Molecules* 25 (2020). DOI: 10.3390/molecules25153498.
- [518] H. Hoang, G. Galliero: Local viscosity of a fluid confined in a narrow pore, *Physical Review E* 86 (2012) 021202. DOI: 10.1103/PhysRevE.86.021202.
- [519] I. Bitsanis, G. Hadziioannou: Molecular dynamics simulations of the structure and dynamics of confined polymer melts, *The Journal of Chemical Physics* 92 (1990) 3827–3847. DOI: 10.1063/1.457840.
- [520] S. Volz, J.-B. Saulnier, M. Lallemand, B. Perrin, P. Depondt, M. Mareschal: Transient Fourier-law deviation by molecular dynamics in solid argon, *Physical Review B* 54 (1996) 340–347. DOI: 10.1103/PhysRevB.54.340.
- [521] T. Haliciolu, G. M. Pound: Calculation of potential energy parameters from crystalline state properties, *Physica Status Solidi (a)* 30 (1975) 619–623. DOI: 10.1002/pssa.2210300223.
- [522] S. Merabia, S. Shenogin, L. Joly, P. Keblinski, J.-L. Barrat: Heat transfer from nanoparticles: A corresponding state analysis, *Proceedings of the National Academy of Sciences* 106 (2009). DOI: 10.1073/pnas.0901372106.
- [523] D. A. Nield, A. V. Kuznetsov, M. Xiong: Thermally developing forced convection in a porous medium: parallel plate channel with walls at uniform temperature,

- with axial conduction and viscous dissipation effects, *International Journal of Heat and Mass Transfer* 46 (2003) 643–651. DOI: 10.1016/S0017-9310(02)00327-7.
- [524] D. A. Nield, A. Bejan: *Convection in porous media*, Springer New York, New York, 2013.
- [525] D. Dai, Y. Zhou, J. Liu: Liquid metal based thermoelectric generation system for waste heat recovery, *Renewable Energy* 36 (2011) 3530–3536. DOI: 10.1016/j.renene.2011.06.012.
- [526] D. Tuckerman, R. Pease: High-performance heat sinking for VLSI, *IEEE Electron Device Letters* 2 (1981) 126–129. DOI: 10.1109/EDL.1981.25367.
- [527] T.-H. Tsai, R. Chein: Performance analysis of nanofluid-cooled microchannel heat sinks, *International Journal of Heat and Fluid Flow* 28 (2007) 1013–1026. DOI: 10.1016/j.ijheatfluidflow.2007.01.007.
- [528] J. P. Holman: *Heat transfer*, McGraw-Hill series in mechanical engineering, 10th ed., McGraw Hill Higher Education, Boston, 2010.
- [529] M. H. Ernst, E. H. Hauge, J. M. J. van Leeuwen: Asymptotic time behavior of correlation functions. III. Local equilibrium and mode-coupling theory, *Journal of Statistical Physics* 15 (1976) 23–58. DOI: 10.1007/BF01012808.
- [530] L. Cai, Y. Uygun, C. Togbé, H. Pitsch, H. Olivier, P. Dagaut, S. M. Sarathy: An experimental and modeling study of *n*-octanol combustion, *Proceedings of the Combustion Institute* 35 (2015) 419–427. DOI: 10.1016/j.proci.2014.05.088.
- [531] B. Rajesh Kumar, S. Saravanan: Use of higher alcohol biofuels in diesel engines: A review, *Renewable and Sustainable Energy Reviews* 60 (2016) 84–115. DOI: 10.1016/j.rser.2016.01.085.
- [532] M. K. Akhtar, H. Dandapani, K. Thiel, P. R. Jones: Microbial production of 1-octanol: A naturally excreted biofuel with diesel-like properties, *Metabolic Engineering Communications* 2 (2015) 1–5. DOI: 10.1016/j.meteno.2014.11.001.
- [533] B. Kerschgens, L. Cai, H. Pitsch, B. Heuser, S. Pischinger: Di-*n*-butylether, *n*-octanol, and *n*-octane as fuel candidates for diesel engine combustion, *Combustion and Flame* 163 (2016) 66–78. DOI: 10.1016/j.combustflame.2015.09.001.

- [534] L. T. Vargas-Ibáñez, J. J. Cano-Gómez, G. A. Iglesias-Silva, I. A. Santos-López, P. Rivas-García, M. M. Alcalá-Rodríguez, P. Zwolinski: Thermophysical and excess properties of diesel + biodiesel with octanol isomers at different temperatures, *Journal of Molecular Liquids* 363 (2022) 119779. DOI: 10.1016/j.molliq.2022.119779.
- [535] A. I. El-Seesy, R. M. El-Zoheiry, A. K. Fouad, A. M. Hussien, S. O. M. Elshabrawy, Z. He, A. Nasser: Impacts of octanol and decanol addition on the solubility of methanol/hydrous methanol/diesel/biodiesel/Jet A-1 fuel ternary mixtures, *RSC Advances* 11 (2021) 18213–18224. DOI: 10.1039/D1RA01625C.
- [536] J. J. Cano-Gómez, G. A. Iglesias-Silva, P. Rivas, C. O. Díaz-Ovalle, F. de Jesús Cerino-Córdova: Densities and viscosities for binary liquid mixtures of biodiesel + 1-butanol, + isobutyl alcohol, or + 2-butanol from 293.15 to 333.15 K at 0.1 MPa, *Journal of Chemical & Engineering Data* 62 (2017) 3391–3400. DOI: 10.1021/acs.jced.7b00440.
- [537] T. Reddyhoff, J. P. Ewen, P. Deshpande, M. D. Frogley, M. D. Welch, W. Montgomery: Macroscale superlubricity and polymorphism of long-chain n-alcohols, *ACS Applied Materials & Interfaces* 13 (2021) 9239–9251. DOI: 10.1021/acsmi.0c21918.
- [538] K. Yagi, J. Sugimura, P. Vergne: Rheological response of fatty alcohols in sliding elastohydrodynamic contacts, *Tribology International* 49 (2012) 58–66. DOI: 10.1016/j.triboint.2011.12.012.
- [539] K. Yagi, P. Vergne: Abnormal film shapes in sliding elastohydrodynamic contacts lubricated by fatty alcohols, *Proceedings of the Institution of Mechanical Engineers, Part J: Journal of Engineering Tribology* 221 (2007) 287–300. DOI: 10.1243/13506501JET253.
- [540] P. Kottenhahn, G. Philipps, S. Jennewein: Hexanol biosynthesis from syngas by *Clostridium carboxidivorans* P7 - product toxicity, temperature dependence and in situ extraction, *Heliyon* 7 (2021) e07732. DOI: 10.1016/j.heliyon.2021.e07732.
- [541] H. W. Oh, S. C. Lee, H. C. Woo, Y. Han Kim: Energy-efficient biobutanol recovery process using 1-heptanol extraction, *Chemical Engineering & Technology* 44 (2021) 2316–2326. DOI: 10.1002/ceat.202100154.
- [542] Z. Lu, S. Dourdain, S. Pellet-Rostaing: Understanding the effect of the phase modifier *n*-octanol on extraction, aggregation, and third-phase appearance in solvent

- extraction, *Langmuir* 36 (2020) 12121–12129. DOI: 10.1021/acs.langmuir.0c01554.
- [543] K. A. Omar, R. Sadeghi: Novel nonanol-based deep eutectic solvents: Thermophysical properties and their applications in liquid-liquid extraction and amino acid detection, *Journal of Molecular Liquids* 336 (2021) 116359. DOI: 10.1016/j.molliq.2021.116359.
- [544] J. J. Segovia, O. Fandiño, E. R. López, L. Lugo, M. Carmen Martín, J. Fernández: Automated densimetric system: Measurements and uncertainties for compressed fluids, *The Journal of Chemical Thermodynamics* 41 (2009) 632–638. DOI: 10.1016/j.jct.2008.12.020.
- [545] R. Span: Multiparameter equations of state, Springer Berlin Heidelberg, Berlin, Heidelberg, 2000.
- [546] R. Leonhard, M. Parche, C. Alvarez-Avila, J. Krauss, B. Rosenau: Pressure-amplified common rail system for commercial vehicles, *MTZ worldwide* 70 (2009) 10–15. DOI: 10.1007/BF03226948.
- [547] R. Battino: Volume changes on mixing for binary mixtures of liquids, *Chemical Reviews* 71 (1971) 5–45. DOI: 10.1021/cr60269a002.
- [548] A. M. F. Palavra, M. A. Tavares Cardoso, J. A. P. Coelho, M. F. B. Mourato: Density measurements of fluids and their mixtures at high pressure, *Chemical Engineering & Technology* 30 (2007) 689–694. DOI: 10.1002/ceat.200700040.
- [549] W. Wagner, R. Kleinrahm: Densimeters for very accurate density measurements of fluids over large ranges of temperature, pressure, and density, *Metrologia* 41 (2004) S24–S39. DOI: 10.1088/0026-1394/41/2/S03.
- [550] J. Troncoso, D. Bessières, C. A. Cerdeiriña, E. Carballo, L. Roman: Automated measuring device of  $(p, \rho, T)$  data, *Fluid Phase Equilibria* 208 (2003) 141–154. DOI: 10.1016/S0378-3812(03)00020-7.
- [551] Y. A. Sanmamed, A. Dopazo-Paz, D. González-Salgado, J. Troncoso, L. Romani: An accurate calibration method for high pressure vibrating tube densimeters in the density interval (700 to 1600)  $\text{kg}\cdot\text{m}^{-3}$ , *The Journal of Chemical Thermodynamics* 41 (2009) 1060–1068. DOI: 10.1016/j.jct.2009.01.007.
- [552] I. M. Lampreia, C. A. Nieto De Castro: A new and reliable calibration method for vibrating tube densimeters over wide ranges of temperature and pressure, *The Journal of Chemical Thermodynamics* 43 (2011) 537–545. DOI: 10.1016/j.jct.2010.11.002.



- [553] J. Staubach, G. Schwarz, S. Möbius, H. Hasse, S. Stephan: Modeling thermodynamic properties of mixtures of  $\text{CO}_2 + \text{O}_2$  in the Allam cycle by equations of state, *International Journal of Thermophysics* 44 (2023) 182. DOI: 10.1007/s10765-023-03297-w.
- [554] S. Stephan, F. Fleckenstein, H. Hasse: Vapor-liquid interfacial properties of the systems (toluene +  $\text{CO}_2$ ) and (toluene +  $\text{N}_2$ ): Experiments, molecular simulation, and density gradient theory, *Journal of Chemical & Engineering Data* 69 (2024) 590–607. DOI: 10.1021/acs.jced.3c00338.
- [555] W. Chapman, K. Gubbins, G. Jackson, M. Radosz: SAFT: Equation-of-state solution model for associating fluids, *Fluid Phase Equilibria* 52 (1989) 31–38. DOI: 10.1016/0378-3812(89)80308-5.
- [556] W. G. Chapman, K. E. Gubbins, G. Jackson, M. Radosz: New reference equation of state for associating liquids, *Industrial & Engineering Chemistry Research* 29 (1990) 1709–1721. DOI: 10.1021/ie00104a021.
- [557] J. Gross, G. Sadowski: Application of the perturbed-chain SAFT equation of state to associating systems, *Industrial & Engineering Chemistry Research* 41 (2002) 5510–5515. DOI: 10.1021/ie010954d.
- [558] F. J. Blas, L. F. Vega: Prediction of binary and ternary diagrams using the statistical associating fluid theory (SAFT) equation of state, *Industrial & Engineering Chemistry Research* 37 (1998) 660–674. DOI: 10.1021/ie970449+.
- [559] S. L. Outcalt, M. O. McLinden: Automated densimeter for the rapid characterization of industrial fluids, *Industrial & Engineering Chemistry Research* 46 (2007) 8264–8269. DOI: 10.1021/ie070791e.
- [560] E. F. May, W. J. Tay, M. Nania, A. Aleji, S. Al-Ghafri, J. P. Martin Trusler: Physical apparatus parameters and model for vibrating tube densimeters at pressures to 140 MPa and temperatures to 473 K, *Review of Scientific Instruments* 85 (2014) 095111. DOI: 10.1063/1.4894469.
- [561] E. F. May, W. J. Tay, M. Nania, A. Aleji, S. Al-Ghafri, J. P. Martin Trusler: Erratum: Physical apparatus parameters and model for vibrating tube densimeters at pressures to 140 MPa and temperatures to 473 K [Rev. Sci. Instrum. 85, 095111 (2014)], *Review of Scientific Instruments* 86 (2015) 049902. DOI: 10.1063/1.4919437.
- [562] J. A. Schroeder, S. G. Penoncello, J. S. Schroeder: A fundamental equation of state for ethanol, *Journal of Physical and Chemical Reference Data* 43 (2014) 043102. DOI: 10.1063/1.4895394.

- [563] E. W. Lemmon, R. Span: Short fundamental equations of state for 20 industrial fluids, *Journal of Chemical & Engineering Data* 51 (2006) 785–850. DOI: 10.1021/je050186n.
- [564] M. Thol, M. A. Javed, E. Baumhögger, R. Span, J. Vrabec: Thermodynamic properties of dodecamethylpentasiloxane, tetradecamethylhexasiloxane, and decamethylcyclopentasiloxane, *Industrial & Engineering Chemistry Research* 58 (2019) 9617–9635. DOI: 10.1021/acs.iecr.9b00608.
- [565] A. C. Rencher, G. B. Schaalje: *Linear models in statistics*, 2nd ed., Wiley-Interscience, Hoboken, 2008.
- [566] T. Boublík: Hardsphere equation of state, *The Journal of Chemical Physics* 53 (1970) 471–472. DOI: 10.1063/1.1673824.
- [567] G. A. Mansoori, N. F. Carnahan, K. E. Starling, J. Leland: Equilibrium thermodynamic properties of the mixture of hard spheres, *The Journal of Chemical Physics* 54 (1971) 1523–1525. DOI: 10.1063/1.1675048.
- [568] J. K. Johnson, J. A. Zollweg, K. E. Gubbins: The Lennard-Jones equation of state revisited, *Molecular Physics* 78 (1993) 591–618. DOI: 10.1080/00268979300100411.
- [569] J. K. Johnson, E. A. Mueller, K. E. Gubbins: Equation of state for Lennard-Jones chains, *The Journal of Physical Chemistry* 98 (1994) 6413–6419. DOI: 10.1021/j100076a028.
- [570] V. Pokorný, V. tejfá, M. Klajmon, M. Fulem, K. Rika: Vapor pressures and thermophysical properties of 1-heptanol, 1-octanol, 1-nonanol, and 1-decanol: Data reconciliation and PC-SAFT modeling, *Journal of Chemical & Engineering Data* 66 (2021) 805–821. DOI: 10.1021/acs.jced.0c00878.
- [571] S. H. Du Plessis, S. A. M. Smith, C. Latsky-Galloway, C. E. Schwarz: Investigation of the low-pressure phase behavior and SAFT modeling of 1-alcohol and *n*-alkane binary systems, *Journal of Chemical & Engineering Data* 69 (2023) 623–638. DOI: 10.1021/acs.jced.3c00346.
- [572] S. A. Smith, J. T. Cripwell, C. E. Schwarz: A quadrupolar SAFT-VR Mie approach to modeling binary mixtures of CO<sub>2</sub> or benzene with *n*-alkanes or 1-alkanols, *Journal of Chemical & Engineering Data* 65 (2020) 5778–5800. DOI: 10.1021/acs.jced.0c00705.

- [573] F. Llovell, L. F. Vega: Global fluid phase equilibria and critical phenomena of selected mixtures using the crossover soft-SAFT equation, *The Journal of Physical Chemistry B* 110 (2006) 1350–1362. DOI: 10.1021/jp0551465.
- [574] M. Almasi, H. Iloukhani, A. Hernández: New experimental data and modeling for the densities and viscosities of the 1,4-dioxane + 1-alkanols (C6 to C10) mixtures, *International Journal of Thermophysics* 44 (2023) 149. DOI: 10.1007/s10765-023-03255-6.
- [575] D. Ambrose, C. Sprake: Thermodynamic properties of organic oxygen compounds XXV. Vapour pressures and normal boiling temperatures of aliphatic alcohols, *The Journal of Chemical Thermodynamics* 2 (1970) 631–645.
- [576] D. Ambrose, J. Ellender, C. Sprake: Thermodynamic properties of organic oxygen compounds XXXV. Vapour pressures of aliphatic alcohols, *The Journal of Chemical Thermodynamics* 6 (1974) 909–914.
- [577] T. Apaev, A. Gylmanov, G. Akhmedova: Measurement of the density of n-octanol over a wide range of temperatures and pressures, *Proceedings of Higher Educational Institutions. Oil and Gas.* (1987) 19–32. DOI: "".
- [578] M. Censky, V. Rohac, K. Ruzicka, M. Fulem, K. Aim: Vapor pressure of selected aliphatic alcohols by ebulliometry. Part 1, *Fluid Phase Equilibria* 298 (2010) 192–198. DOI: 10.1016/j.fluid.2010.06.019.
- [579] Y. V. Efremov: Density, surface tension, vapour pressures and critical parameters of alcohols, *Journal of Applied Chemistry of the USSR* 40 (1966) 1240–1247.
- [580] G. H. Findenegg: Dichte und Ausdehnungskoeffizienten einiger flüssiger Alkohole und Carbonsäuren, *Monatshefte für Chemie/Chemical Monthly* 104 (1973) 998–1007. DOI: 10.1007/BF00903916.
- [581] J. L. Hales, J. H. Ellender: Liquid densities from 293 to 490 K of nine aliphatic alcohols, *The Journal of Chemical Thermodynamics* 8 (1976) 1177–1184. DOI: 10.1016/0021-9614(76)90126-9.
- [582] H. R. Kemme, S. I. Kreps: Vapor pressure of primary n-alkyl chlorides and alcohols, *Journal of Chemical & Engineering Data* 14 (1969) 98–102.
- [583] J. N'Guimbi, H. Kasehgari, I. Mokbel, J. Jose: Tensions de vapeur d'alcools primaires dans le domaine 0,3 Pa à 1,5 kPa, *Thermochimica Acta* 196 (1992) 367–377. DOI: 10.1016/0040-6031(92)80100-B.

- [584] H. Sackmann, F. Sauerwald: Dichtemessungen XIV, *Zeitschrift für Physikalische Chemie* 195 (1950) 295–312.
- [585] M. Schmitt, H. Hasse: Phase Equilibria for Hexyl Acetate Reactive Distillation, *Journal of Chemical & Engineering Data* 50 (2005) 1677–1683. DOI: 10.1021/je050141m.
- [586] A. Shakhverdiev, Y. M. Naziev, D. T. Safarov: Thermische Eigenschaften von Einigen aliphatischen Alkoholen nahe an der Dampf-Fluessig-Phasenubergangslinie, *Journal of Applied Chemistry of the USSR* 65 (1992) 1631–1637.
- [587] C. Smyth, W. Stoops: The dielectric polarization of liquids. VI. Ethyl iodide, ethanol, normal-butanol and normal-octanol, *Journal of the American Chemical Society* 51 (1929) 3312–3329.
- [588] V. Stejfa, M. Fulem, K. Ruzicka, P. Matejka: Vapor pressures and thermophysical properties of selected hexenols and recommended vapor pressure for hexan-1-ol, *Fluid Phase Equilibria* 402 (2015) 18–29. DOI: 10.1016/j.fluid.2015.05.026.
- [589] J. A. White, S. Zhang: Renormalization group theory for fluids, *The Journal of Chemical Physics* 99 (1993) 2012–2019. DOI: 10.1063/1.465263.
- [590] E. Brown: On the thermodynamic properties of fluids, *Bulletin de l'Institut International du Froid Annexe 1* (1960) 169–178.
- [591] U. K. Deiters, A. Neumaier: Computer simulation of the characteristic curves of pure fluids, *Journal of Chemical & Engineering Data* 61 (2016) 2720–2728. DOI: 10.1021/acs.jced.6b00133.
- [592] U. K. Deiters, K. M. d. Reuck: Guidelines for publication of equations of state I. Pure fluids (Technical Report), *Pure and Applied Chemistry* 69 (1997) 1237–1250. DOI: 10.1351/pac199769061237.
- [593] R. Span, W. Wagner: On the extrapolation behavior of empirical equations of state, *International Journal of Thermophysics* 18 (1997) 1415–1443. DOI: 10.1007/BF02575343.
- [594] H. Renneis, S. Stephan: Characteristic curves of polar fluids: (I) The two-center Lennard-Jones plus dipole fluid, *International Journal of Thermophysics* 45 (2024) 77. DOI: 10.1007/s10765-024-03366-8.

- [595] H. Renneis, S. Stephan: Characteristic curves of polar fluids: (II) The two-center Lennard-Jones plus quadrupole fluid, *International Journal of Thermophysics* 45 (2024) 73. DOI: 10.1007/s10765-024-03367-7.
- [596] K. Paduszyski, M. Wickowski, M. Okuniewski, U. Domaska: New phase equilibrium data at ambient and high pressure for strongly asymmetric mixtures containing menthol, *Journal of Molecular Liquids* 286 (2019) 110819. DOI: 10.1016/j.molliq.2019.04.096.
- [597] F. E. Alaoui, E. A. Montero, G. Qiu, F. Aguilar, J. Wu: Liquid density of biofuel mixtures: 1-Heptanol+heptane system at pressures up to 140 MPa and temperatures from 298.15 K to 393.15 K, *The Journal of Chemical Thermodynamics* 65 (2013) 174–183. DOI: 10.1016/j.jct.2013.05.051.
- [598] V. Altunin, E. Konikevich: Generalized equation of state of liquid aliphatic alcohols of normal structure, *Journal of Applied Chemistry of the USSR* 3 (1980) 97–106. DOI: "".
- [599] F. Audonnet, A. A. H. Pádua: Density and viscosity of mixtures of n-Hexane and 1-Hexanol from 303 to 423 K up to 50 MPa., *International Journal of Thermophysics* 23 (2002) 1537–1550. DOI: 10.1023/a:1020785816403.
- [600] M. Basu, T. Samanta, D. Das: Volumetric and compressibility studies on tri-n-butyl phosphate (TBP)-phase modifier (1-octanol, 1-decanol and isodecanol) interactions from T=(298.15 to 323.15)K, *The Journal of Chemical Thermodynamics* 70 (2014) 1–12. DOI: 10.1016/j.jct.2013.10.018.
- [601] W. E. Danforth: The dielectric constant of liquids under high pressure, *Physical Review* 38 (1931) 1224–1235. DOI: 10.1103/physrev.38.1224.
- [602] M. J. Dávila, R. Alcalde, M. Atilhan, S. Aparicio:  $P\rho T$  measurements and derived properties of liquid 1-alkanols, *The Journal of Chemical Thermodynamics* 47 (2012) 241–259. DOI: 10.1016/j.jct.2011.10.023.
- [603] M. Diaz Peña, G. Tardajos: Isothermal compressibilities of n-1-alcohols from methanol to 1-dodecanol at 298.15, 308.15, 318.15, and 333.15 K, *The Journal of Chemical Thermodynamics* 11 (1979) 441–445. DOI: 10.1016/0021-9614(79)90121-6.
- [604] U. Domaska, M. Zawadzki, A. Lewandowska: Effect of temperature and composition on the density, viscosity, surface tension, and thermodynamic properties of binary mixtures of N-octylisoquinolinium bis(trifluoromethyl)sulfonylimide with alcohols, *The Journal of Chemical Thermodynamics* 48 (2012) 101–111. DOI: 10.1016/j.jct.2011.12.003.

- [605] N. Dubey: Micellar properties and related thermodynamic parameters of aqueous anionic surfactants in the presence of monohydric alcohols, *Journal of Chemical & Engineering Data* 56 (2011) 3291–3300. DOI: 10.1021/je101358p.
- [606] G. P. Dubey, P. Kaur: Thermodynamic, transport and excess properties of 2-butoxy ethanol +1-alkanol (C6,C8,C10) at different temperatures, *The Journal of Chemical Thermodynamics* 64 (2013) 239–248. DOI: 10.1016/j.jct.2013.04.021.
- [607] M. Dzida, P. Góralski: Excess molar heat capacities for (decan-1-ol+n-heptane) at temperatures from (290 to 318) K. Experimental results and theoretical description using the ERAS model, *The Journal of Chemical Thermodynamics* 38 (2006) 962–969. DOI: 10.1016/j.jct.2005.10.009.
- [608] M. Dzida: Speeds of sound, densities, isobaric thermal expansion, compressibilities, and internal pressures of heptan-1-ol, octan-1-ol, nonan-1-ol, and decan-1-ol at temperatures from (293 to 318) K and pressures up to 100 MPa, *Journal of Chemical & Engineering Data* 52 (2007) 521–531. DOI: 10.1021/je0604378.
- [609] A. Estrada-Baltazar, J. I. S. López-Lázaro, G. A. Iglesias-Silva, J. Barajas-Fernández: Density and surface tension of binary mixture of 1-nonanol +n-octane, +n-nonane, and +n-decane from (293.15 to 323.15) K at P = 0.1 MPa, *The Journal of Chemical Thermodynamics* 150 (2020) 106225. DOI: 10.1016/j.jct.2020.106225.
- [610] C. Fan, Y. Zhuang, C. Han, M. Cao, F. Yang, X. Liu, Y. Chen: Study of volume properties of N, N-dimethylcyclohexylamine and alcohols binary mixtures at different temperatures and 0.1 MPa, *The Journal of Chemical Thermodynamics* 161 (2021) 106532. DOI: 10.1016/j.jct.2021.106532.
- [611] F. Forghani, H. Iloukhani, K. Khanlarzadeh: Excess molar enthalpies of monoethanolamine (MEA) + primary alkan-1-ols (C3-C6) and their fitting with Wilson, NRTL and UNIQUAC models at 298.15 K, *Journal of Solution Chemistry* 51 (2022) 1–13. DOI: 10.1007/s10953-021-01130-2.
- [612] B. García, S. Aparicio, A. M. Navarro, R. Alcalde, J. M. Leal: Measurements and modeling of thermophysical behavior of (C1 - C4) alkylbenzoate/ (C1 - C11) alkan-1-ol mixed solvents, *The journal of physical chemistry. B* 108 (2004) 15841–15850. DOI: 10.1021/jp0485439.
- [613] S. K. Garg, T. S. Banipal, J. C. Ahluwalia: Densities, molar volumes, cubic expansion coefficients, and isothermal compressibilities of 1-alkanols from 323.15

- to 373.15 K and at pressures up to 10 MPa, *Journal of Chemical & Engineering Data* 38 (1993) 227–230. DOI: 10.1021/jc00010a010.
- [614] I. Golubev, T. Vasilkovskaya, V. Zolin, A. Shelkovenko: Density of isoamyl and heptyl alcohols at various temperatures and pressures, *Journal of Engineering Physics and Thermophysics* 40 (1981) 194–198. DOI: 10.1007/BF00826030.
- [615] A. Guzmán-López, G. A. Iglesias-Silva, F. Reyes-García, A. Estrada-Baltazar, M. Ramos-Estrada: Densities and viscosities for binary liquid mixtures of n-undecane + 1-heptanol, 1-octanol, 1-nonanol, and 1-decanol from 283.15 to 363.15 K at 0.1 MPa, *Journal of Chemical & Engineering Data* 62 (2017) 780–795. DOI: 10.1021/acs.jced.6b00834.
- [616] A. Gylmanov, T. Apaev, L. Akhmedov, S. Lipovetskii: Experimental study of the density of n-amyl and n-hexyl alcohols, *News of Higher Educational Institutions. Oil and Gas*. 7 (1979) 55–56. DOI: "".
- [617] M. Habibullah, I. M. M. Rahman, M. A. Uddin, M. Anowar, M. Alam, K. Iwakabe, H. Hasegawa: Densities, viscosities, and speeds of sound of binary mixtures of heptan-1-ol with 1,4-dioxane at temperatures from (298.15 to 323.15) K and atmospheric pressure, *Journal of Chemical & Engineering Data* 58 (2013) 2887–2897. DOI: 10.1021/jc400512u.
- [618] J. D. d. O. Henriques, F. H. B. Sosa, R. M. Dias, P. F. M. Martinez, M. C. Da Costa: Flash point and excess molar volumes of binary mixtures containing d-limonene and alcohol compounds from propanol to dodecanol, *The Journal of Chemical Thermodynamics* 150 (2020) 106224. DOI: 10.1016/j.jct.2020.106224.
- [619] F. J. Hoyuelos, B. García, R. Alcalde, S. Ibeas, J. M. Leal: Shear viscosities of binary mixtures of pyrrolidin-2-one with C6-C10 n-alkan-1-ols, *Journal of the Chemical Society, Faraday Transactions* 92 (1996) 219–225. DOI: 10.1039/FT9969200219.
- [620] G. A. Iglesias-Silva, A. Guzmán-López, G. Pérez-Durán, M. Ramos-Estrada: Densities and viscosities for binary liquid mixtures of n-undecane + 1-propanol, + 1-butanol, + 1-pentanol, and + 1-hexanol from 283.15 to 363.15 K at 0.1 MPa, *Journal of Chemical & Engineering Data* 61 (2016) 2682–2699. DOI: 10.1021/acs.jced.6b00121.
- [621] P. Kaur, G. P. Dubey: Thermo physical and FT-IR study on binary mixtures of 2-isopropoxy ethanol and alcohols at different temperatures, *Journal of Molecular Liquids* 233 (2017) 479–486. DOI: 10.1016/j.molliq.2017.03.039.

- [622] M.-J. Lee, T.-J. Ku, H.-m. Lin: (Pressure+volume+temperature) properties for binary oligomeric solutions of poly(ethylene glycol mono-4-octylphenyl ether) with 1-octanol or acetophenone at pressures up to 50MPa, *The Journal of Chemical Thermodynamics* 41 (2009) 1178–1185. DOI: 10.1016/j.jct.2009.05.007.
- [623] I. Mamedov, A. Aliev: Study of the equation of state of aqueous solutions of alcohols, *Winiti, Code 17-82, Moscow* (1982) 1 – 3. DOI: "".
- [624] S. Matsuo, T. Makita: Volumetric properties of 1-alkanols at temperatures in the range 298 - 348 K and pressures up to 40 MPa, *International Journal of Thermophysics* 10 (1989) 885–897. DOI: 10.1007/bf00514483.
- [625] S. Nayar, A. P. Kudchadker: Densities of some organic substances, *Journal of Chemical & Engineering Data* 18 (1973) 356–357. DOI: 10.1021/jc60059a007.
- [626] A. Pimentel-Rodas, L. A. Galicia-Luna, J. J. Castro-Arellano: Capillary viscometer and vibrating tube densimeter for simultaneous measurements up to 70 MPa and 423 K, *Journal of Chemical & Engineering Data* 61 (2016) 45–55. DOI: 10.1021/acs.jced.5b00152.
- [627] A. Pimentel-Rodas, L. A. Galicia-Luna, J. J. Castro-Arellano: Viscosity and density of n-alcohols at temperatures between (298.15 and 323.15) K and pressures up to 30 MPa, *Journal of Chemical & Engineering Data* 64 (2019) 324–336. DOI: 10.1021/acs.jced.8b00812.
- [628] C. N. Pinto, G. Z. Frugoli, P. M. Florido, G. V. Atzingen, C. E. Rodrigues, C. B. Gonçalves: Viscosities and densities of fatty alcohol mixtures from 298.15 to 338.15 K: Estimation by Kay's rule and prediction by the UNIFAC-VISCO and GC-UNIMOD group contribution methods, *Journal of Chemical & Engineering Data* 64 (2019) 1937–1947. DOI: 10.1021/acs.jced.8b00992.
- [629] X. Qin, S. Yang, J. Zhao, L. Wang, Y. Zhang, X. Qin, D. Luo: Density and viscosity for the ternary mixture of 1,3,5-trimethyladamantane + 1,2,3,4-tetrahydronaphthalene + n-octanol and corresponding binary systems at T = (293.15 to 343.15) K, *The Journal of Chemical Thermodynamics* 168 (2022) 106726. DOI: 10.1016/j.jct.2022.106726.
- [630] S. L. Randzio, J.-P. Grolier, J. R. Quint: Thermophysical properties of 1-hexanol over the temperature range from 303 K to 503 K and at pressures from the saturation line to 400 MPa, *Fluid Phase Equilibria* 110 (1995) 341–359. DOI: 10.1016/0378-3812(95)02761-3.



- [631] M. A. Rauf, G. H. Stewart, A. Farhataziz: Viscosities and densities of binary mixtures of 1-alkanols from 15 to 55°C, *Journal of Chemical & Engineering Data* 28 (1983) 324–328. DOI: 10.1021/je00033a012.
- [632] L. F. Sanz, J. A. González, I. La García de Fuente, J. C. Cobos, F. Hevia: Thermodynamics of mixtures with strong negative deviations from Raoult's law. XVIII: Excess molar enthalpies for the (1-alkanol + cyclohexylamine) systems at 298.15 K and modelling, *The Journal of Chemical Thermodynamics* 157 (2021) 106395. DOI: 10.1016/j.jct.2021.106395.
- [633] B. Sarkoohaki, M. Almasi, M. Karimkhani: Correlation studies of cyclohexanone/(C5-C10) alkan-1-ol binary mixtures: PC-SAFT model and free volume theory, *Journal of Chemical & Engineering Data* 63 (2018) 2257–2265. DOI: 10.1021/acs.jced.8b00201.
- [634] A. Shakhverdiev, B. T. Akhmed: The density of n-heptyl and n-nonyl alcohols at high temperatures, *Thermophysics of High Temperatures* 36 (1998) 572–576. DOI: "".
- [635] A. Shelkovenko, V. Zolin, T. Vasilkovskaya, I. Golubev: Thermodynamic properties of n-propyl and isopropyl alcohols, *Winiti*, Code 1109-83, Moscow (1983) 1–13. DOI: "".
- [636] G. W. Smith, L. V. Sorg: The measurement of boundary tension by the pendant-drop method. I. The aliphatic alcohols, *The Journal of Physical Chemistry* 45 (1941) 671–681. DOI: 10.1021/j150409a011.
- [637] K. Sreenivasulu, V. Govinda, P. Venkateswarlu, K. Sivakumar: Thermodynamic properties of non-electrolyte solutions, *Journal of Thermal Analysis and Calorimetry* 115 (2014) 1805–1811. DOI: 10.1007/s10973-013-3395-6.
- [638] U. Sülzner, G. Luft: Effect of hydrogen bonding on the viscosity of alcohols at high pressures, *International Journal of Thermophysics* 18 (1997) 1355–1367. DOI: 10.1007/bf02575339.
- [639] M. A. Uddin, A. Sanaullah, F. Yeasmin, M. Habibullah, K. Iwakabe, I. M. Rahman: Temperature-induced variations in the thermophysical properties of the binary mixtures of heptan-1-ol with cumene, or mesitylene: An experimental and theoretical approach, *Journal of Molecular Liquids* 297 (2020) 111900. DOI: 10.1016/j.molliq.2019.111900.
- [640] J. L. Valencia, D. González-Salgado, J. Troncoso, J. Peleteiro, E. Carballo, L. Romaní: Thermophysical characterization of liquids using precise density and iso-

- baric heat capacity measurements as a function of pressure, *Journal of Chemical & Engineering Data* 54 (2009) 904–915. DOI: 10.1021/je8006875.
- [641] J. L. Valero-Hernández, G. A. Iglesias-Silva, M. Ramos-Estrada: Densities and viscosities for binary liquid mixtures of n-aldehydes + ethanol from 283.15 to 343.15 K at 0.1 MPa, *Journal of Chemical & Engineering Data* 67 (2022) 2879–2898. DOI: 10.1021/acs.jced.2c00226.
- [642] X. Wang, X. Wang, B. Song: Densities and viscosities of binary mixtures of 2,2,4-trimethylpentane + 1-propanol, + 1-pentanol, + 1-hexanol, and + 1-heptanol from (298.15 to 323.15) K, *Journal of Chemical & Engineering Data* 60 (2015) 1664–1673. DOI: 10.1021/je501041r.
- [643] X. Wang, Y. Ma, J. Huo, J. Liu, S. Wang, L. Fang, Z. Zhao: Viscosity measurement and correlation research of one biodiesel component (methyl octanoate) with five 1-alcohols, *Fuel* 324 (2022) 124441. DOI: 10.1016/j.fuel.2022.124441.
- [644] C.-H. Yu, F.-N. Tsai: Excess volumes of binary mixtures of benzene + 1-alkanols at 298.15 and 308.15 K, *Journal of Chemical & Engineering Data* 39 (1994) 441–443. DOI: 10.1021/je00015a008.
- [645] A. Zúñiga-Moreno, L. A. Galicia-Luna, F. F. Betancourt-Cárdenas, J. M. Bernal-García: Compressed liquid densities and excess molar volumes of CO<sub>2</sub> + hexan-1-ol mixtures from (313 to 363) K and pressures up to 25 MPa, *Journal of Chemical & Engineering Data* 51 (2006) 1723–1730. DOI: 10.1021/je060154f.
- [646] A. Zúñiga-Moreno, L. A. Galicia-Luna: Densities, isothermal compressibilities, and isobaric thermal expansivities of hexan-2-ol, octan-1-ol, and decan-1-ol from (313 to 363) K and pressures up to 22 MPa, *Journal of Chemical & Engineering Data* 52 (2007) 1773–1783. DOI: 10.1021/je700145e.
- [647] A. Zúñiga-Moreno, L. A. Galicia-Luna, F. F. Betancourt-Cárdenas: Densities and derived thermodynamic properties of 1-heptanol and 2-heptanol at temperatures from 313 K to 363 K and pressures up to 22 MPa, *The Journal of Chemical Thermodynamics* 40 (2008) 96–106. DOI: 10.1016/j.jct.2007.05.007.
- [648] T. Lafitte, D. Bessieres, M. M. Piñeiro, J.-L. Daridon: Simultaneous estimation of phase behavior and second-derivative properties using the statistical associating fluid theory with variable range approach, *The Journal of Chemical Physics* 124 (2006) 024509. DOI: 10.1063/1.2140276.

- [649] T. Lafitte, M. M. Piñeiro, J.-L. Daridon, D. Bessières: A comprehensive description of chemical association effects on second derivative properties of alcohols through a SAFT-VR approach, *The Journal of Physical Chemistry B* 111 (2007) 3447–3461. DOI: 10.1021/jp0682208.
- [650] S. Stephan, M. Urschel: Characteristic curves of the Mie fluid, *Journal of Molecular Liquids* 383 (2023) 122088. DOI: 10.1016/j.molliq.2023.122088.
- [651] O. L. Boshkova, U. K. Deiters: Soft repulsion and the behavior of equations of state at high pressures, *International Journal of Thermophysics* 31 (2010) 227–252. DOI: 10.1007/s10765-010-0727-7.
- [652] E. Mühlegger, K. Langenbach: Investigation of the density dependence of the influence parameter, *International Journal of Thermophysics* 44 (2023) 173. DOI: 10.1007/s10765-023-03281-4.
- [653] B. Breure, C. J. Peters: Modeling of the surface tension of pure components and mixtures using the density gradient theory combined with a theoretically derived influence parameter correlation, *Fluid Phase Equilibria* 334 (2012) 189–196. DOI: 10.1016/j.fluid.2012.08.010.
- [654] V. L. Popov: *Kontaktmechanik und Reibung: ein Lehr- und Anwendungsbuch von der Nanotribologie bis zur numerischen Simulation*, Springer, Berlin, 2009.
- [655] A. W. Islam, E. S. Carlson: Viscosity models and effects of dissolved CO<sub>2</sub>, *Energy & Fuels* 26 (2012) 5330–5336. DOI: 10.1021/ef3006228.
- [656] L. C. Burrows, F. Haeri, P. Cvetic, S. Sanguinito, F. Shi, D. Tapriyal, A. Goodman, R. M. Enick: A literature review of CO<sub>2</sub>, natural gas, and water-based fluids for enhanced oil recovery in unconventional reservoirs, *Energy & Fuels* 34 (2020) 5331–5380. DOI: 10.1021/acs.energyfuels.9b03658.
- [657] B. Kunstmann, I. Wlokas, M. Kohns, H. Hasse: Simulation study of superheating in evaporating droplets of (TTIP + p-xylene) in spray flame synthesis, *Applications in Energy and Combustion Science* 15 (2023) 100156. DOI: 10.1016/j.jaecs.2023.100156.
- [658] R. A. Svehla: Estimated viscosities and thermal conductivities of gases at high temperatures, Technical Report NASA-TR-R-132, Lewis Research Center, Cleveland, Ohio, 1962.
- [659] E. Johannessen, J. Gross, D. Bedeaux: Nonequilibrium thermodynamics of interfaces using classical density functional theory, *The Journal of Chemical Physics* 129 (2008) 184703. DOI: 10.1063/1.3009182.

- [660] K. Stephan, K. Lucas: Viscosity of dense fluids, Springer US, Boston, 1979.
- [661] J. Mairhofer: A residual entropy scaling approach for viscosity based on the GERG-2008 equation of state, *Industrial & Engineering Chemistry Research* 60 (2021) 2652–2662. DOI: 10.1021/acs.iecr.0c04938.
- [662] I. H. Bell: Entropy scaling of viscosity – I: A case study of propane, *Journal of Chemical & Engineering Data* 65 (2020) 3203–3215. DOI: 10.1021/acs.jced.0c00209.
- [663] X. Yang, X. Xiao, E. F. May, I. H. Bell: Entropy scaling of viscosity - III: Application to refrigerants and their mixtures, *Journal of Chemical & Engineering Data* 66 (2021) 1385–1398. DOI: 10.1021/acs.jced.0c01009.
- [664] X. Yang, D. Kim, E. F. May, I. H. Bell: Entropy scaling of thermal conductivity: Application to refrigerants and their mixtures, *Industrial & Engineering Chemistry Research* 60 (2021) 13052–13070. DOI: 10.1021/acs.iecr.1c02154.
- [665] X. Li, K. Kang, Y. Gu, X. Wang: Viscosity prediction of pure refrigerants applying the residual entropy scaling theory coupled with a Generalized Chart parametrization method for the Statistical Associating Fluid Theory, *Journal of Molecular Liquids* 367 (2022) 120479. DOI: 10.1016/j.molliq.2022.120479.
- [666] A. Jäger, L. Steinberg, E. Mickoleit, M. Thol: Residual entropy scaling for long-chain linear alkanes and isomers of alkanes, *Industrial & Engineering Chemistry Research* 62 (2023) 3767–3791. DOI: 10.1021/acs.iecr.2c04238.
- [667] T. Zeiner, S. Enders: Phase behavior of hyperbranched polymer solutions in mixed solvents, *Chemical Engineering Science* 66 (2011) 5244–5252. DOI: 10.1016/j.ces.2011.07.016.
- [668] O. Lobanova, A. Mejía, G. Jackson, E. A. Müller: SAFT- $\gamma$  force field for the simulation of molecular fluids 6: Binary and ternary mixtures comprising water, carbon dioxide, and n -alkanes, *The Journal of Chemical Thermodynamics* 93 (2016) 320–336. DOI: 10.1016/j.jct.2015.10.011.
- [669] O. Lötgering-Lin, J. Gross: Group contribution method for viscosities based on entropy scaling using the perturbed-chain polar statistical associating fluid theory, *Industrial & Engineering Chemistry Research* 54 (2015) 7942–7952. DOI: 10.1021/acs.iecr.5b01698.
- [670] M. Hopp, J. Gross: Thermal conductivity of real substances from excess entropy scaling using PCP-SAFT, *Industrial & Engineering Chemistry Research* 56 (2017) 4527–4538. DOI: 10.1021/acs.iecr.6b04289.

- [671] M. Hopp, J. Mele, J. Gross: Self-diffusion coefficients from entropy scaling using the PCP-SAFT equation of state, *Industrial & Engineering Chemistry Research* 57 (2018) 12942–12950. DOI: 10.1021/acs.iecr.8b02406.
- [672] O. Lötgering-Lin, M. Fischer, M. Hopp, J. Gross: Pure substance and mixture viscosities based on entropy scaling and an analytic equation of state, *Industrial & Engineering Chemistry Research* 57 (2018) 4095–4114. DOI: 10.1021/acs.iecr.7b04871.
- [673] M. Hopp, J. Mele, R. Hellmann, J. Gross: Thermal conductivity via entropy scaling: An approach that captures the effect of intramolecular degrees of freedom, *Industrial & Engineering Chemistry Research* 58 (2019) 18432–18438. DOI: 10.1021/acs.iecr.9b03998.
- [674] M. Hopp, J. Gross: Thermal conductivity from entropy scaling: A group-contribution method, *Industrial & Engineering Chemistry Research* 58 (2019) 20441–20449. DOI: 10.1021/acs.iecr.9b04289.
- [675] J. Zmpitas, J. Gross: Modified Stokes-Einstein equation for molecular self-diffusion based on entropy scaling, *Industrial & Engineering Chemistry Research* 60 (2021) 4453–4459. DOI: 10.1021/acs.iecr.0c06090.
- [676] L. T. Novak: Fluid viscosity-residual entropy correlation, *International Journal of Chemical Reactor Engineering* 9 (2011) 1–27. DOI: 10.2202/1542-6580.2839.
- [677] L. T. Novak: Predictive corresponding-states viscosity model for the entire fluid region: n-Alkanes, *Industrial & Engineering Chemistry Research* 52 (2013) 6841–6847. DOI: 10.1021/ie400654p.
- [678] L. T. Novak: Predicting fluid viscosity of nonassociating molecules, *Industrial & Engineering Chemistry Research* 54 (2015) 5830–5835. DOI: 10.1021/acs.iecr.5b01526.
- [679] A. Dehlouz, J.-N. Jaubert, G. Galliero, M. Bonnissel, R. Privat: Entropy scaling-based correlation for estimating the self-diffusion coefficients of pure fluids, *Industrial & Engineering Chemistry Research* 61 (2022) 14033–14050. DOI: 10.1021/acs.iecr.2c01086.
- [680] A. Dehlouz, J.-N. Jaubert, G. Galliero, M. Bonnissel, R. Privat: Combining the entropy-scaling concept and cubic- or SAFT equations of state for modelling thermal conductivities of pure fluids, *International Journal of Heat and Mass Transfer* 196 (2022) 123286. DOI: 10.1016/j.ijheatmasstransfer.2022.123286.

- [681] A. Dehlouz, R. Privat, G. Galliero, M. Bonnissel, J.-N. Jaubert: Revisiting the entropy-scaling concept for shear-viscosity estimation from cubic and SAFT equations of state: Application to pure fluids in gas, liquid and supercritical states, *Industrial & Engineering Chemistry Research* 60 (2021) 12719–12739. DOI: 10.1021/acs.iecr.1c01386.
- [682] W. A. Fouad, L. F. Vega: Transport properties of HFC and HFO based refrigerants using an excess entropy scaling approach, *The Journal of Supercritical Fluids* 131 (2018) 106–116. DOI: 10.1016/j.supflu.2017.09.006.
- [683] L. Yelash, M. Müller, W. Paul, K. Binder: Artificial multiple criticality and phase equilibria: an investigation of the PC-SAFT approach, *Physical Chemistry Chemical Physics* 7 (2005) 3728–3732. DOI: 10.1039/B509101M.
- [684] R. Privat, R. Gani, J.-N. Jaubert: Are safe results obtained when the PC-SAFT equation of state is applied to ordinary pure chemicals?, *Fluid Phase Equilibria* 295 (2010) 76–92. DOI: 10.1016/j.fluid.2010.03.041.
- [685] I. H. Bell: Entropy scaling of viscosity – I: Predictive scheme for normal alkanes, *Journal of Chemical & Engineering Data* 65 (2020) 5606–5616. DOI: 10.1021/acs.jced.0c00749.
- [686] W. P. Krekelberg, M. J. Pond, G. Goel, V. K. Shen, J. R. Errington, T. M. Truskett: Generalized Rosenfeld scalings for tracer diffusivities in not-so-simple fluids: Mixtures and soft particles, *Physical Review E* 80 (2009) 061205. DOI: 10.1103/PhysRevE.80.061205.
- [687] S. Pieprzyk, D. M. Heyes, A. C. Braika: Thermodynamic properties and entropy scaling law for diffusivity in soft spheres, *Physical Review E* 90 (2014) 012106. DOI: 10.1103/PhysRevE.90.012106.
- [688] N. Gnan, T. B. Schrøder, U. R. Pedersen, N. P. Bailey, J. C. Dyre: Pressure-energy correlations in liquids. IV. Isomorphs in liquid phase diagrams, *The Journal of Chemical Physics* 131 (2009) 234504. DOI: 10.1063/1.3265957.
- [689] T. B. Schrøder, N. Gnan, U. R. Pedersen, N. P. Bailey, J. C. Dyre: Pressure-energy correlations in liquids. V. Isomorphs in generalized Lennard-Jones systems, *The Journal of Chemical Physics* 134 (2011) 164505. DOI: 10.1063/1.3582900.
- [690] I. H. Bell: Probing the link between residual entropy and viscosity of molecular fluids and model potentials, *Proceedings of the National Academy of Sciences* 116 (2019) 4070–4079. DOI: 10.1073/pnas.1815943116.

- [691] Y. Zhang, W. G. Chapman: Modeling thermodynamic properties of isomeric alkanes with a new branched equation of state, *Industrial & Engineering Chemistry Research* 57 (2018) 1679–1688. DOI: 10.1021/acs.iecr.7b03951.
- [692] I. G. Economou: Statistical associating fluid theory: A successful model for the calculation of thermodynamic and phase equilibrium properties of complex fluid mixtures, *Industrial & Engineering Chemistry Research* 41 (2002) 953–962. DOI: 10.1021/ie0102201.
- [693] A. Müller, J. Winkelmann, J. Fischer: Backbone family of equations of state: 1. Nonpolar and polar pure fluids, *AIChE Journal* 42 (1996) 1116–1126. DOI: 10.1002/aic.690420423.
- [694] U. Weingerl, M. Wendland, J. Fischer, A. Müller, J. Winkelmann: Backbone family of equations of state: 2. Nonpolar and polar fluid mixtures, *AIChE Journal* 47 (2001) 705–717. DOI: 10.1002/aic.690470317.
- [695] R. L. Cotterman, B. J. Schwarz, J. M. Prausnitz: Molecular thermodynamics for fluids at low and high densities. Part I: Pure fluids containing small or large molecules, *AIChE Journal* 32 (1986) 1787–1798. DOI: 10.1002/aic.690321104.
- [696] R. L. Cotterman, J. M. Prausnitz: Molecular thermodynamics for fluids at low and high densities. Part II: Phase equilibria for mixtures containing components with large differences in molecular size or potential energy, *AIChE Journal* 32 (1986) 1799–1812. DOI: 10.1002/aic.690321105.
- [697] G. M. Kontogeorgis, M. L. Michelsen, G. K. Folas, S. Derawi, N. Von Solms, E. H. Stenby: Ten years with the CPA (cubic-plus-association) equation of state. Part 1. Pure compounds and self-associating systems, *Industrial & Engineering Chemistry Research* 45 (2006) 4855–4868. DOI: 10.1021/ie051305v.
- [698] J. Staubach, S. Stephan: Prediction of thermodynamic properties of fluids at extreme conditions: Assessment of the consistency of molecular-based models, in: J. C. Aurich, C. Garth, B. S. Linke (Eds.), *Proceedings of the 3rd Conference on Physical Modeling for Virtual Manufacturing Systems and Processes*, Springer International Publishing, Cham, 2023, pp. 170–188. DOI: 10.1007/978-3-031-35779-4\_10.
- [699] J. S. Rowlinson, F. L. Swinton: *Liquids and liquid mixtures: Butterworths monographs in chemistry*, Butterworth-Heinemann, Oxford, 2013.
- [700] D. Berthelot: Sur le melange des gaz, *Comptes rendus hebdomadaires des séances de l'Académie des sciences* 126 (1898) 1703 – 1706.

- [701] G. M. Kontogeorgis, I. V. Yakoumis, H. Meijer, E. Hendriks, T. Moorwood: Multicomponent phase equilibrium calculations for water-methanol-alkane mixtures, *Fluid Phase Equilibria* 158-160 (1999) 201–209. DOI: 10.1016/S0378-3812(99)00060-6.
- [702] A. Gonzalez, L. Pereira, P. Paricaud, C. Coquelet, A. Chapoy: Modeling of transport properties using the SAFT-VR Mie equation of state, in: SPE Annual Technical Conference and Exhibition, SPE, Houston, 2015, p. D031S043R005. DOI: 10.2118/175051-MS.
- [703] J. Gross: An equation-of-state contribution for polar components: Quadrupolar molecules, *AIChE Journal* 51 (2005) 2556–2568. DOI: 10.1002/aic.10502.
- [704] N. M. Al-Saifi, E. Z. Hamad, P. Englezos: Prediction of vapor-liquid equilibrium in water-alcohol-hydrocarbon systems with the dipolar perturbed-chain SAFT equation of state, *Fluid Phase Equilibria* 271 (2008) 82–93. DOI: 10.1016/j.fluid.2008.06.015.
- [705] I. H. Bell, R. Hellmann, A. H. Harvey: Zero-density limit of the residual entropy scaling of transport properties, *Journal of Chemical & Engineering Data* 65 (2020) 1038–1050. DOI: 10.1021/acs.jced.9b00455.
- [706] M. Thol, G. Rutkai, A. Köster, R. Lustig, R. Span, J. Vrabec: Equation of state for the Lennard-Jones fluid, *Journal of Physical and Chemical Reference Data* 45 (2016) 023101. DOI: 10.1063/1.4945000.
- [707] S. Deublein, B. Eckl, J. Stoll, S. V. Lishchuk, G. Guevara-Carrion, C. W. Glass, T. Merker, M. Bernreuther, H. Hasse, J. Vrabec: ms2: A molecular simulation tool for thermodynamic properties, *Computer Physics Communications* 182 (2011) 2350–2367. DOI: 10.1016/j.cpc.2011.04.026.
- [708] C. W. Glass, S. Reiser, G. Rutkai, S. Deublein, A. Köster, G. Guevara-Carrion, A. Wafai, M. Horsch, M. Bernreuther, T. Windmann, H. Hasse, J. Vrabec: ms2: A molecular simulation tool for thermodynamic properties, new version release, *Computer Physics Communications* 185 (2014) 3302–3306. DOI: 10.1016/j.cpc.2014.07.012.
- [709] P. Vargas, E. Munoz, L. Rodriguez: Second virial coefficient for the Lennard-Jones potential, *Physica A* (2001).
- [710] B. Widom: Some topics in the theory of fluids, *The Journal of Chemical Physics* 39 (1963) 2808–2812. DOI: 10.1063/1.1734110.



- [711] U. K. Deiters, T. Kraska: High-pressure fluid phase equilibria: Phenomenology and computation, *Supercritical fluid science and technology*, Elsevier, Amsterdam, Boston, 2012.
- [712] C. R. Wilke: A viscosity equation for gas mixtures, *The Journal of Chemical Physics* 18 (1950) 517–519. DOI: 10.1063/1.1747673.
- [713] A. Wassiljewa: Wärmeleitung in Gasgemischen, *Physikalische Zeitschrift* 5 (1904) 737.
- [714] E. A. Mason, S. C. Saxena: Approximate formula for the thermal conductivity of gas mixtures, *The Physics of Fluids* 1 (1958) 361–369. DOI: 10.1063/1.1724352.
- [715] J. Vrabec, J. Stoll, H. Hasse: A set of molecular models for symmetric quadrupolar fluids, *The Journal of Physical Chemistry B* 105 (2001) 12126–12133. DOI: 10.1021/jp012542o.
- [716] J. Gross, J. Vrabec: An equation-of-state contribution for polar components: Dipolar molecules, *AIChE Journal* 52 (2006) 1194–1204. DOI: 10.1002/aic.10683.
- [717] N. A. Lai, T. T. H. Phan: Review of the BACKONE equation of state and its applications, *Molecular Physics* 115 (2017) 1041–1050. DOI: 10.1080/00268976.2016.1218562.
- [718] B. Saleh, G. Koglbauer, M. Wendland, J. Fischer: Working fluids for low-temperature organic Rankine cycles, *Energy* 32 (2007) 1210–1221. DOI: 10.1016/j.energy.2006.07.001.
- [719] Dortmund Data Bank, 2024, [www.ddbst.com](http://www.ddbst.com), 2024.
- [720] J. Grace, G. Kennedy: The melting curve of five gases to 30 kb, *Journal of Physics and Chemistry of Solids* 28 (1967) 977–982. DOI: 10.1016/0022-3697(67)90214-4.
- [721] P. Linstrom: NIST Chemistry WebBook, NIST Standard Reference Database 69, 1997. DOI: 10.18434/T4D303.
- [722] G. P. Dubey, M. Sharma: Excess volumes, densities, speeds of sound, and viscosities for the binary systems of 1-octanol with hexadecane and squalane at (298.15, 303.15 and 308.15) K, *International Journal of Thermophysics* 29 (2008) 1361–1375. DOI: 10.1007/s10765-008-0491-0.

- [723] D. Ducoulombier, H. Zhou, C. Boned, J. Peyrelasse, H. Saint-Guirons, P. Xans: Pressure (1-1000 bars) and temperature (20-100°C) dependence of the viscosity of liquid hydrocarbons, *The Journal of Physical Chemistry* 90 (1986) 1692–1700. DOI: 10.1021/j100399a047.
- [724] J. A. Wesselingh, R. Krishna: *Mass transfer in multicomponent mixtures*, 1st ed., Delft Univ. Press, Delft, 2000.
- [725] R. Evans, G. Dal Poggetto, M. Nilsson, G. A. Morris: Improving the interpretation of small molecule diffusion coefficients, *Analytical Chemistry* 90 (2018) 3987–3994. DOI: 10.1021/acs.analchem.7b05032.
- [726] A. Vignes: Diffusion in binary solutions. Variation of diffusion coefficient with composition, *Industrial & Engineering Chemistry Fundamentals* 5 (1966) 189–199. DOI: 10.1021/i160018a007.
- [727] L. Darken: Diffusion, mobility and their interrelation through free energy in binary metallic systems, *Transactions of the AIME* 175 (1948) 184.
- [728] I. H. Bell, J. C. Dyre, T. S. Ingebrigtsen: Excess-entropy scaling in supercooled binary mixtures, *Nature Communications* 11 (2020) 4300. DOI: 10.1038/s41467-020-17948-1.
- [729] H. A. Lorentz: Ueber die Anwendung des Satzes vom Virial in der kinetischen Theorie der Gase, *Annalen der Physik* 248 (1881) 127–136. DOI: 10.1002/andp.18812480110.
- [730] J. Burger, E. Ströfer, H. Hasse: Production process for diesel fuel components poly(oxyethylene) dimethyl ethers from methane-based products by hierarchical optimization with varying model depth, *Chemical Engineering Research and Design* 91 (2013) 2648–2662. DOI: 10.1016/j.cherd.2013.05.023.
- [731] N. Schmitz, J. Burger, E. Ströfer, H. Hasse: From methanol to the oxygenated diesel fuel poly(oxyethylene) dimethyl ether: An assessment of the production costs, *Fuel* 185 (2016) 67–72. DOI: 10.1016/j.fuel.2016.07.085.
- [732] C. F. Breitzkreuz, N. Schmitz, E. Ströfer, J. Burger, H. Hasse: Design of a Production Process for Poly(oxyethylene) Dimethyl Ethers from Dimethyl Ether and Trioxane, *Chemie Ingenieur Technik* 90 (2018) 1489–1496. DOI: 10.1002/cite.201800038.
- [733] T. Beutler, N. Prchal, M. Günthner: Numerical modeling of diesel and poly(oxyethylene) dimethyl ether spray in a high pressure chamber using the fischer

- primary breakup model, *Automotive and Engine Technology* 7 (2022) 409–426. DOI: 10.1007/s41104-022-00120-w.
- [734] J. Burger, M. Siegert, E. Ströfer, H. Hasse: Poly(oxymethylene) dimethyl ethers as components of tailored diesel fuel: Properties, synthesis and purification concepts, *Fuel* 89 (2010) 3315–3319. DOI: 10.1016/j.fuel.2010.05.014.
- [735] M. L. Botero, Y. Huang, D. L. Zhu, A. Molina, C. K. Law: Synergistic combustion of droplets of ethanol, diesel and biodiesel mixtures, *Fuel* 94 (2012) 342–347. DOI: 10.1016/j.fuel.2011.10.049.
- [736] B. Lump, D. Rothe, C. Pastötter, R. Lämmermann, E. Jacob: Oxymethylene ethers as diesel fuel additives of the future, *MTZ worldwide* 72 (2011) 34–38.
- [737] C. F. Breitzkreuz, A. Holzer, T. Fuchs, M. Günthner, H. Hasse: Miscibility in systems containing (poly(oxymethylene) ethers (OME) + hydrocarbons + water), *Fuel* 338 (2023) 127337. DOI: 10.1016/j.fuel.2022.127337.
- [738] C. K. Law: Internal boiling and superheating in vaporizing multicomponent droplets, *AIChE Journal* 24 (1978) 626–632. DOI: 10.1002/aic.690240410.
- [739] C. R. Wilke, P. Chang: Correlation of diffusion coefficients in dilute solutions, *AIChE Journal* 1 (1955) 264–270. DOI: 10.1002/aic.690010222.
- [740] M. Schappals, T. Breug-Nissen, K. Langenbach, J. Burger, H. Hasse: Solubility of Carbon Dioxide in Poly(oxymethylene) Dimethyl Ethers, *Journal of Chemical & Engineering Data* 62 (2017) 4027–4031. DOI: 10.1021/acs.jced.7b00718.
- [741] P. S. Tofts, D. Lloyd, C. A. Clark, G. J. Barker, G. J. M. Parker, P. McConville, C. Baldock, J. M. Pope: Test liquids for quantitative MRI measurements of self-diffusion coefficient in vivo, *Magnetic Resonance in Medicine* 43 (2000) 368–374. DOI: 10.1002/(sici)1522-2594(200003)43:3<368::aid-mrm8>3.0.co;2-b.
- [742] J. H. Dymond, K. R. Harris: The temperature and density dependence of the self-diffusion coefficient of n-hexadecane, *Molecular Physics* 75 (1992) 461–466. DOI: 10.1080/00268979200100351.
- [743] K. R. Harris, B. Ganbold, W. S. Price: Viscous Calibration Liquids for Self-Diffusion Measurements, *Journal of Chemical & Engineering Data* 60 (2015) 3506–3517. DOI: 10.1021/acs.jced.5b00246.
- [744] J. J. C. Shieh, P. A. Lyons: Transport properties of liquid n-alkanes, *The Journal of Physical Chemistry* 73 (1969) 3258–3264. DOI: 10.1021/j100844a017.

- [745] J. Chen, J. Zhang: Determination of liquid diffusion coefficients for binary systems by improved metallic diaphragm cell method, *Gao Xiao Hua Xue Gong Cheng Xue Bao/Journal of Chemical Engineering of Chinese Universities* 6 (1992) 196 – 201.
- [746] M. L. P. Price, D. Ostrovsky, W. L. Jorgensen: Gas-phase and liquid-state properties of esters, nitriles, and nitro compounds with the OPLS-AA force field, *Journal of Computational Chemistry* 22 (2001) 1340–1352. DOI: 10.1002/jcc.1092.
- [747] R. A. Messerly, M. C. Anderson, S. M. Razavi, J. R. Elliott: Mie 16-6 force field predicts viscosity with faster-than-exponential pressure dependence for 2,2,4-trimethylhexane, *Fluid Phase Equilibria* 495 (2019) 76–85. DOI: 10.1016/j.fluid.2019.05.013.
- [748] I. J. Prentice, X. Liu, O. A. Nerushev, S. Balakrishnan, C. R. Pulham, P. J. Camp: Experimental and simulation study of the high-pressure behavior of squalane and poly- $\alpha$ -olefins, *The Journal of Chemical Physics* 152 (2020) 074504. DOI: 10.1063/1.5139723.
- [749] J. Bezanson, A. Edelman, S. Karpinski, V. B. Shah: Julia: A fresh approach to numerical computing, *SIAM Review* 59 (2017) 65–98. DOI: 10.1137/141000671.
- [750] Y. Naziev, A. Gazanov, A. Gumbatov, A. Abasov: Experimentelle Untersuchung der Wärmekapazität von flüssigen binären n-Hexan-Benzol-Mischungen, *Izvestiya Vysshikh Uchebnykh Zavedenii, Neft i Gaz* 29 (1986) 51–54.
- [751] S. Kravchun: Thermal conductivity of binary liquid systems, *Russian Journal of Physical Chemistry A* 60 (1986) 2176–2179.
- [752] L. Miller, P. C. Carman: Self-diffusion in mixtures. Part 4. – Comparison of theory and experiment for certain gas mixtures, *Transactions of the Faraday Society* 57 (1961) 2143–2150. DOI: 10.1039/TF9615702143.
- [753] B. Eckl, J. Vrabec, H. Hasse: Set of molecular models based on quantum mechanical ab initio calculations and thermodynamic data, *The Journal of Physical Chemistry B* 112 (2008) 12710–12721. DOI: 10.1021/jp803341h.
- [754] D. J. L. Prak, B. G. Lee, J. S. Cowart, P. C. Trulove: Density, viscosity, speed of sound, bulk modulus, surface tension, and flash point of binary mixtures of butylbenzene + linear alkanes (n-decane, n-dodecane, n-tetradecane, n-hexadecane, or n-heptadecane) at 0.1 MPa, *Journal of Chemical & Engineering Data* 62 (2016) 169–187. DOI: 10.1021/acs.jced.6b00542.

- [755] M. A. Aissa, I. R. Radovi, Z. V. Simi, M. L. Kijevanin: Thermodynamic and transport properties of ternary mixture (ethyl oleate + n-hexadecane + 1-butanol) and its binary constituents (ethyl oleate + 1-butanol and ethyl oleate + n-hexadecane) at different temperatures and atmospheric pressure, *Journal of Molecular Liquids* 317 (2020) 114186. DOI: 10.1016/j.molliq.2020.114186.
- [756] M. H. H. Fechter, P. Haspel, C. Hasse, A. S. Braeuer: Vapor pressures and latent heats of vaporization of Poly(oxymethylene) Dimethyl Ethers (OME3 and OME4) up to the vicinity of the critical temperature, *Fuel* 303 (2021) 121274. DOI: 10.1016/j.fuel.2021.121274.
- [757] M.-R. Kang, H.-Y. Song, F.-x. Jin, J. Chen: Synthesis and physicochemical characterization of polyoxymethylene dimethyl ethers, *Journal of Fuel Chemistry and Technology* 45 (2017) 837–845. DOI: 10.1016/s1872-5813(17)30040-3.
- [758] R. L. Rowley, W. V. Wilding, J. L. Oscarson, Y. Yang, N. A. Zundel, T. E. Daubert, R. P. Danner: DIPPR data compilation of pure chemical properties, 2003.
- [759] R. Krishna, J. M. van Baten: The Darken relation for multicomponent diffusion in liquid mixtures of linear alkanes: An investigation using molecular dynamics (MD) simulations, *Industrial & Engineering Chemistry Research* 44 (2005) 6939–6947. DOI: 10.1021/ie050146c.
- [760] P. W. M. Rutten: Diffusion in liquids, PhD thesis, TU Delft, Delft, 1992.
- [761] J. Li, H. Liu, Y. Hu: A mutual-diffusion-coefficient model based on local composition, *Fluid Phase Equilibria* 187-188 (2001) 193–208. DOI: 10.1016/S0378-3812(01)00535-0.



# Appendix

## A Supporting Information for Chapter 2

### A.1 Simulation Details

The software package *ms2* [464] was used for the simulations performed in this work. Simulations were carried out with 5,000 particles. The Gear-predictor-corrector integrator was used with a time step of  $\Delta\tau = 0.001 \sigma(M/\varepsilon)^{1/2}$ . The simulations were conducted in the *NVT* ensemble with  $1 \times 10^5$  equilibration time steps and  $5 \times 10^6$  production time steps. Periodic boundary conditions were applied in all directions. The shear viscosity, thermal conductivity, and self-diffusion coefficient were sampled using the Green-Kubo [97, 98] formalism with a correlation length of  $10^4$  time steps for  $\rho \geq 0.1 \sigma^{-3}$  and  $10^5$  time steps for  $\rho < 0.1 \sigma^{-3}$ . Details on the computational procedure of the Green-Kubo implementation in *ms2* are given in Refs. [707, 708]. For the simulations at  $\rho < 0.01 \sigma^{-3}$ , a different computational setup was used. These simulations were conducted with the software package LAMMPS [298]. Number of particles, time step, ensemble, and boundary conditions were the same as above. The number of equilibration and production time steps were adjusted for the low-density simulations to  $10^6$  and  $10^8$ , respectively. The shear viscosity and thermal conductivity were calculated with the Green-Kubo method with correlation lengths of  $2 \times 10^6$  ( $\rho = 10^{-2} \sigma^{-3}$  and  $\rho = 5 \times 10^{-3} \sigma^{-3}$ ) and  $5 \times 10^6$  ( $\rho = 10^{-3} \sigma^{-3}$ ) time steps. The self-diffusion coefficient was calculated by the Einstein method [14] based on the mean squared displacement.

## A.2 Discussion of Data Sets

Figs. A.1 - A.3 show the relative deviations  $\delta Y$  (cf. Eq. (2)) of the entropy scaling model and the simulation data for the shear viscosity, thermal conductivity, and self-diffusion coefficient as a function of temperature, respectively. All data are shown, i.e. both

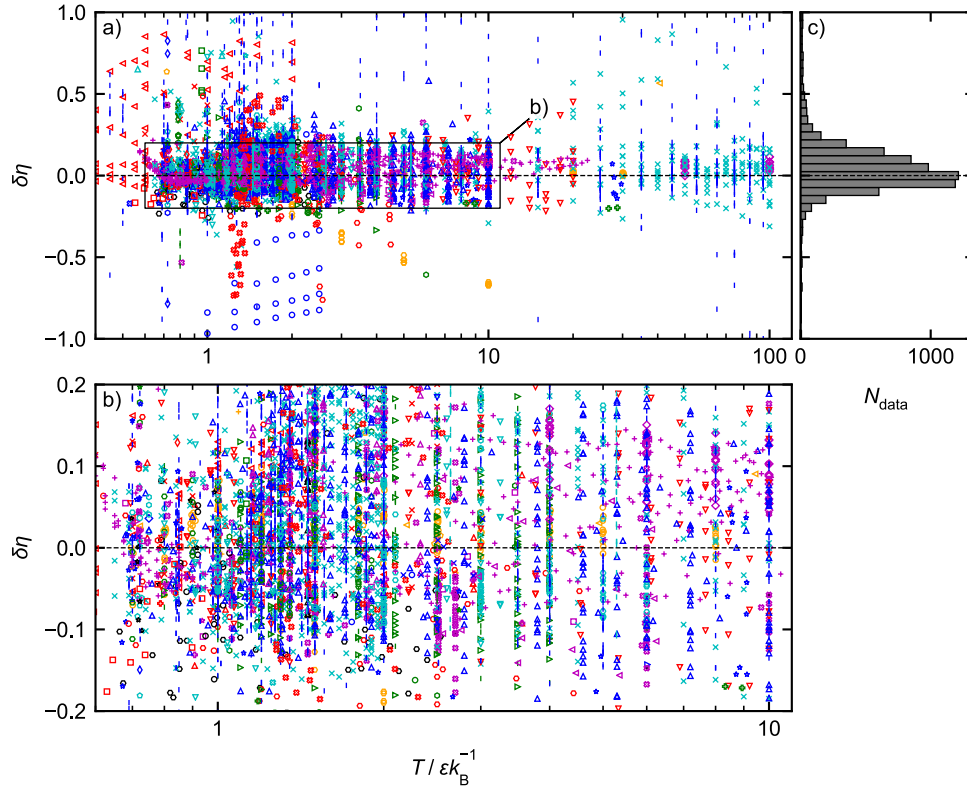


**Figure A.1:** Relative deviation of the simulation data from the entropy scaling model for the shear viscosity  $\delta\eta$  (cf. Eq. (2)) as a function of temperature. All data are shown (including those identified as outliers). The dashed line represents the entropy scaling model. Symbols as introduced in Fig. 4. Error bars are omitted to avoid visual clutter. Panel b) is a magnified view of a part of panel a). Panel c) shows a histogram of the relative deviations.

the confirmed data and outliers. For the shear viscosity, the model has a tendency to underestimate the computer experiment data, cf. Fig. A.1 a). There are no systematic temperature-dependent deviations – the deviations at high temperatures are similar to those at moderate temperatures (which is different for  $\lambda$  and  $D$  – see below). For the triple point temperature  $T_{\text{tr}} = 0.69 \epsilon k_B^{-1}$  [238] and below (mainly metastable liquid simulations, cf. Fig. 3), large deviations were observed. Several data points from the reproducibility study from *Fleckenstein et al.* [200] (blue vertical lines) significantly



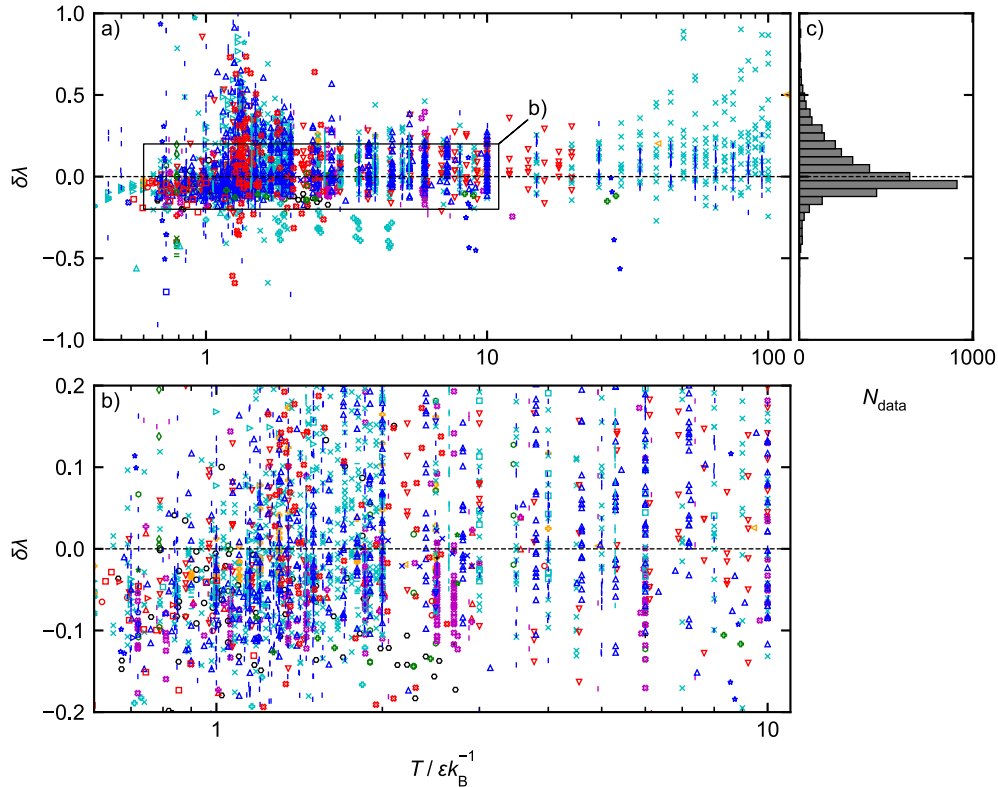


**Figure A.2:** Relative deviation of the simulation data from the entropy scaling model for the thermal conductivity  $\delta\lambda$  (cf. Eq. (2)) as a function of temperature. All data are shown (including those identified as outliers). The dashed line represents the entropy scaling model. Symbols as introduced in Fig. 4. Error bars are omitted to avoid visual clutter. Panel b) is a magnified view of a part of panel a). Panel c) shows a histogram of the relative deviations.

exceed the entropy scaling model. Most of these data points at high temperatures can be traced back to the NEMD simulation data reported therein. Several of these data points were identified as outliers (see Supporting Information). At high temperatures, the thermal (undirected) particle velocities are large and thus, it is difficult to determine the velocity profile that is required for the evaluation of the shear viscosity by NEMD simulations. Furthermore, significant deviations were observed for the data reported by *Baidakov et al.* [184] (red triangles pointing left), cf. Fig. A.1 a). A significant amount of these data points lies in the solid-liquid two-phase region or beyond the melting line (cf. Fig. 3). Since data are only scarcely available in these regions for comparison, the MoDOD algorithm does not identify all of these data as outliers. The data from *Michels and Trappeniers* [145] (orange hexagons) show a peculiar temperature dependence (cf. Fig. A.1), which is reflected by the fact that around two third of the according data

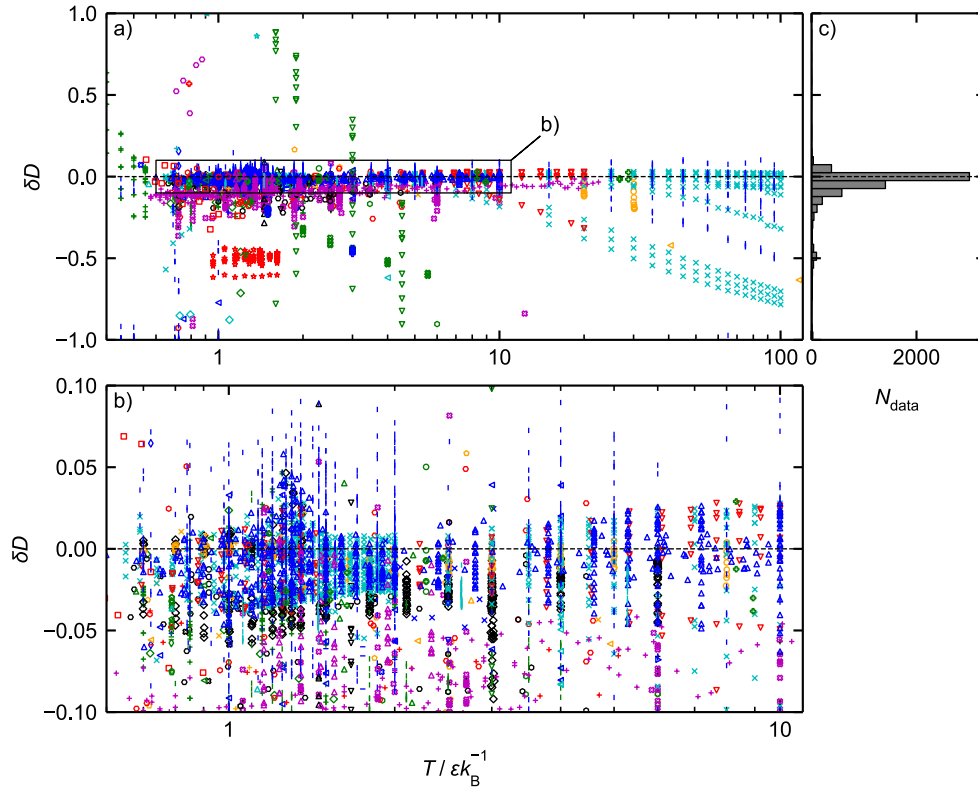


**Figure A.3:** Relative deviation of the simulation data from the entropy scaling model for the self-diffusion coefficient  $\delta D$  (cf. Eq. (2)) as a function of temperature. All data are shown (including those identified as outliers). The dashed line represents the entropy scaling model. Symbols as introduced in Fig. 4. Error bars are omitted to avoid visual clutter. Panel b) is a magnified view of a part of panel a). Panel c) shows a histogram of the relative deviations.

were identified as outliers. For some data points reported by *Thomas and Rowley* [176] (green triangles pointing right), significant deviations are observed, cf. Fig. A.1 a) and c). Most of these data points are at high density liquid states and were identified as outliers. This is in line with a statement of the authors regarding the reliability of these very high-density data [176], which was determined by a specific approach. Similarly, a significant amount of data from *Heyes* [144] (red hexagons) deviate from most other data, cf. Fig. A.1 a) and c), especially for densities  $\rho < 0.6 \sigma^{-3}$  and temperatures  $T > 1.2 \epsilon k_B^{-1}$  (see electronic Supporting Information). Most of these data points were also identified as outliers. This might be due to the fact that the NEMD method applied in Ref. 144 has difficulties under these conditions. Some systematic positive deviations were observed for simulation data from this work (cyan crosses) at extreme temperatures, cf. Fig. A.1. These deviations are mainly caused by the model: At high temperatures  $T > 20 \epsilon k_B^{-1}$

and densities  $\rho > 1.8 \sigma^{-3}$ , the employed EOS exhibits artifacts, which yields an unreliable description of the entropy. Yet, practically no data points in the region where the Kolafa-Nezbeda EOS exhibits artifacts were identified as outliers, which supports the robustness of the MoDOD method. Details are given in the Supporting Information.

For the thermal conductivity (cf. Fig. A.2), also several aspects regarding specific data sets were observed. The thermal conductivity data reported by *Borgelt et al.* [156] (black hexagons) (all at  $\rho = 0.7802 \sigma^{-3}$  and  $0.66 \leq T / \varepsilon k_{\text{B}}^{-1} \leq 2.71$ ) slightly underestimates the other simulation data, cf. Fig. A.2 a) and b). Nevertheless, the deviations of the data from *Borgelt et al.* do not exceed the overall scatter of the thermal conductivity data to be identified as outliers with the MoDOD test. Also for the data of *Heyes* [203] (turquoise pluses), systematic deviations from the majority of the other data are observed. These deviations support the findings from the MoDOD test, which identified most of these data points as outliers. This might be due to the relatively large time step used in Ref. 203 and the special NEMD method used therein. The data from *Ashurst and Hoover* from 1975 [139] (blue stars) show a large scatter with respect to the entropy scaling base line, cf. Fig. A.2 a). This is in line with the fact that several of these data points were identified as outliers. The same holds for the first simulation data set reported for the thermal conductivity by *Levesque et al.* [138] in 1973 (blue square). Some of the data from *Fleckenstein et al.* [200] (blue vertical lines) overestimate the thermal conductivity in the vicinity of the critical point. Most of these data points were sampled with different NEMD methods, whereof some were identified as outliers.

For the self-diffusion coefficient, the deviation plot in Fig. A.3 yields additional insights regarding the quality of individual data sets. The systematic deviations in the extreme temperature region are again due to the artifact of the base line model at  $\rho > 2 \sigma^{-3}$ . Systematic deviations were observed for the studies from *Michels and Trappeniers* from 1975 [215] and 1978 [217] (blue crosses and green pluses, respectively). Both data sets systematically underestimate the remainder of the data. The deviations increase with rising temperature. This is in line with the fact that many of these data points were identified as outliers. The defects of these data are probably due to the relatively short sampling time and small number of particles used in the simulations [215, 217]. The data from *Heyes et al.* [140] (blue diamonds) and *Heyes* [153] (pink crosses) systematically underestimate the majority of the simulation data, which is also reflected by the MoDOD test that identified around 30% of these data as outliers. The same holds for the data of *Borgelt et al.* [156] (black hexagons), whereof about 40% were identified as outliers. The data from *Oderji et al.* [183] (orange circles) are in good agreement with most of the other simulation data up to about  $T = 10 \varepsilon k_{\text{B}}^{-1}$ , cf. Fig. A.3 a) and c). At higher temperatures, the data from *Oderji et al.* deviate from the base line model and other simulation data, cf. Fig. A.3 a). Hence, these data might have a defect, which is

supported by the results from the CE test, cf. Fig. 9.

### A.3 Overview of Other Properties Reported in the References

Table A.1 gives an overview for the data of other properties (not shear viscosity, thermal conductivity, or self-diffusion coefficient), e.g. caloric or entropic properties. The listed publications and data reported therein are not part of the original (static property) Lennard-Jones database [73].

**Table A.1:** Overview of (static) thermodynamic properties reported in the references considered in this work. The columns indicate (from left to right) the authors, year of publication, properties given, and number of data points. In the third column, the variables indicate the pressure  $p$ , internal energy  $u$ , isochoric and isobaric heat capacities  $c_v$  and  $c_p$ , isothermal compressibility  $\beta$ , configurational entropy  $s_{\text{conf}}$ , and derivatives of the Helmholtz energy  $\tilde{a}_{ij}$  [706].

Authors	Year	Properties	#
<i>Fincham and Heyes</i> [143]	1983	$c_v, u$	11
<i>Heyes</i> [218]	1983	$c_v, c_p, \beta$	10, 15, 15
<i>Heyes</i> [203]	1984	$c_v$	36
<i>Heyes</i> [148]	1987	$u$	126
<i>Levesque and Verlet</i> [149]	1987	$u, c_v$	3
<i>Heyes</i> [153]	1988	$u$	210
<i>Wei-Zhong et al.</i> [224]	2008	$u$	1
<i>Oderji et al.</i> [183]	2011	$\beta$	1
<i>Fertig and Stephan</i> [112]	2023	$\tilde{a}_{ij}$	26
<i>Fleckenstein et al.</i> [200]	2024	$u$	1497
<i>Saric et al.</i> [202]	2024	$s_{\text{conf}}$	120
<i>Schmitt et al.</i> [52]	2024	$s_{\text{conf}}$	196

## A.4 Heat Maps of the Statistical Uncertainties of the Data

The mean relative statistical uncertainties reported in the database (using all data) are depicted in heat maps as a function of  $T$  and  $\rho$  in Fig. A.4.

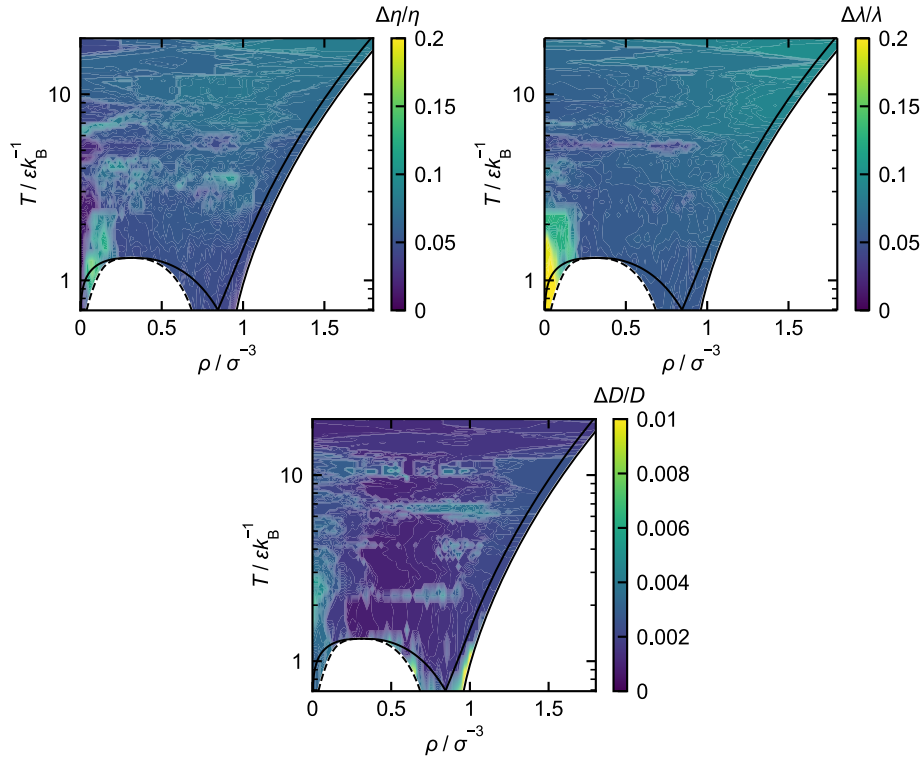


**Figure A.4:** Heat maps of the relative statistical uncertainty of the data points for the shear viscosity  $\Delta\eta/\eta$  (top left), thermal conductivity  $\Delta\lambda/\lambda$  (top right), and self-diffusion coefficient  $\Delta D/D$  as a function of temperature  $T$  and density  $\rho$ . The color encodes the uncertainty as given by the colorbar. The phase envelopes are the same as in Fig. 3.

The statistical uncertainties of the shear viscosity and thermal conductivity are largest in the subcritical gas phase region. Especially the uncertainty of the thermal conductivity data strongly increases there. For the other state regions, the uncertainties are uniformly distributed with a slight tendency of increasing uncertainty with rising temperature. The uncertainty of the self-diffusion coefficient data is not elevated in the gas phase region. There are larger uncertainties in the liquid phase state region and in the metastable regions including the metastable SLE and VLE regions.

## A.5 Outliers in the Phase Diagram

Fig. A.5 shows the data points identified as outliers in the  $T - \rho$  plane. In general, the

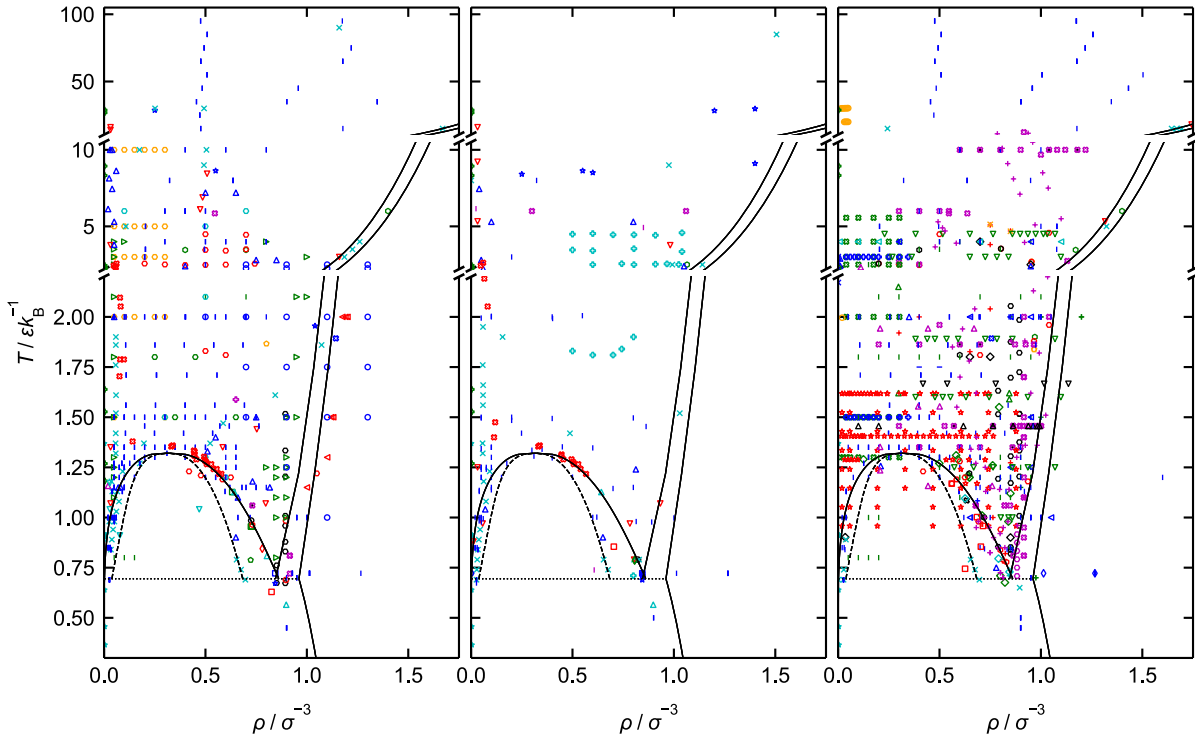


**Figure A.5:** Data points identified as outliers for the shear viscosity (left), thermal conductivity (middle), and self-diffusion coefficient (right) as a function of  $T$  and  $\rho$ . Symbols and lines are the same as in Fig. 3.

data points identified as outliers are distributed across the entire phase diagram, which includes gas, liquid, supercritical, and metastable states. For the shear viscosity, an increased number of data points at high liquid densities and in the metastable liquid-solid region were identified as outliers, which can be attributed to the difficulties for the simulation techniques there. Data points in the unstable regions are not in all cases identified as outliers, which is mostly due to the fact that the data points in their neighborhood also exhibit similar deviations from the model, cf. Eq. (3). Moreover, the neighborhood  $M_j$  is often sparsely populated for data points in the unstable region, which makes the MoDOD algorithm reluctant to identify a data point as an outlier.

## A.6 Evaluation of the Critical Region

In Fig. A.6, the deviations of the data points with respect to the base line models in the vicinity of the critical point are given. For the shear viscosity, there are positive deviations independent of density or temperature. This is probably due to the poor description of the entropy by the Kolafa-Nezbeda EOS in the vicinity of the critical point. For the thermal conductivity, the deviations of the simulation data from the reference model show systematic deviations when approaching the critical point – both

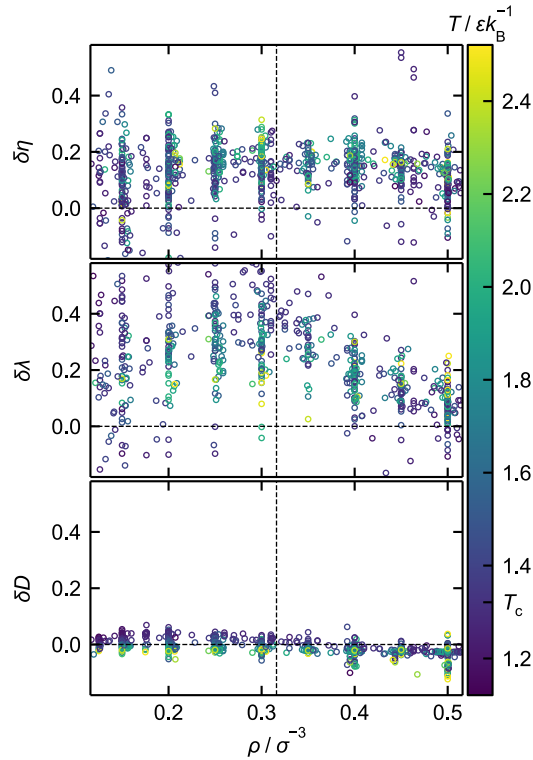


**Figure A.6:** Relative deviations of the simulation data and the entropy scaling model for the shear viscosity  $\delta\eta$  (top), thermal conductivity  $\delta\lambda$  (middle), and self-diffusion coefficient  $\delta D$  (bottom) as a function of the density  $\rho$  for state points in the vicinity of the critical point with  $T_c - 0.1\epsilon k_B^{-1} < T < T_c + 1.2\epsilon k_B^{-1}$  and  $\rho_c - 0.2\sigma^{-3} < \rho < \rho_c + 0.2\sigma^{-3}$ . The dashed lines represent the entropy scaling model. The color of the symbols indicates the temperature.

for the density and temperature dependence. Regarding the density dependence, the deviations exhibit a maximum at the critical density as can be seen in Fig. A.6. This is due to the critical enhancement of the thermal conductivity [128]. For the self-diffusion coefficient, the deviations are consistently smaller and a critical enhancement is visible. However, for temperatures near the critical point, the deviations are positive, i.e. the simulation data are underestimated by the base line model. For higher temperatures, this relation is reversed and the base line model tends to overestimate the simulation data. This behavior can be attributed to the scaling behavior of the Kolafa-Nezbeda EOS in that region.

## A.7 Artifact of Kolafa-Nezbeda EOS at High Temperatures and Densities

For the self-diffusion coefficient, there are some data sets at high temperatures and pressures that seem to have a strong systematic deviation. These spurious deviations are due to the unphysical behavior of the Kolafa-Nezbeda EOS in this (small) state region which is demonstrated in the following. Fig. A.7 shows the isentropes calculated with the Kolafa-Nezbeda EOS in the entire  $T - \rho$  phase diagram up to  $T = 100 \varepsilon k_B^{-1}$ . For densities  $\rho > 1.8 \sigma^{-3}$  and temperatures  $T > 15 \varepsilon k_B^{-1}$ , which is outside of the validity

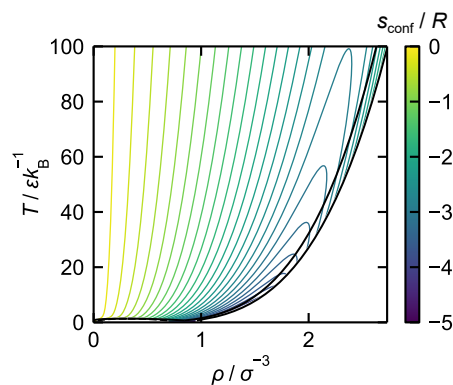


**Figure A.7:** Phase diagram of the Lennard-Jones fluid. Black lines represent the phase envelopes. Colored lines represent isentropes calculated with the Kolafa-Nezbeda EOS [136]. The melting and the freezing lines (black) were taken from Ref. 238. The color indicates the entropy value of a given isentrope.

range of that EOS, the isentropes exhibit a maximum temperature, which is unphysical. Due to this artifact of the EOS, the entropy scaling model yields erroneous values in this region leading to large deviations. As the outlier detection method *MoDOD* [135] is a conservative approach and takes such deviations implicitly into account, these data points were not identified as outliers. An artifact of the Kolafa-Nezbeda LJ EOS was also identified by *Stephan and Deiters* [50] using the characteristic curve test approach. Yet, this test revealed an artificial behavior (for the *Amagat* curve) beyond the freezing line at extreme temperatures and densities. In this work, it becomes clear that the Kolafa-Nezbeda EOS shows artifacts already in the fluid region at extreme temperatures and densities based on the behavior of the entropy. This underlines the statement that passing the characteristic curve test is necessary, but not sufficient to prove the thermodynamic consistency of an EOS model. Nevertheless, the characteristic curve test correctly indicated issues in that state region.



## A.8 Deviation Plots of Selected Data Sets

Fig. A.8 shows the deviation plot of the data sets with high accuracy as mentioned in the Chapter 2, namely Refs. 171, 183, 194, 196, 197, 199, 202 for the viscosity, Refs. 114, 153, 199, 202, 211 for the thermal conductivity, and Refs. 52, 118, 183, 199 for the self-diffusion coefficient. The data show significantly less scatter compared to all data (cf. Chapter 2). These data sets comprise more than 1000 data points for each of the three transport properties and span over a wide temperature and density range.

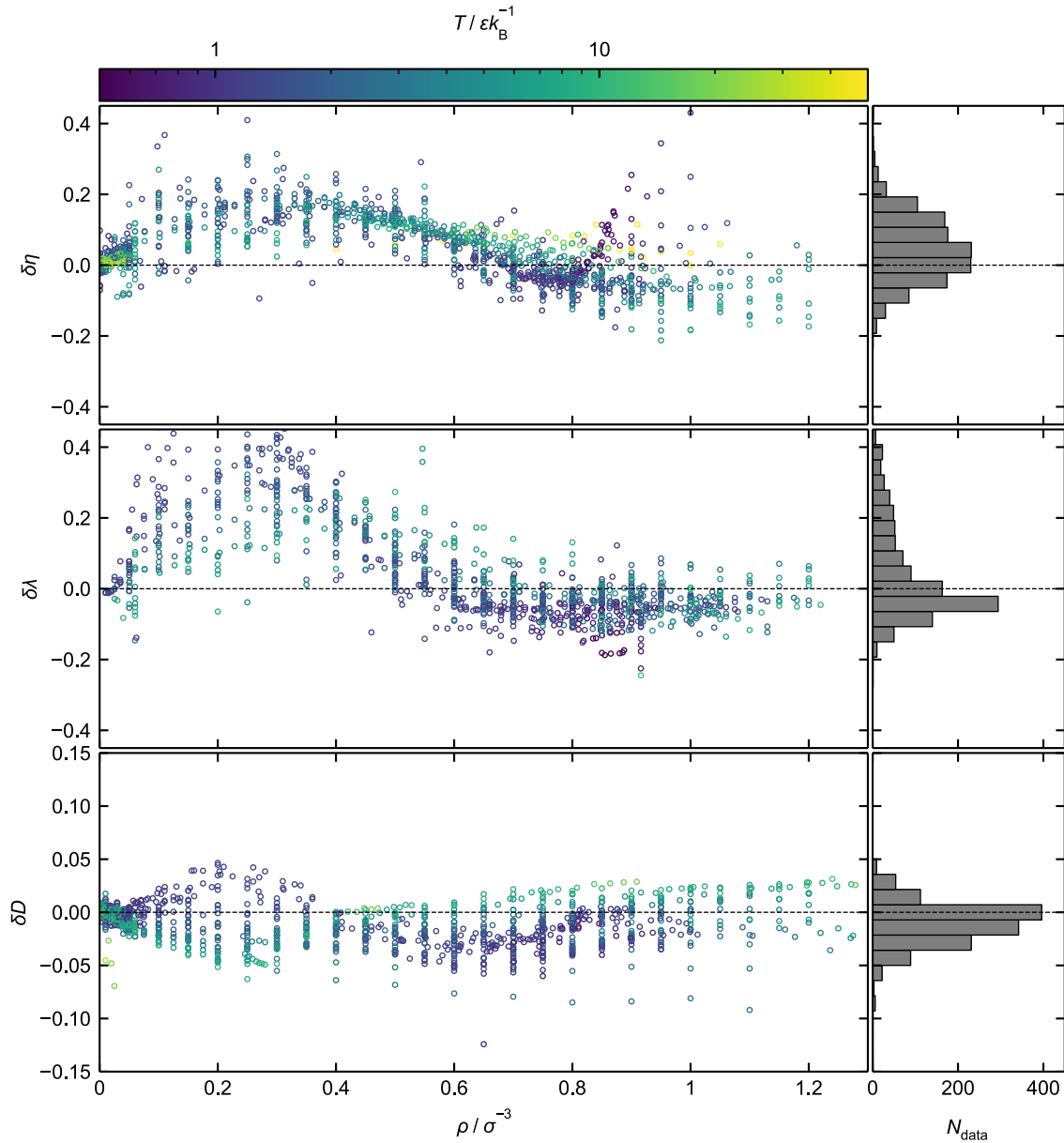


**Figure A.8:** Relative deviation of the simulation data from the entropy scaling model for the shear viscosity  $\delta\eta$  (top), thermal conductivity  $\delta\lambda$  (middle), and self-diffusion coefficient  $\delta D$  (cf. Eq. (2)) as a function of the density (left) and corresponding histograms of the relative deviations (right). Only confirmed data from Refs. 171, 183, 194, 196, 197, 199, 202 ( $\eta$ ), 114, 153, 199, 202, 211 ( $\lambda$ ), and 52, 118, 183, 199 ( $D$ ) are shown. The dashed line represents the entropy scaling model. Error bars are omitted to avoid visual clutter. The color indicates the temperature.

# B Supporting Information for Chapter 3

## B.1 Finite Size Analysis

The finite size dependency of the results was analysed by conducting simulations of *n*-decane with the Potoff force field at  $T = 373.15$  K and  $\rho = 0.66836$  g/ml with six different box sizes that contained 200, 400 (used in this work for *n*-decane simulations), 1000, 2000, 5000, and 10000 molecules, respectively. For every box size, 20 replica simulations have been conducted and the procedure described in Chapter 3 was applied to calculate the viscosity and the self-diffusion coefficient. The results of these simulations are given in Fig. B.1 as function of the inverse box length  $1/L$ . For the viscosity, all results are within their error bars. Thus, there is no size dependency of the viscosity results. For the self-diffusion coefficient, it is known that there is a box size dependency when using the Einstein relation and a correction term was proposed [122]. In Fig. B.1, the raw results without correction (circles) as well as the final values as used in this work (diamonds) are shown. The thermodynamic limit ( $L \rightarrow \infty$ ) can be calculated by extrapolating a linear fit on the uncorrected values to  $1/L = 0$ . The results in Fig. B.1 show that the correction term produces good results in accordance with the result calculated from extrapolating to the thermodynamic limit.

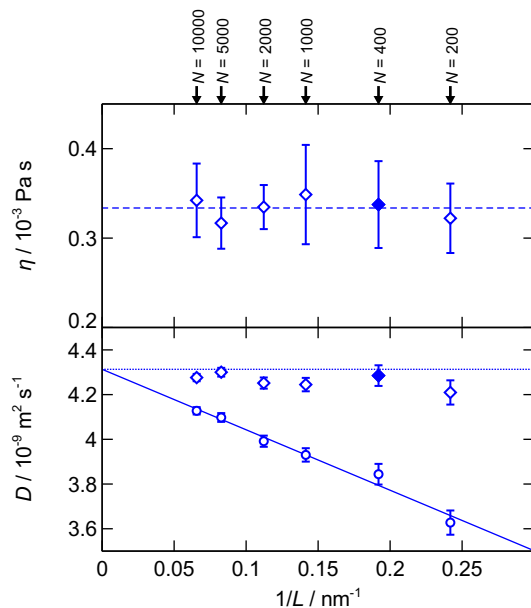


**Figure B.1:** Viscosity  $\eta$  (top) and self-diffusion coefficient  $D$  (bottom) as function of the inverse box length  $1/L$  of  $n$ -decane at  $T = 373.15$  K and  $\rho = 0.66836$  g/ml calculated using the Potoff force field. Top: The dashed line represents the mean viscosity values as calculated from all box lengths. Bottom: The solid line represents a linear fit on the self-diffusion values and the dotted line the thermodynamic limit ( $1/L = 0$ ) as obtained from the linear fit. Filled symbols represent the values used in this work.

## B.2 Choice of Integrator for All-atom Simulations

The all-atom force fields (excluding the reactive force fields) have been used with the RESPA multiple timestep integrator to reduce the computational costs of these simulations. The computational costs of all-atom force fields is in particular high as they usually use 3-4 times more interaction sites compared to united-atom force fields by nature. Additionally, they need a smaller time step as they include C-H bonds that obey high frequencies. To still conserve the total energy of the system, the time step has to be very small. This can be fixed by a multiple time step integrator like RESPA. Therefore, simulations of  $n$ -C10 with the COMPASS force field have been conducted with three different integration schemes in advance. The three integration schemes are the standard velocity Verlet algorithm [14] with a time step of  $\Delta t = 0.25$  fs and the RESPA multiple time step method [295] with a maximal time step of  $\Delta t = 1$  fs and  $\Delta t = 2$  fs. The results of these simulations are shown in Fig. B.2. For all three properties ( $\rho$ ,  $\eta$ , and  $D$ ), the simulation results agree within their error bars. Based on this results, the RESPA integrator with a maximal time step of  $\Delta t = 2$  fs was used for the all-atom force fields as the computational costs are reduced by more than a factor of 8 (Verlet) or 1.5 (RESPA with  $\Delta t = 1$  fs).

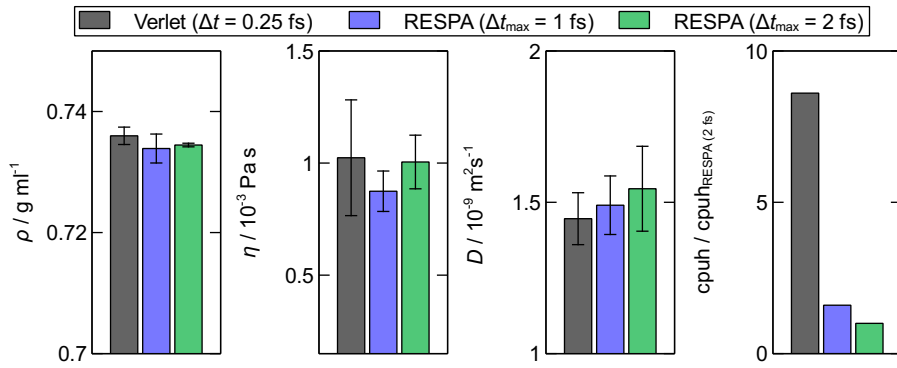


**Figure B.2:** Density  $\rho$ , viscosity  $\eta$ , self-diffusion coefficient  $D$ , and the computational costs  $cpu_{\text{h}}$  (from left to right) calculated from simulations of  $n$ -C10 with the COMPASS force field at  $p = 100$  MPa and  $T = 373.15$  K with three different integration schemes. Details on the different integration schemes are given in the text.

### B.3 Long $NpT$ Run

To ensure equilibration in the  $NpT$  simulations, a long  $NpT$  simulation run of 100 ns was conducted (see Fig. B.3). The total energy  $E_{\text{tot}}$  and the density  $\rho$  over time show

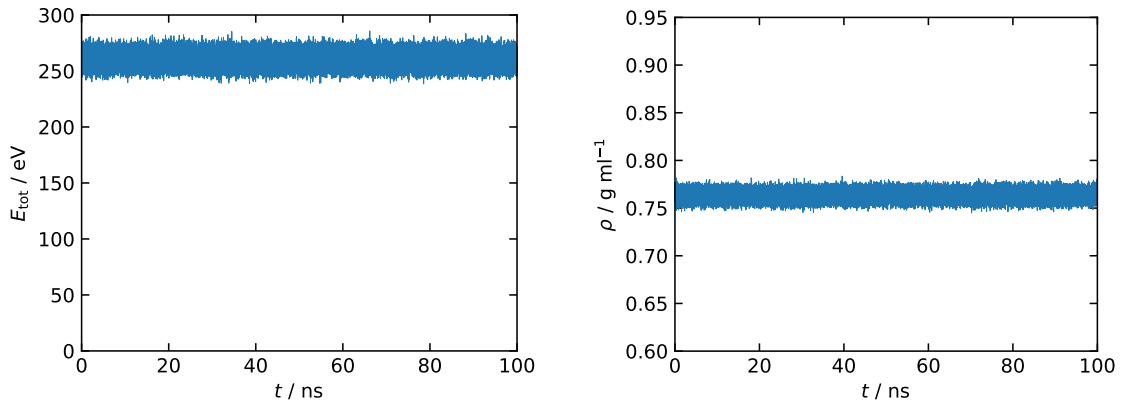


**Figure B.3:** Total energy of the system  $E_{\text{tot}}$  and the density  $\rho$  as a function of the simulation time  $t$  for TRI with the Potoff force field at  $p = 0.1$  MPa and  $T = 373.15$  K.

that there is no shift. The equilibrated state is reached after few timesteps ( $t_{\text{sim}} < 1$  ns).

### B.4 Influence of the Cutoff Criterion in the TDM

The cutoff criterion  $\sigma(t_{\text{cut}})/\eta(t_{\text{cut}})$  of the time decomposition method was set to 0.4. It determines the time at which the autocorrelation function is cut to remove noise from the evaluation. To ensure a proper choice of the criterion, a series of 20 simulations of

*n*-octane modeled by the TraPPE force field at  $\rho = 0.764 \text{ g ml}^{-1}$  and  $T = 293 \text{ K}$  was evaluated to calculate the viscosity using cut criteria from 0.2 to 0.8. The results are shown in Fig. B.4. The cutoff criterion does not have an influence on the simulation

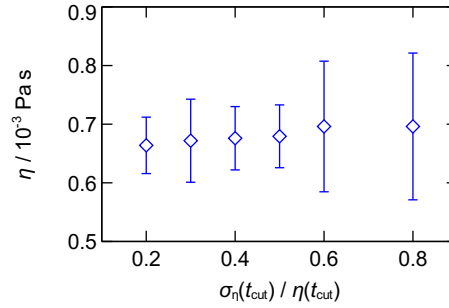


**Figure B.4:** Viscosity  $\eta$  as function of the cutoff criterion  $\sigma(t_{\text{cut}})/\eta(t_{\text{cut}})$  of the TDM for *n*-octane modeled by the TraPPE force field with  $\rho = 0.764 \text{ g ml}^{-1}$  and  $T = 293 \text{ K}$ .

result. All results are within their error bars. For large values of  $\sigma(t_{\text{cut}})/\eta(t_{\text{cut}})$  ( $\geq 6$ ), the calculated uncertainty increases.

## B.5 Force Field Parameters

In this section, the force fields that were used in Chapter 3, are presented together with their parameters. The following functions were used to describe the interaction potentials  $U$ :

$$U(r) = C\varepsilon \left[ \left( \frac{\sigma}{r} \right)^n - \left( \frac{\sigma}{r} \right)^m \right] \quad \text{with} \quad C = \left( \frac{n}{n-m} \right) \left( \frac{n}{m} \right)^{\frac{m}{n-m}} \quad (\text{B.1})$$

$$U(r) = k_2(r - r_0)^2 \quad (\text{B.2})$$

$$U(r) = k_2(r - r_0)^2 + k_3(r - r_0)^3 + k_4(r - r_0)^4 \quad (\text{B.3})$$

$$U(\theta) = l_2(\theta - \theta_0)^2 \quad (\text{B.4})$$

$$\begin{aligned} U(\theta) = & l_2(\theta - \theta_0)^2 + l_3(\theta - \theta_0)^3 + \\ & l_4(\theta - \theta_0)^4 + k_2(r_{ij} - r_1)(r_{jk} - r_2) + \\ & N_1(r_{ij} - r_1)(\theta - \theta_0) + N_2(r_{jk} - r_2)(\theta - \theta_0) \end{aligned} \quad (\text{B.5})$$

$$U(\phi) = c_0 + c_1(1 + \cos(\phi)) + c_2(1 + \sin(2\phi)) + c_3(1 + \cos(3\phi)) \quad (\text{B.6})$$

$$U(\phi) = 0.5c_1(1 + \cos(\phi)) + 0.5c_2(1 - \cos(2\phi)) + 0.5c_3(1 + \cos(3\phi)) + 0.5k_4(1 - \cos(4\phi)) \quad (\text{B.7})$$

$$\begin{aligned}
U(\phi, \theta, r) = & \sum_3^{n=1} c_n(1 - \cos(n\phi - \phi_n)) + \\
& (r_{jk} - r_2)(B_1 \cos(\phi) + B_2 \cos(2\phi) + B_3 \cos(3\phi)) + \\
& (r_{ij} - r_1)(B_4 \cos(\phi) + B_5 \cos(2\phi) + B_6 \cos(3\phi)) + \\
& (r_{kl} - r_3)(B_7 \cos(\phi) + B_8 \cos(2\phi) + B_9 \cos(3\phi)) + \\
& (\theta_{ijk} - \theta_1)(L_1 \cos(\phi) + L_2 \cos(2\phi) + L_3 \cos(3\phi)) + \\
& (\theta_{jkl} - \theta_2)(L_4 \cos(\phi) + L_5 \cos(2\phi) + L_6 \cos(3\phi)) + \\
& M_1(\theta_{ijk} - \theta_1)(\theta_{jkl} - \theta_2) \cos(\phi) \quad (\text{B.8})
\end{aligned}$$

$$\begin{aligned}
U(\phi, \theta) = & M_1(\theta_{ijk} - \theta_1)(\theta_{kjl} - \theta_2) \cos(\phi) \\
& M_2(\theta_{ijk} - \theta_1)(\theta_{ijl} - \theta_2) \cos(\phi) \\
& M_3(\theta_{ijl} - \theta_1)(\theta_{kjl} - \theta_2) \cos(\phi) \quad (\text{B.9})
\end{aligned}$$

### B.5.1 UA Force Fields

The non-bonded parameters of the TraPPE, Potoff, and TAMie force field are given in Tab. B.1 - B.3. All three force fields use the same intramolecular parameters. The bond, angle, and dihedral interaction parameters are given in Tab. B.4 - B.6.

**Table B.1:** Non-bonded interaction parameters of the TraPPE force field. Parameters given for the Lennard-Jones potential (see Eq. (B.1) with  $n = 12$  and  $m = 6$ ).

Site	$\varepsilon$ / eV	$\sigma$ / Å	Ref.
CH <sub>3</sub>	0.008445	3.75	[37]
CH <sub>2</sub>	0.003964	3.95	[37]
CH	0.000862	4.68	[310]

**Table B.2:** Non-bonded interaction parameters of the Potoff force field. Parameters given for the Mie potential (see Eq. (B.1)).

Site	$n$	$m$	$\varepsilon/eV$	$\sigma/\text{\AA}$	Ref.
CH <sub>3</sub>	16	6	0.010449	3.783	[38]
CH <sub>2</sub>	16	6	0.005257	3.99	[38]
CH	16	6	0.001206	4.70	[311]

**Table B.3:** Non-bonded interaction parameters of the TAMie force field. Parameters given for the Mie potential (see Eq. (B.1)).

Site	$n$	$m$	$\varepsilon/eV$	$\sigma/\text{\AA}$	Ref.
CH <sub>3</sub>	14	6	0.011747	3.60	[39]
CH <sub>2</sub>	14	6	0.004560	4.04	[39]
CH	14	6	0.001253	4.37	[312]

**Table B.4:** Bond interaction parameters of the UA force fields. Parameters given for the harmonic potential (see Eq. (B.2)).

Bond	$k_2/eV\text{\AA}^{-1}/\text{\AA}$	Ref.
CH <sub>x</sub> -CH <sub>y</sub>	11.6216 1.54	[37, 389]
CH <sub>3</sub> -CH <sub>y</sub> (only TAMie)	11.6216 1.74	[39, 389]

**Table B.5:** Angle interaction parameters of the UA force fields. Parameters given for the harmonic potential (see Eq. (B.4)).

Angle	$l_2/eV$	$\theta_0/^\circ$	Ref.
CH <sub>x</sub> -CH <sub>2</sub> -CH <sub>y</sub>	2.6929	114	[37]
CH <sub>x</sub> -CH-CH <sub>y</sub>	2.6929	112	[310]



**Table B.6:** Dihedral interaction parameters of the TraPPE force field. Parameters given for the Fourier potential (see Eq. (B.6)).

Dihedral	$c_0/\text{eV}$	$c_1/\text{eV}$	$c_2/\text{eV}$	$c_3/\text{eV}$	Ref.
$\text{CH}_x\text{-CH}_2\text{-CH}_2\text{-CH}_y$	0	0.03059	-0.00588	0.06819	[37]
$\text{CH}_x\text{-CH}_2\text{-CH-CH}_y$	-0.02163	0.03695	-0.00964	0.03803	[310]

## B.5.2 OPLS

The non-bonded parameters of the OPLS force field are given in Tab. B.7. The bond, angle, and dihedral interaction parameters are given in Tab. B.8 - B.10.

**Table B.7:** Non-bonded interaction parameters and charges of the OPLS force field. Parameters given for the Lennard-Jones potential (see Eq. (B.1) with  $n = 12$  and  $m = 6$ ).

Site	$\varepsilon/\text{eV}$	$\sigma/\text{\AA}$	$q/e$	Ref.
C ( $\text{CH}_3$ )	0.002862	3.5	-0.18	[34]
C ( $\text{CH}_2$ )	0.002862	3.5	-0.12	[34]
C ( $\text{CH}$ )	0.002862	3.5	-0.06	[34]
H	0.001301	2.5	0.06	[34]

**Table B.8:** Bond interaction parameters of the OPLS force field. Parameters given for the harmonic potential (see Eq. (B.2)).

Bond	$k_2/\text{eV}\text{\AA}^{-1}$	$r_0/\text{\AA}$	Ref.
C-C	11.6216	1.529	[34]
C-H	14.7438	1.090	[34]

**Table B.9:** Angle interaction parameters of the OPLS force field. Parameters given for the harmonic potential (see Eq. (B.4)).

Angle	$l_2/\text{eV}$	$\theta_0/^\circ$	Ref.
C-C-C	2.5303	112.7	[34]
C-C-H	1.6262	110.7	[34]
H-C-H	1.4310	107.8	[34]

**Table B.10:** Dihedral interaction parameters of the OPLS force field. Parameters given for the OPLS potential (see Eq. (B.7)).

Dihedral	$c_1/\text{eV}$	$c_2/\text{eV}$	$c_3/\text{eV}$	Ref.
C-C-C-C	0.07545	-0.00681	0.01210	[34]
C-C-C-H	0.0	0.0	0.01587	[34]
H-C-C-H	0.0	0.0	0.01379	[34]

### B.5.3 L-OPLS

The non-bonded parameters of the L-OPLS force field are given in Tab. B.11. The C-C bond potential of the L-OPLS is given in Tab. B.8. The C-H is rigid with a distance of  $r_0 = 1.09 \text{ \AA}$ . The angle interaction parameters of the L-OPLS force field are the same as those of the OPLS force field (see Tab. B.9). The dihedral parameters are given in Tab. B.12.

**Table B.11:** Non-bonded interaction parameters and charges of the L-OPLS force field. Parameters given for the Lennard-Jones potential (see Eq. (B.1) with  $n = 12$  and  $m = 6$ ).

Site	$\varepsilon/\text{eV}$	$\sigma/\text{\AA}$	$q/e$	Ref.
C (CH <sub>3</sub> )	0.002862	3.5	-0.222	[307]
C (CH <sub>2</sub> )	0.002862	3.5	-0.148	[307]
C (CH)	0.002862	3.5	-0.06	[307]
H (CH <sub>3</sub> )	0.001301	2.5	0.074	[307]
H (CH <sub>2</sub> )	0.001140	2.5	0.074	[307]
H (CH)	0.001301	2.5	0.06	[307]

**Table B.12:** Dihedral interaction parameters of the L-OPLS force field. Parameters given for the OPLS potential (see Eq. (B.7)).

Dihedral	$c_1/\text{eV}$	$c_2/\text{eV}$	$c_3/\text{eV}$	Ref.
C-C-C-C	0.02796	-0.00929	0.00773	[307]
C-C-C-H	0.0	0.0	0.01301	[746]
H-C-C-H	0.0	0.0	0.01301	[746]

### B.5.4 COMPASS

The parameters for the non-bonded (cf. Table B.13), the bond (cf. Table B.14) the angle (cf. Table B.15), the dihedral (cf. Table B.16), and the improper (cf. Table B.17) interactions are given in the following.

**Table B.13:** Non-bonded interaction parameters and charges of the COMPASS force field. Parameters given for the Mie potential (see Eq. (B.1)) with  $n = 9$  and  $m = 6$ .

Site	$\varepsilon/\text{eV}$	$\sigma/\text{\AA}$	$q/e$	Ref.
C (CH <sub>3</sub> )	0.002689	3.8540	-0.159	[35]
C (CH <sub>2</sub> )	0.002689	3.8540	-0.106	[35]
C (CH)	0.001735	3.8540	-0.053	[35]
H	0.000997	2.8780	0.053	[35]

**Table B.14:** Bond interaction parameters of the COMPASS force field. Parameters given for the quartic potential (see Eq. (B.3)).

Bond	$k_2/\text{eV}\text{\AA}^{-2}$	$k_3/\text{eV}\text{\AA}^{-3}$	$k_4/\text{eV}\text{\AA}^{-4}$	$r_0/\text{\AA}$	Ref.
C-C	12.9949	-21.7588	29.4794	1.530	[35]
C-H	14.9606	-30.0032	36.6253	1.101	[35]

**Table B.15:** Angle (3-body) interaction parameters of the COMPASS force field. Parameters given for the potential given by Eq. (B.5). The equilibrium bonds  $r_1$  and  $r_2$  are given in Table B.14.

Angle ( $i-j-k$ )	$l_2/\text{eV}$	$l_3/\text{eV}$	$l_3/\text{eV}$	$\theta_0/^\circ$	$k_2/\text{eV}$	$N_1/\text{eV}$	$N_2/\text{eV}$	Ref.
C-C-C	1.7136	-	-	112.67	0.0	0.3476	0.3476	[35]
		0.3228	0.4145					
C-C-H	1.7976	-	0.2224	110.77	0.1469	0.9000	0.4953	[35]
		0.4598						
H-C-H	1.7190	-	-	107.66	0.2312	0.7850	0.7850	[35]
		0.5603	0.1055					

**Table B.16:** Dihedral (4-body) interaction parameters of the COMPASS force field. Parameters given for the potential given by Eq. (B.8). The equilibrium bonds  $r_1-r_3$  as well as the equilibrium angles  $\theta_1-\theta_2$  are given in Table B.14 and B.15.

Dihedral ( $i-j-k-l$ )	$c_1/\text{eV}$	$c_2/\text{eV}$	$c_3/\text{eV}$	$B_1/\text{eV}\text{\AA}^{-1}$	$B_2/\text{eV}\text{\AA}^{-1}$	$B_3/\text{eV}\text{\AA}^{-1}$	Ref.
C-C-C-C	0.0	0.0022	-0.0062	-0.7713	-0.3117	0.0	[35]
C-C-C-H	0.0	0.0014	-0.0073	-0.6452	-0.1586	-0.0136	[35]
H-C-C-H	-0.0062	0.0027	-0.0066	-0.6184	-0.0231	-0.0211	[35]
	$B_4/\text{eV}\text{\AA}^{-1}$	$B_5/\text{eV}\text{\AA}^{-1}$	$B_6/\text{eV}\text{\AA}^{-1}$	$B_7/\text{eV}\text{\AA}^{-1}$	$B_8/\text{eV}\text{\AA}^{-1}$	$B_9/\text{eV}\text{\AA}^{-1}$	
C-C-C-C	-0.0032	0.0	0.0	-0.0032	0.0	0.0	[35]
C-C-C-H	0.0108	0.0105	-0.0040	0.0035	0.0026	0.0096	[35]
H-C-C-H	0.0092	0.0135	0.0034	0.0092	0.0135	0.0034	[35]
	$L_1/\text{eV}$	$L_2/\text{eV}$	$L_3/\text{eV}$	$L_4/\text{eV}$	$L_5/\text{eV}$	$L_6/\text{eV}$	
C-C-C-C	0.0169	-0.0136	0.0060	0.0169	-0.0136	0.0060	[35]
C-C-C-H	-0.0106	0.0	-0.0049	0.0135	0.0196	-0.0086	[35]
H-C-C-H	-0.0351	0.0242	-0.0107	-0.0351	0.0242	-0.0107	[35]
	$M_1/\text{eV}$						
C-C-C-C	-0.9560						[35]
C-C-C-H	-0.7009						[35]
H-C-C-H	-0.5448						[35]

**Table B.17:** Improper (4-body) interaction parameters of the COMPASS force field. Parameters given for the potential given by Eq. (B.9). The equilibrium angles  $\theta_1 - \theta_3$  are given in Table B.15. The atom  $j$  defines the central atom of the improper.

Improper ( $i - j - k - l$ )	$M_1$ /eV	$M_2$ /eV	$M_3$ /eV	Ref.
C-C-C-C	-0.0075	-0.0075	-0.0075	[35]
C-C-C-H	-0.0572	-0.0572	0.0051	[35]
H-C-C-H	0.0119	-0.0209	0.0119	[35]
H-C-H-H	-0.0137	-0.0137	-0.0137	[35]

### B.5.5 MARTINI

The coarse-grained models of all five substances as used in this work are shown in Fig. B.5.

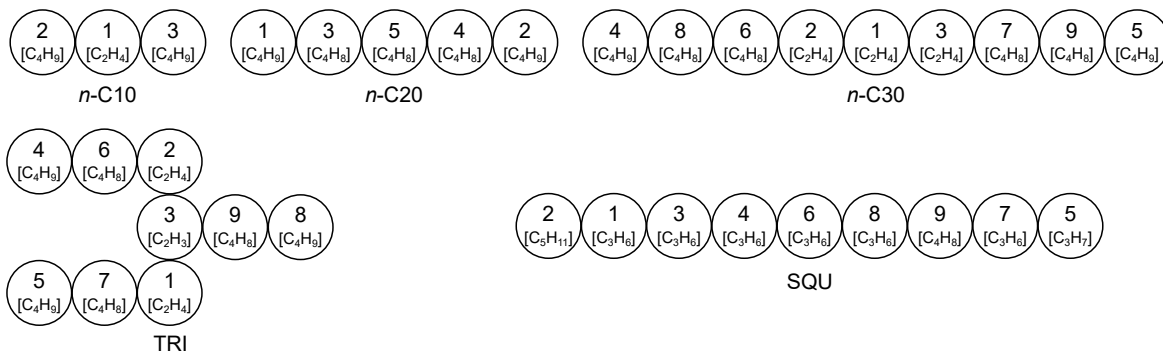


**Figure B.5:** Coarse grained models for the Martini force field used in this work.

The parameters for the non-bonded, the bond, and the angel interaction potentials are given in Tab. B.18 – B.20.

**Table B.18:** Non-bonded interaction parameters of the MARTINI force field as used in this work. Parameters given for the Lennard-Jones potential (see Eq. (B.1) with  $n = 12$  and  $m = 6$ ).

Molecule	Interaction sites	$\varepsilon / \text{eV}$	$\sigma / \text{\AA}$
<i>n</i> -C10, <i>n</i> -C20, <i>n</i> -C30, TRI	C <sub>2</sub> H <sub>4</sub> – C <sub>2</sub> H <sub>4</sub>	0.0363	4.7
	C <sub>4</sub> H <sub>x</sub> – C <sub>4</sub> H <sub>y</sub>	0.0321	4.7
	C <sub>2</sub> H <sub>4</sub> – C <sub>4</sub> H <sub>y</sub>	0.0363	4.7
SQU	C <sub>x</sub> H <sub>y</sub> – C <sub>x</sub> H <sub>y</sub>	0.0363	4.7

**Table B.19:** Bond interaction parameters of the MARTINI force field as used in this work. Parameters given for the harmonic bond potentials (see Eq. (B.2)).

Molecule	Bond	$k_2 / \text{eV}\text{\AA}^{-1}$	$r_0 / \text{\AA}$	Bond	$k_2 / \text{eV}\text{\AA}^{-1}$	$r_0 / \text{\AA}$
<i>n</i> -C10	1 – 2	0.0648	3.390	1 – 3	0.0648	3.410
<i>n</i> -C20	1 – 3	0.0648	4.942	2 – 4	0.0648	4.930
	3 – 5	0.0648	5.001	4 – 5	0.0648	4.977
<i>n</i> -C30	1 – 2	0.0648	3.291	1 – 3	0.0648	3.291
	2 – 6	0.0648	4.452	3 – 7	0.0648	4.425
	4 – 8	0.0648	5.600	5 – 9	0.0648	5.667
	6 – 8	0.0648	5.667	7 – 9	0.0648	5.654
TRI	1 – 3	0.0648	3.290	1 – 7	0.0648	4.420
	2 – 3	0.0648	3.348	2 – 6	0.0648	4.608
	3 – 9	0.0648	4.608	4 – 6	0.0648	5.782
	5 – 7	0.0648	5.869	8 – 9	0.0648	5.884
SQU	1 – 2	0.0648	3.290	1 – 3	0.0648	4.420
	3 – 4	0.0648	3.348	4 – 6	0.0648	4.608
	5 – 7	0.0648	4.608	6 – 8	0.0648	5.782
	7 – 9	0.0648	5.869	8 – 9	0.0648	5.884

**Table B.20:** Angle interaction parameters of the MARTINI force field as used in this work. Parameters given for the harmonic angle potentials (see Eq. (B.4)).

Molecule	Angle	$l_2/\text{eV}$	$\theta_0/^\circ$	Angle	$l_2/\text{eV}$	$\theta_0/^\circ$
<i>n</i> -C10	2 – 1 – 3	0.1296	143.1			
<i>n</i> -C20	1 – 3 – 5	0.1296	142.5	2 – 4 – 5	0.1296	142.4
	3 – 5 – 4	0.1296	143.6			
<i>n</i> -C30	2 – 1 – 3	0.1296	137.1	1 – 2 – 6	0.1296	131.4
	1 – 3 – 7	0.1296	130.7	2 – 6 – 8	0.1296	137.5
	3 – 7 – 9	0.1296	139.7	4 – 8 – 6	0.1296	137.7
	5 – 9 – 7	0.1296	136.8			
TRI	3 – 1 – 7	0.1296	102.4	1 – 3 – 2	0.1296	117.5
	1 – 3 – 9	0.1296	119.1	1 – 7 – 5	0.1296	132.8
	3 – 2 – 6	0.1296	136.0	2 – 3 – 9	0.1296	87.8
	2 – 6 – 4	0.1296	138.8	3 – 9 – 8	0.1296	137.5
SQU	2 – 1 – 3	0.1296	119.3	1 – 3 – 4	0.1296	138.7
	3 – 4 – 6	0.1296	120.3	4 – 6 – 8	0.1296	135.4
	5 – 7 – 9	0.1296	140.8	6 – 8 – 9	0.1296	126.1
	7 – 9 – 8	0.1296	126.9			

### B.5.6 Reactive Force Fields

For both reactive force fields, external input files have been used. The *CHON-2017\_weak* version of the ReaxFF is provided in the Supplementary Material of Ref. [308]. For the AIREBO-M, the file distributed by LAMMPS (Version 3 March 2020) was used (*CH.airebo-m*).

## B.6 Validation

In the following, the implementation of some force fields as used in this work is validated using literature data. As can be seen in Fig. B.6 - B.10, the results agree well with the values given in the literature.



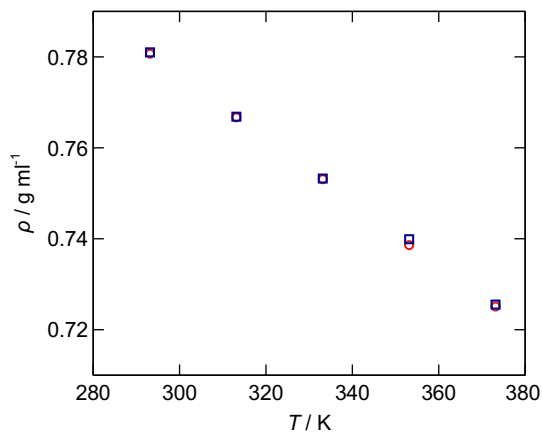


**Figure B.6:** Validation of the ReaxFF force field with data from *Morrow and Harrison* [280] for the density  $\rho$  of *n*-hexadecane as function of temperature  $T$  at a pressure  $p = 0.1$  MPa. Blue squares represent the result from this work and red circles the results from literature.

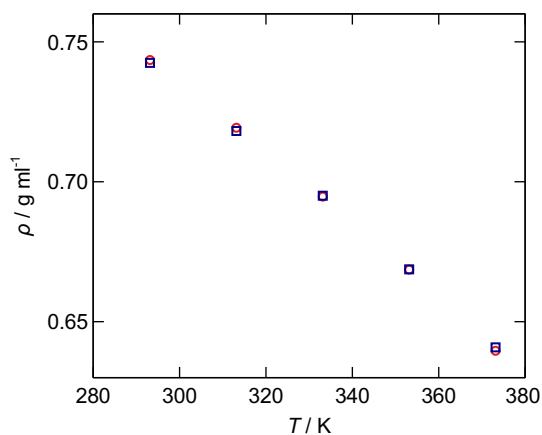


**Figure B.7:** Validation of the AIREBO-M force field with data from *Morrow and Harrison* [280] for the density  $\rho$  of *n*-hexadecane as function of temperature  $T$  at a pressure  $p = 0.1$  MPa. Blue squares represent the result from this work and red circles the results from literature.

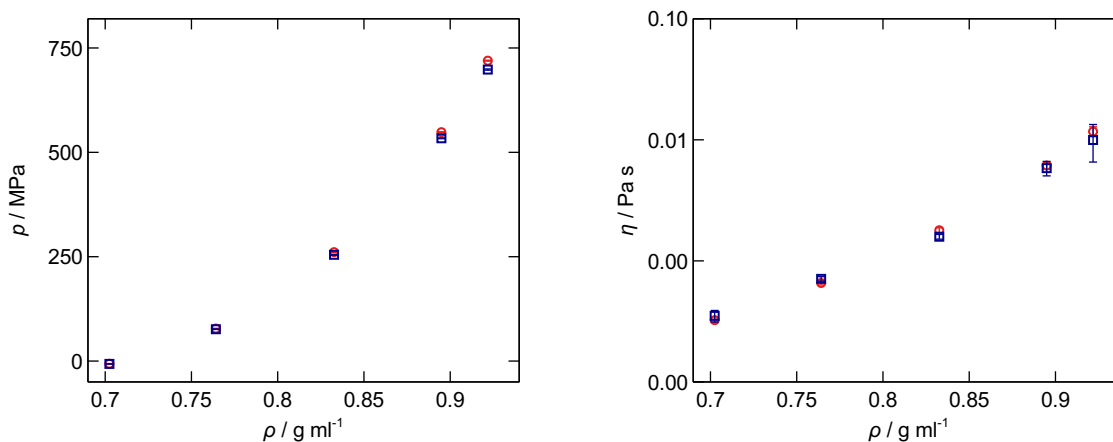


**Figure B.8:** Validation of the TraPPE force field with data from *Messerly et al.* [747] for the pressure  $p$  and the viscosity  $\eta$  of  $n$ -octane as function of density  $\rho$  at a temperature  $T = 293$  K. Blue squares represent the result from this work and red circles the results from literature.

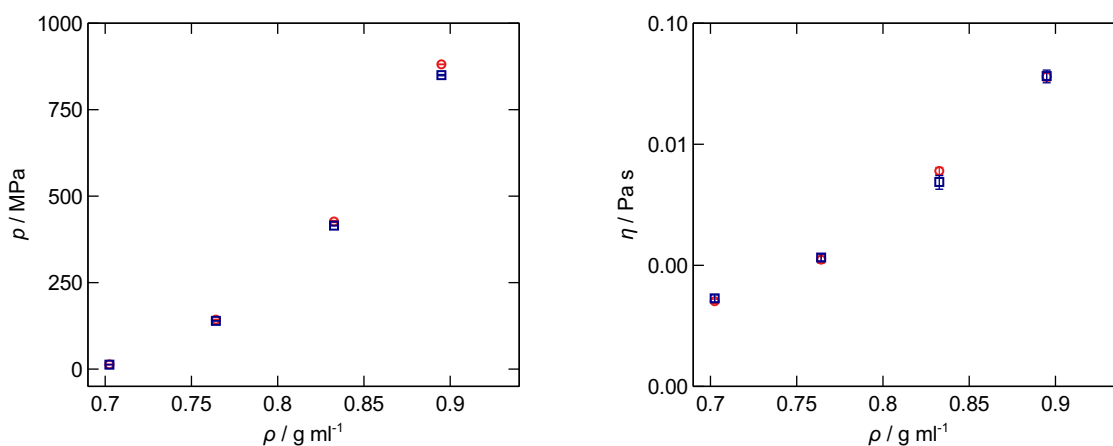


**Figure B.9:** Validation of the TAMie force field with data from *Messerly et al.* [747] for the pressure  $p$  and the viscosity  $\eta$  of  $n$ -octane as function of density  $\rho$  at a temperature  $T = 293$  K. Blue squares represent the result from this work and red circles the results from literature.

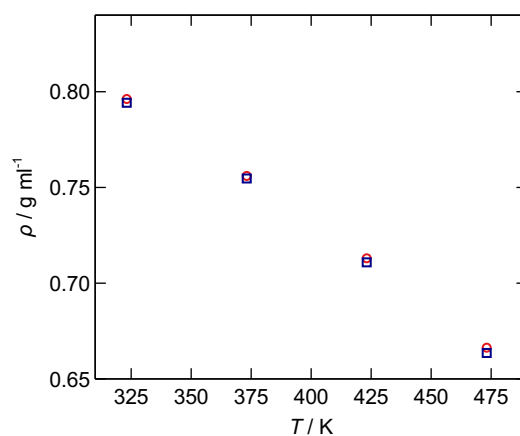


**Figure B.10:** Validation of the MARTINI force field with data from *Papavasileiou et al.* [289] for the density  $\rho$  of *n*-dodecane as function of temperature  $T$  at a pressure  $p = 0.1$  MPa. Blue squares represent the result from this work and red circles the results from literature.

## B.7 Correlations of Experimental Data

Eq. (B.10) was used to fit the experimental data.

$$y/[y] = \frac{a_0 + a_1(T/K) + a_2(p/\text{MPa}) + a_3(p/\text{MPa})^2 + a_4(T/K)(p/\text{MPa})}{1 + b_1(T/K) + b_2(p/\text{MPa}) + b_3(T/K)(p/\text{MPa})} \quad (\text{B.10})$$

Table B.21 shows the units of the properties used for the fits with Eq. (B.10).

**Table B.21:** Units of the correlations used with Eq. (B.10).

$y$	$[y]$
$\rho$	g/ml
$\eta$	Pa s
$D$	m <sup>2</sup> /s
$\lambda$	W/(K m)

The references of the experimental data are given in Chapter 3. Table B.22 contains the fitted parameters as well as the AAD of the fits for all properties with experimental data available.

## B.8 Correlations of Simulation Data

The parameters for the properties without experimental data available are given in Table B.23.

**Table B.23:** Correlation parameters for Eq. (B.10) with  $a_1 = 0$ ,  $a_4 = 0$ ,  $b_1 = 0$ , and  $b_3 = 0$ .

Substance	Property	$a_0$	$a_2$	$a_3$	$b_2$	AAD / %
<i>n</i> -C20	log( $D$ )	-2.09e1	-8.06e-3	4.77e-6	6.19e-16	0.07
<i>n</i> -C30	log( $\eta$ )	-5.86e0	7.22e-3	-3.64e-6	1.01e-15	0.34
TRI	$\rho$	7.64e-1	4.36e-3	5.33e-7	4.75e-3	0.01
	log( $D$ )	-2.22e1	-1.76e-1	-4.57e-5	7.23e-3	0.03
SQU	log( $D$ )	-2.22e1	-2.03e-2	4.68e-6	3.31e-4	0.02

They were fitted to the simulation results of the Potoff force field.

**Table B.22:** Correlation parameters for Eq. (B.10).

Substance	Property	$a_0$	$a_1$	$a_2$	$a_3$	$a_4$	$b_1$	$b_2$	$b_3$	AAD / %
<i>n</i> -C10	$\rho$	9.44e-1	-8.35e-4	3.43e-3	1.11e-6	6.23e-6	-1.43e-4	3.52e-3	9.16e-6	0.13
	$\log(\eta)$	8.64e1	-8.17e-1	1.57e0	1.03e-3	-8.56e-3	7.14e-2	-1.23e-1	1.0e-3	1.4
	$\log(D)$	-4.51e1	-2.43e-1	1.52e-1	-6.65e-5	-2.23e-3	1.60e-2	-140e-2	1.22e-4	1.61
<i>n</i> -C20	$\rho$	9.57e-1	-8.23e-4	4.64e-3	1.38e-6	4.47e-6	-3.13e-4	5.04e-3	6.35e-6	0.16
	$\log(\eta)$	1.05e1	-9.09e-2	2.49e-1	7.36e-5	-8.84e-4	6.94e-3	-2.01e-2	1.07e-4	0.43
<i>n</i> -C30	$\rho$	9.64e-1	-7.42e-4	5.66e-3	1.41e-6	2.58e-6	-2.51e-4	6.13e-3	4.13e-6	0.13
	$\log(D)$	-1.64e7	-1.17e5	6.00e4	-2.67e1	-7.67e2	7.42e3	-5.82e3	3.98e1	1.22
TRI	$\log(\eta)$	1.82e7	-8.32e4	1.44e5	4.59e1	-4.49e2	5.87e3	-9.9e3	5.38e1	3.19
SQU	$\rho$	9.96e-1	-7.03e-4	5.46e-4	2.55e-7	8.42e-6	-7.82e-5	1.52e-4	9.88e-6	0.28
	$\log(\eta)$	2.65e7	-1.18e5	2.37e5	8.14e1	-7.05e2	8.11e3	-1.4e4	7.44e1	5.12

## B.9 Radius of Gyration

The radius of gyration was calculated for all simulations. The results are shown in Fig. B.11 for all molecules and force fields. There is only a weak pressure dependency

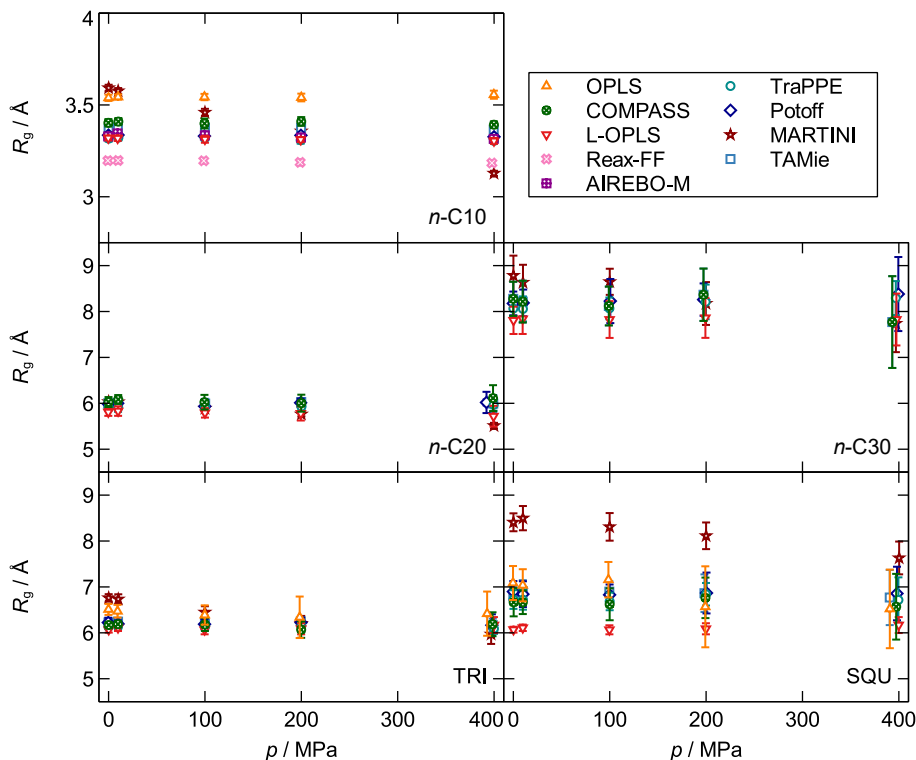


**Figure B.11:** Radius of gyration  $R_g$  of  $n$ -C10,  $n$ -C20,  $n$ -C30, TRI, and SQU at  $T = 373.15$  K as a function of the pressure  $p$ . Colored symbols indicate the simulation results for the different force fields.

of  $R_g$ . Especially the simulations with the MARTINI force field show a decrease of the radius of gyration with increasing pressure. The strong decrease of  $R_g$  for pressures  $p > 50$  MPa observed by *Prentice et al.* [748] for SQU with the L-OPLS force field could not be confirmed. The radius of gyration was averaged over all pressures for every force field and molecule. The results are shown in Fig. B.12. The radius of gyration increases with increasing chainlength for the linear alkanes as expected. The two branched alkanes show lower radii of gyration compared to their isomer  $n$ -C30. TRI (long branches) exhibits thereby smaller radius of gyration than SQU (short branches). The different force fields show very similar results for the radius of gyration. Only the simulations with the OPLS force field for  $n$ -C20 and  $n$ -C30 and the MARTINI force field for SQU deviate from the other force fields. For OPLS, this is already known as its results for long linear alkanes show unphysical behavior (see Section B.10). The deviation of the MARTINI force field for SQU can be explained by the representation by MARTINI as a linear chain (see Section B.5).

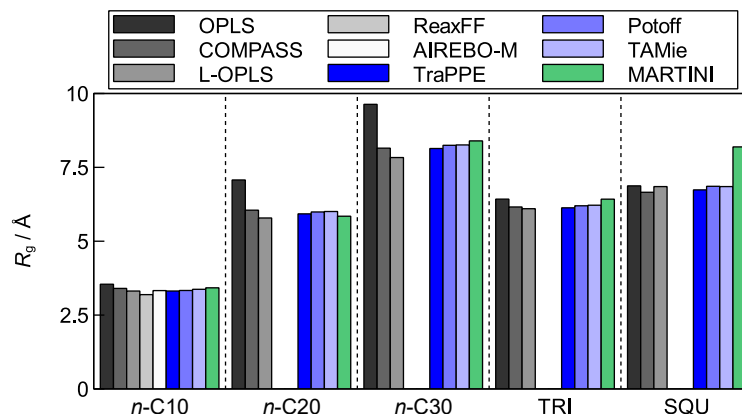


**Figure B.12:** Averaged radius of gyration  $R_g$  of *n*-C10, *n*-C20, *n*-C30, TRI, and SQU at  $T = 373.15$  K for the different force fields averaged over all state points.

## B.10 OPLS Simulations of *n*-Icosane and *n*-Triacontane

The simulations for *n*-icosane (*n*-C20) and *n*-triacontane (*n*-C30) with the OPLS force field exhibit an unphysical transition to a gel-like phase, which has already been described by Ref. [307]. Therefore, these simulations were discarded in Chapter 3. For transparency, these results are shown here in the Supplementary Material. A screenshot of such a gel-like phase of *n*-icosane (*n*-C20) at a density of 0.833 g/ml is shown in Fig. B.13.

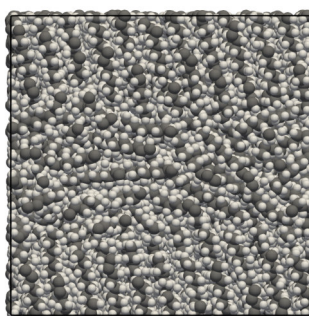


**Figure B.13:** Screenshot of an *NVT* simulation of *n*-icosane (*n*-C20) at  $\rho = 0.833$  g/ml and  $T = 373.15$  K. The single sites are colored as follows: gray - carbon, white - hydrogen.

The backbones of the *n*-icosane (*n*-C20) molecules are blockwise structured in parallel. In measurements, the phase transition to solid-like phase is observed at significantly lower temperatures than considered in this work [307]. In general, the single replica simulations exhibit different metastable states and are inhomogeneous. The transition to the gel-like phase strongly influences the prediction of the density and leads to high

uncertainties of the pressure in the  $NVT$  simulations due to different degrees of structuring in the set of replica simulations. Additionally the densities calculated from the preliminary  $NpT$  simulations do not reproduce the pressure in the  $NVT$  simulations which is why the OPLS simulations do not match the prescribed pressures. This structuring can only be observed for  $n$ -icosane ( $n$ -C20) and  $n$ -triacontane ( $n$ -C30) modeled by the OPLS force field.

The results for the densities of  $n$ -C20 and  $n$ -C30 calculated with the OPLS force field are shown in Fig. B.14. For both substances, the simulations show large deviations

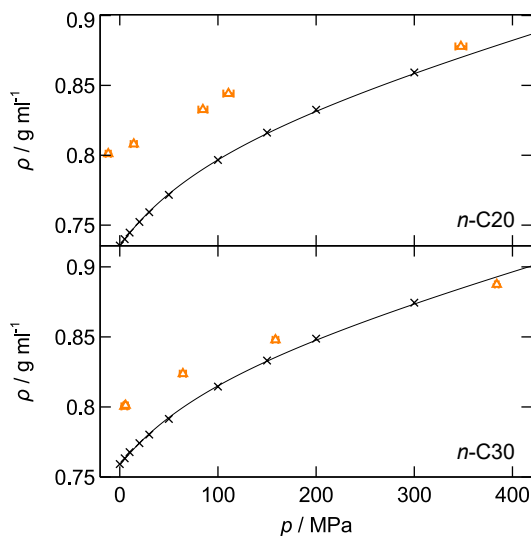


**Figure B.14:** Density  $\rho$  as function of pressure  $p$  for  $n$ -C20 and  $n$ -C30. Symbols indicate the simulation results for the OPLS force field. Lines represent the empirical correlations (black solid lines in cases where exp. data was used). All properties given for the temperature  $T = 373.15$  K.

to the experimental data. Except for the highest pressure, the densities are strongly overestimated.

In Fig. B.15, the viscosity results for  $n$ -C20 and  $n$ -C30 simulated with the OPLS force field are displayed. For nearly all state points, the OPLS force fields overestimated the experimental data by more than one order of magnitude. The increased viscosity is a result of the decreased mobility of the molecules due to the structuring.

The results for the self-diffusion coefficient of  $n$ -C20 and  $n$ -C30 of the OPLS force field are shown in Fig. B.16. As expected from the increased viscosity, the OPLS force field underestimates the experimental data.



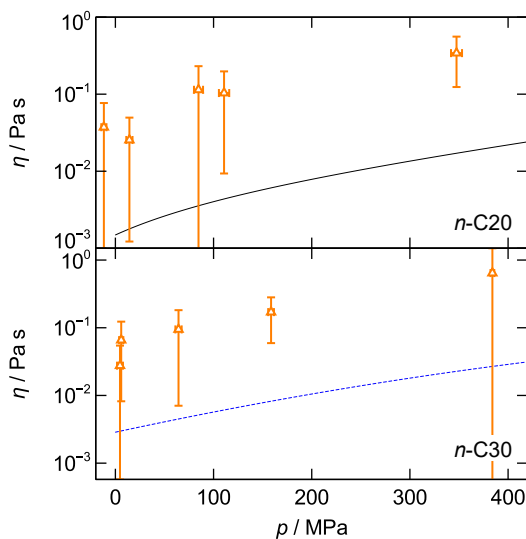


**Figure B.15:** Viscosity  $\eta$  as function of pressure  $p$  for  $n$ -C20 and  $n$ -C30. Symbols indicate the simulation results for the OPLS force field. Lines represent the empirical correlations (black solid lines in cases where exp. data was used; blue dotted lines in cases where the Potoff force field was used). All properties given for the temperature  $T = 373.15$  K.

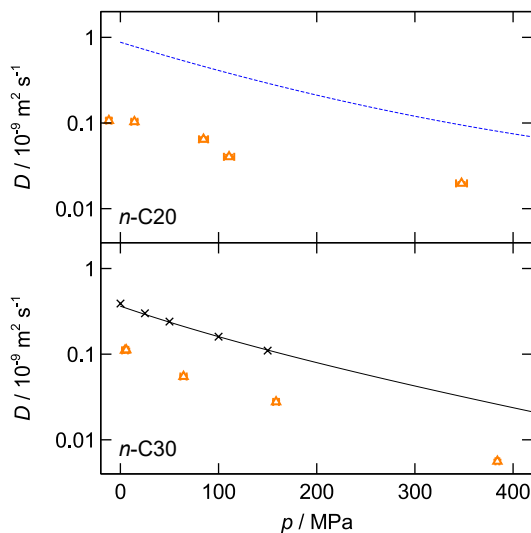


**Figure B.16:** Self-diffusion coefficient  $D$  as function of pressure  $p$  for  $n$ -C20 and  $n$ -C30. Symbols indicate the simulation results for the OPLS force field. Lines represent the empirical correlations (black solid lines in cases where exp. data was used; blue dotted lines in cases where the Potoff force field was used). All properties given for the temperature  $T = 373.15$  K.

## B.11 Relation Between Viscosity and Self-diffusion

Fig. B.17 shows the linear relation between the self-diffusion coefficient and the viscosity as predicted by the Stokes-Einstein relation [342]. Using the Stokes-Einstein equation

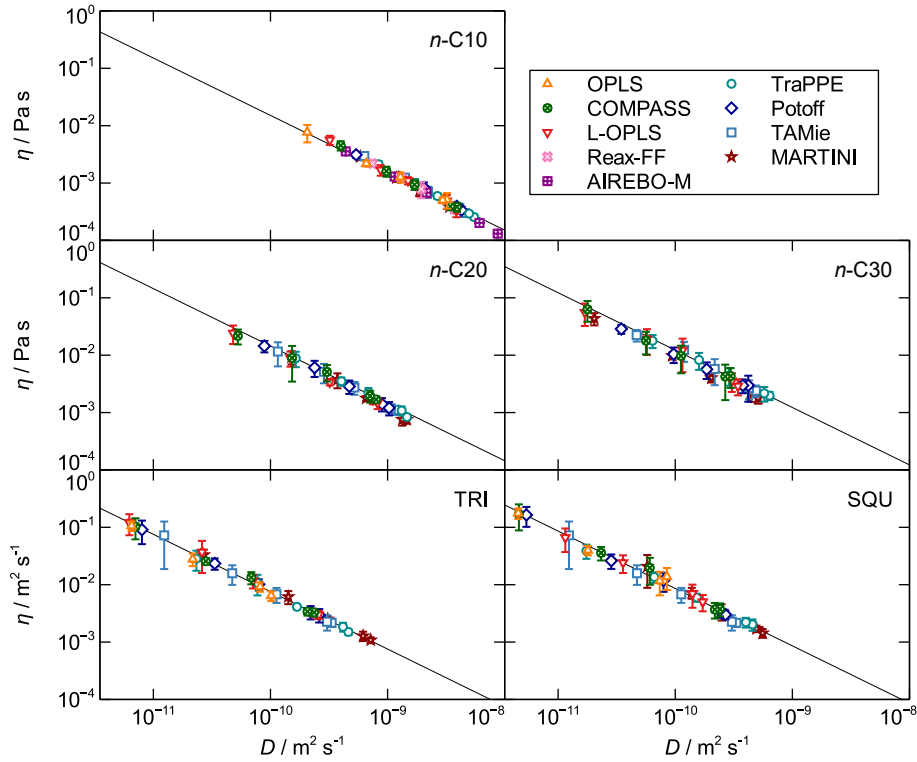


**Figure B.17:** Viscosity  $\eta$  as function of the self-diffusion coefficient  $D$  for  $n$ -C10,  $n$ -C20,  $n$ -C30, TRI, and SQU. Symbols indicate the simulation results for the different force fields. All properties given for the temperature  $T = 373.15$  K and pressures  $p = 0.1 - 400$  MPa.

(see Eq. (B.11)), the hydrodynamic radii  $r_h$  were calculated for each state point.

$$D = \frac{k_B T}{6\pi\eta R_h} \quad (\text{B.11})$$

The results are given in Fig. B.18. A dependency of the hydrodynamic radius  $R_h$  on the pressure is hardly detectable. Thus, a breakdown of the Stokes-Einstein relation for high pressure as observed by Ref. [748] is not found. However, the values for the hydrodynamic radius of SQU are in accordance with the values given by *Prentice et al.* for low pressure ( $p < 50$  MPa).

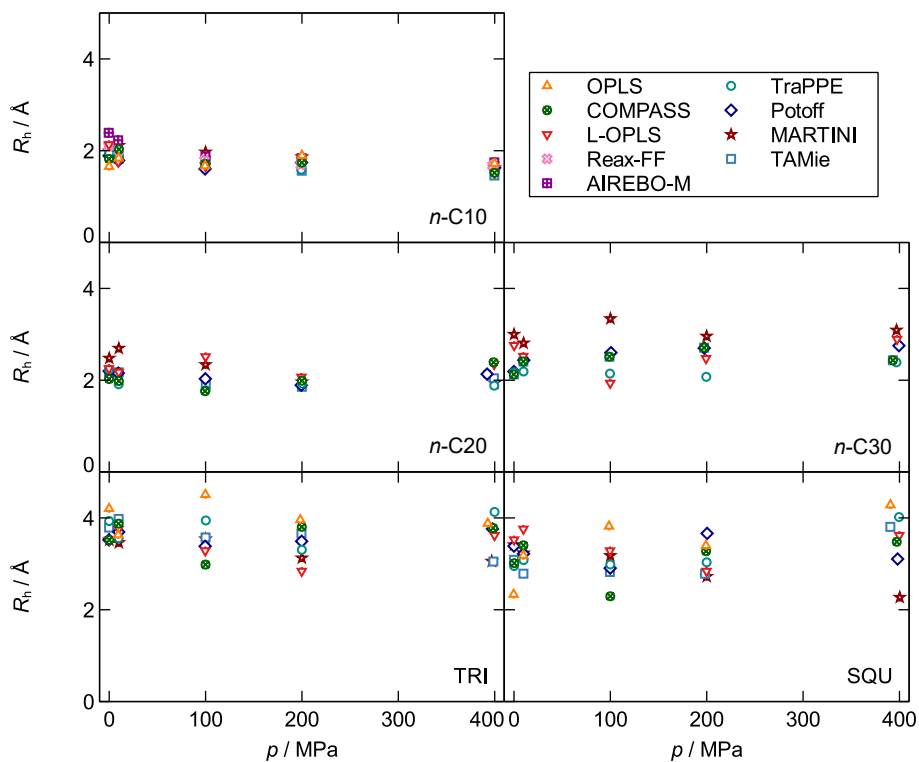


**Figure B.18:** Hydrodynamic radius  $R_h$  of  $n$ -C10,  $n$ -C20,  $n$ -C30, TRI, and SQU at  $T = 373.15$  K as a function of the pressure  $p$ . Colored symbols indicate the simulation results for the different force fields.

The hydrodynamic radius was also averaged over all pressures for every force field and molecule. The results are shown in Fig. B.19.

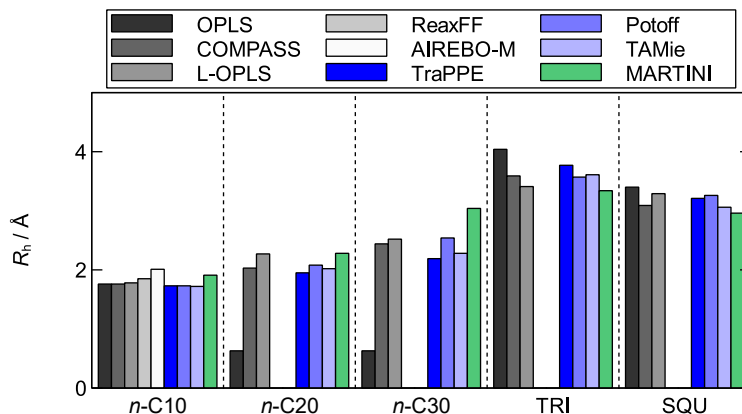


**Figure B.19:** Averaged radius of gyration  $R_h$  of  $n$ -C10,  $n$ -C20,  $n$ -C30, TRI, and SQU at  $T = 373.15$  K for the different force fields averaged over all state points.

The results are similar to the radius of gyration (see Fig. B.12). The force fields are mostly consistent in their prediction of the hydrodynamic radius except the OPLS force field for  $n$ -C20 and  $n$ -C30. Due to its unphysical properties for long linear alkanes, it

predicts smaller values than all other force fields. In general, the hydrodynamic radius is smaller than the radius of gyration which is in accordance with Ref. [748].

## B.12 Results for the MARTINI Force Field with Time Scaling

In Fig. B.20 and B.21, the results for the viscosity and the self-diffusion coefficient calculated by the MARTINI force field with time scaling are compared to the original MARTINI results without time scaling. For the time scaling, a scaling factor  $k_t = 4$  was applied. The viscosity and the self-diffusion coefficient with time scaling were calculated from the original values of the MARTINI force field by  $\eta_{\text{scaled}} = \eta \cdot k_t$  and  $D_{\text{scaled}} = D/k_t$ , respectively. For both properties, the predictions by the MARTINI force field worsen

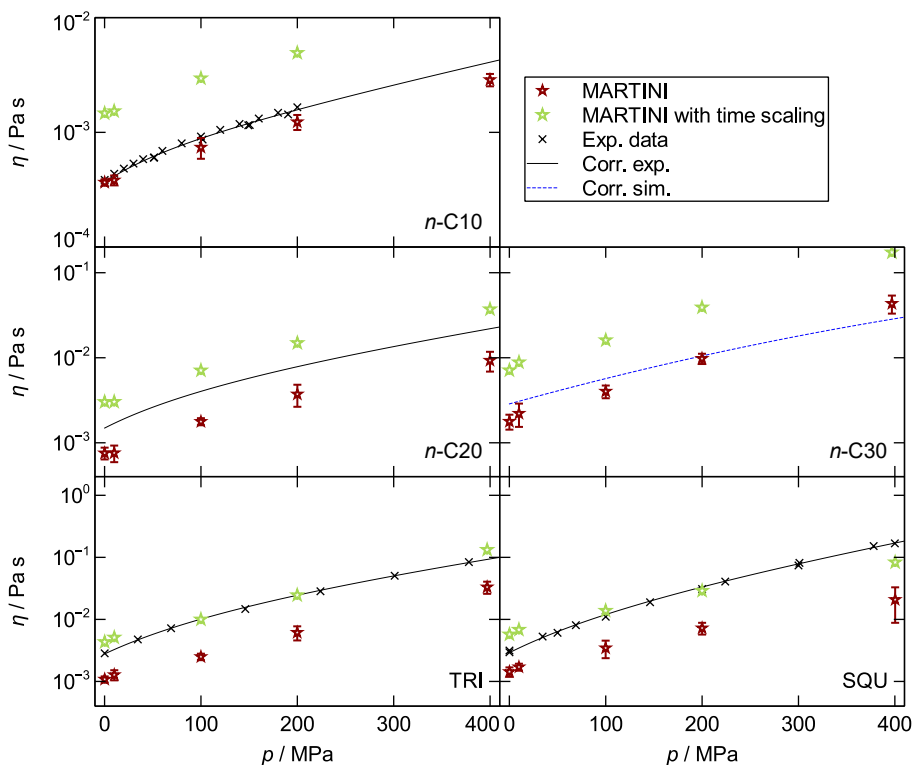


**Figure B.20:** Viscosity  $\eta$  of  $n$ -C10,  $n$ -C20,  $n$ -C30, TRI, and SQU at  $T = 373.15$  K as a function of the pressure  $p$ . Stars indicate the simulation results for the MARTINI force field without (dark red) and with scaling (light green) and the black crosses are experimental data points. Black solid lines are correlations of the experimental data, blue broken lines are correlations of the simulation data with the Potoff force field.

for the linear alkanes. They overestimate the viscosity and underestimate the self-diffusion clearly for all three substances where the original MARTINI without time scaling provided good predictions. In contrast, the predictions for the branched alkanes

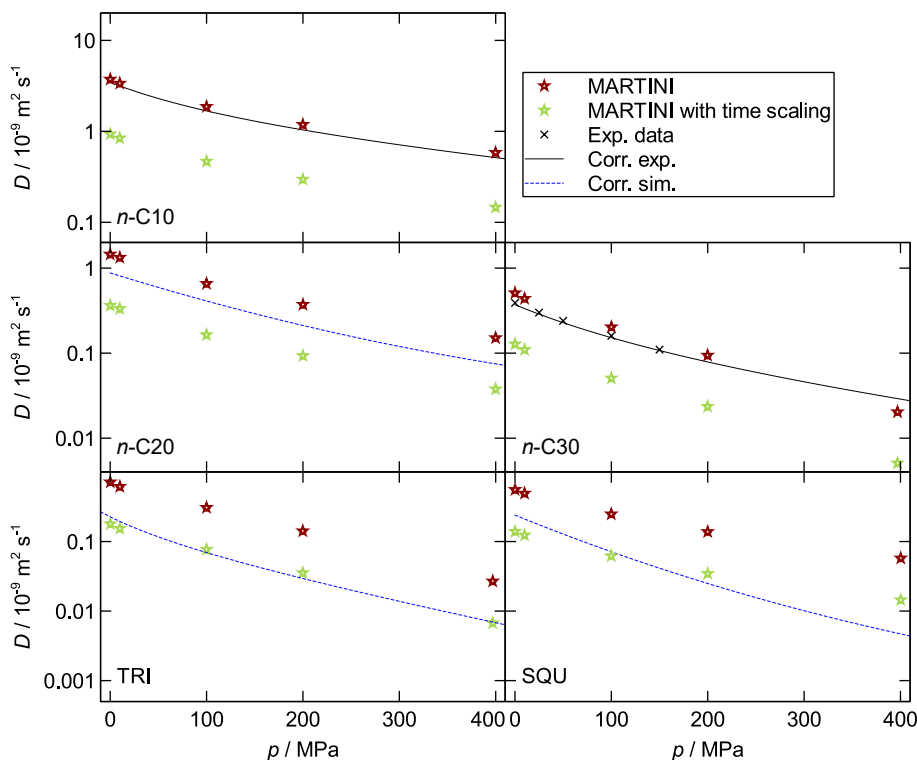


**Figure B.21:** Self-Diffusion  $D$  of  $n$ -C10,  $n$ -C20,  $n$ -C30, TRI, and SQU at  $T = 373.15$  K as a function of the pressure  $p$ . Stars indicate the simulation results for the MARTINI force field without (dark red) and with scaling (light green) and the black crosses are experimental data points. Black solid lines are correlations of the experimental data, blue broken lines are correlations of the simulation data with the Potoff force field.

improve: The viscosity is underestimated and the self-diffusion is overestimated without time scaling. With time scaling, the deviations to the experimental values decrease. Overall, the time scaling does not improve the results throughout all substances and state points. Additionally, the factor itself is kind of arbitrary. For example, the standard scaling factor  $k_t = 4$  was derived from the comparison of the diffusional dynamics of water in CG simulations and experiments. Higher scaling factors (5-10) have been also used for different systems [313].

## B.13 Uncertainties of the Simulations for the Computational Costs

The uncertainties shown in Fig. B.22 give an impression of the statistical quality of the simulations that were compared by their computational costs. For the viscosity,  $\Delta\eta$  is between 7.4 % and 22 % of the computed value. The uncertainty of the self-diffusion coefficient is smaller in the range between 1 % and 1.6 %. For both properties, the

uncertainties of the AA force fields tends to be slightly larger than the uncertainties of the UA and CG force fields. For the self-diffusion, this trend is even more mitigated.

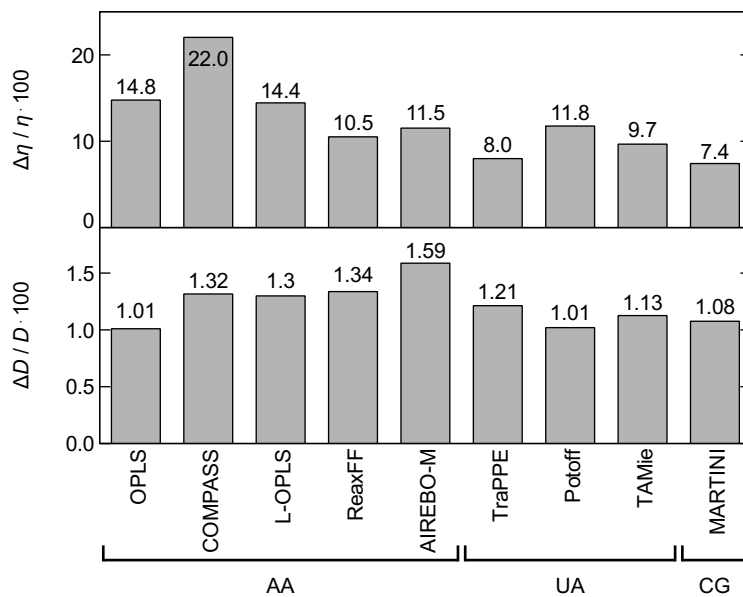


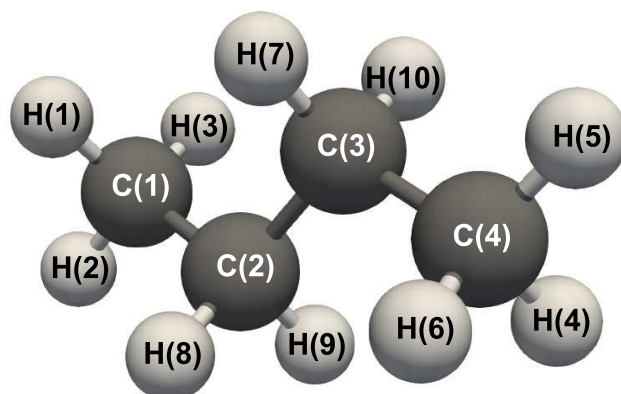
**Figure B.22:** Uncertainties of the viscosity  $\Delta\eta$  and the self-diffusion coefficient  $\Delta D$  of all force fields for 20 replica simulations with  $T = 373.15\text{K}$  and  $\rho = 0.67982\text{g/ml}$ .

# C Supporting Information for Chapter 4

## C.1 Further Details on the Data Scheme and Data Format

### C.1.1 Tags of Interaction Sites Modeling Hydrogen Atoms

The tags for interaction sites modeling a hydrogen atom in all-atom force fields have a special format regarding the last two parts of the tag format. Since hydrogen atoms can only form a single first-order bond, hydrogen atoms would have tags of the form "part1-part2-1-1". To increase the quality of information in the tag, the last two parts of the tag are modified for hydrogen atoms: The third part of the tag thereby describes, which atom is modeled by the interaction site to which the hydrogen atom under consideration is bound. The last part of the tag is a tuple divided by a backslash "\". The first part of the tuple specifies the number of bonds of the interaction site to which the hydrogen atom under consideration is bound. In case of non-cyclic molecular structures, the second part of the tuple describes the highest bond order of the interaction site to which the hydrogen atom under consideration is bound. Therein, the number of bonds neglects bonds to hydrogen atoms. Fig. C.1 shows an all-atom model of a n-pentane molecule, in which each interaction site has been assigned its corresponding tag. For cyclic molecular structures see the following section.



H(1) - H(6): A-H-C-1\1      C(1) & C(4): A-C-1-1  
 H(7) - H(10): A-H-C-2\1      C(2) & C(3): A-C-2-1

**Figure C.1:** All-atom model of the n-pentane molecule with tags assigned to the interaction sites.

### C.1.2 Tags of Interaction Sites Modeling Cyclic Structures

The tags for interaction sites modeling an atom or a group of atoms within a cyclic molecular structure have a special format regarding the last two parts of the tag format. The second part of the tag is preceded by a "C" to indicate that the interaction site under consideration is located in a cyclic molecular structure. The last part of the tag, on the other hand, consists of several flags separated by a hyphen "/". The first flag describes the functional group within the ring. Table C.1 gives examples of flags used in the data format.

Further flags are an alphabetical listing of all second parts of the tags of the interaction sites bond to the interaction site under consideration. In the case that the part of the considered interaction site is "CC", another flag is appended. This appended flag

**Table C.1:** Flags representing a functional group within a cyclic molecular structure. \* Only for cycloalkanes with a ring size of five or six. \*\* Only for cycloalkanes with a ring size of six.

Abbreviation	Functional group
CA	cycloalkane
E*	ether
diE(1,3)*	1,3 di-ether
diE(1,4)*	1,4 di-ether
triE**	tri-ether
Aro	benzene



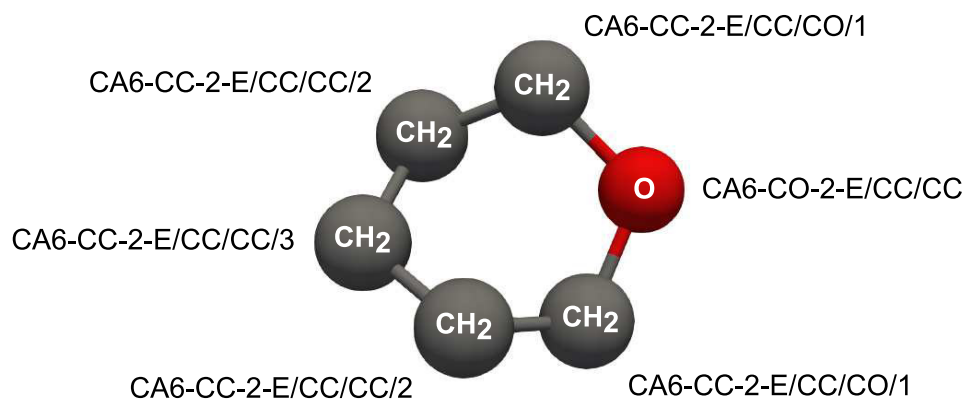


**Figure C.2:** Model of a cyclic molecular structure and the tags associated with the interaction site.

describes the minimum distance of the considered interaction site to another site within the ring whose second part of the tag is not "CC". In case of a pure "CC" ring, the flag has the value "0". Fig. C.2 shows a model of an united-atom cyclic molecular structure and the tags associated with each interaction site. For all-atom modeled hydrogen atoms that are bound to a cyclic molecular structure, only the last tag is altered compared to the description in the previous section. The last tag follows the same rules described in this section.

### C.1.3 Non-Transferable Models of Molecules in the Data Scheme

Some transferable force fields also include models of molecules that are intrinsically non-transferable and parameters are fitted for each component-specific force field model. Hence, for specific molecules, exceptions from the transferable model framework are defined and component-specific models are used. For example, water molecules often possess parameters which are exclusively used for this particular molecular model and cannot be applied to any other molecule. The data scheme presented in this chapter is capable of incorporating these component-specific force field models by assigning them a new functional group. Therefore, the first tag is an abbreviation representing the functional group. The other tags follow the principles of the data scheme outlined in Chapter 4. Analogously, interaction sites modeling an atom or group of atoms within a cyclic molecular structure in a non-transferable model can be assigned a new flag representing the functional group.

### C.1.4 Details on Rigid, Flexible, and Semi-Flexible Force Fields

For rigid force fields, all bond lengths, bond angles or torsion angles are constrained. Semi-flexible force fields allow that individual bond lengths, bond angles or torsion angles are constrained. The TraPPE-UA force field for example uses rigid bond lengths for all bonds, whereas bond angles and torsion angles are not constrained – in most cases. Certain molecular structures (e.g. benzene) are also constrained with respect to their bond angles and torsion angles. Constrained bond lengths or bond angles are given the  $ID_i = 0$  and the parameter  $p_0$  takes either the constrained bond length or the constrained bond angle. All other parameters take the value '-'. In the case of a constrained torsion angle, both the potential and all parameters take the value '-'.

### C.1.5 Specifications for Special Cis/Trans Torsion Potentials

To distinguish between cis and trans configurations, further metadata is required. Therefore, for isomerism-dependent torsion potentials, the potentials for both configurations are given by specifying two potential functions, parameter sets and meta data separated by a slash. The first data refers to the cis configuration and the second to the trans configuration.

## C.2 Application to the TraPPE-UA, OPLS-AA, and Potoff Force Fields

The TraPPE-UA, OPLS-AA, and Potoff transferable force fields were implemented in the TUK-FFDat data format. The corresponding files are provided in the Zenodo repository 436 in the three files "TUK-FFDat\_TraPPE-UA.xlsx", "TUK-FFDat\_OPLS-AA.xlsx", and "TUK-FFDat\_Potoff.xlsx".

It should be noted that the extension of the TraPPE-UA force field from *Zhang et al.* [384] was used, since perfluoranes have a backbone consisting of "CF<sub>x</sub>" interaction sites instead of "CH<sub>x</sub>" interaction sites. In the special case of perfluoranes, each interaction site "CF<sub>x</sub>" is assigned the first and second part of the interaction site tag "A-PF" instead of the regular alkane tag of "A-C".

## C.3 Building a TUK-FFDat Force Field File

For force field developers, a blank `.xlsx` TUK-FFDat template (`template.xlsx`) is provided that can be used to create new transferable force field files. The template consists of seven tabs (`intermolecular`, `bond`, `angle`, `torsion`, `improper`, `1n_potential`, `special`) – analogue to the interaction types (cf. Tables 8 - 13). The headers of the tables are colored in dark green in the template. The names of the headers may not be changed as they are part of the data format. The body of the table is colored light green. This body needs to be filled with the actual force field data as outlined in Tables 8 - 13. Examples how the force field data needs to be filled are given via the TraPPE, OPLS-AA, and Potoff force field (see above). For each of the seven tabs, the columns defined by the data format are present. Since the number of parameters is variable for each interaction, additional columns can be added (see Tables 8 - 13, and 15 for details). In the template, placeholders (orange colored) for additional columns are added for clarity. The parameters have to be numbered in ascending order (`p1`, `p2`, `p3`, ...) and its names have to be inserted in the respective header cells. Hence, the number of columns varies according to the number of parameters used in a given force field. Moreover, the number of parameters and columns is indirectly coded in the `ID` variable of each tab. Any number of rows can be used within the limits of the `.xlsx` file format. The `.xlsx` file can then be converted to an SQL database with the tools described in the next section.

## C.4 The Handling of the Conversion Tools

The python scripts `"xlsx2SQL.py"` and `"SQL2xlsx.py"` are designed to run under python 3. The requirements for running the scripts given in the Zenodo repository 436 is a computer on which python 3 and the package manager "pip" are installed. Further python modules needed to run the scripts `"xlsx2SQL.py"` and `"SQL2xlsx.py"` that are specified in the file `"requirements.txt"` and can be installed with the help of the package manager "pip". Using the command line, the directory in which the file `"requirements.txt"` was downloaded needs to be navigated to. The following command is then to be entered into the command line:

```
$ pip install -r requirements.txt
```

Both python scripts `"xlsx2SQL.py"` and `"SQL2xlsx.py"` require two arguments each. The script `"xlsx2SQL.py"` reads in an `.xlsx` spread sheet file containing a transferable force field in the TUK-FFDat data format and outputs an SQL script that sets up a

corresponding SQL database containing the transferable force field. The first argument to this script is the name of the `.xlsx` spread sheet file including the file extension `.xlsx`. The second argument is the name of the SQL script to be generated – also including the corresponding file extension `.sql`. The `.xlsx` spread sheet file should have the same structure as the files `.xlsx` given in the Zenodo repository 436, which means that the names and headers of the individual tables must be identical.

The python script `"SQL2xlsx.py"` is the counterpart to the `"xlsx2SQL.py"` script. It reads in an SQL script that sets up a database and then outputs an `.xlsx` spread sheet file. The first argument to this script is the name of the SQL script including the file extension `.sql`. The second argument is the name of the `.xlsx` spread sheet file to be generated – also including the corresponding file extension `.xlsx`.

Thus, the two scripts `"xlsx2SQL.py"` and `"SQL2xlsx.py"` can be executed with the following commands via the command line:

```
$ python3 xlsx2SQL.py input.xml output.sql
```

or accordingly:

```
$ python3 SQL2xlsx.py input.sql output.xml
```

## C.5 Comparison with Literature Data

The implemented force fields were validated using literature data. Figs. C.3, C.4, and C.5, show the results for the TraPPE, OPLS-UA, and the TAMie force field. For the TraPPE and the TAMie force field, simulations were carried out based on the *MolMod* implementation and the results were compared with those from *Messerly et al.* [291]. For the OPLS-UA force field, results from the *MolMod* implementation were compared with those from *Schappals et al.* [90]. The results obtained from the force fields from the *MolMod* implementation are in very good agreement with the results from the literature in all cases.

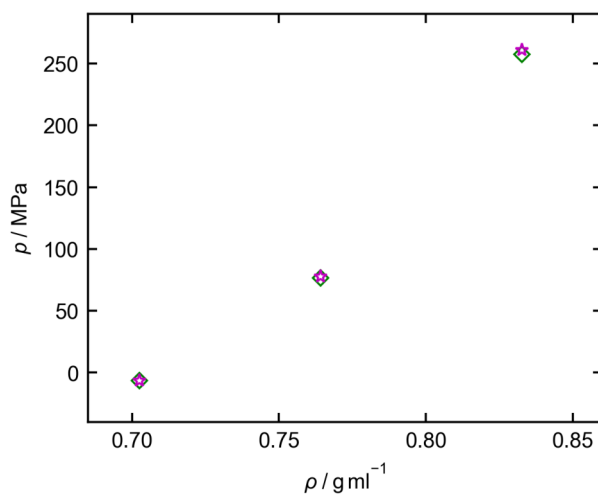


**Figure C.3:** Pressure of *n*-octane for the TraPPE force field from this work (green diamonds) in comparison with results from *Messerly et al.* [291] (magenta stars) as function of the density  $\rho$  at  $T = 293$  K.

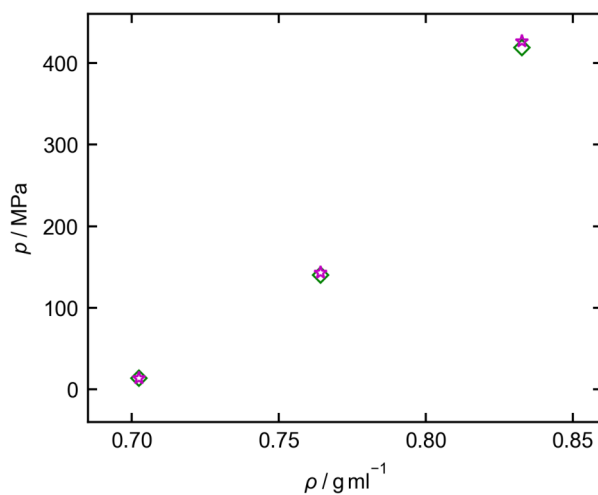


**Figure C.4:** Pressure of *n*-octane for the TAMie force field from this work (green diamonds) in comparison with results from *Messerly et al.* [291] (magenta stars) as function of the density  $\rho$  at  $T = 293$  K.

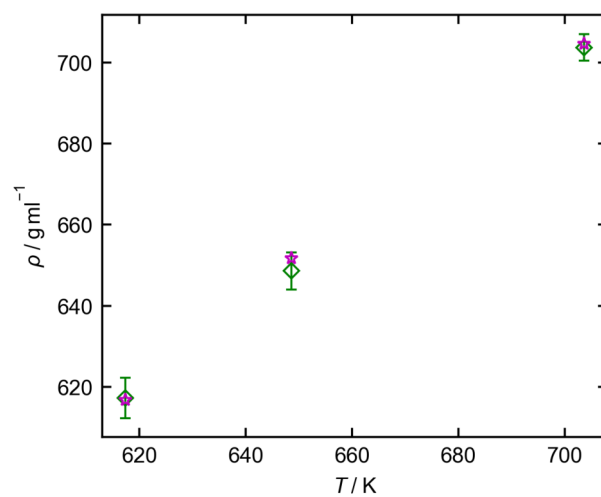


**Figure C.5:** Density of  $n$ -butane for the OPLS-UA force field from this work (green diamonds) in comparison with results from *Schappals et al.* [90] (magenta stars) as function of the temperature  $T$  at  $p = 41$  MPa.

## D Supporting Information for Chapter 5

### D.1 Cumulative Kinetic Energy

Fig. D.1 shows a typical result for the kinetic energy  $E$  added to the hot wall and removed from the cold wall by the thermostats as a function of the simulation time  $t$  during the sampling phase of the simulation. The linear dependency indicates a steady-state.

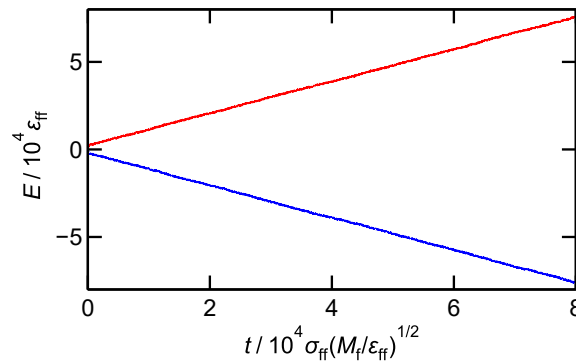


**Figure D.1:** Cumulative kinetic energy  $E$  added to the hot wall (red) and the cold wall (blue) by the thermostats as a function of the simulation time  $t$  in the 4 million time steps of the sampling phase. Data taken from simulation 1, cf. Table 23.

### D.2 Influence of the Channel Width $H$ and the Wall Temperature $T_w$

The simulations 28 – 62 (cf. Tab. II) were used to study the influence of the channel width on the Kapitza length. As shown in Fig. D.2, the Kapitza length  $L_K$  is practically independent of the channel width  $H$ .

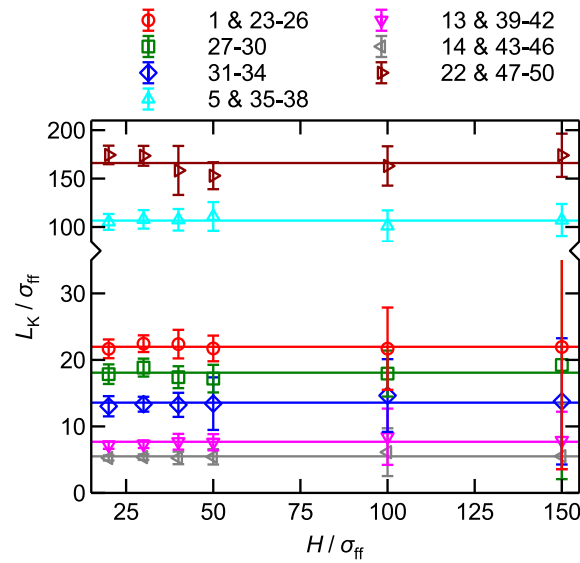


**Figure D.2:** Influence of the channel width  $H$  on the Kapitza length  $L_K$ . Results from the simulations (symbols) are indicated in the legend; the numbers correspond to the simulation number given in Table 23. The solid lines represent the mean values of the respective simulations.

The influence of the temperature difference between the fluid in the center of the channel and the wall  $\Delta T_w$  was studied by the simulations 63 – 74 (cf. Table 23). The results of these simulations are shown in Fig. D.3 and reveal that  $\Delta T_w$  has no significant influence on  $L_K$  in the range of values studied in Chapter 5, i.e. the results scatter around a common mean value.



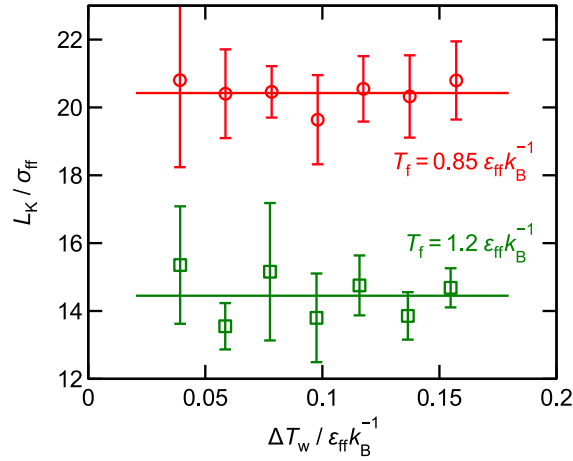


**Figure D.3:** Dependence of the temperature difference between the fluid in the center of the channel and the wall  $\Delta T_w$  on the Kapitza length  $L_K$ . Results from the simulations 63 – 68 (red symbols) and 69 – 74 (green symbols), cf. Table 23. The red and green solid lines represent the mean value of the respective simulations.

### D.3 Density Profiles Near the Solid Surface

Fig. D.4 shows that the solid-fluid interaction energy  $\varepsilon_{sf}$  has an important influence on the fluid structure at the interface. Not only the width of the maxima depend on  $\varepsilon_{sf}$ , but also their position. As expected, low numbers of  $\varepsilon_{sf}$  lead to less ordering. A high ordering in the adsorption layer leads to an increased heat transfer resistance of the interface

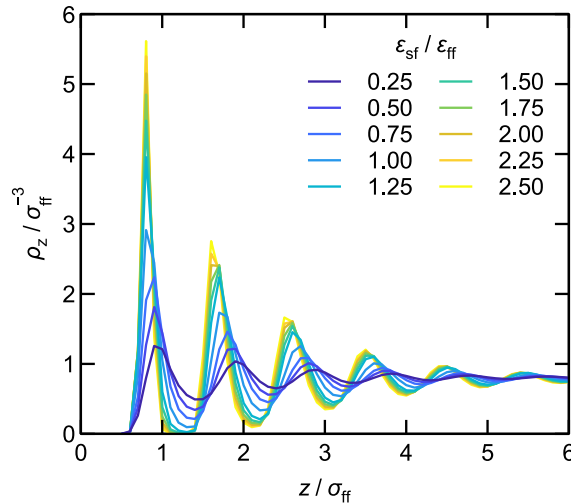


**Figure D.4:** Density profile  $\rho_z$  of the fluid at the solid-fluid interface for different solid-fluid interaction energies  $\varepsilon_{sf}$ . The bulk density is  $\rho_f = 0.8 \sigma_{ff}^{-3}$ . Results from the simulations 1 and 10 – 18, cf. Table 23.

Fig. D.5 shows the influence of the fluid temperature  $T_f$  on the structure of the fluid

at the interface. Fig. D.5 reveals that high temperatures lead to a decrease of the structuring due to a larger fluid particle mobility.

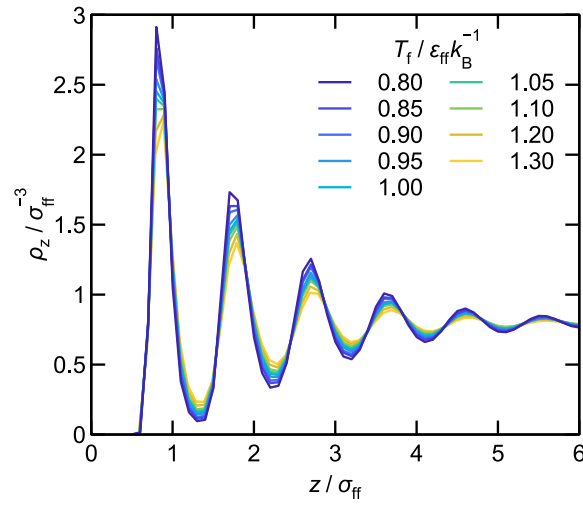


**Figure D.5:** Density profile  $\rho_z$  of the fluid at the solid-fluid interface for different fluid temperatures  $T_f$ . The bulk density is  $\rho_f = 0.8 \sigma_{ff}^{-3}$ . Results from the simulations 1 – 9, cf. Table 23.

In Fig. D.6, the structuring of the fluid is plotted for ten different mean fluid densities along supercritical isotherm  $T = 1.3 \varepsilon_{ff} k_B^{-1}$ . It reveals that the number of adsorption layers and thus the structuring of the fluid near the wall increases with increasing density.

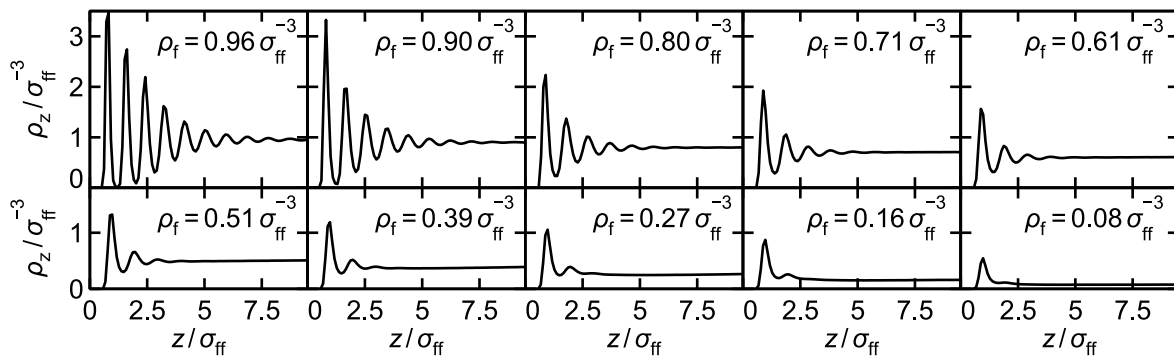


**Figure D.6:** Density profile  $\rho_z$  of the fluid for ten bulk densities  $\rho_f$  at a temperature of  $T = 1.3 \varepsilon_{ff} k_B^{-1}$ . The mean bulk fluid density is indicated in each subplot. Results from the simulations 9, 97, 99, 101, 103, 105, 107, 109, 112, and 113, cf. Table 23.

# E Supporting Information for Chapter 6

## E.1 Multi-parameter EOS of Calibration Fluids

In Fig. E.1, the densities calculated from the multi-parameter EOS for the reference fluids ethanol and toluene [562, 563] are compared to experimental data from the Dortmund Database (DDB) [719]. The mean average deviations of the depicted data from the EOS are 0.06 % for ethanol and 0.075 % for toluene.

## E.2 Estimation of the Calibration Uncertainty

$$u_{\text{cal,r}}(\rho)$$

The calibration uncertainty  $u_{\text{cal,r}}(\rho)$  was estimated similar to Eq. (32) as

$$u_{\text{cal,r}}(\rho) = \sqrt{u_{\text{fit,r}}^2 + u_{\text{EOS-Eth,r}}^2 + u_{\text{EOS-Tol,r}}^2}, \quad (\text{E.1})$$

where  $u_{\text{fit,r}} = 0.000232$  is the standard uncertainty of the calibration fit,  $u_{\text{EOS-Eth,r}} = 0.00028$  and  $u_{\text{EOS-Tol,r}} = 0.00036$  are the standard uncertainties of the data which obey a smaller deviation than the mean average deviations given in the section before. This data reduction was implemented to remove the influence of outliers and get a real estimation of the uncertainty. The resulting uncertainty for the calibration is  $u_{\text{cal,r}}(\rho) = 0.0005$ .

## E.3 Parameters of Empirical Correlations $\rho_{\text{corr}}(T, p)$

The parameters of the empirical correlations (cf. Eq. (33)) are given in Table E.1.

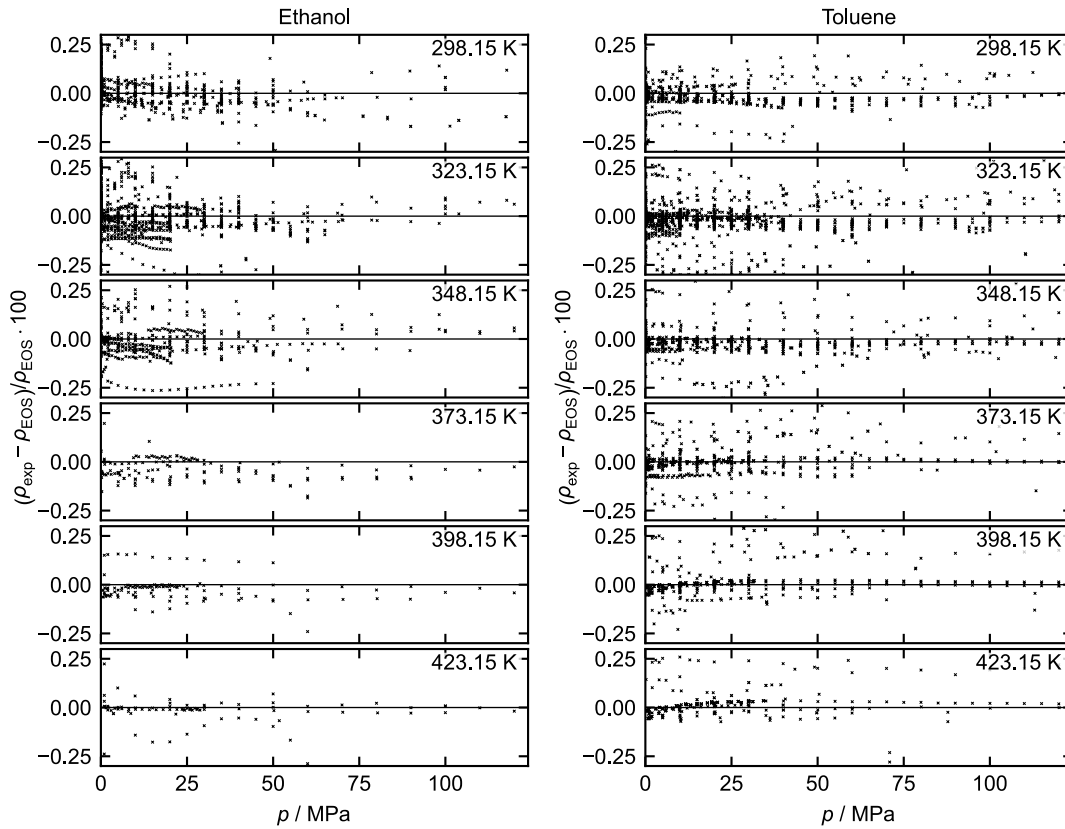


**Figure E.1:** Relative deviations of experimental data and results from the multiparameter EOS as a function of the pressure  $p$  for the reference fluids ethanol and toluene. Experimental data  $\rho_{\text{exp}}$  were taken from the DDB [719]. The EOS from Refs. 562 (ethanol) and 563 (toluene) were used to calculate the densities  $\rho_{\text{EOS}}$ .

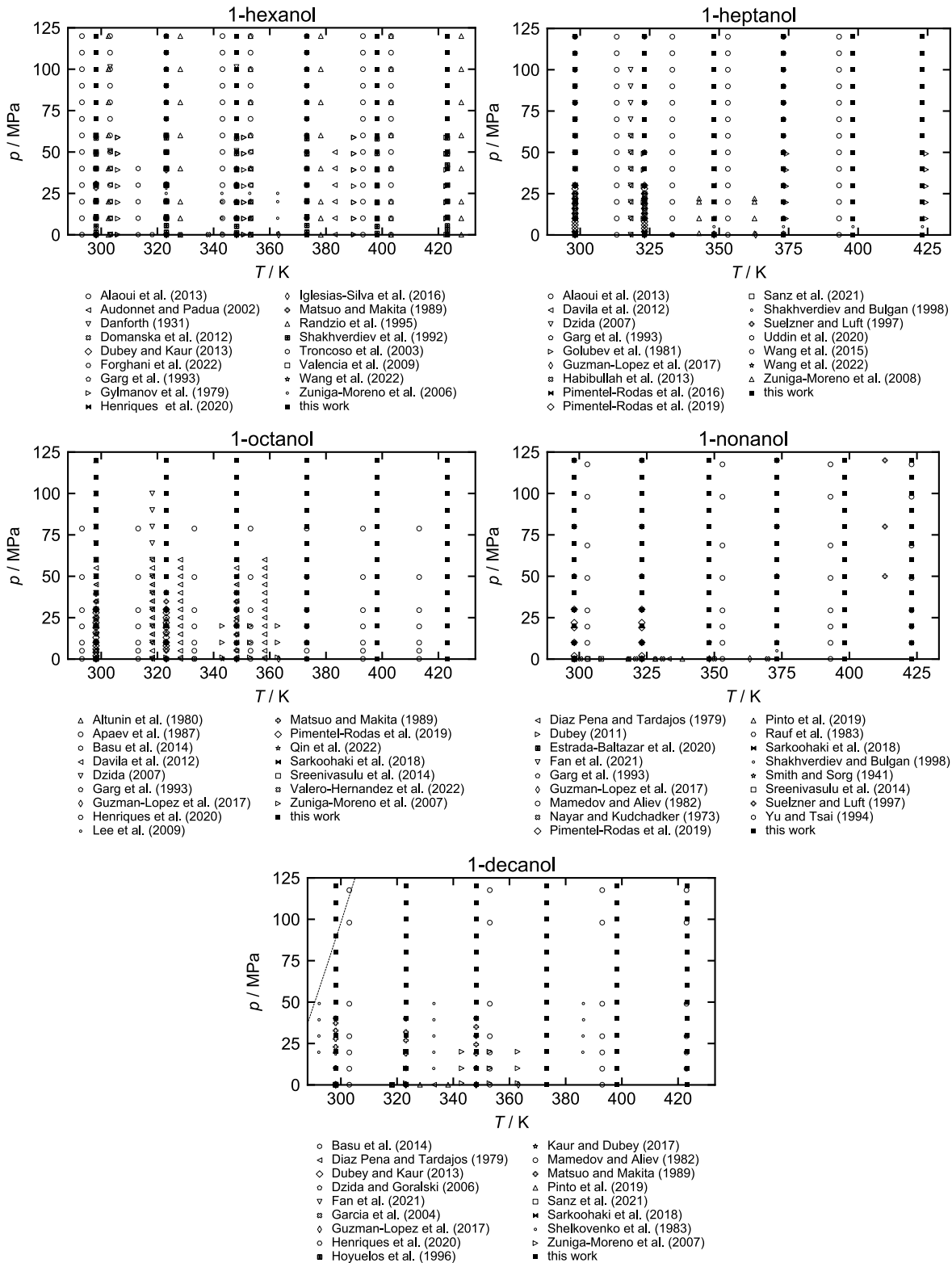
**Table E.1:** Parameters of the empirical correlations  $\rho_{\text{corr}}(T, p)$  (cf. Eq. (33)) for the 1-alcohols studied in this work.

	1-hexanol	1-heptanol	1-octanol	1-nonanol	1-decanol
$c_0 / 10^2$	9.202185	9.202185	9.518282	9.486945	9.030465
$c_1 / 10^{-1}$	-0.211634	-0.211634	-1.943067	-1.695094	1.071356
$c_2 / 10^{-1}$	-0.011168	-0.011168	-0.008145	-0.008269	-0.012203
$c_3 / 10^{-1}$	3.731305	3.731305	3.642881	3.586195	3.585842
$c_4 / 10^{-8}$	1.209565	1.209565	1.058661	1.008344	0.965867
$c_5 / 10^{-8}$	3.520952	3.520952	2.783496	2.593317	2.500269
$c_6 / 10^{-8}$	-3.315736	-3.315736	-2.781481	-2.624923	-2.515265

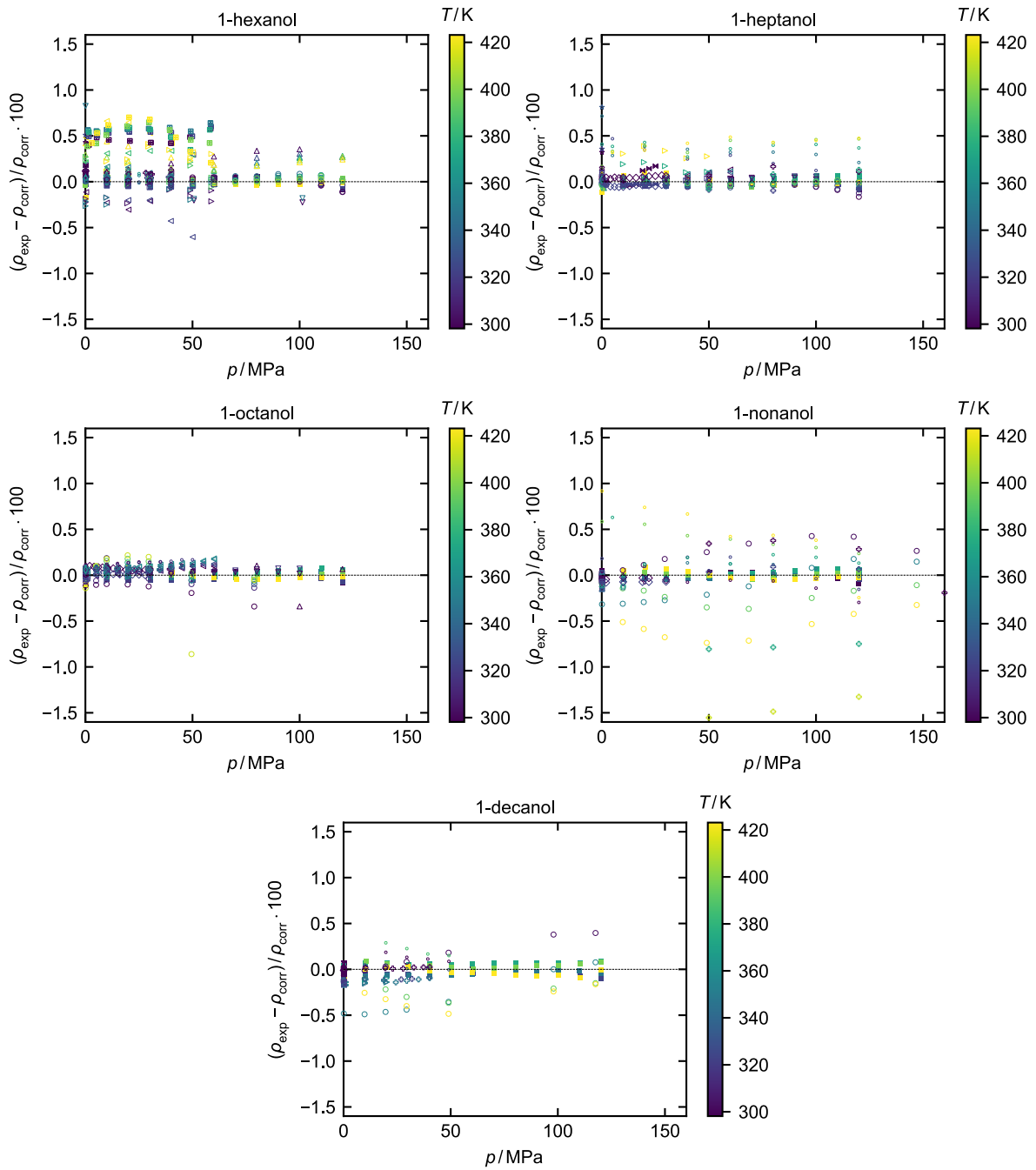
## E.4 Literature Data

Fig. E.2 shows the available literature data for the density of the five 1-alcohols for  $298.15 \leq T/\text{K} \leq 423.15$  and  $0.1 \leq p/\text{MPa} \leq 120$ . Experimental data are available for all five substances. Most experiments were conducted at ambient conditions. In general, data is sparse especially for elevated pressures ( $p \gtrsim 50$  MPa) and temperatures ( $T \gtrsim 380$  K). The density data for 1-hexanol are distributed relatively uniformly in the considered pressure and temperature range. The availability of experimental density data tends to decrease with increasing chain length.

In addition to Figs. 49 - 50, Fig. E.3 shows the deviations of the experimental data of this work as well as the literature data are shown as function of the pressure. In contrast to the Figs. 49 - 50 (which are limited to deviations between -0.4% and 0.4% for better visibility), deviations up to 1.6% are displayed in Fig. E.3 to also include large deviations. For 1-nonanol, the literature data scatter most and do not agree with each other (especially Refs. 623, 634, 638). These data points obey both, positive and negative deviations to the empirical model of this work. Due to this distribution of the deviations and the fact, that other references (only available for  $p < 35$  MPa) agree well with the results of this work, the data from these references are assumed to be outliers. This is also the reason for the higher  $\text{AAD}_{g,\text{corr}}^{\text{lit}}$  for 1-nonanol (see Table 32).



**Figure E.2:** State points (temperature  $T$  and pressure  $p$ ) where measurements are available in literature (including measurements of this work) for 1-hexanol, 1-heptanol, 1-octanol, 1-nonanol, and 1-decanol. The dashed line represents a correlations for the solid-liquid equilibrium of 1-decanol from Ref. 596.



**Figure E.3:** Relative deviations between experimental density data (symbols) and the empirical correlation, cf. Eq. (33), (baseline) as a function of the pressure  $p$ . Symbols are the same as in Fig. E.2 (individually for each substance). The color indicates the temperature.

## E.5 Details on the Fitting Procedure

For the fitting procedure of the component-specific models, the error for the vapor pressure was weighted five times more than the error of the saturated densities and the

**Table E.2:** Result of the fit: Deviations of the EOS models to the reference data used for the fit for the vapor pressure  $\text{AAD}_{p^s, \text{EOS}}^{\text{lit}}$ , the saturated liquid densities  $\text{AAD}_{\rho^s, \text{EOS}}^{\text{lit}}$ , and the homogeneous state liquid density  $\text{AAD}_{\rho, \text{EOS}}^{\text{th}}$ .

	1-hexanol	1-heptanol	1-octanol	1-nonanol	1-decanol
	$\text{AAD}_{p^s, \text{EOS}}^{\text{lit}} / \%$				
PC-SAFT	0.31	0.84	0.98	0.74	0.92
SAFT-VR Mie	0.21	0.77	0.99	0.99	1.24
soft SAFT	0.37	0.7	0.92	1.16	1.4
CPA	0.49	0.88	0.94	0.51	0.93
	$\text{AAD}_{\rho^s, \text{EOS}}^{\text{lit}} / \%$				
PC-SAFT	0.76	0.41	0.56	0.65	0.73
SAFT-VR Mie	0.92	0.56	0.24	0.51	0.65
soft SAFT	1.3	1.68	1.2	2.11	1.67
CPA	1.11	1.39	1.59	1.45	1.25
	$\text{AAD}_{\rho, \text{EOS}}^{\text{th}} / \%$				
PC-SAFT	0.49	0.57	0.66	0.91	0.99
SAFT-VR Mie	0.4	0.31	0.2	0.38	0.73
soft SAFT	0.61	0.97	0.61	1.59	0.93
CPA	1.13	1.34	1.37	1.54	1.52

homogeneous bulk densities. Thus, the objective function

$$\Delta = \frac{5}{N_{p^s}} \sum_i^{N_{p^s}} \left( \frac{p_{\text{exp}}^v - p_{\text{EOS}}^v}{p_{\text{exp}}^v} \right)^2 + \frac{1}{N_{\rho^s}} \sum_i^{N_{\rho^s}} \left( \frac{\rho_{\text{exp}}^{\text{sat}} - \rho_{\text{EOS}}^{\text{sat}}}{\rho_{\text{exp}}^{\text{sat}}} \right)^2 + \frac{1}{N_{\rho}} \sum_i^{N_{\rho}} \left( \frac{\rho_{\text{exp}} - \rho_{\text{EOS}}}{\rho_{\text{exp}}} \right)^2, \quad (\text{E.2})$$

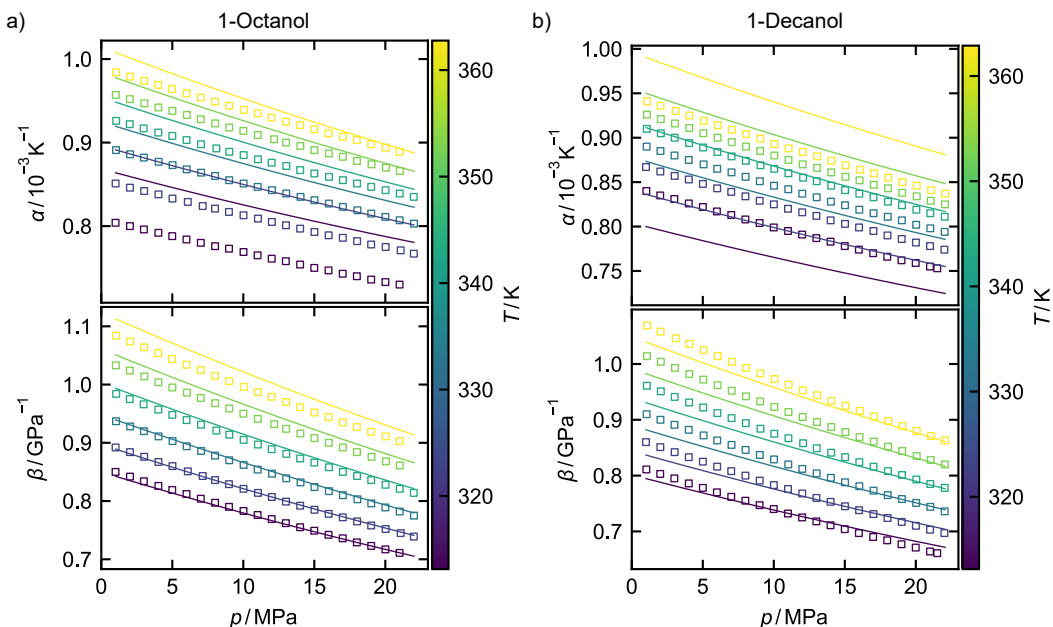
was used.

Table E.2 reports the results of the fits of the component-specific models developed in this work for the vapor pressure, the saturated density, and the homogeneous state liquid density. The AADs are calculated using the data used for the fit, which comprise literature data for the vapor pressure and saturated liquid density as well as the measured densities from this work. Details on the fitting procedure are given in Chapter 6.



## E.6 Comparison of the Second-Order Derivative Properties to Literature Data

Fig. E.4 shows a comparison of the thermal expansion coefficient  $\alpha$  and the isothermal compressibility  $\beta$  calculated from the empirical model (cf. Eq. (3)) with literature data for 1-octanol and 1-decanol. For the thermal expansion coefficient, the AADs between



**Figure E.4:** Thermal expansion coefficient  $\alpha$  (top) and isothermal compressibility  $\beta$  as function of pressure  $p$  for 1-octanol (a) and 1-decanol (b). Lines are the results from this work calculated from Eqs. (3) - (5). Symbols are results from Ref. 646. The color indicates the temperature.

the empirical model and the literature data (cf. Eq. (9)) are 3.2% and 2.8% for 1-octanol and 1-decanol, respectively. For the isothermal compressibility, the agreement to the literature data is higher resulting in lower average deviations (AADs: 1.0% for 1-octanol and 1.3% for 1-decanol). All deviations to literature data are within the given uncertainties of  $U_r(\alpha) = U_r(\beta) = 0.08$  for 1-octanol and  $U_r(\alpha) = 0.12$  as well as  $U_r(\beta) = 0.14$  for 1-decanol (see Chapter 6).

## E.7 EOS Parameters from the Literature

For the studied alcohols, there are also EOS component-specific models available in literature for the EOS frameworks used in this work. Only for soft SAFT, no models are available for 1-nonanol and 1-decanol. The references for these EOS models are given in Table E.3. All models include association but no polar contribution.

**Table E.3:** References of the substance-specific EOS parameters for the 1-alcohols applied in this work.

EOS	1-hexanol	1-heptanol	1-octanol	1-nonanol	1-decanol
PC-SAFT	570	570	570	570	570
SAFT-VR Mie	571	571	572	572	572
soft SAFT	573	573	573	-	-
CPA	574	574	574	574	574

To compare these models, the AADs for the vapor pressure, saturated liquid density, and the homogeneous state liquid density were calculated (which corresponds to the data used for fitting the component-specific EOS models in this work). The resulting AADs are given in Table E.4. Additionally, the results for the density, thermal expansion

**Table E.4:** Deviations of the EOS models from literature to experimental data of the vapor pressure  $\text{AAD}_{p^s, \text{EOS}}^{\text{lit}}$ , the saturated liquid densities  $\text{AAD}_{\rho^s, \text{EOS}}^{\text{lit}}$  and the compressed liquid density  $\text{AAD}_{\rho, \text{EOS}}^{\text{th}}$ .

	1-hexanol	1-heptanol	1-octanol	1-nonanol	1-decanol
	$\text{AAD}_{p^s, \text{EOS}}^{\text{lit}} / \%$				
PC-SAFT	0.59	0.96	1.12	0.8	1.18
SAFT-VR Mie	3.52	7.84	2.39	1.37	5.19
soft SAFT	27.69	28.52	25.91		
CPA	7.13	18.31	9.8	11.04	8.02
	$\text{AAD}_{\rho^s, \text{EOS}}^{\text{lit}} / \%$				
PC-SAFT	0.66	0.63	0.54	0.33	0.84
SAFT-VR Mie	0.78	2.4	0.35	0.54	1.26
soft SAFT	0.21	0.42	1.17		
CPA	1.43	1.31	1.63	2.12	1.2
	$\text{AAD}_{\rho, \text{EOS}}^{\text{th}} / \%$				
PC-SAFT	0.59	0.47	0.69	1.4	2.03
SAFT-VR Mie	0.33	1.93	0.16	0.46	0.77
soft SAFT	0.37	0.66	1.62		
CPA	1.2	1.15	1.38	1.36	1.49

coefficient, and the isothermal compressibility of these models are shown in Fig. E.5. The soft SAFT EOS was used here without a crossover term, even though the parameters were fitted using a version that includes a crossover term [573].

For three out of the four EOS models, the deviations of the vapor pressure, i.e.  $\text{AAD}_{p^s, \text{EOS}}^{\text{lit}}$ ,

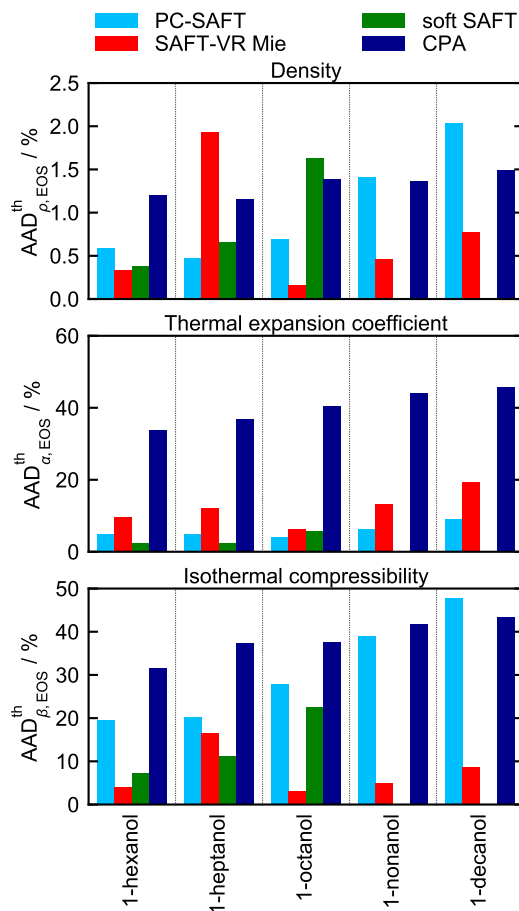


**Figure E.5:** Average absolute deviations of the EOS results  $\text{AAD}_{Y,\text{EOS}}^{\text{th}}$  for the density  $\rho$ , the thermal expansion coefficient  $\alpha$ , and the isothermal compressibility  $\beta$  for the five 1-alcohols using the EOS models from literature [570–574]. The AAD were computed with respect to the reference data from this work 'th'.

are significantly larger than the ones from this work. This is probably due to a different target function used in the fitting procedure with less weight on the vapor pressure, besides a different set of experimental data. The target function is not given in most of the publications which hinders the reproducibility of the given results. The extremely high deviations of the vapor pressure description by the soft SAFT EOS, cf. Table E.4, are possibly related to the fact that a crossover term was used in the original publication.

Compared to the models parameterized in this work (see Chapter 6), the results for the density show slightly higher deviations for most of the substances. This is due to the parametrization, as the models from the literature were only adjusted to vapor pressure and saturated liquid density data. Nevertheless, also the models from the literature yield relatively small deviations of only up to around 2 %. As already seen for the models adjusted in this work, the SAFT-VR Mie shows the overall lowest deviations (with one exception for 1-heptanol). Some effects can be found for both, the models from the literature and from this work: For both, the soft SAFT and CPA EOS, the

deviations increase with increasing chain length for all three properties ( $\rho$ ,  $\alpha$ ,  $\beta$ ). Also, the pressure dependence of the density, i.e. the isothermal compressibility, is described very well by nearly all the SAFT-VR Mie models.

## E.8 *Brown's* Characteristic Curves

Fig. E.6 shows *Brown's* characteristic curves for 1-hexanol, 1-heptanol, 1-nonanol, and 1-decanol as obtained by the PC-SAFT, SAFT-VR Mie, soft SAFT, and CPA EOS. Qualitatively, the behavior of the characteristic curves is the same for a given EOS model for the different alcohols. Hence, the defects are likely not a results of the component-specific parameters, but a result of the fundamental mathematical form of a given molecular-based EOS – as expected.

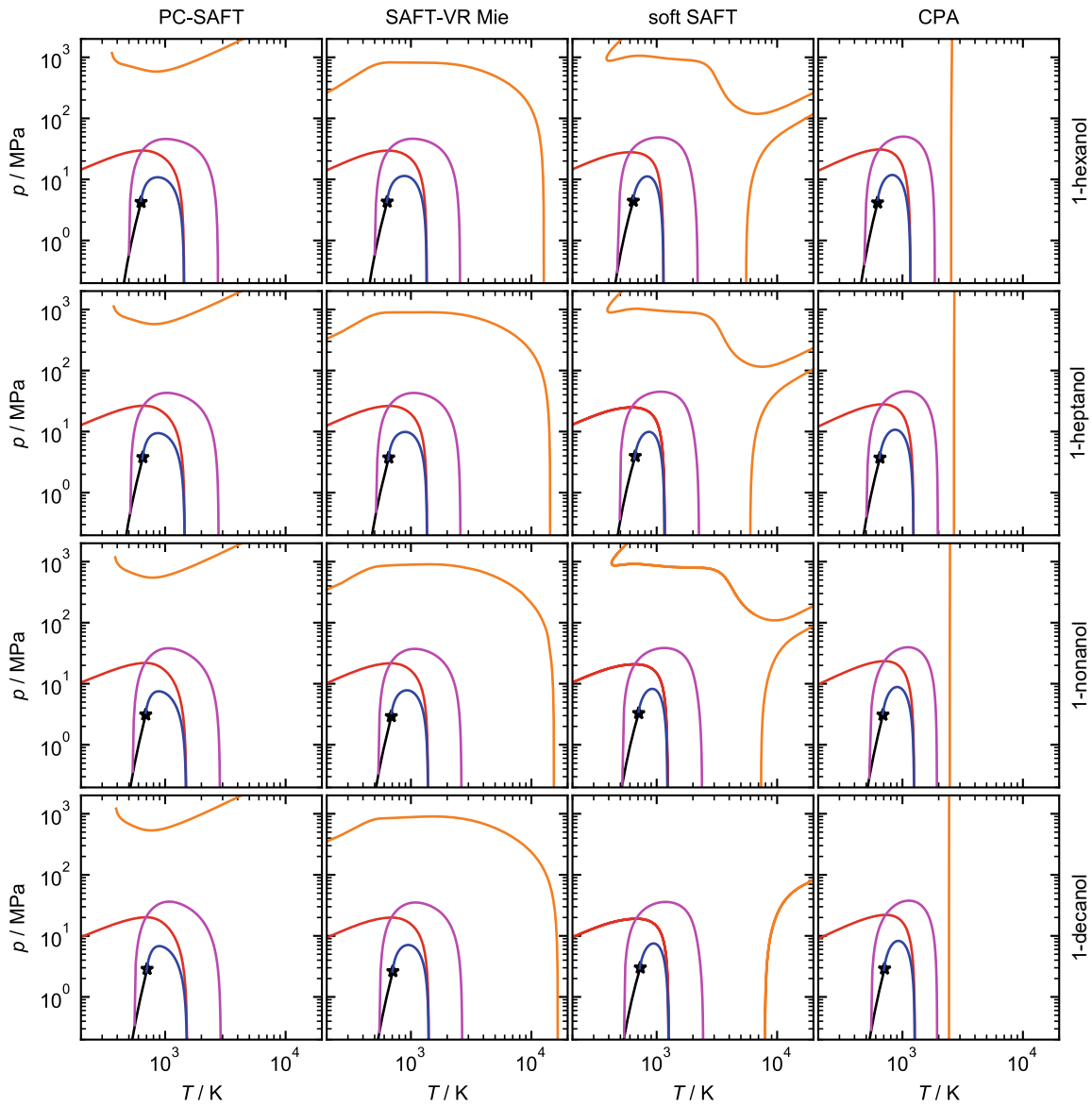


**Figure E.6:** Characteristic curves of 1-hexanol, 1-heptanol, 1-nonanol, and 1-decanol (top to bottom) calculated by the PC-SAFT EOS, SAFT-VR Mie EOS, soft SAFT EOS, and CPA EOS (left to right): Zeno curve (red), Amagat curve (orange), Boyle curve (blue), and Charles curve (purple). Black solid lines and the stars represent the vapor pressure curve and the critical point, respectively, as calculated by the corresponding EOS.

# F Supporting Information for Chapter 7

## F.1 Phase Diagrams of Viscosity, Thermal Conductivity, and Self-Diffusion

Fig. 56 of this work schematically shows the fluid phase diagram for the three transport properties (viscosity, thermal conductivity, and self-diffusion). The topologies of these diagrams are discussed here in more detail. The viscosity and the thermal conductivity exhibit the same qualitative characteristics. First, both transport properties increase with increasing pressure in all fluid phase state regions. For the states  $p < p_c$  and  $T < T_c$ , liquid and gaseous isotherms can be easily distinguished. Liquid isotherms start on the saturated liquid curve and lie above the VLE, i.e. higher viscosity or thermal conductivity in the liquid phase state than the corresponding value of the saturated liquid at the corresponding pressure. The larger the temperature of an isotherm in the liquid phase state region, the lower is the corresponding viscosity and thermal conductivity. The isotherms in the gas region start in the limit  $p \rightarrow 0$  and are nearly horizontal as the transport properties of gases only depend on the temperature, as also indicated by the Chapman-Enskog theory [75]. Here, the temperature dependency is inverted compared to the liquid phase state region: The viscosity and thermal conductivity increase with increasing temperature. The gaseous isotherms end in the saturated vapor curve and exhibit higher viscosities than the corresponding saturated vapor at the same pressure, i.e. the isotherms lie above the saturated vapor curve. The critical isotherm has similar characteristics as the gaseous isotherms for  $T > p_c$ . At the critical point, the viscosity and thermal conductivity strongly increases. The supercritical isotherms show also the same characteristics as the gaseous isotherms for  $p < p_c$ , but their values are higher than the ones of the critical isotherm. For  $T > T_c$ , the supercritical isotherms cross both the critical isotherm and other supercritical isotherms with lower temperature. This is due to the inversion of the temperature dependency. In the metastable and unstable region, the viscosity and the thermal conductivity steadily increase from the saturated vapor to the saturated liquids. As expected, they obey a pressure maximum on the vapor-side

spinodal and a pressure minimum on the liquid-side spinodal.

The self-diffusion coefficient behaves qualitatively different compared to the viscosity and the thermal conductivity. For the whole phase diagram of  $D(T, p)$ , the self-diffusion coefficient increases with increasing temperature and decreases with increasing pressure. Hence, the self-diffusion coefficient of the saturated liquid is smaller than of the saturated vapor phase at the same pressure. Therefore, the gas state points lie above the VLE region, i.e. the self-diffusion coefficient of the homogeneous gas phase states is larger than its corresponding values of the saturated vapor at the same pressure. Consequently, the self-diffusion coefficient of the liquid phase state region is lower than its corresponding values of the saturated liquid at the same pressure. The supercritical isotherms do not cross each other (as there is no change in the temperature dependency from gas to liquid states). In contrast to the viscosity and the thermal conductivity, the self-diffusion steadily decreases from the gas to the liquid in the metastable and unstable region.

## F.2 Scaled Chapman-Enskog Transport Properties

$\eta_{\text{CE}}^+$ ,  $\lambda_{\text{CE}}^+$ , and  $D_{\text{CE}}^+$

The unscaled Chapman-Enskog transport properties are given as [75]

$$\eta_{\text{CE}} = \frac{5}{16} \sqrt{\frac{M k_{\text{B}} T}{\pi N_{\text{A}}}} \frac{1}{\sigma_{\text{CE}}^2 \Omega^{(2,2)}}, \quad (\text{F.1})$$

$$\lambda_{\text{CE}} = \frac{75}{64} k_{\text{B}} \sqrt{\frac{R T}{M \pi}} \frac{1}{\sigma_{\text{CE}}^2 \Omega^{(2,2)}}, \quad (\text{F.2})$$

$$D_{\text{CE}} \rho = \frac{3}{8} \sqrt{\frac{M k_{\text{B}} T}{\pi N_{\text{A}}}} \frac{1}{\sigma_{\text{CE}}^2 \Omega^{(1,1)}}, \quad (\text{F.3})$$

where  $\rho$  is the mass density in  $\text{kg m}^{-3}$  and  $\Omega^{(1,1)}$  and  $\Omega^{(2,2)}$  are the reduced collision integrals (see Chapter 7). These properties are now scaled according to Eqs. (44) - (46) using the relation

$$\lim_{\rho_{\text{N}} \rightarrow 0} \left( \frac{\partial(-s_{\text{conf}}/R)}{\partial \rho_{\text{N}}} \right)_T = T \frac{\text{d}B}{\text{d}T} + B, \quad (\text{F.4})$$

where  $B$  is the second virial coefficient. The resulting scaled Chapman-Enskog equations are

$$\eta_{\text{CE}}^+ = \eta_{\text{CE}} \frac{1}{\sqrt{Mk_B/N_A T}} \left( T \left( \frac{dB}{dT} \right) + B \right)^{2/3}, \quad (\text{F.5})$$

$$\lambda_{\text{CE}}^+ = \lambda_{\text{CE}} \frac{1}{k_B \sqrt{RT/M}} \left( T \left( \frac{dB}{dT} \right) + B \right)^{2/3}, \quad (\text{F.6})$$

$$D_{\text{CE}}^+ = D_{\text{CE}} \rho \frac{1}{\sqrt{Mk_B/N_A T}} \left( T \left( \frac{dB}{dT} \right) + B \right)^{2/3}. \quad (\text{F.7})$$

Inserting Eqs. (F.1) - (F.3) into (F.5) - (F.7) yields the Eqs. (48) - (50).

### F.3 Isentropes of the LJ fluid

The configurational entropy  $s_{\text{conf}}$  as calculated from first principle molecular dynamics simulations are given in Fig. F.1 in a  $T - \rho$  diagram. Additional to the simulation results, isentropes have been calculated by the Kolafa-Nezbeda EOS. The simulation results agree well with the EOS.

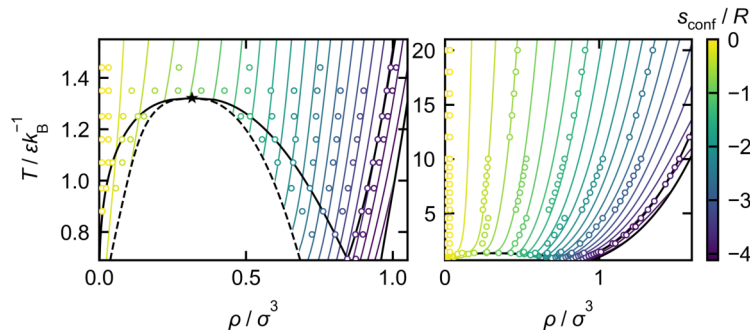


**Figure F.1:** Results of the 196 state points (squares) of the Lennard-Jones fluid simulations conducted to adjust the universal parameters of the model. The symbols represent the simulation state points and the lines are isentropes calculated by the Kolafa-Nezbeda EOS [136]. The color of the symbols and the lines indicate the configurational entropy  $s_{\text{conf}} / R$ . The phase envelopes are depicted as black solid lines. The binodal and the critical point are taken from a Ref. [73], the spinodal from Ref. [706], and the freezing and melting lines from Ref. [238].

### F.4 EOS Parameters

The EOS parameters of the substance models were taken from the literature [40, 41, 62, 63, 558, 694, 695, 697, 702–704]. They are given in Table F.1 - F.6 for the PC-



SAFT EOS, SAFT-VR Mie EOS, soft SAFT EOS, PACT+B EOS, BACKONE EOS, and the sCPA EOS, respectively. The parameters for methane used with the EOS from *Stephan et al.* were taken from the MolMod database [63] and are  $M = 16.043 \text{ kg mol}^{-1}$ ,  $\sigma = 3.7281 \text{ \AA}$ , and  $\varepsilon/k_B = 148.55 \text{ K}$  for the molar mass, the size parameter, and the energy parameter.

The segment number  $m$  is used in Eq. (47) to scale the configurational entropy. For EOS that do not use the segment number  $m$  explicitly, namely the PACT+B EOS, the BACKONE EOS, and the sCPA EOS, the equivalent parameters describing the molecular elongation or anisotropy are used. For the PACT+B EOS, the segment parameter  $c$  was used and for the BACKONE EOS, the anisotropic parameter  $\alpha$ . For methanol modeled by the sCPA EOS,  $m$  was set to 2. For the two model fluids, the LJ and LJTS fluid,  $m$  was set to 1.

**Table F.1:** PC-SAFT EOS parameters used in this work: The columns indicate the substance name, molar mass  $M$ , segment number  $m$ , segment diameter  $\sigma$ , segment dispersion energy  $\varepsilon$ , dipole moment  $\mu$ , quadrupole moment  $Q$ , bonding type scheme of association, association radius  $\kappa$ , association energy  $\varepsilon_{AB}$ , and the reference where the parameters were taken from. The 2B association scheme was used.

Substance	$M$ g/mol	$m$	$\sigma$ Å	$\varepsilon/k_B$ K	$\mu$ $D$	$Q$ $D\text{Å}$	$\kappa$	$\varepsilon_{AB}/k_B$ K	Ref.
<i>n</i> -butane	58.123	2.3316	3.7086	222.88	0	0	0	0	[40]
<i>n</i> -hexadecane	226.45	6.6485	3.9552	254.7	0	0	0	0	[40]
carbon-dioxide	44.01	1.5131	3.1869	163.33	0	4.4	0	0	[703]
1-octanol	130.23	4.403	3.6943	260.9	1.7	0	0.00261	2700.3	[704]

**Table F.2:** SAFT-VR Mie EOS parameters used in this work: The columns indicate the substance name, molar mass  $M$ , segment number  $m$ , segment diameter  $\sigma$ , segment dispersion energy  $\varepsilon$ , repulsive exponent  $\lambda_r$ , attractive exponent  $\lambda_a$ , bonding type scheme of association, association radius  $\kappa$ , association energy  $\varepsilon_{AB}$ , and the reference where the parameters were taken from. The attractive exponent was 6 for all substances, i.e.  $\lambda_a = 6$ . The 2B association scheme was used.

Substance	$M$ g/mol	$m$	$\sigma$ Å	$\varepsilon/k_B$ K	$\lambda_r$	$\kappa$	$\varepsilon_{AB}/k_B$ K	Ref.
<i>n</i> -hexane	86.177	2.1097	4.423	354.38	17.203	0	0	[41]
benzene	78.114	1.9163	4.0549	372.59	14.798	0	0	[41]
nitrogen	28.01	1.4214	3.176	72.438	9.8749	0	0	[702]
1-propanol	60.096	2.3356	3.5612	227.66	10.179	0.35377	2746.2	[41]

**Table F.3:** Soft SAFT EOS parameters used in this work: The columns indicate the substance name, molar mass  $M$ , segment number  $m$ , segment diameter  $\sigma$ , segment dispersion energy  $\varepsilon$ , and the reference where the parameters were taken from.

Substance	$M$	$m$	$\sigma$	$\varepsilon/k_B$	Ref.
	g/mol		Å	K	
propene	42.08	1.9681	3.566	206.561	[558]

**Table F.4:** PACT+B EOS parameters used in this work: The columns indicate the substance name, molar mass  $M$ , segment parameter  $c$ , characteristic temperature  $T^*$ , soft core volume  $v^*$ , and the reference where the parameters were taken from.

Substance	$M$	$c$	$T^*$	$v^*$	Ref.
	g/mol		K	cm <sup>3</sup> mol <sup>-1</sup>	
cyclohexane	84.162	1.705	358.5	61.71	[695]

**Table F.5:** BACKONE EOS parameters used in this work: The columns indicate the substance name, molar mass  $M$ , anisotropic parameter  $\alpha$ , characteristic temperature  $T_0$ , characteristic density  $\rho_0$ , dipole moment  $\mu$ , the quadrupole moment  $Q$ , and the reference where the parameters were taken from.

Substance	$M$	$\alpha$	$T_0$	$\rho_0$	$\mu$	$Q$	Ref.
	g/mol		K	mol/l	D	DÅ	
R134a	102.04	1.4287	332.07	4.957	2.99218	8.22875	[694]

**Table F.6:** sCPA EOS parameters used in this work: The columns indicate the substance name, molar mass  $M$ , co-volume parameter  $b$ , energy parameter  $a_0$ , energy parameter  $c_1$ , bonding type scheme of association, association energy  $\varepsilon_{AB}$ , association volume  $\beta$ , and the reference where the parameters were taken from. The 3B association scheme was used.

Substance	$M$	$b$	$a_0$	$c_1$	$\varepsilon_{AB}$	$\beta$	Ref.
	g/mol	l/mol	K	mol/l	bar l/mol <sup>-1</sup>		
methanol	102.04	0.0334	4.5897	1.0068	160.7	0.0344	[697]

## F.5 Component-Specific Entropy Scaling Parameters

Tables F.7 - F.9 contains the component-specific parameters of the pure substance entropy scaling models summarized in Table 34.

**Table F.7:** Entropy scaling parameters of all component-specific models for the viscosity including the substance name and the parameters  $\alpha_{0,i}^{(\eta)}$ ,  $\alpha_{\ln,i}^{(\eta)}$ ,  $\alpha_{1,i}^{(\eta)}$ ,  $\alpha_{2,i}^{(\eta)}$ , and  $\alpha_{3,i}^{(\eta)}$ .

Substance $i$	$\alpha_{0,i}^{(\eta)}$	$\alpha_{\ln,i}^{(\eta)}$	$\alpha_{1,i}^{(\eta)}$	$\alpha_{2,i}^{(\eta)}$	$\alpha_{3,i}^{(\eta)}$
LJ	0	-3.218	3.29	-0.071	0.151
LJTS	0	-0.075	0.756	0.4	0.113
methane	0	-1.963	2.157	0.121	0.125
<i>n</i> -butane	0	-14.165	13.97	-2.382	0.501
<i>n</i> -hexane	0	-1.906	2.883	0.178	0.152
<i>n</i> -hexane <sup>a</sup>	0	-2.135	2.991	0.207	0.142
<i>n</i> -hexadecane	0	10.987	-6.898	3.01	0.172
propene	0	-29.914	29.005	-7.646	1.407
cyclohexane	0	-11.074	10.705	-1.759	0.415
benzene	0	-7.591	7.779	-1.152	0.363
nitrogen	-0.013	-2.291	3.005	-0.037	0.25
carbon dioxide	0	-9.576	9.498	-1.76	0.418
methanol	0.118	-12.592	11.046	-2.159	0.444
1-propanol	0	0	0	0.69	0.158
1-octanol	0	-18.349	18.866	-3.858	0.807
R134a	0	-4.92	4.288	0.065	0.083

<sup>a</sup>only fitted to exp. data with  $p \leq 10$  MPa.

**Table F.8:** Entropy scaling parameters of all component-specific models for the thermal conductivity including the substance name and the parameters  $\alpha_{0,i}^{(\lambda)}$ ,  $\alpha_{\ln,i}^{(\lambda)}$ ,  $\alpha_{1,i}^{(\lambda)}$ ,  $\alpha_{2,i}^{(\lambda)}$ , and  $\alpha_{3,i}^{(\lambda)}$ .

Substance $i$	$\alpha_{0,i}^{(\lambda)}$	$\alpha_{\ln,i}^{(\lambda)}$	$\alpha_{1,i}^{(\lambda)}$	$\alpha_{2,i}^{(\lambda)}$	$\alpha_{3,i}^{(\lambda)}$
LJ	1	3.892	-2.24	0.008	0.985
LJTS	1	-23.5	22.5	-6.678	1.851
methane	1	6.789	-3.655	-0.312	1.095
<i>n</i> -butane	3.962	98.222	-82.974	20.079	1.073
<i>n</i> -hexane	8.971	-6.462	8.837	-3.673	3.602
<i>n</i> -hexadecane	39.064	0	0	6.413	17.801
propene	3.418	6.022	-2.581	0.717	2.274
cyclohexane	10.121	0	0	0.466	1.691
benzene	6.224	-3.916	5.903	-2.205	2.755
nitrogen	1.322	-21.803	21.88	-6.878	2.875
carbon dioxide	1.668	-31.829	32.545	-10.475	3.313
methanol	2.147	-3.268	7.385	-2.678	1.007
1-propanol	4.872	25.028	-14.238	4.503	0.866
1-octanol	11.186	-63.034	65.556	-7.559	5.549
R134a	3.536	-12.106	13.7	-3.933	1.758

**Table F.9:** Entropy scaling parameters of all component-specific models for the self-diffusion coefficient including the substance name and the parameters  $\alpha_{0,i}^{(D)}$ ,  $\alpha_{\ln,i}^{(D)}$ ,  $\alpha_{1,i}^{(D)}$ ,  $\alpha_{2,i}^{(D)}$ , and  $\alpha_{3,i}^{(D)}$ .

Substance $i$	$\alpha_{\ln,i}^{(D)}$	$\alpha_{1,i}^{(D)}$	$\alpha_{2,i}^{(D)}$	$\alpha_{3,i}^{(D)}$
LJ	4.402	-4.178	0.868	-1.135
LJTS	0	0	-0.672	-0.818
methane	-0.911	0.15	0.021	-0.982
<i>n</i> -butane	0	0	-3.507	-0.997
<i>n</i> -hexane	0	0	-2.095	-0.609
<i>n</i> -hexadecane	0	0	-7.316	-2.958
cyclohexane	0	0	-0.243	-1.757
benzene	0	0	0.979	-1.999
carbon dioxide	0	0	0	-3.491
methanol	0	-1.015	2.512	-2.170
1-octanol	0	0	0.497	-3.341

## F.6 Details on Entropy Scaling Framework

Here, details on the entropy scaling framework are given. If the function  $Y_{\text{CE}}^+(T)$  becomes negative with increasing temperature due to the behavior of the EOS in the zero-density limit, the value  $\min(Y_{\text{CE}}^+(T))$  is set to  $Y_{\text{CE}}^+(T = 0.6T_{\text{Boyle}})$  with  $T_{\text{Boyle}}$  being the *Boyle* temperature of the respective substance. This choice is adapted from the temperature of the minimum of  $Y_{\text{CE}}^+(T)$  of the LJ fluid.

In the following, the equations for the macroscopic scaling as well as the correlation functions are given for mixtures. The CE-scaled viscosity and thermal conductivity are defined analogue to Eq. (56). Therein, the low-density (LD) and the high-density (HD) scaling are defined as

$$\widehat{Y}_{\text{LD,mix}}^+ = \frac{Y_{\text{LD,mix}}^+}{Y_{\text{CE,mix}}^+}, \quad (\text{F.8})$$

and

$$\widehat{Y}_{\text{HD,mix}}^+ = \frac{Y_{\text{HD,mix}}^+}{\min(Y_{\text{CE}}^+)}, \quad (\text{F.9})$$

where  $Y_{\text{LD,mix}}^+$  and  $Y_{\text{HD,mix}}^+$  are the scaled transport properties of the mixture in the

LD and HD regions, respectively. The scaled Chapman-Enskog property  $Y_{\text{CE,mix}}^+$  are calculated according to Eqs. (65) - (66) from the zero-density limits of the pure components. The minimum of the scaled Chapman-Enskog property  $\min(Y_{\text{CE}}^+)$  is computed from the minima of the zero-density transport properties of the pure components by Eqs. (65) - (66). The macroscopically scaled values of a mixture  $\eta_{\text{mix}}^+$  and  $\lambda_{\text{mix}}^+$  are defined as

$$\eta_{\text{mix}}^+ = \eta_{\text{mix}} \frac{\rho_{\text{N,mix}}^{-2/3}}{\sqrt{M_{\text{mix}} T k_{\text{B}} / N_{\text{A}}}} \left( \frac{-s_{\text{conf,mix}}}{R} \right)^{2/3}, \quad (\text{F.10})$$

$$\lambda_{\text{mix}}^+ = \lambda_{\text{mix}} \frac{\rho_{\text{N,mix}}^{-2/3}}{k_{\text{B}} \sqrt{RT / M_{\text{mix}}}} \left( \frac{-s_{\text{conf,mix}}}{R} \right)^{2/3}, \quad (\text{F.11})$$

$$(\text{F.12})$$

where  $\rho_{\text{N,mix}}$  is the number density of the mixture,  $M_{\text{mix}}$  is the mean molar mass of the mixture calculated by Eq. (63), and  $s_{\text{conf,mix}}$  is the configurational entropy of the mixture. The configurational entropy is calculated from the EOS model and is a function of the temperature, pressure, and composition, i.e.  $s_{\text{conf,mix}} = s_{\text{conf,mix}}(T, p, \underline{x})$ . The correlation functions  $\ln(\widehat{\eta}^+(\tilde{s}_{\text{conf,mix}}))$  and  $\widehat{\lambda}^+(\tilde{s}_{\text{conf,mix}})$  are given as

$$\left. \begin{aligned} \ln(\widehat{\eta}_{\text{mix}}^+(\tilde{s}_{\text{conf}})) \\ \widehat{\lambda}_{\text{mix}}^+(\tilde{s}_{\text{conf}}) \end{aligned} \right\} = \frac{\alpha_{0,\text{mix}} + \alpha_{\ln,\text{mix}}^{(Y)} \ln(\tilde{s}_{\text{conf}} + 1) + \alpha_{1,\text{mix}}^{(Y)} \tilde{s}_{\text{conf}} + \alpha_{2,\text{mix}}^{(Y)} (\tilde{s}_{\text{conf}})^2 + \alpha_{3,\text{mix}}^{(Y)} (\tilde{s}_{\text{conf}})^3}{1 + g_1^{(Y)} \log(\tilde{s}_{\text{conf}} + 1) + g_2^{(Y)} \tilde{s}_{\text{conf}}} \quad (\text{F.13})$$

according to Eq. (58). The parameters  $\alpha_{0,\text{mix}}^{(Y)}$ ,  $\alpha_{\ln,\text{mix}}^{(Y)}$ ,  $\alpha_{1,\text{mix}}^{(Y)}$ ,  $\alpha_{2,\text{mix}}^{(Y)}$ , and  $\alpha_{3,\text{mix}}^{(Y)}$  are calculated according to Eq. (67) from the component-specific entropy scaling parameters.

## F.7 Implementation of the Entropy Scaling Framework

An implementation of the introduced entropy scaling framework is available on GitHub as Julia [749] module. The module implements all equations introduced in Chapter 7 and enables an application of the framework. Implementations of the applied equations of state are not included and have to be added externally. However, the repository contains a ready-to-use example to model the viscosity of methane by the Peng-Robinson (PR) EOS.

## F.8 Comparison of EOS for Modeling the Viscosity of Methane

Three different EOS, namely the EOS from *Stephan et al.*, the PC-SAFT EOS, and the BACKONE EOS, were used for modeling the viscosity of methane. For all three EOS, the same experimental viscosity data were used to adjust the entropy scaling parameters and four parameters were adjusted for each EOS. The EOS parameters for the component models were taken from Refs. [40, 63, 694]. In Table F.10, the mean average deviations obtained for the three models are given.

**Table F.10:** Mean average deviations  $\overline{\delta\eta}$  obtained for the three EOS.

EOS	$\overline{\delta\eta} / \%$
<i>Stephan et al.</i>	2.99
PC-SAFT	2.67
BACKONE	2.90

All models have similar mean average deviations with less than 3 %. The lowest mean average deviations is achieved using the PC-SAFT EOS with  $\overline{\delta\eta} = 2.67\%$ . The model using the EOS from *Stephan et al.* has the largest mean average deviation with nearly 3 %. This can be contributed to the underlying component-specific EOS parameters used to calculate the configurational entropy. For the PC-SAFT and BACKONE EOS, these parameters were directly fitted to experimental data of methane. The EOS from *Stephan et al.* is a EOS for the LJ model fluid and the parameter were taken from the *MolMod* database [63].

In Fig. F.2, the scaling behavior of the three models is compared. Despite the slightly larger mean average deviation, the scaling obtained from the LJ EOS from *Stephan et al.* shows a more robust behavior compared to the other two models. For the PC-SAFT and the BACKONE EOS, some larger deviations are identified.



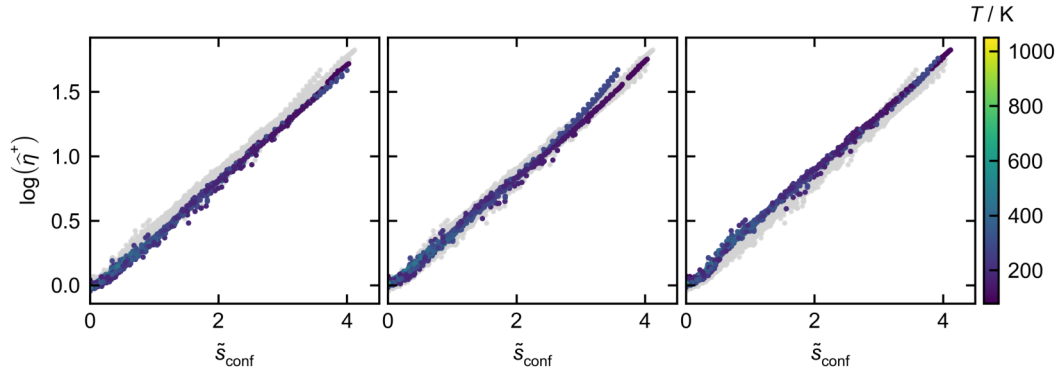


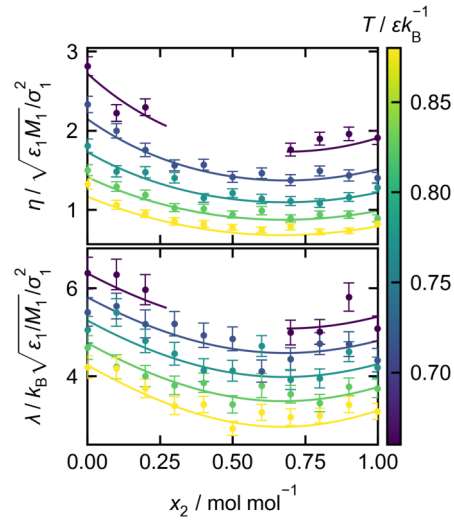
**Figure F.2:** CE-scaled viscosity  $\widehat{\eta}^+$  of methane as function of the reduced configurational entropy  $\tilde{s}_{\text{conf}}$  using the EOS from *Stephan et al.* (left), the PC-SAFT EOS (middle), and the BACKONE EOS (right). Symbols are the data points derived from experimental data ( $\eta$  from experimental data and  $\tilde{s}_{\text{conf}}$  from the EOS). The color indicates the temperature. The results from the respective other two EOS are illustrated as light grey symbols in the background.

## F.9 LJTS Mixture

The results for the viscosity and the thermal conductivity of the LJTS mixture with  $\sigma_2 = \sigma_1$ ,  $\varepsilon_2 = 0.9\varepsilon_1$ , and  $\xi = 0.85$  [62] are given in Fig. F.3. The PeTS EOS [108] is used to model the pure components and the mixtures. The results are shown over the entire composition range for five temperatures. For the temperature range  $0.715 \leq T / \varepsilon k_B^{-1} \leq 0.88$ , the mixture exhibits a low-boiling azeotrope [62]. For the lowest given temperature  $T = 0.66 \varepsilon / k_B$ , heteroazeotropic behavior is observed [62] which is why there is a miscibility gap at  $p = 0.1 \varepsilon \sigma^{-3}$ . For all other temperatures, the viscosity and the thermal conductivity exhibit a minimum at a molar fraction of  $x_2 \approx 0.7 \text{ mol mol}^{-1}$ , which approximately corresponds to the azeotropic point. As already seen for the other LJ mixture discussed in Chapter 7, the predictions by the entropy scaling model are in good agreement with the simulation data for all temperatures.

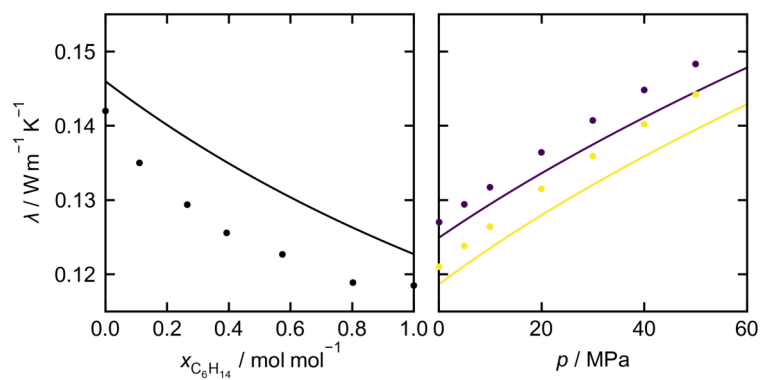
## F.10 Thermal Conductivity of Mixture Benzene + *n*-Hexane

Fig. F.4 shows the results for the thermal conductivity of the mixture benzene + *n*-hexane. The thermal conductivity is given as function of the mole fraction of *n*-hexane  $x_{\text{C}_6\text{H}_{14}}$  at the temperature  $T = 294.7 \text{ K}$ . Additionally, the thermal conductivity is shown as function of the pressure for a constant composition of  $x_{\text{C}_6\text{H}_{14}} = 0.73113 \text{ mol mol}^{-1}$  at two temperatures. All state points are in the liquid region. The thermal conductivity



**Figure F.3:** Viscosity  $\eta$  (top) and thermal conductivity  $\lambda$  (bottom) of a LJTS mixture with  $\sigma_2 = \sigma_1$ ,  $\epsilon_2 = 0.9\epsilon_1$ , and  $\xi = 0.85$  [62] as function of the mole fraction  $x_2$ . Molecular simulation data (symbols) from Ref. [62] and predictions with entropy scaling (lines). The colors indicate the temperature. The pressure is  $p = 0.1 \epsilon \sigma^{-3}$ . The entropy scaling results were obtained with the PeTS EOS.

decreases with increasing mole fraction  $x_{\text{C}_6\text{H}_{14}}$  as the thermal conductivity of benzene is smaller than that of  $n$ -hexane and the mixture behavior is nearly linear. With increasing pressure, the thermal conductivity of the mixture with constant composition increases. In total, the thermal conductivity of all included state points only varies in a small range between  $0.12 \text{ W m}^{-1} \text{ K}^{-1}$  and  $0.15 \text{ W m}^{-1} \text{ K}^{-1}$ . For all state points, the entropy scaling model slightly overestimates the experimental values. This can already be seen for the pure components in the  $\lambda - x_{\text{C}_6\text{H}_{14}}$  plot. The mean relative deviation is  $\overline{\delta\lambda} = 3.47\%$ , which is in the range of the pure component models (with  $\overline{\delta\lambda} = 2.93\%$  for benzene and  $\overline{\delta\lambda} = 3.01\%$  for  $n$ -hexane).



**Figure F.4:** Thermal conductivity  $\lambda$  of the mixture benzene + *n*-hexane as function of the mole fraction  $x_{\text{C}_6\text{H}_{14}}$  of *n*-hexane (left) at  $T = 294.7 \text{ K}$  and of the pressure  $p$  with  $x_{\text{C}_6\text{H}_{14}} = 0.73113 \text{ mol mol}^{-1}$  and  $T / \text{K} = 303.15$  (darkblue) and  $323.15$  (yellow) (right). Experimental data [750, 751] (symbols) and entropy scaling (lines). The entropy scaling results were obtained with the SAFT-VR Mie EOS.

# G Supporting Information for Chapter 8

## G.1 Entropy Scaling of infinite dilution diffusion coefficients

In the following, the scaling for infinite dilution diffusion coefficients is described in detail. The infinite dilution diffusion coefficient  $D_i^\infty$  is scaled by the temperature  $T$ , the number density  $\rho_N$ , and the configurational entropy of the solvent  $s_{\text{conf}} = s_{\text{conf}}(T, \rho)$ . Thereby, the modified Rosenfeld-scaled diffusion coefficient  $D_i^{\infty, \circ}$  is dimensionless and defined as

$$D_i^{\infty, \circ} = D_i^\infty \frac{\rho_N^{1/3}}{\sqrt{RT/M_{\text{CE}}}} \left( \frac{-s_{\text{conf}}}{R} \right)^{2/3}, \quad (\text{G.1})$$

where  $R$  is the universal gas constant. The molar mass  $M_{\text{CE}}$  is adapted from the Chapman-Enskog theory as

$$M_{\text{CE}} = \frac{2}{1/M_i + 1/M_j}, \quad (\text{G.2})$$

where  $M_i$  and  $M_j$  are the molar masses of the pure components. The modified Rosenfeld-scaled diffusion coefficient  $D_i^{\infty, \circ}$  (denoted by the 'o') exhibits some scattering in the zero-density limit for  $s_{\text{conf}} \rightarrow 0$ . Therefore, the scaling is further modified using the Chapman-Enskog diffusion coefficient  $D_{\text{CE},i}^\circ$ . This follows the scaling procedure from Chapter 7 used for pure component self-diffusion coefficients. The scaled Chapman-Enskog infinite dilution diffusion coefficient  $D_{\text{CE},i}^{\infty, \circ}$  is only a function of the temperature and given as

$$D_{\text{CE},i}^{\infty, \circ} = \frac{3}{8\sqrt{\pi}} \frac{1}{\sigma_{ij}^2 \Omega^{(1,1)}} \left( T \left( \frac{dB}{dT} \right) + B \right)^{2/3}, \quad (\text{G.3})$$

where  $B$  is the second virial coefficient of the solvent at a given temperature (which is computed from the EOS model),  $\sigma_{ij}$  is the cross-interaction Lennard-Jones size parameter, and  $\Omega_{ij}^{(1,1)} = \Omega^{(1,1)}(T k_B \varepsilon_{ij}^{-1})$  is the collision integral for diffusion [9, 126]. The Lennard-Jones parameter  $\sigma_{ij}$  and  $\varepsilon_{ij}$  are calculated according to the Lorentz-Berthelot

combining rules [700, 729] from the pure component interaction parameters as

$$\sigma_{ij} = \frac{\sigma_i + \sigma_j}{2} \quad \text{and} \quad (\text{G.4})$$

$$\varepsilon_{ij} = \sqrt{\varepsilon_j \varepsilon_i}. \quad (\text{G.5})$$

The Lennard-Jones parameters  $\sigma_i$ ,  $\sigma_j$ ,  $\varepsilon_i$ , and  $\varepsilon_j$  of a given pure (possibly real) components are calculated by the corresponding states principle with the Lennard-Jones fluid as reference from the critical temperature  $T_{c,j}$  and the critical pressure  $p_{c,j}$  of the solvent as  $\varepsilon_j = T_{c,j} k_B / 1.321$  and  $\sigma_j = (\varepsilon_j 0.129 / p_{c,j})^{1/3}$ .

The CE-scaled infinite dilution diffusion coefficient  $\widehat{D}_i^{\infty, \circ}$  is then constructed from the low-density region (LD) and high-density region (HD) as

$$\widehat{D}_i^{\infty, \circ} = \underbrace{\frac{D_i^{\infty, \circ}}{D_{\text{CE},i}^{\infty, \circ}}}_{\text{LD}} W(\tilde{s}_{\text{conf}}) + \underbrace{\frac{D_i^{\infty, \circ}}{\min(D_{\text{CE},i}^{\infty, \circ})}}_{\text{HD}} (1 - W(\tilde{s}_{\text{conf}})), \quad (\text{G.6})$$

where  $\tilde{s}_{\text{conf}} = -s_{\text{conf}} / (Rm)$  is the reduced configurational entropy using the chain length parameter of the EOS model  $m$  of the solvent and  $W$  is a continuous step function (see Ref. 52). The function  $W$  establishes a smooth transition from the low-density region to the high-density region. In the low-density region (LD,  $\tilde{s}_{\text{conf}} < 0.5$ ), the Rosenfeld-scaled diffusion coefficient is divided by the corresponding scaled Chapman-Enskog diffusion coefficient. In the high-density region (HD,  $\tilde{s}_{\text{conf}} \geq 0.5$ ), the Rosenfeld-scaled diffusion coefficient is divided by the minimum of  $D_{\text{CE},i}^{\infty, \circ}$ , i.e.  $\min D_{\text{CE},i}^{\infty, \circ}$ . This results in a continuous, monovariate function  $\widehat{D}_i^{\infty, \circ} = \widehat{D}_i^{\infty, \circ}(\tilde{s}_{\text{conf}})$ .

The scaled infinite dilution coefficient  $\widehat{D}_i^{\infty, \circ}$  is modeled by the empirical function

$$\ln(\widehat{D}_i^{\infty, \circ}) = \frac{\alpha_{0,ij}^{(D^\infty)} + \alpha_{\ln,ij}^{(D^\infty)} \ln(\tilde{s}_{\text{conf}} + 1) + \alpha_{1,ij}^{(D^\infty)} \tilde{s}_{\text{conf}} + \alpha_{2,ij}^{(D^\infty)} (\tilde{s}_{\text{conf}})^2 + \alpha_{3,ij}^{(D^\infty)} (\tilde{s}_{\text{conf}})^3}{1 + g_1^{(D)} \ln(\tilde{s}_{\text{conf}} + 1) + g_2^{(D)} \tilde{s}_{\text{conf}}}, \quad (\text{G.7})$$

where  $\alpha_{0,ij}^{(D^\infty)}$ ,  $\alpha_{\ln,ij}^{(D^\infty)}$ ,  $\alpha_{1,ij}^{(D^\infty)}$ ,  $\alpha_{2,ij}^{(D^\infty)}$ , and  $\alpha_{3,ij}^{(D^\infty)}$  are system-dependent parameters and  $g_1^{(D)} = 0.6632$  and  $g_2^{(D)} = 9.4714$  are global parameters fitted to the self-diffusion coefficient of the Lennard-Jones fluid [52]. The system-dependent parameters  $\alpha_{k,ij}^{(D^\infty)}$  are fitted to experimental data of the pseudo-pure component, i.e. the diffusion-coefficients at infinite dilution, individually for each system. The mathematical form of the model proposed here for the infinite dilution diffusion coefficients is equivalent to that proposed for pure component self-diffusion coefficients in Chapter 7. The fact that this yields excellent and very similar results (see main body of this work and results shown below) supports the physical picture that infinite dilution self-diffusion coefficients can be interpreted as a pseudo-pure component property. Moreover, both limits (cf. Fig. 1

in main body) are thereby treated consistently.

## G.2 Entropy Scaling of Diffusion Coefficients in Mixtures

The models for the limiting cases  $\widehat{D}_i^{\text{pure},\circ}$ ,  $\widehat{D}_i^{\text{pure},\circ}$ ,  $\widehat{D}_i^{\infty,\circ}$ , and  $\widehat{D}_j^{\infty,\circ}$ , can be used for predicting both self-diffusion coefficients as well as the Maxwell-Stephan and the Fickian diffusion coefficient in the mixture, i.e.  $D_i(x_j)$ ,  $D_j(x_j)$ ,  $D_{ij}(x_j)$ , and  $D_{ij}(x_j)$ . The main feature for these predictions into the mixture at a given composition is the configurational entropy of the mixture, i.e.  $s_{\text{conf}} = s_{\text{conf}}(T, \rho, \underline{x})$ . To predict the self-diffusion coefficient of a component  $i$  in a mixture with component  $j$ , i.e.  $D_i = D_i(T, \rho, \underline{x})$ , the limiting case models are the self-diffusion of the pure component  $i$  and the diffusion of infinitely diluted component  $i$  in the solvent  $j$ , i.e. the models describing  $\widehat{D}_i^{\text{pure},\circ}(\tilde{s}_{\text{conf}})$  and  $\widehat{D}_i^{\infty,\circ}(\tilde{s}_{\text{conf}})$ . For the Maxwell-Stefan diffusion coefficient  $D_{ij} = D_{ij}(T, \rho, \underline{x})$ , the limiting case models are the infinite dilution diffusion coefficients, i.e. the models describing  $\widehat{D}_i^{\infty,\circ}$  and  $\widehat{D}_j^{\infty,\circ}$ . The methodology for all three cases is similar and is described in the following. The Fickian diffusion coefficient is predicted via the Maxwell-Stefan diffusion coefficient and the thermodynamic factor described by the EOS mixture model.

The CE-scaled self-diffusion coefficients, i.e.  $\widehat{D}_i^\circ$  or  $\widehat{D}_j^\circ$ , and the CE-scaled Maxwell-Stefan diffusion coefficient  $\widehat{D}_i^\circ$  in the mixture are predicted using the same ansatz as that for the limiting case models

$$\ln(\widehat{\Lambda}^\circ) = \frac{\alpha_{0,ij}^{(\Lambda)} + \alpha_{\ln,ij}^{(\Lambda)} \ln(\tilde{s}_{\text{conf}} + 1) + \alpha_{1,ij}^{(\Lambda)} \tilde{s}_{\text{conf}} + \alpha_{2,ij}^{(\Lambda)} (\tilde{s}_{\text{conf}})^2 + \alpha_{3,ij}^{(\Lambda)} (\tilde{s}_{\text{conf}})^3}{1 + g_1^{(D)} \ln(\tilde{s}_{\text{conf}} + 1) + g_2^{(D)} \tilde{s}_{\text{conf}}}, \quad (\text{G.8})$$

where  $s_{\text{conf}} = s_{\text{conf}}(T, \rho, \underline{x})$  is the configurational entropy of the mixture and  $\Lambda$  is either a self-diffusion coefficient or the Maxwell-Stefan diffusion coefficient, i.e.  $\Lambda \in \{D_i, D_j, D_{ij}\}$ . The parameters  $\beta_{ij}^{(\Lambda)} \in \{\alpha_{0,ij}^{(\Lambda)}, \alpha_{\ln,ij}^{(\Lambda)}, \alpha_{1,ij}^{(\Lambda)}, \alpha_{2,ij}^{(\Lambda)}, \alpha_{3,ij}^{(\Lambda)}\}$  are predicted using mixing rules as

$$\beta_{ij}^{(D_i)} = x_i \beta^{(D_i^{\text{pure}})} + x_j \beta^{(D_i^\infty)}, \quad (\text{G.9})$$

$$\beta_{ij}^{(D_j)} = x_i \beta^{(D_j^\infty)} + x_j \beta^{(D_j^{\text{pure}})}, \quad (\text{G.10})$$

$$\beta_{ij}^{(D_{ij})} = x_i \beta^{(D_j^\infty)} + x_j \beta^{(D_i^\infty)}, \quad (\text{G.11})$$

for the self-diffusion coefficients of components  $i$  and  $j$  and the Maxwell-Stefan diffusion coefficient, respectively.

Kinetic gas theory enables the prediction of both the mutual diffusion coefficient and the self-diffusion coefficients at  $\rho \rightarrow 0$  (based on molar masses and parameters describing

the pair collisions). Also temperature dependence of the diffusion coefficients in gases at low densities is captured. The mutual diffusion coefficient in gases does not depend on the composition for these mixtures and  $D_{ij} = \mathcal{D}_{ij}$ . The Chapman-Enskog self-diffusion coefficients in the mixture  $D_{i,CE}^\circ(\underline{x})$  and  $D_{i,CE}^\infty(\underline{x})$  are calculated according to *Miller and Carman* [752] as

$$\frac{1}{D_{CE,i}^\circ} = \frac{x_i}{D_{CE,i}^{\text{pure},\circ}} + \frac{x_j}{D_{CE,i}^{\infty,\circ}} \quad \text{and} \quad (\text{G.12})$$

$$\frac{1}{D_{CE,j}^\circ} = \frac{x_j}{D_{CE,j}^{\text{pure},\circ}} + \frac{x_i}{D_{CE,j}^{\infty,\circ}}, \quad (\text{G.13})$$

where the Rosenfeld-scaled self-diffusion coefficients of the pure components  $D_{CE,i}^{\text{pure},\circ}$  and  $D_{CE,j}^{\text{pure},\circ}$  are adapted from Ref. [52] as

$$D_{CE,i}^{\text{pure},\circ} = \frac{3}{8\sqrt{\pi}} \frac{1}{\sigma_i^2 \Omega_i^{(1,1)}} \left( T \left( \frac{dB}{dT} \right) + B \right)^{2/3}, \quad (\text{G.14})$$

and the Rosenfeld-scaled infinite dilution diffusion coefficients  $D_{CE,i}^{\infty,\circ}$  and  $D_{CE,j}^{\infty,\circ}$  are given by Eq. (G.3). For the Maxwell-Stefan diffusion coefficient in the mixture, the corresponding Chapman-Enskog diffusion coefficient is given as

$$\mathcal{D}_{CE,ij}^\circ = \frac{3}{8\sqrt{\pi}} \frac{1}{\sigma_{ij}^2 \Omega_{ij}^{(1,1)}} \left( T \left( \frac{dB}{dT} \right) + B \right)^{2/3}, \quad (\text{G.15})$$

where  $B$  is the second virial coefficients of the mixture calculated as

$$B = x_i^2 B_i + x_i x_j B_{ij} + x_j^2 B_j, \quad (\text{G.16})$$

where  $B_i$  and  $B_j$  are the second virial coefficients of the pure components and  $B_{ij}$  is cross second virial coefficient.

For determining the minimum of  $\Lambda_{CE}^\circ$ , i.e.  $\min(\Lambda_{CE}^\circ)$ , the mixing rule proposed by *Miller and Carman* [752] are employed, for both the self-diffusion coefficients as well as for the Maxwell-Stefan diffusion coefficient as

$$\frac{1}{\min D_{CE,i}^\circ} = \frac{x_i}{\min D_{CE,i}^{\text{pure},\circ}} + \frac{x_j}{\min D_{CE,i}^{\infty,\circ}}, \quad (\text{G.17})$$

$$\frac{1}{\min D_{CE,j}^\circ} = \frac{x_i}{\min D_{CE,j}^{\infty,\circ}} + \frac{x_j}{\min D_{CE,j}^{\text{pure},\circ}}, \quad (\text{G.18})$$

$$\frac{1}{\min \mathcal{D}_{CE,ij}^\circ} = \frac{x_i}{\min D_{CE,j}^{\infty,\circ}} + \frac{x_j}{\min D_{CE,i}^{\infty,\circ}}. \quad (\text{G.19})$$

The reference mass  $M_{\text{ref}}$  is calculated as

$$M_{\text{ref}}^{D_i} = x_i M_i + x_j M_{\text{CE}} \quad \text{and} \quad (\text{G.20})$$

$$M_{\text{ref}}^{D_j} = x_i M_{\text{CE}} + x_j M_j, \quad (\text{G.21})$$

for the self-diffusion coefficients  $D_i$  and  $D_j$ , respectively. For the Maxwell-Stefan diffusion coefficient, the reference mass is equal to  $M_{\text{CE}}$ , i.e.  $M_{\text{ref}} = M_{\text{CE}}$  (see main body of this work).

The entropy scaling methodology proposed in this work enables the predictions of the 'transformed' diffusion coefficients  $\widehat{D}_i^\circ$ ,  $\widehat{D}_j^\circ$ , and  $\widehat{D}_{ij}^\circ$  (Chapman-Enskog and Rosenfeld scaled properties). For computing the 'normal' diffusion coefficients  $D_j$ ,  $D_i$ ,  $D_{ij}$ , and  $D_{ij}$ , the transformation formalism is reverted in a straightforward way that is briefly illustrated in the following for convenience. The 'normal' diffusion coefficients  $D_i$ ,  $D_j$ , and  $D_{ij}$  are calculated from the corresponding scaled value  $\widehat{D}_i^\circ$ ,  $\widehat{D}_j^\circ$ , and  $\widehat{D}_{ij}^\circ$  as

$$D_i = \frac{\widehat{D}_i^\circ}{\frac{W(\tilde{s}_{\text{conf}})}{D_{i,\text{CE}}^\circ} + \frac{1-W(\tilde{s}_{\text{conf}})}{\min(D_{i,\text{CE}}^\circ)}} \frac{\sqrt{RT/M_{\text{ref}}^{D_i}}}{\rho_{\text{N}}^{1/3}} \left( \frac{-s_{\text{conf}}}{R} \right)^{-2/3}, \quad (\text{G.22})$$

$$D_j = \frac{\widehat{D}_j^\circ}{\frac{W(\tilde{s}_{\text{conf}})}{D_{j,\text{CE}}^\circ} + \frac{1-W(\tilde{s}_{\text{conf}})}{\min(D_{j,\text{CE}}^\circ)}} \frac{\sqrt{RT/M_{\text{ref}}^{D_j}}}{\rho_{\text{N}}^{1/3}} \left( \frac{-s_{\text{conf}}}{R} \right)^{-2/3}, \quad (\text{G.23})$$

$$D_{ij} = \frac{\widehat{D}_{ij}^\circ}{\frac{W(\tilde{s}_{\text{conf}})}{D_{ij,\text{CE}}^\circ} + \frac{1-W(\tilde{s}_{\text{conf}})}{\min(D_{ij,\text{CE}}^\circ)}} \frac{\sqrt{RT/M_{\text{CE}}}}{\rho_{\text{N}}^{1/3}} \left( \frac{-s_{\text{conf}}}{R} \right)^{-2/3}, \quad (\text{G.24})$$

where the number density  $\rho_{\text{N}}$  and the configurational entropy  $s_{\text{conf}}$  are evaluated at a given mixture state point ( $pT\underline{x}$  or  $\rho T\underline{x}$ ).

### G.3 Simulation Details

Molecular dynamics (MD) simulations for determining the infinite dilution diffusion coefficients in two binary Lennard-Jones systems were conducted in this work. The Lennard-Jones potential between two particles  $i$  and  $j$  is defined as

$$u_{ij} = 4\varepsilon_{ij} \left[ \left( \frac{\sigma_{ij}}{r_{ij}} \right)^{12} - \left( \frac{\sigma_{ij}}{r_{ij}} \right)^6 \right], \quad (\text{G.25})$$

where  $u_{ij}$  is their potential energy,  $r_{ij}$  the distance between both particles, and  $\sigma_{ij}$  and  $\varepsilon_{ij}$  the size and energy parameters of the particles, respectively. For both systems, the size parameters of both components were equal, i.e.  $\sigma_2 = \sigma_1$ . The energy parameter was  $\varepsilon_2 =$



$0.9\varepsilon_1$  for the first system and  $\varepsilon_2 = 0.5\varepsilon_1$  for the second system. The potential parameters for the interaction of unlike particles were calculated according to Eqs. (G.4) and (G.5), whereas the Berthelot combining rule was modified by a single state-independent mixture parameter  $\xi_{ij}$  as

$$\varepsilon_{ij} = \xi_{ij}\sqrt{\varepsilon_i\varepsilon_j} \quad (\text{G.26})$$

to establishing a non-ideality in the system. The parameter  $\xi_{ij}$  was chosen to be  $\xi_{ij} = 1.2$  in the first system (the particles have a strong cross affinity) and  $\xi_{ij} = 0.85$  in the second system (the particles have a particularly weak cross affinity). Both mixtures are highly non-ideal with a high-boiling azeotrope (first mixture) and a miscibility gap (second mixture).

For each system, simulations at 114 state points in the gas, liquid, metastable vapor-liquid, metastable solid-liquid, and supercritical region (of the solvent) were carried out (see Fig. 2 in the main text). For each temperature-pressure pair, three simulations in the vicinity of the infinite dilution limit ( $x_2 = 0.001, 0.005, 0.01 \text{ mol mol}^{-1}$ ) were carried out. The three simulations were used to extrapolate to infinite dilution ( $x_2 \rightarrow \infty$ ) in a post-processing (see below).

The simulations were performed with the software *ms2*[464]. Each simulation consisted of 5,000 particles. The Gear-predictor-corrector algorithm was used for time integration with a time step of  $\Delta\tau = 0.001\sigma\sqrt{\varepsilon^{-1}M}$ . The simulations were conducted in the isochoric-isothermal (NVT) ensemble with  $10^5$  equilibration time steps and  $5 \cdot 10^6$  production time steps. Periodic boundary conditions were applied in all directions. The self-diffusion coefficient of component 2  $D_2$  was sampled using the Green-Kubo formalism with a correlation length of  $10^4$  time steps for  $\rho \geq 0.1\sigma_1^{-3}$  and  $10^5$  time steps for  $\rho < 0.1\sigma_1^{-3}$ . The infinite dilution diffusion coefficient  $D_2^\infty$  at a given temperature-density pair was computed by linear extrapolation from the results at finite dilution, cf. Fig. G.1. The configurational entropy  $s_{\text{conf}}$  was determined in the simulations using the relation

$$s_{\text{conf}} = \frac{u_{\text{conf}}}{T} - \frac{p}{\rho T} - \sum_{i=1}^2 \frac{\mu_{\text{conf},i}}{T}, \quad (\text{G.27})$$

where  $u_{\text{conf}}$  is the configurational internal energy and  $\mu_{\text{conf},i}$  is the chemical potential of component  $i$ . The chemical potentials were sampled using *Widom's* test particle method [710].

Additionally, a real system, the binary mixture benzene (1) + isobutane (2), was investigated by the same methodology. The component-specific force fields from Refs. [349, 753] – taken from the MolMod database [63] – were used to model benzene and isobutane. In total, 29 state points were investigated in the liquid, gas, and supercriti-

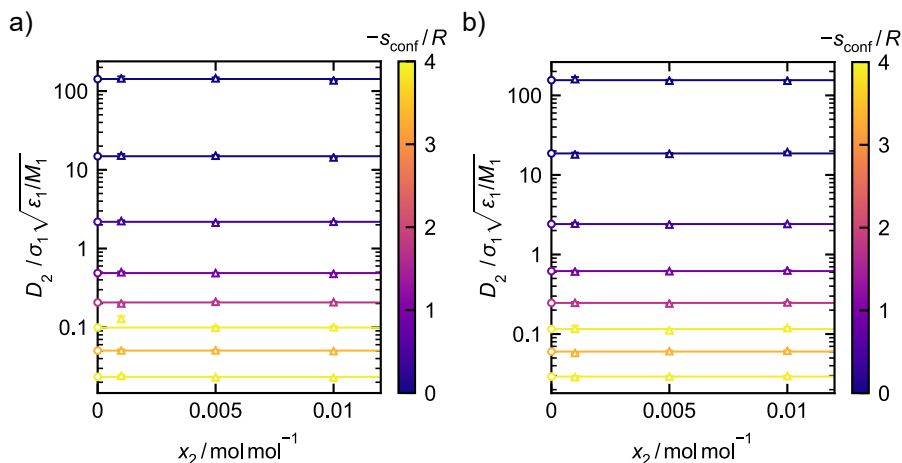


**Figure G.1:** Self-diffusion coefficient  $D_2$  as function of the mole fraction  $x_2$  for eight state points (exemplarily chosen) in two Lennard-Jones systems with a)  $\sigma_2 = \sigma_1$ ,  $\varepsilon_2 = 0.9\varepsilon_1$ ,  $\varepsilon_{12} = 1.2\sqrt{\varepsilon_1\varepsilon_2}$  (a) and  $\sigma_2 = \sigma_1$ ,  $\varepsilon_2 = 0.5\varepsilon_1$ , and  $\varepsilon_{12} = 0.85\sqrt{\varepsilon_1\varepsilon_2}$  (b). Triangles are the simulation results for the self-diffusion coefficient  $D_2$ , the circles are the extrapolated infinite dilution diffusion coefficients  $D_2^\infty$ , and the lines represent the linear extrapolations. The color indicates the configurational entropy.

cal regions. The time step was 0.329 fs for simulations with  $\rho > 8.9 \text{ mol l}^{-1}$  and 0.987 fs elsewhere. Each simulation consisted of 4096 molecules – 4 benzene molecules and 4092 isobutane molecules ( $x_1 \approx 0.001 \text{ mol mol}^{-1}$ ). The simulations were equilibrated for  $5 \cdot 10^5$  time steps and the actual production run consisted of  $6 \cdot 10^6$  time steps. The self-diffusion coefficient of benzene  $D_1$  was sampled using the Green-Kubo formalism with a correlation length  $10^4$  time steps. As for the Lennard-Jones systems, the chemical potential was sampled using *Widom's* test particle method to calculate the configurational entropy (see Eq. (G.27)). The second virial coefficient as well as its temperature derivative was calculated for all considered temperatures.

## G.4 Component-Specific EOS Models

The entropy scaling framework proposed in this work for the prediction of mixture diffusion coefficients can be coupled with practically any molecular-based equation of state (and with minor adjustments also with empirical multiparameter EOS [545], e.g. regarding the molecular property parameters  $m$ ,  $\varepsilon$ ,  $\sigma$ ). In this work, the Kolafa-Nezbeda EOS was used for modeling the Lennard-Jones model mixtures and the PC-SAFT EOS for modeling the real substance mixtures. The Kolafa-Nezbeda EOS was found to be the most accurate and robust EOS for modeling thermodynamic properties of the Lennard-Jones fluid [83, 234]. Also the PC-SAFT EOS is known to often yield good predictions for thermodynamic mixture properties [553, 554].

The component-specific PC-SAFT EOS models for the real substances were taken from Ref. 40. The parameters are given in Table G.1. The binary interaction parameters  $\xi_{ij}$  of all real substance systems were kept to unity in this work. Hence, the mixture diffusion coefficients are described in a fully predictive way. For applications, the binary interaction parameter could be adjusted to experimental data to improve the model performance.

**Table G.1:** Component-specific PC-SAFT EOS parameters from the literature used in the present work. The columns indicate (from left to right): The substance name, segment diameter  $\sigma$ , segment dispersion energy  $\varepsilon$ , and chain length parameter  $m$ .

substance	$\sigma$ Å	$\varepsilon/k_B$ K	$m$	reference
<i>n</i> -hexane	3.7983	236.77	3.0576	[40]
<i>n</i> -heptane	3.8049	238.40	3.4831	
<i>n</i> -dodecane	3.8959	249.21	5.306	
<i>n</i> -hexadecane	3.9552	254.70	6.6485	
OME <sub>2</sub>	3.55	260	3.258	[740]
OME <sub>3</sub>	3.55	260	4.046	
OME <sub>4</sub>	3.55	260	4.834	
toluene	3.7169	285.69	2.8149	[40]

## G.5 Entropy Scaling Models

The entropy scaling limiting case model parameters (pure component and pseudo-pure component) used in this work are reported in Table G.2. Additionally, the references of the experimental data used for the parameter adjustment are given. For the infinite dilution diffusion coefficients, only up to two component-specific parameters were used due to small number of experimental data available. The other parameters were set to 0.

**Table G.2:** Component-specific entropy scaling parameters (see Eq. (G.7)) used in the present work. The columns indicate (from left to right): the system, the property, the parameters  $\alpha_{2,i}$  and  $\alpha_{3,i}$  as well as the reference where experimental data were taken from. The parameters  $\alpha_{0,i}$ ,  $\alpha_{ln,i}$ ,  $\alpha_{1,i}$  were set to zero (since only few data were available).

system	property	$\alpha_{2,i}$	$\alpha_{3,i}$	data source
<i>n</i> -hexane (1) + <i>n</i> -dodecane (2)	$D_1$	-2.5414	-1.9186	329
	$D_2$	-4.3257	-3.2885	
	$D_1^\infty$	0.0	-5.3751	744
	$D_2^\infty$		-3.1396	
toluene (1) + <i>n</i> -hexane (2)	$D_1^\infty$	-4.0978	-1.0285	745
	$D_2^\infty$	-2.6050	-1.5678	
OME <sub>2</sub> (1) + <i>n</i> -dodecane (2)	$D_1$	0.130	-3.629	134
	$D_1^\infty$	-1.300	-4.272	
	$D_2^\infty$	-0.120	-3.527	
OME <sub>2</sub> (1) + <i>n</i> -hexadecane (2)	$D_2$	-2.970	-5.194	
	$D_1^\infty$	2.362	-6.650	
	$D_2^\infty$	-1.590	-2.958	
OME <sub>3</sub> (1) + <i>n</i> -dodecane (2)	$D_1$	-1.932	-3.582	
	$D_1^\infty$	-2.629	-3.905	
	$D_2^\infty$	-1.459	-3.716	
OME <sub>3</sub> (1) + <i>n</i> -hexadecane (2)	$D_1^\infty$	-2.580	-4.684	
	$D_2^\infty$	-1.572	-3.835	
OME <sub>4</sub> (1) + <i>n</i> -dodecane (2)	$D_1$	-1.782	-4.489	
	$D_1^\infty$	-3.536	-3.454	
	$D_2^\infty$	-1.530	-4.434	
OME <sub>4</sub> (1) + <i>n</i> -hexadecane (2)	$D_1^\infty$	-1.605	-5.183	
	$D_2^\infty$	-0.431	-5.103	

## G.6 Established Methods for Predicting Infinite Dilution Diffusion Coefficients

The SEGWE model of Evans et al.[725] for predicting the diffusion coefficient of solute "1" at infinite dilution in a solvent "2"  $D_{12}^\infty$  is given by

$$D_{12}^{\infty, \text{SEGWE}} / \text{m}^2 \text{ s}^{-1} = \frac{(k_{\text{B}} / \text{J K}^{-1})(T / \text{K}) \left[ \frac{3\alpha}{2} + \frac{1}{1+\alpha} \right]}{6\pi (\eta_2 / \text{Pa} \cdot \text{s}) \sqrt[3]{\frac{3(M_1 / \text{g mol}^{-1})}{4\pi(\rho_{\text{eff}} / \text{g m}^{-3})(N_{\text{A}} / \text{mol}^{-1})}}} \quad (\text{G.28})$$

$$\alpha = \sqrt[3]{\frac{(M_2 / \text{g mol}^{-1})}{(M_1 / \text{g mol}^{-1})}}$$

where  $k_{\text{B}}$  is Boltzmann's constant,  $T$  is the temperature,  $\eta_2$  is the dynamic viscosity of the solvent "2",  $M_1$  is the molar mass of the solute "1",  $M_2$  is the molar mass of the solvent "2",  $\rho_{\text{eff}} = 619 \text{ kg m}^{-3}$  is an "effective density", the number of which was fitted to the literature data by the authors [725] and  $N_{\text{A}}$  is Avogadro's constant.

The model of Wilke and Chang [739] (WC) is given by

$$D_1^{\infty, \text{WC}} / \text{m}^2 \text{ s}^{-1} = 7.4 \cdot 10^{-12} \frac{\sqrt{\Phi_2 (M_2 / \text{g mol}^{-1})} (T / \text{K})}{(\eta_2 / \text{cP}) (v_1 / \text{cm}^3 \text{ mol}^{-1})^{0.6}} \quad (\text{G.29})$$

where  $\Phi_2$  is the association factor of the solvent "2" which was set to 1 here in all cases, and  $v_1$  is the liquid molar volume of the pure solute "1" at their normal boiling point [739].

Data for the dynamic viscosity  $\eta_2$  of alkanes [754, 755] and of OME [756, 757] were taken from the literature. Data for the liquid molar volume of the solutes at their normal boiling point  $v_1$  were computed from correlations from DIPPR [758] and Burger et al. [730].

## G.7 Scaling Behavior of Pure Components and at Infinite Dilution

For the Lennard-Jones model systems, a quasi-universality is observed using the applied scaling, which is evident by the representation of  $\widehat{D}_2^{\infty, \circ}$  by the global model from Ref. 52, which was only fitted to pure-component self-diffusion coefficient data. Hence, the correlation developed in Ref. 52 using pure-component self-diffusion coefficient data of

the Lennard-Jones fluid also describes the infinite dilution diffusion coefficient data from this work.

In Fig. G.2, the scaling of the pure component self-diffusion coefficient is compared with the scaling of the infinite dilution diffusion coefficient. Both CE-scaled diffusion coef-

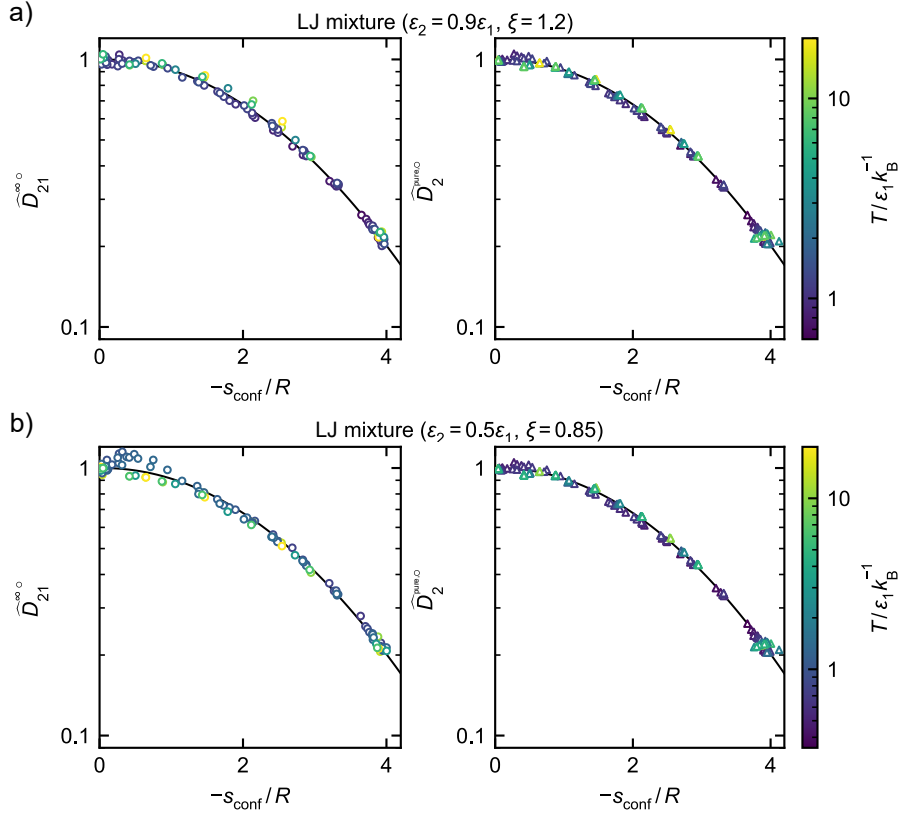


**Figure G.2:** Scaled infinite dilution diffusion coefficient  $\widehat{D}_2^{\infty,\circ}$  (left) and self-diffusion coefficient  $\widehat{D}_2^{\text{pure},\circ}$  (right) for two Lennard-Jones systems (a and b) as a function of the configurational entropy  $s_{\text{conf}}$ . The symbols are simulation results from this work ( $\widehat{D}_2^{\infty,\circ}$ ) and from Ref. 52 ( $\widehat{D}_2^{\text{pure},\circ}$ ). The color of the symbols indicates the temperature. The black solid line is the entropy scaling model.

ficients show a monovariate behavior over the entire range of configurational entropies and all temperatures. To quantify this, a measure  $\Delta_\Lambda$  was defined as

$$\Delta_\Lambda = \sqrt{\frac{1}{N_\Lambda} \sum_i^{N_\Lambda} (\Lambda_{\text{sim},i} - \Lambda_{\text{mod},i})^2}, \quad (\text{G.30})$$

where  $\Lambda \in \{\widehat{D}_2^{\text{pure},\circ}, \widehat{D}_2^{\infty,\circ}\}$ ,  $N_\Lambda$  is the respective number of simulation data points,  $\Lambda_{\text{sim},i}$  are diffusion coefficients obtained from the simulations, and  $\Lambda_{\text{mod},i}$  the values calculated from the entropy scaling model. The obtained values are  $\Delta_{\widehat{D}_2^{\text{pure},\circ}} \approx 1.244$  and  $\Delta_{\widehat{D}_2^{\infty,\circ}} \approx 1.254$  for first system and  $\Delta_{\widehat{D}_2^{\text{pure},\circ}} \approx 1.244$  and  $\Delta_{\widehat{D}_2^{\infty,\circ}} \approx 1.254$  for the second Lennard-Jones system.

## G.8 Results for the Lennard-Jones Mixtures at Different Pressures

Fig. G.3 shows the application of the entropy scaling model to the Lennard-Jones mixture with  $\varepsilon_2 = 0.9\varepsilon_1$  and  $\varepsilon_{12} = 1.2\sqrt{\varepsilon_1\varepsilon_2}$  at different pressures (corresponding to Fig. 3 of the main body). The predictions from the entropy scaling model are compared to

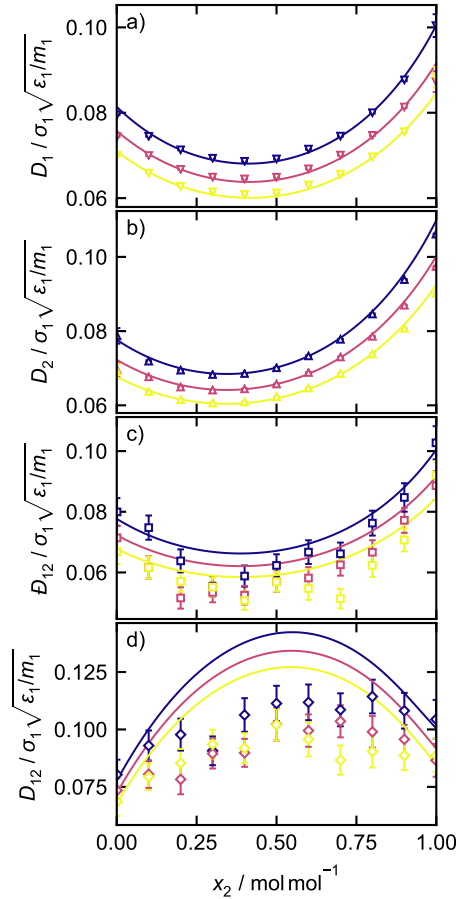


**Figure G.3:** Diffusion coefficients in the Lennard-Jones system with  $\sigma_2 = \sigma_1$ ,  $\varepsilon_2 = 0.9\varepsilon_1$ , and  $\varepsilon_{12} = 1.2\sqrt{\varepsilon_1\varepsilon_2}$  as a function of the mole fraction  $x_2$  at  $T = 0.92 k_B\varepsilon_1^{-1}$ . a) Self-diffusion coefficient of component 1  $D_1$ ; b) Self-diffusion coefficient of component 2  $D_2$ ; c) Maxwell-Stefan diffusion coefficient  $\mathcal{D}_{12}$ ; d) Fickian diffusion coefficient  $D_{12}$ . Lines are the predictions from the entropy scaling model. Symbols are simulation results from Ref. 112. The entropy scaling model was used in combination with the Kolafa-Nezbeda EOS [136]. The colors indicate the pressure  $p \in \{0.13, 0.26, 0.39\} \sigma_1^3 \varepsilon_1^{-1}$  (yellow to dark purple).

simulation data from Ref. 112. The results for different pressures are very similar to those for different temperatures (see main body of this work): The agreement between the predictions from the entropy scaling model and simulation data is very good for both self-diffusion coefficients. For the mutual diffusion coefficients, some deviations are

observed.

## G.9 Comparison of Entropy Scaling to the Vignes and Darken Models

The Vignes equation [726] is an often applied, simple model for calculating Maxwell-Stefan diffusion coefficients in mixtures based on the infinite dilution diffusion coefficients. It is written as

$$D_{ij} = (D_i^\infty)^{x_j} (D_j^\infty)^{x_i}. \quad (\text{G.31})$$

Besides the Vignes model, the generalized Darken model [759] is often applied and found to be superior in some cases [13]. For binary mixtures, it is defined as

$$D_{ij} = x_i \left( x_i^{(m)} D_j^\infty + x_j^{(m)} D_j^{(\text{pure})} \right) + x_j \left( x_i^{(m)} D_i^{(\text{pure})} + x_j^{(m)} D_i^\infty \right), \quad (\text{G.32})$$

where  $x_i^{(m)}$  and  $x_j^{(m)}$  are the mass fractions of the components  $i$  and  $j$ , respectively. Both the Vignes and the Darken model only require information on the limiting case diffusion coefficients, like the entropy scaling model proposed in this work.

In Fig. G.4, the predictions from the entropy scaling model proposed in this work are compared to the results from the Vignes model and the generalized Darken model for both Lennard-Jones mixtures. Both mixtures show a strongly non-ideal behavior (see main text and above). For both mixtures, the entropy scaling model provides a reasonable description of the Maxwell-Stefan diffusion coefficient in the mixture. The Vignes and Darken models are not able to capture the trend of  $D_{12}$  in the first Lennard-Jones system (see Fig. G.4a). For the second system (see Fig. G.4b), the predictions by the Vignes equation show a wrong curvature compared to the simulation data and, most importantly, do not capture the liquid-liquid equilibrium (LLE). Both empirical models (Vignes and Darken) do not comprise information on the liquid-liquid miscibility gap. The entropy scaling model proposed in this work, on the other hand, inherently captures the LLE due to the coupling with the EOS model and also describes the diffusion coefficients of the coexisting phases, metastable phases, supercritical phases etc. However, no computer experiment data is available for the coexisting phase diffusion coefficients for validation.



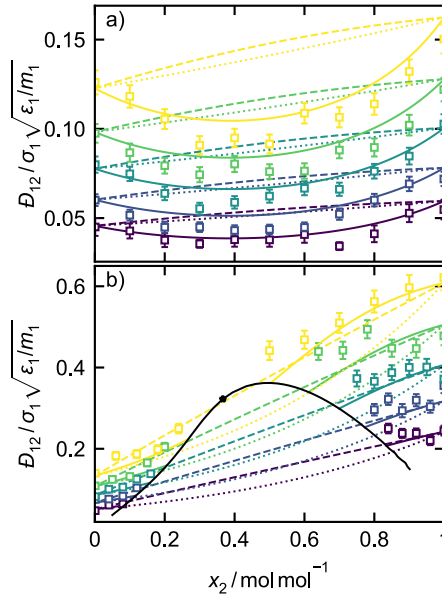


**Figure G.4:** Comparison of MD reference data to the entropy scaling model proposed in this work, the Vignes model, and the Darken model for the Maxwell-Stefan diffusion coefficient. Results for two binary Lennard-Jones systems (a:  $\sigma_2 = \sigma_1$ ,  $\epsilon_2 = 0.9\epsilon_1$ ,  $\epsilon_{12} = 1.2\sqrt{\epsilon_1\epsilon_2}$ , b:  $\sigma_2 = \sigma_1$ ,  $\epsilon_2 = 0.5\epsilon_1$ ,  $\epsilon_{12} = 0.85\sqrt{\epsilon_1\epsilon_2}$ ) as a function of the mole fraction  $x_2$  at  $p = 0.13\sigma_1^3\epsilon_1^{-1}$  (a) and  $p = 0.26\sigma_1^3\epsilon_1^{-1}$  (b). Symbols indicate simulation results from Ref. 112. Solid lines are predictions from the entropy scaling model obtained in combination with the Kolafa-Nezbeda EOS. Dotted lines are results from the Vignes model (cf. Eq. (G.31)) and dashed lines from the generalized Darken model (cf. Eq. (G.32)). The colors indicate the temperature  $T \in \{0.79, 0.855, 0.92, 0.985, 1.05\} k_B\epsilon_1^{-1}$  (blue to yellow). The black line indicate the liquid-liquid equilibrium diffusion coefficient and the star the critical point.

## G.10 Scaled Diffusion Coefficient of Mixtures

Fig. G.5 shows the scaling behavior of mixtures for the two Lennard-Jones systems and a real substance system. For the two considered Lennard-Jones systems, both scaled self-diffusion coefficients and the scaled Maxwell-Stefan diffusion coefficient collapse on one line, which is a special feature of the considered Lennard-Jones mixtures. As a result, a single set of parameters is able to describe all three diffusion coefficients. The scattering of the Maxwell-Stefan diffusion coefficients is larger than that for the self diffusion coefficients, which is due to the scattering of the reference data. For the real substance system  $n$ -hexane (1) +  $n$ -dodecane (2), results for both scaled self-diffusion coefficients  $\widehat{D}_1^\circ$  and  $\widehat{D}_2^\circ$  are shown. The corresponding, non-scaled results are shown in Fig. 4 of the main text. The data and models for the pure component self-diffusion coefficient and the pseudo-pure component infinite dilution diffusion coefficient differ significantly. The self-diffusion coefficients in the mixture ( $0 < x_2/\text{mol mol}^{-1} < 1$ ) lie

between both curves. The entropy scaling model connects both lines (here at a given  $T$  and  $p$ ) and is thus able to predict these points. The link is primarily established via the entropy of the mixture and mixing and combination rules built in the entropy scaling model.

Fig. G.5 demonstrates the two central elements of the proposed methodology: (1) the infinite dilution diffusion coefficient, if scaled as proposed in this work, exhibit a monovariate relation and can be treated as a pseudo-pure component, which enables the scaling of that property. The scaling can be used for predicting infinite dilution diffusion coefficients far beyond the range of available data based on that scaling. (2) The predictions of the diffusion coefficients into the mixture do not follow the monovariate scaling behavior. Yet, the entropy of the mixture in combination with appropriately designed mixing and combination rules enable the prediction of the diffusion coefficients in the mixture in the scaled variables. For the limiting cases of the pure components and the pseudo-pure components, empirical models for describing the scaled diffusion coefficient are required in this framework. Yet, these models require only very few parameters, e.g. 1 or 2 parameters were used for the real substance cases studied in this work (cf. Table G.2). From these few parameters, the model (1) can predict the corresponding diffusion coefficient practically in the entire fluid state region, cf. for example Fig. G.2. For the main part of the novel framework, i.e. the prediction of the different diffusion coefficients in the mixture  $D_i(x_j)$ ,  $D_j(x_j)$ ,  $D_{ij}(x_j)$ , no adjustable parameters are required. The mechanisms for establishing the link between the limiting case diffusion coefficients (pure component and pseudo-pure component) are analogue and consistent to the mechanisms usually used for predicting the viscosity and thermal conductivity of mixtures by entropy scaling. Albeit, significantly more complex in the case of diffusion since different diffusion coefficients are described in a single and consistent framework. However, strong non-idealities of the Maxwell-Stefan diffusion coefficients, especially in binary mixtures of an alcohol and a non-polar substance [760], may not be covered by the proposed framework. The description of these non-idealities, which might be due to local composition phenomena [761], requires modifications of the introduced framework as well as of the underlying EOS models.

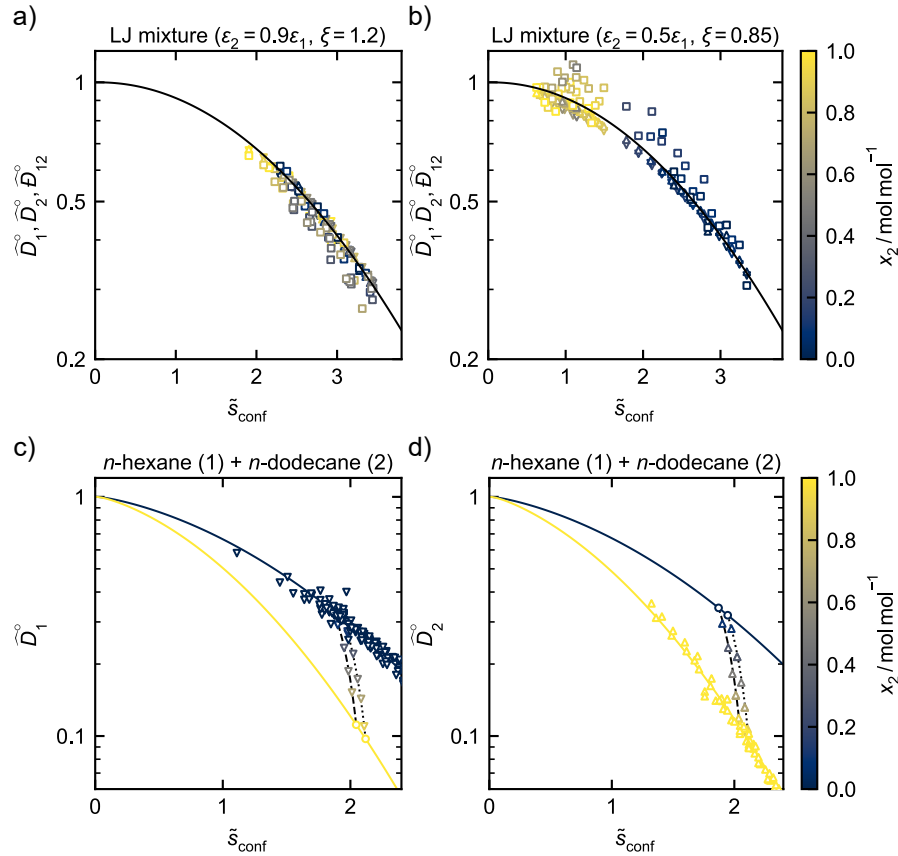


**Figure G.5:** Scaled diffusion coefficients as a function of the configurational entropy  $\tilde{s}_{\text{conf}}$  in different mixtures. a & b: Lennard-Jones mixtures. c & d: Mixture *n*-hexane (1) + *n*-dodecane (2). Symbols are scaled simulation results (a & b) or experimental data (c & d) [62, 744]. Triangles: Self-diffusion coefficients; squares: Maxwell-Stefan diffusion coefficient; circles: Infinite dilution diffusion coefficients. a + b: The solid line represents the global entropy scaling model for the diffusion coefficients of the Lennard-Jones fluid [52]. c: The yellow and the dark blue lines represent the entropy scaling models for  $D_1$  and  $D_1^\infty$ , respectively. d: The dark blue and the yellow lines represent the entropy scaling model for  $D_2$  and  $D_2^\infty$ , respectively. c & d: Black dotted and dashed lines are results from the entropy scaling model for constant temperature (dotted:  $T = 298.15 \text{ K}$ , dashed:  $T = 308.15 \text{ K}$ ) computed over the entire composition range, i.e.  $0 < x_2 / \text{mol mol}^{-1} < 1$ .



# Declaration

This dissertation contains material that has been published previously or that is included in submitted publications. In the following, these publications are listed together with a statement on the contributions of the author of the present dissertation.

- S. Schmitt, T. Vo, M.P. Lautenschlaeger, S. Stephan, H. Hasse: Molecular dynamics simulation study of heat transfer across solid-fluid interfaces in a simple model system, *Molecular Physics*, 120 (2022) e2057364, DOI: 10.1080/00268976.2022.2057364.  
*The author carried out the MD simulations, implemented the post-processing, and evaluated the results. The author wrote the manuscript.*
- S. Schmitt, F. Fleckenstein, H. Hasse, S. Stephan: Comparison of Force Fields for the Prediction of Thermophysical Properties of Long Linear and Branched Alkanes, *The Journal of Physical Chemistry B*, 127 (2023) 1789-1802, DOI: 10.1021/acs.jpcc.2c07997.  
*The author carried out the MD simulations, implemented the post-processing, and evaluated the results. The author wrote the manuscript.*
- G. Kanagalingam, S. Schmitt, F. Fleckenstein, and S. Stephan: Data Scheme and Data Format for Transferable Force Fields for Molecular Simulation, *Scientific Data* 10 (2023) 495, DOI: 10.1038/s41597-023-02369-8.  
*The author developed the data format together with Gajanan Kanagalingam, Florian Fleckenstein, and Simon Stephan. The author wrote parts of the manuscript.*
- S. Schmitt, G. Kanagalingam, F. Fleckenstein, D. Froescher, H. Hasse, and S. Stephan: Extension of the MolMod Database to Transferable Force Fields, *Journal of Chemical Information and Modeling* 63 (2023) 7148-7158, DOI: 10.1021/acs.jcim.3c01484.  
*The author implemented the force fields together with Florian Fleckenstein and Gajanan Kanagalingam. The author wrote the manuscript.*
- S. Schmitt, H. Hasse, and S. Stephan: Entropy Scaling Framework for Transport Properties using Molecular-based Equations of State, *Journal of Molecular Liquids* 395 (2024) 123811,

DOI: 10.1016/j.molliq.2023.123811.

*The author developed and implemented the framework. The author wrote the manuscript.*

- S. Mross, S. Schmitt, S. Stephan, K. Münnemann, and H. Hasse: Diffusion Coefficients in Mixtures of Poly(Oxymethylene) Dimethyl Ethers with Alkanes, *Industrial & Engineering Chemistry Research* 63 (2024) 1662-1669, DOI: 10.1021/acs.iecr.3c03839.  
*The author carried out the entropy scaling modeling. The author wrote the corresponding part of the manuscript.*
- S. Schmitt, H. Hasse, and S. Stephan: Measurements and Equation of State Modeling of the Density of Five 1-Alcohols (C6C10) at Pressures of up to 120 MPa, *Journal of Chemical & Engineering Data* 69 (2024) 2967-2983, DOI: 10.1021/acs.jced.4c00265.  
*The author procured and commissioned the experimental setup and carried out the experiments and the post-processing and modeling. The author wrote the manuscript.*
- S. Schmitt, H. Hasse, S. Stephan: Entropy Scaling for Diffusion Coefficients in Mixtures, submitted (2024).  
*The author developed and implemented the framework. The author wrote the manuscript.*
- S. Schmitt, J. Vrabec, H. Hasse, S. Stephan: Transport Properties of the Lennard-Jones Fluid: Database and Data Assessment, to be submitted (2024).  
*The author collected, compiled, and assessed the database. The author wrote the manuscript.*

Furthermore, the author contributed to the following publications that are relevant for this thesis and are cited therein:

- S. Schmitt, S. Stephan, B. Kirsch, J.C. Aurich, E. Kerscher, H.M. Urbassek, H. Hasse: Molecular Simulation Study on the Influence of the Scratching Velocity on Nanoscopic Contact Processes, *2nd International Conference of the DFG International Research Training Group 2057 - Physical Modeling for Virtual Manufacturing (iPMVM 2020)*, 89 (2021) 17:1-17:16, DOI: 10.4230/OASiCs.iPMVM.2020.17.
- S. Schmitt, S. Stephan, B. Kirsch, J.C. Aurich, H.M. Urbassek, H. Hasse: Molecular Dynamics Simulation of Cutting Processes: The Influence of Cutting Fluids at the Atomistic Scale, In: *Proceedings of the 3rd Conference on Physical Modeling*

*for Virtual Manufacturing Systems and Processes*, Springer International Publishing, Cham (2023) 260-280,  
DOI: 10.1007/978-3-031-35779-4\_14.

- S. Stephan, S. Schmitt, H. Hasse, and H. M. Urbassek: Molecular Dynamics Simulation of the Stribeck Curve: Boundary Lubrication, Mixed Lubrication, and Hydrodynamic Lubrication on the Atomistic Level, *Friction* 11(2023) 2342-2366, DOI: 10.1007/s40544-023-0745-y.
- P. Wingerts Zahn, S. Schmitt, S. Thielen, M. Oehler, B. Magyar, O. Koch, H. Hasse, and S. Stephan: Measurement, Modelling, and Application of Lubricant Properties at Extreme Pressures, *Tribologie und Schmierungstechnik* 70 (2023) 5-12,  
DOI: 10.24053/TuS-2023-0017.
- D. Schaefer, B. Kunstmann, S. Schmitt, H. Hasse, and M. Kohns: Explosions of Nanodroplets Studied with Molecular Dynamics Simulations, *Physics of Fluids* 36 (2024) 037129,  
DOI: 10.1063/5.0190455.





# Student Theses

The following student theses were prepared under the supervision of the author of the present doctoral thesis in the frame of his research:

- J. Stumpf: Investigation of Thermal Processes in Nanotribological Systems by Molecular Dynamics Simulations. Bachelor thesis, Laboratory of Engineering Thermodynamics (LTD), TU Kaiserslautern (2021).
- T. Just: Development of a Program for Thermal Elastohydrodynamic Simulations Using Equations of State from Molecular Thermodynamics. Student thesis, Laboratory of Engineering Thermodynamics (LTD), TU Kaiserslautern (2021).
- J. Wagner: Molecular Simulations of the Thermal Conductivity of the Lennard-Jones Solid. Bachelor thesis, Laboratory of Engineering Thermodynamics (LTD), TU Kaiserslautern (2021).
- R. Al-Khamissi: Molecular Simulation of Isoprenol. Bachelor thesis, Laboratory of Engineering Thermodynamics (LTD), TU Kaiserslautern (2021).
- F. Fleckenstein: Molecular Simulation of Transport Properties of Lubricants. Master thesis, Laboratory of Engineering Thermodynamics (LTD), TU Kaiserslautern (2021).
- M. Christely: Reproducibility of Molecular Dynamics Simulations. Student thesis, Laboratory of Engineering Thermodynamics (LTD), TU Kaiserslautern (2022).
- T. Just: Development of a Program for Thermal Elastohydrodynamic Simulations Using Equations of State from Molecular Thermodynamics. Bachelor thesis, Laboratory of Engineering Thermodynamics (LTD), TU Kaiserslautern (2022).
- J. Wagner: Commissioning of a High-Pressure Density Meter. Student thesis, Laboratory of Engineering Thermodynamics (LTD), TU Kaiserslautern (2022).
- M. Christely: Reproducibility of Molecular Simulations. Diploma thesis, Laboratory of Engineering Thermodynamics (LTD), TU Kaiserslautern (2022).
- F. Lorig: Implementation of the friction theory in MicTherm. Student thesis, Laboratory of Engineering Thermodynamics (LTD), RPTU Kaiserslautern (2023).

- I. Javaid: Measurement of the Density of Polyalphaolefin Lubricants at High Pressures. Student thesis, Laboratory of Engineering Thermodynamics (LTD), RPTU Kaiserslautern (2023).
- F. Bartzack: Measurement of the Viscosity of Model Lubricants at High Pressure. Student thesis, Laboratory of Engineering Thermodynamics (LTD), RPTU Kaiserslautern (2023).
- S. Hofäcker: Application of Entropy Scaling for the Modeling of Transport Properties Using Molecular-based Equations of State. Master thesis, Laboratory of Engineering Thermodynamics (LTD), RPTU Kaiserslautern (2023).
- R. Loubet: Measurement and modeling of the density of fluids at high pressure. Master thesis, Laboratory of Engineering Thermodynamics (LTD), RPTU Kaiserslautern (2024).
- J. Noss: Measurement and modeling of the viscosity at high pressure. Master thesis, Laboratory of Engineering Thermodynamics (LTD), RPTU Kaiserslautern (2024).
- J. Hoffmann: Modeling Transport Properties with Methods from Molecular Thermodynamics. Master thesis, Laboratory of Engineering Thermodynamics (LTD). RPTU Kaiserslautern (2024).

# Curriculum Vitae

Name: Sebastian Schmitt  
Place of birth: Neunkirchen/Saar  
Nationality: German

## Education

2000 – 2004 Elementary School Furpach  
2004 – 2012 Gymnasium am Steinwald  
Degree: Allgemeine Hochschulreife  
2012 – 2017 Technische Universität Kaiserslautern  
Program: Maschinenbau  
Degree: Bachelor of Science  
2017 – 2019 Technische Universität Kaiserslautern  
Program: Computational Engineering  
Degree: Master of Science

## Professional

2019 – 2024 Research Associate at the Laboratory of Engineering  
Thermodynamics (LTD), RPTU Kaiserslautern  
Prof. Dr.-Ing. Hans Hasse